07:53:51 OCA PAD AMENDMENT - PROJECT HEADER INFORMATION 08/18/92

Active

Project #: E-20-686 Cost share #: E-20-318 Rev #: 1
Center # : 10/24-6-R7055-0A0 Center shr #: 10/22-1-F7055-0A0 OCA file #:
Work type : RES
Contract#: 14-08-0001-G1886 Mod #: 01 Document : GRANT
Prime #: Contract entity: GTRC

Subprojects ? : N CFDA:
Main project #: PE #:

Project unit: CIVIL ENGR Unit code: 02.010.116
Project director(s):
GEORGAKAKOS A P CIVIL ENGR (404)894-2240

Sponsor/division names: US DEPT OF INTERIOR / GEOLOGICAL SURVEY
Sponsor/division codes: 111 / 002

Award period: 900917 to 930630 (performance) 930930 (reports)

Sponsor amount	New this change	Total to date
Contract value	0.00	169,725.00
Funded	0.00	169,725.00
Cost sharing amount		185,230.00

Does subcontracting plan apply ?: N

Title: IMPACTS OF GLOBAL WARMING ON RESERVOIR SYSTEM MANAGEMENT

PROJECT ADMINISTRATION DATA

OCA contact: E. Faith Gleason 894-4820

Sponsor technical contact

MELVIN LEW
(703)648-6811

U.S. GEOLOGICAL SURVEY
WATER RESOURCES DIVISION--MS 424
12201 SUNRISE VALLEY DRIVE
RESTON, VA 22092

Sponsor issuing office

WILLIAM L. POLLOCK, MS 205C
(703)648-7383

U.S. GEOLOGICAL SURVEY
OFFICE OF PROCUREMENT AND CONTRACTS
12201 SUNRISE VALLEY DRIVE
RESTON, VA 22092

Security class (U,C,S,TS) : U ONR resident rep. is ACO (Y/N): N
Defense priority rating : NA supplemental sheet
Equipment title vests with: Sponsor GIT X

Administrative comments -
REVISION NO. 01 EXTENDS THE BUDGET AND PROJECT PERIODS TO JUNE 30, 1992

GEORGIA INSTITUTE OF TECHNOLOGY
OFFICE OF CONTRACT ADMINISTRATION

NOTICE OF PROJECT CLOSEOUT

Closeout Notice Date 01/26/94

Project No. E-20-686 Center No. 10/24-6-R7055-0A0

Project Director GEORGAKAKOS A P School/Lab CIVIL ENGR

Sponsor US DEPT OF INTERIOR/GEOLOGICAL SURVEY

Contract/Grant No. 14-08-0001-G1886 Contract Entity GTRC

Prime Contract No. _____

Title IMPACTS OF GLOBAL WARMING ON RESERVOIR SYSTEM MANAGEMENT

Effective Completion Date 930630 (Performance) 930930 (Reports)

Closeout Actions Required:	Y/N	Date Submitted
Final Invoice or Copy of Final Invoice	Y	931129
Final Report of Inventions and/or Subcontracts	Y	
Government Property Inventory & Related Certificate	N	
Classified Material Certificate	N	
Release and Assignment	N	
Other _____	N	

Comments _____

Subproject Under Main Project No. _____

Continues Project No. _____

Distribution Required:

Project Director	Y
Administrative Network Representative	Y
GTRI Accounting/Grants and Contracts	Y
Procurement/Supply Services	Y
Research Property Managment	Y
Research Security Services	N
Reports Coordinator (OCA)	Y
GTRC	Y
Project File	Y
Other CARL BAXTER-FMD	Y
_____	N

NOTE: Final Patent Questionnaire sent to PDPI.

E20-686
7

Selected Water Resources Abstracts
Input Transaction Form

3. Accession No.
W

4. Title
IMPACTS OF GLOBAL WARMING ON RESERVOIR SYSTEMS,

7. Author(s)
GEORGAKAKOS, A.P., GEORGAKAKOS, K.P.,

9. Organization
SCHOOL OF CIVIL ENGINEERING, GEORGIA INSTITUTE OF TECHNOLOGY

10. Project No.

11. Contract/Grant No.
14-08-0001-G1886

15. Supplementary Notes

USGS Water Resources Investigations Report, Vol I and II, Grant # 14-08-0001-G1886, August 1993, p. 345.

16. Abstract

Examined is the sensitivity of reservoir systems to changes in their climatic forcing. Coupled forecast-control procedures were developed to simulate operational flow forecasting and reservoir management decisions. These procedures involve large-scale opeational hydrologic/hydraulic models (i.e., the Modified Sacramento Model and the Un. of Iowa Forecast System), probabilistic schemes for extended flow forecasts based on conditional ensemble flow forecasting (i.e., the National Weather Service Extended Streamflow Prediction scheme), and a new reservoir control approach based on a set description of the various uncertainties.

The coupled forecast-control scheme was first applied to the operation of the Saylorville reservoir in the upper Des Moines river basin (midwest). Side-by-side simulation experiements with current operational practises showed that it improved reservoir operations, entirely avoiding floods and droughts. Second, the impacts of a potential climate change were examined using historical analogues of low, intermediate, and high streamflow periods. It was shown that reservoirs can be operated to mitigate the adverse effects of climatic change with the aid of effective forecast-control procedures. On the contrary, heuristic management practises could not readily adapt to changing hydrologic circumstances, causing frequent flooding and water shortages.

Results from three General Circulation Models (GCMs) were used to establilsh plausible scenarios for Lake Lanier in the Chattahoochee River Basin (southeast). Under a doubled atmospheric CO_2 scenario, inflow volumes would be reduced significantly, causing the lake to experience frequent and severe droughts. However, the use of effective streamflow forecasting and reservoir control procedures can ease these consequences.

17a. Descriptors

Climatology, Hydrometeorology, River Forecasting, Reservoirs, Operations & Management, Floods, Water Supply, Hydropower

17c. COWRR Field & Group

Climate Change 02C
Reservoir Mgt. 05G

18. Availability

BOFRS, USGS, BOX 25425
Denver CO. 80225

Send to:
Water Resources Scientific Information Center
GEOLOGICAL SURVEY, Mail Stop 425
U.S. DEPARTMENT OF THE INTERIOR
Reston, Va. 22092

Abstractors

Institution

NEW CONTROL CONCEPTS FOR UNCERTAIN WATER RESOURCES SYSTEMS: 1, THEORY

Aris P. Georgakakos and Huaming Yao

School of Civil Engineering, Georgia Institute of Technology, Atlanta

A major complicating factor in water resources systems management is handling unknown inputs. Stochastic optimization provides a sound mathematical framework but requires that enough data exist to develop statistical input representations. In cases where data records are insufficient (e.g., extreme events) or atypical of future input realizations, stochastic methods are inadequate. This article presents a control approach where input variables are only expected to belong in certain sets. The objective is to determine sets of admissible control actions guaranteeing that the system will remain within desirable bounds. The solution is based on Dynamic Programming and derived for the case where all sets are convex polyhedra. A companion paper addresses specific applications and problems in relation to reservoir system management.

1. INTRODUCTION

Many water resources systems can be represented by difference equations describing the evolution of a pivotal quantity, called state, in response to controllable and uncontrollable inputs:

$$S(k+1) = A(k)\,S(k) + B(k)\,u(k) + G(k)\,w(k), \quad k=0,1,...,N-1, \tag{1}$$

where $\mathbf{S}(k)$ is the n_s-dimensional state vector; $\mathbf{u}(k)$ is the n_u-dimensional control vector, $\mathbf{w}(k)$ is the n_w-dimensional input vector; and $\mathbf{A}(k)$, $\mathbf{B}(k)$, and $\mathbf{G}(k)$ are $(n_s \times n_s)$-, $(n_s \times n_u)$-, and $(n_s \times n_w)$-dimensional matrix coefficients respectively encoding the system layout and the interaction among its constituent elements. Examples include reservoir systems where state variables (states) represent reservoir storages, control variables (controls) represent releases or power generation hours, and input variables (inputs) represent reservoir inflows [*Loucks et al., 1980, Wasimi and Kitanidis, 1983, Trezos and Yeh, 1987, Georgakakos, 1989, and others*]; groundwater systems where states may represent hydraulic heads and/or pollutant concentrations, controls may represent pumping rates, and inputs may represent boundary conditions [see, among others, *Willis and Finney, 1985, Georgakakos and Vlatsa, 1991*]; and

wastewater treatment processes where states are organic and inorganic constituent concentrations, controls are recycling rates, and inputs are wastewater loading characteristics [*Harris, 1977, Kabouris and Georgakakos, 1990, and others*]. Typically, the state and control vectors are restricted within certain acceptable ranges,

$$\begin{aligned} S^{\min}(k) \le S(k) \le S^{\max}(k), \quad k=0,1,\ldots,N, \\ u^{\min}(k) \le u(k) \le u^{\max}(k), \quad k=0,1,\ldots,N-1, \end{aligned} \tag{2}$$

where the upper and lower bounds may represent physical capacities or operational requirements.

The purpose of a control scheme is to determine control vector sequences able to guide the system to meet its objectives over an operational horizon. The control process is seriously complicated, however, by the fact that future system inputs are typically unknown. The traditional approach is to develop probabilistic input descriptions and optimize system performance in some average sense. However, this may not always be possible or sound.

In many cases, existing data records are simply not long enough to establish probabilistic models, and we are forced to make assumptions which in the end cannot be corroborated. And even if sufficient data records exist, probabilistic input models and, consequently the associated control policies, become inadequate for extreme events where observations are sparse. In yet other circumstances, existing data records are atypical of future input realizations due to natural or anthropogenic causes (e.g., global climate changes). On such occasions, probabilistic input characterizations are inappropriate even in the average sense.

Lastly, stochastic control policies can at best guarantee that the system will not violate its bounds with certain probability. They cannot explicitly control the magnitude of the violation. During extreme input episodes, however, the operational goal becomes just that: Take permissible actions guaranteeing that system states stay within acceptable limits. Namely, during crises system operators are not at all concerned with optimizing system performance; they only wish to avoid actions that may endanger or damage the system.

To address the previous concerns, in this work we take a different tact. Rather than relying on probabilistic characterizations, we assume that future inputs are only restricted to belong in certain sets. The boundaries of these sets may represent minimum and maximum input estimates or other extreme levels, against which a sound operational policy is to be developed. In this framework, the purpose of the control process is to determine admissible controls such that system states remain within their acceptable limits as long as system inputs take on values from the specified input sets.

2. Dynamic Programming Solution

Glover and Schweppe [1971] and *Bertsekas and Rhodes [1971]* proposed a general solution for the previous problem using Dynamic Programming. The solution process is illustrated in Figure 1 and explained below:

In what follows, $\{\Omega_s(k), k=0,1,...,N\}$ denotes the sequence of acceptable state sets, $\{\Omega_u(k), k=0,1,...,N-1\}$ the sequence of admissible control sets, and $\{\Omega_w(k), k=0,1,...,N-1\}$ the input set sequence.

Define the modified state set $\Omega_m(N)$ as follows:

$$\Omega_m(N) = \{S \in R^n: [S + G(N-1)\, w(N-1)] \in \Omega_s(N),\ \forall\, w(N-1) \in \Omega_w(N-1)\}. \qquad (3)$$

Namely, $\Omega_m(N)$ contains all vectors **S** such that [S + G(N-1) w(N-1)] belongs to the state set $\Omega_s(N)$ for any input vector in $\Omega_w(N-1)$.

Define the reduced state set $\Omega_r(N-1)$ as follows:

$$\Omega_r(N-1) = \{S \in \Omega_s(N-1):\ \exists\, u(N-1) \in \Omega_u(N-1):\ [A(N-1)\, S + B(N-1)\, u(N-1)] \in \Omega_m(N)\}. \qquad (4)$$

Namely, $\Omega_r(N-1)$ includes all acceptable state vectors **S** for which there exists an admissible control vector **u**(N-1) such that [**A**(N-1) **S** + **B**(N-1) **u**(N-1)] belongs to the modified state set $\Omega_m(N)$. The significance of the previous sets is that if the system state S(N-1) reaches set $\Omega_r(N-1)$, there exists an admissible control vector that can transfer it to an acceptable terminal state S(N) for any input vector in $\Omega_w(N-1)$.

One can proceed similarly to define the modified and reduced state sets for the previous time:

$$\Omega_m(N-1) = \{S \in R^n: [S + G(N-2)\, w(N-2)] \in \Omega_r(N-1),\ \forall\, w(N-2) \in \Omega_w(N-2)\}, \qquad (5)$$

(Note that $\Omega_m(N-1)$ is defined based on $\Omega_r(N-1)$, not $\Omega_s(N-1)$.)

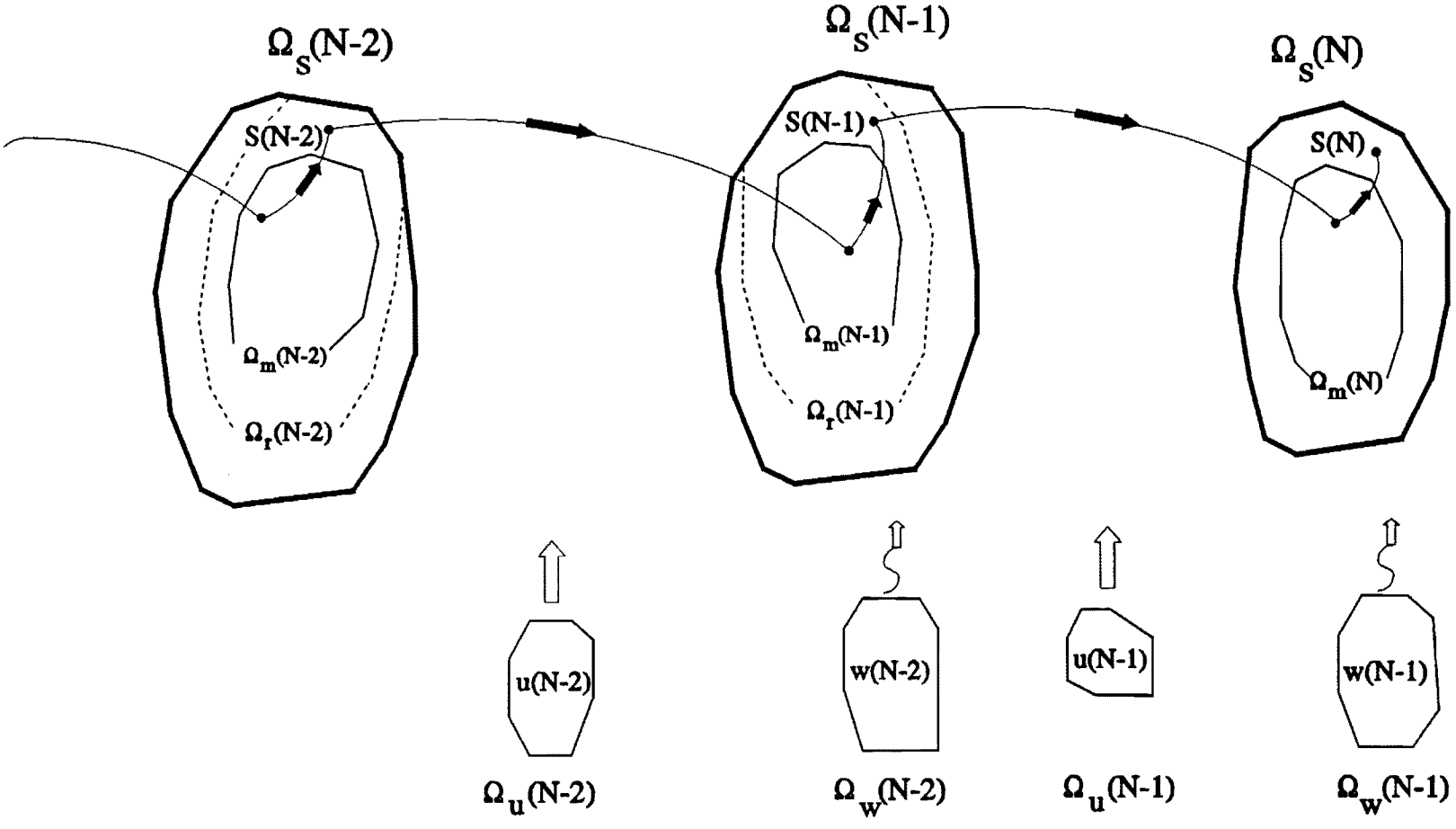

Figure 1: Dynamic Programming Solution of the Set Control Problem

$$\Omega_r(N\text{-}2) = \{S \in \Omega_s(N\text{-}2) : \exists\, u(N\text{-}2) \in \Omega_u(N\text{-}2) : \quad (6)$$
$$[A(N\text{-}2)\, S + B(N\text{-}2)\, u(N\text{-}2)] \in \Omega_m(N\text{-}1)\} .$$

Thus, if the system reaches set Ω_m(N-2), there exist control vectors **u**(N-2) and **u**(N-1) such that states S(N-1) and S(N) remain within the acceptable limits for any input realizations {**w**(N-2), **w**(N-1)} from the specified input sets.

The previous considerations can recursively be repeated in the reverse time direction, k = N-3, N-4, ... , 0. The problem has a feasible solution (i.e., there exist a control sequence able to keep the state vectors within their acceptable sets) if the sets thus derived are nonempty and the reduced state set $\Omega_r(0)$ includes the initial state vector S(0). Note, however, that the previous solution process does not determine which controls to use. Specific control vectors can be selected only as the system evolves and the state variable values become known. This and other related issues will further be discussed in a subsequent section.

As usual, Dynamic Programming led to a theoretically elegant solution. The practical implementation of this solution, however, presents an equally elegant challenge. *Glover and Schweppe [1971]* and *Bertsekas and Rhodes [1971]* proposed ellipsoidal approximation algorithms based on Schweppe's bounding ellipsoidal approximation theory [*Schweppe, 1973*]. The idea is to approximate all sets by bounding ellipsoids and develop recursive relationships for the computation of the modified and reduced state sets. Since ellipsoids are characterized by their center vector and principal axes, the set computation is reduced to a recursive computation of these attributes. However, the required approximations quickly result in empty modified and reduced state sets, and the algorithms falsely indicate infeasibility.

Another approach is to define state, control, and input sets as convex polyhedra and develop efficient procedures to compute the modified and reduced state sets. It turns out that the modified and reduced state sets are also convex polyhedra defined by their perpendicular vectors and support functions. This is the approach we adopt herein because it is exact and naturally suitable for water resources systems. Our work follows that of

Bertsekas and Rhodes [1971] (although most of the material was developed independently) but also contains several extensions and refinements.

3. Derivation of the Modified State Set $\Omega_m(k)$

The modified state set $\Omega_m(k)$, k=N, N-1, ..., 1, is defined by Equation (5). $\Omega_m(k)$ includes all state vectors **X** such that vectors [**X** + G(k-1)**w**(k-1)] belong to the reduced state set $\Omega_r(k)$ for any (or all) **w**(k-1) in $\Omega_w(k-1)$. Let $\Omega_r(k)$ be a convex polyhedron in the n_s-dimensional space $\mathbf{R}^{n_s}$ of the state vector elements S_1, S_2, ..., and S_{n_s}. (A polyhedron is a set bounded by hyperplanes. A hyperplane is a straight line in $\mathbf{R}^2$ and a two-dimensional plane in $\mathbf{R}^3$. A set Ω is convex if the line segment joining any two points in Ω also belongs in Ω.) Furthermore, let the reduced state set $\Omega_r(k)$ be known by its support function $\phi_r(\eta)$. (This information is available by the computations of the following section.) Namely, let $\Omega_r(k)$ be the following set (*Schweppe, 1973*)

$$\Omega_r(k) = \{S:\ S'\eta \le \phi_r(\eta),\ \textit{for all}\ \eta,\ \eta'\eta = 1\},$$
$$\text{where } \phi_r(\eta) = \underset{\text{all } S \in \Omega_r(k)}{\text{maximum}}\{S'\eta\}. \tag{7}$$

Figure 2 provides a graphical interpretation of the support function in two dimensions and demonstrates that a convex polyhedron can be completely defined by the support function values at only a finite number of vectors η: the vectors perpendicular to its bounding hyperplanes. Thus, we will assume that $\Omega_r(k)$ is defined as follows:

$$\Omega_r(k) = \{S:\ S'\eta_i \le \phi_r(\eta_i),\ i = 1,\ldots,n_r\}, \tag{8}$$

where n_r is the number of bounding hyperplanes. It is noted that the use of unit vectors is only a matter of convenience and, especially in the case of polyhedra, non-unit vectors will also serve our purpose as long as the support function $\phi()$ is defined accordingly.

By our earlier definitions, the reduced state set $\Omega_r(k)$, the modified state set $\Omega_m(k)$, and the input set $\Omega_w(k-1)$ are related as follows:

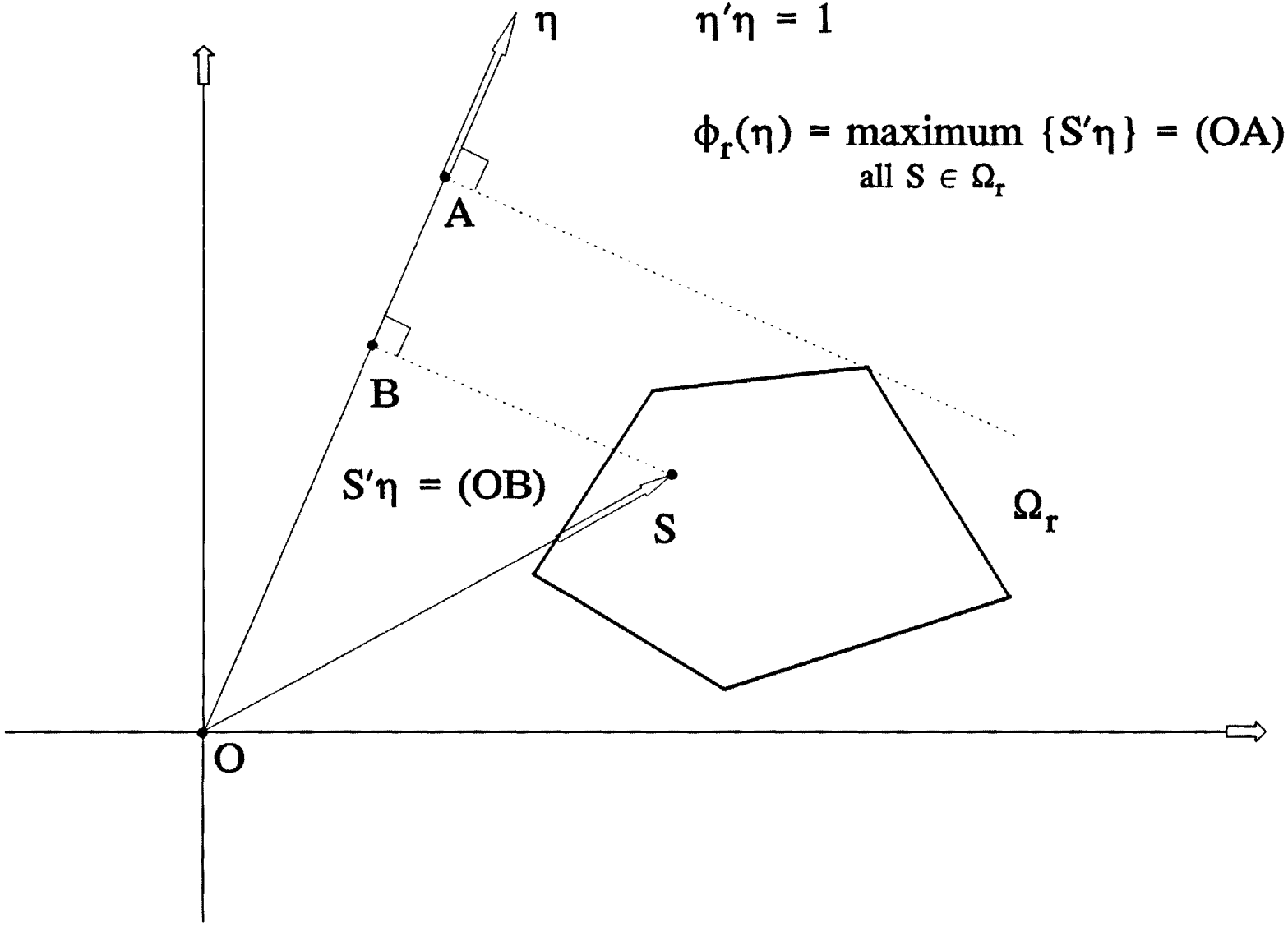

Figure 2: The Support Function of a Convex Polyhedron

$$\Omega_r(k) = \{S:\ S = X + G(k-1)w(k-1),\ \text{for any } X \in \Omega_m(k) \text{ and any } w(k-1) \in \Omega_w(k-1)\}\ . \quad (9)$$

The modified state set $\Omega_m(k)$ will be completely defined if its support function value can be computed for any vector η. Let $\phi_m()$ and $\phi_w()$ represent the support functions of the modified state and input sets respectively. Then,

$$\begin{aligned}
\phi_r(\eta) &= \underset{\substack{X \in \Omega_m(k) \\ w(k-1) \in \Omega_w(k-1)}}{\text{maximum}} [X + G(k-1)w(k-1)]'\eta \\
&= \underset{X \in \Omega_r(k)}{\text{maximum}} X'\eta + \underset{w(k-1) \in \Omega_w(k-1)}{\text{maximum}} w'(k-1)G'(k-1)\eta \qquad (10) \\
&= \phi_m(\eta) + \phi_w[G'(k-1)\eta], \\
&\text{all } \eta'\eta = 1\ ,
\end{aligned}$$

and therefore,

$$\phi_m(\eta) = \phi_r(\eta) - \phi_w[G'(k-1)\eta]\ , \text{ for all } \eta'\eta = 1\ . \qquad (11)$$

Although $\Omega_m(k)$ is now fully defined, it would be computationally more economical to restrict Equation (11) to vectors η perpendicular to its bounding hyperplanes. It turns out that the hyperplanes of $\Omega_m(k)$ are parallel to those of $\Omega_r(k)$, and consequently vectors $\{\eta_i,\ i=1,\ ...,\ n_r\}$ associated with Equation (8) are sufficient for the definition of $\phi_m()$ and $\Omega_m(k)$.

Figure 3 provides a graphical proof of this fact by deriving set $\Omega_m(k)$ from $\Omega_r(k)$ and $\Omega_{Gw}(k-1)$ in two dimensions. Points (vectors) A, B, C, D, and E are on the boundary hyperplanes of $\Omega_r(k)$. The dashed polygons originating from each point are obtained by subtracting the vectors defining the $\Omega_{Gw}(k-1)$ corner points. Set $\Omega_m(k)$ is the polygon circumscribed by the interior corner points of the dashed polygons, as A, B, C, D, and E trace the periphery of $\Omega_r(k)$. By construction, if a point (vector) belongs to $\Omega_m(k)$, adding any vector within $\Omega_{Gw}(k-1)$ generates points (vectors) inside $\Omega_r(k)$.

In summary, the modified state set $\Omega_m(k)$ can be determined as follows:

$$\Omega_m(k) = \{X:\ X'\eta_i \le \phi_m(\eta_i) = \phi_r(\eta_i) - \phi_w[G'(k-1)\eta_i],\ i = 1,...,n_r\}\ , \qquad (12)$$

where η_i, $i = 1,...,n_r$, are perpendicular to the bounding hyperplanes of $\Omega_r(k)$.

$\phi_w[G'(k-1)\eta_i)$ can be specified by solving the following Linear Programming (LP) problem:

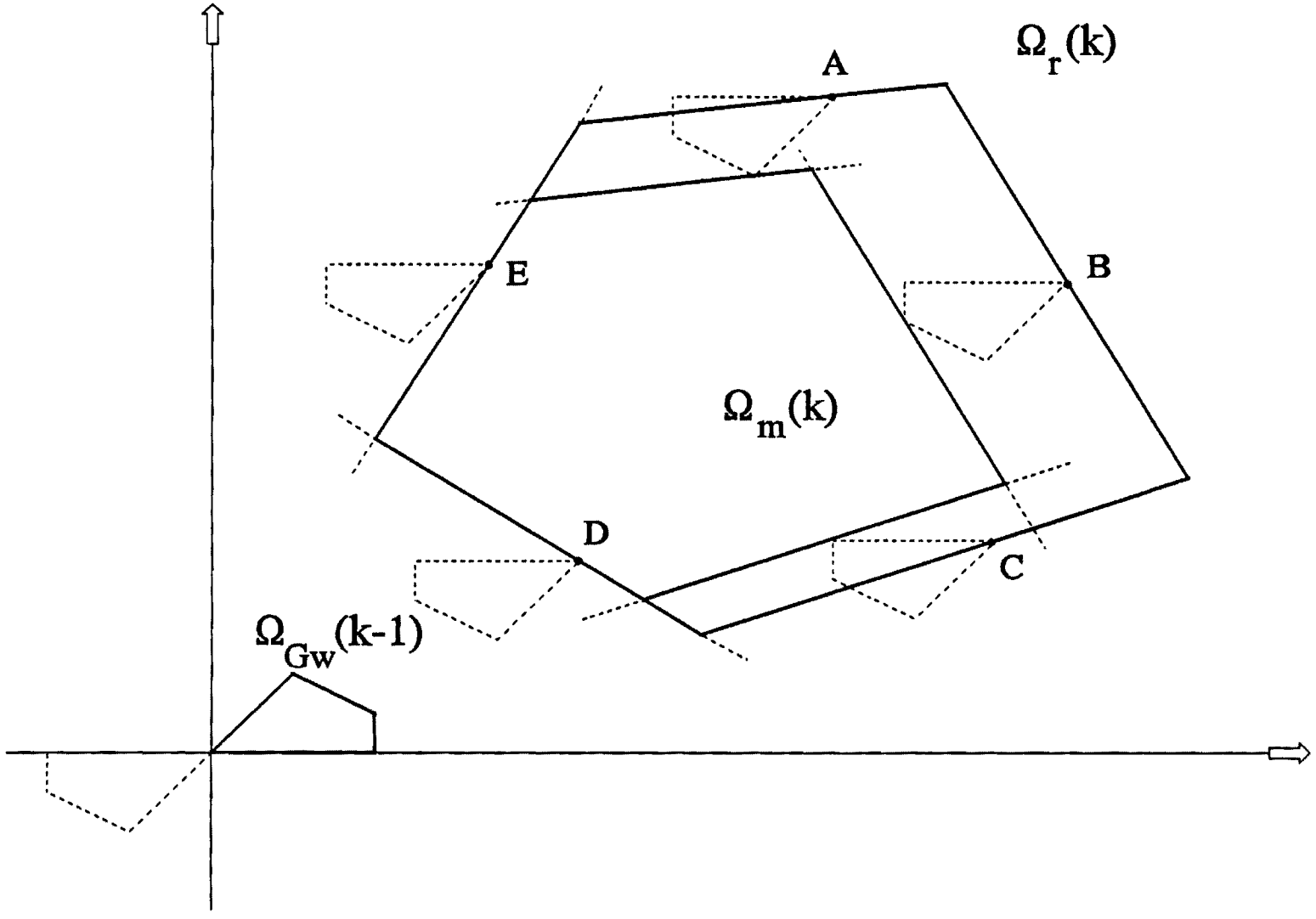

Figure 3: Derivation of $\Omega_m(k)$

$$\underset{\text{all } w}{\text{Maximize}}\ J = w'G'(k-1)\eta_i$$

$$\text{subject to} \tag{13}$$

$$w'e_j \le \phi_w(e_j),\ j = 1,\ldots,n_w,$$

where e_j, $j=1,\ldots,n_w$, represent unit vectors perpendicular to the bounding hyperplanes of $\Omega_w(k-1)$. $\phi_w[G'(k-1)\eta_i)$ is equal to the optimum value of J.

It is finally possible that set $\Omega_m(k)$ has fewer bounding hyperplanes than $\Omega_r(k)$. Namely depending on the shape of $\Omega_{Gw}(k-1)$, some hyperplanes may vanish. (One can easily envision this possibility with the aid of Figure 3.) It is generally desirable to discard unnecessary hyperplanes to reduce the computational overhead. To determine hyperplane redundancy, let $\zeta(\zeta_1, \zeta_2,\ldots, \zeta_{n_s})$ be any fixed unit vector and $X(X_1, X_2,\ldots, X_{n_s})$ be any vector in $\Omega_m(k)$. The projection of X on ζ is given by the inner product

$$J = X'\zeta = X_1\zeta_1 + X_2\zeta_2 + \cdots + X_{n_s}\zeta_{n_s}. \tag{14}$$

The vector X^* whose coordinates maximize (or minimize) J is a corner point of $\Omega_m(k)$. (For example, (OC′) in Figure 4 is the maximum projection length of all points in $\Omega_m(k)$.) Thus, a corner point can be found by solving the following LP problem: Find $X(X_1, X_2,\ldots, X_{n_s})$ which maximize/minimize J given by Equation (14) subject to inequalities (12). Furthermore, if any single inequality is replaced by a strict equality, the solution of this Linear Program will provide a corner point on the associated hyperplane. However, if the hyperplane is redundant, LP will indicate infeasibility. The corresponding inequality and hyperplane can then be discarded. This procedure should be repeated n_r times to test the redundancy of all hyperplanes. One can avoid multiple LP solutions by selecting a vector ζ which is not perpendicular to any hyperplane. To guarantee this fact, ζ should not be collinear with any vector η_i, $i=1,\ldots,n_r$.

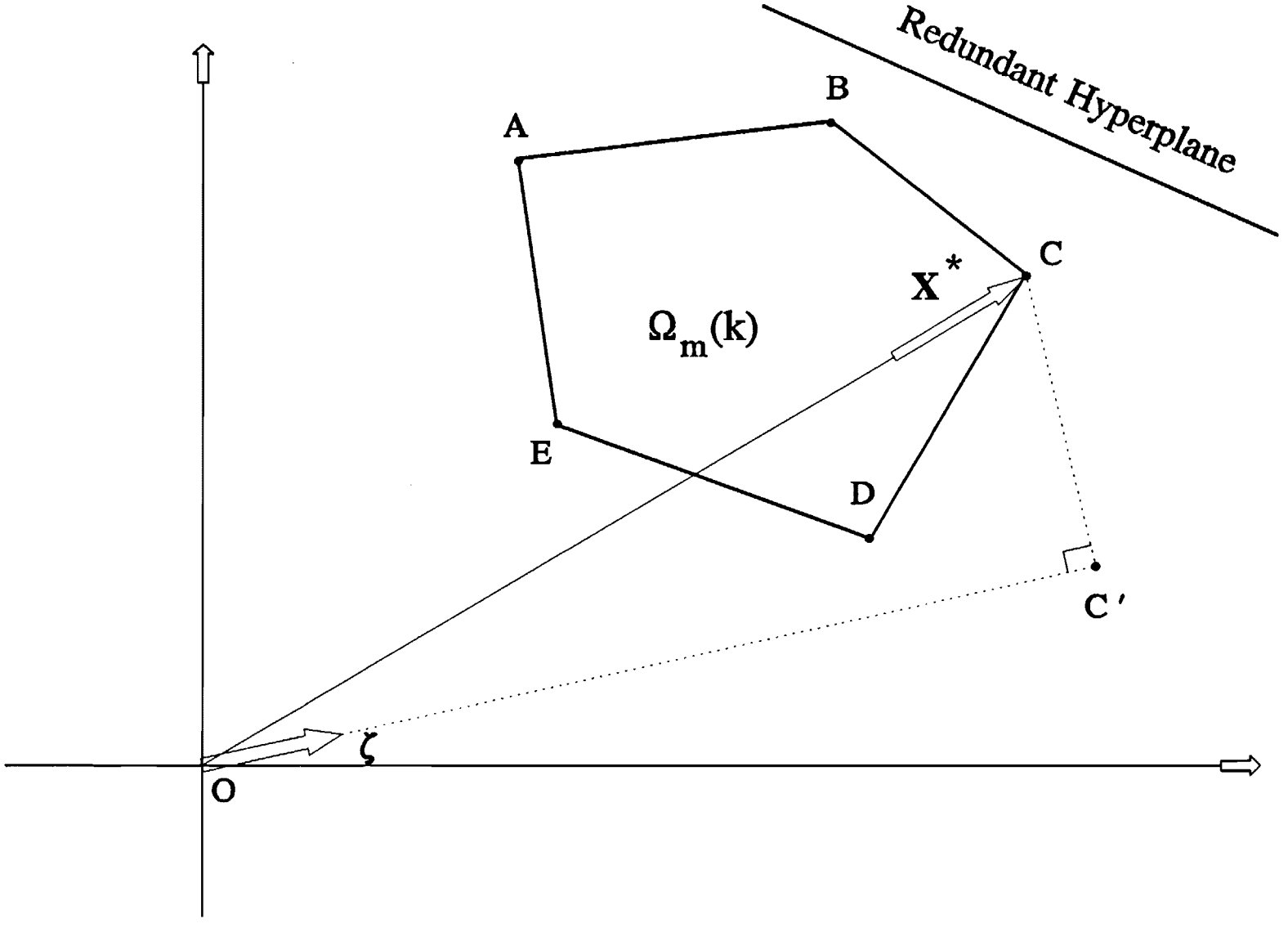

Figure 4: Determining the Corner Points of $\Omega_m(k)$

4. Derivation of the Reduced State Sets $\Omega_r(k)$

The reduced state set $\Omega_r(k)$, k=N-1, N-2, ..., 0, was defined as follows (cf. Equation (6)):

$$\Omega_r(k) = \{S \in \Omega_s(k) : \exists\, u(k) \in \Omega_u(k) : [A(k)\,S + B(k)\,u(k)] \in \Omega_m(k+1)\}\,. \tag{15}$$

The derivation of $\Omega_r(k)$ involves the following set operations: (1) Derivation of set $\Omega_{Bu}(k)$ including all vectors $\mathbf{B}(k)\mathbf{u}(k)$ such that $\mathbf{u}(k) \in \Omega_u(k)$; (2) Derivation of set $\Omega_{AS}(k)$ with all vectors $\mathbf{X}$ such that there exist vectors (at least one) in $\Omega_{Bu}(k)$ that transfer $[\mathbf{X} + \mathbf{B}(k)\mathbf{u}(k)]$ in $\Omega_m(k+1)$; (3) Derivation of set $\Omega_o(k)$ including all vectors $\mathbf{S}$ such that $\mathbf{A}(k)\mathbf{S} \in \Omega_{AS}(k)$; and (4) Derivation of $\Omega_r(k) = \Omega_o(k) \cap \Omega_S(k)$ (set intersection), where $\Omega_S(k)$ denotes the admissible state set (depicted in Figure 1).

For the first set operation, the problem is as follows: Given that $\Omega_u(k)$ is defined by

$$\Omega_u(k) = \{u:\ u'\eta_i \le \phi_u(\eta_i),\ i = 1,\ldots,n_u\}, \tag{16}$$

namely, by the values of its support function at the vectors perpendicular to its bounding hyperplanes, find the vectors perpendicular to the hyperplanes of $\Omega_{Bu}(k)$ and the associated support function values. The following result holds for the case where $\mathbf{B}(k)$ is an invertible matrix (see appendix for a proof):

$$\begin{gathered}\Omega_{Bu}(k) = \{X:\ X'\theta_i \le \phi_u(\eta_i),\ i = 1,\ldots,n_u\},\\ \text{where } \theta_i = (B'(k))^{-1}\,\eta_i,\ i = 1,\ldots,n_u.\end{gathered} \tag{17}$$

If there are more $\mathbf{B}(k)$ rows than columns (most usual case when $\mathbf{B}(k)$ is not invertible), one can still use the previous result by augmenting $\mathbf{B}(k)$ (and the state equations) to include columns corresponding to fictitious control variables with empty feasible ranges. This technique is further discussed and illustrated in the companion article. If the rank of $\mathbf{B}(k)$ is less than the dimension of its rows or columns, in all likelihood the state equations are ill-posed and some may be redundant.

The second set operation calls for the derivation of set $\Omega_{AS}(k)$ with all vectors $\mathbf{X}$ such

that there exist vectors in $\Omega_{Bu}(k)$ which transfer $[\mathbf{X} + \mathbf{B}(k)\mathbf{u}(k)]$ in $\Omega_m(k+1)$. The above is equivalent to finding a set $\Omega_{AS}(k)$ such that for all vectors $\mathbf{Z} \in \Omega_m(k+1)$ and $\mathbf{Y} \in \Omega_{Bu}(k)$, there holds $\mathbf{Z} - \mathbf{Y} = \mathbf{X} \in \Omega_{AS}(k)$. The equivalence of these two statements can be easily demonstrated by showing that the set $\Omega_{AS}(k)$ corresponding to the first is a subset of the set corresponding to the second and vice-versa. Thus, $\Omega_{AS}(k)$ is the vector sum of $\Omega_m(k+1)$ and $\Omega'_{Bu}(k)$, where $\Omega_{Bu}(k)$ is the set including all vectors $[-\mathbf{B}(k)\mathbf{u}(k)]$. As shown in the previous section (Equation 10), the support function of $\Omega_{AS}(k)$ can then be computed from the support functions of $\Omega_m(k+1)$ and $\Omega_{Bu}(k)$ as follows:

$$\begin{aligned}
\phi_{AS}(\eta) &= \underset{\substack{Z \in \Omega_m(k+1) \\ Y \in \Omega_{Bu}(k)}}{\text{maximum}} [Z - Y]'\eta \\
&= \underset{Z \in \Omega_m(k+1)}{\text{maximum}} Z'\eta - \underset{Y \Omega_{Bu}(k)}{\text{maximum}} Y'\eta \\
&= \phi_m(\eta) - \phi_{Bu}(\eta), \\
&\text{all } \eta'\eta = 1 .
\end{aligned} \tag{18}$$

The minimal set of vectors η where the support function has to be evaluated includes all vectors perpendicular to the hyperplanes of both $\Omega_m(k+1)$ and $\Omega_{Bu}(k)$. Thus, $\Omega_{AS}(k)$ is defined by

$$\begin{aligned}
\Omega_{AS}(k) = \{X:\ & X'\eta_i \le \phi_m(\eta_i) - \phi_{Bu}(\eta_i),\ i = 1,\ldots,n_m,\ \textit{and} \\
& X'\theta_j \le \phi_m(\theta_j) - \phi_{Bu}(\theta_j),\ j = 1,\ldots,n_u\} ,
\end{aligned} \tag{19}$$

where $\phi_m(\eta_i)$, $i = 1,\ldots,n_m$, are provided by the computations of the previous section (Equation 12 and discussion thereafter) and $\phi_{Bu}(\theta_j)$, $j = 1,\ldots,n_u$, are as specified in Equation (17) above.

Figure 5 illustrates how $\Omega_{AS}(k)$ is graphically constructed in two dimensions. Let ABCD represent set $\Omega_m(k+1)$. Hyperplanes A'D, DC, CB, and AB (solid lines) of $\Omega_{AS}(k)$ are respectively parallel to hyperplanes AD, DC, CB, and AB of $\Omega_m(k+1)$ and include points which can be transferred to $\Omega_m(k+1)$ only by one corner vector of $\Omega_{Bu}(k)$. The additional hyperplanes needed to define $\Omega_{AS}(k)$, namely, A'A, AA, CC, and BB, are parallel to those of $\Omega'_{Bu}(k)$ which is the set symmetric to $\Omega_{Bu}(k)$ about the origin. The

sets resulting by subtracting the corner point vectors of $\Omega_{Bu}(k)$ from each corner point of $\Omega_m(k+1)$ (dashed line polygons in Figure 5) are simply parallel translations of $\Omega'_{Bu}(k)$ as though each corner point of $\Omega_m(k+1)$ were the origin of the axes. Namely, $\Omega_{AS}(k)$ is the polyhedron circumscribed by the exterior corner points of $\Omega'_{Bu}(k)$ as it traces the periphery of $\Omega_m(k+1)$.

The third set operation calls for determining set $\Omega_o(k)$ from $\Omega_{AS}(k)$. By noting that $\mathbf{S} = \mathbf{A}^{-1}$ **(A S)** and applying the lema associated with Equation (17), set $\Omega_o(k)$ can be determined by

$$\Omega_o(k) = \{X:\ X'\rho_i \le \phi_{AS}(\rho_i),\ i = 1,\ldots,n_{AS}\},$$
$$\text{where } \rho_i = A'(k)\,e_i,\ i = 1,\ldots,n_{AS}, \tag{20}$$

and e_i, $i=1,\ldots,n_{AS}$, includes all vectors η_i, $i=1,\ldots,n_m$, and θ_j, $j=1,\ldots,n_u$, associated with Equation (19) ($n_{AS}=n_m+n_u$).

Finally, set $\Omega_r(k)$ can be derived as the intersection of $\Omega_o(k)$ and $\Omega_S(k)$. In mathematical form, this intersection is determined by

$$\Omega_r(k) = \{X: X'\eta_i \le \text{minimum}[\phi_S(\eta_i), \phi_o(\eta_i)],\ i = 1,\ldots,n_S, \textit{ and}$$
$$X'\rho_j \le \text{minimum}[\phi_S(\rho_j), \phi_o(\rho_j)],\ j = 1,\ldots,n_o\}, \tag{21}$$

where $\phi_S()$, η_i, $i=1,\ldots,n_S$, represent the support function and associated vector set for $\Omega_S(k)$, and $\phi_o()$, ρ_j, $j=1,\ldots,n_o$, represent the support function and associated vector set for $\Omega_o(k)$. The validity of the above statement is illustrated in Figure 6.

As with the modified state set, some of the hyperplanes associated with the reduced state set computed above may be redundant and should be discarded using the procedure outlined at the end of the previous section.

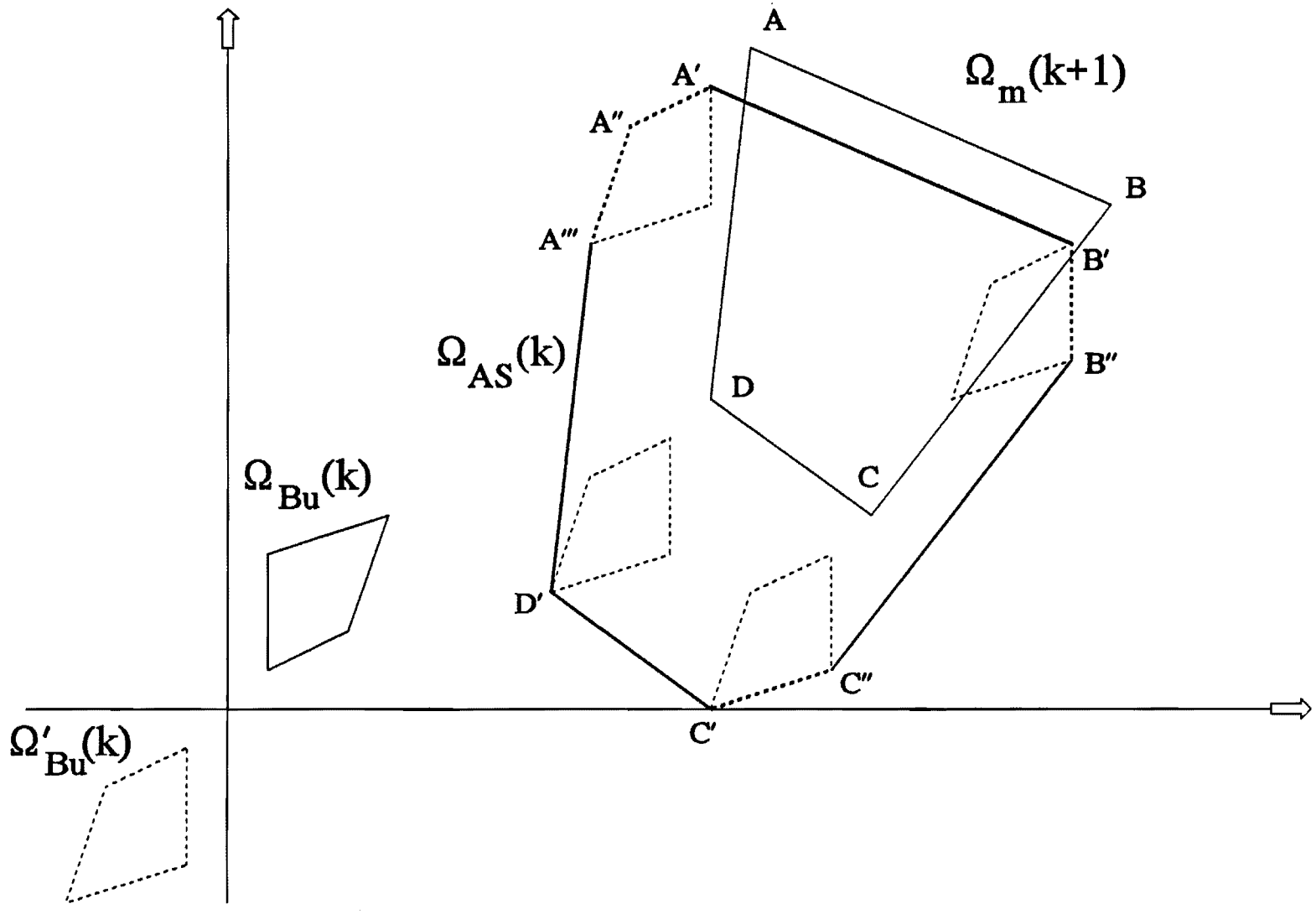

Figure 5: Derivation of $\Omega_{AS}(k)$

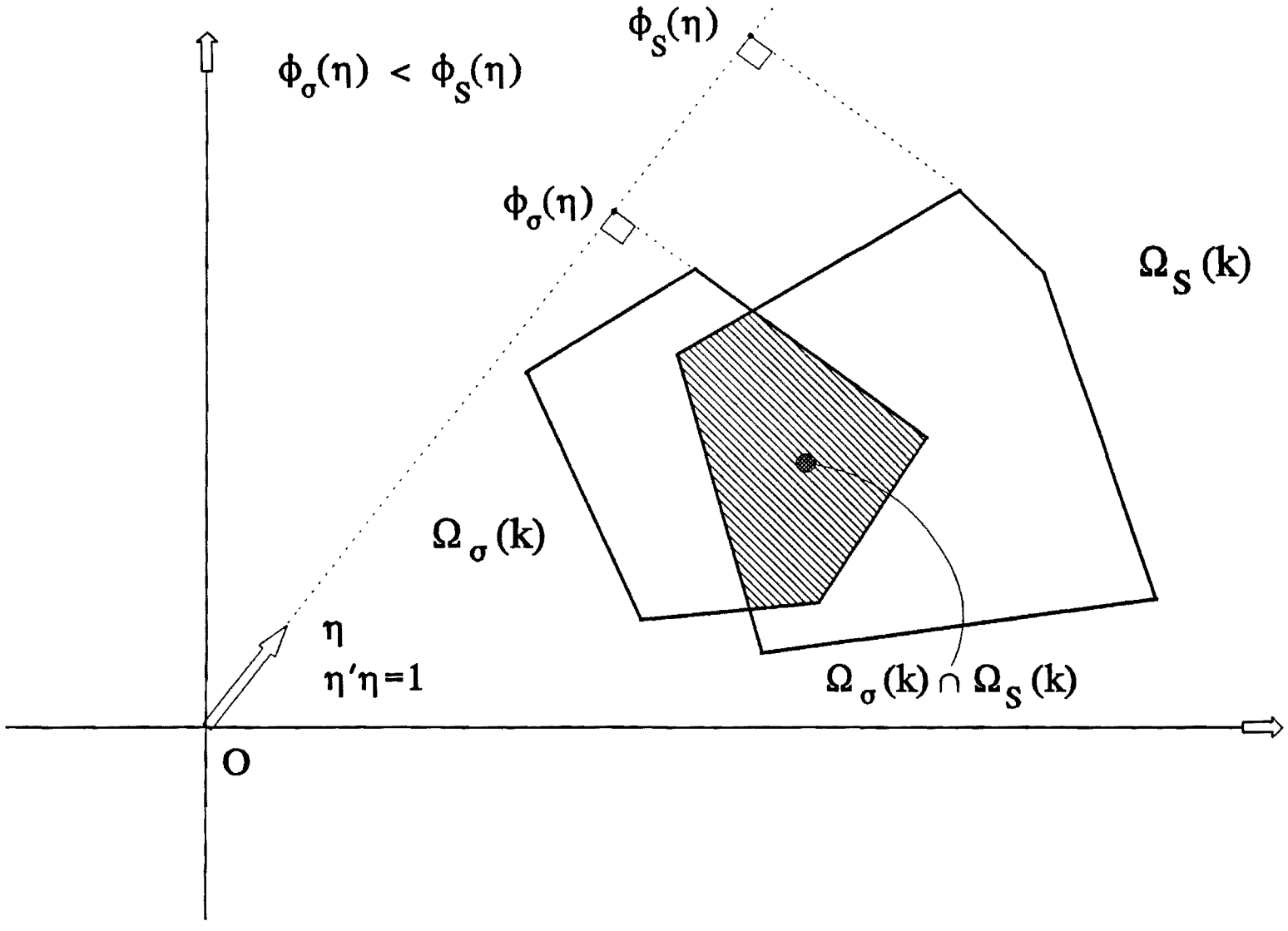

Figure 6: Set Intersection

5. REAL-TIME IMPLEMENTATION

The computation of the modified and reduced state sets can thus proceed from the terminal time N to the initial time 0. The problem has a solution (namely, there exists a feasible control sequence that guarantees that the state variables will remain within their admissible limits for any input realization within the specified input sets) if the reduced state set $\Omega_r(0)$ at time 0 is nonempty and includes the initial state vector S(0). The determination of these solutions has yet to be discussed.

Assuming that S(0) is known, the state equation describes the transition to state S(1) by

$$S(1) = A(0)\,S(0) + B(0)\,u(0) + G(0)\,w(0)\,. \tag{22}$$

The issue here is to determine an admissible control subset whose vectors guarantee that whatever the input w(0), the state S(1) will be within the reduced state set $\Omega_r(1)$. Equivalently, this subset should be such that vector $[\mathbf{A}(0)\mathbf{S}(0)+\mathbf{B}(0)\mathbf{u}(0)]$ always belongs in the modified state set $\Omega_m(1)$. The set $\Omega_{Bu}(0)$ that satisfies this requirement is obviously a parallel translation of $\Omega_m(1)$ by the vector A(0)S(0). More formally, $\Omega_{Bu}(0)$ can be defined by

$$\Omega_{Bu}(0) = \{X:\ X'\eta_i \le \phi_m(\eta_i) - S'(0)\,A'(0)\,\eta_i,\ i = 1,\ldots,n_m\}\,, \tag{23}$$

where $\phi_m()$, η_i, $i=1,\ldots,n_m$, represent the support function and associated vector set for $\Omega_m(1)$ already determined by the D.P. procedure.

The admissible control set $\Omega_c(0)$ can finally be obtained from the lema associated with Equation (17) and an intersection with $\Omega_u(0)$ (Equation 21). Any control vector in the set $\Omega_c(0)$ guarantees that (**a**) state S(1) will be feasible and (**b**) there will exist **u**(k), $k=1,2,\ldots,N-1$, vector sequences which will produce feasible states all through the control horizon. Subsequent sets $\Omega_c(k)$, $k=1,2,\ldots,N-1$, can be obtained by similar considerations as the system evolves and the state values S(k), $k=1,2,\ldots,N-1$, become known.

6. AN EXAMPLE AND A COMPARISON

To provide some computational insight for the theory presented earlier, we first solve a two-dimensional problem with four time steps. The state equation is as follows:

$$\begin{bmatrix} S_1(k+1) \\ S_2(k+1) \end{bmatrix} = \begin{bmatrix} 1 & 0 \\ 0 & 1 \end{bmatrix} \begin{bmatrix} S_1(k) \\ S_2(k) \end{bmatrix} + \begin{bmatrix} -1 & 0 \\ 1 & -1 \end{bmatrix} \begin{bmatrix} u_1(k) \\ u_2(k) \end{bmatrix} + \begin{bmatrix} 1 & 0 \\ 0 & 1 \end{bmatrix} \begin{bmatrix} w_1(k) \\ w_2(k) \end{bmatrix},$$
$$k = 0,1,2,3, \quad \begin{bmatrix} S_1(0) = 4 \\ S_2(0) = 4 \end{bmatrix}, \tag{24}$$

where the state, input, and control sets are shown below:

$$\Omega_S(k) = \left\{ \begin{matrix} 0 \le S_1(k) \le 10 \\ 0 \le S_2(k) \le 15 \end{matrix} \right\}, \; k = 0,1,2,3,4,$$
$$\Omega_w(k) = \left\{ \begin{matrix} 0 \le w_1(k) \le 3 \\ 0 \le w_2(k) \le 3 \end{matrix} \right\}, \; k = 0,1,2,3, \tag{25}$$
$$\Omega_u(k) = \left\{ \begin{matrix} 0 \le u_1(k) \le 2 \\ 0 \le u_2(k) \le 2 \end{matrix} \right\}, \; k = 0,1,2,3.$$

It is noted that the above formulation could represent a two-reservoir cascade. In hyperplane form, the constraints become

$$\begin{matrix} \Omega_S \end{matrix} \qquad \begin{matrix} \Omega_w \end{matrix} \qquad \begin{matrix} \Omega_u \end{matrix}$$
$$\begin{bmatrix} 1\,S_1(k) + 0\,S_2(k) \le 10 \\ (-1)\,S_1(k) + 0\,S_2(k) \le 0 \\ 0\,S_1(k) + 1\,S_2(k) \le 15 \\ 0\,S_1(k) + (-1)\,S_2(k) \le 0 \end{bmatrix}, \begin{bmatrix} 1\,w_1(k) + 0\,w_2(k) \le 3 \\ (-1)\,w_1(k) + 0\,w_2(k) \le 0 \\ 0\,w_1(k) + 1\,w_2(k) \le 3 \\ 0\,w_1(k) + (-1)\,w_2(k) \le 0 \end{bmatrix}, \begin{bmatrix} 1\,u_1(k) + 0\,u_2(k) \le 2 \\ (-1)\,u_1(k) + 0\,u_2(k) \le 0 \\ 0\,u_1(k) + 1\,u_2(k) \le 2 \\ 0\,u_1(k) + (-1)\,u_2(k) \le 0 \end{bmatrix}, \tag{26}$$

where the support function ($\phi(\eta)$) values are given by the right-hand side of the above inequalities, and the coordinates of the associated vectors (η) are the coefficients on the left-hand side. In this example, the constraint sets and matrices **A**, **B**, and **G** are time-invariant.

Set Ω_{Bu} is also time-invariant and can be obtained by the lema of Equation (17):

$$\Omega_{Bu} \begin{bmatrix} (-1)u_1(k) + 0u_2(k) \le 2 \\ 1u_1(k) + 0u_2(k) \le 0 \\ (-1)u_1(k) + (-1)u_2(k) \le 2 \\ 1u_1(k) + 1u_2(k) \le 0 \end{bmatrix}. \tag{27}$$

The computation of the modified and reduced state sets proceeds as explained earlier in this article. The derived sets are depicted in Figure 7 and their hyperplane forms are summarized in Table 1.

Due to limited control capability (compare input and control sets in Equation (25)), the modified and reduced state sets become smaller as the solution proceeds from the final to the initial time. Since $\Omega_r(0)$ contains the initial state vector, the problem has a feasible solution. The real-time control set that ensures feasibility is depicted in the last graph of Figure 7 (shaded region). Any control actions such that $\{0 \le u_1(0) \le 2$ and $1 \le u_2(0) \le 2\}$ place the state vector within the modified state set at the next time step and guarantee the existence of subsequent feasible decisions.

The second computational experiment aims at comparing the polyhedral control algorithm discussed earlier with an ellipsoidal approximation algorithm proposed by *Bertsekas and Rhodes [1971]*. The basis of this approach is to create ellipsoidal approximations of all sets and develop recursive relationships for the ellipsoid centers and principle axes. These relationships are similar to the Ricatti equations encountered in Linear Quadratic Gaussian control problems.

The system is again described by Equation (24) and the state, input, and control sets are as follows:

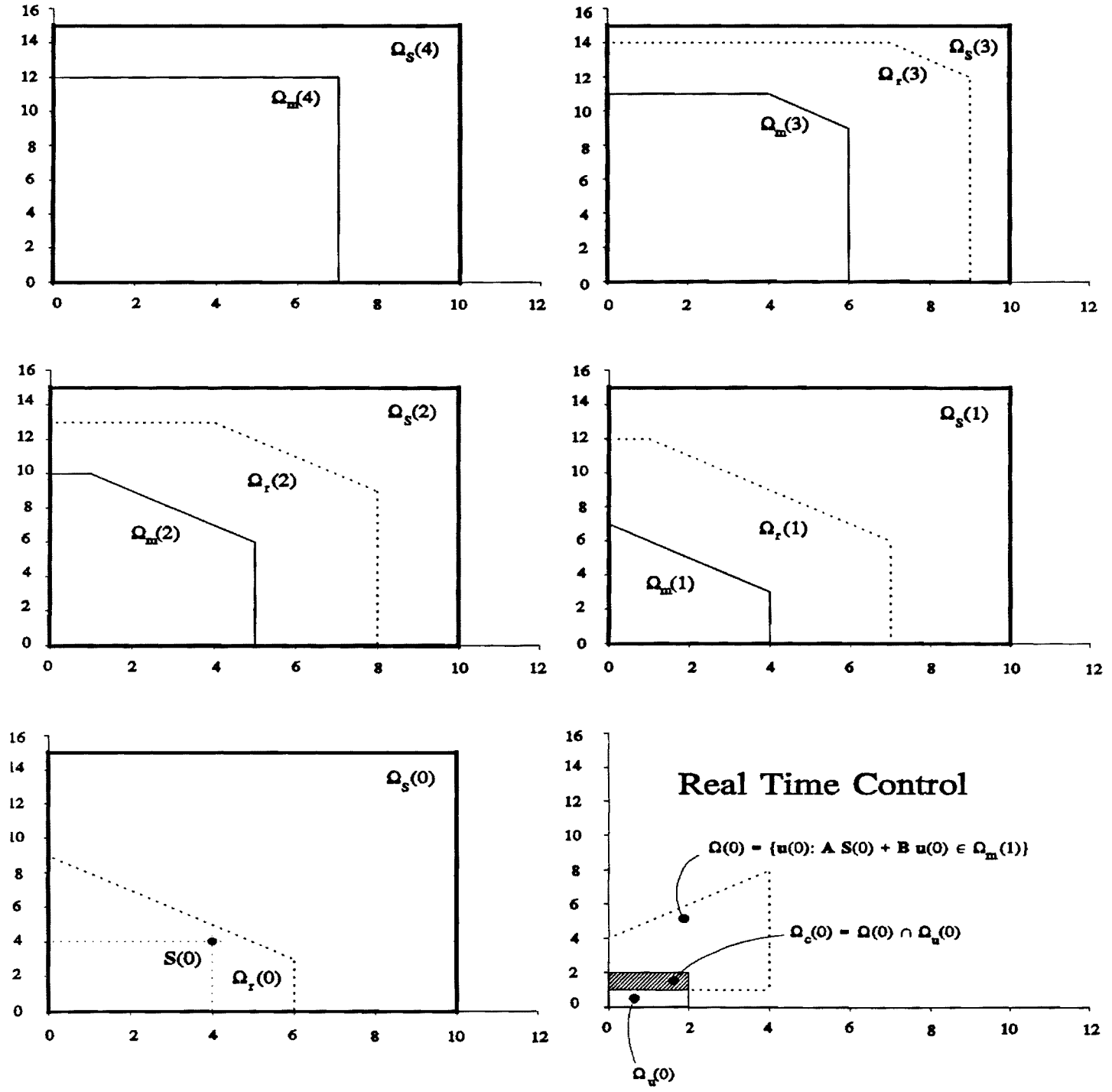

Figure 7: State and Control Sets for the Example

Table 1: Modified and Reduced State Sets for the Example

N	$\Omega_m(N)$	$\Omega_r(N)$
4	$1S_1 + 0S_2 \le 7$ $(-1)S_1 + 0S_2 \le 0$ $0S_1 + 1S_2 \le 12$ $0S_1 + (-1)S_2 \le 0$	
3	$1S_1 + 0S_2 \le 6$ $(-1)S_1 + 0S_2 \le 0$ $0S_1 + 1S_2 \le 11$ $0S_1 + (-1)S_2 \le 0$ $1S_1 + 1S_2 \le 15$	$1S_1 + 0S_2 \le 9$ $(-1)S_1 + 0S_2 \le 0$ $0S_1 + 1S_2 \le 14$ $0S_1 + (-1)S_2 \le 0$ $1S_1 + 1S_2 \le 21$
2	$1S_1 + 0S_2 \le 5$ $(-1)S_1 + 0S_2 \le 0$ $0S_1 + 1S_2 \le 10$ $0S_1 + (-1)S_2 \le 0$ $1S_1 + 1S_2 \le 11$	$1S_1 + 0S_2 \le 8$ $(-1)S_1 + 0S_2 \le 0$ $0S_1 + 1S_2 \le 13$ $0S_1 + (-1)S_2 \le 0$ $1S_1 + 1S_2 \le 17$
1	$1S_1 + 0S_2 \le 4$ $(-1)S_1 + 0S_2 \le 0$ $0S_1 + (-1)S_2 \le 0$ $1S_1 + 1S_2 \le 7$	$1S_1 + 0S_2 \le 7$ $(-1)S_1 + 0S_2 \le 0$ $0S_1 + 1S_2 \le 12$ $0S_1 + (-1)S_2 \le 0$ $1S_1 + 1S_2 \le 13$
0		$1S_1 + 0S_2 \le 6$ $(-1)S_1 + 0S_2 \le 0$ $0S_1 + (-1)S_2 \le 0$ $1S_1 + 1S_2 \le 9$

$$\Omega_S(k) = \left\{ \begin{matrix} -37.5 \le S_1(k) \le 37.5 \\ -31 \le S_2(k) \le 31 \end{matrix} \right\}, \; k = 0,1,\ldots,15,$$

$$\Omega_w(k) = \left\{ \begin{matrix} -10 \le w_1(k) \le 10 \\ -15 \le w_2(k) \le 15 \end{matrix} \right\}, \; k = 0,1,\ldots,14, \tag{36}$$

$$\Omega_u(k) = \left\{ \begin{matrix} -10 \le u_1(k) \le 10 \\ -22 \le u_2(k) \le 22 \end{matrix} \right\}, \; k = 0,1,\ldots,14.$$

For the ellipsoidal approximation algorithm, the state, input, and control sets are the smallest ellipses enveloping the previous rectangles.

Figure 8 portrays the resulting modified and reduced state sets for both set computation approaches at times 15, 14, 13, 12, 1, and 0. Until time 12, both approaches produce feasible results, although the polyhedral modified and reduced sets are significantly larger. At time 11, the ellipsoidal algorithm terminates indicating infeasibility, while the polyhedral approach remains feasible until time 0. This experiment shows that the required ellipsoidal approximations underestimate the feasible regions and cause early algorithm termination.

6. CONCLUSION

Uncertain water resources systems are disturbed by inputs for which we frequently have limited information. Rather than using statistical input descriptions, herein we introduce an alternative approach based on set characterization of uncertainty. The resulting control problem calls for finding the set of admissible actions that ensures that the system stays within its bounds for the duration of the operational horizon. The solution is derived using Dynamic Programming and is implemented for the case where all sets are convex polyhedra.

The set control approach is motivated by the need to guide the operation of water resources systems under extreme or relatively unknown input circumstances. More specific applications in relation to reservoir systems are discussed in the companion paper.

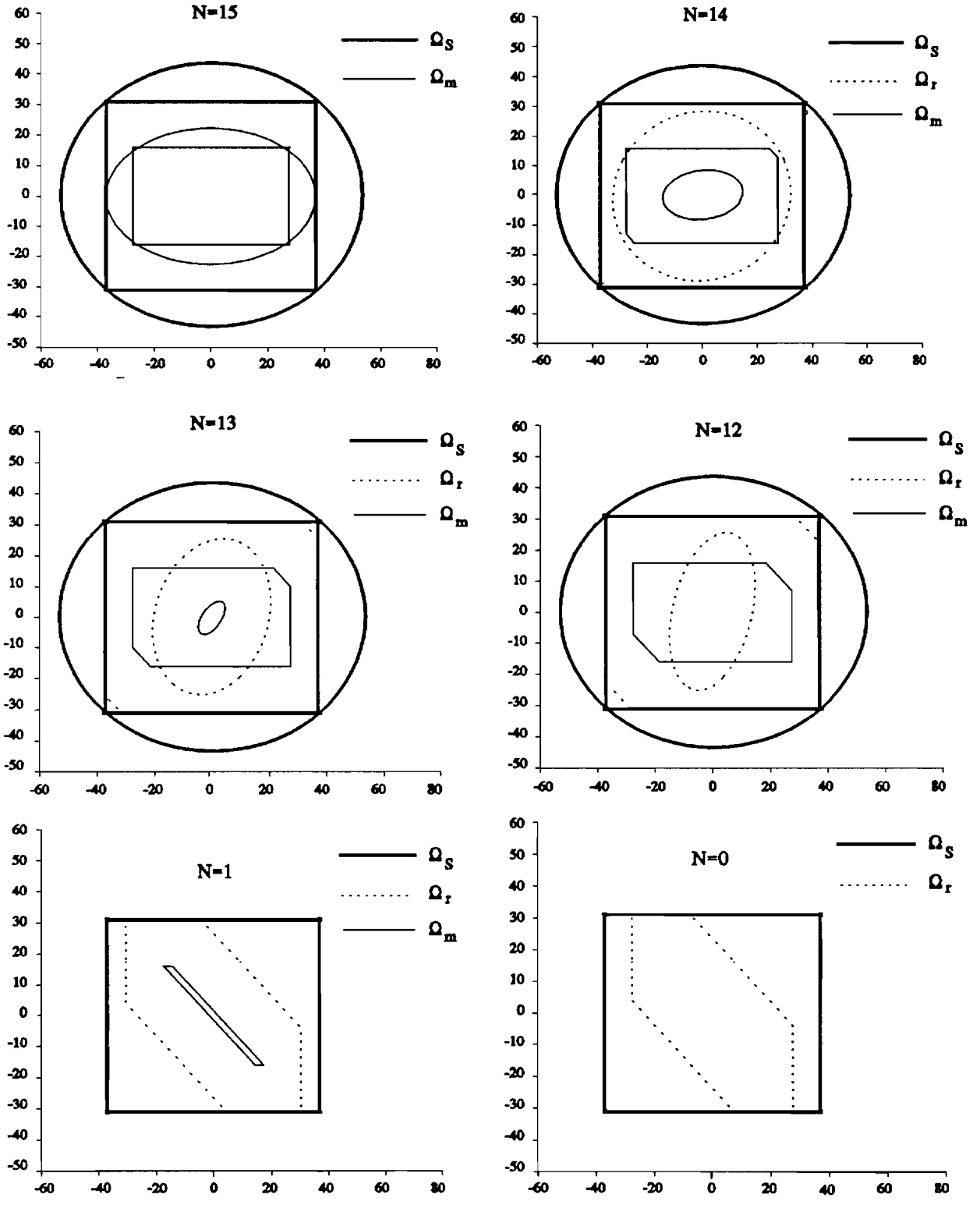

Figure 8: A Comparison of Polyhedral and Ellipsoidal Set Algorithms

ACKNOWLEDGEMENT

This work was partially funded by the U.S. Geological Survey under Research Contract No. 14-08-0001-G1886.

REFERENCES

Bertsekas, D.P. and I.B. Rhodes, On the minimax reachability of target sets and target tubes, *Automatica*, Vol. 7, 233-247, 1971.

Georgakakos, A.P., Extended Linear Quadratic Gaussian (ELQG) control: Further extensions, *Water Resources Research*, 25(2), 191-201, 1989.

Georgakakos, A.P., and D.A. Vlatsa, Stochastic control of groundwater systems, *Water Resources Research*, 27(8), 2077-2090, 1991.

Glover, J.D., and F.C. Schweppe, Control of linear dynamic systems with set-constrained disturbances, IEEE Transactions of Automatic Control, 16(5), 411-423, 1971.

Grygier, J.C., and J.R. Stedinger, Algorithms for optimizing hydropower system operation, *Water Resources Research*, 21(1), 1-10, 1985.

Harris, C.J., Modelling and adaptive control of urban wastewater treatment plants, in *Environmental Systems Planning, Design, and Control*, Proceedings IFAC Symposium, Kyoto, Japan, 1977.

Kabouris , J.C., and A.P. Georgakakos, Optimal control of the activated sludge process, *Water Research*, 24(10), 1197-1208, 1990.

Loucks, D.P., J. R. Stedinger, and D. A. Haith, *Water resource systems planning and analysis*, Prentice Hall, 1981.

Schweppe, F.C., *Uncertain Dynamic Systems*, Prentice Hall, 1973.

Trezos, T., and W.W-G. Yeh, Use of stochastic dynamic programming for reservoir management, *Water Resources Research*, 23(6), 983-996, 1987.

Wasimi, S.A., and P.K. Kitanidis, Real-time forecast and daily operation of a multireservoir system during floods by Linear Quadratic Gaussian Control, *Water Resources Research*, 19(6), 1511-1522, 1983.

Willis, R., and B.A. Finney, Optimal control of nonlinear groundwater hydraulics: Theoretical development and numerical experiments, *Water Resources Research*, 21(10), 1476-1482, 1985.

APPENDIX

Lema: Let Ω_x be a set characterized by

$$\Omega_x = \{X:\ X'\eta_i \le \phi_x(\eta_i),\ i = 1,\ldots,n_x\} \tag{37}$$

and **B** an invertible matrix. Then, the set Ω_y of all vectors **Y** such that **Y = B X** is defined by

$$\begin{gathered}\Omega_y = \{Y:\ Y'\theta_i \le \phi_x(\eta_i),\ i = 1,\ldots,n_x\},\\ \text{where } \theta_i = (B')^{-1}\eta_i,\ i = 1,\ldots,n_x.\end{gathered} \tag{38}$$

Proof: Let (ABCDE) and (abcde) (Figure 9) represent sets Ω_x and Ω_y respectively, and let vectors η_i and θ_i be perpendicular to hyperplanes AB and ab. To establish a relationship between η_i and θ_i, we start from the implications of orthogonality between these vectors and any other vector on the corresponding hyperplanes:

$$\begin{gathered}(\overline{ab})'\theta_i = 0 = (\overline{Ob} - \overline{Oa})'\theta_i = [B(\overline{OB}) - B(\overline{OA})]'\theta_i = (\overline{AB})'B'\theta_i\\ \textit{and}\\ (\overline{AB})'\eta_i = 0.\end{gathered} \tag{39}$$

The above relationships suggest that vectors η_i and $\mathbf{B}'\theta_i$ are collinear (parallel) and consequently, a set of θ_i vectors perpendicular to the hyperplanes of Ω_y can be obtained from

$$B'\theta_i = \eta_i \rightarrow \theta_i = (B')^{-1}\eta_i. \tag{40}$$

To fully characterize Ω_y, we additionally need the support function values $\phi_m(\theta_i)$, θ_i, $i=1,\ldots,n_x$. Using the definition and the previous result, we obtain

$$\begin{aligned}\phi_y(\theta_i) &= \underset{Y\in\Omega_y}{maximum}\ Y'\theta_i = \underset{X\in\Omega_x}{maximum}\ X'B'\theta_i\\ &= \underset{X\in\Omega_x}{maximum}\ X'B'(B')^{-1}\eta_i = \underset{X\in\Omega_x}{maximum}\ X'\eta_i\\ &= \phi_x(\eta_i).\end{aligned} \tag{41}$$

It is noted that even though η_i may be unit vectors, vectors θ_i may not have unit length. However, one can easily normalize them and scale the support function values accordingly:

$$e_i = \theta_i / |\theta_i|$$

$$\phi_y(e_i) = \phi_y(\theta_i) / |\theta_i|, \tag{42}$$

where $|\cdot|$ represents vector norm.

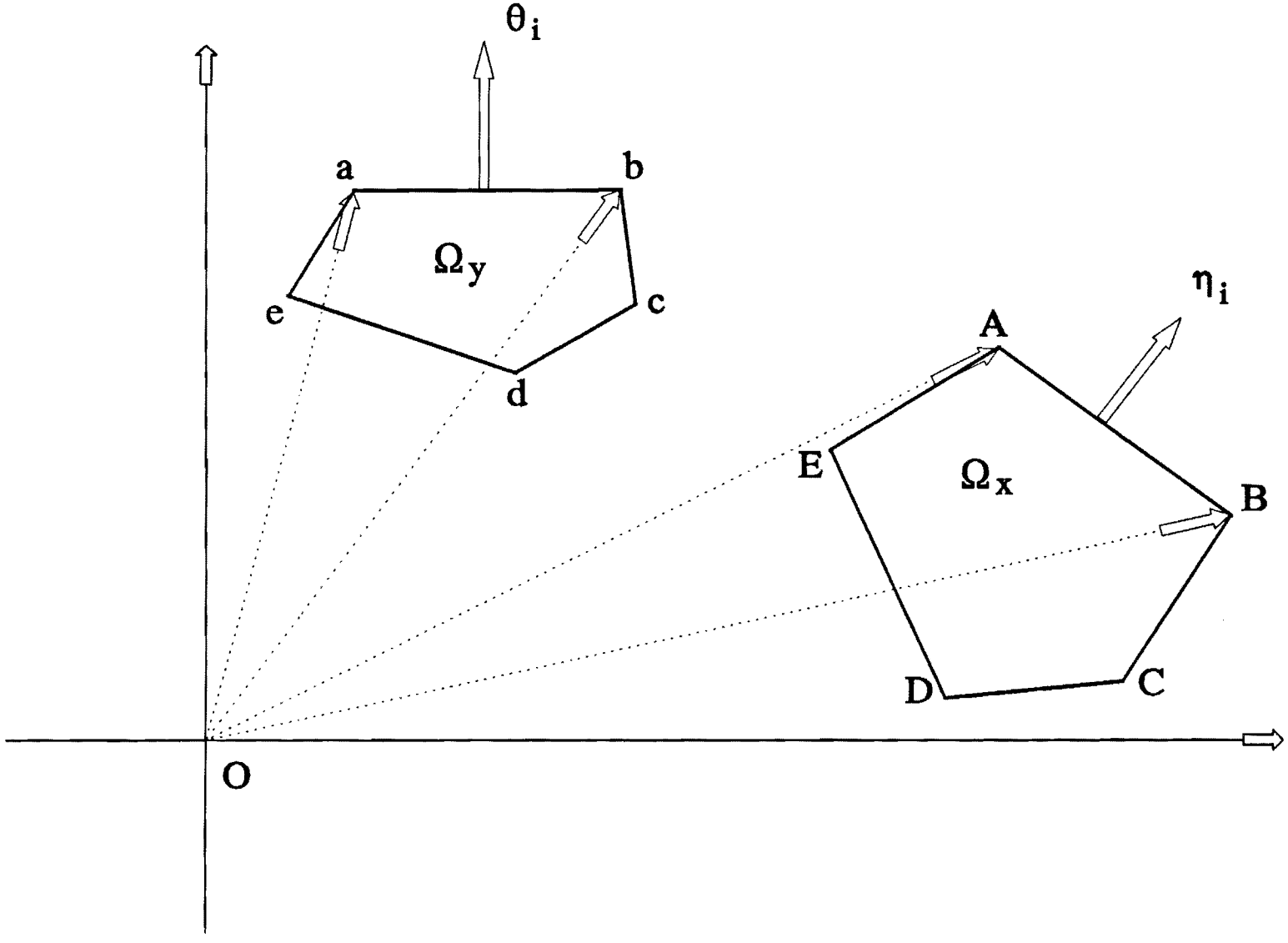

Figure 9: Linear Set Transformations

NEW CONTROL CONCEPTS FOR UNCERTAIN WATER RESOURCES SYSTEMS: 2, RESERVOIR MANAGEMENT

Huaming Yao and Aris P. Georgakakos

School of Civil Engineering, Georgia Institute of Technology, Atlanta

Reservoir management decisions continuously strive to balance conflicting risks and benefits. Hydrologic uncertainty is a major complicating factor, especially during extreme events when data are sparse and probabilistic characterizations are less reliable. The set control approach offers an alternative by assuming that inputs are unknown but bounded. The solution provides a set of control actions which guarantee that the system will operate within the stated constraints for a certain time horizon. The method is applied to a three-reservoir system in the southeastern U.S.

1. INTRODUCTION

The need to handle uncertainty in reservoir management is widely recognized by practicing and research professionals and continues to motivate new management approaches [*Foufoula-Georgiou and Kitanidis, 1988, Kelman et al., 1990, Georgakakos, 1989, 1992*]. The common theme is to rely on probability theory to model random quantities and then develop suitable optimization schemes to control the probability distribution of storage, release, energy generation, and other key system variables. The basic suppositions are (**a**) that enough data are available to validate the descriptions of the uncertain elements and (**b**) that the system operator has the ability to balance abstract concepts such as risks of not meeting certain objectives or expected output levels among themselves and over time.

Data availability undermines stochastic methods when they are most valuable: during hydrologic extremes. Data deficiencies for extreme floods and droughts usually weaken model predictions and limit management options. What is more, potentially new climatic regimes may totally invalidate existing observation records.

Amidst crises situations, system operators are also faced with nontrivial challenges. At the onset of droughts, they must decide whether to reduce outflow or continue with their normal release schedules. In retrospect, one option is better than the other, but at the time when the decision is made each option involves risks. Anticipating floods, reservoir operators should evacuate enough storage to avoid damage-causing outflows and energy-

wasting spillage. Over- or under-estimating this storage again involves risks. Risks are associated with almost every decision in reservoir operations, but it is unclear how reservoir operators should try to appreciate and balance them. Stochastic management methods are useful, but they can only control the probability of extreme events and not their magnitude [*Georgakakos, 1989*]. And, as already mentioned, probability estimates can only be as good as the available data.

As an alternative, in this work we develop operational choices that are easier to understand and offer some guarantees. Using the set control approach, we derive sets of control actions guaranteeing that the system will meet its constraints (satisfy water supplies, maintain outflow below damaging levels, or cover a dependable energy commitment). The guarantees are valid for a certain length of time and for all inflow sequences bounded by specific ranges. The inflow bounds are selected by the operator and should reflect extreme hydrologic circumstances against which the system is to be controlled. This selection affects the size of the admissible control sets and the length of the operational horizon during which the system can fully meet the stated constraints. Bounds associated with more extreme hydrologies result in shorter guaranteed operational horizons and smaller admissible control sets. Although this judgement involves risks, it is also more meaningful and reassuring, especially during crises. The operators can select any control action within the specified sets and be confident that the system will not violate the stated constraints at least for the duration of the operational horizon.

This article examines this approach as it applies to flood and drought management and hydropower operations. Some potential applications for reservoir design and operational policy determination are also briefly discussed.

2. FLOOD AND DROUGHT MANAGEMENT / RESERVOIR DESIGN

The following discussion, although general, will make reference to a three-reservoir cascade as an example and test case study. This system is located on the Savannah River in the southeastern U.S. and is described in *Georgakakos* [*1989, 1992*]. For the purposes of this section (namely, to investigate issues exclusive of hydropower), the system is modelled by the following water balance state equation:

$$\begin{bmatrix} S_1(k+1) \\ S_2(k+1) \\ S_3(k+1) \end{bmatrix} = \begin{bmatrix} 1 & 0 & 0 \\ 0 & 1 & 0 \\ 0 & 0 & 1 \end{bmatrix} \begin{bmatrix} S_1(k) \\ S_2(k) \\ S_3(k) \end{bmatrix} + \begin{bmatrix} -1 & 0 & 0 \\ 1 & -1 & 0 \\ 0 & 1 & -1 \end{bmatrix} \begin{bmatrix} u_1(k) \\ u_2(k) \\ u_3(k) \end{bmatrix} + \begin{bmatrix} 1 & 0 & 0 \\ 0 & 1 & 0 \\ 0 & 0 & 1 \end{bmatrix} \begin{bmatrix} w_1(k) \\ w_2(k) \\ w_3(k) \end{bmatrix}, \qquad (1)$$

$$k = 0,1,\ldots,N-1,$$

where $S_i(k)$, $u_i(k)$, and $w_i(k)$ respectively represent storage, release, and inflow volumes for reservoir $i=1,2,3$. Table 1 reports permissible storage and release ranges reflecting water conservation and flood control objectives, and Figure 1 depicts the weekly inflow ranges. These ranges were obtained, somewhat arbitrarily, using the third lowest and third highest inflow values on record (63 years).

The first question is whether the system can control inflows without violating the stated constraints, namely, without effecting water shortages ($u_3(k) < 2.2$ bcf/week) or damage-causing outflows ($u_3(k) > 18$ bcf/week). The answer is far from obvious since system inflow ($w_1(k)+w_2(k)+w_3(k)$) saturates the admissible range of $u_3(k)$ for more than one third of the year (rainy season).

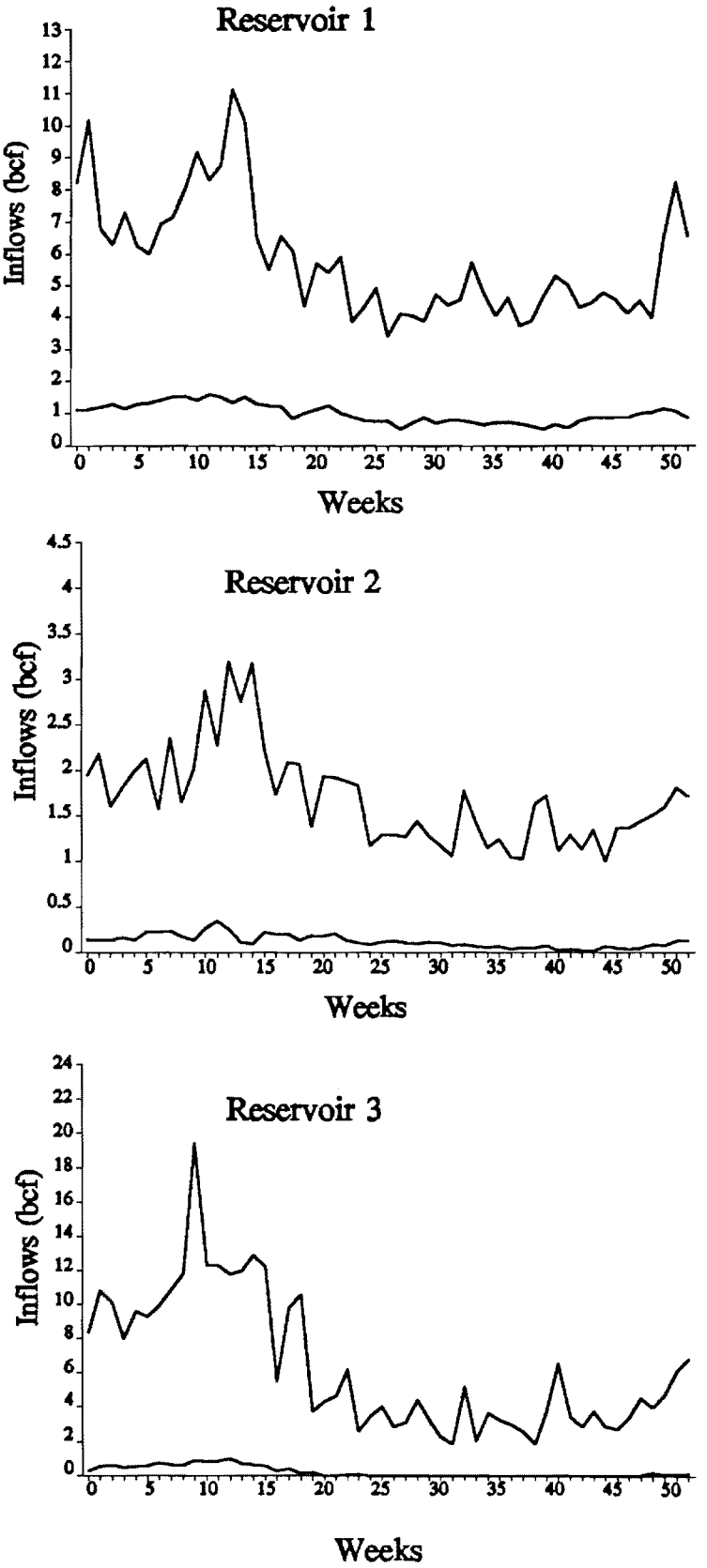

Figure 1: Reservoir Inflow Ranges

Table 1: Reservoir Storage and Release Constraints

	Minimum	Maximum
Reservoir 1		
Storage (bcf)	79.25	123.8
Release (bcf / week)	0.0	18.0
Reservoir 2		
Storage (bcf)	34.2	50.8
Release (bcf/week)	0.0	18.0
Reservoir 3		
Storage (bcf)	69.71	125.95
Release (bcf/week)	2.2	18.0

To provide a partial answer to this question, we run the set control algorithm (*Georgakakos and Yao, companion article*) with a time horizon of 52 weeks. The algorithm terminates successfully and generates the following reduced state set at time zero:

$$\Omega_r(0) = \left\{ \begin{array}{r} (-0.7071)S_1 + (-0.7071)S_2 + 0S_3 \le -80.2213 \\ 0.5774S_1 + 0.5774S_2 + 0.5774S_3 \le 140.4670 \\ -0.5774)S_1 + (-0.5774)S_2 + (-0.5774)S_3 \le -129.8806 \\ 1S_1 + 0S_2 + 0S_3 \le 123.8 \\ (-1)S_1 + 0S_2 + 0S_3 \le -79.25 \\ 0S_1 + 1S_2 + 0S_3 \le 50.8 \\ 0S_1 + (-1)S_2 + 0S_3 \le -34.2 \\ 0S_1 + 0S_2 + 1S_3 \le 125.93 \\ 0S_1 + 0S_2 + (-1)S_3 \le -69.71 \end{array} \right\}. \qquad (2)$$

If this set contains the initial storage values, there exist feasible release sequences that maintain all reservoir storages within their acceptable limits independently of what inflows materialize, provided that they are within the specified bounds. The set of admissible

control actions that guarantee feasibility is also determined for initial storage values $S_1(0)=100$, $S_2(0)=45$, and $S_3(0)=95$ bcf:

$$\Omega_c(0) = \left\{ \begin{array}{r} 0.7071u_1 + (-0.7071)u_2 + 0u_3 \le 2.7209 \\ (-0.7071)u_1 + 0.7071u_2 + 0u_3 \le 7.7442 \\ 1u_1 + 0u_2 + 0u_3 \le 18.0 \\ (-1)u_1 + 0u_2 + 0u_3 \le 0.0 \\ 0u_1 + 1u_2 + 0u_3 \le 18.0 \\ 0u_1 + (-1)u_2 + 0u_3 \le 0.0 \\ 0u_1 + 0u_2 + 1u_3 \le 17.2403 \\ 0u_1 + 0u_2 + (-1)u_3 \le -14.7040 \end{array} \right\}. \quad (3)$$

To test the validity of the results, we run simulation experiments. Each simulation begins with the generation of a 52-week, random inflow sequence for each system reservoir. These sequences can be determined in several ways. One approach is to generate inflow values uniformly (equally likely) within each weekly range. The result would be a totally random sequence, but one with very little probability of being consistently high or low (as in wet and dry years). Furthermore, the yearly volume of such sequences usually has a much wider range than actually observed. To avoid these inconsistencies, the inflow sequences were constructed as follows: The yearly inflow ranges for the entire system and each reservoir were first determined using the third lowest and third highest annual inflows on record. A uniform value within each range was then generated. Next, the annual inflow values of each reservoir were appropriately normalized to agree with the system value. Lastly, uniform inflows were obtained within each weekly range and subsequently adjusted to conform to the respective annual inflow values for each reservoir.

At each time period k (week) of the simulation horizon, a control vector was also randomly generated from the corresponding real-time control set $\Omega_c(k)$. The inflow and control vectors were then used in Equation (1) to determine the storage values for the next time step $k+1$. Based on these values and the reduced and modified state sets derived by the set control approach for time $k+2$, a new real-time control set $\Omega_c(k+1)$ was determined and the procedure was repeated until the end of the year. The simulation process was applied to 30 different random inflow sequences with the results shown on Figure 2. The

figure includes the simulated storage and release sequences (solid lines) along with their associated bounds (dashed lines) and indicates that the set control approach accomplishes the objective of maintaining system storages within their limits using only feasible releases. The fact that the reservoirs experience drawdowns is a consequence of the manner in which the applied releases are obtained. It turns out that random release selection from the $\Omega_c(k)$ sets leads to reservoir depletion. Note, however, that this does not forewarn that the control process will become infeasible. What will happen is that sets $\Omega_c(k)$ will shift towards low release regions of the feasible control sets $\Omega_u(k)$.

To see the effect of other selection rules, we run additional simulation experiments using the release vector associated with the $\Omega_c(k)$ corner point closest to the axis origin (Figures 3). The system is again contained within the specified constraints in all simulations, but reservoir storages now tend to be in the proximity of their upper bounds. The applied releases are generally lower than in the previous case, although specific release levels may be higher depending on the seasonal inflow range and the value of storage.

Hence, the selection of applied releases can drastically influence the state of the system, this being a strength and an open question. From the operational point of view and especially during crises, it is comforting to know that any control action from the $\Omega_c(k)$ sets will not force violation of the stated bounds. However, a relevant question is how to establish an appropriate selection mechanism to coerce the system to evolve in a desirable manner. Desirability implies that each possible system sequence has some distinct value to the system users, and this premise is beyond the stated scope of the set control approach which simply aims to guarantee system feasibility. Nevertheless, it is a question of practical interest and will be taken up again in the conclusion section.

The purpose of the above experiments was to see whether the system is controllable in view of the imposed constraints. The answer was positive but partial because the results do not guarantee feasibility beyond the 52-week control horizon. In fact if the control horizon is extended to over 90 weeks, the set control approach terminates identifying empty modified state sets. Infeasibility means that there is no guarantee that the system can be contained within the stated limits so far in advance. The reason is that the minimum required release of 2.2 bcf/week from the 3rd reservoir is higher than the average lower

inflow bound (~1.396 bcf/week). Eventually, this disparity renders the process infeasible. Note, however, that infeasibilities may occur even if average inflow is higher than the required draft. Such is the case when the upper release bound of the third reservoir is reduced below 16 bcf/week, despite an average upper inflow bound of 13.9 bcf/week. The process becomes infeasible due to large seasonal inflow bound fluctuations.

To understand the nature of the solution when no infeasibility is encountered, we run a 5-year (260-week) control experiment with a lower release bound of 1.39 bcf/week. The results show that after the first year (as the solution proceeds backwards), the modified and reduced state sets exhibit annual periodicity. For the problem stated, the reduced state sets determine the regions where the storages ought to be located in any given week so that the system can continue its feasible operation independently of inflow realization. In an attempt to visualize these three dimensional sets, Figure 4a shows the projection of the minimum set distance on the storage of the 3rd reservoir (solid lines). The shapes for the other reservoirs are identical but contained within the respective bounds. The lower boundary of these regions reflects drought concerns, building up at the beginning of the dry season and easing off as time progresses. During the same period and with no fear of floods, the system can maintain high storages, while the rest of the time, it must make room for high inflows. By contrast, Figure 4b gives the same results when the lower bound for u_3 is 2.2 bcf/week. The figure shows how quickly the feasible region contracts as its lower boundary rises to guarantee a higher draft. Eventually the reduced set becomes empty and the procedure is unable to guarantee feasibility so far in advance. The length of the feasible horizon depends on the seasonal and relative variation of inflow, storage, and release constraints and is a measure of system reliability.

The reduced state sets extend the concept of the rule curves commonly used in reservoir operation. A rule curve suggests a target storage sequence that balances various system objectives in an acceptable manner. A reduced state set sequence guarantees that the system will simultaneously meet these objectives at all times. The advantage of the latter approach is that it considers all system storages simultaneously and guarantees feasibility. A relative disadvantage is that the sets are expressed as a system of inequalities (e.g., Equation 2) that storages must satisfy in each period.

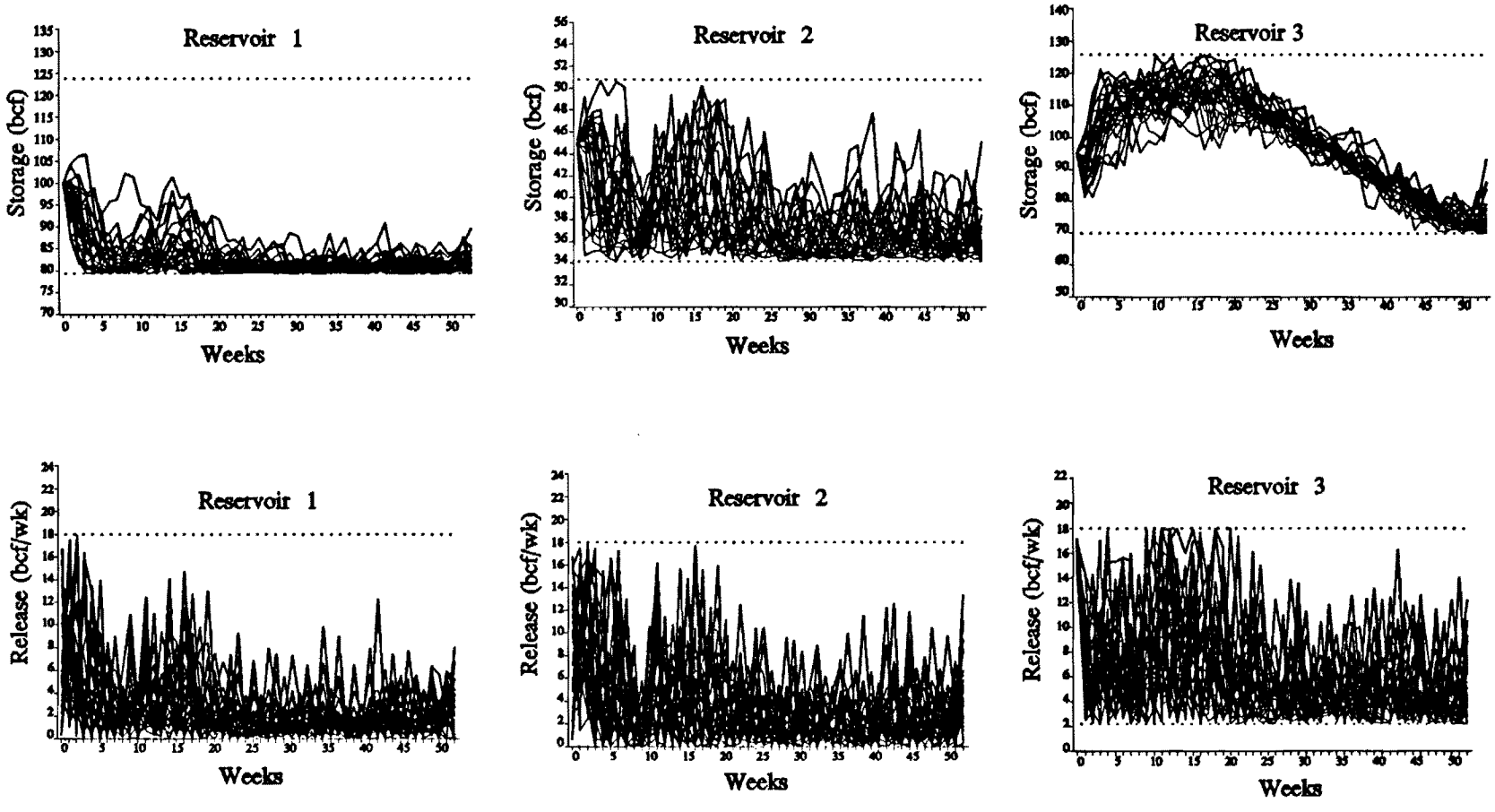

Figure 2: Simulation with Random Release Selection

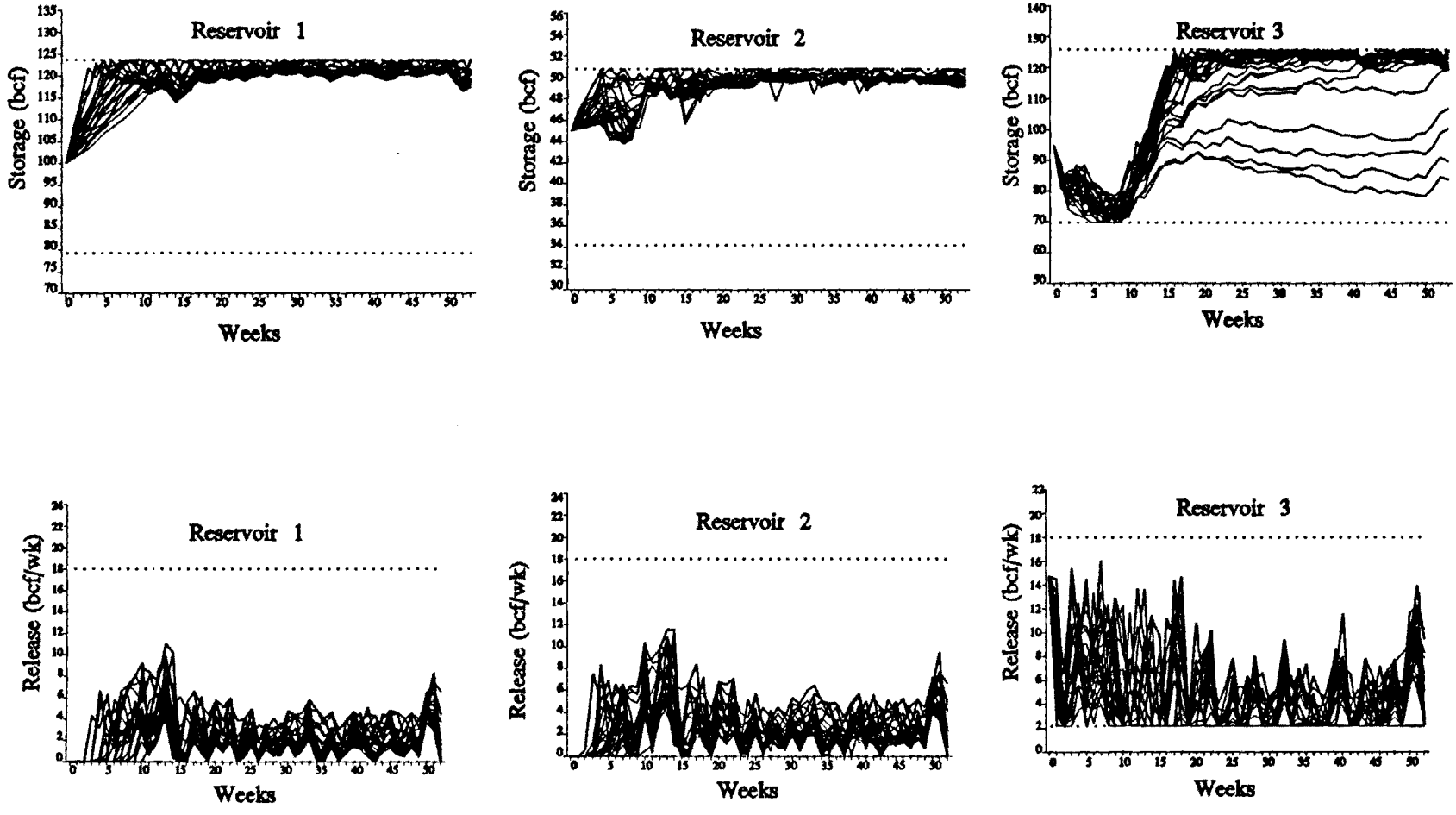

Figure 3: Simulation with Low Release Selection

Clearly, the set control approach can be used in various reservoir operation and design issues. Three examples of practical interest would be to determine (**a**) the minimum and maximum release levels that can be met given an inflow pattern, (**b**) the maximum inflow range that can be controlled for a given output pattern, or (**c**) the system configuration (reservoir capacities) guaranteeing that the desirable output levels will be met given an inflow pattern. In all cases, one can solve the problem such that the objective is always met or such that it is met only within a specified time horizon. The latter case implies that the operation is sequential. This and other issues are discussed in the following section.

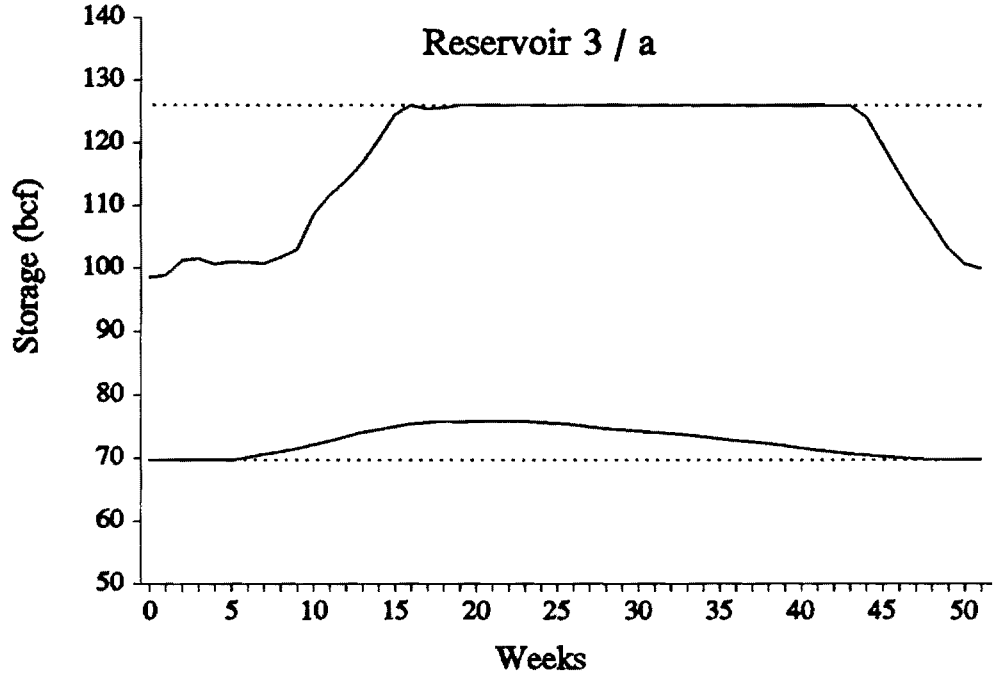

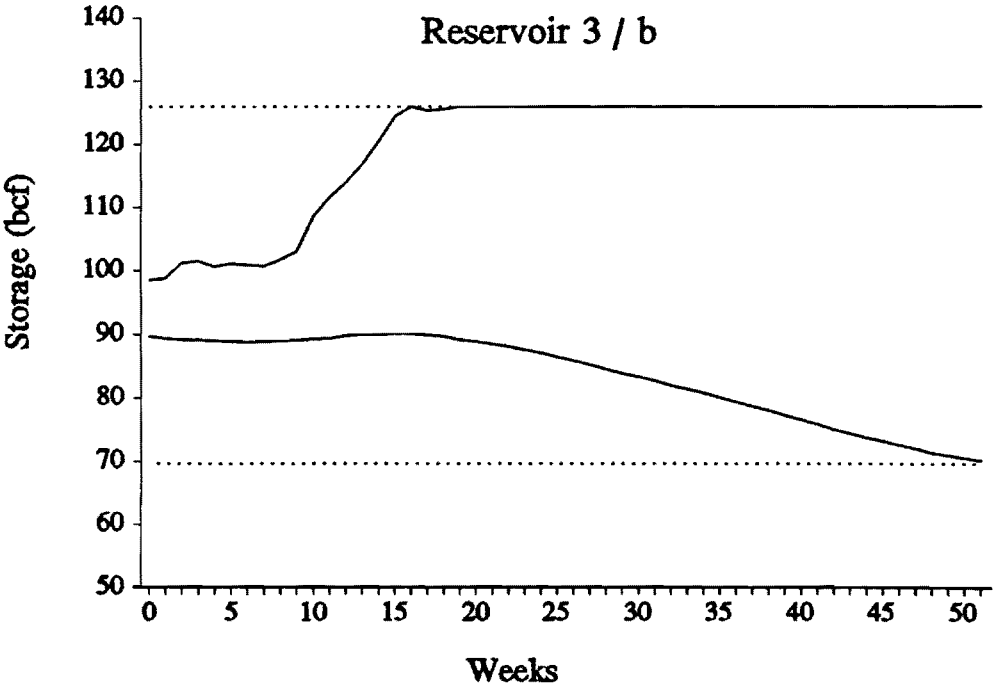

Figure 4: Reduced State Sets for Draft Levels (a) 1.39 bcf/wk and (b) 2.2 bcf/wk

3. HYDROPOWER

Hydropower adds nonlinear elements to the reservoir management problem and raises more questions in reference to the set control approach. To include hydropower considerations, we modify the state equation as follows (*Georgakakos, 1992*):

$$\begin{bmatrix} S_1(k+1) \\ S_2(k+1) \\ S_3(k+1) \end{bmatrix} = \begin{bmatrix} 1 & 0 & 0 \\ 0 & 1 & 0 \\ 0 & 0 & 1 \end{bmatrix} \begin{bmatrix} S_1(k) \\ S_2(k) \\ S_3(k) \end{bmatrix} + \begin{bmatrix} -b_1(k) & 0 & 0 \\ b_1(k) & -b_2(k) & 0 \\ 0 & b_2(k) & -b_3(k) \end{bmatrix} \begin{bmatrix} t_1(k) \\ t_2(k) \\ t_3(k) \end{bmatrix} + \begin{bmatrix} 1 & 0 & 0 \\ 0 & 1 & 0 \\ 0 & 0 & 1 \end{bmatrix} \begin{bmatrix} w_1(k) \\ w_2(k) \\ w_3(k) \end{bmatrix}, \quad (4)$$

$$k = 0,1,\ldots,N-1,$$

where

$$b_i(k) = \sum_{j=1}^{n_i} u_{ij}(k), \quad i = 1,2,3, \quad (5)$$

with $u_{ij}(k)$ being the discharge from the j^{th} turbine of the i^{th} reservoir, $t_i(k)$ the generation hours during period k, and n_i the number of turbines at reservoir i.

Turbine discharge depends (nonlinearly) on reservoir storage and power output and complicates the solution process since the matrix multiplying the control vector [t(k)] is now a function of the state. Products of set quantities cannot be explicitly handled in the framework suggested earlier [*Georgakakos and Yao, companion article*], but one can usually overcome this predicament by following a well-established engineering rule: [*Scweppe, 1973*] "When faced with a nonlinear problem, linearize." In this context, this would imply that coefficients $b_i(k)$ be computed for a particular storage and power level and treated as constants at each time period k. The same approach is usually employed in stochastic control problems with the linearization performed around the most likely state sequence. The difficulty in this case is that a single most likely sequence does not exist; all sequences with vectors from the reduced state sets are equally likely. Thus, linearization introduces approximations and invalidates the one-time solution approach adopted in the previous section. Instead, a sequential scheme where an N-period set control problem is solved at each decision time has distinct advantages.

In a sequential scheme, linearization can be performed around the initial state vector, which is expected to stay representative for some time. Eventually, the state will digress from the locale of the initial vector and will render the process approximate. However, the error is mitigated by the sequential mode of operation where decisions are always selected from the initial control set $\Omega_c(0)$. It is noted, however, that in some cases the procedure may become infeasible, even though the reduced and modified state sets are nonempty.

The above formulation can also reflect release constraints by specifying lower and upper bounds for the control vector $\mathbf{t}(k)$ such that the products $[b_i(k)\ t_i(k)]$ are within the allowable range. Constraints on energy generation can also be included: Let $P_i(k)$, represent the cumulative power output from all turbines at hydroelectric facility i and time period k. Then, the requirement that energy generation satisfy a minimum commitment $E^{min}(k)$ can be enforced as follows:

$$P_1(k)\,t_1(k) + P_2(k)\,t_2(k) + P_3(k)\,t_3(k) \geq E^{min}(k)\,. \qquad (6)$$

This inequality simply defines another bounding hyperplane for the control set $\Omega_u(k)$ and can easily be handled by the set control approach. Thus, the proposed formulation may be used to derive control policies (energy generation schedules) guaranteed to meet a dependable energy sequence, in addition to storage and release constraints.

To gain some insight with the above formulation, we run simulation experiments. The problem is solved with a control horizon of 10 weeks, sequentially at each week of a 10-year simulation horizon. The output of each plant equals its nominal power capacity, 430 MW for Reservoir 1, 375 MW for Reservoir 2, and 350 MW for Reservoir 3. Figure 5 shows the dependence of total turbine discharge on reservoir storage at these power levels. The curves take into account tailrace effects and are based on the power-(net hydraulic head)-discharge relationships reported by *Georgakakos [1991, Appendix A]*. The Ω_s and Ω_w sets are as in the previous section. The control set Ω_t reflects the restriction that generation hours be in the (0 to 168)-hour range per week, total system energy exceed a dependable energy commitment (Eq. 3), and weekly average outflow of the third reservoir be greater than 1.4 billion cubic feet. The last requirement is enforced as follows: At the beginning of each week, the discharge, $Q_3(k)$, from Reservoir 3 is determined based on its initial

storage and Figure 5. Then, the generation hours for Reservoir 3 are constrained by

$$t_3(k) \geq t_3^{\min}(k) = \frac{1.4 \cdot 10^9}{60 \cdot 60 \cdot Q_3(k)}, \quad \text{all } k, \tag{7}$$

where $Q_3(k)$ is expressed in cubic feet per second and $t_3^{\min}(k)$ in hours. It is noted that $P_1(k)$, $P_2(k)$, and $P_3(k)$ are herein arbitrarily set equal to nominal plant capacities. Alternatively, they may reflect contracted power outputs necessitating turbine overload or underload conditions. Furthermore, one may determine the power output of each turbine so as to meet the power contracts and additionally maximize plant efficiency [*Georgakakos, 1992*].

Figure 6 displays the results from 10 such simulations. Storage and generation sequences are only shown for Reservoir 3. Those of the other two reservoirs are qualitatively similar. Total system energy generation is plotted on the third graph along with the dependable energy requirement (thicker line). It can be seen that storage stays within the specified bounds and the generation hours are such that the minimum weekly outflow of 1.4 billion cubic feet is always met. Turbine outflow usually suffices to maintain storage within the desirable bounds; however, on four occasions spillways are also activated (generation greater than 168 hours). System energy generation always satisfies the dependable energy commitment. This commitment may be increased but with no guarantee that it will then be met.

For example, the first graph on Figure 7 displays the energy generation results for another 10-year simulation series where dependable energy requirements are increased by 25%. The system state and control variables stay within the desirable limits, but energy generation occasionally fails to meet the respective targets. The simulation program is such that when the control algorithm identifies infeasibility (empty reduced and modified state sets), it reduces the dependable energy requirements by a certain percentage and repeats the computations until the problem becomes feasible. The worst violation requires that energy commitment be decreased by 40%.

To explore the effect of the control horizon, we repeated the above simulation series with a control horizon of 20 weeks. The results shown on the second graph on Figure 7 indicate that violations of lesser magnitude occur more frequently (the worst violation

requires 30% reduction of the original target). This happens because the control algorithm anticipates potential infeasibilities further in advance and begins to reduce energy generation early on. When the worst violation actually arrives, it is not as serious as in the 10-week control horizon case.

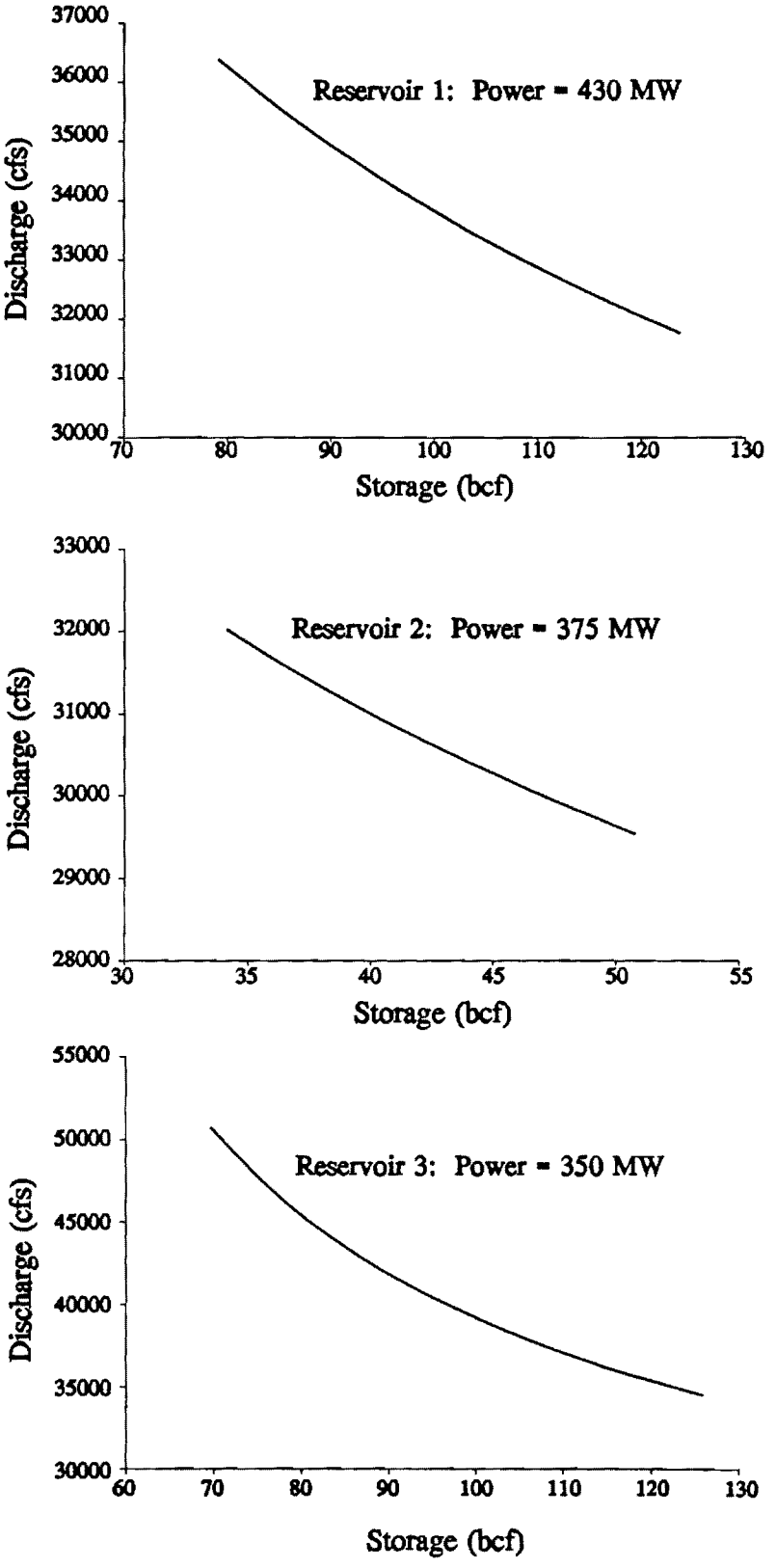

Figure 5: Turbine Discharge versus Storage

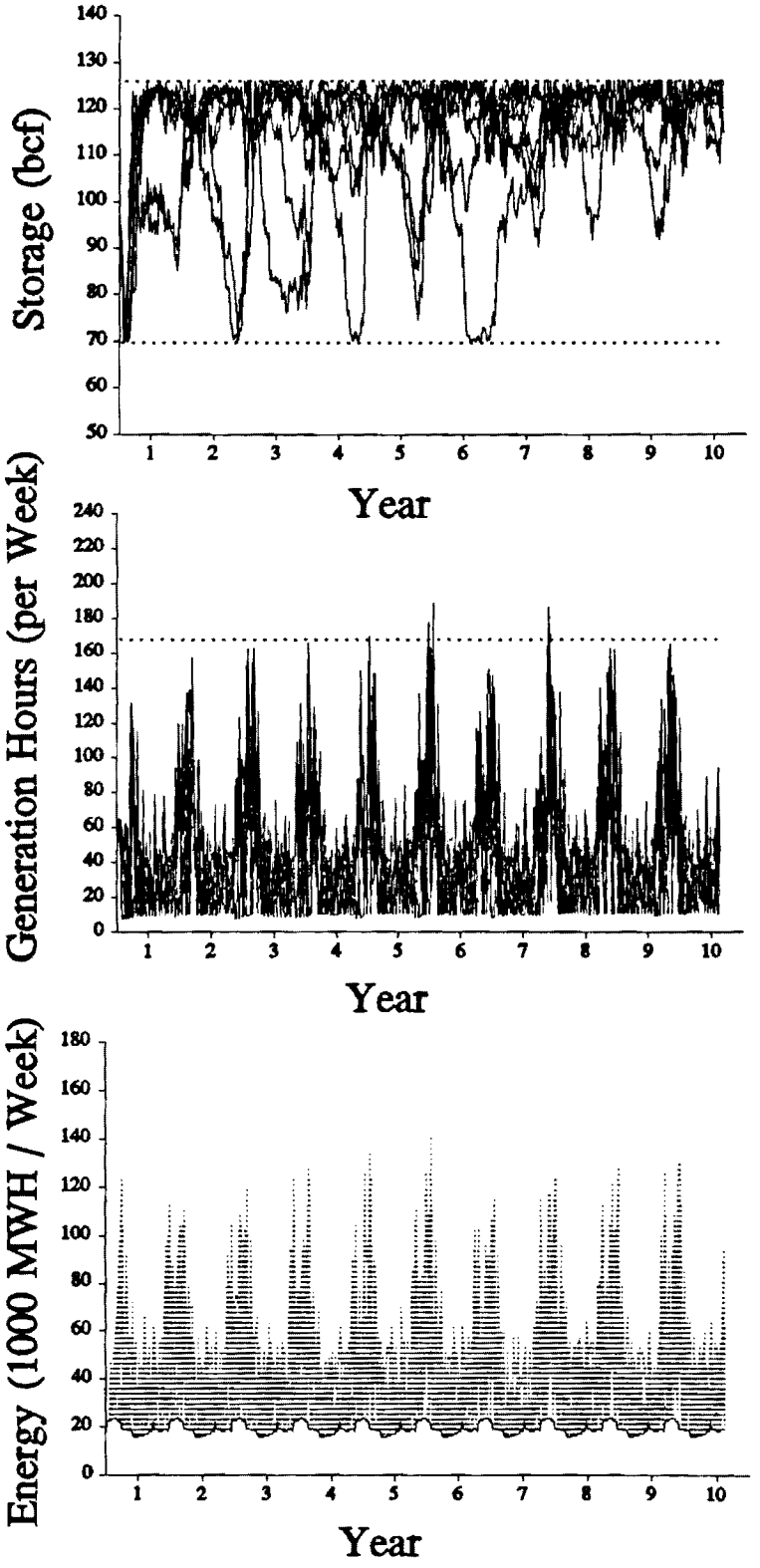

Figure 6: Simulations Experiments

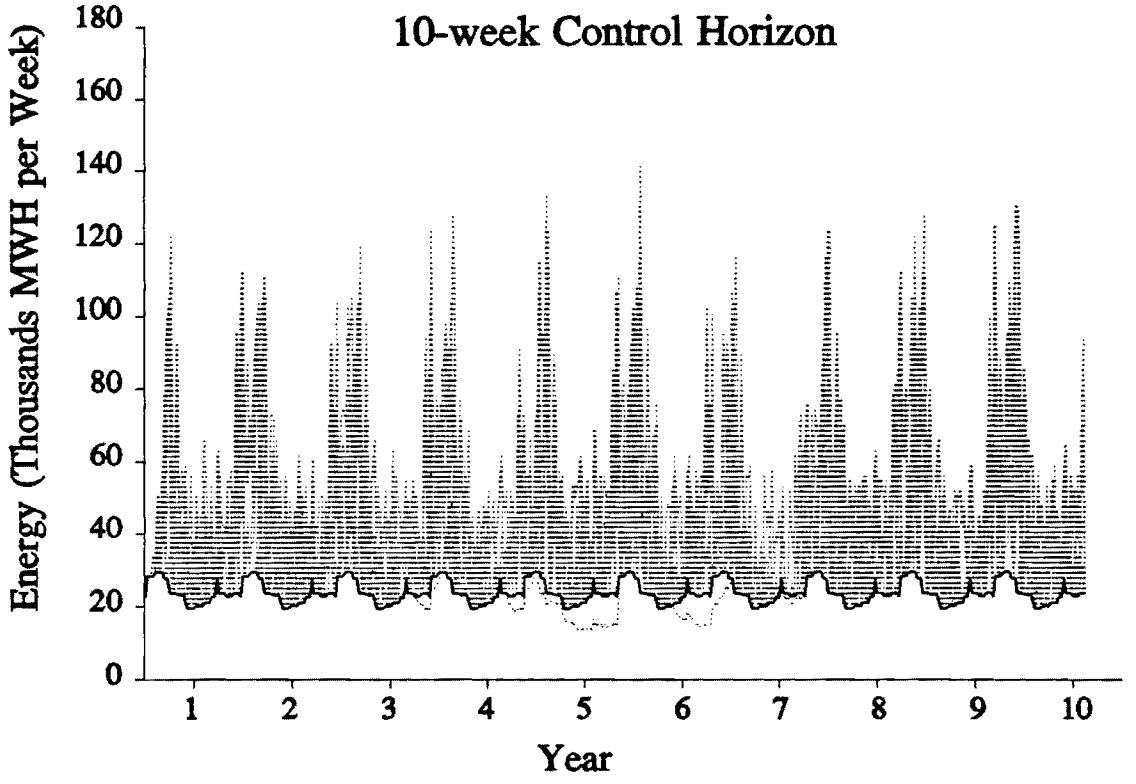

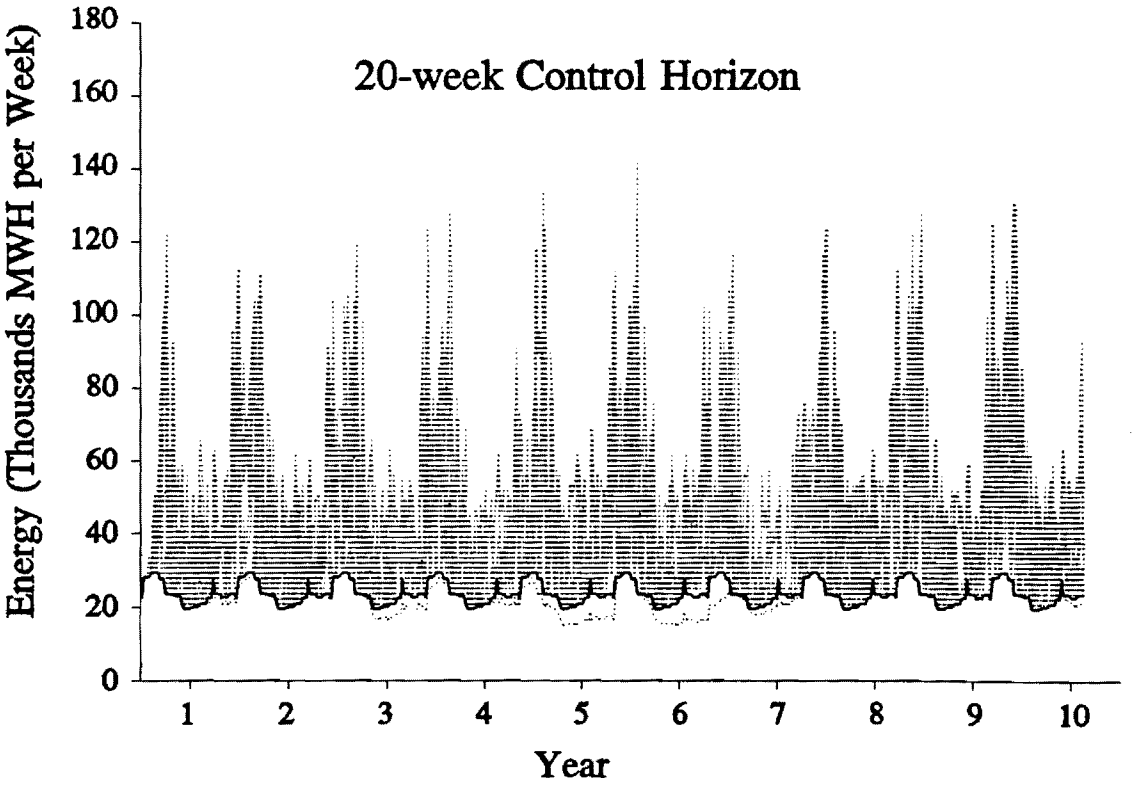

Figure 7: Simulation with Higher Energy Commitments and Different Control Horizons

4. ENERGY VALUE

As the power industry moves toward an open market system, hydropower operation focuses on the value of energy. To address some of the related issues, the system model of the previous section can be expanded to include an additional state variable:

$$V(k+1) = V(k) + \lambda(k)\,[P_1(k)\,t_1(k) + P_2(k)\,t_2(k) + P_3(k)\,t_3(k)], \quad V(0) = 0,$$
$$k = 0,1,\ldots,N-1, \tag{8}$$

where V(k) is the cumulative value of energy up to time k, and $\lambda(k)$ is the value of energy at period k, reflecting the avoided cost of alternative energy sources. The power outputs $P_1(k)$, $P_2(k)$ and $P_3(k)$ are fixed as in the previous section, and $t_1(k)$, $t_2(k)$, and $t_3(k)$ are the control variables representing generation hours. A problem of interest would be to develop operational policies that meet the constraints described in the previous section and in addition guarantee that the energy value at time N exceeds a minimum threshold V^{min}:

$$V(N) \geq V^{min}. \tag{9}$$

As seen by the new system state equation,

$$\begin{bmatrix} S_1(k+1) \\ S_2(k+1) \\ S_3(k+1) \\ V(k+1) \end{bmatrix} = \begin{bmatrix} 1 & 0 & 0 & 0 \\ 0 & 1 & 0 & 0 \\ 0 & 0 & 1 & 0 \\ 0 & 0 & 0 & 1 \end{bmatrix} \begin{bmatrix} S_1(k) \\ S_2(k) \\ S_3(k) \\ V(k) \end{bmatrix} + \begin{bmatrix} -b_1(k) & 0 & 0 \\ b_1(k) & -b_2(k) & 0 \\ 0 & b_2(k) & -b_3(k) \\ \lambda(k)\,P_1(k) & \lambda(k)\,P_2(k) & \lambda(k)\,P_3(k) \end{bmatrix} \begin{bmatrix} t_1(k) \\ t_2(k) \\ t_3(k) \end{bmatrix} + \begin{bmatrix} 1 & 0 & 0 \\ 0 & 1 & 0 \\ 0 & 0 & 1 \end{bmatrix} \begin{bmatrix} w_1(k) \\ w_2(k) \\ w_3(k) \end{bmatrix}$$
$$= A\,S(k) + B(k)\,t(k) + G\,w(k),$$
$$k = 0,1,\ldots,N-1, \tag{10}$$

this problem has more state than control variables and is not directly amenable to the set control approach presented earlier. The problem is that the derivation of the reduced state sets, (lema (17) in *Georgakakos and Yao, companion article*) requires that the coefficient matrix B(k) is invertible. To overcome this limitation, we can enforce invertibility by including an additional column and a fourth control variable, $t_4(k)$:

$$B(k)\,t(k) = \begin{bmatrix} -b_1(k) & 0 & 0 & 0 \\ b_1(k) & -b_2(k) & 0 & 0 \\ 0 & b_2(k) & -b_3(k) & 0 \\ \lambda(k)\,P_1(k) & \lambda(k)\,P_2(k) & \lambda(k)\,P_3(k) & -1 \end{bmatrix} \begin{bmatrix} t_1(k) \\ t_2(k) \\ t_3(k) \\ t_4(k) \end{bmatrix}. \qquad (11)$$

The new column vector can have any form as long as it makes B(k) invertible. However, the new control variable should have an empty feasible range:

$$0 \le t_4(k) \le 0, \quad k = 0,1,\ldots,N-1. \qquad (12)$$

The above modification does not alter the character of the original system. (The proof that the two equations essentially describe the same system is trivial.) It only facilitates the application of the set derivation procedures discussed earlier.

In summary, the set control problem amounts to finding feasible control policies for the system (10), (11), and (5) such that all storage variables remain feasible (see Table 1) subject to constraints (6), (7), (9), and (12). The λ-values assumed for this computational experiment are shown below and are roughly indicative of the energy generation cost ($/MWH, weekly average) in the southeastern U.S.:

$$\lambda(k) = \begin{cases} 19, & \text{if } 1 \le k \le 13 \\ 24, & \text{if } 14 \le k \le 26 \\ 31, & \text{if } 27 \le k \le 39 \\ 19, & \text{if } 40 \le k \le 52 \end{cases} \qquad (13)$$

Annual energy generation is to always exceed 27.3 million dollars ($=V^{min}$), and the dependable energy sequence is 60% of the one reported previously. To determine the system potential to operate under these constraints, we performed the following computational experiment: First, the control model was run with a 52-week planning horizon to determine the reduced state sets. To simplify the procedure, the linearization of the B(k) matrices was performed around the initial storage values for all k. Then, the system operation was simulated over 50 weekly sequences of one year duration. Figure 8 includes some results related to energy generation. The first graph depicts the value of annual energy from each simulation and shows that it is always greater than the specified

minimum. In fact, for V^{min} greater than this value, the control problem becomes infeasible. One can reduce the planning horizon to achieve feasibility but forgo the 52-week operational guarantee. The second graph portrays the energy generation sequences for which the annual energy value is almost equal to V^{min}. Actual energy generation always meets the specified dependable sequence. Storage and generation hour sequences are also feasible but are not shown. The computations are performed on a 486/33 microcomputer and take approximately 1 minute.

It is noted that the formulation of this section may also be used to control the system such that annual energy amounts and outflow volumes exceed certain levels. The first case can be analyzed by the same formulation after λ is omitted. The second would require that Equation (8) be replaced with one describing the cumulative outflow volume.

4. CONCLUSION

Reservoir management is complicated by uncertain inputs whose probabilistic characterization is occasionally unreliable. Examples are the hydrologic extremes of floods and droughts whose natural data-deficiencies invalidate stochastic forecasting and optimization models. As an alternative, this article discusses potential reservoir management applications of the set control approach (*Georgakakos and Yao, companion article*). Common to all applications is the premise that the operator wishes to have a set of policies which are guaranteed to meet all system constraints rather than optimize specific objectives. We feel that this mode of operation is more meaningful under crises situations. Potential reservoir design applications were also mentioned.

Reservoir systems usually operate under normal hydrologic conditions and only occasionally experience extreme events. During the former, stochastic methods are appropriate and can usefully guide system operations. Our future research focuses on the development of a hybrid control model which uses stochastic menthods during normal circumstances but switches to the set control approach at the onset of critical periods.

ACKNOWLEDGEMENT

This work was partially funded by the U.S. Geological Survey under Contract No. 14-08-0001-G1886.

REFERENCES

Foufoula-Georgiou, E., and P. K. Kitanidis, Gradient dynamic programming for stochastic control of multidimensional water resources systems, *Water Resources Research*, 24(8), 1345-1359, 1988.

Georgakakos, A. P., Extended Linear Quadratic Gaussian (ELQG) control: Further extensions, *Water Resources Research*, 25(2), 191-201, 1989.

Georgakakos, A. P., Optimal regulation of the Savannah River system, *Technical Report* for U.S. Army Corps of Engineers Research Contract No. DACW21-88-C-0043, School of Civil Engineering, Georgia Tech, May 1991.

Georgakakos, A. P., Operational tradeoffs in reservoir control, *Water Resources Research*, under review, 1992.

Kelman, J., J. R. Stedinger, L. A. Cooper, E. Hsu, and S.-Q. Yuan, Sampling stochastic dynamic programming applied to reservoir operation, *Water Resources Research*, 26(3), 447-454, 1990.

Schweppe, F., *Uncertain dynamic systems*, Prentice Hall, 1973.

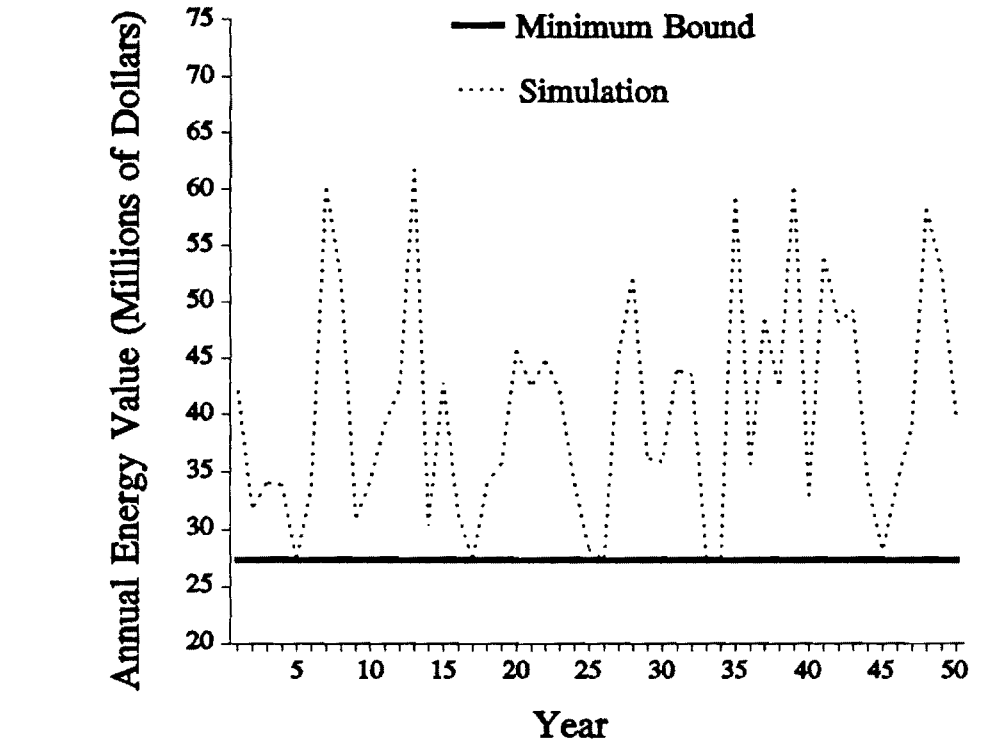

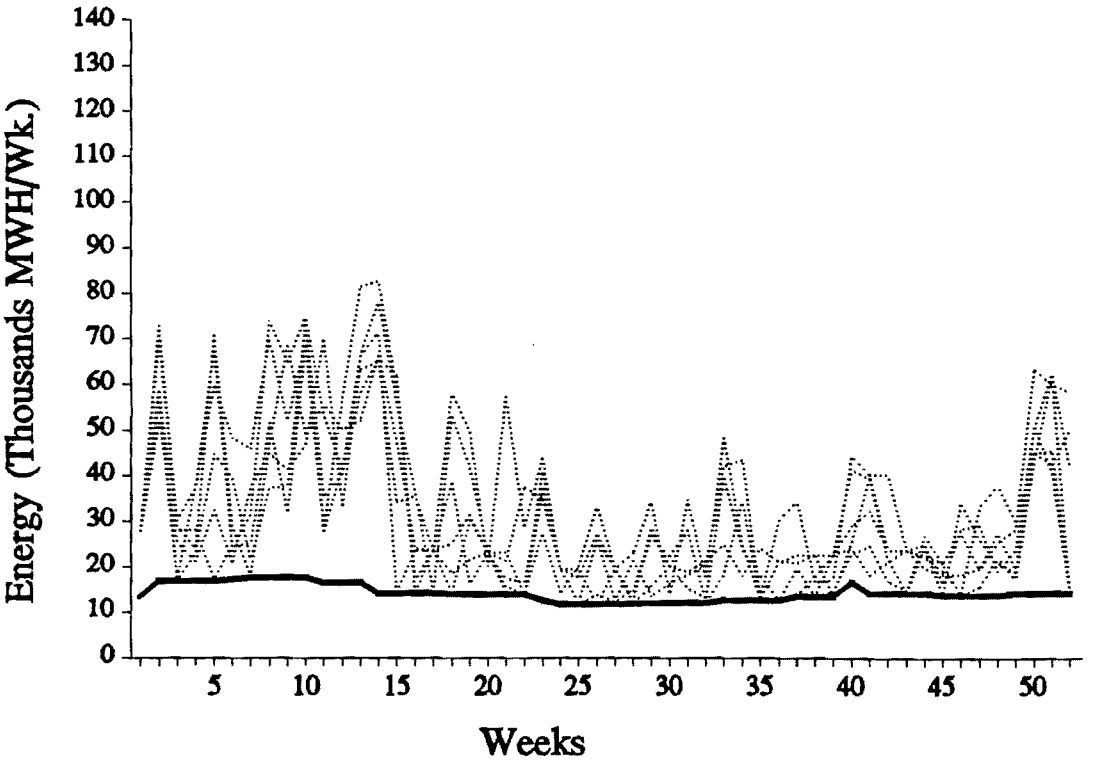

Figure 8: Energy Value Simulations

E 20-686
2

THE UNIVERSITY OF IOWA

1 July 1992

Professor Aris P. Georgakakos
School of Civil Engineering
Georgia Institute of Technology
Atlanta, Georgia 30332

Dear Aris:

I attach a paper (to be submitted to *Water Resources Research*) summarizing our recent research activities. The paper constitutes our second progress report on the USGS Award (Georgia Tech subcontract E-20-686-S1). I shall be happy to answer questions you may have on the manuscript.

Sincerely,

Konstantine P. Georgakakos, Sc.D.
Associate Professor, CEE
Research Engineer, IIHR

Encl.

Iowa City, Iowa 52242 U.S.A. Institute of Hydraulic Research 319/335-5237 Telex: 756569 FAX 319/335-5238 Bitnet ID: AEGCRAPA@UIAMVS

Georgia Tech

School of Civil Engineering

Georgia Institute of Technology
Atlanta, Georgia 30332-0355

Tel.: (404) 894-2240
Fax: (404) 894-2278

E20 2

7 July 1992

William Pollock
Office of Procurements and Contracts
United States Geological Survey
Mail Stop 205C
12201 Sunrise Valley Dr.
Reston Virginia 22092

Dear Mr. Pollock:

Enclosed please find the second progress report for Research Project 14-08-0001-G1886. This package includes the reports from both participating institutions, namely, Georgia Tech and The University of Iowa. The Georgia Tech report consists of a two-part paper that was submitted to Water Resources Research in March and has been accepted for publication. The University of Iowa report is again a paper which will be submitted to either the same journal or the Journal of Climate. We apologize for the delay. We were under the impression that only yearly reports are now required. This material was ready in March. Also, thank you for granting us the no cost extension till next June.

If you have any comments or questions, please contact me.

Most Sincerely,

Aris P. Georgakakos
Associate Professor of
Hydrology and Water Res.

CLIMATIC FORCING AND LAND-SURFACE FEEDBACK IN CONTINENTAL WATERSHEDS
Part I: Temporal Analysis

Konstantine P. Georgakakos and Deg-Hyo Bae
Department of Civil and Environmental Engineering
and Iowa Institute of Hydraulic Research
The University of Iowa
Iowa City, Iowa 52242

and

Daniel R. Cayan
Climate Research Division, 0224
Scripps Institution of Oceanography
University of California, San Diego
La Jolla, California 92093-0224

April 1992

To be submitted to the Journal of Climate or Water Resources Research

ABSTRACT

A multi-pronged study of the linkage between meteorology/climate and hydrology of temperate latitude catchments on daily to decade time scales is presented. The effort uses the detailed hydrology provided by a hydrologic catchment model, adapted from the operational streamflow forecast model of the NWS River Forecast System. The model is tuned to respond to observed daily precipitation and potential evaporation input. Results from the Bird Creek basin with outlet near Sperry, Oklahoma, and from the Boone River basin with outlet at Webster City, Iowa, indicate that the model quite accurately simulates the observed daily discharge over 40 years at each of the two basins. Linkage between the hydrological components and both local and regional-to-hemispheric atmospheric variability is studied, both for atmosphere-forcing-hydrology and hydrology-forcing-atmosphere.

Daily precipitation and potential evaporation within the Bird Creek and the Boone River basins in the Central U.S. yield a detailed hydrological budget over approximately 40 years so that interannual and shorter term variability can be investigated. This budget provides an estimate of components such as upper and lower zone soil moisture, which are not available from conventional observations or parameterizations. Previous studies have identified soil moisture as an important influence on local-to-regional scale atmospheric variability through its effect on the surface energy balance, especially over mid-continental regions during spring and summer. Large scale relationships between the hydrology and regional-to-hemispheric atmospheric fields, as well as connections to local meteorological variables, are examined. The present paper is the first in a sequence of two papers. Here we focus on the results of a local-temporal analysis. In a companion paper (Cayan and Georgakakos, in this issue) we present results of a spatial hydroclimatic analysis.

An important conclusion of this study is that the model used is capable of successfully simulating basin processes over climate scales, thus producing reliable estimates of soil water interdecadal variability. This study also shows that two similar central-US basins with areas of about 2000 sqkm, that differ in the temperature regime and in the soil water capacity, behave quite differently when forced by the atmosphere. The northern basin that has higher capacity for holding soil water under unsaturated conditions appears to be more resilient to seasonal and interdecadal changes in local hydrometeorological forcing. The southern basin exhibits strong summer feedback to the local atmosphere through evapotranspiration. No significant local hydrologic cycles were detected for the two study basins, and an analysis of the two generated 40-year records of estimated daily values of soil water revealed a multitude of spatial time scales, some exceeding the separation distance of the basins. For both basins, the time scale of the atmospheric forcing variables was very short compared to the rather long time scale of the soil water content.

1. Introduction

a. Background and Scope

This is the first in a series of two papers which have as a theme the interaction of land-surface hydrology with the atmospheric forcing of precipitation and potential evaporation. The general goal of the relevant on-going research effort is to improve our understanding of atmospheric and land surface processes through which the energy and water balance of the earth's surface is maintained. The subject and the regional focus of this work is highly-relevant to the Global Energy and Water Cycle Experiment (GEWEX), including the GEWEX Continental-Scale International Project. One of our study basins (Boone River, Iowa) lies within the Mississippi River basin, which has been identified as the preferred site of the GEWEX Continental-Scale Project (WMO, 1990, p. 38).

Soil moisture to a depth of 1 to 2 meters is the primary hydrologic state variabe that controls and is controlled by land surface processes. Any assessment of forcing/feedback mechanisms between the land surface and the atmosphere will have to involve soil moisture. The primary difficulty with such hydroclimatic studies is the absence of long time series of reliable soil moisture data that characterize the soil moisture temporal variability over the area of hydrologic catchments (e.g., 1000 km^2 or greater). It is timely, however, to examine the forcing/feedback mechanisms on regional scales to assess the natural variability of regional climatic variables for establishing a base for studies aiming at the assessment of potential regional climate change effects. Thus, until such time when long and reliable time series of soil moisture become available, land-surface/atmosphere interaction studies will have to rely on surrogate measures of soil moisture variability.

Toward this goal, this work explores the ability of a physically-based conceptual catchment model (adapted from the operational streamflow forecast model of the U.S. National Weather Service River Forecast System) to capture daily-interannual variations of surface hydrological components in two watersheds over the central United States. In addition to the utility of a better description of the variability of the catchment surface hydrology, this work helps determine its linkage (forcing and feedback) to the atmospheric circulation and attendant larger-than-catchment scale surface variations. A primary aim of present day climate change research is to provide reliable predictions of global climate change and associated regional implications on time scales ranging from seasons to a century or more. The research presented here in contributes to a better understanding of future climate variations by exploring the natural variability within a several decade record at typical mid-latitude and mid-continental watersheds. The records from the study basins contain a broad spectrum of natural hydrological variations ranging from floods to extended multi-year droughts. In addition, the present study indicates the regional feedbacks that are pertinent to a hydrologic and water resources impact assessment. It also establishes the capability

of physically-based hydrologic models to perform well in long term simulations under a changing climate.

The implicit premise is that if a model, that generates indices of basin soil moisture, produces reliable and accurate daily flow simulations over long periods of time and in various hydroclimatic regimes, then such model can be used to generate estimates of interdecadal soil moisture variability. In the present work, "reliable and accurate" means cross-correlations between *daily* observed and simulated flow that are higher than 0.8, as computed over a period of forty years for two mid-continental watersheds in different hydroclimatic regimes. The close nonlinear relationship between the rainfall-runoff process and the soil water content is exemplified in Figure 1, which shows a period of record for one of the study basins (Bird Creek with outlet near Sperry, OK). It can be seen that the 37 mm/day rainfall rate on 22 August 1971 produced negligible runoff, while a lower rainfall rate on the 25 September 1971 produced a flood of almost the same magnitude as the one produced on 19 September 1971 by a rainfall rate of 70 mm! Such nonlinear runoff production can only be explained using the water content of the upper soil (estimated by the rainfall-runoff model used in this work and depicted in a thick solid line in Figure 1). While the soil water content was below 60 mm on the 21st of August, it was near the saturation capacity of 135 mm on the 19th and 25th of September.

Within this framework, the proposed work concerns itself with land hydrology in specific drainage basins, and how it interacts with atmospheric forcing of temperature and precipitation on local and regional, as well as on daily and seasonal scales. In particular, we utilize physically-based models of drainage basin response as a means to determine internally consistent scenarios of observed (e.g., temperature, precipitation and pan evaporation) and unobserved hydrometeorological variables (e.g., upper and lower soil moisture, evapotranspiration) spanning several decades in the past. Calibration and verification of such models to the specific drainage basins with data that span several decades is an important aspect of the work that assures model ability to represent drainage basin dynamics given interdecadal climate variability. The model-produced time series are utilized in a temporal (this paper) and spatial (Cayan and Georgakakos, this issue) analysis with the purpose to determine characteristic hydrometeorological time scales, feedbacks with regional atmospheric circulation (i.e., pressure and temperature patterns), and spatial relationships between hydrologic variables under specific regional "climates".

The objectives of the temporal analysis are:

1. Assessment of the performance of the hydrologic model with historical daily data for long periods of simulation that include several atmospheric circulation regimes.
2. Study of the seasonal and inter-decadal behavior of the model-computed soil moisture indices.
3. Relationship of surface and sub-surface Hydrology to climatic forcing/response in time for specific catchments in the continental United States.

4. Inter-comparison of 1, 2 and 3 above for two different regions of the mid-continental United States

b. Relations to other studies

Aspects of this study are related to the recent works of Gleick (1987), Schaake (1990) and Lettenmaier and Gan (1990). The following are differences which would undoubtedly cause significant differences in results on the aspects of the subject research that might be of a similar scope to those published:

1. The testing of the connections of drainage basin hydrology (in this case the detailed output from the hydrologic model) to local and large scale atmospheric forcing/response is new and has not been documented in the literature.
2. The study is a dual "attack" by a land-surface hydrology group and a climate analysis group, as warranted by the hydrometeorological character of the processes involved. This hydrologic-meteorological "marriage" allows exploration of both detailed drainage-basin hydrology and atmospheric variability such as atmospheric circulation.
3. Our focus is for rainfall-driven drainage basin hydrology as opposed to snowmelt-driven hydrology (e.g., work by Lettenmaier and Gan, 1990) with dynamics simulated in temporal scales down to days as opposed to months (e.g., work by Gleick, 1987, and Schaake, 1990). The latter has important consequences for basins subject to runoff on daily time scales.
4. The study includes a diagnostic part where a lengthy past record is used with the hydrologic model to establish regional feedbacks between climatic and hydrologic variables.
5. The spatial relationship of regional circulation patterns and the strength of the regional circulation is investigated (Cayan and Georgakakos, this issue) by examining two regions of the Continental United States in the central plains when concurrent soil anomalies in hydrologic variables (such as soil moisture) occur.

c. Methodology

Our methodology consists of calibrating-verifying the simulations of the hydrologic model for the two drainage basins of study and for the historical data that span several decades, then using the model-generated time series of hydrologic variables (such as soil moisture content) together with the time series of the observed atmospheric variables in a temporal local analysis. The temporal local analysis entails computing time series of anomalies (after the seasonal variation has been subtracted) of model-generated and observed variables that show the temporal behavior during wet and dry spells. Auto-correlation and cross-correlation coefficients are computed in an effort to diagnose causative relationships among the different atmospheric and hydrologic variables

at the drainage basin local level. Finally, we examine the differences among our diagnosis results for the two drainage basins.

The next section presents a brief description of the two application drainage basins followed by a section describing the hydrologic model used. The study is a data intensive one, and section 4 presents issues of data availability and data quality control. Section 5 discusses model calibration and verification, while section 6 presents the main results of the temporal analysis. Important conclusions are presented in section 7.

2. Description of study drainage basins

We have selected headwater basins (basins with no upstream inflow) of a similar area. Such basins are the 2344-sqkm Bird Creek basin with outlet near Sperry, Oklahoma, and the 2160-sqkm Boone River basin with outlet at Webster City. Figures 2a and 2b show the hydrologic maps of the basins with the location of the nearest precipitation, temperature and pan evaporation stations indicated on the maps. Figure 2c shows the location of the basins within the United States. The basins have longitudes near 90W, while they differ in their latitudes by more than 5 degrees. Table 1 provides a summary of available data for each basin. The period of record from 1949 through 1988 is available for all but a few of the indicated stations. Staff of the Office of Hydrology has calibrated the soil moisture accounting component of the hydrologic model for the Bird Creek basin as part of the operational flow prediction process. The model has been calibrated for the Boone River basin as part of this study, and in a collaborative effort with the Army Corps of Engineers District Office at Rock Island, Illinois.

Table 2 presents the long-term average hydrometeorological characteristics of the area for each of the two study basins. It is noted that the Boone River basin "climate" is similar to the Bird Creek basin one but with cooler average temperatures. Hydrological ramifications of these differences, along with attendant differences in the influencing atmospheric circulation, are examined in a later section in this paper and in Cayan and Georgakakos (this issue). Figure 3 presents the 5-day averaged seasonal variation of the runoff ratios (flow/rainfall) and climate ratios (potential evapotranspiration/rainfall) for Bird Creek and Boone River. It is shown that the runoff ratios for Bird Creek and Boone River are about the same, both exhibiting important seasonal features. The runoff ratio is greatest in late winter/early spring with mean values exceeding 0.5, and least in mid-summer with a mean value less than 0.1. The maximum value for Boone River lags that of Bird Creek by a month. The climate ratios also exhibit strong seasonality, and important differences between Bird Creek and Boone River. The annual average value of the climate ratio for Boone River is close to 1 with 5-day mean values that have relatively small

seasonal departures from that annual average value. On the other hand, Bird Creek with an annual average value also close to 1 exhibits pronounced seasonality, varying from a) "wet climate" values near 0.5 in winter, spring, and late fall to b) "arid climate" values with a maximum of 2.5 in summer. For such a basin, using annual climate ratio values to characterize its climate becomes meaningless.

3. Model description

We have utilized a conceptual rainfall-runoff model complemented with a kinematic channel routing component for the translation and attenuation of the generated runoff downstream to the catchment outlets. The model used constitutes the deterministic component of an operational model (Hydrologic Forecast System - HFS, Georgakakos and Smith, 1990) that is currently under operational testing by several River Forecast Centers across the United States for adoption in routine operational use. For ease of reference, we will call it the 3R model (Rainfall-Runoff-Routing model). It is based on the Sacramento model as the hydrologic soil moisture accounting component for the study of the rainfall-runoff process on the hydrologic catchment scale.

The Sacramento model is used routinely by field offices (River Forecast Centers) of the Office of Hydrology, National Weather Service, NOAA to issue short (e.g., Peck, 1976) and medium range (a few months) (e.g., Day, 1985; Smith, et al. 1991) flood and low flow forecasts. Compared to other models such as the Antecedent Precipitation Index (API) models also in operational use by the field offices (e.g., Georgakakos, 1987), it has the advantage that it is physically-based, in that it distinguishes upper-soil and lower-soil moisture storage and groundwater storage; it has a variable impervious area that expands as the soils become saturated; and it simulates the soil-wetting front after a storm in a realistic manner. Compared to more complex finite-difference and finite-element models of surface and subsurface response it has the advantage that it can be adequately calibrated from the available historical drainage basin record of daily rainfall, pan evaporation or temperature and streamflow, and in addition it does not require excessive CPU time for the simulation of the drainage basin processes over several decades. Its very good performance in simulating accurately the six-hourly and daily flows from drainage basins has been demonstrated by Georgakakos, et al. (1988), Georgakakos and Smith (1990), and in the Model Validation section of this paper using a 40-year long record. For the purpose of the proposed work, this model can be considered as a state-of-the-science hydrologic model for climate studies in specific watersheds. For example, the models used in Global Circulation Models (GCMs), such as the GISS and the GFDL GCMs, are very crude approximations of the Sacramento model.

The Sacramento model has been recently documented in Georgakakos (1986); it accepts mean areal precipitation and mean areal potential evapotranspiration as input, and produces total channel inflow as output. The model is of the spatially lumped type with a variable impervious area to account for spatial soil saturation effects. The runoff production mechanism is a saturation excess mechanism. The flow components contributing to the total channel inflow are direct runoff from impervious areas, surface runoff in cases of excessive rainfall rates, interflow through the upper soil layers, and groundwater flow. The model subdivides the drainage basin into two zones, an upper and a lower zone. The upper zone simulates water stored in the upper soil layers which is available for evapotranspiration, percolation, surface runoff and interflow. The lower zone simulates the bulk of soil moisture and groundwater storage. Both zones have tension-water elements and free-water elements. The former simulates water which can be extracted only via evapotranspiration, while the later simulates water that is "free" to move under the action of gravity. The upper soil zone contains one tension and one free water element, while the lower zone contains one tension and two free water elements in order to capture the observed nonlinear baseflow. An additional-impervious area storage element was introduced by the model creators in an effort to account for the temporal changes of the saturated soil area during flooding events and, therefore, to partially account for the spatial distribution of that area as a function of time.

Several versions of the Sacramento Model have been published in the literature. The original version (Burnash, Ferral and McGuire, 1973) was a discrete-time model. Kitanidis and Bras (1978) presented a simplified state-space form of the discrete-time version, thus, allowing the propagation of uncertainty from the model input to the model output via a state estimator. Georgakakos (1986) presented and tested successfully a continuous-time state-space form of the model differential equations that closely approximates the original discrete-time version. It is this model that is used in the 3R model and which we have used to simulate hydrologic catchment processes. Peck (1976) and, more recently, Brazil (1989) document methodologies for parameter estimation from input-output data. The model has been successfully coupled to unit hydrographs and reservoir-type channel routing models (e.g., Georgakakos et al., 1988, and Georgakakos and Smith, 1990) for the real-time prediction of streamflows in headwater basins. The Sacramento model coupled with the NWS snow-melt model has been used previously by Lettenmaier and Gan (1990) to assess potential climatic impacts to small drainage basins in the Western United States subject to snowmelt runoff.

For the important channel routing component of the model we have used the kinematic routing procedure in Georgakakos and Bras (1982) suitable for use in headwater drainage basins. A series of conceptual linear channel reservoirs was used to simulate water wave attenuation and translation in basin channels. The number of the conceptual reservoirs and their common time constant were two parameters whose values were estimated from existing flow data.

The interested reader is referred to Georgakakos, et al.(1988) for a detailed description and mathematical formulation of the rainfall-runoff and channel routing components of the 3R model.

4. Input data and data quality control

As mentioned above, the required model-input data is daily time series of rain gauge rainfall, pan evaporation or derived potential evapotranspiration. Daily streamflow time series is also used for calibration and verification. Our data source is the climate and discharge data routinely collected by co-operative observers and stored on optical disks distributed by EARTHINFO Inc. The choice of this database was based on the fact that it has a good coverage of the continental United States, it is easily accessible, and it contains long time series records.

The temperature records and the discharge records for the catchments of study were of good quality and quite complete. There were several issues, however, associated with the use of the available data to estimate mean areal precipitation and evapotranspiration. In the following, we present those issues for each data type together with the associated data quality control procedures.

a. Mean areal precipitation

At first, the models are spatially lumped and, thus, one has to compute mean areal rainfall data over the drainage basin of interest from sparse raingauge data in and around the basin. This is a research issue in itself as evidenced by the work of Krajewski (1987). For the purposes of this work and given the fact that our drainage basins are in non-mountainous areas (central US plains), the spatial averaging procedure presently employed by the Office of Hydrology of the National Weather Service was used. The procedure, documented by Larson (1975), and Larson and VanDemark (1979) consists of an inverse-quadratic distance weighting of raingauge observations for each grid point of a regular grid superimposed over the drainage basin. The raingauge observations are selected so that at least one observation exists in each of the four quadrants originating from the grid point of interest. When estimates of rainfall have been obtained for all the grid points, an arithmetic average of the values gives the mean areal rainfall estimate over the drainage basin. The procedure is repeated at each time step (of daily duration in this work) with the weights for all the grid points precomputed. Computation of new weights is required when one or more raingauge stations report "missing" data.

For relatively flat areas and when there are several raingauge stations, the procedure tends to give mean areal rainfall estimates close to the arithmetic average of the raingauge observations. Summer convective activity in regions of sparse raingauges would tend to make the NWS estimates deviate from the straight arithmetic average estimate.

The procedure proposed does not produce estimates of the error in the computed mean areal rainfall, as the modern minimum variance interpolation methods do (e.g., Kriging as in Krajewski, 1987). It does has the advantage of being efficient in its use of CPU time. The effect of the number of raingauge stations on the cross-correlation coefficient of the daily observed and simulated flow, computed for the 40-year record, is given in Figure 4 for the 2160-sqkm Boone River basin. The model has been calibrated with the maximum number of 11 raingauge stations as described in the Calibration section, and for each case of raingauge number less than 11, the set of raingauge stations with the best performance is the one for which results are reported in Figure 4. It can be seen that improvement in cross-correlation coefficient is dramatic as the number of raingauges increases from 1 to 5, but after that very little improvement is offered by additional raingauges. Analogous results hold for the 2344-sqkm Bird Creek basin in Oklahoma. These results are indications of the adequacy (as far as flow simulation is concerned) of the 11 raingauge stations to represent mean areal rainfall over the catchments.

In case a particular station contained "missing" data for a particular period, such station was removed from the set that contributed to the mean areal precipitation estimates during that period. Such occurrences were rare, and, thus, no "filling" procedures for missing raingauge data were used.

For the case of the Boone River basin and during the winter months, the type of precipitation (rain vs. snow) was determined on the basis on the surface air temperature.

b. Mean areal potential evapotranspiration

The second issue associated with data is the computation of mean areal potential evapotranspiration series from incomplete station pan-evaporation data. The number of stations in the US reporting daily pan evaporation data is considerably smaller than the number of stations reporting daily rainfall and temperature (min and max). Thus, the station closest to the basin was used as representative of the pan evaporation estimates over the drainage basin of interest. Also, it is common with the cooperative observer pan evaporation data that the observations were taken at irregular intervals in some months of the year (usually the colder months) with the existence of several zeros followed by an abnormally high value. We distributed the high value uniformly between the previous consecutive days that have zeros and the current day. As an example, Figure 5a shows the daily pan evaporation data reported for all the months of February in the historical calibration period from September 1956 through November 1978 for the station Hulah Dam in north-central Oklahoma. The aforementioned problem is clearly depicted by the sequence of several zero values before an unrealistically high (for the month of February) pan evaporation value is reported. Our redistribution approach gives the result in Figure 5b, that appears consistent with winter evaporation in that area as assessed by the daily values that were not preceded by zeros.

A problem with the pan evaporation data is the missing values. The 40-year record of pan evaporation is about 75 percent complete for the Bird Creek basin (Hulah Dam recording site) and about 60 percent complete for the Boone River basin (Ames recording site). Fortunately, the majority of missing values are during the low-evaporation cold winter months. For a continuous simulation, as was performed in this work, continuous records are necessary. In order to fill the missing data, we used locally calibrated regressions by month between the daily pan evaporation and the concurrent daily surface air temperatures (min and max) observed at the same station. The use of temperature as an explanatory variable is necessitated by the fact that it is usually the variable with the most complete daily record observed very near or at the site of the pan evaporation station. Table 3 presents the results of such a regression analysis between daily pan evaporation and maximum temperature for the Hulah Dam station in north-central Oklahoma. This station was used to provide pan evaporation data for the Bird Creek basin. Analogous results are in Table 4 for the Ames pan evaporation station in central Iowa used to provide pan evaporation data for the Boone River basin. The Tables show the mean value and variance of the estimates of the regression coefficients a_0 through a_n for each month. In parenthesis shown are the resulting percent reduction in variance, the average daily pan evaporation and the percent missing values for each month. The maximum daily temperature was the variable that explained most of the variance in pan evaporation series. Polynomials of up to order 4 were fitted for each month. The order of the fitting polynomial that is displayed in Tables 3 and 4 was selected considering the variance of the coefficient estimates and the reduction of variance of the observed time series of pan evaporation. The regression explains a larger percent of the pan evaporation time series variance during the spring and summer months in Boone River. It is also evident from the table that missing values constitute mainly a winter problem when pan evaporation is lowest. Thus, evaporation computation values are to be trusted least during that season.

Once a complete pan evaporation series has been determined, conversion to potential evapotranspiration was accomplished, as is the case in the operational environment, by monthly correction coefficients. Usually, such coefficients exist for the drainage basins for which the Staff of the Office of Hydrology has calibrated the Sacramento model. Estimates of such coefficients are also published in the literature (e.g., Saxton and McGuinness, 1982, pg. 235, and Farnsworth, et al. 1982). We used what was available for the drainage basins under study and, then, adjusted such coefficients for a better model calibration to the long record as necessary. Table 5 presents the set of the monthly correction coefficients used for each of the two basins. In the case of the Boone River, we have included in parenthesis the estimated monthly averaged potential evapotranspiration for each of the months with no pan evaporation data. For those months, in the absence of daily potential evapotranpiration values, we have used the monthly averaged values as a best estimate of the potential evapotranspiration for each day of the month. It is noted that the

higher correction coefficients of the Boone River basin, especially for summer and early fall months are consistent with the increased role that crop transpiration plays for the Boone River basin. The later basin is in agricultural land with corn and soybeans being the main crops (growing season from May through August with 10 to 20 percent of canopy transpiring in October).

5. Model calibration and verification

It is hydrologic practice to use a split sample approach for the calibration and verification of mathematical models that are used in flow prediction. Such an approach was followed in this work. It is noted, however, that the length of the daily record for the basins that contains at least a standard climate period of 30 years and the purpose of the model use (soil moisture inference rather than flow prediction) may allow parameter estimation and fine-tuning using the total record. This issue of inference on climate scales given long records is an open issue, and more research is needed in this area.

a. Model calibration

Model calibration entails the determination of values for the parameters of the Sacramento and the nonlinear channel routing models. It is noted that calibration of the channel model parameters is necessary for the verification of the model with daily data and for daily basin outflow analysis. Soil saturation levels in different soil zones, flow-rate constants through the various soil zones, and the magnitude of permanently impervious and pervious areas within the drainage basin under consideration constitute the parameter vector for the Sacramento component. The nonlinear channel routing component is based on a power function relationship between the water stored within a channel reach and the outflow from that reach at a certain time. The coefficient and the exponent in the power function are channel component parameters.

Estimation of the values of model parameters was based on a combination of manual and automated procedures. Initial parameter estimation was done manually using various information sources for each basin, such as basin maps, soil information, vegetation and crop information, land use, previous calibrations for the basin or similar basins and the record of flow (e.g., Peck 1976). Once reasonable initial parameter values had been obtained, a guided downhill simplex method was used (e.g., Press, et al. 1989, pp. 289-293) to improve the parameter estimates. The criterion used was the cross correlation between observed and simulated daily flow. Once convergence was obtained, the calibration was fine-tuned manually using hydrologic criteria such

as the hydrograph peak magnitude and timing for significant flow events and the simulation error during extended low flow periods.

For the Bird Creek basin, the soil model has been calibrated by NWS-Office of Hydrology Staff as part of a forecast system (NWSRFS) that included unit hydrograph components. Such components have been replaced in the 3R model by nonlinear channel routing components (e.g., see Georgakakos and Smith, 1990). We "fine-tuned" the calibration of the Sacramento component parameters with the data from the calibration period (1956 through 1978) and calibrated the nonlinear channel routing component parameters for the Bird Creek basin. For fine tuning, periods of high flows and periods of low flows were examined separately and emphasis was placed on the daily flows rather than on summary statistics. Thus, accurate prediction of hydrograph peaks in terms of timing and magnitude guided this stage of calibration. An additional aspect of the calibration was to adjust the pan coefficients that were used to compute potential evapotranspiration from pan evaporation data so that the simulated outflow volume computed over the record matches the one observed. Table 6 presents the estimated values of the 3R model-parameters for the Bird Creek basin.

The Boone River basin with outlet at Webster City, Iowa was calibrated as part of the present research effort. Estimation consisted of the initial manual calibration phase based on topographic, land use and land cover characteristics, soil maps and a twenty-year calibration flow record (1968-1988). Then, as was the case for Bird Creek, the downhill simplex method followed by a "fine-tuning" manual calibration with emphasis on hydrologic criteria completed the parameter estimation phase. For this basin it was considered necessary to process the raw precipitation data through a snow accumulation and ablation model. The operational NWS snow model based on a surface-air temperature index approach (Anderson, 1973) was used. The model correction factor for the gage measurement deficiency was adjusted during the calibration period to improve the model performance during snowmelt periods. In addition to the snow model, and because of the pronounced frozen ground effects evident in this basin, the frozen ground procedure of the NWS as detailed in Anderson and Newman (1984) was also used. Freezing in a moist soil results in the reduction of the rates of soil moisture movement. The effects become less pronounced with decreasing soil moisture content. The parameters of the frozen ground model were those suggested by Anderson and Newman (1984) for the basins in Minnesota and Wisconsin. Table 6 presents the estimated values of the 3R model parameters for the Boone River basin in Iowa.

Comparison of the values of parameters between the two model basins reveals that they are basically similar. Notable differences exist in the soil capacities for tension water, with the Iowan basin having 35 percent higher capacity, thus retaining water for longer periods available for evaporation and transpiration. Such a difference is consistent with the fact that crops such as corn do better in Iowan soils. The Bird Creek basin carries a higher capacity for free water that

generates baseflow which together with the longer time constant of the primary free baseflow reservoir makes for longer baseflow recession hydrographs. An additional difference between the basins is manifested in the difference of the values of the channel flow times. The lower average channel slope of the Boone River basin makes for a flow time that is three times longer than the flow time in the Bird Creek basin, which has approximately the same area and shape.

b. Model verification

This is an important aspect of the subject research, since it helps establish model credibility in reproducing unobservable hydrologic features of drainage basins. The historical record of observed daily discharge that spans several decades is the main "ground truth" time series which the model-simulated discharge time series are compared with. Verification was done both at the monthly average level as is reproduced in Figures 6a-b and 7a-b for the Bird Creek and Boone River basins, respectively, but also at the daily level as is shown for the same basins in Figures 8a-b and 9a-b (Bird Creek), and 10a-b (Boone River). The solid lines in Figures 6a-b and 7a-b are the monthly averaged values of the observed discharge at the Bird Creek catchment outlet for the total historical period of record: January 1949 through December 1988, that includes both calibration and verification periods. The dashed line represents the corresponding simulated discharge. It is seen that at the monthly level of averaging the 3R model performs very well in reproducing features of the observed record. For example and for the Bird Creek basin, the low flow period from 1952 through 1957 has been accurately reproduced by the model. Similarly, the very high flow periods of the late fifties and late-eighties have also been accurately reproduced. It is also evident that the model responds with time constants similar to those of the observed record. Analogous comments can be made for the Boone River basin results in Figures 7a-b. The high flows of the early fifties and the sixties (verification period) have been simulated well, as are the low flows of the late fifties. In a few instances of high flow periods, i.e., in 1951, and 1961 of the verification period and in 1975 of the calibration period, the model substantially overestimated peak flow.

The seasonal variation of the sample long-term average and standard deviation of the observed 5-day averaged flows is well reproduced by the simulated flows. Figure 8a for Bird Creek and Figure 10a for Boone River show the observed (solid line) and simulated (dashed line) 40-year averages of each of the 73 5-day averaged flows in a year. Analogous plots for the sample standard deviation over 40 years of the same quantities are in Figures 8b for Bird Creek and in 10b for Boone River. The seasonal variability of the flow variance is reproduced remarkably well by the model for both basins. It is only the early spring average flows in Bird Creek that have been somewhat underestimated by the 3R model. Snowmelt events might be responsible for this discrepancy, as snow accumulation and ablation effects were ignored there.

The good model performance in reproducing the daily flows at the Bird Creek basin can be seen in Figures 9a and 9b. Both the periods depicted are typical of other periods in record with very low flows interrupted by sharply rising hydrographs that have been reproduced remarkably well, while the hydrograph shape has been preserved by the 3R model predictions. For example and in terms of statistics, the prediction residuals corresponding to Figure 9a (a three-month period of daily flows) had a mean that was 10 percent of the mean of the observed record, and a variance that was 20 percent of the observed record variance. The corresponding figures for the piece of record of Figure 9b are: 7 percent for the mean and 30 percent for the variance. The good reproduction of the low flows and the isolated fast rising hydrographs of Figure 9b speaks of the accurate representation of the upper soil characteristics in this period by the model.

The total-record sample cross-correlation between the observed and the simulated daily discharges at the Bird Creek catchment outlet was found to be equal to 0.85 while at the Boone River outlet it was 0.84, with a predictions residual mean that was less than 5 percent of the sample mean of the observed discharge time series for Bird Creek and 6 percent for Boone River. The model explained 74 percent of the daily observations variance for Bird Creek and 67 percent of the Boone River daily-flow variance.

It is thus concluded that the model is capable in reproducing the variability of the unobservable hydrologic variables such as upper soil moisture levels at least during the historical-record period and as an average over the drainage basin area (of the order of 2000 sqkm).

6. Temporal Analysis

Under the heading temporal analysis we include statistical analysis of time series of hydrologic and atmospheric variables that characterize the local hydrometeorological environment of a particular drainage basin. Thus, we have obtained second moment sample properties (i.e., sample means, variances, auto- and cross-correlation functions) of the observed time series of local temperature (daily min and max series), of observed and simulated discharge at the basin outlet, of observed mean areal rainfall over the basin, of mean areal observed potential and model-generated actual evapotranspiration, and of model-generated upper and lower soil water content. In particular, we have applied the temporal analysis on the anomalies of the variables with respect to their long term means rather than on the variables themselves for each of the time series. The anomalies are defined as the difference from the daily mean of each of the time series values as computed from all values in the record with the same date. Such an analysis assumes nonstationarity in the mean and has been commonly used to describe and diagnose period climate variations (e.g., Namias, 1978; Cayan and Peterson, 1989).

The purpose of this analysis is to: (1) establish the time scale of each variable for each of the three basins; (2) to attempt to determine feedbacks from the soil moisture to the local atmosphere (e.g., is the soil moisture forcing the surface temperature in relatively dry periods); (3) to determine whether there are differences in the results for high versus low soil moisture conditions and for high versus low flows; (4) to determine the seasonal character of the time series and of their cross-correlation properties; and (5) to compare the hydroclimatology of the two study basins.

Note that for the conclusions of the temporal analysis to hold true for the true hydrologic variables, it is only required that the second moment properties of the anomalies of the model-generated hydrologic variables to have the same temporal characteristics with the second moment properties of the anomalies of the true such variables. This is a much less stringent requirement than the requirement that the values of the the model-generated hydrologic variables (such as soil moisture) should represent exactly the true (but not observed) such variables.

a. Soil water

The monthly anomalies of upper and lower soil water are presented in Figures 11a-b for Bird Creek and in Figures 12a-b for Boone River in units of standard deviations and for the 40-year record. Upper soil water is the sum of the model upper zone tension and free water contents, and lower soil water is the sum of the model lower zone tension and free water contents. A smoothing algorithm was applied on the monthly data to show the low frequency variation on annual time scales. It is evident that low frequency variations of upper and soil water are very similar for each of the two basins, and that negative anomalies, corresponding to drier than average soil conditions, have larger magnitudes than positive anomalies. The latter feature is largely due to the runoff generating mechanism of the upper soil that prohibits large positive soil anomalies. The Figures also show important similarities between the soil moisture histories of the two basins. The low soil water periods of the mid and late fifties and the wetter than average early sixties are features of both basin histories. There are important differences, too. Examples are the out of phase period in late sixties between the soil water histories of the two basins, and the absence of the Boone River extended dry period 1976-1978 in the history of the Bird Creek soil water content. Such similarities and differences are indicative of the disparate scales soil water dynamics possesses, that include localized and mesoscale phenomena.

The seasonal variation of the upper (solid line) and lower (dashed line) soil water averaged over 5-day periods are depicted in Figures 13 (Bird Creek) and 14 (Boone River). There is a pronounced seasonal cycle with maxima in the spring (upper soil) and summer (lower soil), and minima in the late summer and early fall. The seasonal cycle is more pronounced in the upper soil water of the Bird Creek basin that reaches 80 percent saturation in the spring to fall to less than 50

percent saturation in late summer. Overall, the Boone River basin exhibits smoother seasonal transitions in saturation ratio, with a stronger gradient in early spring due to significant snowmelt. The results in Figures 13 and 14 indicate that the Boone River model soils are more moist on the average than the Bird Creek soils, in accordance to the observed soil types in the basins of study. There is a three month delay in the maximum of the lower soil water after the maximum of the upper soil water in both basins.

Figures 13 and 14, when used in conjunction with Figures 8a and 10a, shed light into the mechanisms of flow production in the two basins over climatic scales. In the Boone River, the first flow peak of Figure 10a is in phase with the peak of the upper soil water in Figure 14. The corresponding 5-day seasonal cycle of the difference between rainfall plus snowmelt and evapotranspiration (P-ET, dotted line) shows maximum net basin inflow during this period. It is clear then that it is upper soil saturation that generates the spring flow peak. The second flow peak in Figure 10a is in phase with the peak of the lower soil water in Figure 14 when the upper soil is still at high levels of saturation and when (P-ET) is still positive. The summer peak is generated, therefore, by saturation of the total soil column, before the high evapotranspiration rates deplete soil moisture. It is notable that the decline in soil water content coincides with the time when P-ET becomes negative. In contrast, Bird Creek exhibits three important flow maxima: one in the spring, one in the summer and one in the fall (Figure 8a). The first two peaks are analogous to those of Boone River (compare Figures 13 and 8a). The last peak in Bird Creek is due to unusually high rainfall in the fall which drives the dry late summer soils to a moist state following a steep gradient. It is clearly the atmosphere in this case that is forcing the land surface! When comparing Figures 13 and 14 it becomes apparent that the Bird Creek basin is a much more dynamic basin as far as the soil water content is concerned, with steeper gradients of P-ET. It is generally expected then that it has a closer association with the local and regional atmosphere than the less responsive Boone River basin, on a time scale spanning a few days. It is also clear that the Boone River basin is likely to be more resilient to changes in local and regional climate.

b. Temporal coherence of local observations and soil water estimates

Study of the seasonal autocorrelations of the observed local hydrometeorological variables including soil water content and actual evapotranspiration (the latter two as estimated by the 3R model) aids the establishment of local temporal scales of the underlying physical processes. As examples of our analysis plots we present in Figure15 the autocorrelation functions of the rainfall, potential evapotranspiration, maximum temperature and upper soil water for Bird Creek, for spring (15a) and summer (15b). Figures 16a (spring) and 16b (summer) show the autocorrelation functions of the same variables for Boone River. Analogous plots have been produced (not

shown) for the rest of the seasons and local hydrometeorological variables for both basins. Important results are outlined next.

For all seasons and both basins, the upper- and lower-soil water autocorrelations persist much longer than the autocorrelations of the extreme daily temperatures, evaporation (actual and potential), and precipitation. As an example and for the Boone River basin, only summer potential evaporation (of the atmospheric-forcing variables) has an autocorrelation value as high as 0.3 at a 10-day lag. In contrast, upper soil water has a value that ranges between 0.7 (lowest during summer) and 0.9 (highest during winter) at the same lag and for the same basin. Assuming that an autocorrelation value of 0.2 or lower indicates absence of a relationship, estimates of the upper bound of time scales can be obtained from the autocorrelation functions.

As regards the atmospheric forcing variables and for Boone River during spring and summer, the time scale of maximum temperature is 10 days, of rainfall is less than 5 days, and of potential evapotranspiration ranges from 10 days in the spring up to a month in the summer (when it attains the largest absolute value). For Bird Creek, the analogous values of the atmospheric-forcing variables for spring and summer are: 5 days in the spring and about a month in the summer for maximum temperature, less than 5 days for rainfall, and 5 days in the spring and more than a month in the summer for potential evapotranspiration. The significant difference between the two basins in the persistence of maximum daily temperature in the summer is an indication of the different forcing/feedback scenarios that the two basins have experienced during the past 40 summers.

As a result of the soil integration effect over time, the basin soil water variables exhibit high persistence for all seasons. In general, the Bird Creek basin exhibits smaller temporal time scales in soil water than the Boone River basin does, and upper soil water is less persistent than lower soil water for both basins. For Bird Creek the scale of the upper soil water is about 1.5 months long in the spring dropping to a value of a month in the summer. The analogous figures for Boone River are: more than 2 months in the spring and about 1.5 months in the summer. There is a discernable seasonal variation of persistence. Time scales are greatest in winter and least in summer for both basins. It is indicative of more intense dynamics in the summer.

The autocorrelation functions of observed and simulated flow for the spring and summer seasons are shown in Figures 17 (Bird Creek) and 18 (Boone River). Typical time scales of flow are 10 to 15 days, with Boone River exhibiting longer time scales indicating that the Bird Creek basin is "flashier" than the Boone River one. Persistence is very similar during spring and summer in Bird Creek, while spring flows in Boone River seem to have longer persistence than summer flows. The two figures show that the persistence of the simulated flows bears good correspondence to that of the observed flows, apart from the long lags (greater than a month) during spring in Boone River where the simulated flows have an autocorrelation value that

underestimates the autocorrelation value of the observed flows (which is quite low). The discrepancy which has also been observed in fall and winter for the Boone River basin is probably related to the persistence properties of the estimates of potential evapotranspiration during those seasons when most of the "missing" data have been detected (see Table 4).

c. Soil water feedbacks to the local atmosphere

Cross-correlation functions were used to detect significant relationships between atmospheric forcing and soil water beyond those that are implicit in the formulation of the 3R model. The cross-correlations were computed using 5-day-averaged data with the seasonal averages over 40 years removed. As an example, we present in Figure 19 the cross-correlation function between rainfall and upper soil water for the Bird Creek basin and for each season using the total record. The corresponding cross-correlation functions between maximum temperature and upper soil water are shown in Figure 20. Positive lags indicate that rainfall (Figure 19) or maximum temperature (Figure 20) lead the upper soil water. As expected, in Figure 19 the maximum of the cross-correlation function occurs on a positive lag (10 days) indicating that rainfall strongly leads upper soil water with a 10-day lag. Such a result is a confirmation of the causal relationship present in the 3R model formulation. Figure 19 also makes apparent that for negative or zero lags there is no relationship between rainfall and soil for all seasons in this basin. This supports the conclusion that no strong local hydrologic cycle exists in this region that would require strong water feedback from the soil to the atmosphere.

The maximum of the cross-correlation function of maximum temperature vs. upper soil water also occurs at short positive lags (5 to 10 days). However there are significant cross-correlation values for negative and zero lags when the upper soil water *leads* maximum temperature in the summer. A cross-correlation value of about -0.5 was found for zero lag and a value of about -0.4 was found for a negative lag of 5 days (Figure 18). Such a result is not an artifact of the model used, as maximum temperature is a model input and soil water is a model output. It indicates the presence of feedback from the soil water to the local (and possibly regional) atmosphere, which is presumably due to evapotranspiration. Drier soil is thus historically associated with hotter surface air. Similar results to those presented in Figures 19 and 20 have been obtained for the Boone River basin. The rainfall vs. upper soil water cross-correlation functions are very similar to those in Figure 19 and are not presented here. Figure 21 presents the maximum temperature vs. upper soil water cross-correlation functions as they are different from those of Figure 20 in that, a) cross-correlation values are generally smaller in Boone River, apart from those computed for the spring season which attain values close to the summer values, and b) the maximum cross-correlation values for spring and summer are at zero lag. The feedback from soil to atmosphere appears to be weaker in this basin.

The fact that the feedback from soil to atmosphere seems to be stronger in the summer, when the soil water content is below average, motivates the study of the cross-correlation function computed for those soil water values that are below a certain set threshold value. Significant results were obtained for the summer season in Bird Creek (Figure 22) and for both the spring and summer seasons in Boone River (Figures 23 and 24). Figure 22 presents the cross-correlation values between maximum temperature and upper soil water for several negative lags (soil water leading maximum temperature) and for several upper soil water threshold values (in mm). On the same plot, an upper bound of the error in computing the correlation coefficient from a small sample is plotted for each case (as the threshold decreases so is the number of pairs that enter the computation). The bound was computed based on $\sigma_\rho = N^{-1/2}$ (applicable for N>20, e.g., Press, et al. 1989, pp. 484-487), and is at $2\sigma_\rho$. It is apparent that the lower the threshold, the stronger the feedback from the soil water to surface air temperature becomes. Cross-correlation values greater than 0.4 have been obtained for negative lags of 5 and 10 days for a relatively wide range of thresholds (20 mm wide). The cross-correlation values reach near 0.6 for excessively dry soils. This rather strong local feedback together with the strong temperature forcing (positive lags in Figure 19) might be the mechanism by which initially dry summers become hotter and drier in this region. No significant feedback was detected in this basin during the spring.

Analogous results for spring and summer in Boone River are shown in Figures 23 and 24, respectively. Feedback is weaker in the summer for Boone River as compared to that of Bird Creek but it is still significant with cross-correlation values that reach -0.5 for a negative 5-day lag. During spring there is a sharp increase in correlation value as the upper soil water becomes progressively drier with values better than -0.6 for up to a 15-day negative lag. Such a result has implications for predictability studies in this basin and indicates the persistent nature of the feedback from soil to atmosphere in this region.

Cross-correlation analysis was also performed between the upper soil and maximum temperature for *increasing* upper soil water threshold values. The strongest correlations exist in the summer season for Bird Creek with values near -0.6 reached for 5- and 10-day negative lags (Figure 25) and when the upper soil was 75 percent saturated. Analogous cross-correlation values for Boone River (not shown) reach -0.4 for 5- and 10-day lags in the spring and for a 5-day lag in the summer.

6. Summary and conclusions

REFERENCES

Anderson, E. A., 1973: National Weather Service River Forecast System-Snow Accumulation and Ablation Model. *NOAA Technical Memorandum NWS HYDRO-17*. Office of Hydrology, National Weather Service, NOAA, Silver Spring, Maryland.

Anderson, E. A.,and P. J. Neuman, 1984: The Role of Snow and Ice in Northern Basin Hydrology. *Proceedings of the Fifth Northern Research Basins Symposium*. Vierumaki, Finland, March 19-23, 1984, pp. 5.1-5.14.

Anthes, Richard A., and Ying-Hwa Kuo, 1986: Namias Symposium, J.O. Roads, ed., *SIO Reference Series 86-17*, August, 1986, pp. 132-147.

Barnston, A. G., and R. E. Livezey, 1987: Classification, Seasonality and Persistence of Low-Frequency Atmospheric Circulation Patterns. *Mon. Wea. Rev., **115**,* 1083-1126, 1987.

Brazil, L., 1989: Multilevel calibration strategy for complex hydrologic simulation models. *NOAA Technical Report, NWS 42*, NOAA - National Weather Service, Silver Spring, Maryland, 178 pages.

Burnash, R. J. C., R. L. Ferral, and R. A. McGuire, 1973: *A generalized streamflow simulation system - Conceptual modeling for digital computers*. National Weather Service - NOAA, and State of California Department of Water Resources Technical Report, Joint Federal-State River Forecast Center, Sacramento, California.

Cayan, Daniel R., and D. H. Peterson, 1989: The Influence of North Pacific Atmospheric Circulation on Streamflow in the West.*Geophysical Monograph 55*, available from U.S. Geological Survey, MS-496, 345 Middlefield Road, Menlo Park, CA 94025.

Day, G. N., 1985: Extended Streamflow Forecasting Using NWSRFS. *J. of Water Resources Planning and Management **111**(2)*, 157-170.

Gelb, A., (ed.), 1974: *Applied Optimal Estimation*, MIT Press, Cambridge, Mass., 203-225.

Georgakakos, K. P., 1986: A generalized stochastic hydrometeorological model for flood and flash-flood forecasting, 1, Formulation. *Water Resources Research **22**(13)*, 2083-2095.

Georgakakos, K. P., 1987: Real Time flash Flood Prediction. *J. Geophysical Research - Atmospheres **92**(D8)*, 9615-9629.

Georgakakos, K. P., and R. L. Bras, 1982: Real time statistically linearized adaptive flood routing. *Water Resources Research **18**(3)*, 513-524.

Georgakakos, K. P., Rajaram, H., and S. G. Li, 1988: On improved operational hydrologic forecasting of streamflows. *IIHR Report No. 325*, Department of Civil and Environmental Engineering and Iowa Institute of Hydraulic Research, The University of Iowa, Iowa City, Iowa, 162 pages.

Georgakakos, K. P., and G. F. Smith, 1990: On improved operational hydrologic forecasting: Results from a WMO real-time forecasting experiment. *Journal of Hydrology **114***, 17-45.

Gleick, P., 1987: Regional Hydrologic Consequences of Increases in Atmospheric CO2 and Other Trace Gases. *Climate Change **10***, 137-161.

Karl, T. R., and Knight, R. W., 1985: Atlas of Monthly and Seasonal Precipitation Departures from Normal (1895-1985) for the Contiguous United States, *Historical Climatology Series 3-12*, p. 213. Available from National Climate Data Center, Asheville, NC.

Karl, Thomas R., 1986: The Relationship of Soil Moisture Parameterizations to Subsequent Seasonal and Monthly Mean Temperature in the United States. *Mon. Wea. Rev., **114***, 675-686.

Kitanidis, P. K., and R. L. Bras, 1978: Real time forecasting of river flows. R. M. Parsons Laboratory for Water Resources and Hydrodynamics, Dept. Civil Engineering, *MIT, Technical Report No. 235*, 324 pages.

Krajewski, W. F., 1987: Cokriging radar-rainfall and rain-gauge data. *J. Geophysical Research - Atmospheres **92(D8)***, 9571-9580.

Larson, L. W., 1975: Precipitation Model. *National Weather Service River Forecast System (NWSRFS) User's Manual*, Hydrologic Research Laboratory, NWS-NOAA, Silver Spring, Maryland.

Larson, L. W., and S. VanDemark, 1979: Mean Areal Precipitation Program (MAP). *National Weather Service River Forecast System (NWSRFS) User's Manual,* Hydrologic Research Laboratory, NWS-NOAA, Silver Spring, Maryland.

Lettenmaier, Dennis P., 1990: Hydrologic Sensitivities of the Sacramento-San Joaquin River Basin, California, to Global Warming. *Water Resources Research, **26(1)***, 69-86.

Namias, Jerome, 1978: Persistence of U.S. Seasonal Temperatures up to One Year. *Mon. Wea. Rev., **106(11)***, 1557-1567.

Peck, E. L., 1976: Catchment modeling and initial parameter estimation for the National Weather Service River Forecast System. *NWS HYDRO-31*, National Weather Service - NOAA, Silver Spring, Maryland.

Press, W. H., Flannery, B. P., Teukolsky, S. A., and W. T. Vetterling, *Numerical Recipies, The Art of Scientific Computing (Fortran Version)*, Cambridge University Press, New York, 702 pages, 1989.

Rajaram, H., and K. P. Georgakakos, 1989: Recursive parameter estimation of hydrologic models. *Water Resources Research 25(2)*, 281-294, 1989.

Rasmusson, Eugene M., 1967: Atmospheric Water Vapor Transport and the Water Balance of North America: Part I. Characteristics of the Water Vapor Flux Field. *Mon. Wea. Rev., **95(7)***, 403-426.

Rind, D., 1982: The Influence of Ground Moisture in North America on Summer Climate as Modelled in the GISS GCM. *Mon. Wea. Rev., **110***, 1487-1494.

Rowntree, P. R., and J. A. Bolton, 1983: Simulations of the Atmospheric Response to Soil Moisture Anomalies over Europe. *Quart. J. Roy. Meteor. Soc.*, ***109***, 501-526.

Schaake, J. C., 1990: From Climate to Flow. *Climate Change and U.S. Water Resources*, ed. P. E. Waggoner, John Wiley and Sons, New York, 177-206.

Smith, J. A., Day. G. N., and M. D. Kane, 1991: A Nonparametric framework for long-range streamflow forecasting. *WMO/TD-No. 428*, World Meteorological Organization, Geneva, Switzerland, 28 pages.

Dool, H. M., 1984: Long-lived Air Temperature Anomalies in the Midlatitudes Forced by the Surface. *Mon. Wea. Rev.*, ***112***, 555-562.

van den Dool, H. M., 1989: Monthly Precipitation-Temperature Relations, the United States, 1931-1987. *Proceedings of the Thirteenth Annual Climate Diagnostics Workshop*, October 31-November 4, 1988.

Walsh, John E., W. H. Jasperson, and B. Ross, 1985: Influences of Snow Cover and Soil Moisture on Monthly Air Temperature. *Mon. Wea. Rev.*, ***113***, 756-768.

Walsh, John E., 1986: Surface-Atmosphere Interactions over the Continents: The Namias Influence. Namias Symposium, J.O. Roads, ed., *SIO Reference Series 86-17*, August, 1986, pp. 121-131.

WMO-World Meteorological Organization, 1990: Scientific Plan for the Global Energy and Water Cycle Experiment. World Climate Research Programme, *WMO/TD - No. 376, WCRP - 40*, Geneva, Switzerland, 83 pages.

Table 1. Basin Description and Data Availability for the Application Drainage Basins

	Basin I	Basin II
Basin Name:	Bird Creek	Boone River
Outflow at:	Sperry, OK	Webster City, IA
Area *(sqkm)*:	2344.	2160.
Pan Evap and Temp Station:	Hulah Dam, OK	Ames, IA
No. Precip Stations:	12	10

Table 2. Hydrometeorological Characteristics of Study Basins.

	Bird Creek	Boone River
Prec*(m/yr)*:	0.9	0.8
Tmax*(dgr F)*:	72	60
Tmin*(dgr F)*:	50	40
Pan Evap*(m/yr)*:	1.8	1.2
Outflow*(m/yr)*:	0.2	0.2
Runoff Coef.: *(Outflow/Prec)*	0.22	0.25

Table 3. Regression Results for Pan Evaporation with Daily Maximum Temperature

Hulah Dam, OK, January 1949 through December 1988

$$Pan\ Evap = a_0 + a_1\ T_{max} + a_2\ T_{max}^2 + a_3\ T_{max}^3$$

MONTH	a_0: Mean	a_0: Variance	a_1: Mean	a_1: Variance	a_2: Mean	a_2: Variance	a_3: Mean	a_3: Variance
January	0.739E+00	0.190E-01	0.102E+00	0.793E-04	0.124E-02	0.166E-07		
(7%	*2.16 mm/d*	*82% missing)*						
February	0.134E+01	0.144E-01	0.909E-01	0.434E-04	0.122E-02	0.715E-08		
(22%	*2.87 mm/d*	*72% missing)*						
March	0.107E+01	0.609E-02	0.165E+00	0.119E-04	0.218E-02	0.198E-08		
(33%	*4.56 mm/d*	*29% missing)*						
April	0.692E+00	0.973E-02	0.197E+00	0.107E-04	0.260E-02	0.194E-08		
(29%	*6.42 mm/d*	*8% missing)*						
May	-0.620E+00	0.221E-01	0.208E+00	0.174E-04	0.267E-02	0.343E-08		
(17%	*6.63 mm/d*	*11% missing)*						
June	-0.288E+01	0.412E-01	0.243E+00	0.220E-04	0.363E-02	0.476E-08		
(17%	*7.88 mm/d*	*9% missing)*						
July	-0.500E+01	0.410E-01	0.269E+00	0.159E-04	0.408E-02	0.375E-08		
(31%	*8.83 mm/d*	*10% missing)*						
August	-0.538E+01	0.366E-01	0.269E+00	0.152E-04	0.413E-02	0.357E-08		
(32%	*8.45 mm/d*	*5% missing)*						
September	0.979E+01	0.299E+00	-0.549E+00	0.111E-02	0.957E-02	0.854E-07	0.157E-03	0.469E-10
(36%	*6.44 mm/d*	*5% missing)*						
October	0.604E+00	0.113E-01	0.126E+00	0.108E-04	0.177E-02	0.199E-08		
(24%	*4.67 mm/d*	*6% missing)*						
November	0.104E+01	0.853E-02	0.100E+00	0.167E-04	0.120E-02	0.268E-08		
(19%	*3.13 mm/d*	*28% missing)*						
December	0.127E+01	0.141E-01	0.662E-01	0.539E-04	0.676E-03	0.103E-07		
(10%	*2.21 mm/d*	*72% missing)*						

Table 4. Regression Results for Pan Evaporation with Daily Maximum Temperature

Ames, IA, January 1949 through December 1988

$$Pan\ Evap = a_0 + a_1\ T_{max} + a_2\ T_{max}^2 + a_3\ T_{max}^3$$

MONTH	a_0: Mean	a_0: Variance	a_1: Mean	a_1: Variance	a_2: Mean	a_2: Variance	a_3: Mean	a_3: Variance
January	----	----	----	----	----	----	----	----
(100% missing)								
February	----	----	----	----	----	----	----	----
(100% missing)								
March	----	----	----	----	----	----	----	----
(100% missing)								
April	0.143E+01	0.321E-01	0.684E-01	0.483E-03	0.614E-02	0.395E-06		
(45%	*4.64mm/d*	*25% missing)*						
May	-0.630E+00	0.124E-01	0.226E+00	0.208E-04	0.293E-02	0.664E-08		
(41%	*6.15mm/d*	*3% missing)*						
June	-0.395E+01	0.417E-01	0.404E+00	0.535E-04				
(36%	*7.22 mm/d*	*3% missing)*						
July	-0.500E+01	0.637E-01	0.404E+00	0.720E-04				
(33%	*6.95 mm/d*	*2% missing)*						
August	0.602E+01	0.147E+01	-0.368E+00	0.749E-02	0.125E-01	0.235E-05		
(33%	*5.82 mm/d*	*1% missing)*						
September	0.369E+01	0.248E+00	-0.206E+00	0.179E-02	0.973E-02	0.780E-06		
(38%	*4.63 mm/d*	*4% missing)*						
October	0.186E+01	0.424E-01	-0.322E-01	0.547E-03	0.564E-02	0.403E-06		
(31%	*3.36 mm/d*	*5% missing)*						
November	----	----	----	----	----	----	----	----
(100% missing)								
December	----	----	----	----	----	----	----	----
(100% missing)								

Table 5. Monthly Pan Evaporation Correction Coefficients

MONTH	BIRD CREEK	BOONE RIVER
January	.23	*(0.5 mm/d)*
February	.23	*(0.6 mm/d)*
March	.22	*(1.2 mm/d)*
April	.22	0.40
May	.36	0.40
June	.47	0.44
July	.48	0.69
August	.48	0.88
September	.46	0.86
October	.43	0.68
November	.29	*(1.0 mm/d)*
December	.23	*(0.5 mm/d)*

Table 6. Estimates of Parameter Values for the Sacramento and Channel Routing Components

PARAMETER	BIRD CREEK	BOONE RIVER
Upper zone tension water capacity	120 *mm*	160 *mm*
Upper zone free water capacity	15 *mm*	10 *mm*
Lower zone tension water capacity	160 *mm*	220 *mm*
Lower zone primary free water capacity	140 *mm*	24 *mm*
Lower zone supplementary free water capacity	14 *mm*	15 *mm*
Interflow coefficient	0.3 day^{-1}	0.17 day^{-1}
Primary baseflow coefficient	0.013 day^{-1}	0.059 day^{-1}
Supplementary baseflow coefficient	0.13 day^{-1}	0.048 day^{-1}
Coefficient of increase in percolation at maximum vertical gradient	48	186
Exponent in percolation function for unsaturated lower zone	2.1	1.8
Fraction of free percolated water	0.02	0.44
Baseflow fraction not flowing through basin outlet	0.78	0.66
Maximum fraction of impervious area	0.17	0.19
Fraction of permanently impervious area	0.001	0.026
Number of linear channel reservoirs for routing	2	2
Time constant of channel flow	1.3 *days*	4 *days*

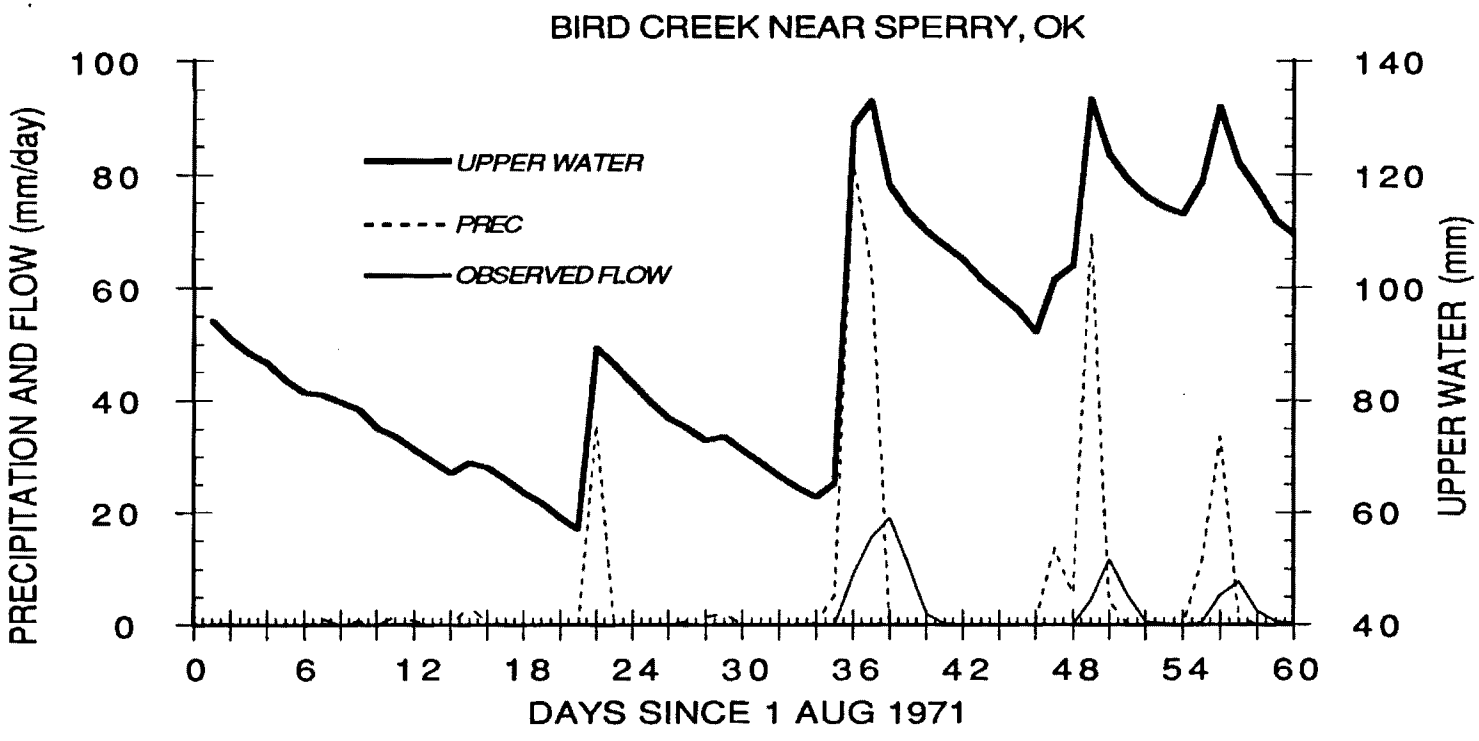
BIRD CREEK NEAR SPERRY, OK
PRECIPITATION AND FLOW (mm/day)
UPPER WATER (mm)
UPPER WATER
PREC
OBSERVED FLOW
100
80
60
40
20
0
140
120
100
80
60
40
0
6
12
18
24
30
36
42
48
54
60
DAYS SINCE 1 AUG 1971

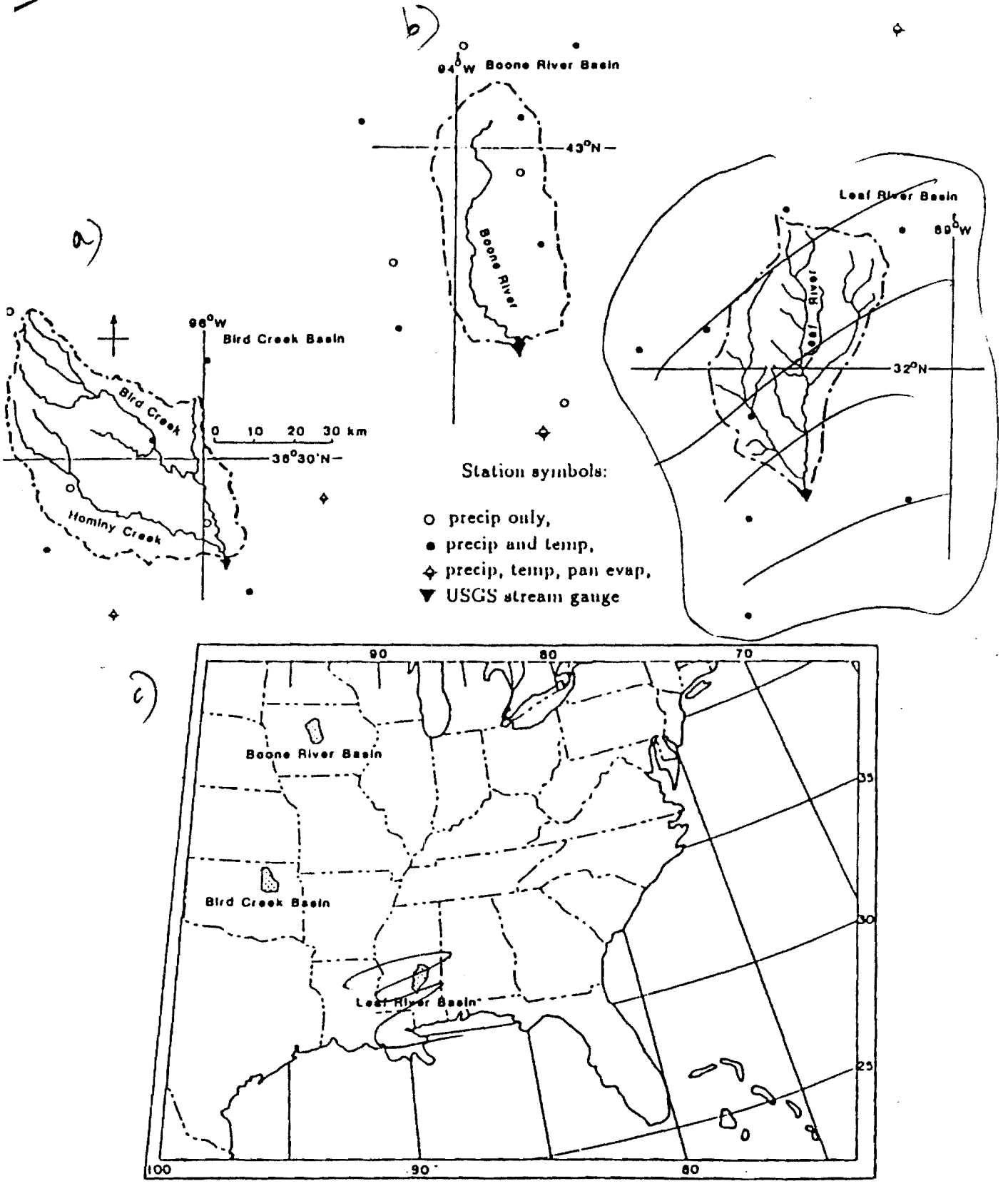

Fig. 1. Bird Creek OK, Boone River IA, ~~and Leaf River, MS~~ catchments and data stations.

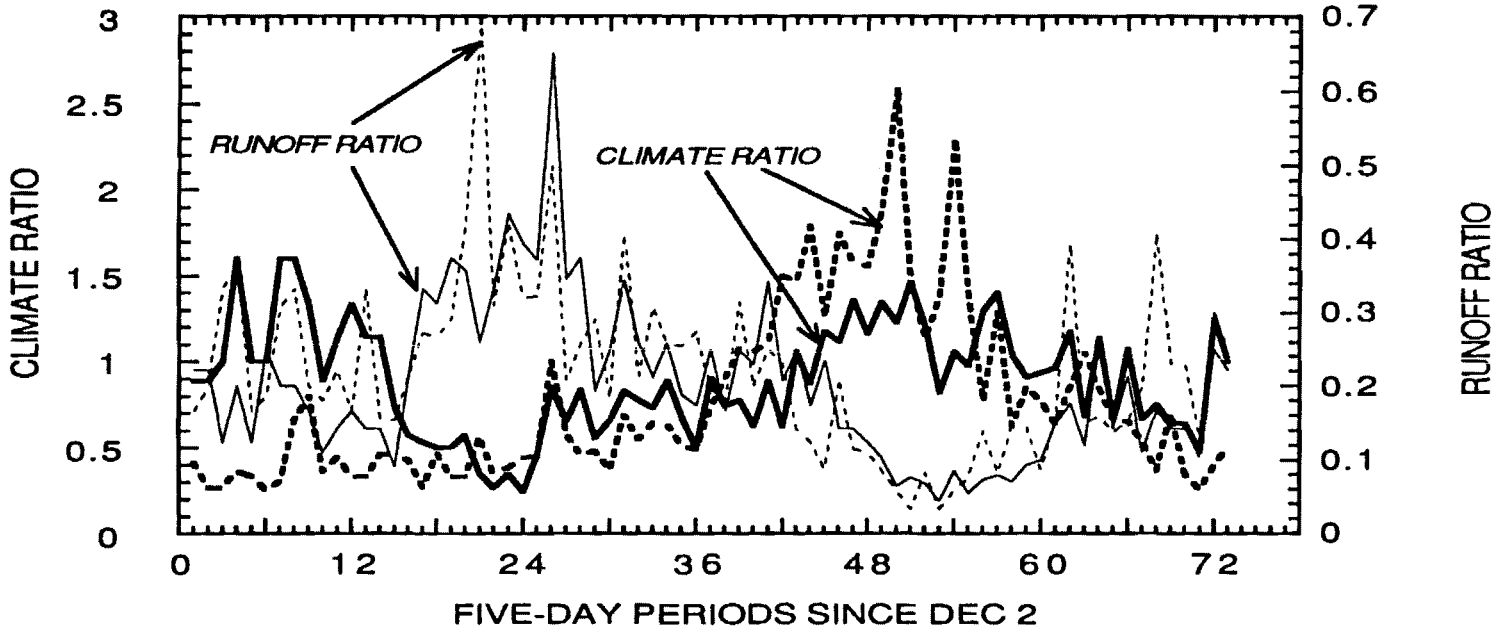
CLIMATE RATIO
RUNOFF RATIO
RUNOFF RATIO
CLIMATE RATIO
3
2.5
2
1.5
1
0.5
0
0.7
0.6
0.5
0.4
0.3
0.2
0.1
0
0
12
24
36
48
60
72
FIVE-DAY PERIODS SINCE DEC 2

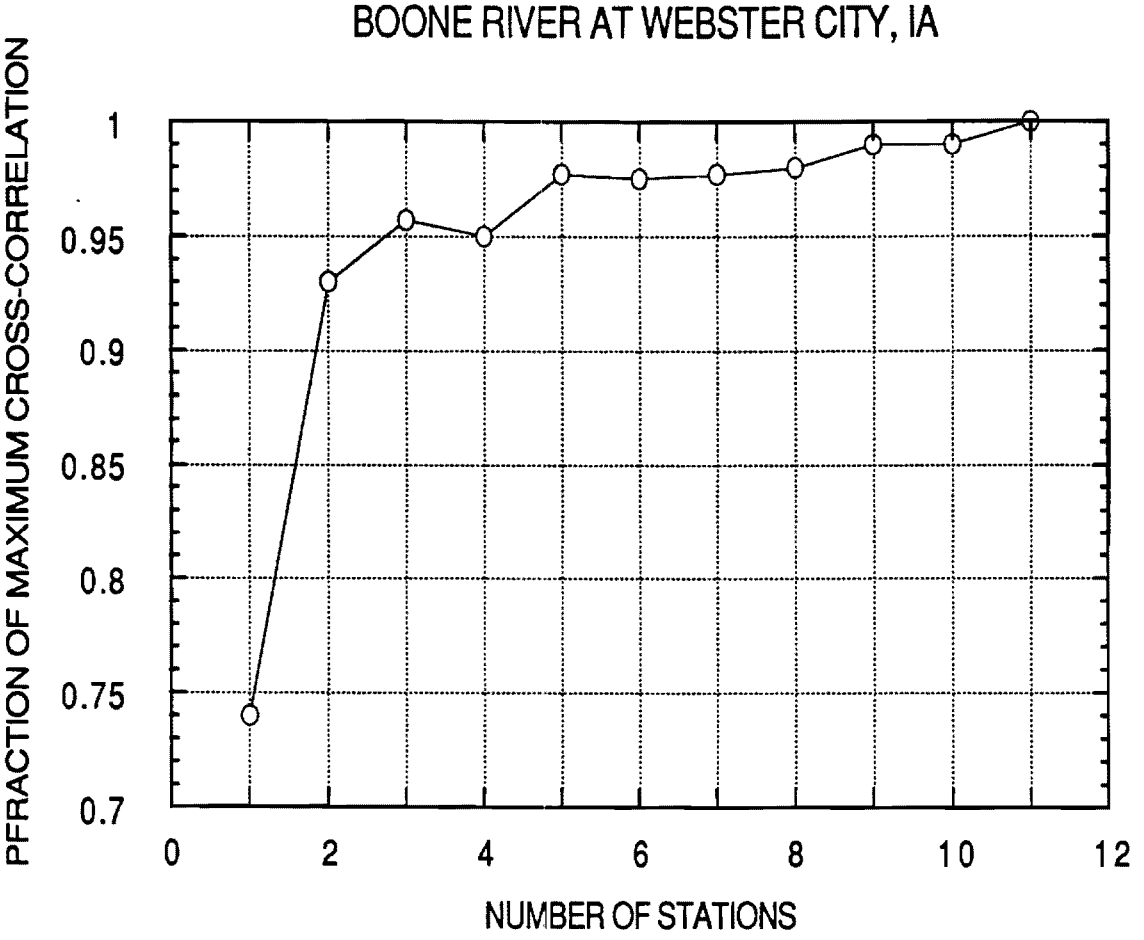
BOONE RIVER AT WEBSTER CITY, IA
PFRACTION OF MAXIMUM CROSS-CORRELATION
1
0.95
0.9
0.85
0.8
0.75
0.7
0
2
4
6
8
10
12
NUMBER OF STATIONS

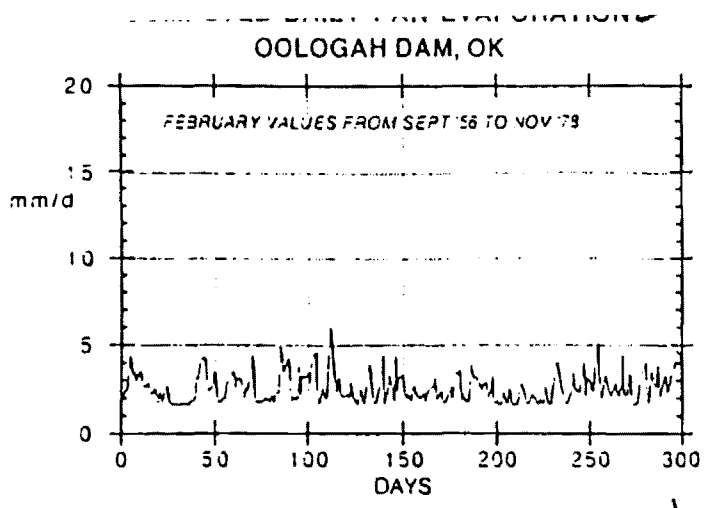

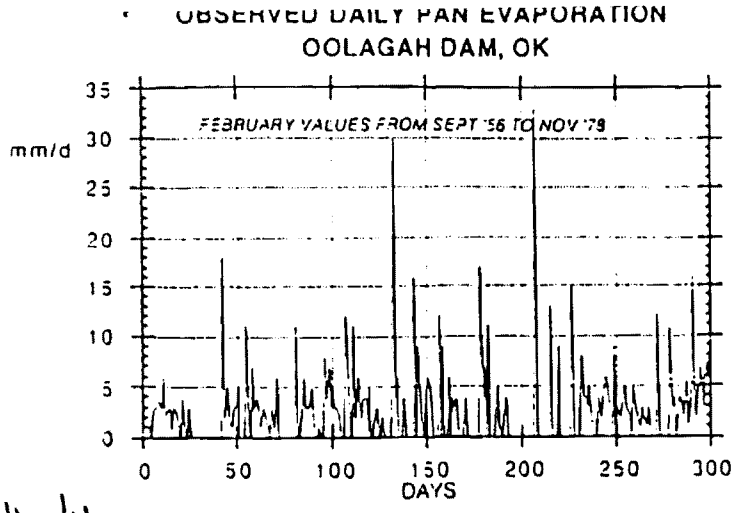

Fig. 2. Daily pan evaporation, a) adjusted, and b) observed for Oologah Dam, OK, Februaries 1957-1973.

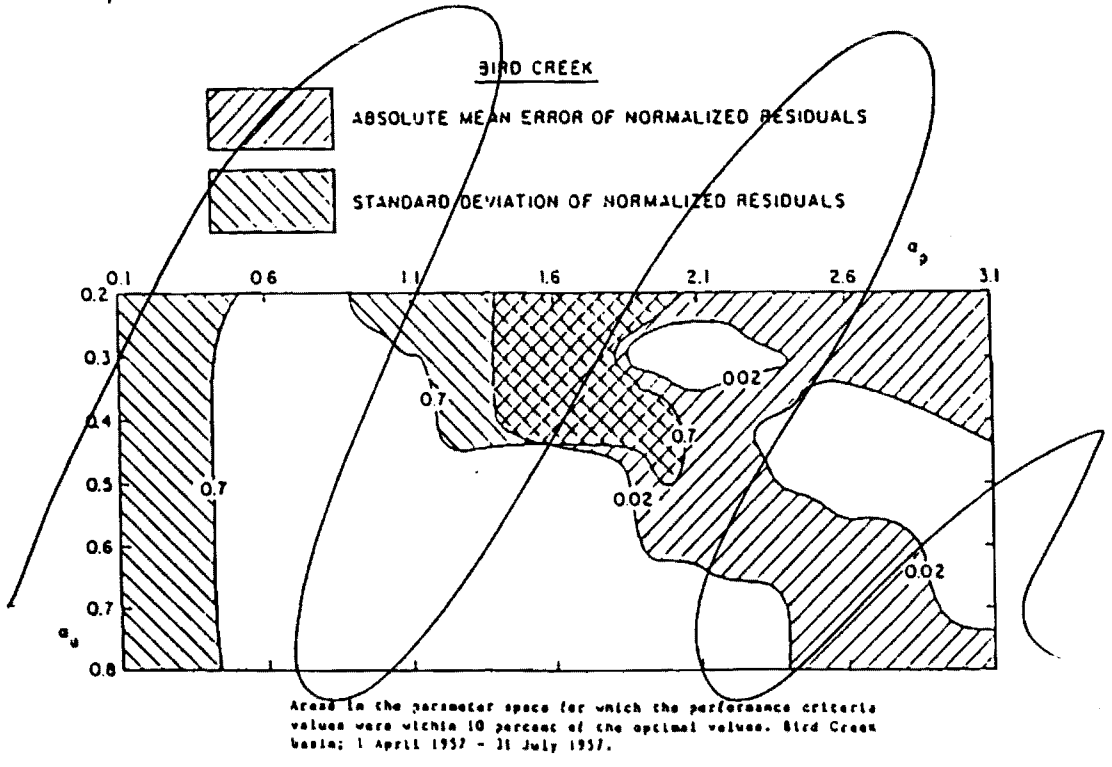

Areas in the parameter space for which the performance criteria values were within 10 percent of the optimal values. Bird Creek basin; 1 April 1957 - 31 July 1957.

Fig. 3. Normalized residuals, stochastic-dynamical HFS model calibration.

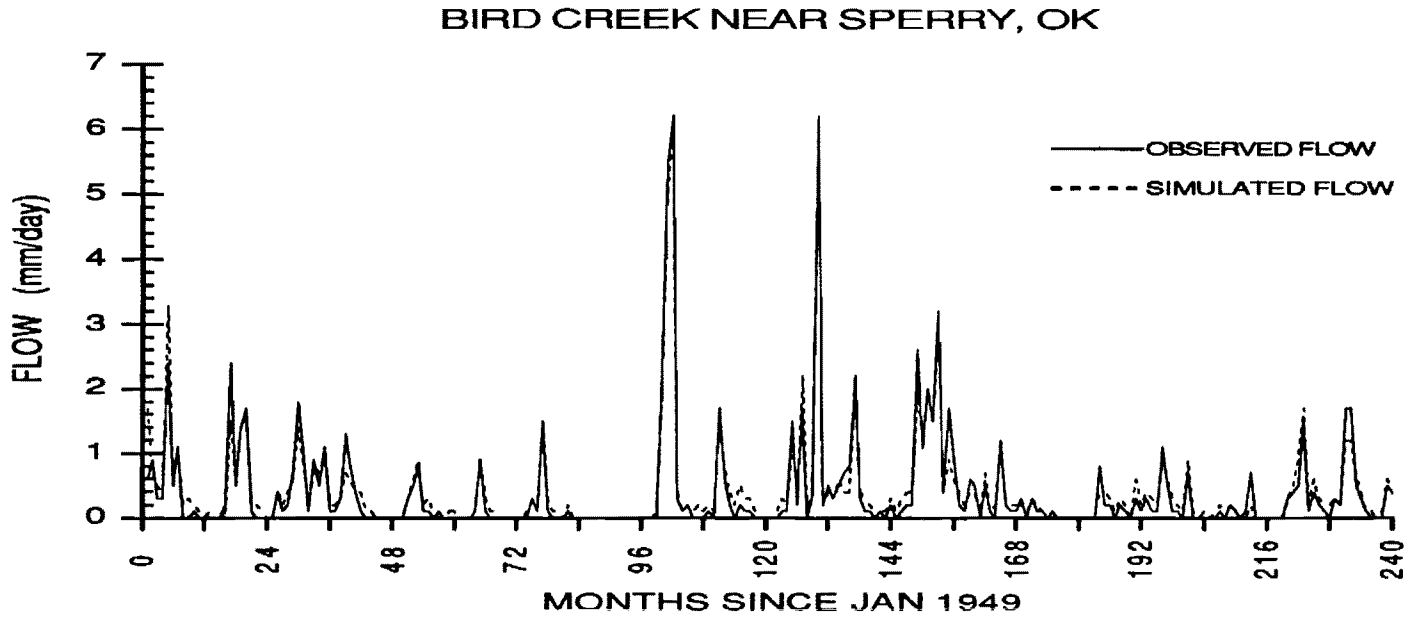
BIRD CREEK NEAR SPERRY, OK
FLOW (mm/day)
0
1
2
3
4
5
6
7
OBSERVED FLOW
SIMULATED FLOW
0
24
48
72
96
120
144
168
192
216
240
MONTHS SINCE JAN 1949

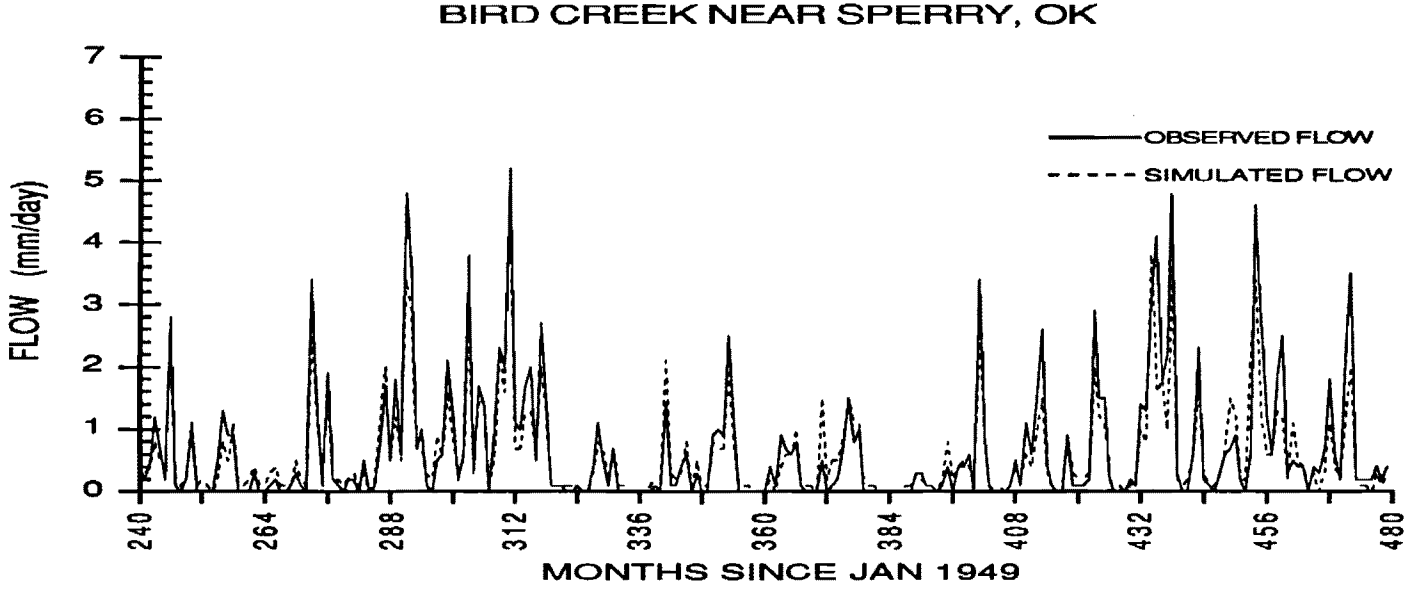
BIRD CREEK NEAR SPERRY, OK
FLOW (mm/day)
0
1
2
3
4
5
6
7
OBSERVED FLOW
SIMULATED FLOW
240
264
288
312
336
360
384
408
432
456
480
MONTHS SINCE JAN 1949

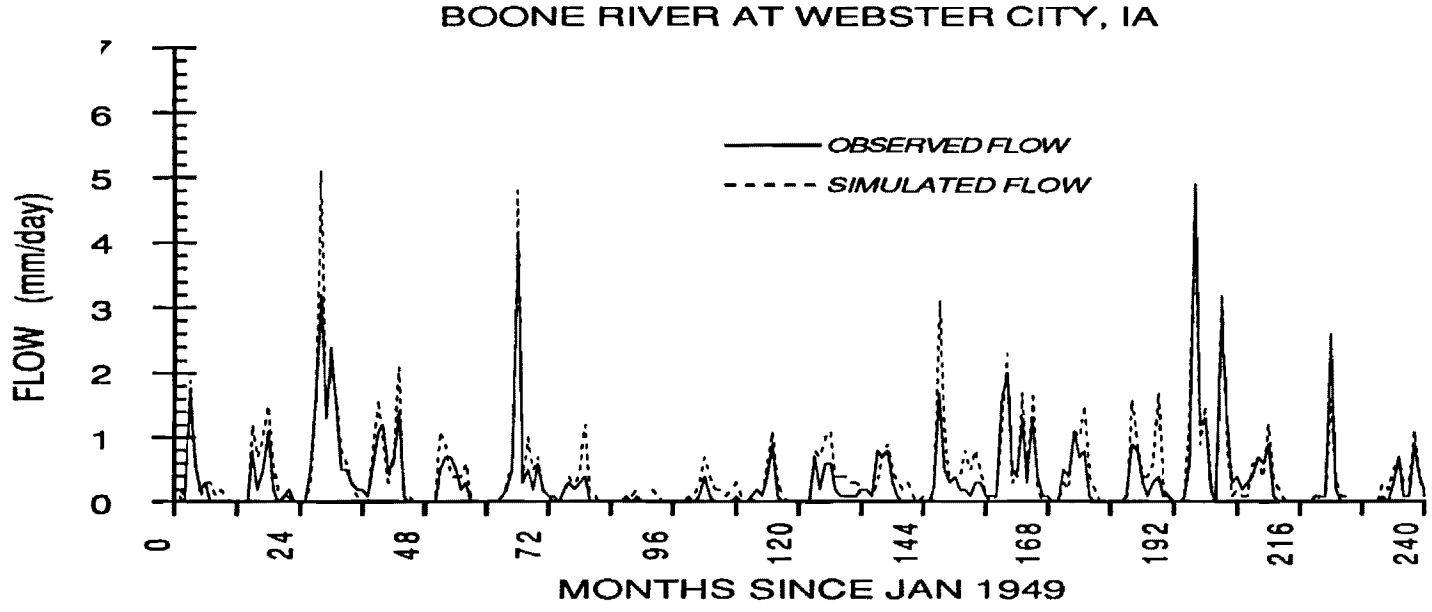
BOONE RIVER AT WEBSTER CITY, IA
OBSERVED FLOW
SIMULATED FLOW
FLOW (mm/day)
0
1
2
3
4
5
6
7
0
24
48
72
96
120
144
168
192
216
240
MONTHS SINCE JAN 1949

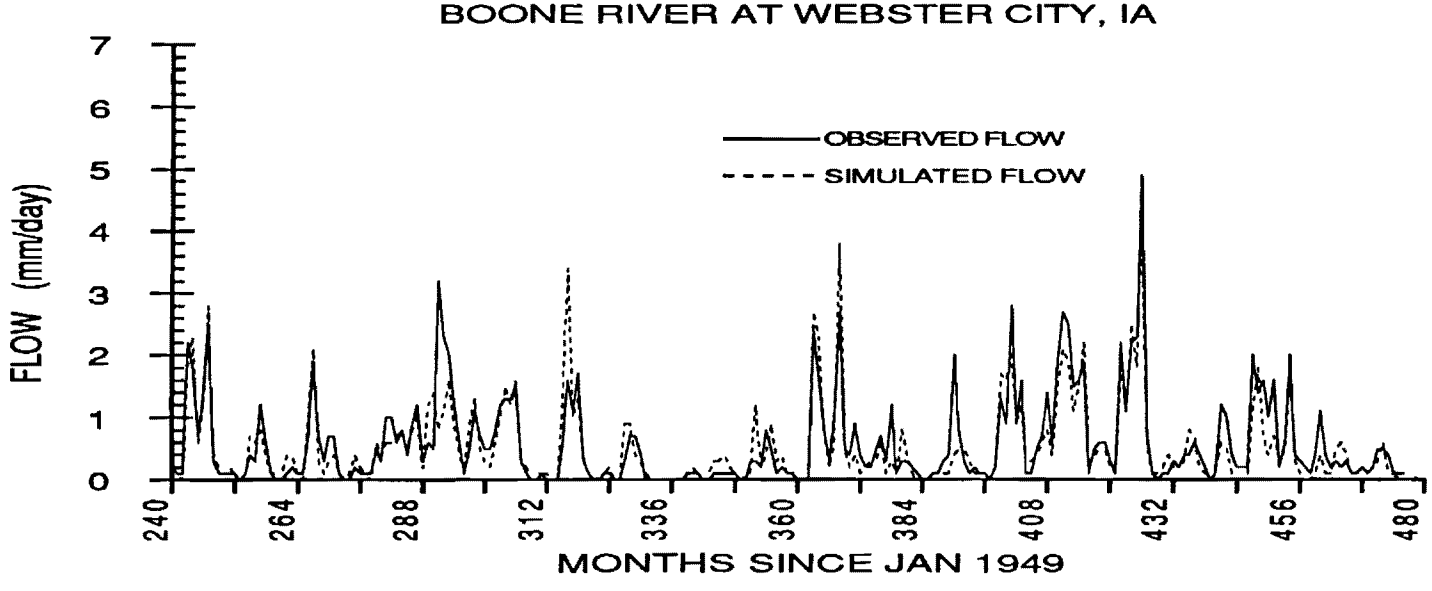
BOONE RIVER AT WEBSTER CITY, IA
OBSERVED FLOW
SIMULATED FLOW
FLOW (mm/day)
0
1
2
3
4
5
6
7
240
264
288
312
336
360
384
408
432
456
480
MONTHS SINCE JAN 1949

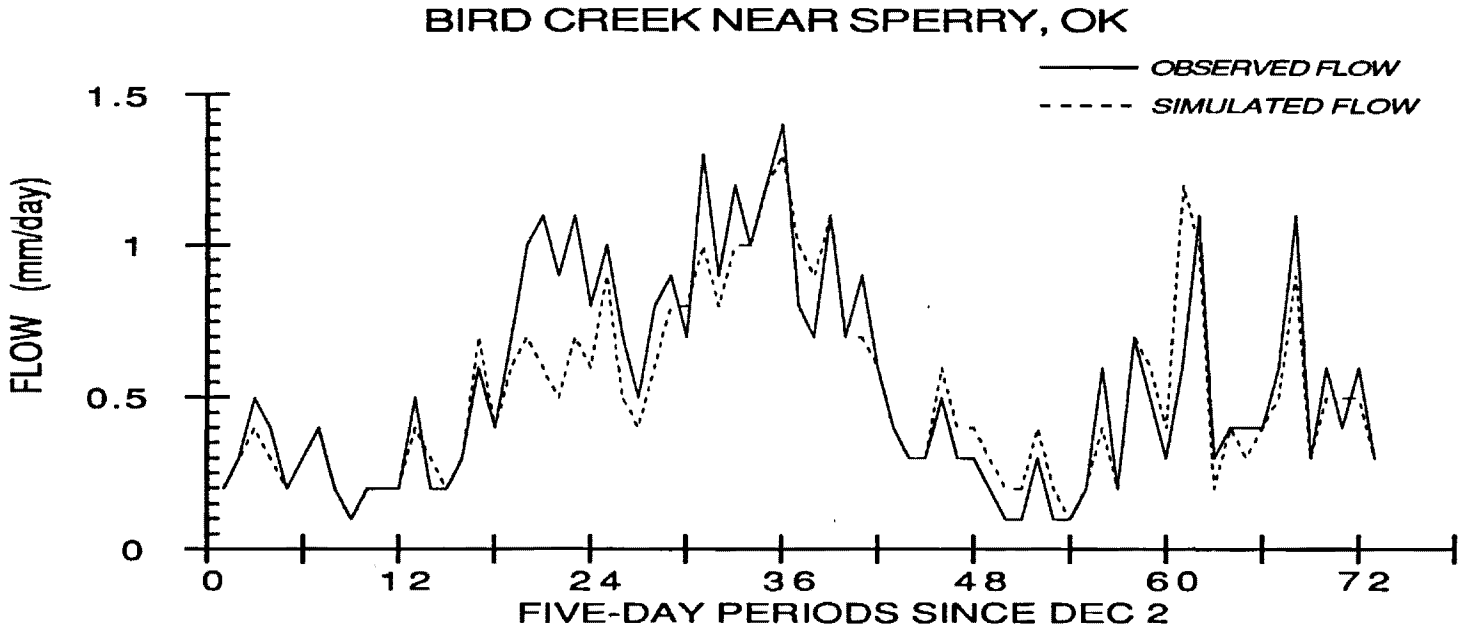
BIRD CREEK NEAR SPERRY, OK
OBSERVED FLOW
SIMULATED FLOW
FLOW (mm/day)
1.5
1
0.5
0
0
12
24
36
48
60
72
FIVE-DAY PERIODS SINCE DEC 2

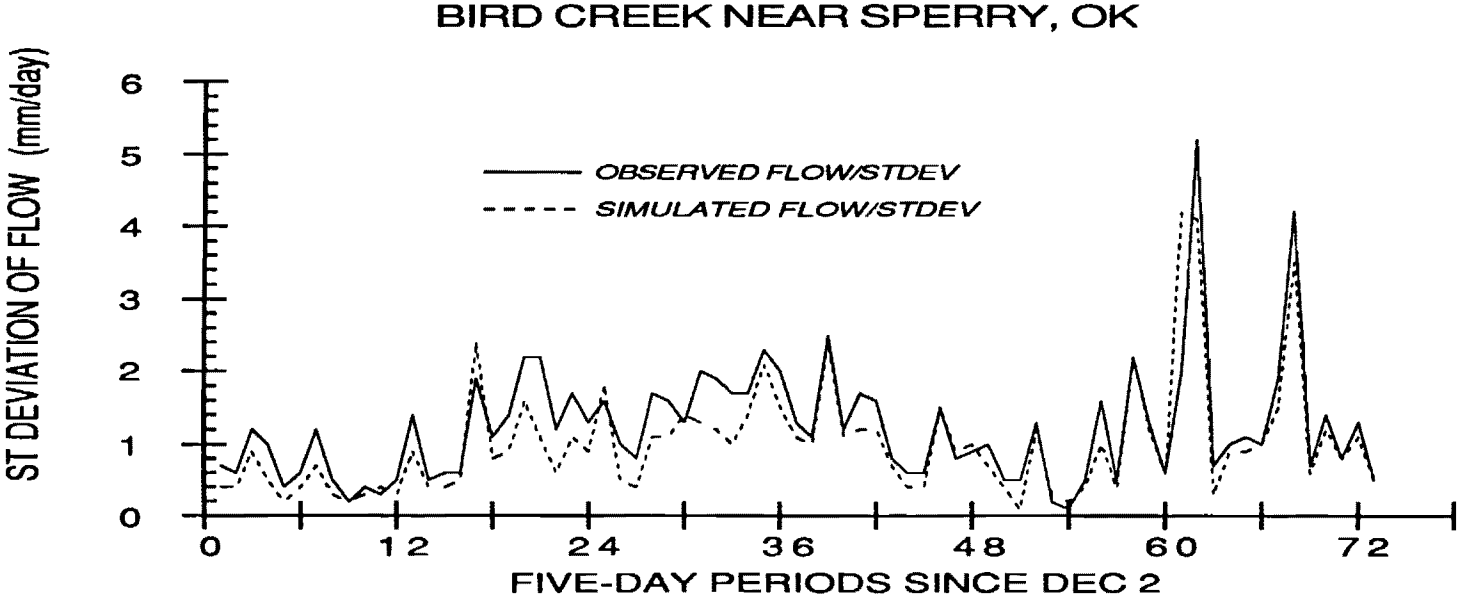
BIRD CREEK NEAR SPERRY, OK
OBSERVED FLOW/STDEV
SIMULATED FLOW/STDEV
ST DEVIATION OF FLOW (mm/day)
6
5
4
3
2
1
0
0
12
24
36
48
60
72
FIVE-DAY PERIODS SINCE DEC 2

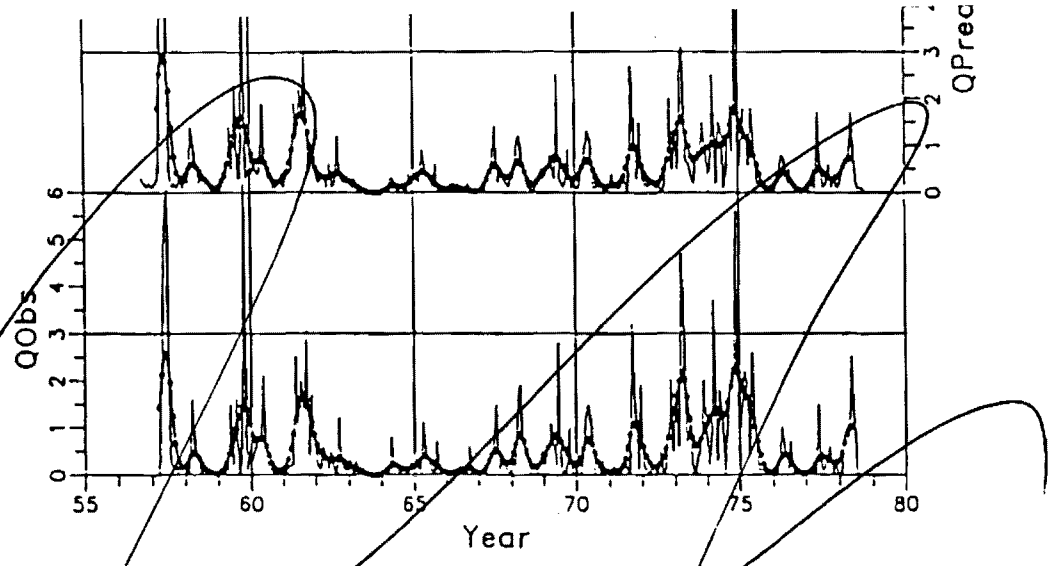

Fig. 4. Bird Creek, OK predicted and observed monthly discharge, 1957-1978. Solid circles show 13-month Guassian low pass filtered discharge.

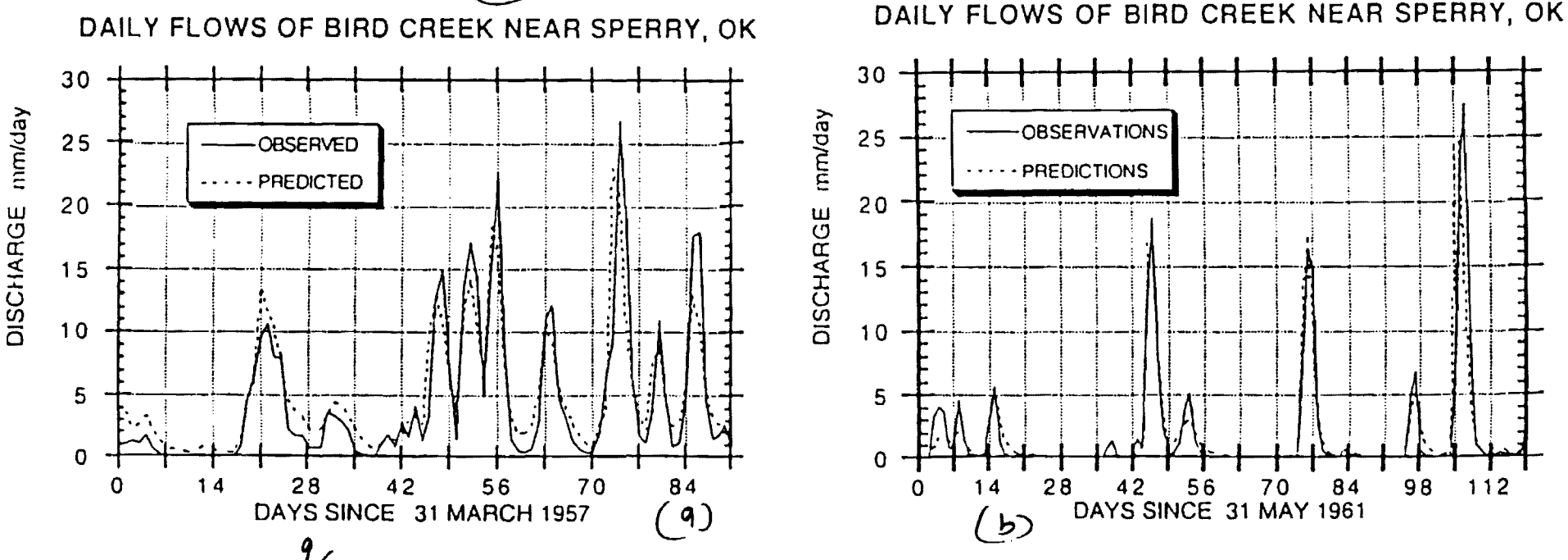

Fig. 5. Bird Creek, OK predicted and observed daily discharge for two high flow periods: *a)* 91 days beginning 31 March, 1957, and *b)* 120 days beginning 31 May, 1961.

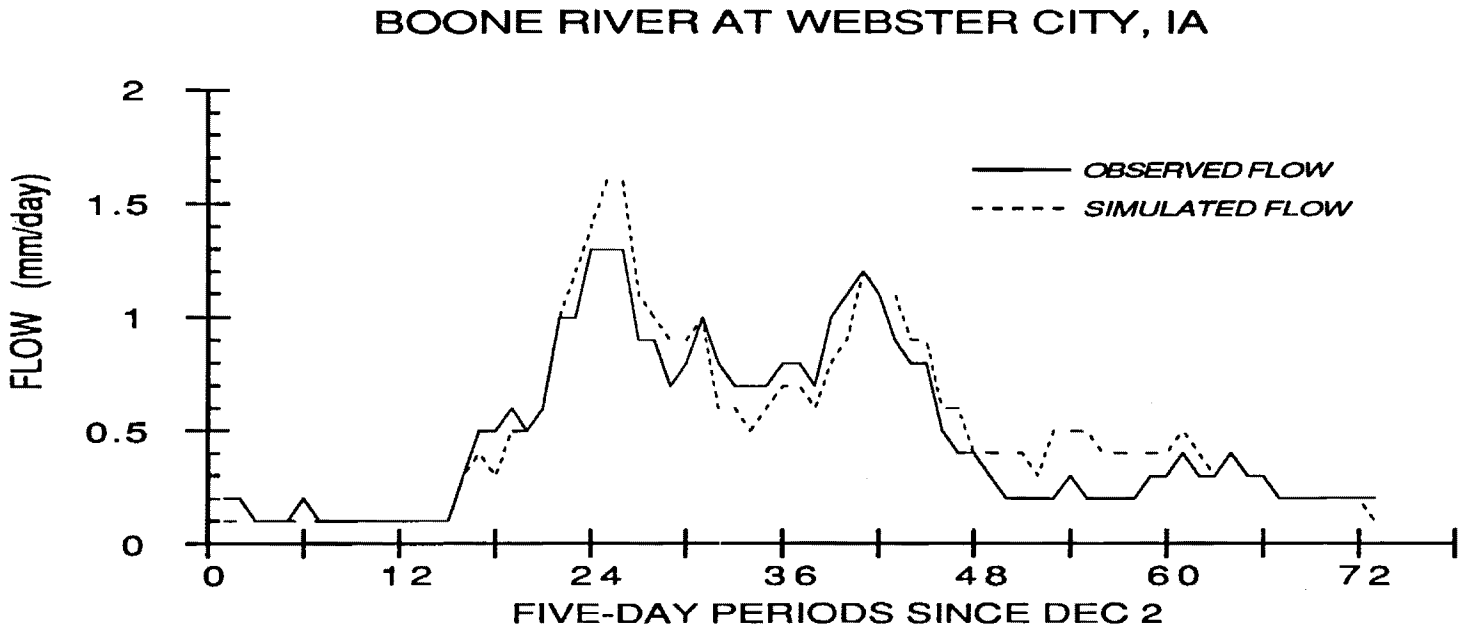
BOONE RIVER AT WEBSTER CITY, IA
FLOW (mm/day)
2
1.5
1
0.5
0
OBSERVED FLOW
SIMULATED FLOW
0
12
24
36
48
60
72
FIVE-DAY PERIODS SINCE DEC 2

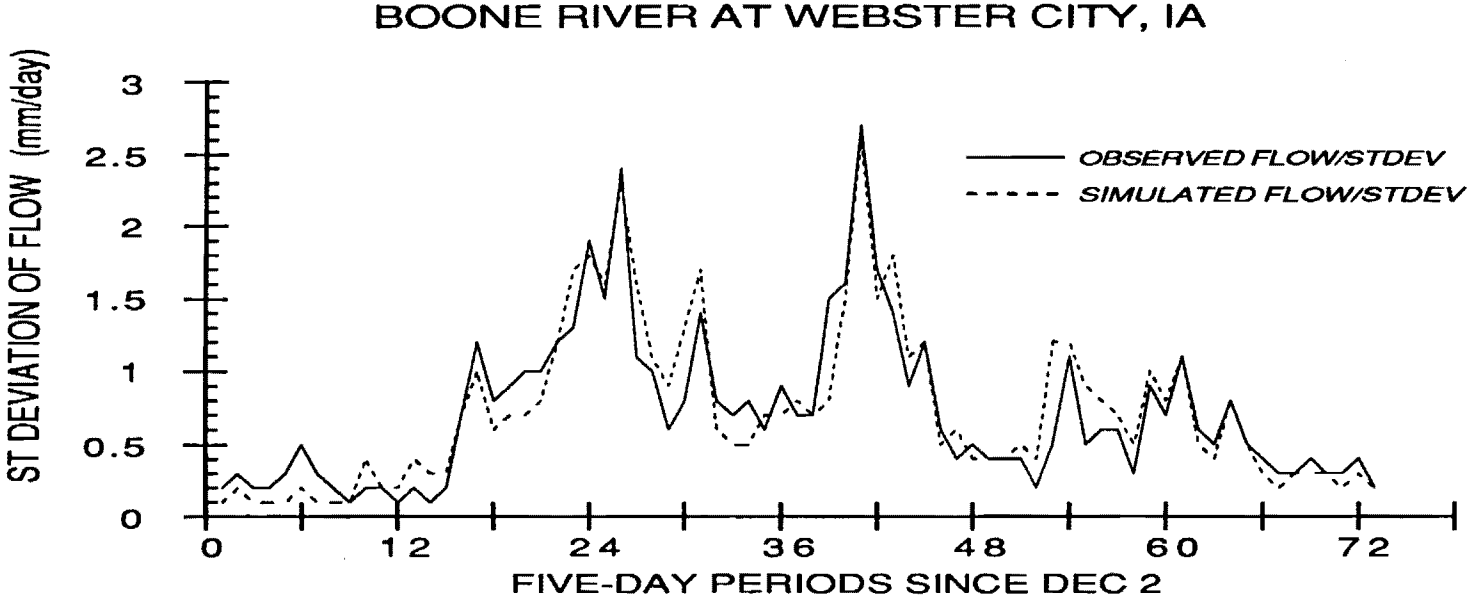
BOONE RIVER AT WEBSTER CITY, IA
ST DEVIATION OF FLOW (mm/day)
3
2.5
2
1.5
1
0.5
0
OBSERVED FLOW/STDEV
SIMULATED FLOW/STDEV
0
12
24
36
48
60
72
FIVE-DAY PERIODS SINCE DEC 2

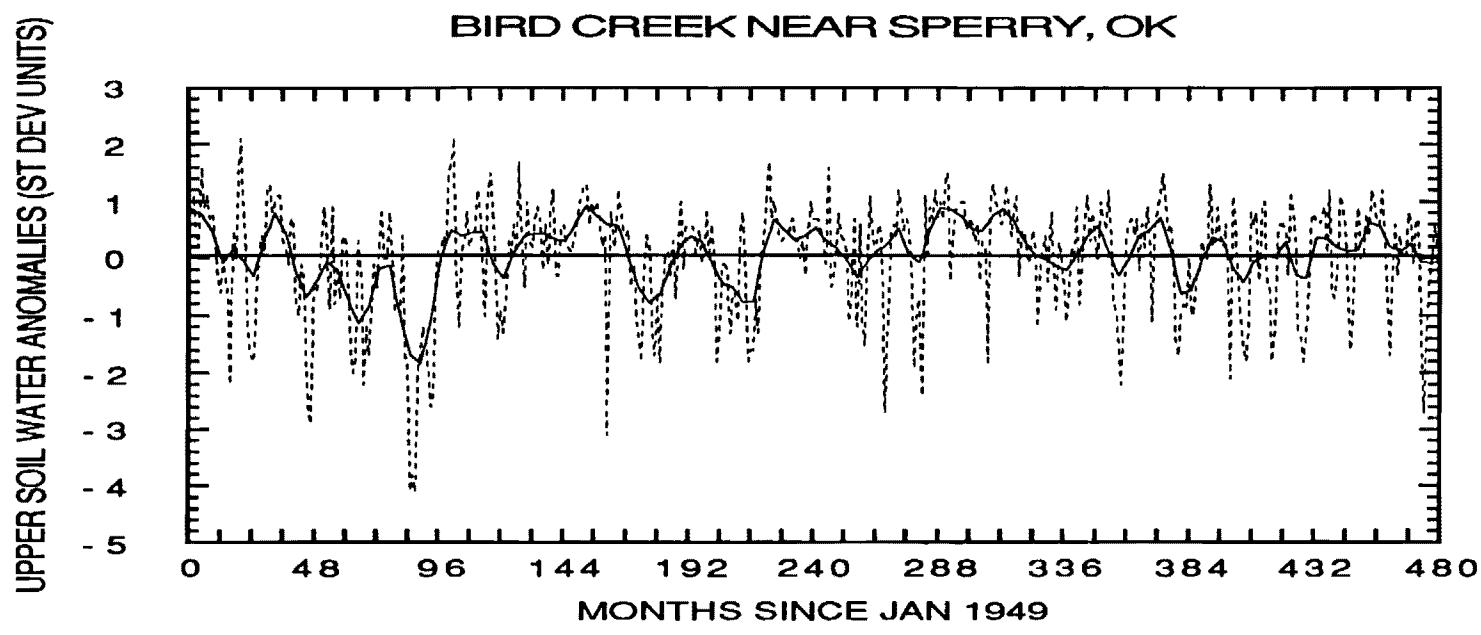
BIRD CREEK NEAR SPERRY, OK
UPPER SOIL WATER ANOMALIES (ST DEV UNITS)
3
2
1
0
- 1
- 2
- 3
- 4
- 5
0
48
96
144
192
240
288
336
384
432
480
MONTHS SINCE JAN 1949

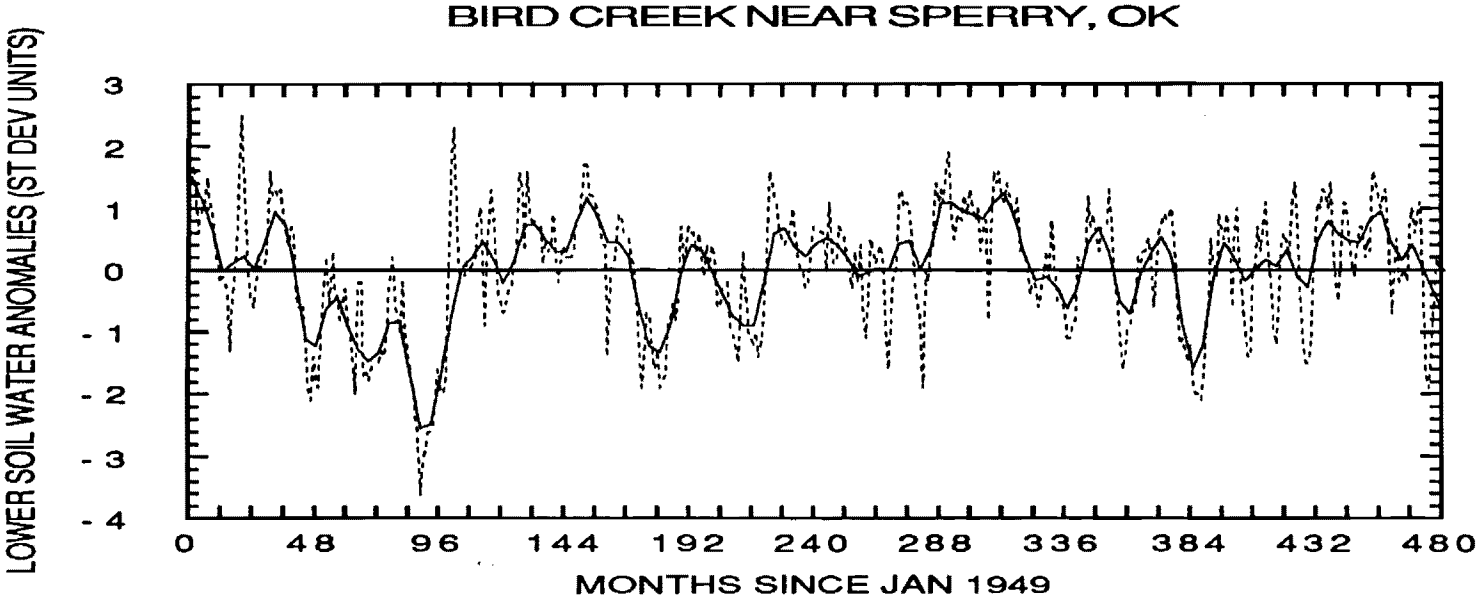
BIRD CREEK NEAR SPERRY, OK
LOWER SOIL WATER ANOMALIES (ST DEV UNITS)
3
2
1
0
- 1
- 2
- 3
- 4
0
48
96
144
192
240
288
336
384
432
480
MONTHS SINCE JAN 1949

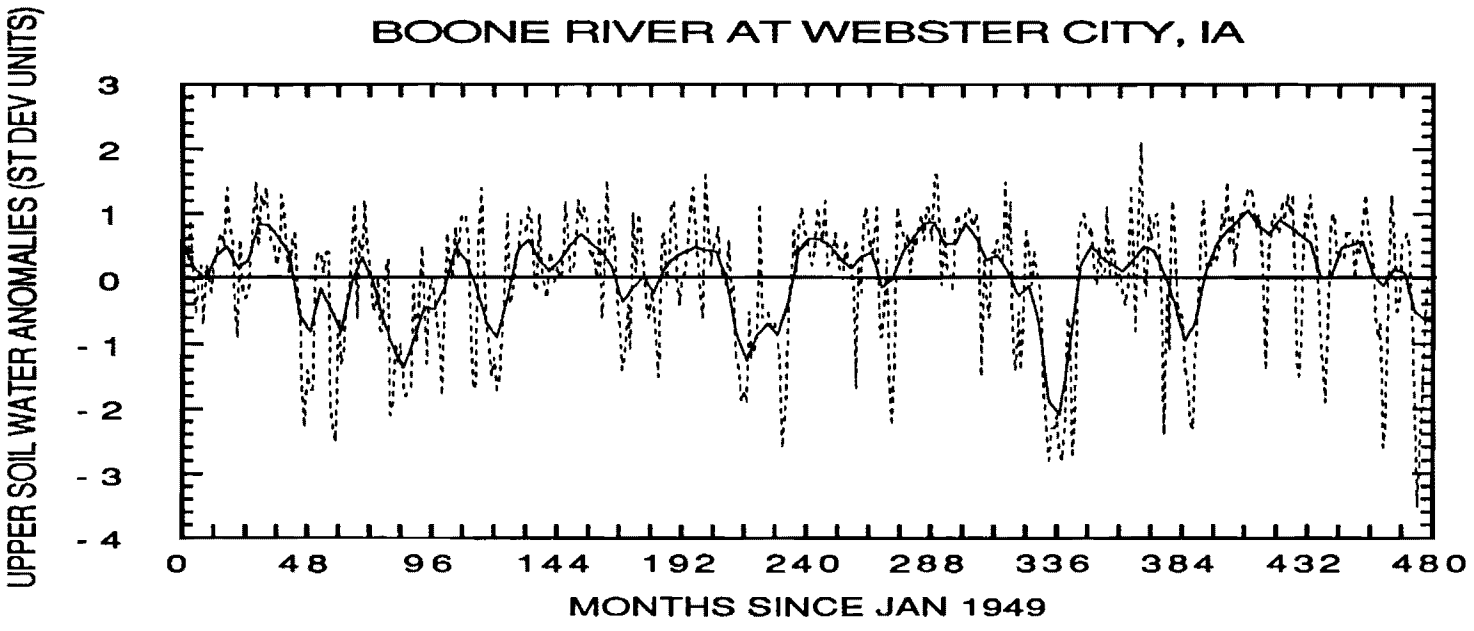
BOONE RIVER AT WEBSTER CITY, IA
UPPER SOIL WATER ANOMALIES (ST DEV UNITS)
3
2
1
0
- 1
- 2
- 3
- 4
0
48
96
144
192
240
288
336
384
432
480
MONTHS SINCE JAN 1949

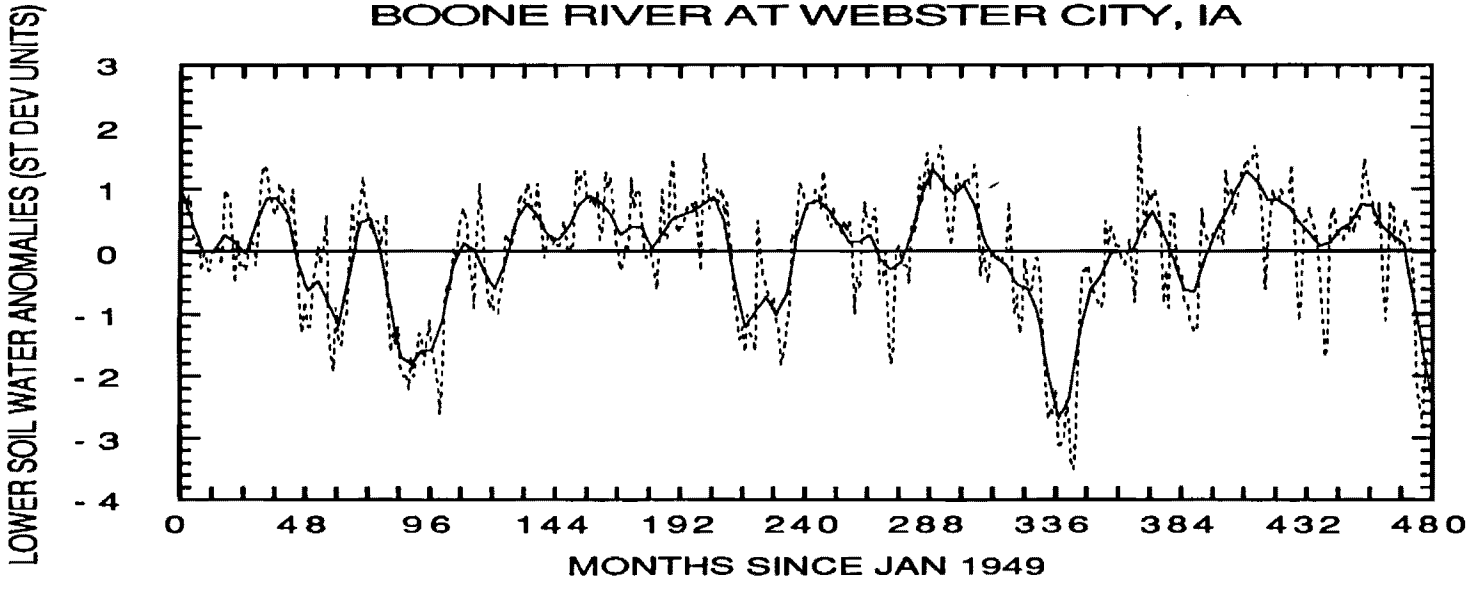
BOONE RIVER AT WEBSTER CITY, IA
LOWER SOIL WATER ANOMALIES (ST DEV UNITS)
3
2
1
0
- 1
- 2
- 3
- 4
0
48
96
144
192
240
288
336
384
432
480
MONTHS SINCE JAN 1949

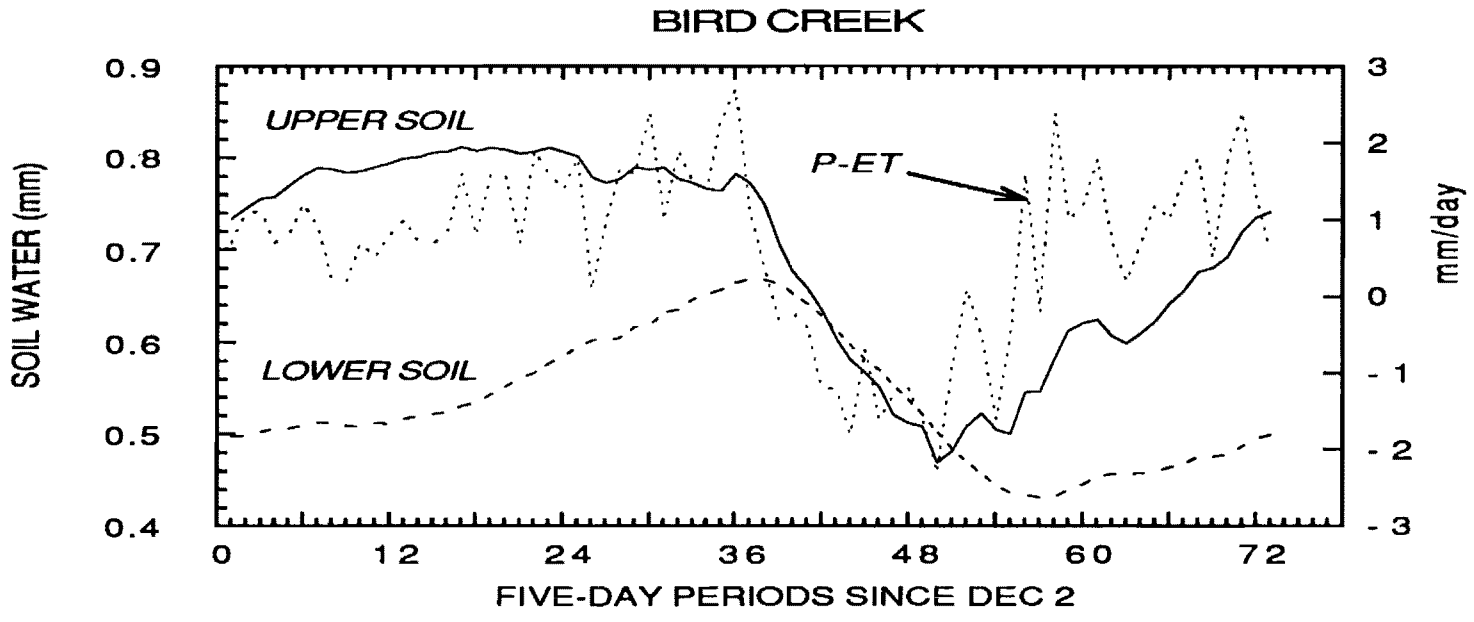
BIRD CREEK
SOIL WATER (mm)
0.9
0.8
0.7
0.6
0.5
0.4
UPPER SOIL
LOWER SOIL
P-ET
3
2
1
0
- 1
- 2
- 3
mm/day
0
12
24
36
48
60
72
FIVE-DAY PERIODS SINCE DEC 2

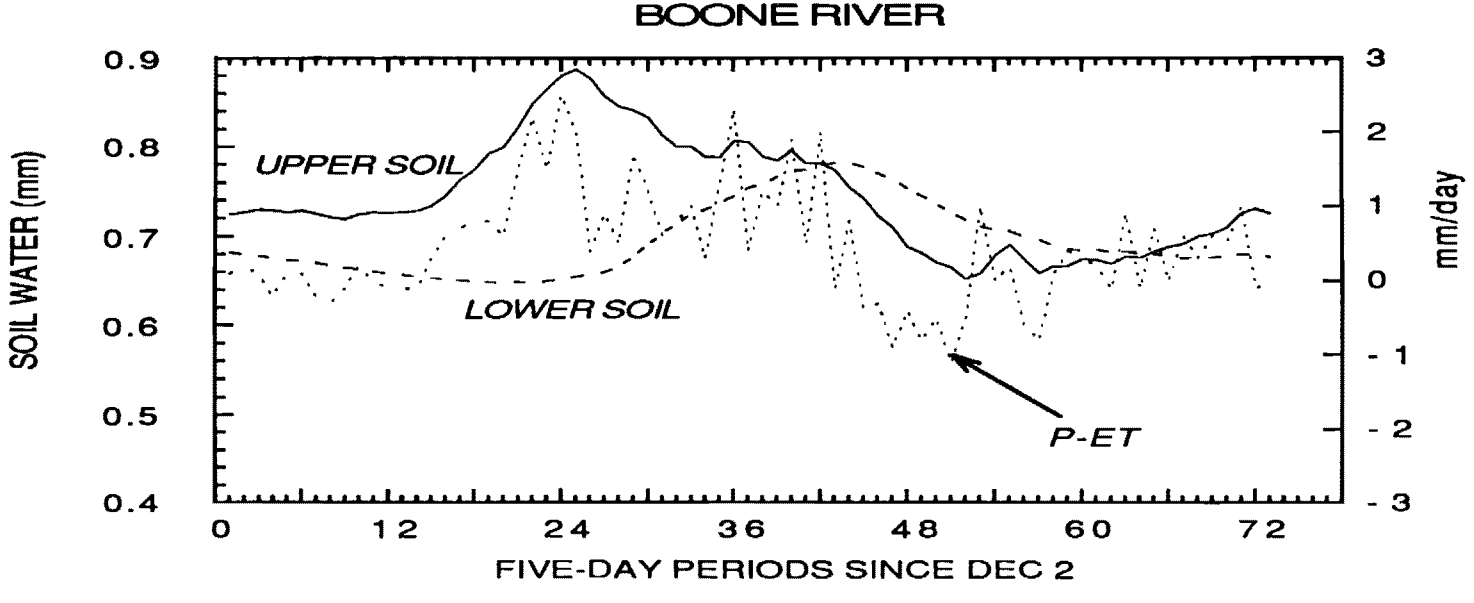
BOONE RIVER
SOIL WATER (mm)
0.9
0.8
0.7
0.6
0.5
0.4
UPPER SOIL
LOWER SOIL
P-ET
3
2
1
0
- 1
- 2
- 3
mm/day
0
12
24
36
48
60
72
FIVE-DAY PERIODS SINCE DEC 2

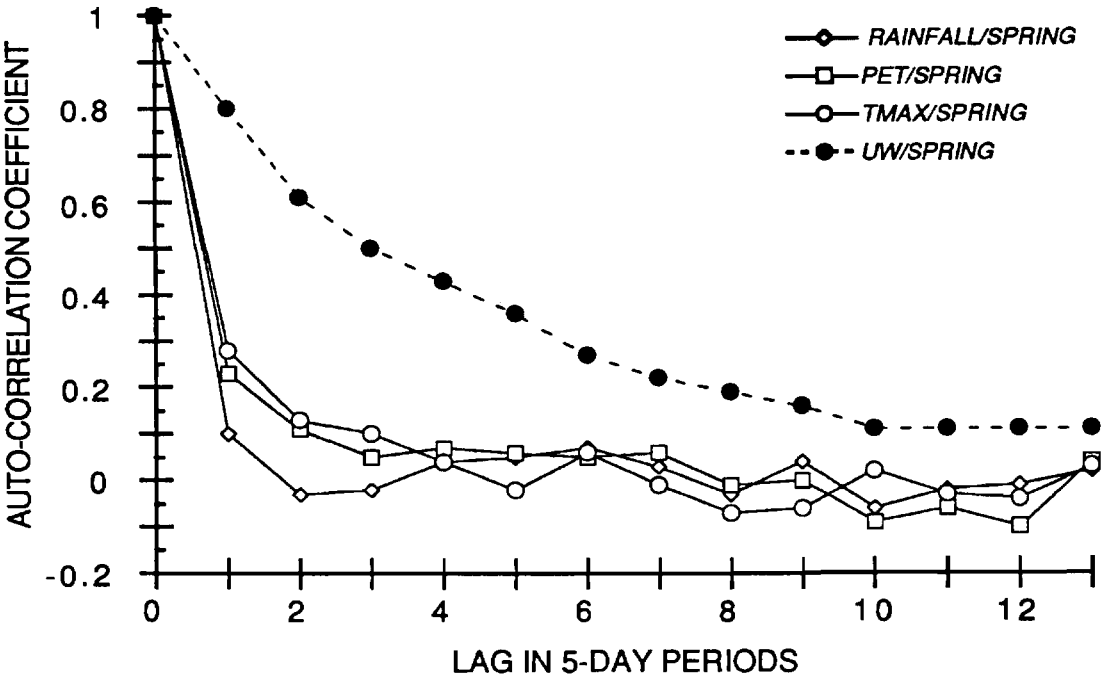
AUTO-CORRELATION COEFFICIENT
1
0.8
0.6
0.4
0.2
0
-0.2
0
2
4
6
8
10
12
LAG IN 5-DAY PERIODS
RAINFALL/SPRING
PET/SPRING
TMAX/SPRING
UW/SPRING

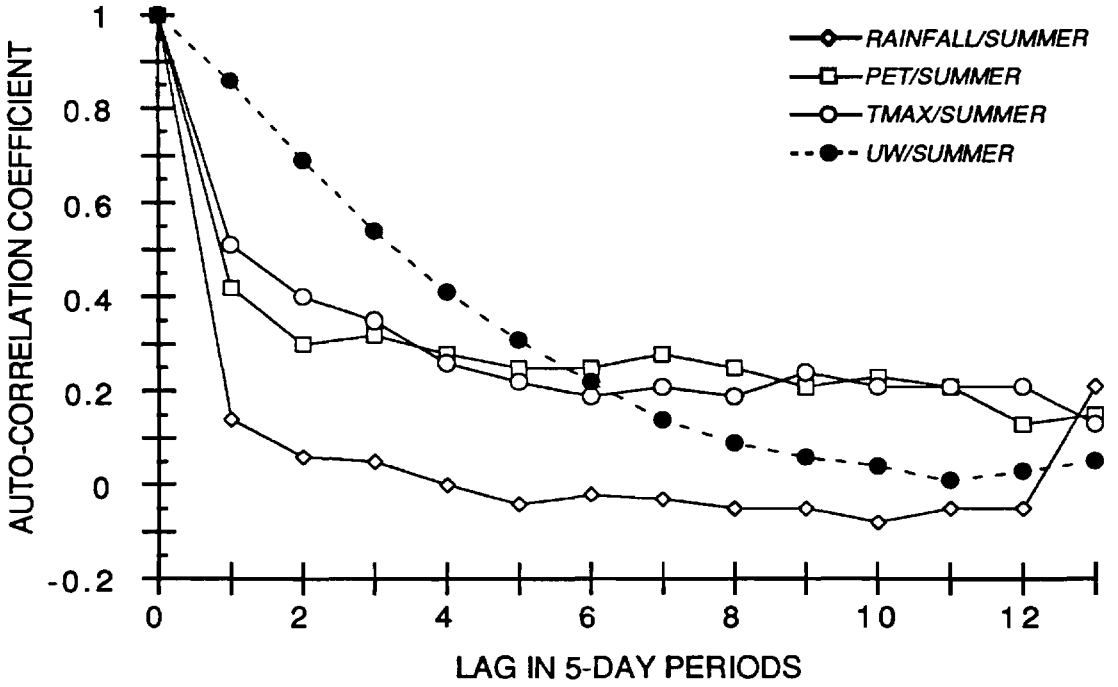
AUTO-CORRELATION COEFFICIENT
1
0.8
0.6
0.4
0.2
0
-0.2
0
2
4
6
8
10
12
LAG IN 5-DAY PERIODS
RAINFALL/SUMMER
PET/SUMMER
TMAX/SUMMER
UW/SUMMER

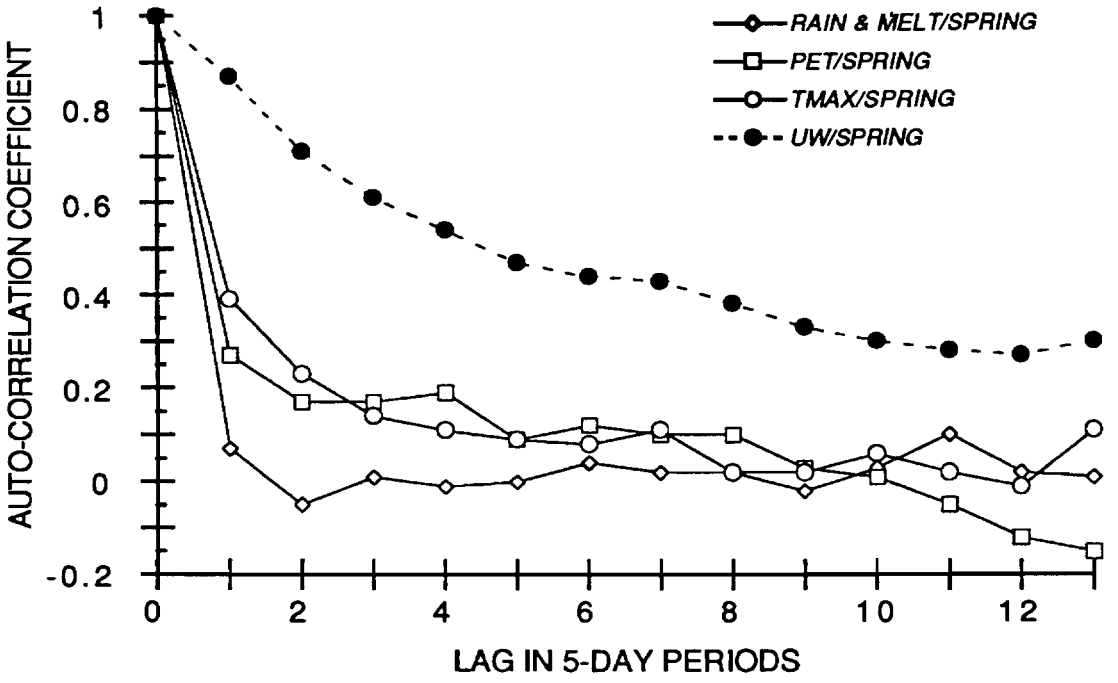
RAIN & MELT/SPRING
PET/SPRING
TMAX/SPRING
UW/SPRING
AUTO-CORRELATION COEFFICIENT
1
0.8
0.6
0.4
0.2
0
-0.2
0
2
4
6
8
10
12
LAG IN 5-DAY PERIODS

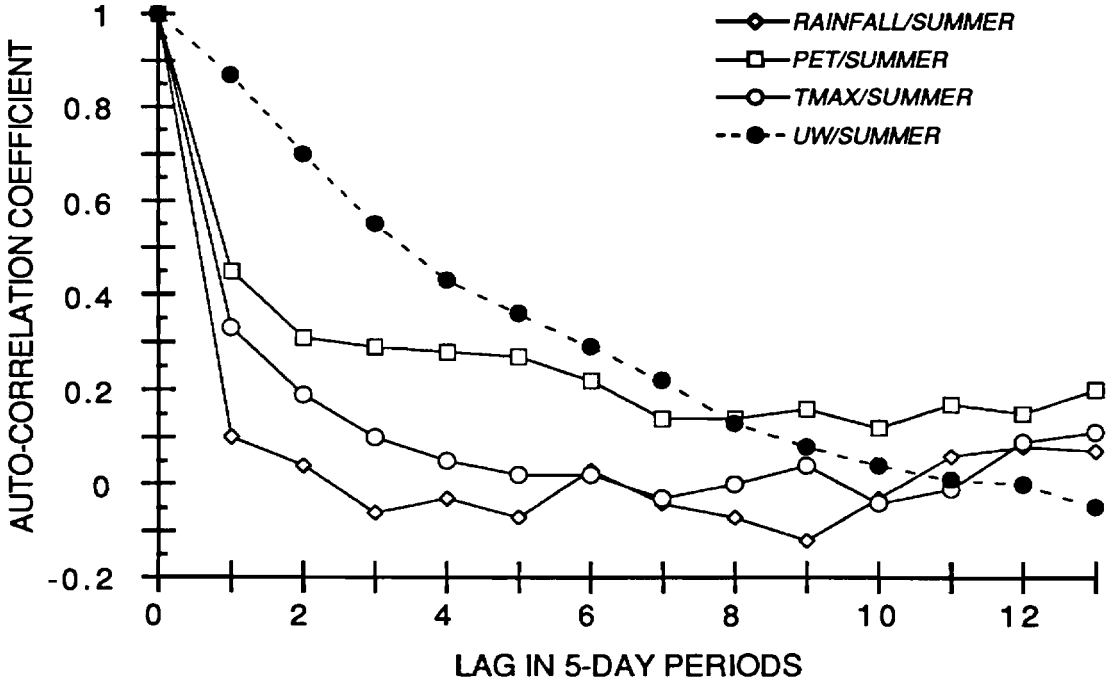
RAINFALL/SUMMER
PET/SUMMER
TMAX/SUMMER
UW/SUMMER
AUTO-CORRELATION COEFFICIENT
1
0.8
0.6
0.4
0.2
0
-0.2
0
2
4
6
8
10
12
LAG IN 5-DAY PERIODS

BIRD CREEK NEAR SPERRY, OK

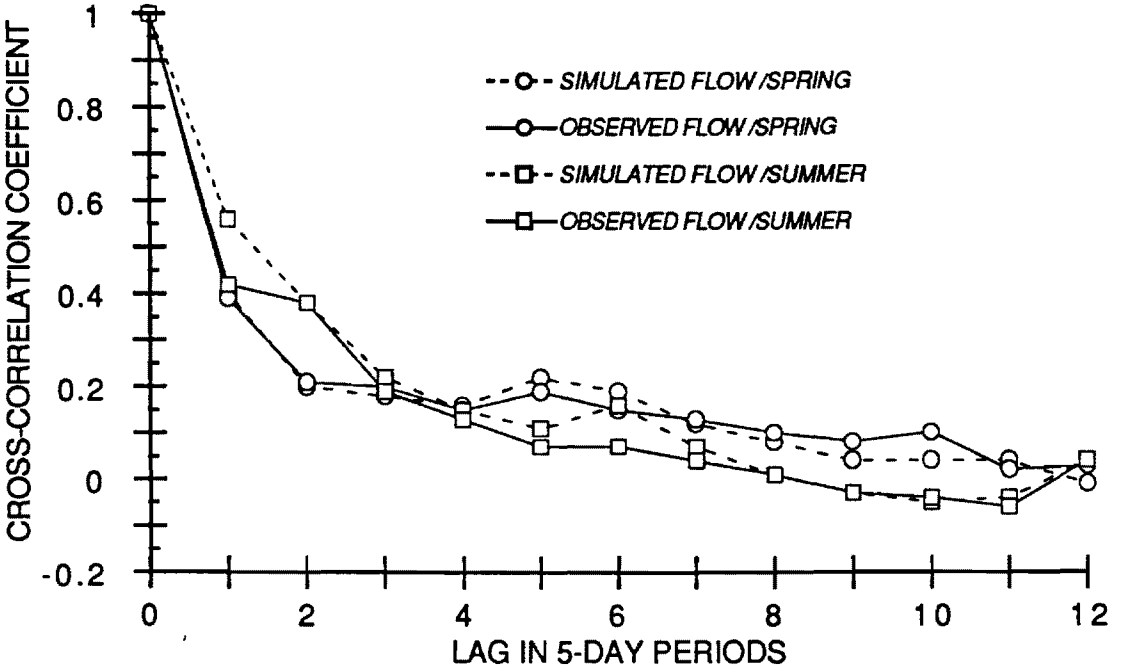

BOONE RIVER AT WEBSTER CITY, IA

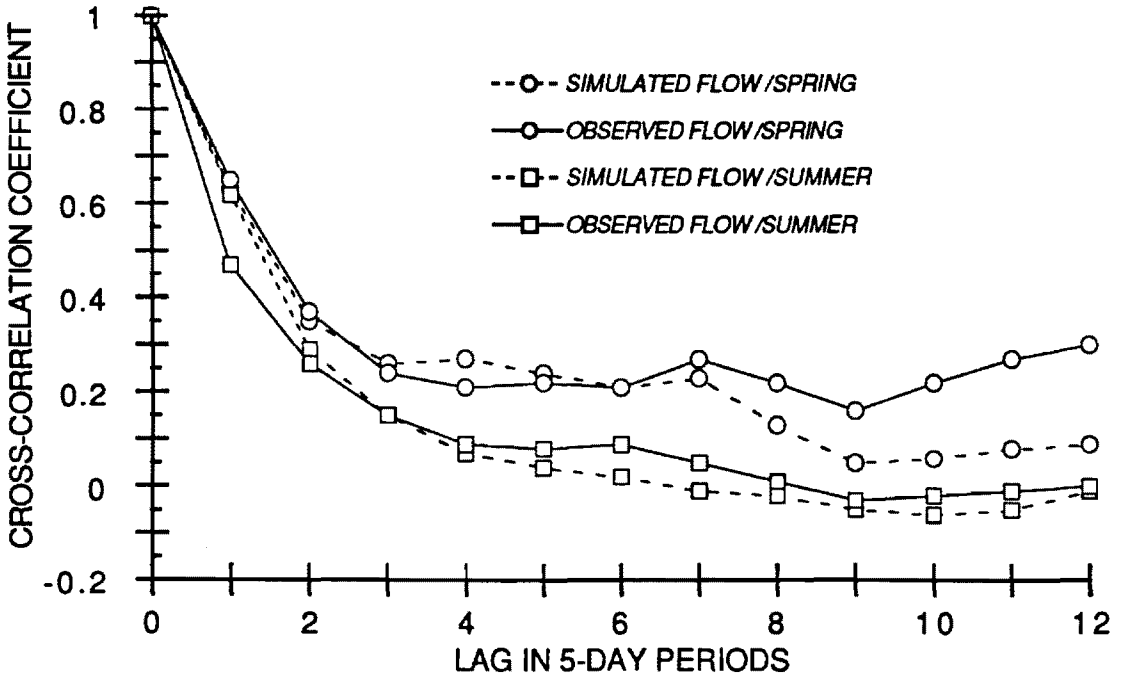

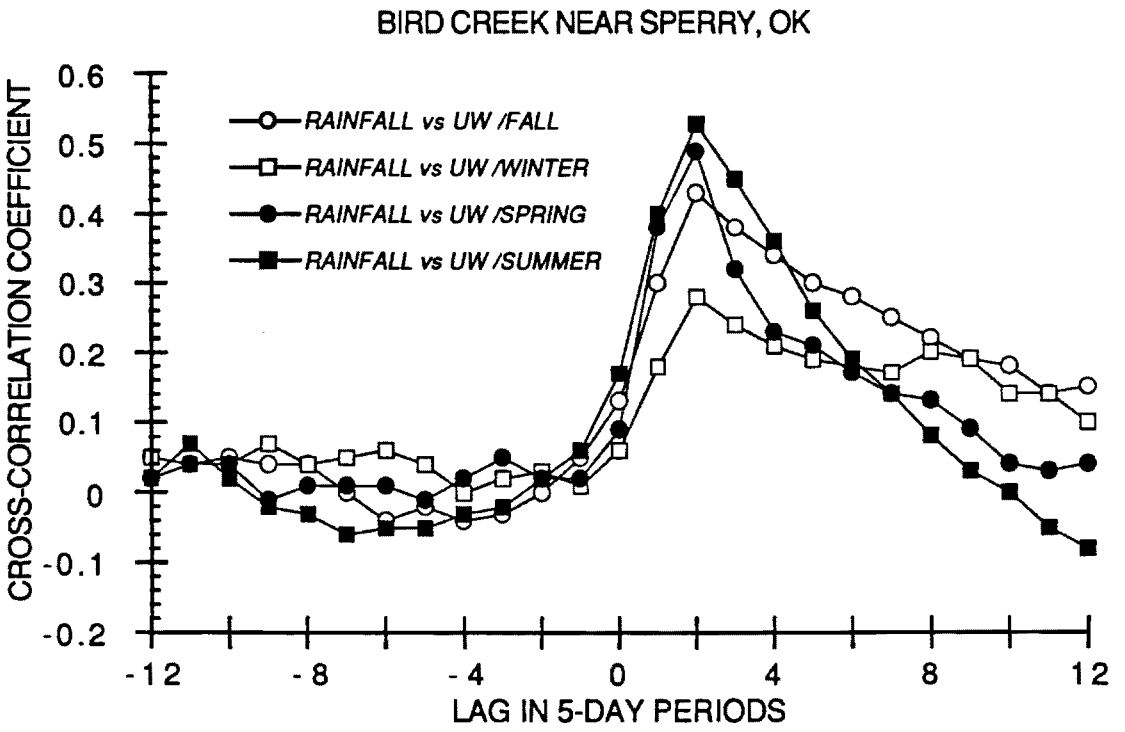
BIRD CREEK NEAR SPERRY, OK
CROSS-CORRELATION COEFFICIENT
0.6
0.5
0.4
0.3
0.2
0.1
0
-0.1
-0.2
RAINFALL vs UW /FALL
RAINFALL vs UW /WINTER
RAINFALL vs UW /SPRING
RAINFALL vs UW /SUMMER
-12
-8
-4
0
4
8
12
LAG IN 5-DAY PERIODS

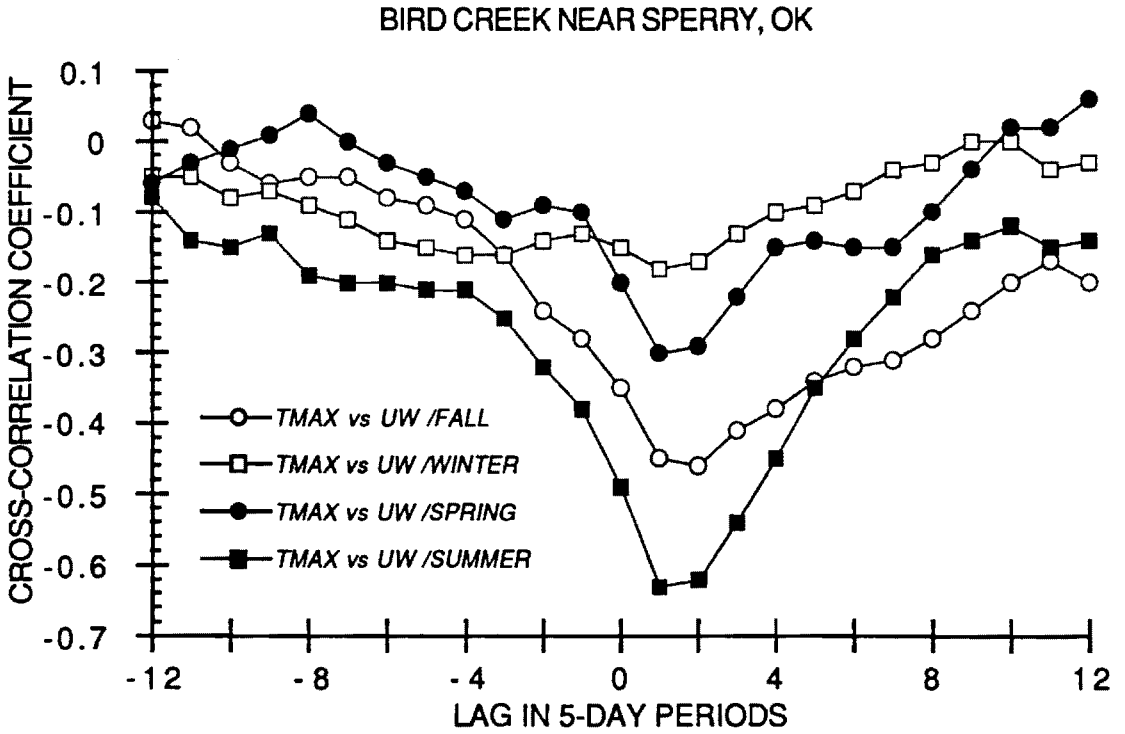
BIRD CREEK NEAR SPERRY, OK
CROSS-CORRELATION COEFFICIENT
0.1
0
-0.1
-0.2
-0.3
-0.4
-0.5
-0.6
-0.7
TMAX vs UW /FALL
TMAX vs UW /WINTER
TMAX vs UW /SPRING
TMAX vs UW /SUMMER
-12
-8
-4
0
4
8
12
LAG IN 5-DAY PERIODS

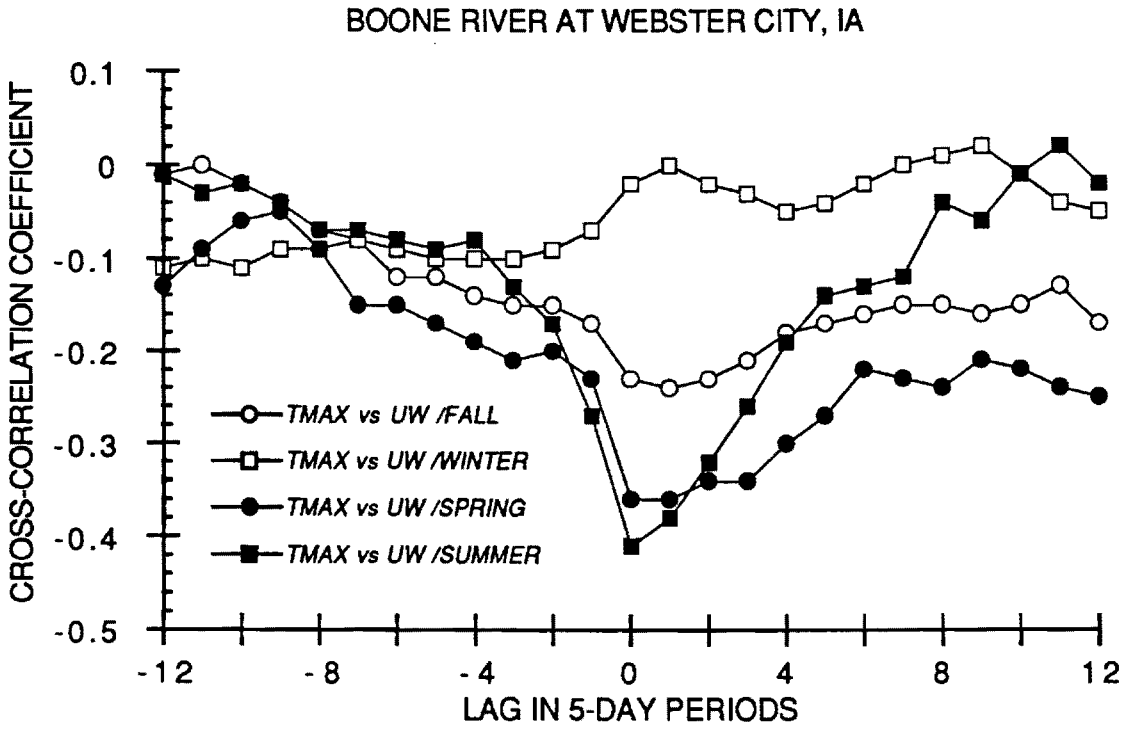
BOONE RIVER AT WEBSTER CITY, IA
CROSS-CORRELATION COEFFICIENT
0.1
0
-0.1
-0.2
-0.3
-0.4
-0.5
-12
-8
-4
0
4
8
12
LAG IN 5-DAY PERIODS
TMAX vs UW /FALL
TMAX vs UW /WINTER
TMAX vs UW /SPRING
TMAX vs UW /SUMMER

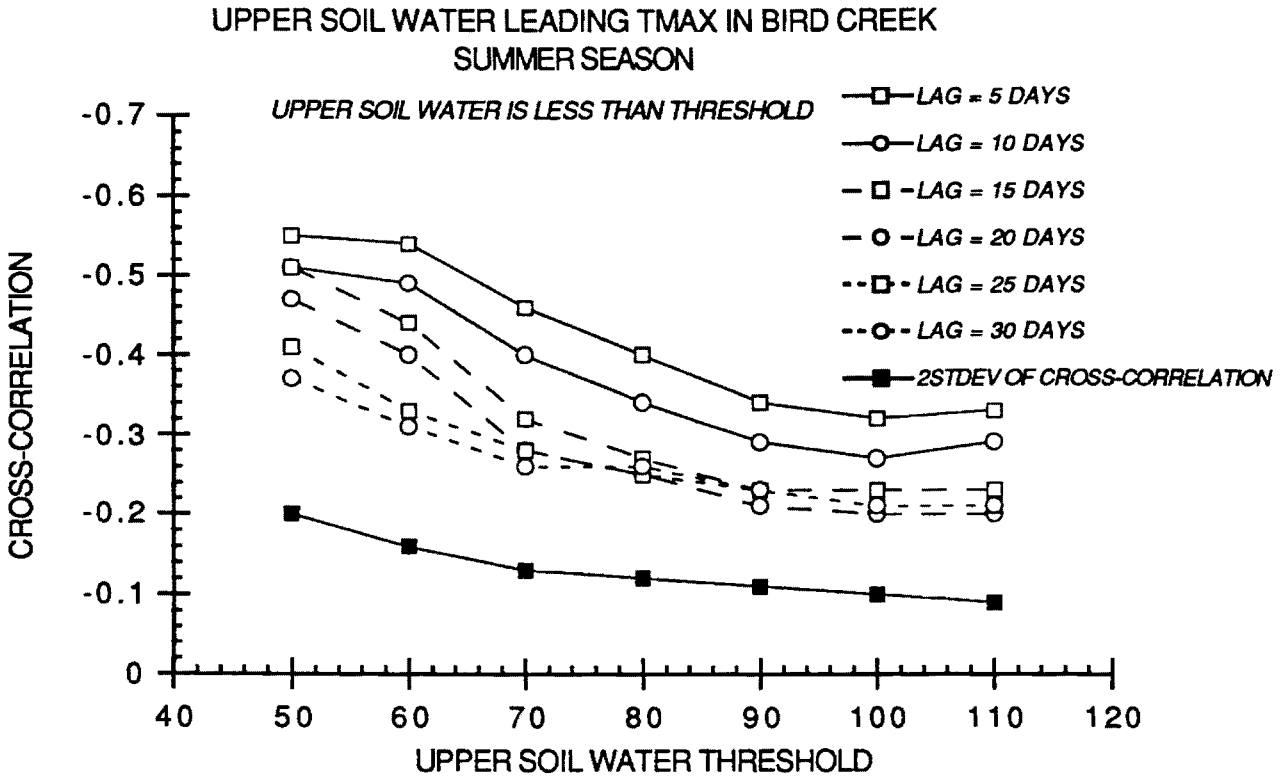
UPPER SOIL WATER LEADING TMAX IN BIRD CREEK
SUMMER SEASON
UPPER SOIL WATER IS LESS THAN THRESHOLD
LAG = 5 DAYS
LAG = 10 DAYS
LAG = 15 DAYS
LAG = 20 DAYS
LAG = 25 DAYS
LAG = 30 DAYS
2STDEV OF CROSS-CORRELATION
CROSS-CORRELATION
-0.7
-0.6
-0.5
-0.4
-0.3
-0.2
-0.1
0
40
50
60
70
80
90
100
110
120
UPPER SOIL WATER THRESHOLD

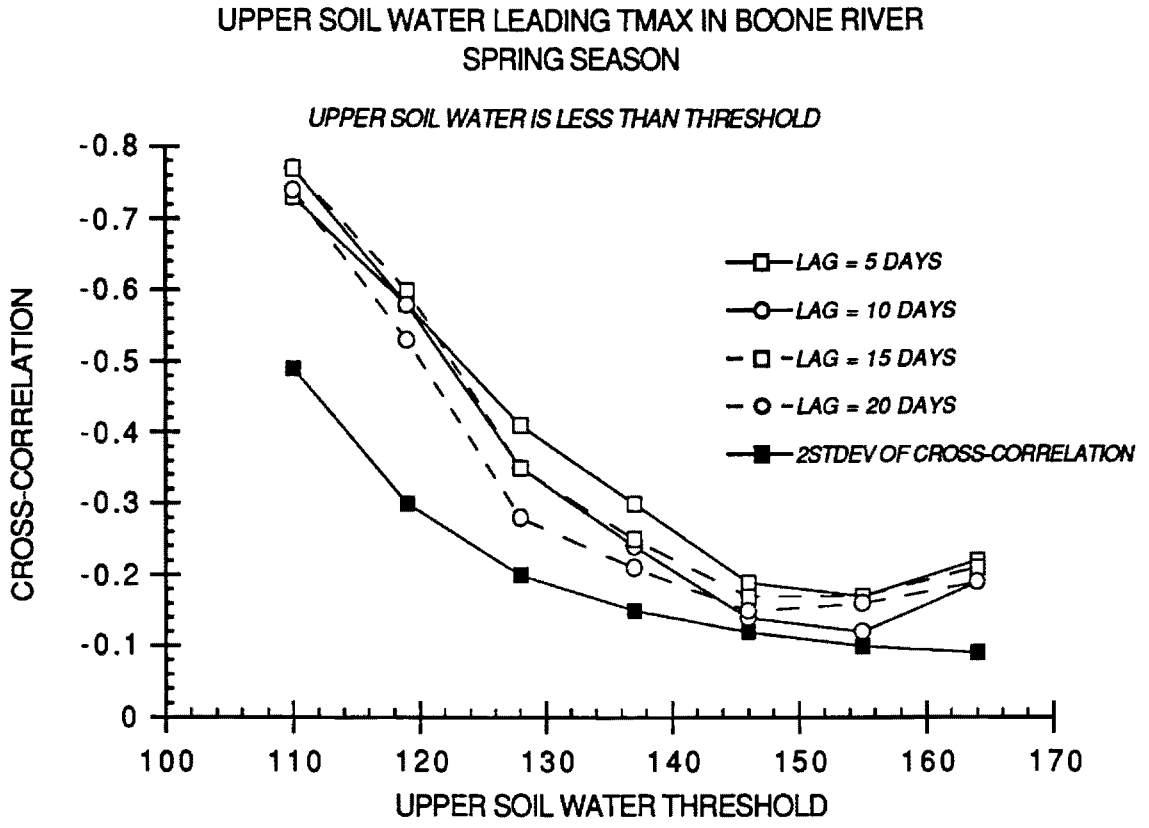
UPPER SOIL WATER LEADING TMAX IN BOONE RIVER
SPRING SEASON
UPPER SOIL WATER IS LESS THAN THRESHOLD
CROSS-CORRELATION
-0.8
-0.7
-0.6
-0.5
-0.4
-0.3
-0.2
-0.1
0
100
110
120
130
140
150
160
170
UPPER SOIL WATER THRESHOLD
LAG = 5 DAYS
LAG = 10 DAYS
LAG = 15 DAYS
LAG = 20 DAYS
2STDEV OF CROSS-CORRELATION

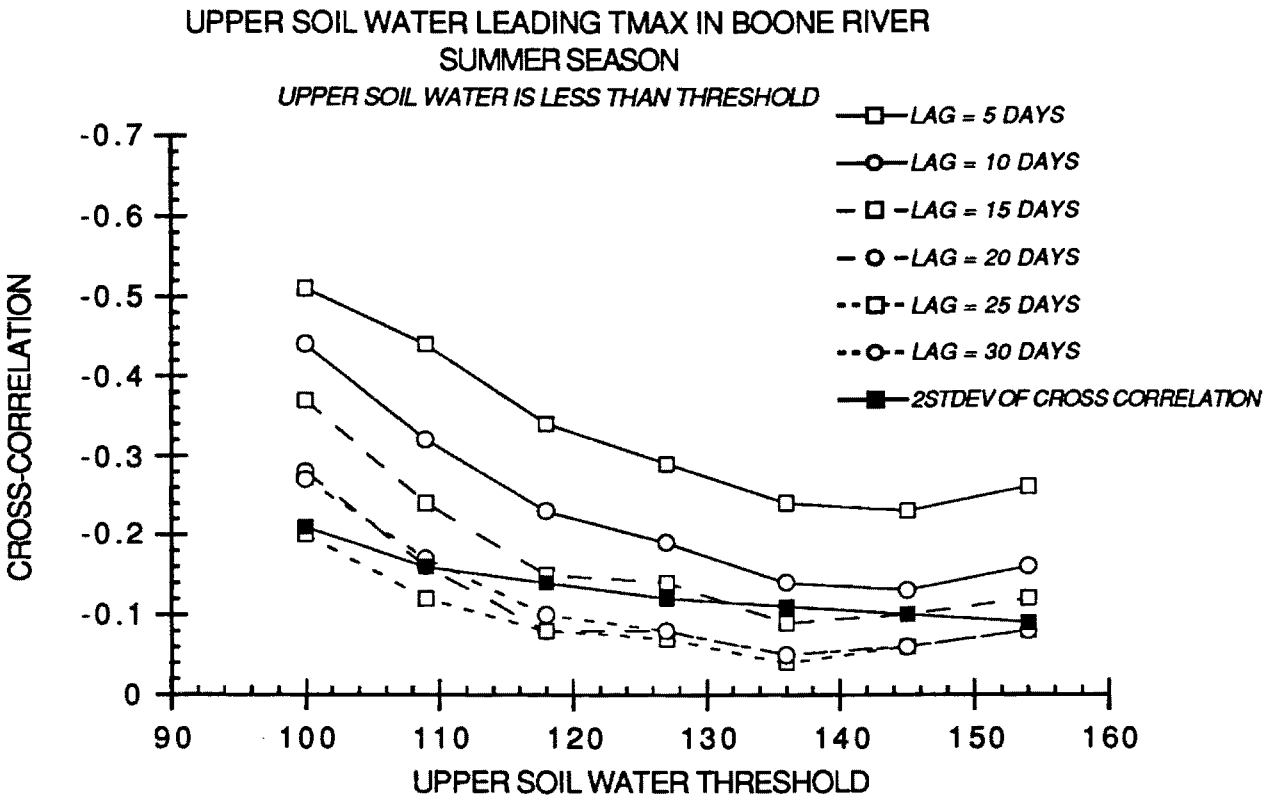
UPPER SOIL WATER LEADING TMAX IN BOONE RIVER
SUMMER SEASON
UPPER SOIL WATER IS LESS THAN THRESHOLD
LAG = 5 DAYS
LAG = 10 DAYS
LAG = 15 DAYS
LAG = 20 DAYS
LAG = 25 DAYS
LAG = 30 DAYS
2STDEV OF CROSS CORRELATION
CROSS-CORRELATION
-0.7
-0.6
-0.5
-0.4
-0.3
-0.2
-0.1
0
90
100
110
120
130
140
150
160
UPPER SOIL WATER THRESHOLD

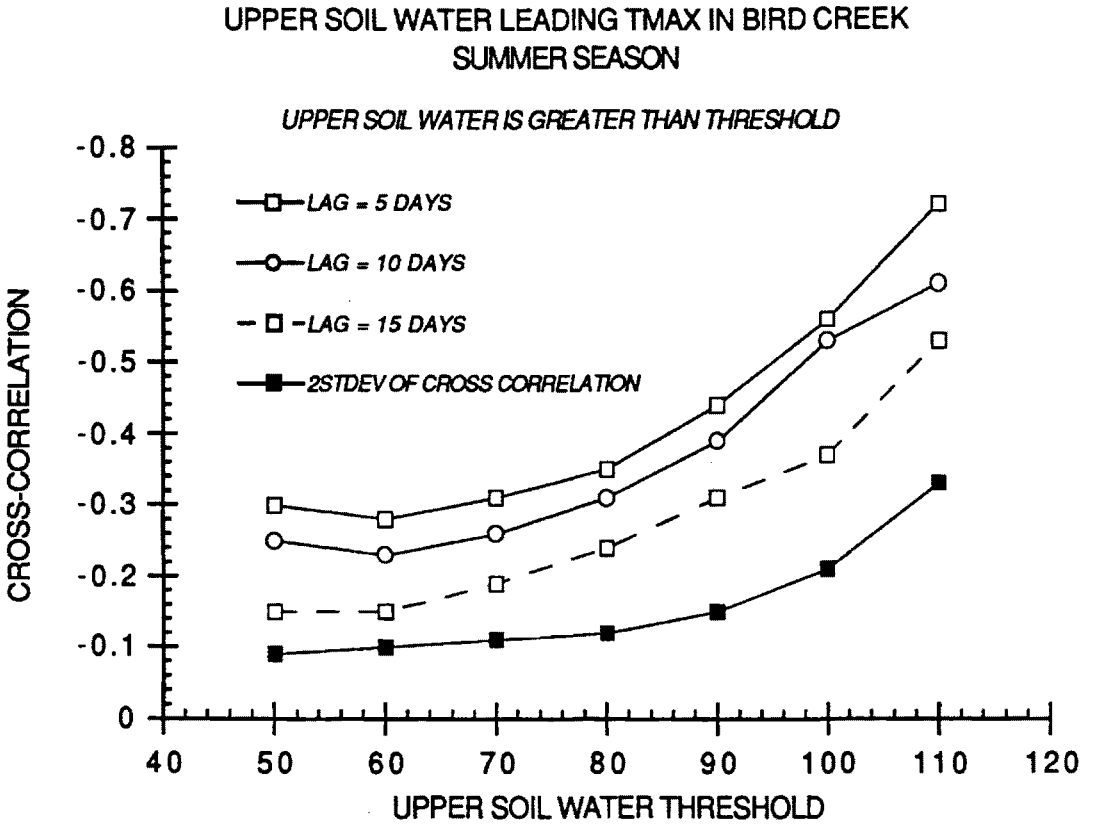
UPPER SOIL WATER LEADING TMAX IN BIRD CREEK
SUMMER SEASON
UPPER SOIL WATER IS GREATER THAN THRESHOLD
LAG = 5 DAYS
LAG = 10 DAYS
LAG = 15 DAYS
2STDEV OF CROSS CORRELATION
CROSS-CORRELATION
-0.8
-0.7
-0.6
-0.5
-0.4
-0.3
-0.2
-0.1
0
40
50
60
70
80
90
100
110
120
UPPER SOIL WATER THRESHOLD

FLOOD PREVENTION USING STREAMFLOW FORECASTS AND RESERVOIR CONTROL SCHEMES

Aris P. Georgakakos, Associate Professor
and
Huaming Yao, Graduate Research Assistant

School of Civil Engineering, Georgia Institute of Technology, Atlanta, GA 30332, USA

ABSTRACT: The purpose of this study is to demonstrate that effective reservoir control schemes combined with inflow forecasting procedures can substantially enhance flood prevention. The approach taken is to simulate and examine the response of a typical reservoir system operated with the aid of such schemes. The results indicate that the benefits are indeed substantial and, most likely, outweigh the cost of implementation.

INTRODUCTION

Reservoir control schemes with inflow forecasting capabilities are expected to improve flood prevention as well as other reservoir system functions. However, a question often raised is whether the benefits from such systems outweigh their costs. The goal of this paper is to provide a partial answer to this question by demonstrating that reservoir control and inflow forecasting procedures can substantially mitigate flood damage frequency and magnitude. The approach taken is to quantify the improvements for a typical three-reservoir system. While to some extent the actual benefits are expected to be system-specific, some general conclusions can still be drawn.

In what follows, the reservoir system used as a case study is described first. Subsequently, a recently developed reservoir control method suitable for water resources management under extreme hydrologic conditions is briefly presented and discussed. Next, a series of three computational experiments is presented where this control method is called upon to guide system operations using inflow forecasts of varying accuracy. Some observations and conclusions are summarized in the last section.

RESERVOIR SYSTEM MODEL

The following discussion makes reference to a three-reservoir cascade as an example and test case. This system is located on the Savannah River in the southeastern U.S. and is described in *Georgakakos* [*1989, 1992*]. For the purposes of this investigation, the system is modelled by the following water balance state equation:

$$\begin{bmatrix} S_1(k+1) \\ S_2(k+1) \\ S_3(k+1) \end{bmatrix} = \begin{bmatrix} 1 & 0 & 0 \\ 0 & 1 & 0 \\ 0 & 0 & 1 \end{bmatrix} \begin{bmatrix} S_1(k) \\ S_2(k) \\ S_3(k) \end{bmatrix} + \begin{bmatrix} -b_1(k) & 0 & 0 \\ b_1(k) & -b_2(k) & 0 \\ 0 & b_2(k) & -b_3(k) \end{bmatrix} \begin{bmatrix} t_1(k) \\ t_2(k) \\ t_3(k) \end{bmatrix} + \begin{bmatrix} 1 & 0 & 0 \\ 0 & 1 & 0 \\ 0 & 0 & 1 \end{bmatrix} \begin{bmatrix} w_1(k) \\ w_2(k) \\ w_3(k) \end{bmatrix}, \quad (1)$$

$$k = 0,1,\ldots,N-1,$$

$$b_i(k) = \sum_{j=1}^{n_i} u_{ij}(k), \quad i = 1,2,3. \quad (2)$$

In the above, $S_i(k)$ and $w_i(k)$ respectively represent storage and inflow volumes for reservoir $i=1,2,3$, $u_{ij}(k)$ is the discharge from the j^{th} turbine of the i^{th} reservoir, $t_i(k)$ represents the generation hours during period k, and n_i is the number of turbines at reservoir i. Table 1 reports relevant reservoir characteristics including permissible storage and release ranges reflecting water conservation and flood control objectives, and Figure 1 depicts extreme daily inflow volume ranges. These ranges represent the lowest and highest inflow values on record (10 years). Figure 2 shows the dependence of total turbine discharge on reservoir storage at power capacity. The curves take into account tailrace effects and are based on the power-(net hydraulic head)-discharge relationships reported by *Georgakakos [1991, Appendix A]*.

Table 1: Reservoir Characteristics

	Reservoir 1	Reservoir 2	Reservoir 3
Min. Storage (bcf)	79.25	34.2	69.71
Max. Storage (bcf)	123.8	50.8	125.95
Min. Release (bcf / day)	0.0	0.0	0.0
Max. Release (bcf / day)	3.0	3.0	3.0
Power Capacity (MW)	430	375	350
Number of Turbines	5	4	7

This system has multiple objectives including flood control, water supply, recreation, pollution abatement, fish and wild life management, and power generation. The purpose of the control scheme is to determine turbine operation schedules (or, equivalently, reservoir releases) to satisfy these objectives as best as possible.

SET CONTROL APPROACH

The Set Control Approach (SCA) was introduced by *Georgakakos and Yao [1992a]* for cases where hydrologic data are insufficient to support probabilistic methods. Such cases include hydrologic extremes (floods and droughts) as well as circumstances where past inflow records are atypical of future realizations (e.g., due to climatic changes). The Set Control Approach makes the assumption that future inputs are only restricted to belong in certain

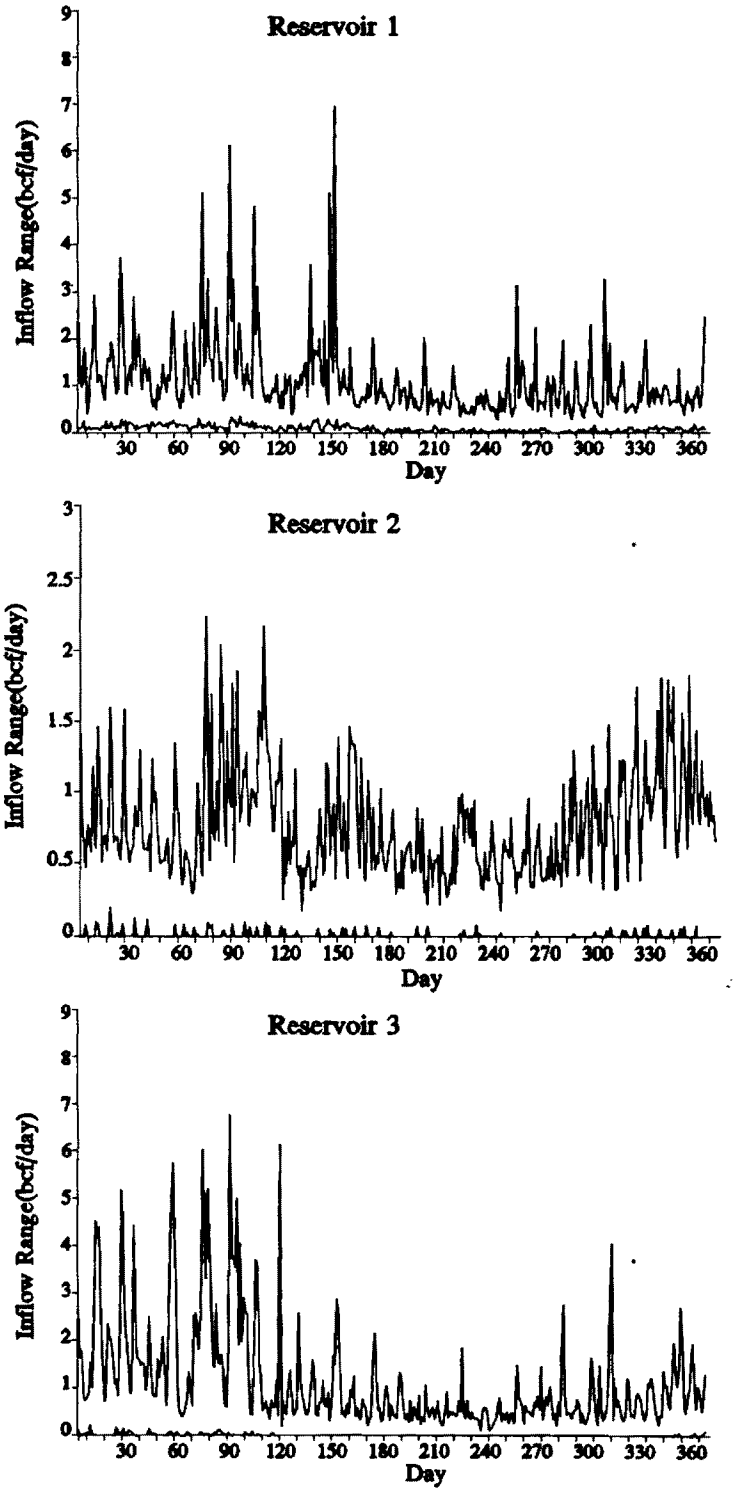

Figure 1: Inflow Bounds

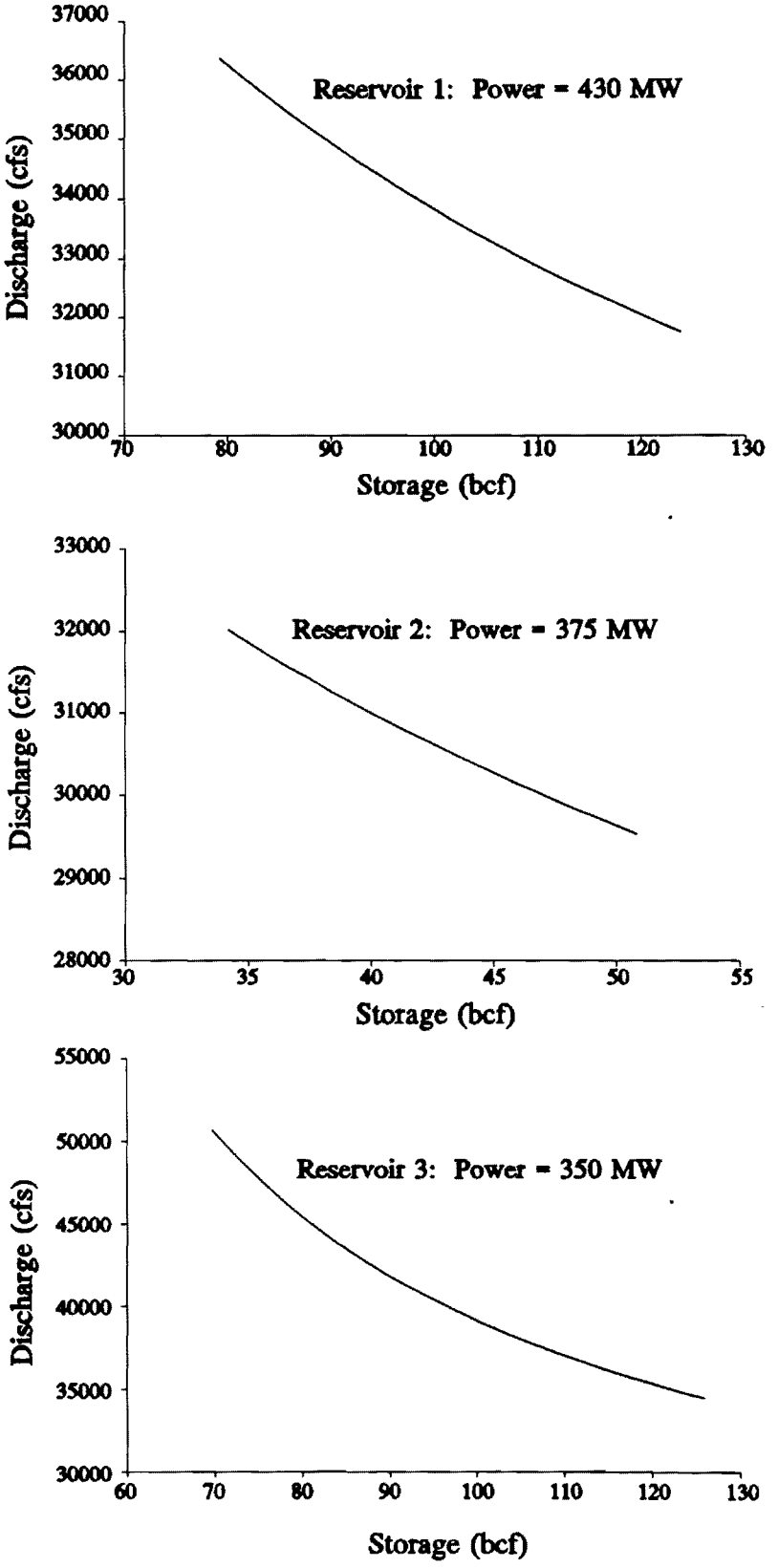

Figure 2: Turbine Discharge Versus Storage

sets. The boundaries of these sets may represent minimum and maximum input estimates or other extreme input levels against which a sound operational policy is to be developed. In this framework, the purpose of the control scheme is to determine admissible control actions such that key system variables stay within acceptable limits as long as system inputs take on values from the specified input sets. In what follows, we outline the basic SCA concepts. For a complete presentation, the reader is referred to *Georgakakos and Yao* [*1992a*] and *Yao and Georgakakos* [*1992*].

Many water resources systems can be represented by difference equations describing the evolution of a pivotal quantity, called state, in response to controllable and uncontrollable inputs:

$$\boldsymbol{S}(k+1) = \boldsymbol{A}(k)\,\boldsymbol{S}(k) + \boldsymbol{B}(k)\,\boldsymbol{u}(k) + \boldsymbol{G}(k)\,\boldsymbol{w}(k), \quad k=0,1,...,N-1, \tag{3}$$

where $\mathbf{S}(k)$ is the n_s-dimensional state vector; $\mathbf{u}(k)$ is the n_u-dimensional control vector, $\mathbf{w}(k)$ is the n_w-dimensional input vector; and $\mathbf{A}(k)$, $\mathbf{B}(k)$, and $\mathbf{G}(k)$ are $(n_s x n_s)$-, $(n_s x n_u)$-, and $(n_s x n_w)$-dimensional matrix coefficients respectively encoding the system layout and the interaction among its constituent elements. Examples include reservoir systems (e.g. the one described earlier) where state variables (states) represent reservoir storages, control variables (controls) represent releases or power generation hours, and input variables (inputs) represent reservoir inflows; groundwater systems where states may represent hydraulic heads and/or pollutant concentrations, controls may represent pumping rates, and inputs may represent boundary conditions [see, among others, *Willis and Finney, 1985, Georgakakos and Vlatsa, 1991*]; and wastewater treatment processes where states are organic and inorganic constituent concentrations, controls are recycling rates, and inputs are wastewater loading characteristics [*Harris, 1977, Kabouris and Georgakakos, 1990, and others*].

Typically, the state and control vectors are restricted within certain acceptable ranges,

$$\begin{aligned} \boldsymbol{S}^{\min}(k) \le \boldsymbol{S}(k) \le \boldsymbol{S}^{\max}(k), \quad k=0,1,...,N, \\ \boldsymbol{u}^{\min}(k) \le \boldsymbol{u}(k) \le \boldsymbol{u}^{\max}(k), \quad k=0,1,...,N-1, \end{aligned} \tag{4}$$

where the upper and lower bounds may represent physical capacities or operational requirements. It is further assumed that system inputs are practically unknown except that they take on values from within specified sets such as:

$$\boldsymbol{w}^{\min}(k) \le \boldsymbol{w}(k) \le \boldsymbol{w}^{\max}(k), \quad k=0,1,...,N-1, \tag{5}$$

where the upper and lower bounds represent extreme input levels against which the system is to be protected. The control problem is to determine admissible controls (4) such that system states remain within their acceptable limits (4), regardless of what inputs materialize from the specified input sets (5).

In what follows, $\{\Omega_s(k), k=0,1,...,N\}$ denotes the sequence of acceptable state sets, $\{\Omega_u(k), k=0,1,...,N-1\}$ the sequence of admissible control sets, and $\{\Omega_w(k), k=0,1,...,N-1\}$ the input set sequence. The solution of the set control problem can be obtained via Dynamic Programming as follows: Define the modified state set $\Omega_m(N)$:

$$\Omega_m(N) = \{S \in R^n: [S + G(N-1)\, w(N-1)] \in \Omega_s(N),\ \forall\, w(N-1) \in \Omega_w(N-1)\}. \qquad (6)$$

Namely, $\Omega_m(N)$ contains all vectors **S** such that [S + G(N-1) w(N-1)] belongs to the state set $\Omega_s(N)$ for any input vector in $\Omega_w(N-1)$.

Define the reduced state set $\Omega_r(N-1)$:

$$\Omega_r(N-1) = \{S \in \Omega_s(N-1):\ \exists\, u(N-1) \in \Omega_u(N-1):\ [A(N-1)\, S + B(N-1)\, u(N-1)] \in \Omega_m(N)\}. \qquad (7)$$

Namely, $\Omega_r(N-1)$ includes all acceptable state vectors **S** for which there exists an admissible control vector **u**(N-1) such that [**A**(N-1) **S** + **B**(N-1) **u**(N-1)] belongs to the modified state set $\Omega_m(N)$. The significance of the previous sets is that if the system state **S**(N-1) reaches set $\Omega_r(N-1)$, there exists an admissible control vector that can transfer it to an acceptable terminal state **S**(N) for any input vector in $\Omega_w(N-1)$.

One can proceed similarly (see Figure 3) to define the modified and reduced state sets for the previous time:

$$\Omega_m(N-1) = \{S \in R^n: [S + G(N-2)\, w(N-2)] \in \Omega_r(N-1),\ \forall\, w(N-2) \in \Omega_w(N-2)\}, \qquad (8)$$

(Note that $\Omega_m(N-1)$ is defined based on $\Omega_r(N-1)$, not $\Omega_s(N-1)$.)

$$\Omega_r(N-2) = \{S \in \Omega_s(N-2):\ \exists\, u(N-2) \in \Omega_u(N-2):\ [A(N-2)\, S + B(N-2)\, u(N-2)] \in \Omega_m(N-1)\}. \qquad (9)$$

Thus, if the system reaches set $\Omega_m(N-2)$, there exist control vectors **u**(N-2) and **u**(N-1) such that states **S**(N-1) and **S**(N) remain within the acceptable limits for any input realizations {**w**(N-2), **w**(N-1)} from the specified input sets.

The previous considerations can recursively be repeated in the reverse time direction, k = N-3, N-4, ... , 0. The problem has a feasible solution (i.e., there exist a control sequence able to keep the state vectors within their acceptable sets) if the sets thus derived are nonempty and the reduced state set $\Omega_r(0)$ includes the initial state vector **S**(0). Note, however, that the previous solution process does not determine which controls to use. Specific control vectors can be selected only as the system evolves and the state variable values become known.

As usual, Dynamic Programming led to a theoretically elegant solution. The practical implementation of this solution, however, presents an equally elegant challenge. *Glover and Schweppe [1971]* and *Bertsekas and Rhodes [1971]* proposed ellipsoidal approximation algorithms based on Schweppe's bounding ellipsoidal approximation theory [*Schweppe, 1973*]. The idea is to approximate all sets by bounding ellipsoids and develop recursive relationships for the computation of the modified and reduced state sets. Since ellipsoids

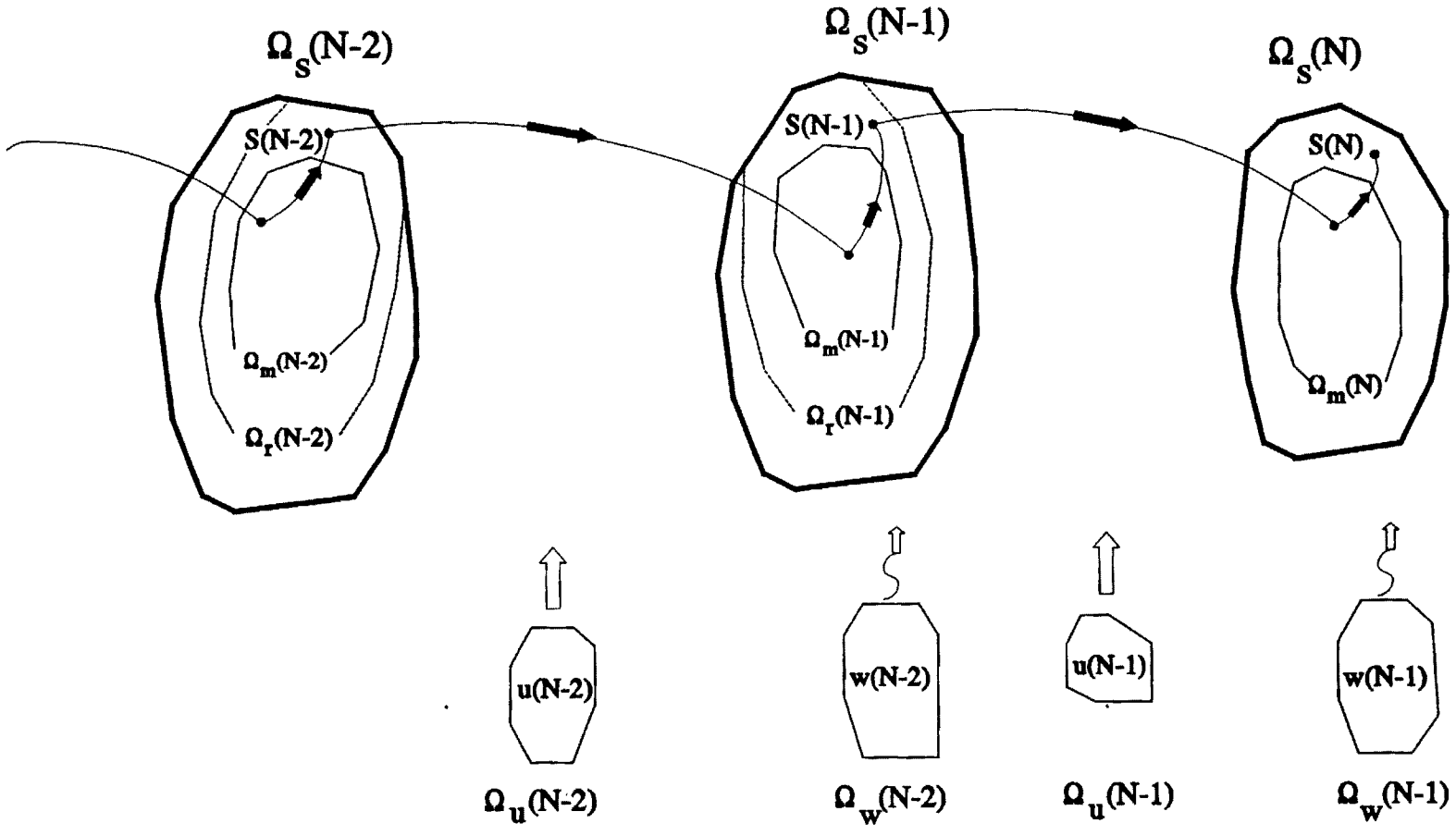

Figure 3: Dynamic Programming Solution of the Set Control Problem

are characterized by their center vector and principal axes, the set computation is reduced to a recursive computation of these attributes. However, the required approximations quickly result in empty modified and reduced state sets, and the algorithms falsely indicate infeasibility.

Another approach is to define state, control, and input sets as convex polyhedra and develop efficient procedures to compute the modified and reduced state sets. It turns out that the modified and reduced state sets are also convex polyhedra defined by their perpendicular vectors and support functions. This is the approach we have adopted because it is exact and naturally suitable for water resources systems. The detail procedures for the modified and reduced state set computations are at the core of the SCA method and are fully described in *Georgakakos and Yao [1992a]*. In what follows, we present some case studies with the Savannah reservoir system.

APPLICATION

The purpose of this section is to illustrate the potential benefits of combined inflow forecast - reservoir control schemes. Our approach is to simulate and assess the performance of the Savannah reservoir system over a 10-year period (1972-1981) under the guidance of the Set Control Approach and various inflow forecasting schemes. Inflow forecasts are assumed to restrict the historical inflow ranges (Figure 1) as follows: The actually observed inflow sequence over the duration of the control horizon is first determined along with the corresponding historical ranges from Figure 1. The range used in the model for each day is centered around the actually observed value and represents a certain percentage of the historical range. As illustrated on Figure 4, these percentages gradually increase from the first to the last day of the control horizon to reflect that forecast quality deteriorates with lead time. The percentages are determined based on the following equation:

$$p(k) = p(1)\,[1.03]^{k-1}, \tag{10}$$

where p(k) denotes the percentage of day k. In the computational experiments to follow, this procedure is employed with $p(1)=0.5$ and $p(1)=0.25$. The results are compared with the case where SCA simply uses the historical inflow ranges from Figure 1 (no forecasting).

The simulation process is as follows: At each day of the simulation horizon, the forecasting model is first activated to determine the inflow ranges over the control horizon, and then the Set Control Approach is employed to generate the feasible control action set. This set includes all possible decisions guaranteeing that the system variables (storage, generation hours, and releases) will observe the stated constraints over the duration of the control horizon. Next, a decision is selected and the system operation is simulated for one time period. The simulation involves the determination of the next day's storages from Equation 1 with $w_i(k)$, $i=1,2,3$, being equal to their historically observed values. This process is repeated sequentially at each day of a 10-year simulation horizon, and system performance is recorded in terms of energy generation, outflow rates, and reservoir storage levels.

Some features common to all experiments are that the Set Control Approach is implemented with a control horizon of 15 days, the decisions selected correspond to the minimum feasible generation hours, the feasible storage range is restricted to the

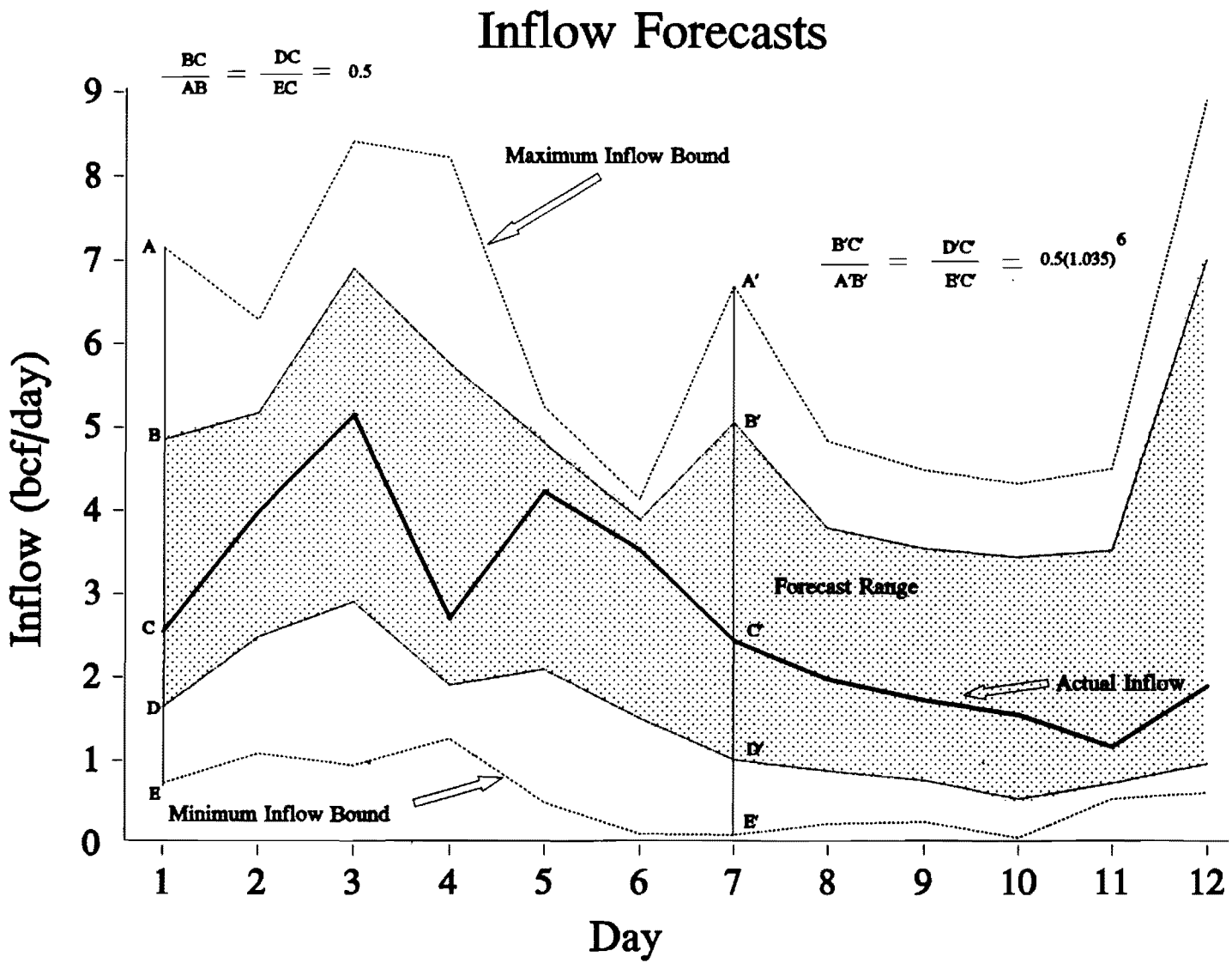

Figure 4: Inflow Forecasting Example

conservation pools, and the determination of turbine discharge over the 15-day control horizon is based on the current storage values. Experiments with a longer control horizon (30 days) were also conducted, but the results are similar to the ones presented herein. The rational for using the most conservative feasible decision is to conserve water and maintain reservoir pools as high as possible. Turbine discharges are determined based on the current storage because it is the best guess of future storage values. Certainly, the storage will eventually digress from this locale. However, the error is mitigated by the sequential mode of operation forcing continuous updating.

Figures 5 and 6 depict the results for the case where no inflow forecasts are used (base case). The graphs in Figure 5 include the storage bounds (dotted lines), the minimum and maximum simulation values for each day (thin solid lines), and the mean simulation storage sequence (thick solid line). The previous statistics were based on 10 simulation storage values for each day of the year. While system storages are maintained within the conservation pools, they tend to fluctuate markedly during the first part of the year (rainy season). Figure 6 includes the associated statistics for the control variables (generation hours per day), with dotted lines again representing bounds and solid lines depicting simulation statistics (minimum, maximum, and mean levels). The notable observation is that energy generation hours are often forced to exceed 24 hours per day in order to keep reservoir storages within the conservation pools. This simply implies that turbine conveyance capacity is not enough to control reservoir storage and water must also be released through the dam spillways. To be sure, the higher the exceedance of the 24-hour threshold, the more severe the flooding effects. More specifically, the highest release from the third reservoir in the cascade is about 3 times higher than the acceptable release bound. What is more, the mean generation sequence also violates the constraint threshold.

Figures 7 and 8 present the simulation results when the Set Control Approach has improved information of the upcoming inflows. This is simulated by using the procedure described previously (Eq. 10) with $p(1)=0.5$. The storage sequences (Figure 7) are again within the conservation zones, but the fluctuation ranges are now tighter. (The mean storage levels are clearly closer to the upper storage bounds.) The associated generation hours (Figure 8) on occasion exceed 24 hours / day, but the magnitude of the violation is much less than in the base case. Better forecasting allows the control model to mitigate flood damage. Nevertheless, the highest outflow is still 1.8 times higher than the acceptable release bound.

This trend continues in the third case (Figures 9 and 10) where inflow forecasting is employed with $p(1)=0.25$. The mean storage sequences have moved even closer to the upper bounds, and the generation hours are for the most part contained within the admissible limits. The magnitude of constraint violations is reduced further, while the distance of the mean generation sequence from the 24-hour bounds indicates that violations occur infrequently.

CONCLUSION

The previous computational experiments demonstrate that inflow forecasting and reservoir control schemes can usefully assist reservoir operations during extreme hydrologic conditions. In particular, better inflow forecasting allows the control model to minimize flood control storage and, at the same time, avoid damage-causing outflows. While, the

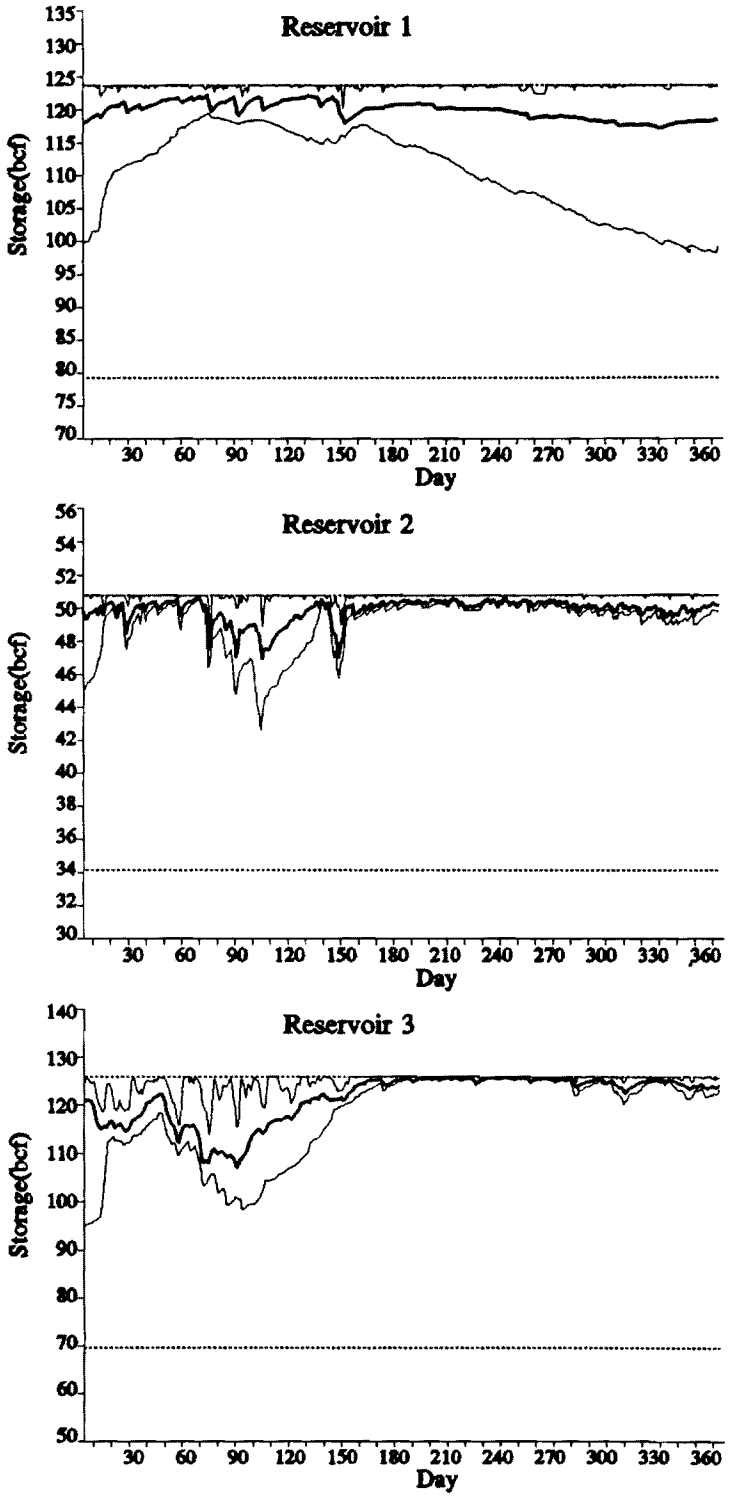

Figure 5: Simulation Storage; Base Case

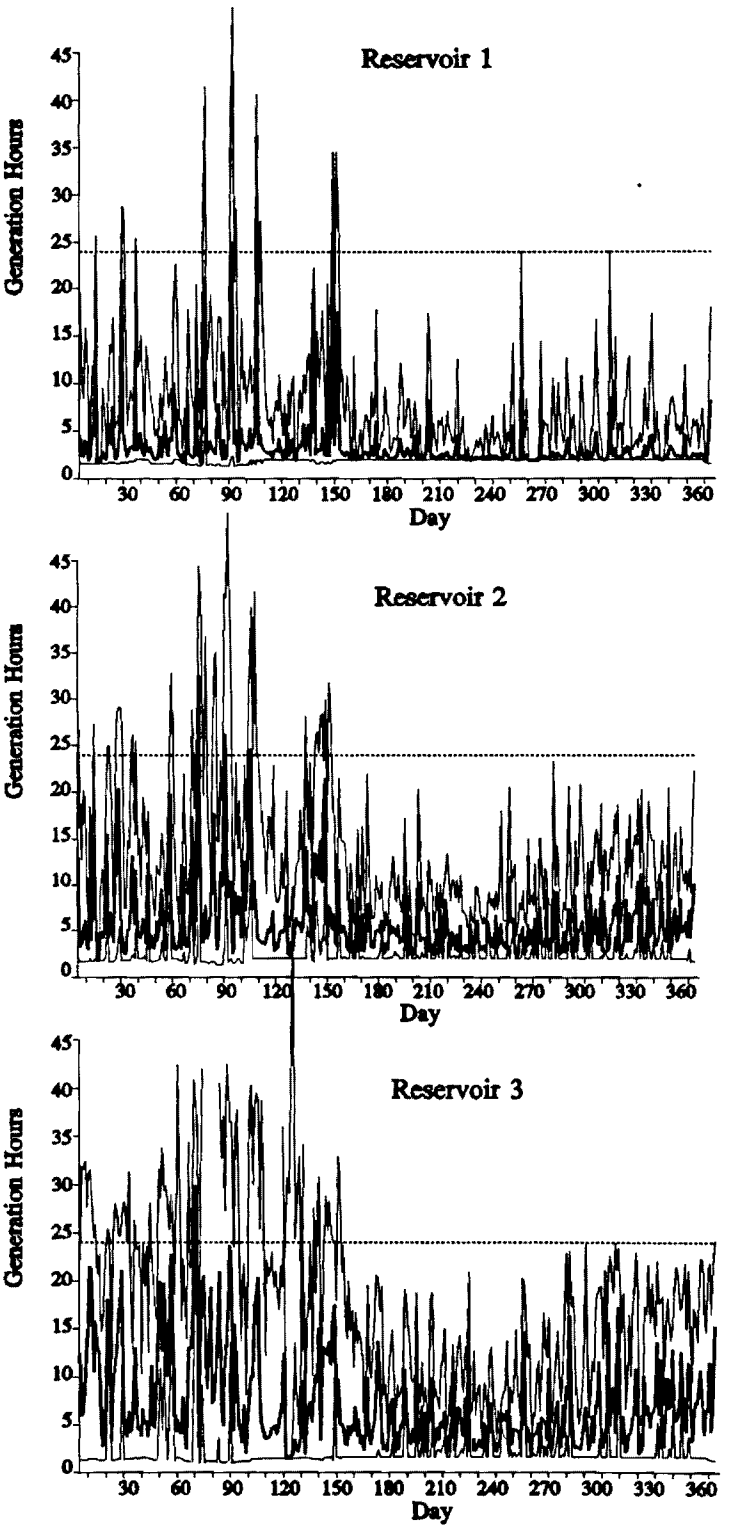

Figure 6: Simulation Gen. Hours; Base Case

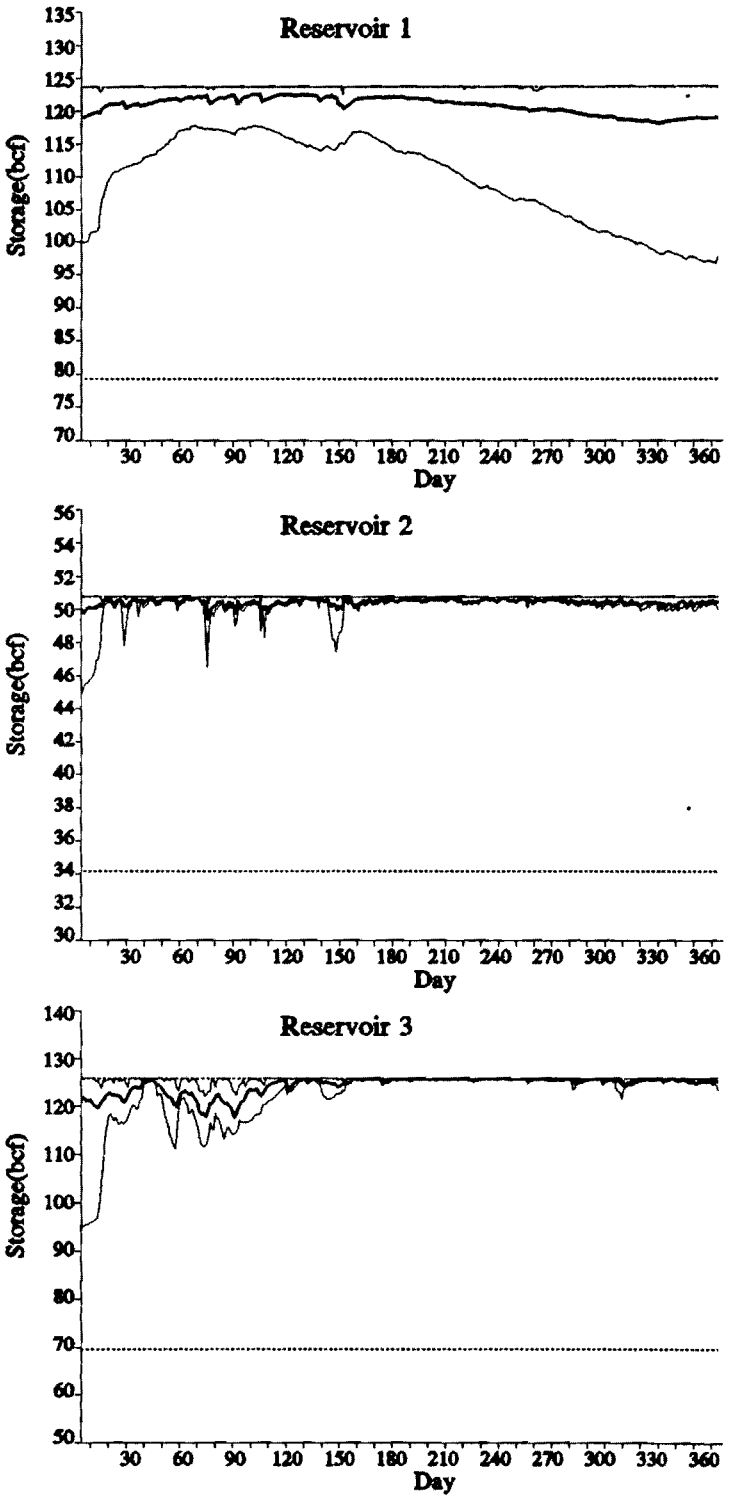

Figure 7: Simulation Storage; P(1)=0.5

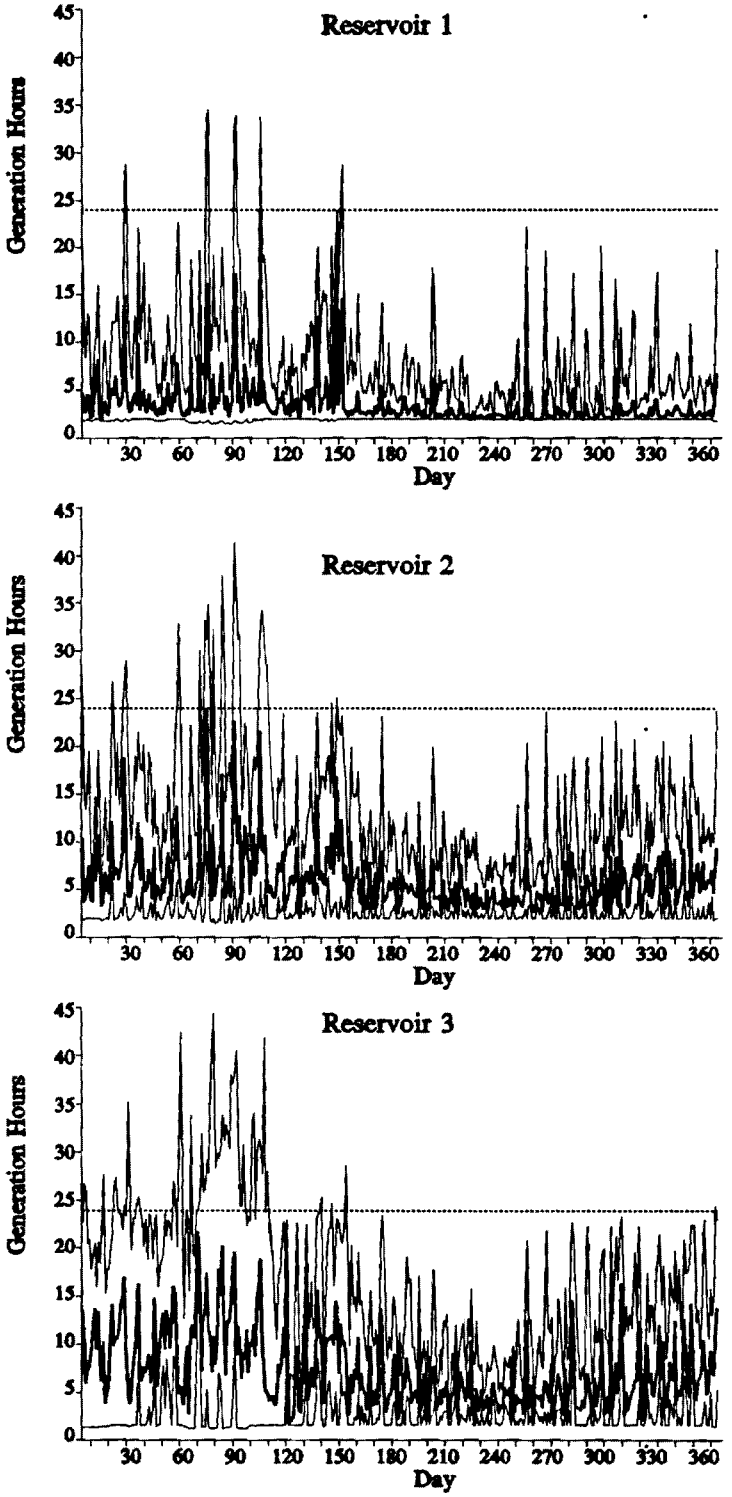

Figure 8: Simulation Gen. Hours;P(1)=0.5

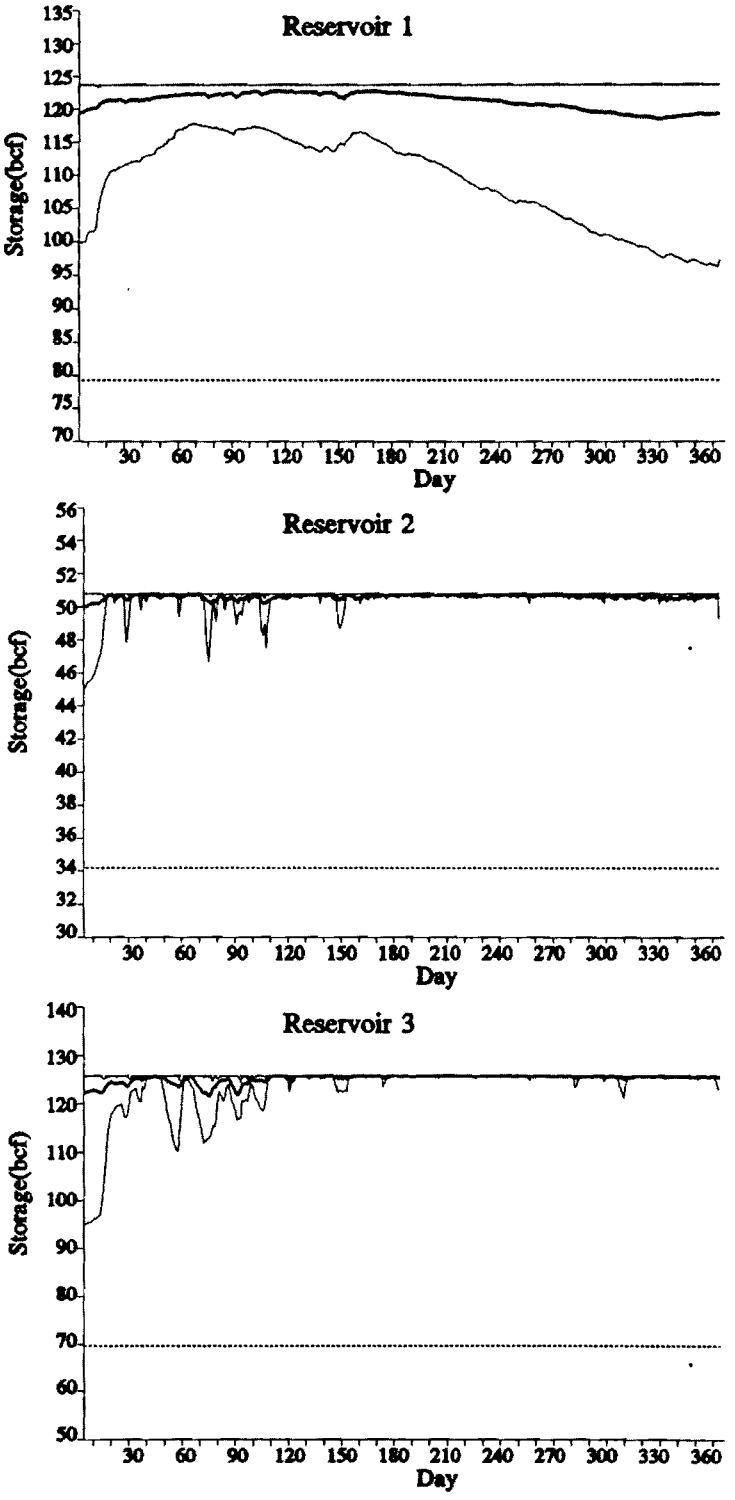

Figure 9: Simulation Storage; P(1)=0.25

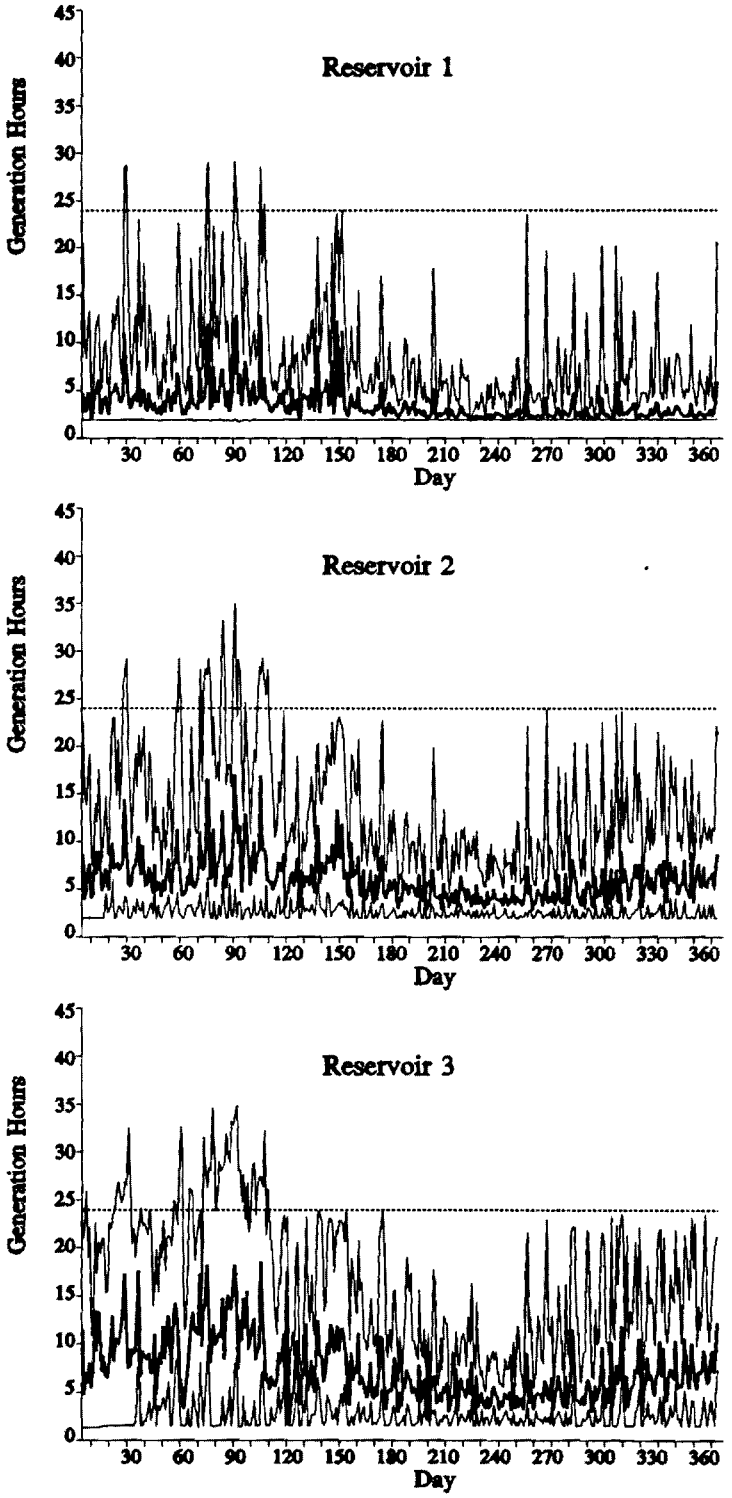

Figure 10: Simulation Gen. Hours; P(1)=0.25

actual forecast quality cannot be quantified before the implementation of a forecast system, the potential reduction of flood damage frequency and magnitude can be substantial. In addition, benefits accrue from energy generation due to higher hydraulic head and less wasted spillage.

Inflow forecasting and reservoir control schemes are also expected to improve the operation of reservoir systems during droughts. In a recent study, *Georgakakos and Yao [1992b]* show that such procedures can help the system meet higher dependable energy commitments and water supply requirements without compromising the associated reliability.

Lastly, it is noted that the Set Control Approach with its set characterization of uncertainty is naturally suitable for water resources management under extreme hydrologic conditions.

ACKNOWLEDGEMENTS

This work was supported in part by the U.S. Geological Survey under Research Contract No. 14-08-0001-G1886. Additional funding was provided by the U.S. Geological Survey as authorized by the Water Resources Act of 1984 and the Georgia Institute of Technology.

REFERENCES

Bertsekas, D.P. and I.B. Rhodes, On the minimax reachability of target sets and target tubes, *Automatica*, Vol. 7, 233-247, 1971.

Georgakakos, A. P., Extended Linear Quadratic Gaussian (ELQG) control: Further extensions, *Water Resources Research*, 25(2), 191-201, 1989.

Georgakakos, A. P., Optimal regulation of the Savannah River system, *Technical Report* for U.S. Army Corps of Engineers Research Contract No. DACW21-88-C-0043, School of Civil Engineering, Georgia Tech, May 1991.

Georgakakos, A. P., Operational tradeoffs in reservoir control, *Water Resources Research*, in press, 1992.

Georgakakos, A.P., and D.A. Vlatsa, Stochastic control of groundwater systems, *Water Resources Research*, 27(8), 2077-2090, 1991.

Georgakakos, A. P., and H. Yao, New control concepts for uncertain water resources systems: 1, Theory, *Water Resources Research*, under review, 1992a.

Georgakakos, A.P. and H. Yao, "A New Reservoir Control Approach with Application to the Management of Lake Lanier," *Technical Completion Report,* Environmental Resour. Center, Dept. of the Interior, USGS, 83p., 1992b.

Glover, J.D., and F.C. Schweppe, Control of linear dynamic systems with set-constrained disturbances, *IEEE Transactions of Automatic Control*, 16(5), 411-423, 1971.

Harris, C.J., Modelling and adaptive control of urban wastewater treatment plants, in *Environmental Systems Planning, Design, and Control*, Proceedings IFAC Symposium, Kyoto, Japan, 1977.

Kabouris , J.C., and A.P. Georgakakos, Optimal control of the activated sludge process, *Water Research*, 24(10), 1197-1208, 1990.

Schweppe, F.C., *Uncertain Dynamic Systems*, Prentice Hall, 1973.

Willis, R., and B.A. Finney, Optimal control of nonlinear groundwater hydraulics: Theoretical development and numerical experiments, *Water Resources Research*, 21(10), 1476-1482, 1985.

SENSITIVITY OF RESERVOIR HYDROSYSTEMS TO POTENTIAL CLIMATE CHANGES

M.G. Mullusky, A.P. Georgakakos[1], D.H. Bae, and K.P. Georgakakos

The University of Iowa
Iowa City, Iowa

[1]Georgia Institute of Technology
Atlanta, Georgia

Operational policies for reservoir systems have been designed based on existing hydroclimatic regimes. Such regimes maybe subject to change as a result of anthropogenic influences. Sensitivity analysis was conducted to assess the robustness of the operating policies to hydroclimatic changes. The analysis is performed within the framework of coupled forecast-control schemes that explicitly account for forecast uncertainty. The application area is the 14,000 square kilometer Upper Des Moines River basin in Minnesota and Iowa. The observed meteorological and hydrological variables have a strong seasonal component with highest flow occurring in spring, and with a second flow peak in the summer season. The area has been subdivided into six sub-catchments. The rainfall-runoff model used for each sub-catchment is an adaptation of the NWS operational Sacramento model, and channel routing is done by the Muskingum-Cunge hydraulic routing scheme, well suited to the mild slopes of the channels. State updating and uncertainty propagation among the model components is performed by a state estimator, using available daily data, (Bae and Georgakakos,1992).

The Extended Streamflow Prediction (ESP) scheme of the NWS has been used to generate probabilistic forecasts up to three months in the future with daily resolution, (Day,1985). The forecasts are updated every 15 days. The Saylorville reservoir on the Upper Des Moines River in Iowa has been used as the application reservoir for the study. The system objectives include water supply, flood prevention and water quality concerns. The control procedure utilizes a numerically-efficient stochastic control algorithm, which explicitly incorporates forecast uncertainty. The procedure for sensitivity analysis consists of establishing baseline performance using historical daily data extending back to the early 1900s. The historical record was subdivided into several pieces which were ranked based on annual-average temperature and precipitation amount. Then, future climate scenerios of increasing temperature decreasing precipitation, increasing temperature, etc, were formed based on the meterological characteristics of the historical pieces. We are in the process of applying the forecast-control procedure to the constructed scenarios and have the results compared to the baseline results for assessing the sensitivity of the procedure to potential future climatic scenarios. The full set of results will be presented at the meeting. We present here initial results of our analysis.

Figure 1 presents the average ESP predictions with a daily resolution for a wet and a dry year made at the first of the month for selected months from March through October. There are 24 realizations of past years used as input to the ESP procedure, and the solid line represents the average of the predictions for each day of the extended

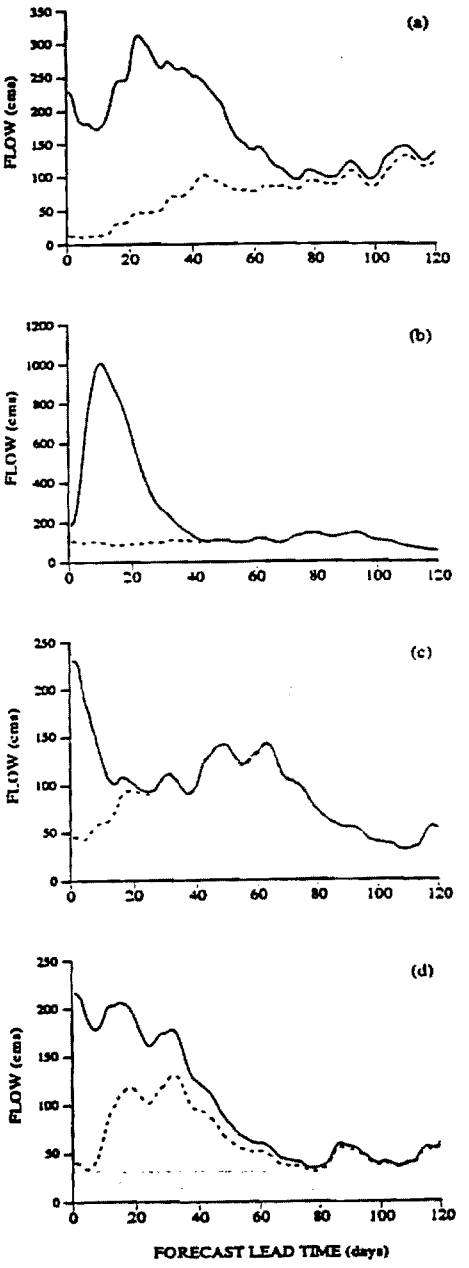

Figure 1. Average ESP predicted flows (in cms) for the wet year (solid line) and the dry year (dashed line) for (a) March, (b) April, (c) May, and (d) June.

forecast period, when initial conditions based on the wet year have been used. The dashed line represents analogous results when the dry year has been used to provide initial conditions for the ESP runs. The length of the forecast period is four months (120 days) in each case. The wet year, 1965, was the second wettest year of the 24 year record of rainfall, and the dry year, 1976, was the driest year of record.

Of particular interest in terms of the impact of having a wet versus a dry year to the management of the reservoir, the largest differences occur in spring (MAM) and early summer and in mid-fall. Thus, it is expected that climatic change toward a wetter or a drier climatic regime would be felt by the operational managers of this particular reservoir in the Central United States during the aforementioned months. It is also interesting to observe that the duration of significant average-prediction differences varies with month. If significant is defined to mean differences greater than 50 cms (~ 1800 cfs), then the duration of such differences in March is about 2 months; in April is about 1.5 months; in May is about 2 weeks; in June it is about a month; in July, August and September there seems to be no significant difference in prediction; and in October it is a little less that 2 months. Such results indicate that the wet year was wet because of high spring and high fall rainfall. The latter was the result of the influence of the remnants of tropical storms, which infrequently affect the fall rainfall of the region.

Figure 2 presents the variation of the predicted standard deviation of the 24 realizations of the ESP runs made for March 1 and June 1 for the wet (solid line) and dry (dashed line) year. It is noted that the variability of the predictions corresponding to individual realizations is as high as the predicted values, with the wet year exhibiting a larger variability than the dry year. Such a result underlies the importance of having modern reservoir management systems capable of accounting for the uncertainty in the flow predictions, as such uncertainty changes when the climatic mean values change.

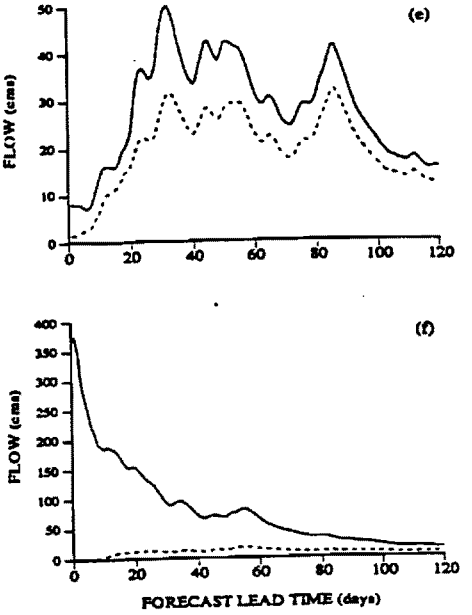

Figure 1 continued. Average ESP predicted flows (in cms) for the wet year (solid line) and the dry year (dashed line) for (e) September, and (f) October.

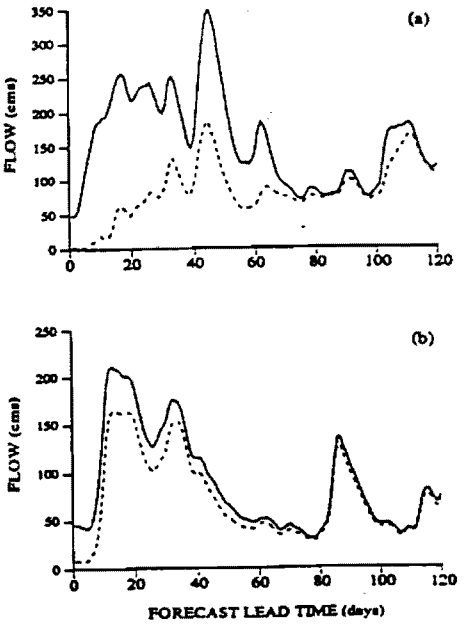

Figure 2. Standard deviation of the ESP predicted flows (in cms) for the wet year (solid line) and the dry year (dashed line) for (a) March and (b) June.

ACKNOWLEDGEMENTS

This work is sponsored by the US Geological Survey Award No. E-20-686-S1 (subcontract to a Georgia Institute of Technology contract); by the Center for Global and Regional Environmental Research (CGRER) of The University of Iowa under seed grant QK96; and by the Iowa Institute of Hydraulic Research through the EPRIa Program, funded by a consortium of mid-western Power Utilities.

REFERENCES

Bae, D.H. and K.P. Georgakakos, "Hydrologic Modeling for Flow Forecasting and Climate Studies in Large Drainage Basins," IIHR Technical Report, Iowa Institute of Hydraulic Research, The University of Iowa, Iowa City, Iowa, 293 pages, 1992. (In press.)

Day, G.N., "Extended Streamflow Forecasting Using NWSRFS," J. Water Resources Planning and Management, ASCE, 111(2), 157-170, 1985.

Progress Report to

U. S. G. S.
Reston, Virginia 22092

Award 14-08-0001-G1886

Impacts of Global Warming on Reservoir System Management

Aris P. Georgakakos[1] and Konstantine P. Georgakakos[2]

[1] School of Civil Engineering, Georgia Institute of Technology, Atlanta, Georgia 30332
[2] Iowa Institute of Hydraulic Research, The University of Iowa, Iowa City, Iowa 52242-1585

March 1993

1. INTRODUCTION

1.1 Problem Addressed

The subject research addresses the question: *How resilient to input forcing changes are large existing water resources reservoir systems?* The question is non-trivial in the context of a potential climate change because: (a) variability in input forcing (i.e., streamflow) critically depends on the variability of meteorological variables which is largely unknown under a potential climatic change on regional scales; (b) the policies for the operation of existing large water resources reservoirs can be improved using modern real-time control concepts and coupled forecast/control systems, so that the reservoir system becomes more robust in its response to enhanced variability and/or trends in inflows on climatic scales; and (c) pronounced nonlinearities and feedbacks exist in the forecast/management components for large reservoirs that make analytical results unreliable and daily simulation with observed data indispensable. The question is very important from the standpoint of water resources availability, ecosystem response and energy production, as the studied large reservoir system has a profound influence on the regional availability of water, protection from excess water (i.e., floods), and assurance of high water quality and regional ecosystem well being.

1.2 Past Relevant Research

NRC (1991) suggests that mitigation actions are likely to reduce the economic effect of a potential climate change on hydrosystems that a pure adaptation strategy would yield. The same report identifies reservoir storage as one of the elements that can moderate climate change effects on water resources. In fact, optimal operation under a potential climate change appears as one engineering approach toward mitigation. Rogers and Fiering (1990) outline the importance of reservoir storage in mitigating input forcing changes using simple models and analytical approaches. They do recommend that more accurate representations are necessary for reliable conclusions. Gleick (1990) discusses vulnerabilities of water supply systems (including reservoir systems) to climatic variability and change. He outlines the importance of studies that quantify the ability of existing reservoir systems to meet this design goals under a potential climate change. Both reservoir systems of the proposed study are in regions identified as vulnerable to flooding and drought with a ratio of reservoir volume to annual supply of less than 0.60. Consequently, special emphasis has been placed in the subject research on the risk of failure of the reservoirs due to extreme forcing.

To the best of the author's knowledge there has not been a study similar to the one outlined here, which uses coupled forecast/control schemes for operational reservoir management under uncertainty and in a climate change context. Previous recent studies have developed a large hydrologic/hydraulic model for the drainage basin of the Iowa reservoir system (Bae and Georgakakos, 1992), and have produced baseline information on the hydroclimatology of the region (selected results are shown herein).

1.3 Outline of Methodology

To answer the posed question of resilience, the following methodology was followed:

1. A physically-based hydrologic/hydraulic model was used to simulate inflows to the reservoir system, given meteorological input of precipitation and potential evapotranspiration. Such a model is necessary to produce a self consistent set of hydrological variables, including soil moisture and actual evapotranspiration, and to provide flow estimates for historical periods with no flow data. Past use of such models on climatic scales has given excellent results (Bae and Georgakakos, 1992).

2. A dataset of historical meteorological and flow data has been assembled for hydrologic /hydraulic model calibration to the local and regional conditions of the basins, and for producing historical climate change analogs. Preliminary analysis has shown that such datasets can be assembled for the study area with records dating back to the early 1900s. Three periods, each 25 years long, would be eventually identified in an effort to study system performance under three different historical climate periods. Such periods would be indexed by the average temperature, precipitation, soil moisture and evapotranspiration.
3. The hydrologic/hydraulic model was used to produce several realizations of future flows for each day of the record using as initial conditions the actual soil moisture conditions for that day (as estimated by the best model simulation with observed data) and as input forcing the trace of the historical realizations of meteorological input variables that correspond to the period under study. This type of methodology is operationally used by the National Weather Service to produce medium range forecasts and it is called Extended Streamflow Prediction (ESP) (Day, 1985). ESP results for the Iowa basin are shown in section 4 of this report.
4. Using the ensemble of forecast realizations by the ESP procedure, a state-of-the-science hybrid stochastic controller (that is based on set theory and on the extended linear quadratic gaussian approach of Georgakakos, 1987, 1989) produced optimal reservoir operating rules that determine releases, storage levels for flood control and hydroelectric power generation. Section 5 presents initial results. Results would eventually be obtained for all three of the aforementioned historical periods and measures of performance relevant to the study would be defined for intercomparison of performance during those periods.

2. CASE STUDY AND DATA

The Saylorville reservoir in central Iowa that accepts inflows from the Upper Des Moines River, draining 14,000 km^2, is the study system. Figure 2.1 shows the drainage basin and the available historical data with daily resolution. Such data is available through the EARTH INFO CD ROM disks that exist at the Hydromet Laboratory of The University of Iowa and cover the proposed areas of study. Many stations have historical records that date since the late 40s and a few have records that date since the beginning of this century. In both cases there are few pan evaporation data stations with data that date since the late 40s. The hydrologic/hydraulic model UIFS, used in this research, requires estimates of mean areal precipitation, mean areal temperature and mean areal potential evapotranspiration over each sub-basin of the system modeled. Such estimates have been produced by Bae and Georgakakos (1992) for the Iowa basin and for the 40-year period from 1948 through 1988, which is the period with most station data.

3. UIFS STREAMFLOW SIMULATION AND PREDICTION MODEL

Bae and Georgakakos (1992) developed, implemented in an operational environment, and tested a physically-based hydrologic/hydraulic model, called the University of Iowa Forecast System (UIFS), suitable for implementation to large basins with several tributary sub-basins and with capability of simulations/predictions with daily resolution. This model was adopted to the local conditions of the basin and was used for the production of flow predictions given meteorological forcing. In the following sections, the model is described briefly and results of its application are reviewed.

3.1 Model Description

The UIFS is based on an adaptation of the operational National Weather Service soil moisture accounting and snow accumulation and ablation models, complemented by a hydraulic

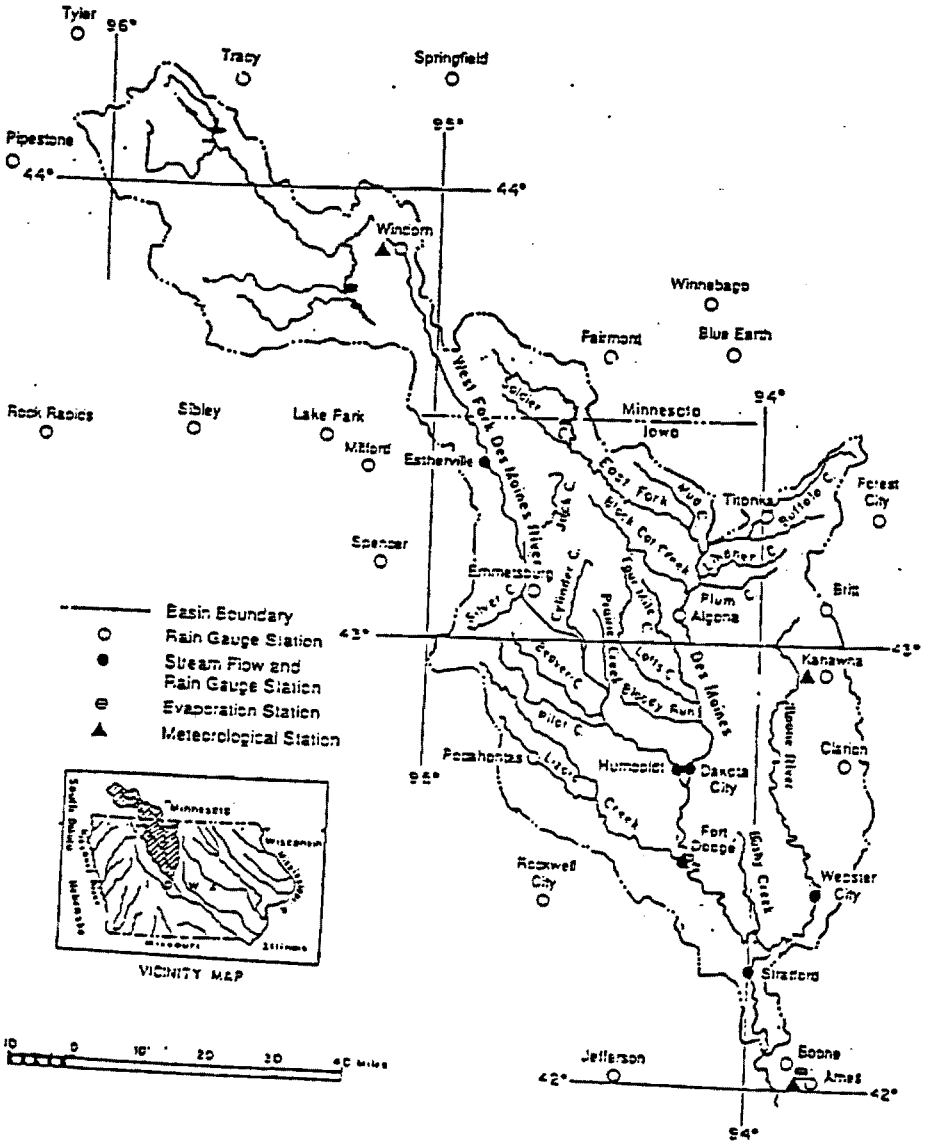

Figure 2.1: Upper Des Moines River basin with outlet at Stratford, Iowa, and stations with daily data on climate scales.

Muskingum-Cunge diffusive channel routing scheme (e.g., Georgakakos, et al. 1990). The UIFS has been designed for application to large basins with identifiable tributary basins. The flows in the tributary basins are computed from the soil moisture accounting and snow models and they are routed through the river channels between tributary outlets and to the large basin outlet using the hydraulic routing component. The soil moisture accounting component divides the soil into two zones in an attempt to simulate the different response of the top soil, including interflow, and the deeper soil that possesses considerably smaller hydraulic conductivities. Interflow, surface runoff, and subsurface baseflow are model outflows in response to precipitation and evapotranspiration forcing. Anderson's (1973) temperature index model (in operational use in the US) has been used as the snow accumulation and ablation component and snowmelt is produced in response to temperature history. Due to space limitations, we refer the interested reader to Georgakakos and Bae (1992, pp. 14-58) for a complete description of model formulation and applicable differential equations.

3.2 Examples of Application

Bae and Georgakakos (1992) have calibrated the UIFS for the Upper Des Moines River basin with outlet at Stratford, Iowa, which is the point of inflow for the Saylorville reservoir. Twenty years of daily data have been used for the calibration that involved a combination of manual and automated procedures and calibration criteria that ranged from statistical quadratic errors to hydrologic criteria of reliable peak flow representation, time to rise to flood levels, etc. Verification was done for a different set of twenty years of daily data. Performance was very good with daily cross-correlation coefficients between observed and simulated flow of 0.86 or better for all tributary basins and at the large basin outlet. It was concluded that the UIFS is a reliable simulator of the daily flows in the Upper Des Moines River basin over climatic scales. As an example, in Figure 3.1 we present the observed seasonal distribution by 5-day periods of the observed average and st. deviation of the flows at two of the tributaries (2160 km^2 Boone River at left and 3512 km^2 West Fork Des Moines at right), together with the corresponding simulated flows. It is clear that the model captures the seasonal flow variability over climate scales (40 years have been used) well. the results also show the variability in flow regimes between tributary basins of the same reservoir system, which is what makes reliable hydrologic simulation indispensable. In the lower panels of Figure 3.1 the traces of the daily values of the soil water content of the lower and upper zones in the aforementioned tributary basins is shown. Significant similarities and differences are observed, with the Boone River basin having a much more pronounced response to atmospheric forcing.

3.4 Extended Streamflow Prediction (ESP)

Day (1985) presented the theory, capabilities and potential applications of the ESP methodology. Smith, et al. (1991) generalized the procedure to a nonparametric statistical framework for long-range streamflow forecasting with hydrologic models. We used ESP with the UIFS to produce operational probabilistic forecasts of future streamflow for the Upper Des Moines River basin under study. Conditional probability distributions with daily resolution were generated for a forecast horizon based on projected realizations by the UIFS using current soil moisture conditions and hypothetical future meteorological forcing that is based on the corresponding historical observed meteorological forcing (i.e., precipitation, temperature and evapotranspiration) for the dates of the forecast horizon. Thus, if there are n years of historical data, an ensemble of n forecast realizations was produced and from those, moments of the implied conditional distributions were constructed (e.g., mean and standard deviation for each day of the forecast horizon). The distribution is conditional on the current soil moisture conditions as current estimates of soil moisture would be used for each ESP run. The ESP/UIFS system is ideal for the

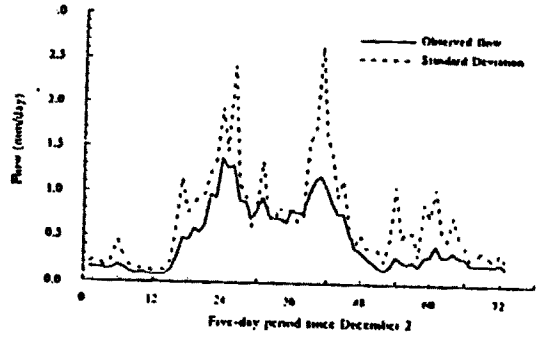

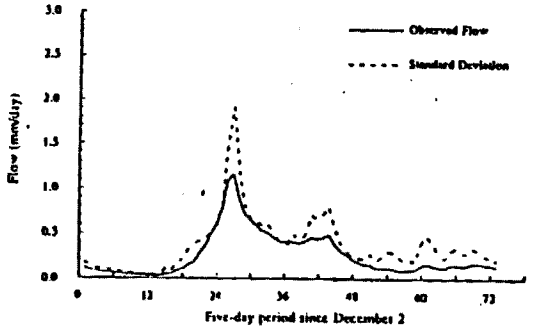

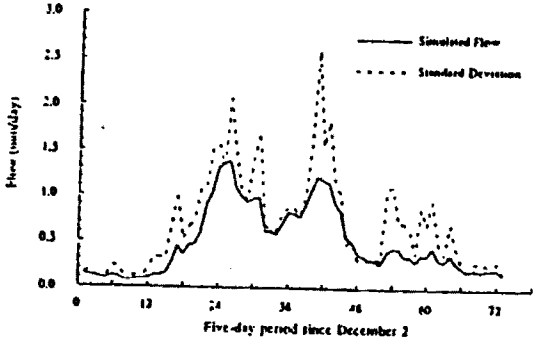

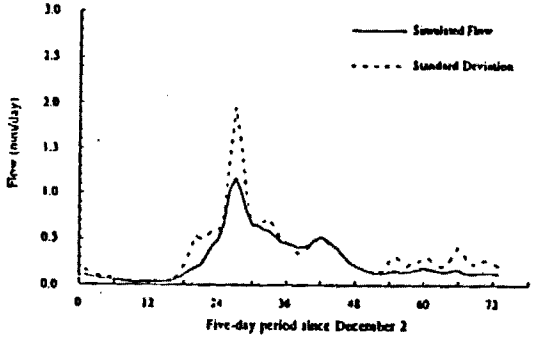

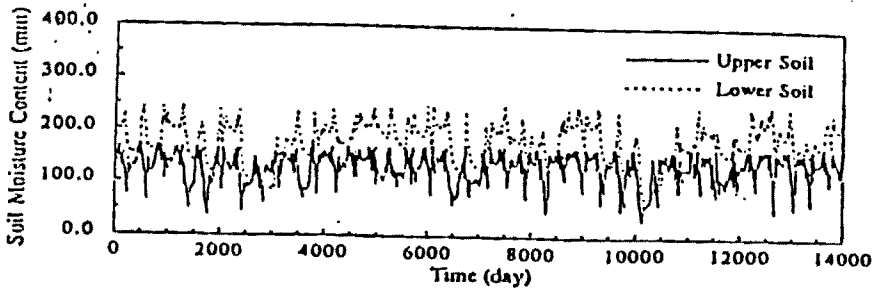

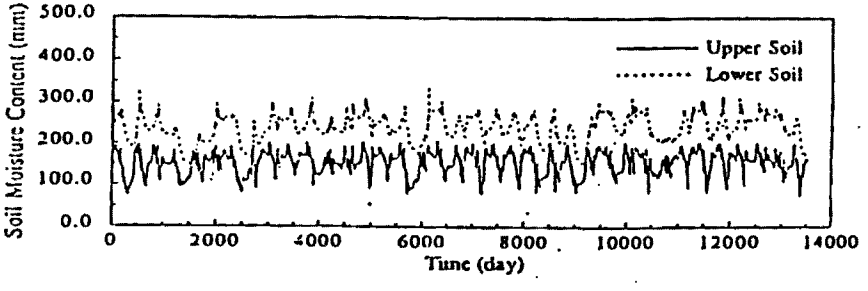

Figure 3.1: UIFS simulation results for sub-basins of the Upper Des Moines River basin. Left panels are for the Boone River basin with outlet at Webster City, Iowa and right panels are for the West Fork Des Moines River basin with outlet at Estherville, Iowa. Description of each panel is in the text.

purposes of this study since it allows for the incorporation of forecast uncertainty in the reservoir control scheme.

Initial results of ESP/UIFS application for the Upper Des Moines River with outlet at Stratford, Iowa are shown in Figure 4.1 with the initial date of forecasts set to April 15. The mean+stdev and mean-stdev of the ESP runs are shown in thick dashed line, together with the mean (in thin dashed line) and the observed flows for the forecast period. In this example a 4-month forecast period was selected. The initial conditions have been selected as to represent the wettest, the driest, the hottest and the coldest years in the 24 year sequence from 1964 through 1988. Pronounced differences are obvious in both the mean projections and in the forecast uncertainty. It is particularly interesting to see the effect of cold vs. hot years on the statistics. A warming trend, then, could alter the way the reservoirs should be operated for resilient response. Also, one can see that it is the wet and cold cases that appear to bring the reservoirs at risk due to occasional large observed flow departures from the historical averages. Such issues will be examined in detail during the next period of this research effort.

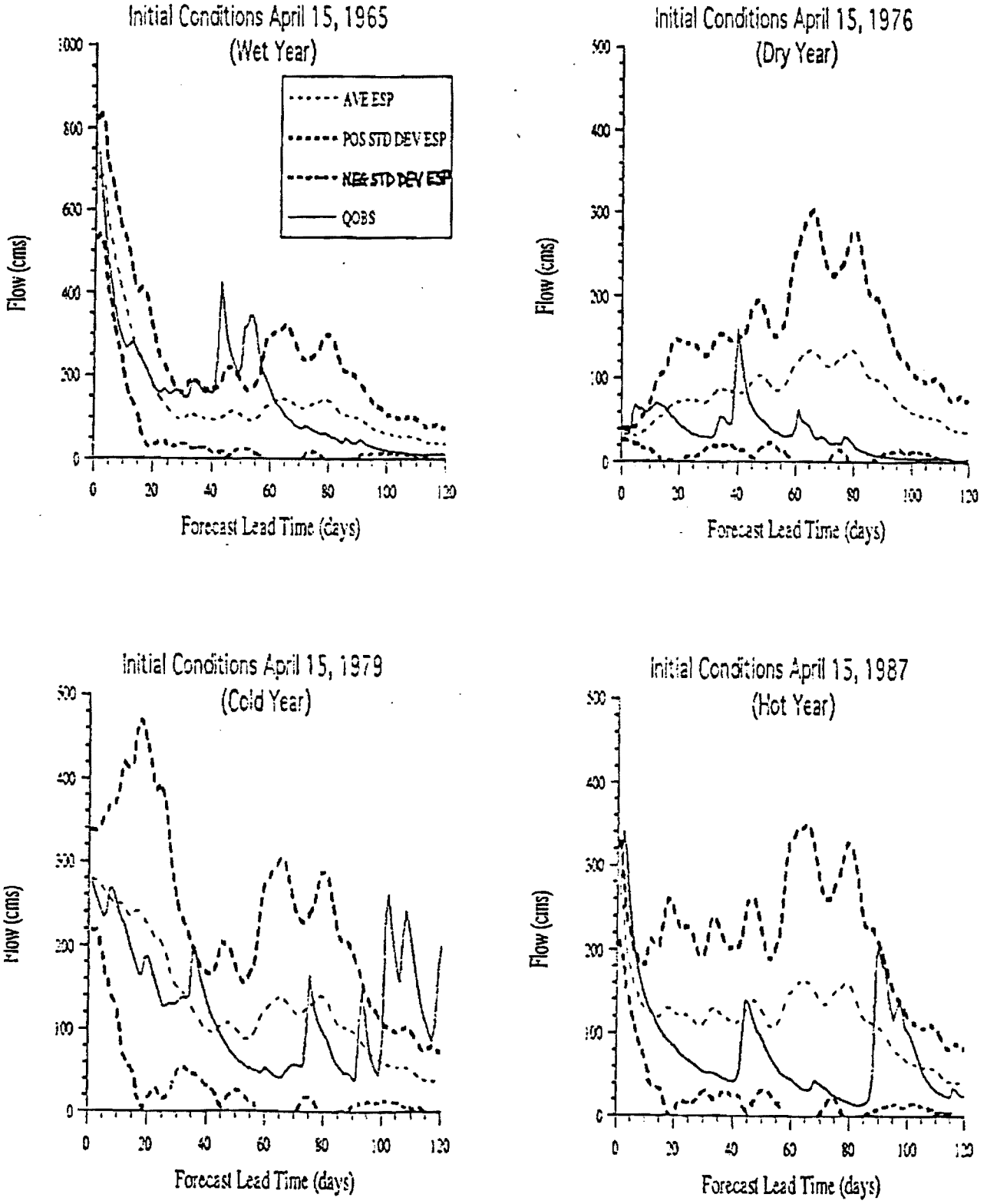

Figure 4.1: ESP runs using the UIFS for the Upper Des Moines River at Stratford, Iowa. Extended predictions out to 4 months in the future with daily resolution are made using twenty four realizations of historical data. All runs have used April 15th as the forecast preparation day. The average of the ESP runs and the one-sigma bounds are shown together with the observed flows.

5. RESERVOIR CONTROL APPROACH

5.1 Set Control Approach

The purpose of the reservoir control procedure is to take advantage of the available storage and change the character of the natural hydrologic inputs so that they best serve the system objectives and operational constraints. Under this research project, our team has developed a new reservoir control method called Set Control Approach *(Georgakakos and Yao, 1992a, and Yao and Georgakakos, 1992)*. This approach has been motivated by the fact that a potential climate change renders past streamflow records atypical of future realizations and invalidates their probabilistic characterizations. The basis of this approach is schematically illustrated in Figure 5.1. Here S(k) represents the vector of reservoir storages experiencing temporal changes (transitions) due to the hydrologic inputs **w**(k) and the controllable inputs **u**(k), the latter being reservoir releases or energy generation hours. The only assumption about the hydrologic inputs is that they take on values from specified sets. The boundaries of these sets can be easily constructed based on inflow traces forecasted by the UIFS model using the ESP procedure, and may represent maximum and minimum inflow levels expected to materialize over the control horizon. Target sets for the reservoir storages S(k) and controllable inputs **u**(k) are also defined based on system physical capacity limitations and operational requirements (imposed, for instance, by flood control, water supply, or pollution abatement). The objective of the set control approach is to determine admissible operational decisions such that system storages remain within their acceptable limits for any possible hydrologic sequence within the specified input sets. For each decision time, this approach determines a set of decision actions guaranteeing that the system will stay within the desirable bounds for the duration of the control horizon. Any decision within this set meets this expectation. The set control approach is especially meaningful during crises when the objective is to avoid decisions that jeopardize system integrity rather than to optimize.

5.2 Preliminary Results of the Combined Forecast-Control Scheme

To simulate potential climate changes, we selected three hydrologic periods exhibiting different streamflow characteristics. These periods are from 1925 to 1949, from 1949 to 1974, and from 1965 to 1988. Figures 5.2 and 5.3 show the monthly means and standard deviations for each period and indicate that both statistics increased with time.

The performance of the combined forecast-control scheme was simulated on a daily basis as follows: First, the forecasting model was run at each day of the simulation horizon to generate a set of 25 inflow traces. These traces were converted into forecast inflow bounds and became input to the control model which, in turn, determined a suitable reservoir release. This release ws applied to the system with the historically observed inflow as input. The resulting storage and actual release values were recorded and the procedure was repeated over the entire simulation horizon. Figures 5.4 through 5.9 show the simulated release and storage sequences, and illustrate that reservoir performance differs from period to period. More specifically, the first hydrologic period (smallest inflow average and variability) is controlled reasonably well with no excessive releases and relatively few

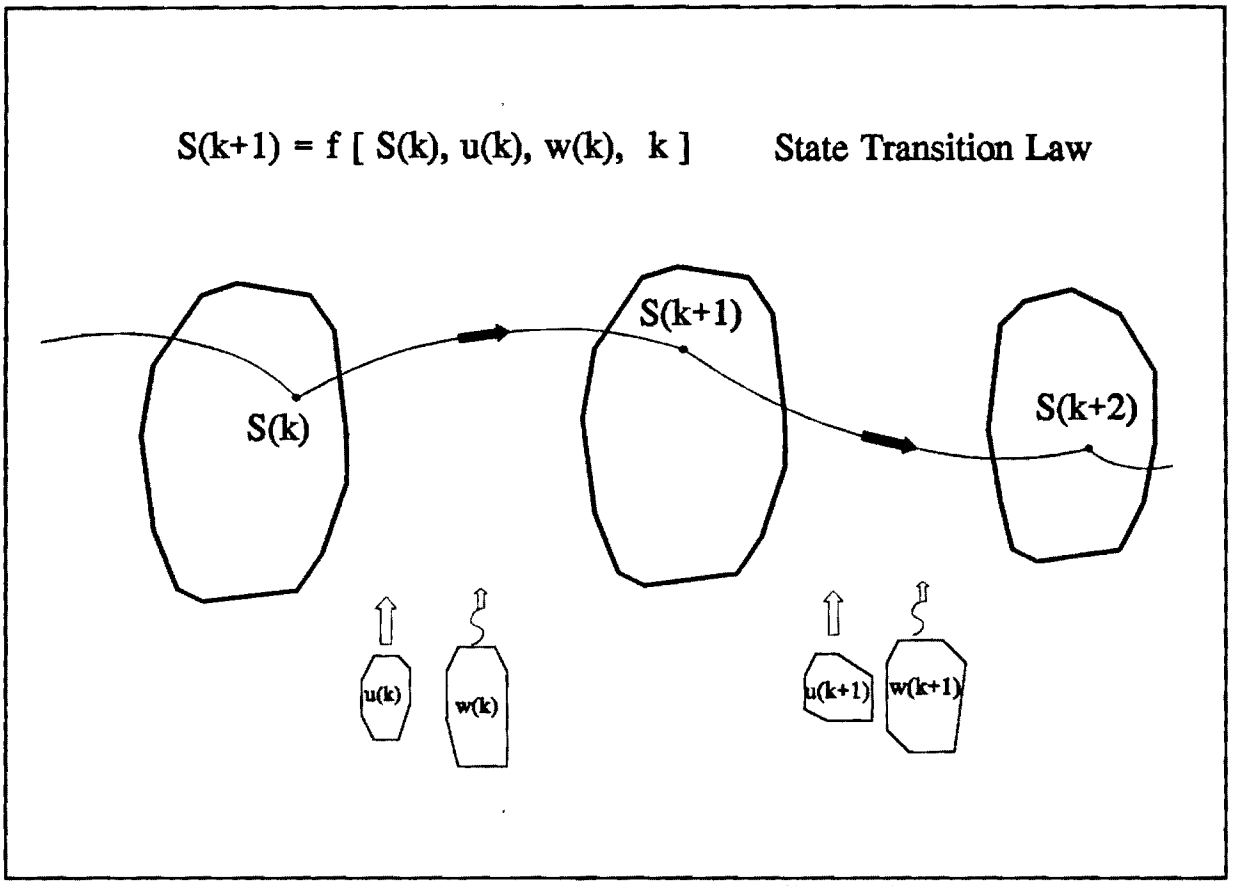

Figure 5.1: Set Control Approach illustration

violations (85 days) of the lower release bound. Despite a substantial change (increase) in the statistics of the inflow process, the second hydrologic period is also handled effectively with only one excessive release (4,300 cfs violation) and 188 days of release deficits. Lastly, the third hydrologic period exhibited 35 days of excessive releases (one of which exceeded 20,000 cfs) and 25 days of release deficits. By contrast, simulation of the current operational practices over the same period shows that excessive releases would reach 32,422 cfs (U.S. Army Corps of Engineers, Rock Island District, personal communication) while the total days of release deficits would be comparable to the results obtained using the forecast - control scheme.

These preliminary results indicate that (**a**) the combined forecast-control scheme generally improves reservoir performance and (**b**) reservoirs can significantly mitigate the effects of climate changes.

6. FURTHER RESEARCH

In the remainder of this project, our research will focus on two broad areas:

(a) Control method improvements: In the results presented earlier, the final decision was selected from the feasible control set in an arbitrary manner. To avoid the arbitrary aspects of this selection, we plan to couple the Set Control Approach with a stochastic control method also developed recently (*Georgakakos, 1987, 1989, 1992a,b*). This method requires a probabilistic model for the hydrologic input forecasts and is designed to optimize system performance in an average sense. Probabilistic characterizations of the hydrologic inputs can again be derived by the inflow traces generated by the UIFS model using the ESP procedure, and consist of the first two or three statistical moments (mean, variance, and skewness) for each period of the control horizon. Through the relationships describing the reservoir system dynamics, these probabilistic forecasts are transformed into forecasts of the system outputs (e.g., storages, energy generation, and downstream streamflow levels). The purpose of the control algorithm is to determine the release or energy generation sequence that maximizes a system performance measure subject to the constraint imposed by the set control approach.

(b) Use of the combined forecast-control scheme to investigate reservoir resilience under a potential climate change. This is the assessment phase of the project and its important role is to reduce the large yield of the results from the previous research tasks to conclusions that are relevant to the issue at hand: the resilience of reservoir systems to a potential climate change. Among the performance measures proposed are: (1) magnitude and frequency of operational requirement violations (e.g., flood stage for high flows and water supply/water quality for low); (2) the length of the control horizon over which the system is guaranteed to meet its operational constraints (the longest the period of guarantee, the lesser the likelihood of extreme risky episodes).

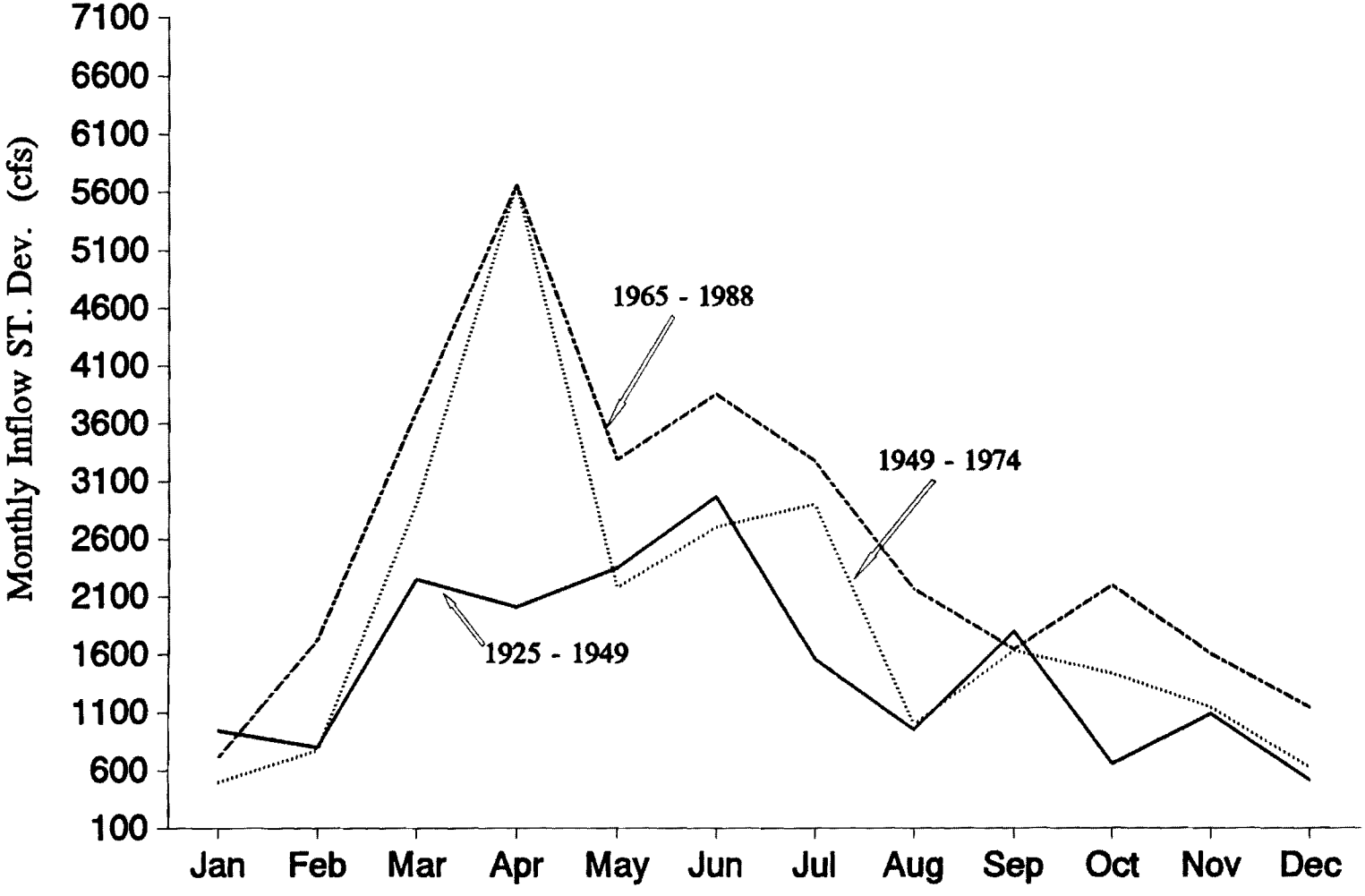

Figure 5.3 Monthly St. deviation for the three test periods

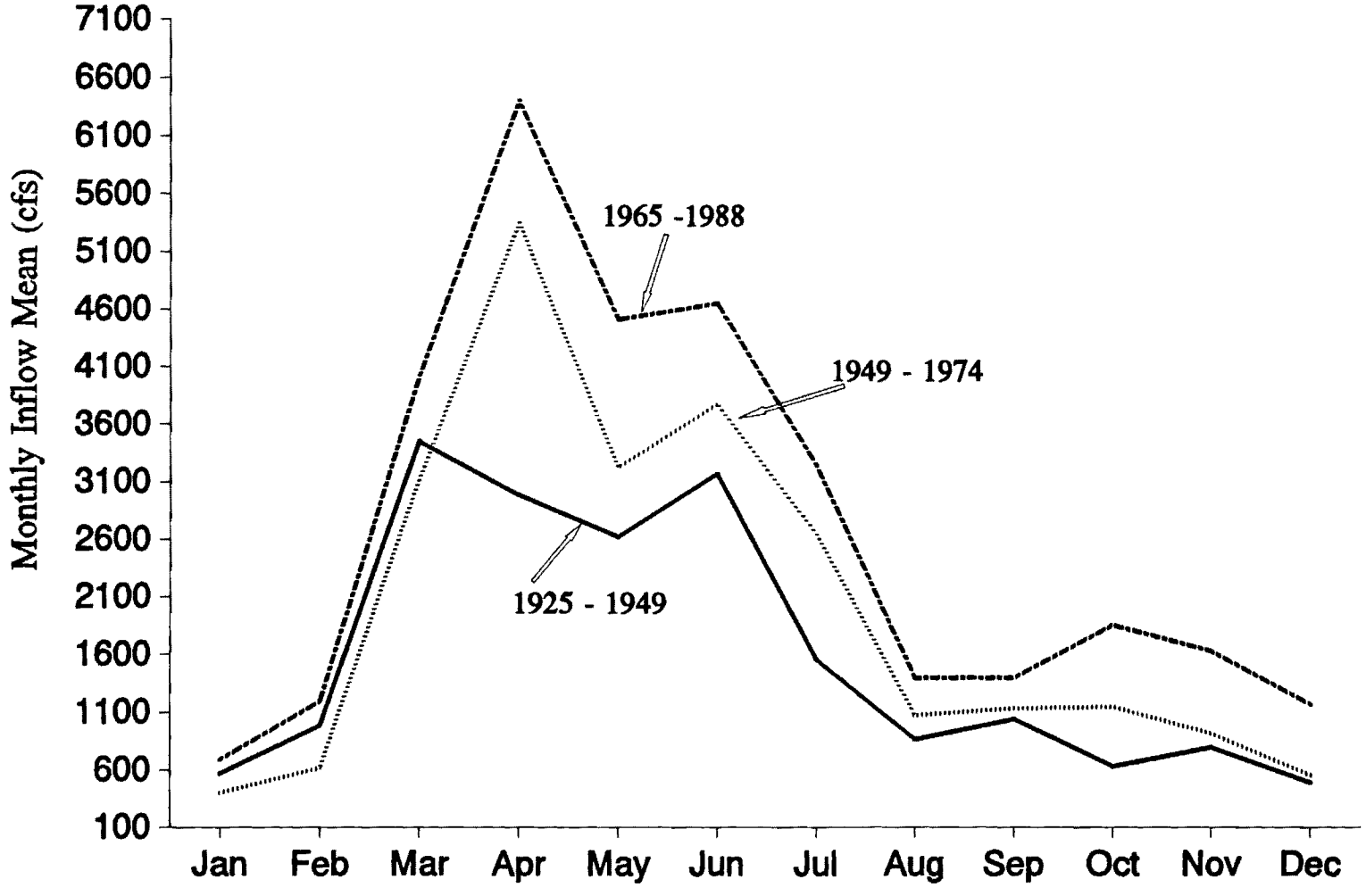

Figure 5.2 Average inflow values for the three test periods

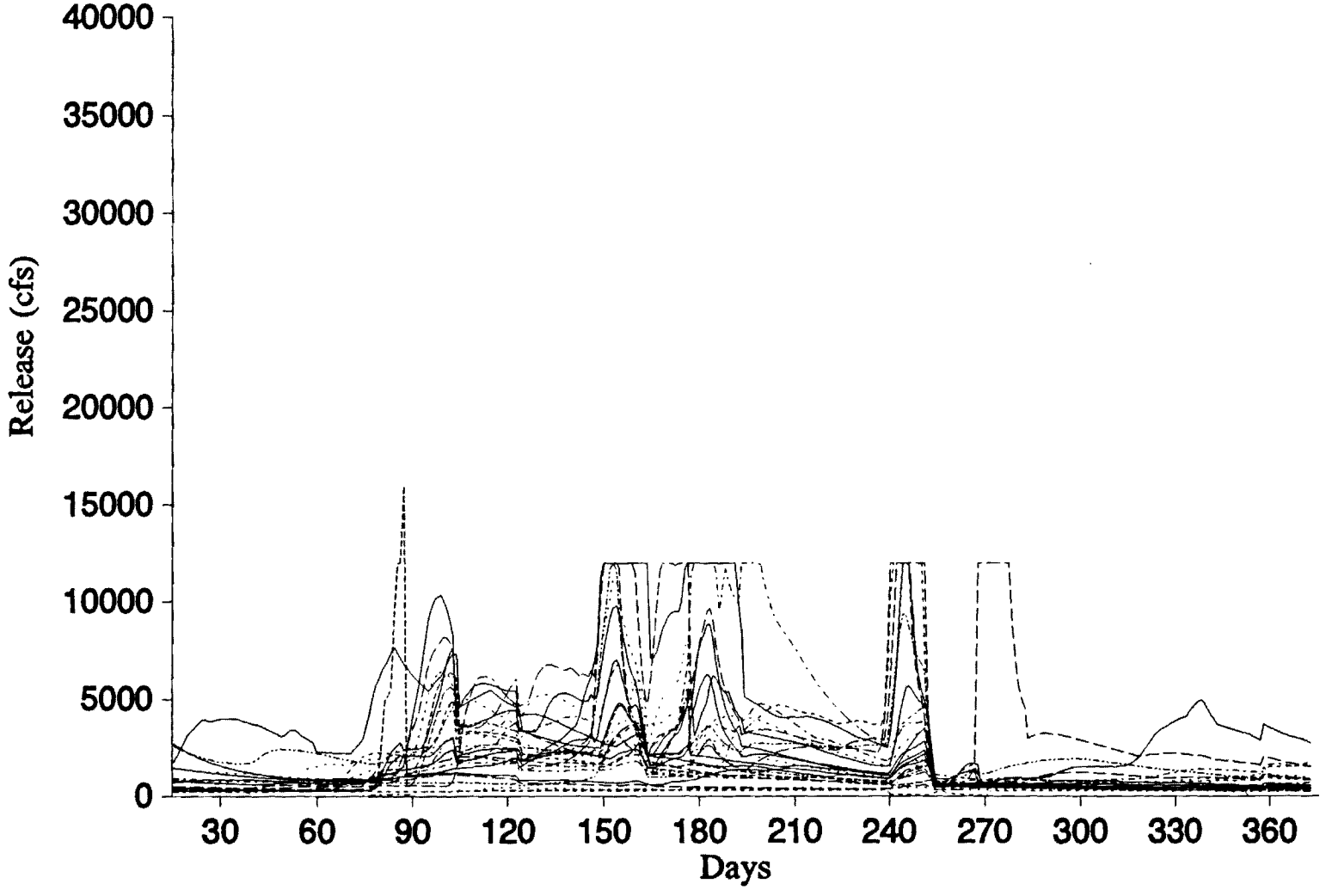

Figure 5.4 Simulted release sequence, 1925 -1949

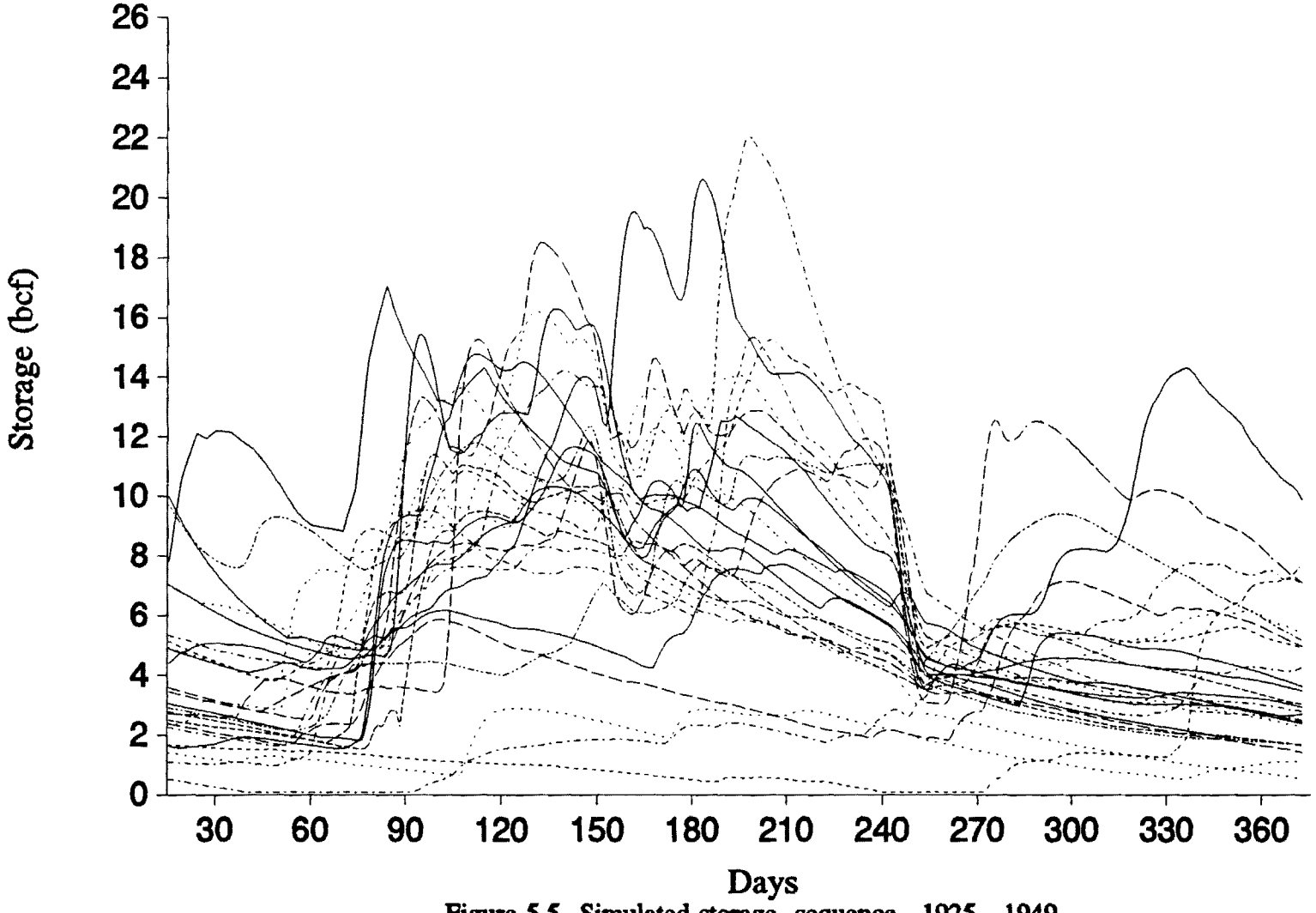

Figure 5.5 Simulated storage sequence , 1925 - 1949

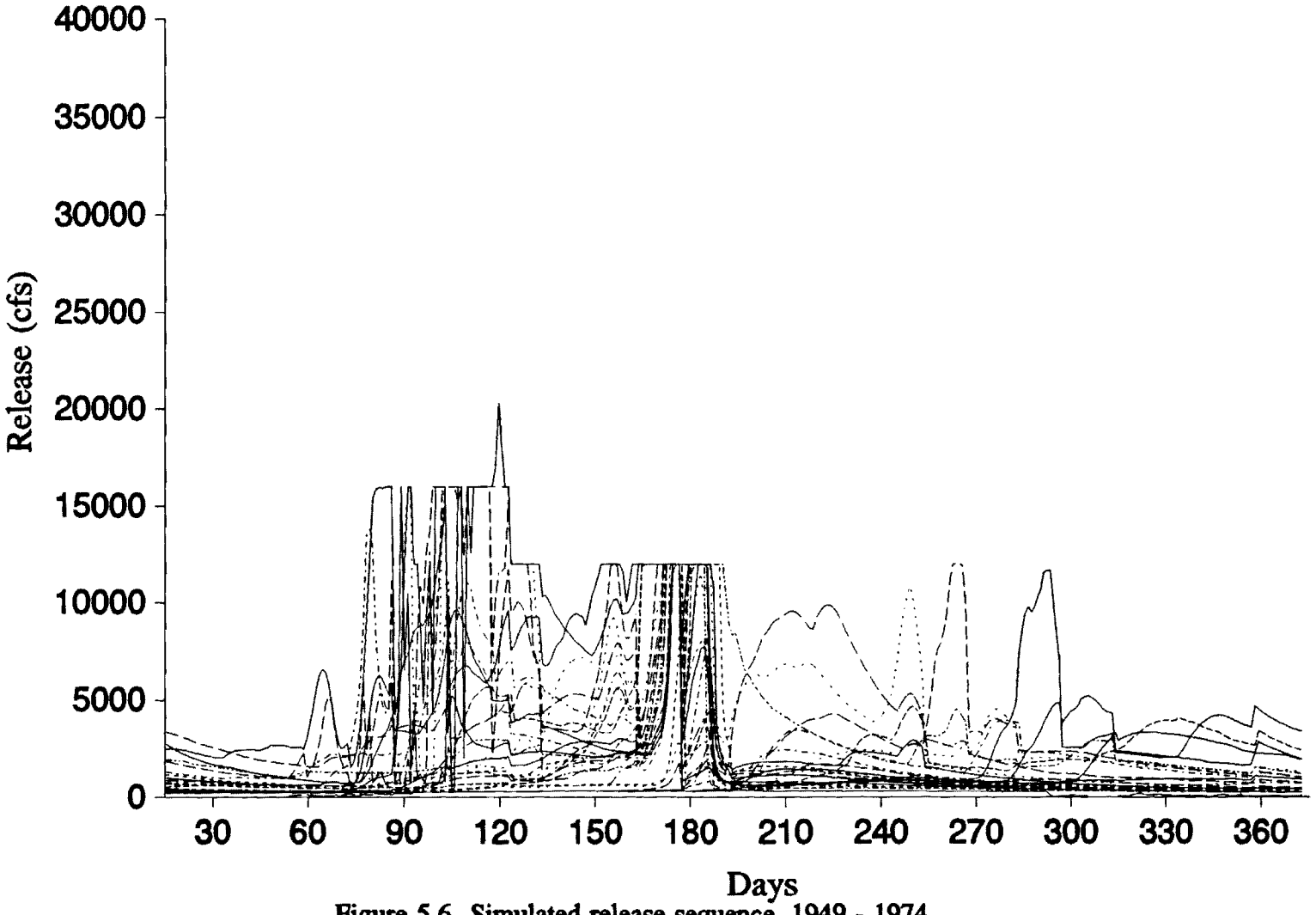

Figure 5.6 Simulated release sequence, 1949 - 1974

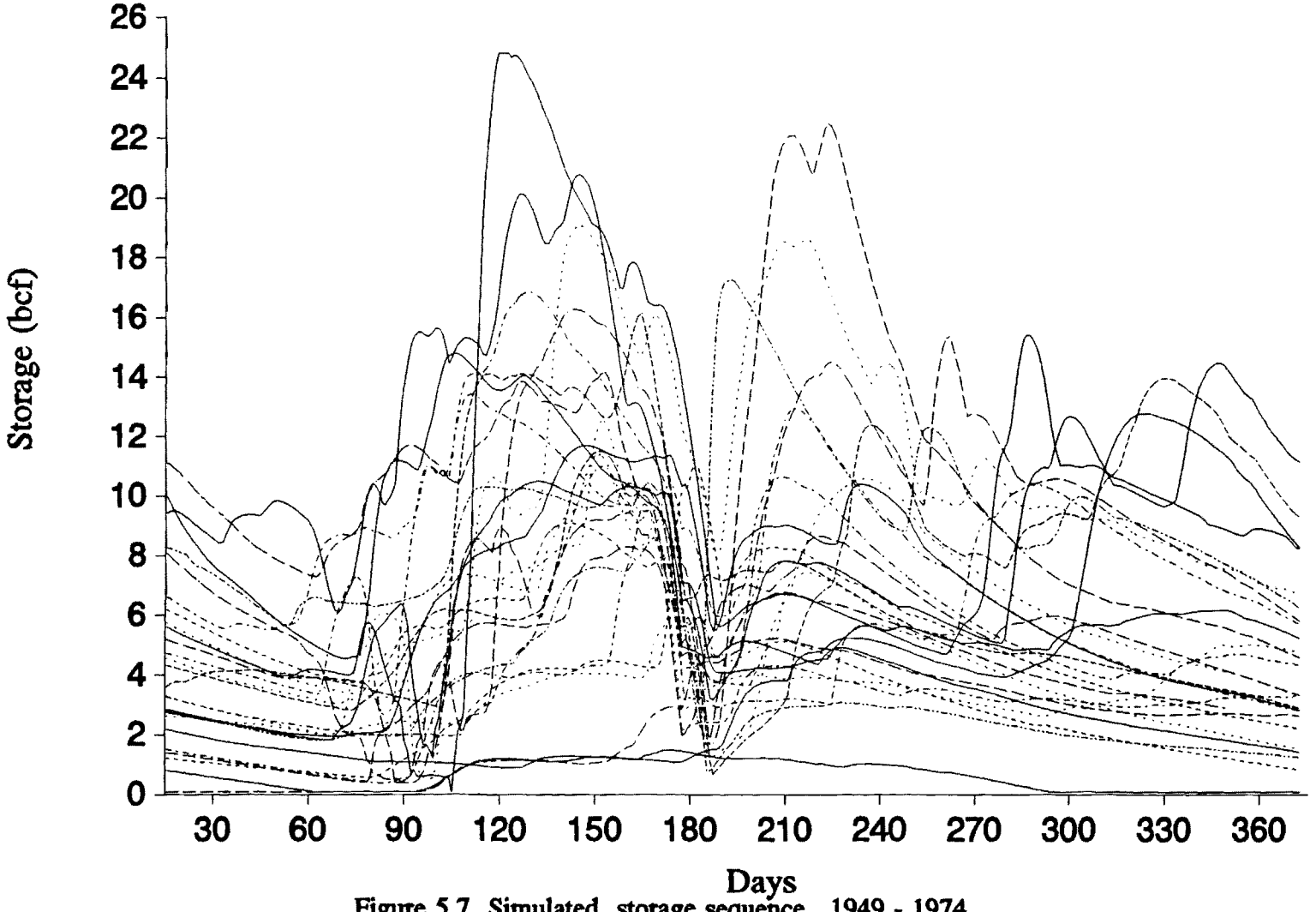

Figure 5.7 Simulated storage sequence, 1949 - 1974

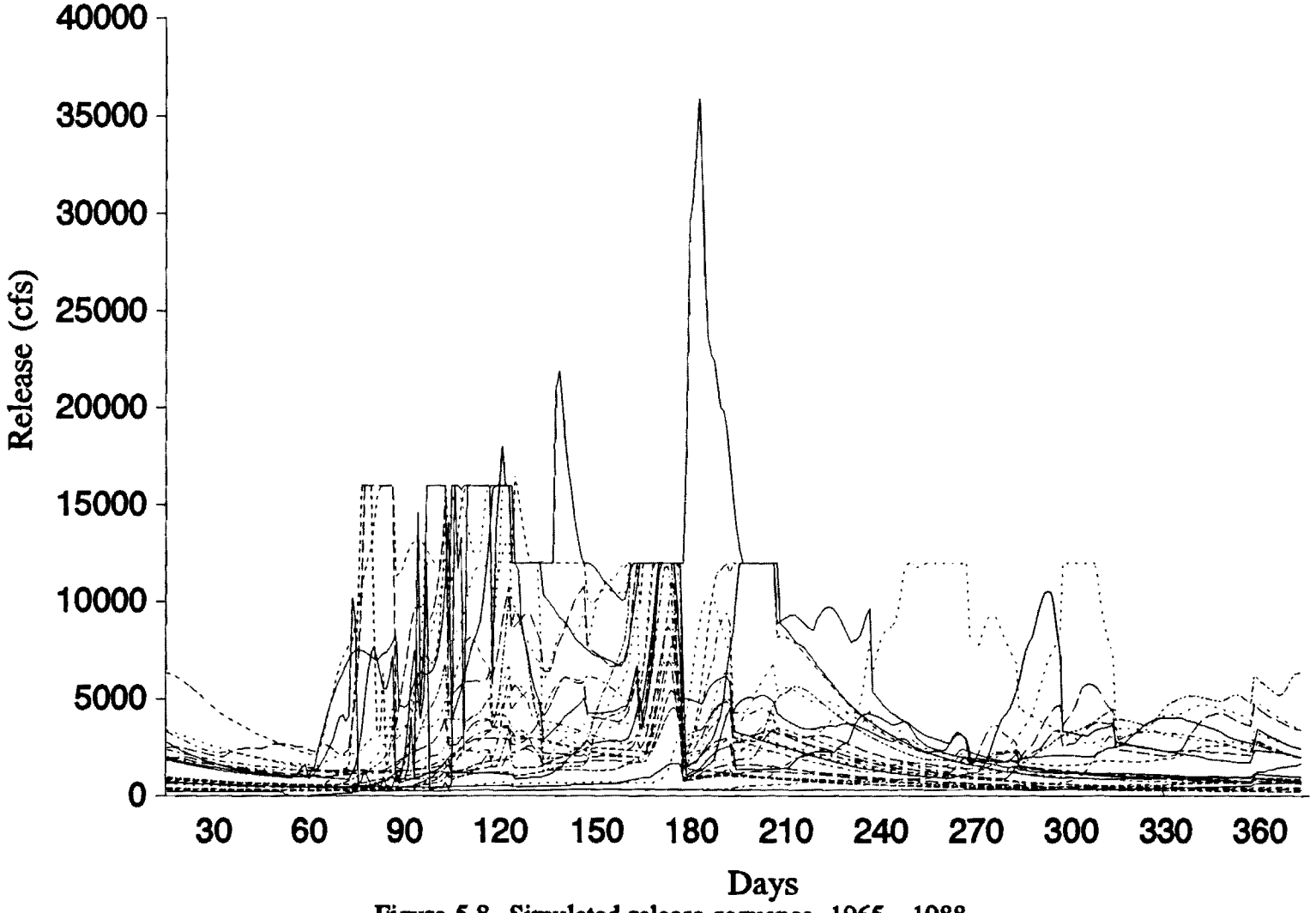

Figure 5.8 Simulated release sequence, 1965 - 1988

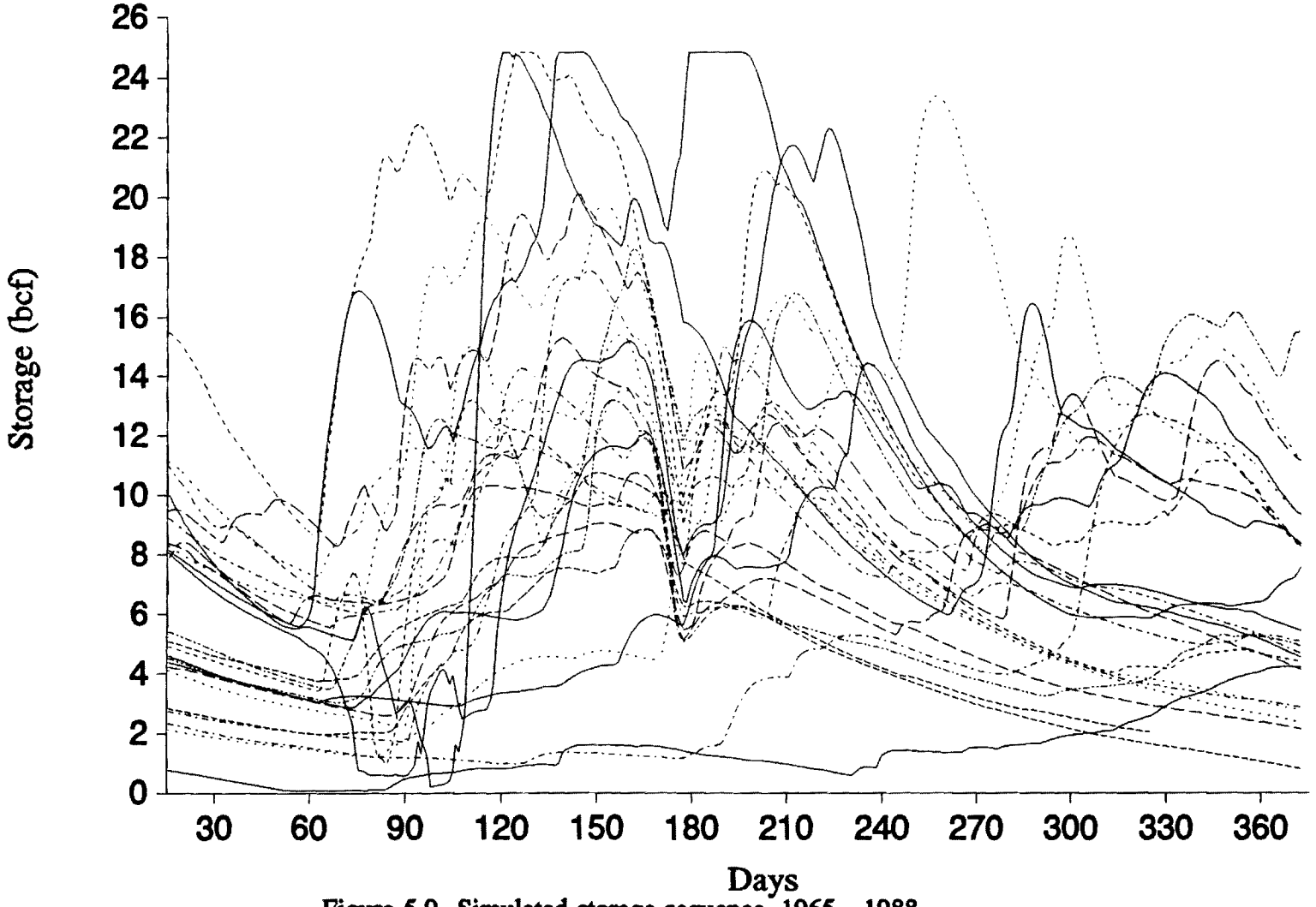

Figure 5.9 Simulated storage sequence, 1965 - 1988

7. REFERENCES

Anderson, E.A., "National Weather Service River Forecast System - Snow Accumulation and Ablation Model," *NOAA Tech. Memo. NWS HYDRO-17,* Silver Spring, Maryland, 1973.

Bae, D.H., and K.P. Georgakakos, "Hydrologic modeling for flow forecasting and climate studies in large drainage basins," *IIHR Report 360,* Department of Civil and Environmental Engineering and Iowa Institute of Hydraulic Research, The University of Iowa, Iowa City, Iowa, 252 pages, 1992.

Day, G.N., "Extended Streamflow Forecasting Using NWSRFS," *J. Water Resources Planning and Management,* 111(2), 157-170, 1985.

Georgakakos, A.P., "Extended Linear Quadratic Gaussian (ELQG) control: Further extensions," *Water Resources Research,* 25(2), 191-201, 1989.

Georgakakos, A.P., "Operational tradeoffs in reservoir control," *Water Resources Research,* 1992a (in press).

Georgakakos, A.P., "A two-level control method for hydropower scheduling," *Water Resources Research,* 1992b (under review).

Georgakakos, A.P., and D.H. Marks, "A stochastic control method for the real-time operation of reservoir systems," *Water Resources Research,* 23(7), 1376-1390, 1987.

Georgakakos, A.P., and H. Yao, "New control concepts for uncertain water resources systems: 1, Theory," *Water Resources Research,* 1992a (in press).

Georgakakos, A.P., Georgakakos, K.P., and E.A. Baltas, "A state-space model for river routing," *Water Resources Research,* 26(5), 827-838, 1990.

Georgakakos, A.P., and H. Yao, "Flood prevention using streamflow forecasting and reservoir control schemes," invited paper, *Proceedings of the U.S.-Taiwan CCNAA-AIT Joint Seminar on Prediction and Damage Mitigation of Meteorologically Induced natural Disasters,* organized by the U.S. National Science Foundation and the ROC National Science Council, Taipei, Taiwan, May 21-24, 1992b.

Gleick, P.H., "Vulnerability of Water Systems," Chapter 10 in *Climate Change and U.S. Water Resources,* Ed. P.E. Waggoner, 223-240, 1990.

National Research Council, Committee on Science, Engineering and Public Policy, *Policy Implications of Greenhouse Warming,* National Academy Press, Washington, DC, 127 pages, 1991.

Rogers, P.P., and M.B. Fiering, "From Flow to Storage," Chapter 9 in *Climate Change and U.S. Water Resources,* Ed. P.E. Waggoner, 207-221, 1990.

Smith, J.A., Day, G.N., and M.D. Kane, "A nonparametric framework for long-range streamflow forecasting," *WMO/TD-No. 428,* World Meteorological Organization, Geneva, Switzerland, 28 pages, 1991.

Yao, H. and A.P. Georgakakos, "New control concepts for uncertain water resources systems: 2, Applications," *Water Resources Research,* 1992 (in press).

IMPACTS OF GLOBAL WARMING ON RESERVOIR SYSTEMS

by

ARIS P. GEORGAKAKOS AND HUAMING YAO

FINAL REPORT: VOLUME I (DRAFT)

United States Geological Survey
Award No. 14-08-0001-G1886

August 1993

School of Civil Engineering
Georgia Institute of Technology
Atlanta, Georgia 30332

FOREWORD

The research work described herein was primarily supported by the United States Geological Survey, Department of the Interior, under USGS award number 14-08-0001-G1886. Additional funding was provided by the United States Geological Survey, Water Resources Institute Program, as authorized by the Water Resources Research Act of 1984 (P.L. 98-242), under Project G-2013(02).

The views and conclusions contained in this document are those of the authors and should not be interpreted as necessarily representing the official policies, either expressed or implied, of the U.S. Government.

We would like to thank Professor Konstantine P. Georgakakos and Ms. Mary G. Mullusky for making the Modified Sacramento forecasting model available to our research. Their cooperative spirit and technical input made our work more meaningful. We are also grateful to Dr. Gary Tasker for expeditiously providing inflow traces reflecting GCM predictions for the Lake Lanier case study. Finally, we are indebted to Mr. William L. Pollock, USGS project coordinator, for kindly accommodating our research needs and reviewing the final reports.

CONTENTS

LIST OF FIGURES

Caption Page No.

LIST OF TABLES

Caption Page No.

1. INTRODUCTION AND OVERVIEW

Climate change is an integral part of Earth's history. (For evidence of long-term changes in regional and global precipitation patterns, the reader is referred to *Bradley, et al., [1987]*, and *Barnett [1986]*; for evidence of change in lake levels, to *Street-Perrott and Harrison [1984]*; and for evidence of trends in global surface temperature, to *Schneider [1989]*. Recent models simulating the global circulation in the atmosphere and oceans predict substantial warming of the Earth's climate if current emission trends of CO_2, methane, and CFCs (Chlorofluorocarbons) continue throughout the world [*Ramanathan, 1988, and Schneider, 1989*]. While state-of-the-science general circulation models are far from being complete, and regional predictions are uncertain [*Bradley, et al., 1987, and Ramanathan, 1988*], there are two compelling reasons for studying the effects of climate change on water resources systems: The first is to determine the robustness of water resources to potential climatic change, and the second is to establish defensive measures for systems that are not resilient to such changes. This information is also useful to basin planners and policy makers who may have to reexamine existing water laws and reevaluate the potential of regional water resources.

Climate changes will undoubtedly impact reservoir system outputs. Wetter climates would potentially enhance energy generation and water availability but increase spillage and flooding. Conversely, drier climates would reduce energy generation and flooding and would strain water supplies and minimum flow requirements. The severity of the impact, however, would depend not just on the volumetric inflow increase or reduction but also on its variability and predictability.

Existing reservoir operation practices are largely based on rule-curves derived via simulation experiments on historical reservoir inflows. Such rules define reservoir zones for flood control and water conservation, and specify seasonal reservoir target levels. However, the validity of these rules is tied to historical weather patterns and can be challenged in the event of major climatic changes. A more appropriate procedure would be to use formal reservoir optimization models reflecting system objective priorities and operational constraints [*TVA, 1988*].

The scope of this research project is (1) to investigate the sensitivity of reservoir systems to potential climate changes and (2) to evaluate whether modern streamflow forecasting and reservoir control methods can be used to mitigate their adverse effects. This research was carried out jointly by two teams, one at Georgia Tech and another at the University of Iowa. The research tasks of both teams are summarized below:

(i) Development and testing of a reservoir control model suitable for a changing hydrologic environment;
(ii) Development and calibration of a physically-based rainfall-runoff model;
(iii) Streamflow forecasting by the rainfall-runoff model and the Extended Streamflow Prediction (ESP) method;
(iv) Coupling of the ESP forecasts with the control model;
(v) Development of historical analogues of potential climatic scenarios;
(vi) Development of inflow traces using General Circulation Model results;
(vii) Evaluation of the forecast-control procedure against current management practices in real-world case studies;
(viii) Comparative assessment of the above procedures in mitigating the effects of climatic changes.

The research procedures and findings of each task are described in the final project report which consists of two volumes. This report is Volume I emphasizing the work performed by the Georgia Tech project team, mainly involved with Tasks (i), (iv), (vi), (vii), and (viii). Volume II emphasizes the work performed by the University of Iowa research team and focuses on the remaining tasks. For continuity, each report reviews or contains elements of the other.

This report is organized as follows: In Chapter 2, we introduce a new control method for the management of uncertain dynamic systems. This method describes system uncertainty using sets rather than statistical methods and derives policies guarantying that the system will remain within its physical and operational constraints. This approach is named Set Control Approach (SCA) and is motivated by the possibility of climatic shifts which are incompatible with historical inflow records and, thus, statistical characterizations. In Chapter 3, we apply the Set Control Approach to common reservoir operation problems such as flood and drought management and energy generation, using the Savannah reservoir system as a case study. We argue that this approach is especially useful during critical hydrologic periods when the objective is not so much to optimize reservoir functions as it is to avoid system failure. In Chapter 4, we describe the coupled forecast-control procedure and evaluate its performance against typical operational practices in side-by-side simulation experiments. This application involves the upper Des Moines river basin and the Saylorville reservoir. The results favor the forecast-control model which proves to be much more effective in avoiding droughts and controlling floods. Using historical analogues of low, intermediate, and high streamflow periods, we also examine the impact of potential climate changes, and conclude that effective forecast-control procedures can mitigate their consequences. In the same chapter, we examine the sensitivity of Lake Lanier to inflow scenarios generated using available GCM results. Our analysis shows that the lake can be

drastically impacted by the potential changes, experiencing frequent and more severe droughts. A key issue, however, is predictability. If inflows are accurately predictable, lake operation can be robust even in adverse climatic conditions. We conclude in Chapter 5 with a summary of our contributions and findings and a short reference to areas needing further research.

2. THE SET CONTROL APPROACH

2.1 INTRODUCTION

Many water resources systems can be represented by difference equations describing the evolution of a pivotal quantity, called state, in response to controllable and uncontrollable inputs:

$$S(k+1) = A(k)\,S(k) + B(k)\,u(k) + G(k)\,w(k), \quad k=0,1,...,N-1, \tag{2.1}$$

where S(k) is the n_s-dimensional state vector; u(k) is the n_u-dimensional control vector, w(k) is the n_w-dimensional input vector; and A(k), B(k), and G(k) are $(n_s x n_s)$-, $(n_s x n_u)$-, and $(n_s x n_w)$-dimensional matrix coefficients respectively encoding the system layout and the interaction among its constituent elements. Examples include reservoir systems where state variables (states) represent reservoir storages, control variables (controls) represent releases or power generation hours, and input variables (inputs) represent reservoir inflows [*Loucks et al., 1980, Wasimi and Kitanidis, 1983, Trezos and Yeh, 1987, Georgakakos, 1989, and others*]; groundwater systems where states may represent hydraulic heads and/or pollutant concentrations, controls may represent pumping rates, and inputs may represent boundary conditions [see, among others, *Willis and Finney, 1985, Georgakakos and Vlatsa, 1991*]; and wastewater treatment processes where states are organic and inorganic constituent concentrations, controls are recycling rates, and inputs are wastewater loading characteristics [*Harris, 1977, Kabouris and Georgakakos, 1990, and others*]. Typically, the state and control vectors are restricted within certain acceptable ranges,

$$\begin{aligned} S^{min}(k) \le S(k) \le S^{max}(k), \quad k=0,1,...,N, \\ u^{min}(k) \le u(k) \le u^{max}(k), \quad k=0,1,...,N-1, \end{aligned} \tag{2.2}$$

where the upper and lower bounds may represent physical capacities or operational requirements.

The purpose of a control scheme is to determine control vector sequences able to guide the system to meet its objectives over an operational horizon. The control process is seriously complicated, however, by the fact that future system inputs are typically unknown. The traditional approach is to develop probabilistic input descriptions and optimize system performance in some average sense. However, this may not always be possible or sound.

In many cases, existing data records are simply not long enough to establish

probabilistic models, and we are forced to make assumptions which in the end cannot be corroborated. Even if sufficient data records exist, probabilistic input models and, consequently the associated control policies, become inadequate for extreme events where observations are sparse. In yet other circumstances, existing data records are atypical of future input realizations due to natural or anthropogenic causes (e.g., global climate changes). On such occasions, probabilistic input characterizations are inappropriate even in the average sense.

Lastly, stochastic control policies can at best guarantee that the system will not violate its bounds with certain probability. They cannot explicitly control the magnitude of the violation. During extreme input episodes, however, the operational goal becomes just that: Take permissible actions guaranteeing that system states stay within acceptable limits. Namely, during crises system operators are not at all concerned with optimizing system performance; they only wish to avoid actions that may endanger or damage the system.

To address the previous concerns, in this work we take a different tact. Rather than relying on probabilistic characterizations, we assume that future inputs are only restricted to belong in certain sets. The boundaries of these sets may represent minimum and maximum input estimates or other extreme levels, against which a sound operational policy is to be developed. In this framework, the purpose of the control process is to determine admissible controls such that system states remain within their acceptable limits as long as system inputs take on values from the specified input sets.

2.2 DYNAMIC PROGRAMMING SOLUTION

Glover and Schweppe [1971] and *Bertsekas and Rhodes [1971]* proposed a general solution for the previous problem using dynamic programming. The solution process is illustrated in Figure 2.1 and explained below:

In what follows, $\{\Omega_s(k), k=0,1,...,N\}$ denotes the sequence of acceptable state sets, $\{\Omega_u(k), k=0,1,...,N-1\}$ the sequence of admissible control sets, and $\{\Omega_w(k), k=0,1,...,N-1\}$ the input set sequence.

Define the modified state set $\Omega_m(N)$ as follows:

$$\Omega_m(N) = \{S \in R^n: [S + G(N-1)\, w(N-1)] \in \Omega_s(N), \quad \forall\, w(N-1) \in \Omega_w(N-1)\}. \tag{2.3}$$

Namely, $\Omega_m(N)$ contains all vectors S such that [S + G(N-1) w(N-1)] belongs to the

state set Ω_s(N) for any input vector in Ω_w(N-1).

Define the reduced state set Ω_r(N-1) as follows:

$$\Omega_r(N-1) = \{S \in \Omega_s(N-1) : \exists\, u(N-1) \in \Omega_u(N-1) : \\ [A(N-1)\, S + B(N-1)\, u(N-1)] \in \Omega_m(N) \}\,. \tag{2.4}$$

Namely, Ω_r(N-1) includes all acceptable state vectors **S** for which there exists an admissible control vector **u**(N-1) such that [**A**(N-1) **S** + **B**(N-1) **u**(N-1)] belongs to the modified state set Ω_m(N). The significance of the previous sets is that if the system state **S**(N-1) reaches set Ω_r(N-1), there exists an admissible control vector that can transfer it to an acceptable terminal state **S**(N) for any input vector in Ω_w(N-1).

One can proceed similarly to define the modified and reduced state sets for the previous time:

$$\Omega_m(N-1) = \{S \in R^n : [S + G(N-2)\, w(N-2)] \in \Omega_r(N-1)\,, \\ \forall\, w(N-2) \in \Omega_w(N-2) \}\,, \tag{2.5}$$

(Note that Ω_m(N-1) is defined based on Ω_r(N-1), not Ω_s(N-1).)

$$\Omega_r(N-2) = \{S \in \Omega_s(N-2) : \exists\, u(N-2) \in \Omega_u(N-2) : \\ [A(N-2)\, S + B(N-2)\, u(N-2)] \in \Omega_m(N-1) \}\,. \tag{2.6}$$

Thus, if the system reaches set Ω_m(N-2), there exist control vectors **u**(N-2) and **u**(N-1) such that states **S**(N-1) and **S**(N) remain within the acceptable limits for any input realizations {**w**(N-2), **w**(N-1)} from the specified input sets.

The previous considerations can recursively be repeated in the reverse time direction, k = N-3, N-4, ... , 0. The problem has a feasible solution (i.e., there exist a control sequence able to keep the state vectors within their acceptable sets) if the sets thus derived are nonempty and the reduced state set Ω_r(0) includes the initial state vector **S**(0). Note, however, that the previous solution process does not determine which controls to use. Specific control vectors can be selected only as the system evolves and the state variable values become known. This and other related issues will further be discussed in Section 2.5.

As usual, dynamic programming leads to a theoretically elegant solution. The practical implementation of this solution, however, presents an equally elegant

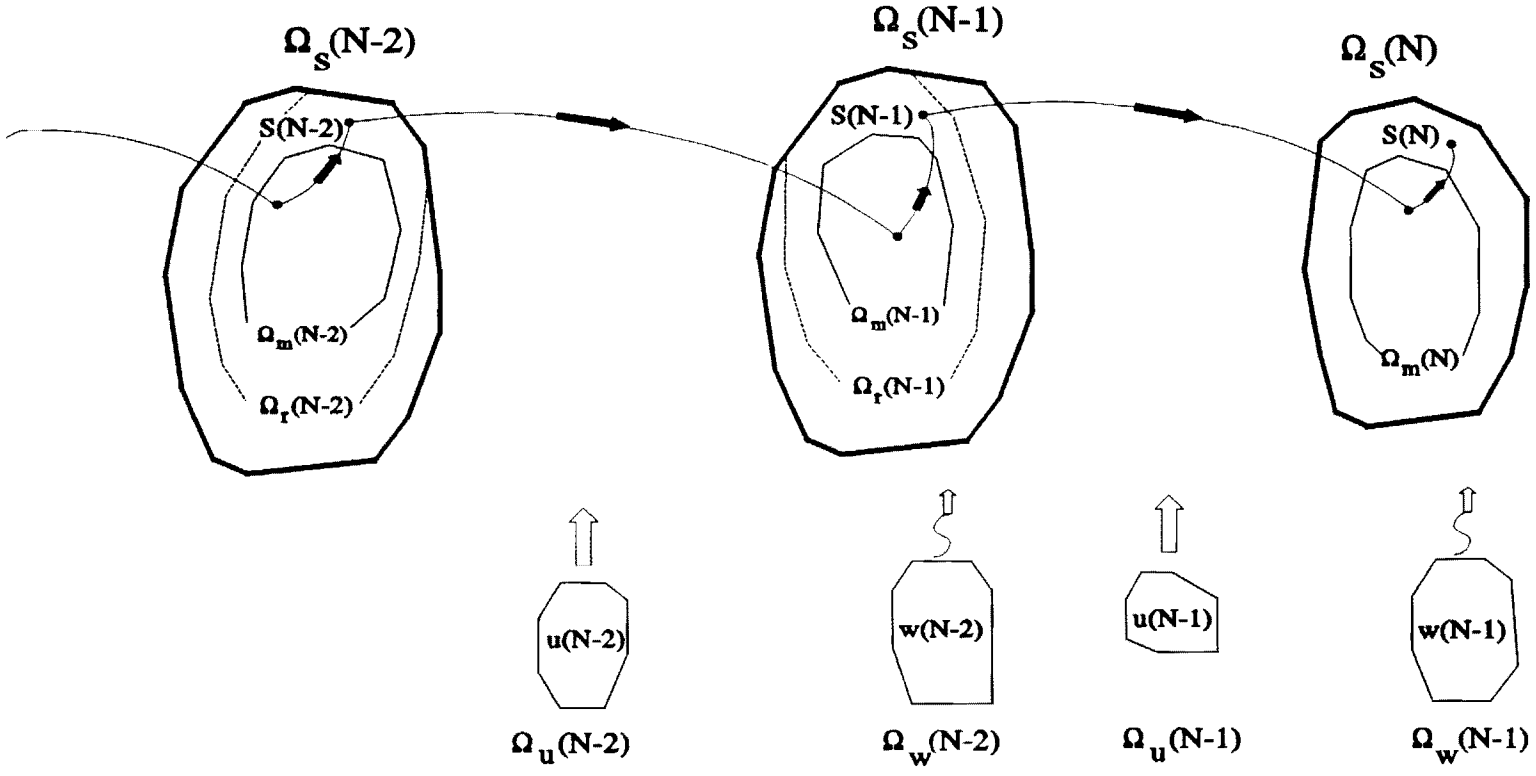

Figure 2.1: Dynamic Programming Solution of the Set Control Problem

challenge. *Glover and Schweppe [1971]* and *Bertsekas and Rhodes [1971]* proposed ellipsoidal approximation algorithms based on Schweppe's bounding ellipsoidalapproximation theory [*Schweppe, 1973*]. The idea is to approximate all sets by bounding ellipsoids and develop recursive relationships for the computation of the modified and reduced state sets. Since ellipsoids are characterized by their center vector and principal axes, the set computation is reduced to a recursive computation of these attributes. However, the required approximations quickly result in empty modified and reduced state sets, and the algorithms falsely indicate infeasibility.

Another approach is to define state, control, and input sets as convex polyhedra and develop efficient procedures to compute the modified and reduced state sets. The modified and reduced state sets then are also convex polyhedra defined by their perpendicular vectors and support functions. This is the approach we adopt herein because it is exact and naturally suitable for water resources systems.

Our work follows that of *Bertsekas and Rhodes* [*1971*] but also contains several extensions and refinements. A significant extension is the applicability to systems with unequal number of state and control variables, a case that arises frequently in water resources systems especially in the management of groundwater aquifers and wastewater treatment plants. Other new contributions include procedures for the computation of the reduced state set, the identification of set infeasibility and hyperplane redundancy, and the determination of the admissible control set in real time. Furthermore, the proofs included in this article are original and are based on the support function concept for convex sets presented by *Schweppe [1973]*. Finally, a comparison of the polyhedral and ellipsoidal approaches quantifies the suboptimality of the latter and illustrates how quickly it becomes infeasible.

2.3 DERIVATION OF THE MODIFIED STATE SET $\Omega_m(k)$

The modified state set $\Omega_m(k)$, k=N, N-1, ..., 1, is defined by Equation (2.5). $\Omega_m(k)$ includes all state vectors $\mathbf{X}$ such that vectors $[\mathbf{X} + \mathbf{G}(k-1)\mathbf{w}(k-1)]$ belong to the reduced state set $\Omega_r(k)$ for any (or all) $\mathbf{w}(k-1)$ in $\Omega_w(k-1)$. Let $\Omega_r(k)$ be a convex polyhedron in the n_s-dimensional space $\mathbf{R}^{n_s}$ of the state vector elements S_1, S_2, ..., and S_{n_s}. (A polyhedron is a set bounded by hyperplanes. A hyperplane is a straight line in $\mathbf{R}^2$ and a two-dimensional plane in $\mathbf{R}^3$. A set Ω is convex if the line segment joining any two points in Ω also belongs in Ω.) Furthermore, let the reduced state set $\Omega_r(k)$ be known by its support function $\phi_r(\eta)$. (This information is available by the computations of the following section.) Namely, let $\Omega_r(k)$ be the following set (*Schweppe, 1973*; *Bishop and Phelps, 1963*)

$$\Omega_r(k) = \{S:\ S'\eta \le \phi_r(\eta),\ \textit{for all}\ \eta,\ \eta'\eta = 1\},$$
$$\text{where } \phi_r(\eta) = \underset{\text{all } S \in \Omega_r(k)}{\text{maximum}} \{S'\eta\}. \tag{2.7}$$

Figure 2.2 provides a graphical interpretation of the support function in two dimensions and demonstrates that a convex polyhedron can be completely defined by the support function values at only a finite number of vectors η: the vectors η_i perpendicular to its bounding hyperplanes. Thus, we will assume that $\Omega_r(k)$ is defined as follows:

$$\Omega_r(k) = \{S:\ S'\eta_i \le \phi_r(\eta_i),\ i = 1,\ldots,n_r\}, \tag{2.8}$$

where n_r is the number of bounding hyperplanes. The use of unit vectors is only a matter of convenience and, especially in the case of polyhedra, non-unit vectors will also serve our purpose as long as the support function $\phi()$ is defined accordingly.

By our earlier definitions, the reduced state set $\Omega_r(k)$, the modified state set $\Omega_m(k)$, and the input set $\Omega_w(k-1)$ are related as follows:

$$\Omega_r(k) = \{S:\ S = X + G(k-1)w(k-1),\ \text{for any } X \in \Omega_m(k) \text{ and any } w(k-1) \in \Omega_w(k-1)\}. \tag{2.9}$$

The modified state set $\Omega_m(k)$ will be completely defined if its support function value can be computed for any vector η. Let $\phi_m()$ and $\phi_w()$ represent the support functions of the modified state and input sets respectively. Then,

$$\begin{aligned}\phi_r(\eta) &= \underset{\substack{X \in \Omega_m(k)\\ w(k-1) \in \Omega_w(k-1)}}{\text{maximum}} [X + G(k-1)w(k-1)]'\eta \\ &= \underset{X \in \Omega_r(k)}{\text{maximum}} X'\eta + \underset{w(k-1) \in \Omega_w(k-1)}{\text{maximum}} w'(k-1)G'(k-1)\eta \\ &= \phi_m(\eta) + \phi_w[G'(k-1)\eta], \\ &\text{all } \eta'\eta = 1,\end{aligned} \tag{2.10}$$

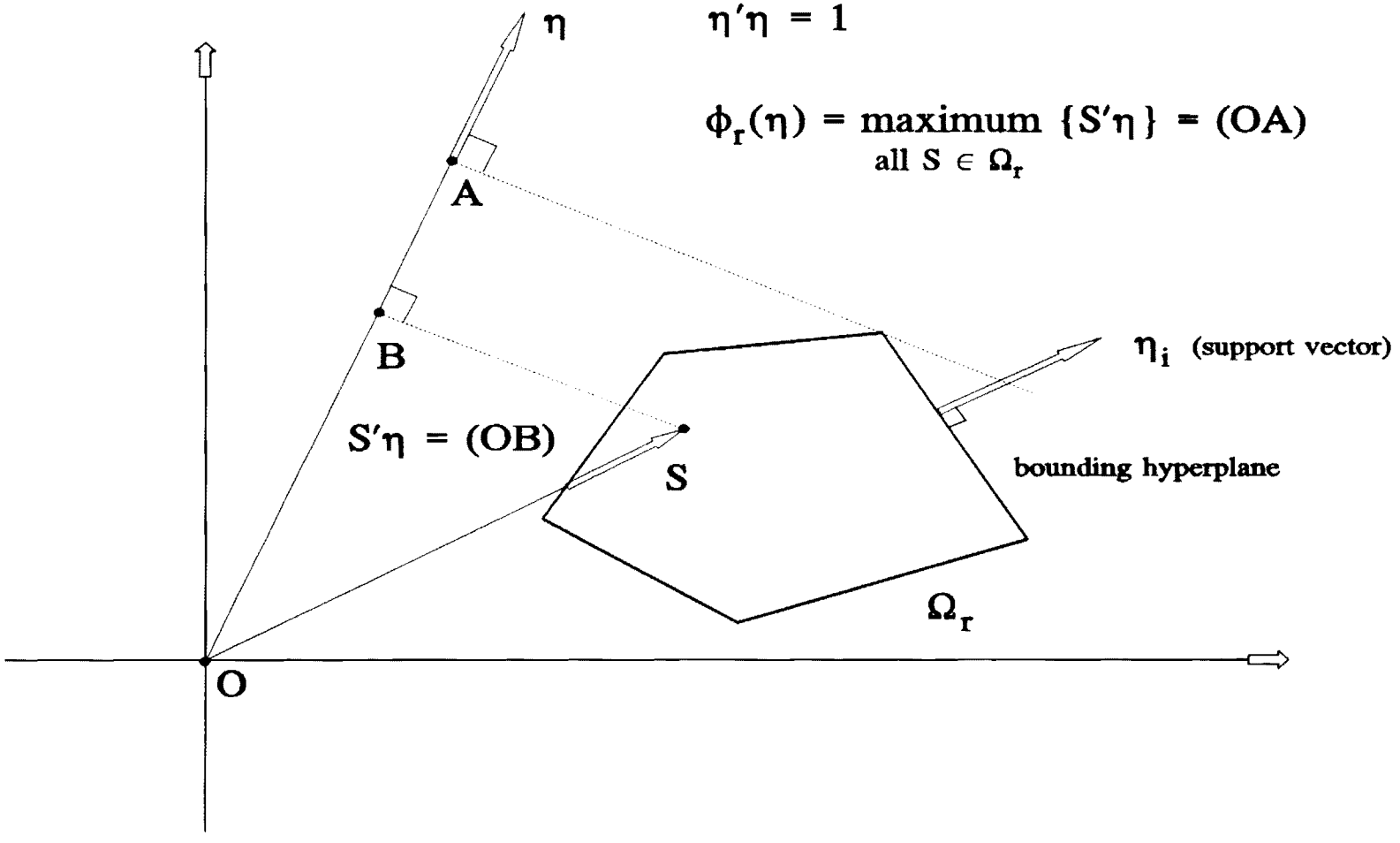

Figure 2.2: The Support Function of a Convex Polyhedron

and therefore,

$$\phi_m(\eta) = \phi_r(\eta) - \phi_w[G'(k-1)\eta], \text{ for all } \eta'\eta = 1. \tag{2.11}$$

Although $\Omega_m(k)$ is now fully defined, it would be computationally more economical to restrict Equation (2.11) to vectors η perpendicular to its bounding hyperplanes. The hyperplanes of $\Omega_m(k)$ are parallel to those of $\Omega_r(k)$, and consequently vectors $\{\eta_i, i=1, ..., n_r\}$ associated with Equation (2.8) are sufficient for the definition of $\phi_m()$ and $\Omega_m(k)$.

Figure 2.3 provides a graphical proof of this fact by deriving set $\Omega_m(k)$ from $\Omega_r(k)$ and $\Omega_{Gw}(k-1)$ in two dimensions. ($\Omega_{Gw}(k-1)$ is the set including all vectors Gw(k-1).) Points (vectors) A, B, C, D, and E are on the boundary hyperplanes of $\Omega_r(k)$. The dashed polygons originating from each point are obtained by subtracting the vectors defining the $\Omega_{Gw}(k-1)$ corner points. Set $\Omega_m(k)$ is the polygon circumscribed by the interior corner points of the dashed polygons, as A, B, C, D, and E trace the periphery of $\Omega_r(k)$. By construction, if a point (vector) belongs to $\Omega_m(k)$, adding any vector within $\Omega_{Gw}(k-1)$ generates points (vectors) inside $\Omega_r(k)$.

In summary, the modified state set $\Omega_m(k)$ can be determined as follows:

$$\Omega_m(k) = \{X: X'\eta_i \le \phi_m(\eta_i) = \phi_r(\eta_i) - \phi_w[G'(k-1)\eta_i],\ i = 1,...,n_r\},$$

where η_i, $i = 1,...,n_r$, are perpendicular to the bounding hyperplanes of $\Omega_r(k)$. **(2.12)**

$\phi_w[G'(k-1)\eta_i]$ can be specified by solving the following linear programming (LP) problem:

$$\underset{\text{all } w}{\text{Maximize}}\ J = w'G'(k-1)\eta_i$$

$$\text{subject to} \tag{2.13}$$

$$w'e_j \le \phi_w(e_j),\ j = 1,...,n_w,$$

where e_j, $j=1,...,n_w$, represent unit vectors perpendicular to the bounding hyperplanes of $\Omega_w(k-1)$. $\phi_w[G'(k-1)\eta_i)$ is equal to the optimum value of J.

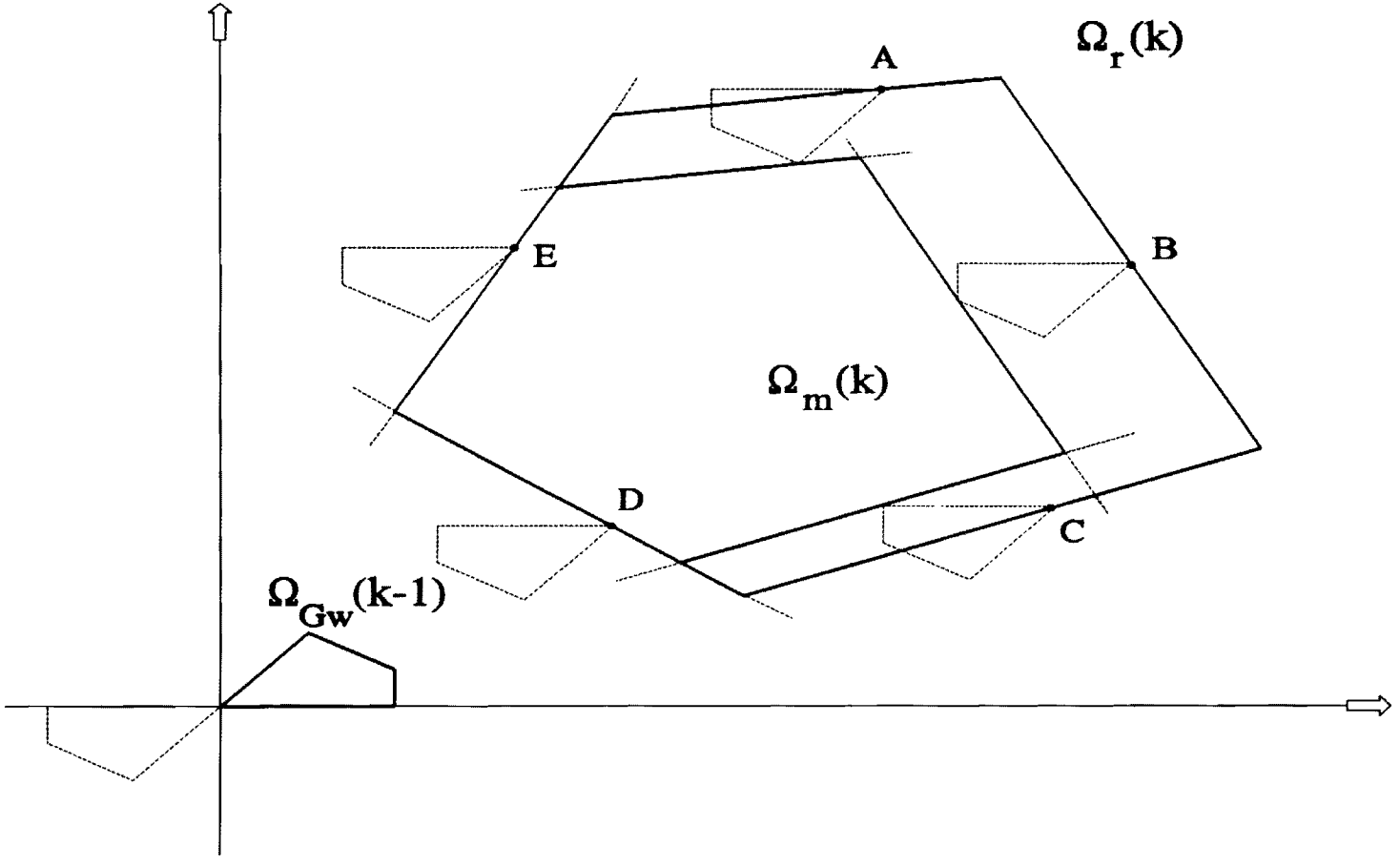

Figure 2.3: Derivation of $\Omega_m(k)$

It is finally possible that set $\Omega_m(k)$ is empty or has fewer bounding hyperplanes than $\Omega_r(k)$. Namely depending on the shape of $\Omega_{Gw}(k-1)$, the previous operations may result in an empty $\Omega_m(k)$ set or cause some hyperplanes to vanish. (One can easily envision this possibility with the aid of Figure 2.3.) If set $\Omega_m(k)$ is empty, then the procedure stops at time k indicating that there does not exist an admissible control sequence that can meet the specified constraints. If $\Omega_m(k)$ is nonempty, discarding unnecessary hyperplanes is generally desirable to reduce the computational overhead. To test for these two conditions, let $\zeta(\zeta_1, \zeta_2, ..., \zeta_{n_s})$ be any fixed unit vector and $\mathbf{X}(X_1, X_2, ..., X_{n_s})$ be any vector in $\Omega_m(k)$. The projection of $\mathbf{X}$ on ζ is given by the inner product

$$J = X'\zeta = X_1 \zeta_1 + X_2 \zeta_2 + \cdots + X_{n_s} \zeta_{n_s}. \tag{2.14}$$

The vector $\mathbf{X}^*$ whose coordinates maximize (or minimize) J is a corner point of $\Omega_m(k)$. (For example, (OC') in Figure 2.4 is the maximum projection length of all points in $\Omega_m(k)$.) Thus, a corner point can be found by solving the following LP problem: Find $\mathbf{X}(X_1, X_2, ..., X_{n_s})$ which maximize/minimize J given by Equation (2.14) subject to inequalities (2.12). If this problem has no feasible solution, set $\Omega_m(k)$ is empty. Furthermore, if any single inequality is replaced by a strict equality, the solution of this Linear Program will provide a corner point on the associated hyperplane. However, if the hyperplane is redundant, LP will indicate infeasibility. The corresponding inequality and hyperplane can then be discarded. This procedure should be repeated n_r times to test the redundancy of all hyperplanes. One can avoid multiple LP solutions by selecting a vector ζ which is not perpendicular to any hyperplane. To guarantee this fact, ζ should not be collinear with any vector η_i, $i = 1, ..., n_r$.

The previous procedure identifies hyperplanes which are completely outside the set $\Omega_m(k)$. However, redundant hyperplanes are also those that pass through a single corner point of this set. To discard these hyperplanes, one can repeat the above procedure using two unit vectors that are negative of one another. If both problems are feasible and have the same solution, the associated hyperplane should be discarded.

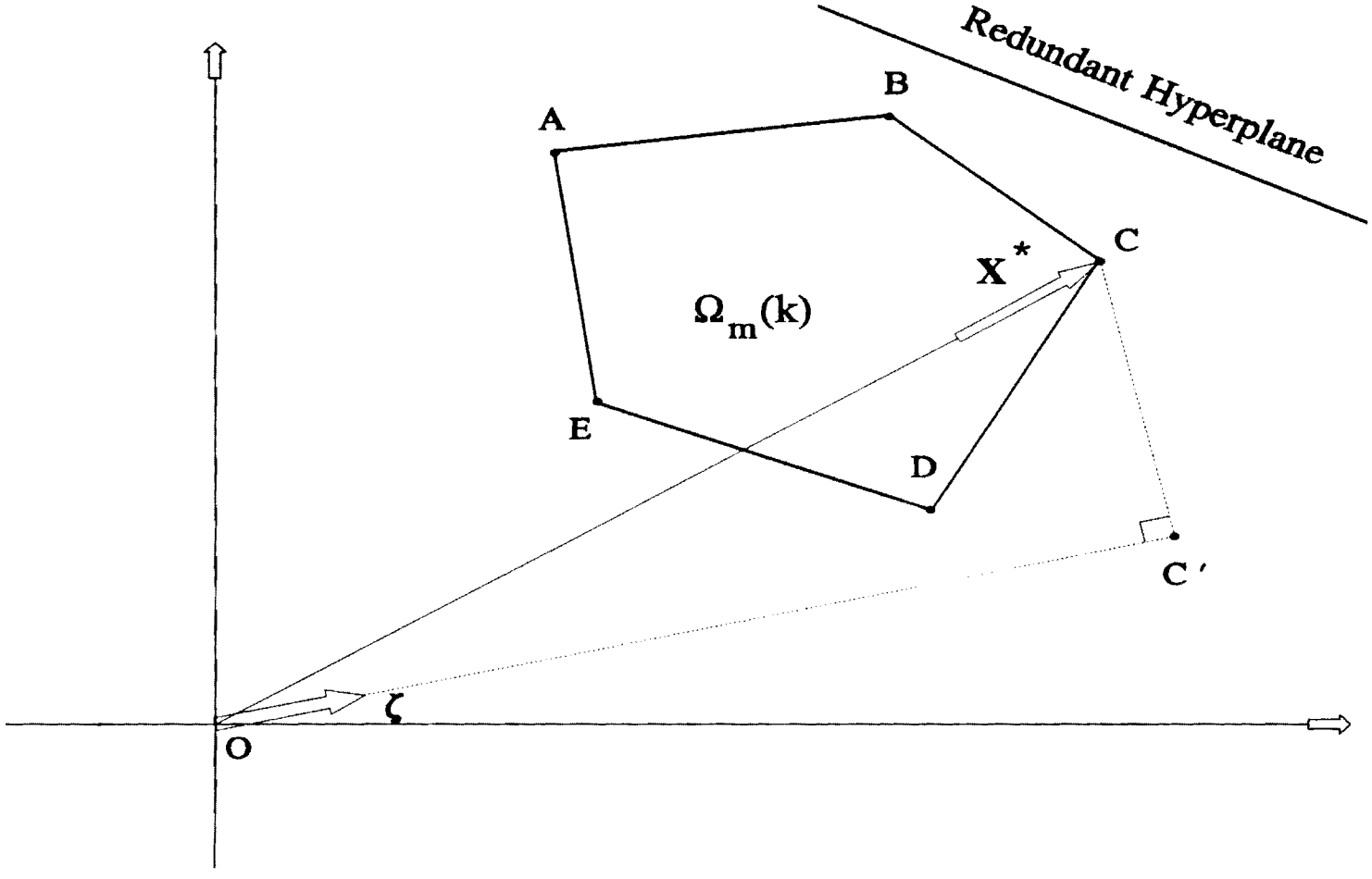

Figure 2.4: Determining the Corner Points of $\Omega_m(k)$

2.4 DERIVATION OF THE REDUCED STATE SETS $\Omega_r(k)$

The reduced state set $\Omega_r(k)$, k=N-1, N-2, ..., 0, was defined as follows (cf. Equation (2.6)):

$$\Omega_r(k) = \{S \in \Omega_s(k) : \exists\, u(k) \in \Omega_u(k) : [A(k)\,S + B(k)\,u(k)] \in \Omega_m(k+1)\}\,. \tag{2.15}$$

The derivation of $\Omega_r(k)$ involves the following set operations: (1) Derivation of set $\Omega_{Bu}(k)$ including all vectors $\mathbf{B}(k)\mathbf{u}(k)$ such that $\mathbf{u}(k) \in \Omega_u(k)$; (2) Derivation of set $\Omega_{AS}(k)$ with all vectors $\mathbf{X}$ such that there exist vectors (at least one) in $\Omega_{Bu}(k)$ that transfer $[\mathbf{X} + \mathbf{B}(k)\mathbf{u}(k)]$ in $\Omega_m(k+1)$; (3) Derivation of set $\Omega_o(k)$ including all vectors S such that $\mathbf{A}(k)\mathbf{S} \in \Omega_{AS}(k)$; and (4) Derivation of $\Omega_r(k) = \Omega_o(k) \cap \Omega_S(k)$ (set intersection), where $\Omega_S(k)$ denotes the admissible state set (depicted in Figure 2.1).

For the first set operation, the problem is as follows: Given that $\Omega_u(k)$ is defined by

$$\Omega_u(k) = \{u:\ u'\mathbf{v}_i \le \phi_u(\mathbf{v}_i),\ i = 1,\ldots,n_u\}, \tag{2.16}$$

namely, by the values of its support function at the vectors perpendicular to its bounding hyperplanes, find the vectors perpendicular to the hyperplanes of $\Omega_{Bu}(k)$ and the associated support function values. The following result holds for the case where $\mathbf{B}(k)$ is an invertible matrix (see appendix for a proof):

$$\Omega_{Bu}(k) = \{X:\ X'\boldsymbol{\theta}_i \le \phi_u(\mathbf{v}_i),\ i = 1,\ldots,n_u\},$$
$$\text{where } \boldsymbol{\theta}_i = (B'(k))^{-1}\mathbf{v}_i,\ i = 1,\ldots,n_u. \tag{2.17}$$

If there are more $\mathbf{B}(k)$ rows than columns (most usual case when $\mathbf{B}(k)$ is not invertible), one can still use the previous result by augmenting $\mathbf{B}(k)$ (and the state equations) to include columns corresponding to fictitious control variables with empty feasible ranges. This technique is further discussed and illustrated in the companion article. If the rank of $\mathbf{B}(k)$ is less than the dimension of its rows or columns, in all likelihood the state equations are ill-posed and some may be redundant.

The second set operation calls for the derivation of set $\Omega_{AS}(k)$ with all vectors $\mathbf{X}$ such that there exist vectors in $\Omega_{Bu}(k)$ which transfer $[\mathbf{X} + \mathbf{B}(k)\mathbf{u}(k)]$ in $\Omega_m(k+1)$. The above is equivalent to finding a set $\Omega_{AS}(k)$ such that for all vectors $\mathbf{Z} \in \Omega_m(k+1)$ and $\mathbf{Y} \in \Omega_{-Bu}(k)$, there holds $\mathbf{Z} + \mathbf{Y} = \mathbf{X} \in \Omega_{AS}(k)$. The equivalence of these two

statements can be easily demonstrated by showing that the set $\Omega_{AS}(k)$ corresponding to the first statement is a subset of the set corresponding to the second and vice-versa. Thus, $\Omega_{AS}(k)$ is the vector sum of $\Omega_m(k+1)$ and $\Omega_{-Bu}(k)$, where $\Omega_{-Bu}(k)$ is the set including all vectors $[-\mathbf{B}(k)\mathbf{u}(k)]$. As shown in the previous section (Equation 2.10), the support function of $\Omega_{AS}(k)$ can then be computed from the support functions of $\Omega_m(k+1)$ and $\Omega_{-Bu}(k)$ as follows:

$$\begin{aligned}
\phi_{AS}(\eta) &= \underset{\substack{Z \in \Omega_m(k+1) \\ Y \in \Omega_{-Bu}(k)}}{\text{maximum}} [Z + Y]'\eta \\
&= \underset{Z \in \Omega_m(k+1)}{\text{maximum}} Z'\eta + \underset{Y \in \Omega_{-Bu}(k)}{\text{maximum}} Y'\eta \\
&= \phi_m(\eta) + \phi_{-Bu}(\eta), \\
&\text{all } \eta'\eta = 1 .
\end{aligned} \tag{2.18}$$

In the above equation, the support vectors and function of $\Omega_{-Bu}(k)$ have not been defined. However, using the support function definition (2.7), one can easily show that the support vectors of $\Omega_{-Bu}(k)$ are negatives of the $\Omega_{Bu}(k)$ support vectors, while the support function values remain the same.

The minimal set of vectors η where the support function has to be evaluated includes all vectors perpendicular to the hyperplanes of both $\Omega_m(k+1)$ and $\Omega_{-Bu}(k)$. Thus, $\Omega_{AS}(k)$ is defined by

$$\begin{aligned}
\Omega_{AS}(k) = \{X:\ & X'\eta_i \le \phi_m(\eta_i) + \phi_{-Bu}(\eta_i),\ i = 1,\ldots,n_m,\ \textit{and} \\
& X'(-\theta_j) \le \phi_m(-\theta_j) + \phi_{-Bu}(-\theta_j),\ j = 1,\ldots,n_u\} ,
\end{aligned} \tag{2.19}$$

where $\phi_m(\eta_i)$, $i=1,\ldots,n_m$, are provided by the computations of the previous section (Equation 2.12 and discussion thereafter) and $\phi_{-Bu}(-\theta_j)$, $j=1,\ldots,n_u$, are equal to $\phi_{Bu}(\theta_j)$, $j=1,\ldots,n_u$ as explained earlier. Figure 2.5 illustrates how $\Omega_{AS}(k)$ is graphically constructed in two dimensions. Let ABCD represent set $\Omega_m(k+1)$. Hyperplanes A'D', D'C', C'B', and A'B' (solid lines) of $\Omega_{AS}(k)$ are respectively parallel to hyperplanes AD, DC, CB, and AB of $\Omega_m(k+1)$ and include points which can be transferred to $\Omega_m(k+1)$ only by a single corner point of $\Omega_{Bu}(k)$. The additional hyperplanes needed to define $\Omega_{AS}(k)$, namely, A'A', A'A', C'C', and B'B', are parallel to those of $\Omega_{Bu}(k)$ which is the set symmetric to $\Omega_{Bu}(k)$ about the origin. The sets resulting by subtracting the corner point vectors of $\Omega_{Bu}(k)$ from each corner point

of $\Omega_m(k+1)$ (dashed line polygons in Figure 2.5) are simply parallel translations of $\Omega_{Bu}(k)$ as though each corner point of $\Omega_m(k+1)$ were the origin of the axes. Namely, $\Omega_{AS}(k)$ is the polyhedron circumscribed by the exterior corner points of $\Omega'_{Bu}(k)$ as it traces the periphery of $\Omega_m(k+1)$.

The third set operation calls for determining set $\Omega_o(k)$ from $\Omega_{AS}(k)$. By noting that $\mathbf{S} = \mathbf{A}^{-1}(\mathbf{A}\,\mathbf{S})$ and applying the lemma associated with Equation (2.17), set $\Omega_o(k)$ can be determined by

$$\Omega_o(k) = \{X:\ X'\rho_i \le \phi_{AS}(e_i),\ i = 1,\ldots,n_{AS}\},$$
$$\text{where } \rho_i = A'(k)\,e_i,\ i = 1,\ldots,n_{AS}, \tag{2.20}$$

and e_i, $i=1,\ldots,n_{AS}$, includes all vectors η_i, $i=1,\ldots,n_m$, and θ_j, $j=1,\ldots,n_u$, associated with Equation (2.19) ($n_{AS}=n_m+n_u$).

Finally, set $\Omega_r(k)$ can be derived as the intersection of $\Omega_o(k)$ and $\Omega_S(k)$. In mathematical form, this intersection is determined by

$$\Omega_r(k) = \{X: X'\tau_i \le \text{minimum}[\phi_S(\tau_i), \phi_o(\tau_i)],\ i = 1,\ldots,n_S, \text{ and}$$
$$X'\rho_j \le \text{minimum}[\phi_S(\rho_j), \phi_o(\rho_j)],\ j = 1,\ldots,n_o\}, \tag{2.21}$$

where $\phi_S()$, τ_i, $i=1,\ldots,n_S$, represent the support function and associated vector set for $\Omega_S(k)$, and $\phi_o()$, ρ_j, $j=1,\ldots,n_o$, represent the support function and associated vector set for $\Omega_o(k)$. The validity of the above statement is illustrated in Figure 2.6.

As with the modified state set, some of the hyperplanes associated with the reduced state set computed above may be redundant and should be discarded using the procedure outlined at the end of the previous section.

2.5. REAL-TIME IMPLEMENTATION

The computation of the modified and reduced state sets can thus proceed from the terminal time N to the initial time 0. The problem has a solution (namely, there exists a feasible control sequence that guarantees that the state variables will remain within their admissible limits for any input realization within the specified input sets) if the reduced state set $\Omega_r(0)$ at time 0 is nonempty and includes the initial state vector $S(0)$. The determination of these solutions has yet to be discussed.

Assuming that S(0) is known, the state equation describes the transition to state S(1)

by

$$S(1) = A(0)\,S(0) + B(0)\,u(0) + G(0)\,w(0)\,. \tag{2.22}$$

The issue here is to determine an admissible control subset whose vectors guarantee that whatever the input $\mathbf{w}(0)$, the state $\mathbf{S}(1)$ will be within the reduced state set $\Omega_r(1)$. Equivalently, this subset should be such that vector $[\mathbf{A}(0)\mathbf{S}(0)+\mathbf{B}(0)\mathbf{u}(0)]$ always belongs in the modified state set $\Omega_m(1)$. The set $\Omega_{Bu}(0)$ that satisfies this requirement is obviously a parallel translation of $\Omega_m(1)$ by the vector $\mathbf{A}(0)\mathbf{S}(0)$. More formally, $\Omega_{Bu}(0)$ can be defined by

$$\Omega_{Bu}(0) = \{X:\ X'\eta_i \le \phi_m(\eta_i) - S'(0)A'(0)\eta_i,\ i = 1,\ldots,n_m\}\,, \tag{2.23}$$

where $\phi_m()$, η_i, $i=1,\ldots,n_m$, represent the support function and associated vector set for $\Omega_m(1)$ already determined by the DP procedure.

The admissible control set $\Omega_c(0)$ can finally be obtained from the lemma associated with Equation (2.17) and an intersection with $\Omega_u(0)$ (Equation 2.21). Any control vector in the set $\Omega_c(0)$ guarantees that (**a**) state $\mathbf{S}(1)$ will be feasible and (**b**) there will exist $\mathbf{u}(k)$, $k=1,2,\ldots,N-1$, vector sequences which will produce feasible states all through the control horizon. Subsequent sets $\Omega_c(k)$, $k=1,2,\ldots,N-1$, can be obtained by similar considerations as the system evolves and the state values $\mathbf{S}(k)$, $k=1,2,\ldots,N-1$, become known.

2.6. AN EXAMPLE

To provide some computational insight for the theory presented earlier, we first solve a two-dimensional problem with four time steps. The state equation is as follows:

$$\begin{bmatrix} S_1(k+1) \\ S_2(k+1) \end{bmatrix} = \begin{bmatrix} 1 & 0 \\ 0 & 1 \end{bmatrix}\begin{bmatrix} S_1(k) \\ S_2(k) \end{bmatrix} + \begin{bmatrix} -1 & 0 \\ 1 & -1 \end{bmatrix}\begin{bmatrix} u_1(k) \\ u_2(k) \end{bmatrix} + \begin{bmatrix} 1 & 0 \\ 0 & 1 \end{bmatrix}\begin{bmatrix} w_1(k) \\ w_2(k) \end{bmatrix},$$
$$k = 0,1,2,3, \quad \begin{bmatrix} S_1(0) = 4 \\ S_2(0) = 4 \end{bmatrix}, \tag{2.24}$$

where the state, input, and control sets are shown below:

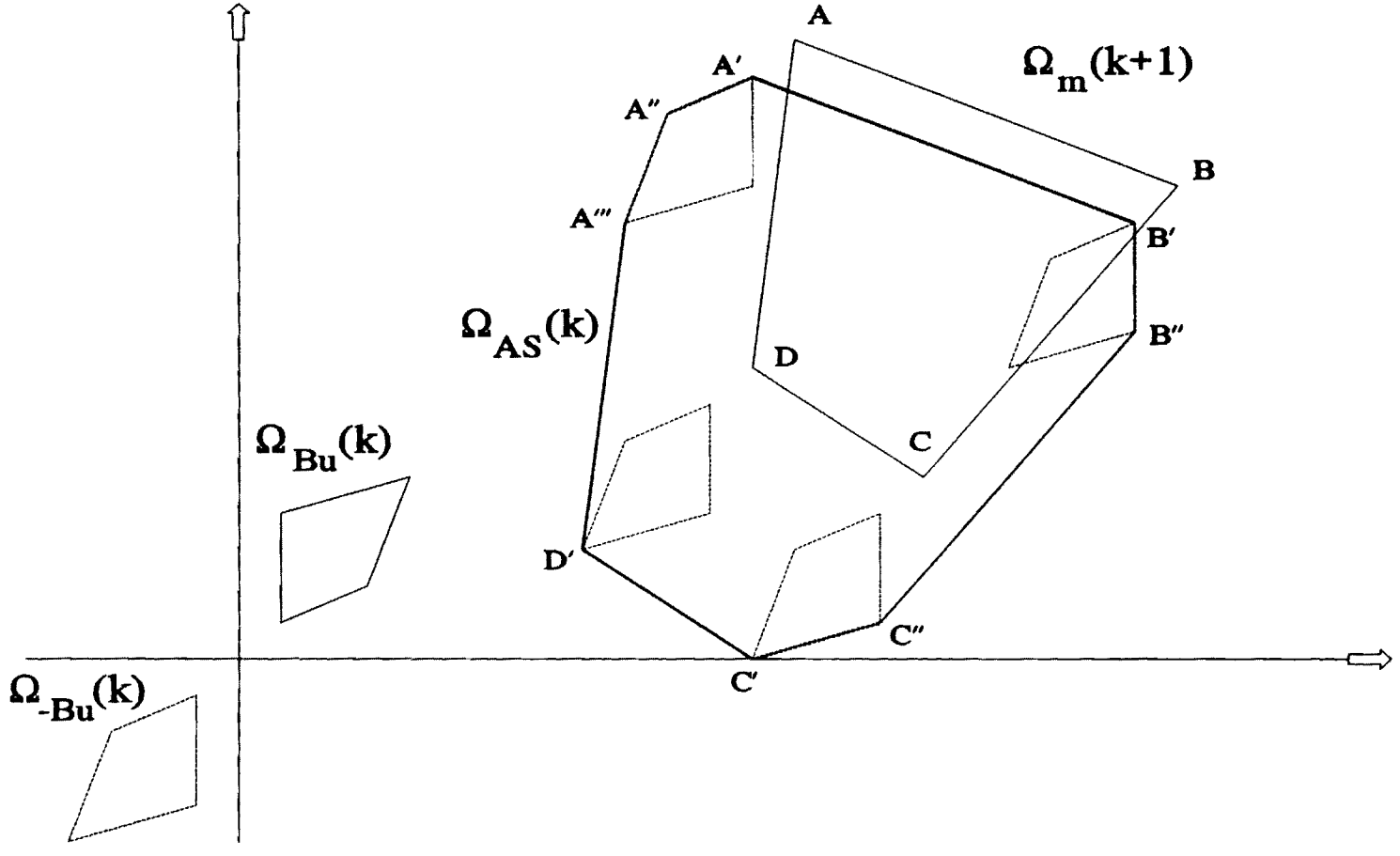

Figure 2.5: Derivation of $\Omega_{AS}(k)$

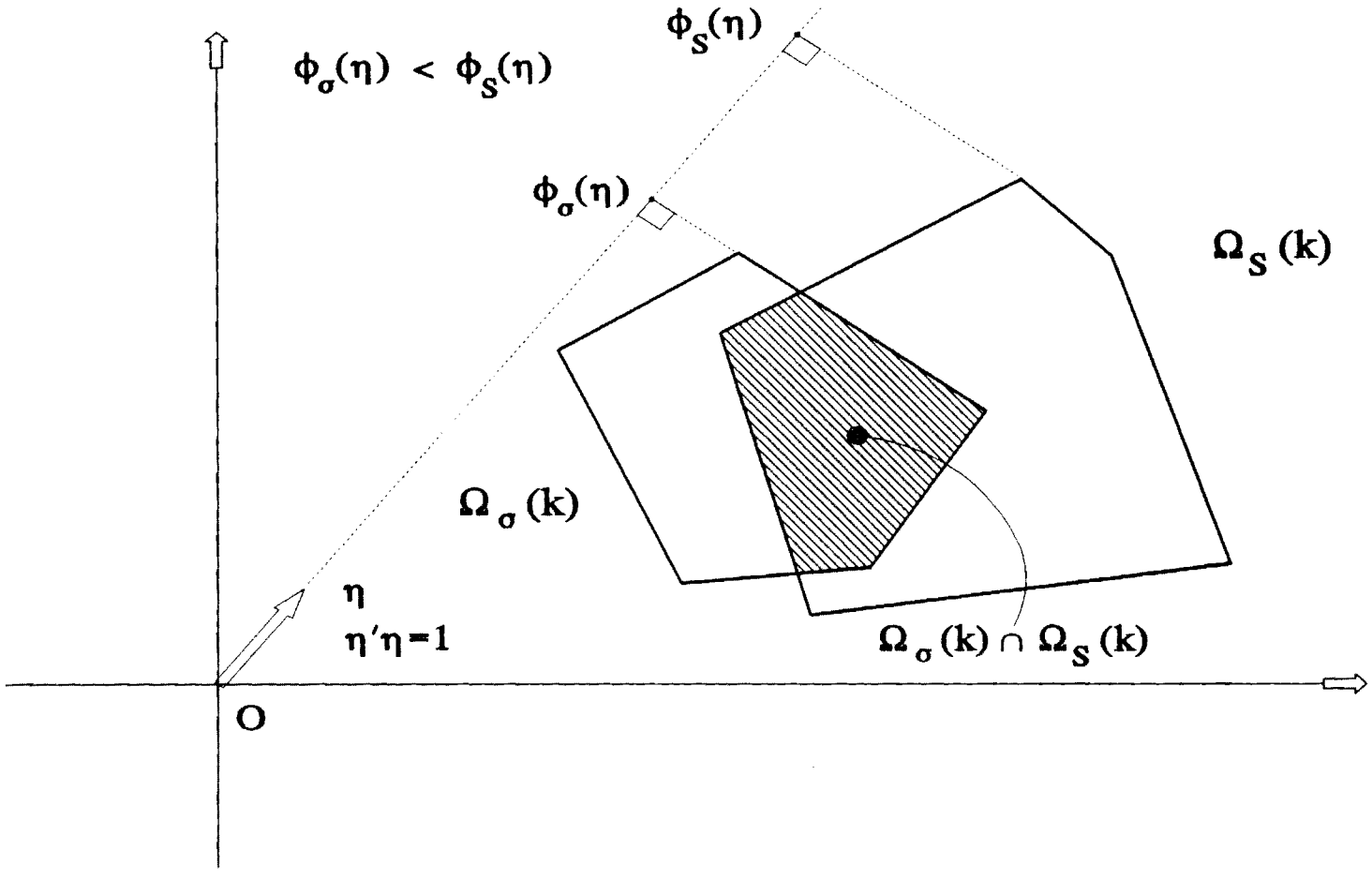

Figure 2.6: Set Intersection

$$\Omega_S(k) = \begin{Bmatrix} 0 \le S_1(k) \le 10 \\ 0 \le S_2(k) \le 15 \end{Bmatrix}, \; k = 0,1,2,3,4,$$

$$\Omega_w(k) = \begin{Bmatrix} 0 \le w_1(k) \le 3 \\ 0 \le w_2(k) \le 3 \end{Bmatrix}, \; k = 0,1,2,3, \tag{2.25}$$

$$\Omega_u(k) = \begin{Bmatrix} 0 \le u_1(k) \le 2 \\ 0 \le u_2(k) \le 2 \end{Bmatrix}, \; k = 0,1,2,3.$$

It is noted that the above formulation could represent a two-reservoir cascade. In hyperplane form, the constraints become

$$\underset{\Omega_S}{\begin{bmatrix} 1\,S_1(k) + 0\,S_2(k) \le 10 \\ (-1)\,S_1(k) + 0\,S_2(k) \le 0 \\ 0\,S_1(k) + 1\,S_2(k) \le 15 \\ 0\,S_1(k) + (-1)\,S_2(k) \le 0 \end{bmatrix}}, \quad \underset{\Omega_w}{\begin{bmatrix} 1\,w_1(k) + 0\,w_2(k) \le 3 \\ (-1)\,w_1(k) + 0\,w_2(k) \le 0 \\ 0\,w_1(k) + 1\,w_2(k) \le 3 \\ 0\,w_1(k) + (-1)\,w_2(k) \le 0 \end{bmatrix}}, \quad \underset{\Omega_u}{\begin{bmatrix} 1\,u_1(k) + 0\,u_2(k) \le 2 \\ (-1)\,u_1(k) + 0\,u_2(k) \le 0 \\ 0\,u_1(k) + 1\,u_2(k) \le 2 \\ 0\,u_1(k) + (-1)\,u_2(k) \le 0 \end{bmatrix}}, \tag{2.26}$$

where the support function ($\phi(\eta)$) values are given by the right-hand side of the above inequalities, and the coordinates of the associated vectors (η) are the coefficients on the left-hand side. In this example, the constraint sets and matrices **A**, **B**, and **G** are time-invariant.

Computation of Sets Ω_{Bu} and Ω_{-Bu}

Let $\mathbf{X}_{Bu}=[\mathbf{X}_{Bu1}\ \mathbf{X}_{Bu2}]'$ denote any vector in set Ω_{Bu}. Then, the support function and vectors of this set are given by (Eq.2.17):

$$\Omega_{Bu}=\{X_{Bu} : X_{Bu}^{t}(B')^{-1}\mathbf{v}_i \le \phi_u(\mathbf{v}_i), i=1,...,4\} \tag{2.27}$$

where ν_i and $\phi_u(\nu_i)$ are the support vector and support function value of set Ω_u respectively,

$$(B')^{-1}=\begin{bmatrix}-1 & -1\\ 0 & -1\end{bmatrix}, \tag{2.28}$$

$$\begin{bmatrix} v_1=[1\ 0]' & \phi_u(v_1)=2\\ v_2=[-1\ 0]' & \phi_u(v_2)=0\\ v_3=[0\ 1]' & \phi_u(v_3)=2\\ v_4=[0\ -1]' & \phi_u(v_4)=0\end{bmatrix}. \tag{2.29}$$

After performing the indicated matrix-vector multiplication, one obtains

$$\begin{matrix}\\ \\ \\ \\ \end{matrix}\begin{matrix}\Omega_{Bu}\end{matrix}$$
$$\begin{bmatrix} -X_{Bu1}+0X_{Bu2}\le 2\\ X_{Bu1}+0X_{Bu2}\le 0\\ -X_{Bu1}-X_{Bu2}\le 2\\ X_{Bu1}+X_{Bu2}\le 0\end{bmatrix}. \tag{2.30}$$

By changing the sign of the left-hand side coefficients, we get set Ω_{-Bu}. Namely,

$$\begin{matrix}\\ \\ \\ \\ \end{matrix}\begin{matrix}\Omega_{-Bu}\end{matrix}$$
$$\begin{bmatrix} X_{Bu1}+0X_{Bu2}\le 2\\ -X_{Bu1}+0X_{Bu2}\le 0\\ X_{Bu1}+X_{Bu2}\le 2\\ -X_{Bu1}-X_{Bu2}\le 0\end{bmatrix}. \tag{2.31}$$

Computation of $\Omega_m(4)$

Reduced state set $\Omega_r(4)$ is the same as $\Omega_S(4)$, and therefore its support function vectors are known. Let $S_m=[S_{m1}\ S_{m2}]'$ denote any vector in set $\Omega_m(4)$. Then, set $\Omega_m(4)$

is given by Equation (2.12):

$$\Omega_m(4)=\{S_m: S_m'\eta_i \le \phi_m(\eta_i) = \phi_r(\eta_i) - \phi_w(G'\eta_i),\ i=1,...,4\}, \tag{2.32}$$

where η_i are the support vectors of $\Omega_r(4)$ as follows (Eq. 2.26):

$$\begin{bmatrix} \eta_1=[1\ 0]' & \phi_r(\eta_1)=10 \\ \eta_2=[-1\ 0]' & \phi_r(\eta_2)=0 \\ \eta_3=[0\ 1]' & \phi_r(\eta_3)=15 \\ \eta_4=[0\ -1]' & \phi_r(\eta_4)=0 \end{bmatrix}. \tag{2.33}$$

$\phi_w[G'\eta_i]$ can be generally computed by solving the following LP problem:

$$\begin{aligned} &\textit{Maximize}\ \ w'G'\eta_i \\ &\textit{Subject to}\ \ w\in\Omega_w, \end{aligned} \tag{2.34}$$

where Ω_w is given by (2.26). The optimal value of $\mathbf{w}'\mathbf{G}'\eta_i$ represents $\phi_w[G'\eta_i]$.

In this example, this optimization problem has a simple solution as illustrated for their support vector η_1:

$$\begin{bmatrix} \textit{Maximize}\ w'G'\eta_1 = \phi_w[G'\eta_1] \\ \textit{Subject to}\ \ w\in\Omega_w \end{bmatrix} = \begin{bmatrix} \textit{Maximize}\ \ w_1 \\ \textit{Subject to}\ \ w\in\Omega_w \end{bmatrix} = 3 \tag{2.35}$$

Thus, the $\Omega_m(4)$ hyperplane associated with η_1 is

$$S_m' \begin{bmatrix} 1 \\ 0 \end{bmatrix} \le 10-3 = 7. \tag{2.36}$$

Similarly, we can compute the other three hyperplanes and specify $\Omega_m(4)$:

$$\Omega_m(4)$$

$$\begin{bmatrix} S_{m1}+0S_{m2} \le 7 \\ -S_{m1}+0S_{m2} \le 0 \\ 0S_{m1}+1S_{m2} \le 12 \\ 0S_{m1}-1S_{m2} \le 0 \end{bmatrix}. \qquad (2.37)$$

After the specification of all relevant hyperplanes, one should check whether the Ω_m set is nonempty and whether it includes redundant hyperplanes. Redundant hyperplanes should be discarded because they unnecessarily increase computational requirement. Procedures for performing these tasks have been outlined in Section 2.3. In this cases, the set is nonempty and does not include redundant hyperplanes.

Computation of set Ω_{AS}

Let $X_{AS}=[X_{AS1}\ X_{AS2}]'$ denote any vector in set Ω_{AS}. Then, Ω_{AS} is given by (Eq. 2.19):

$$\begin{aligned} \Omega_{AS}(3)=\{X_{AS}:\ & X'_{AS}\eta_i \le \phi_m(\eta_i)+\phi_{-BU}(\eta_i),\quad i=1,...,4, \\ & X'_{AS}\theta_j \le \phi_m(\theta_j)+\phi_{-BU}(\theta_j),\quad j=1,...,4\} \end{aligned} \qquad (2.38)$$

where η_i are the support vectors of set $\Omega_m(4)$, and θ_j are the support vectors of set Ω_{-Bu}. For each η_i and θ_j, $\phi_m(\eta_i)$ and $\phi_{-Bu}(\theta_j)$ are known. To compute $\phi_{-Bu}(\eta_i)$ and $\phi_m(\theta_j)$, one needs to solve the following LP problems:

$$\begin{aligned} &\textit{Maximize } X'_{Bu}\eta_i = \phi_{-Bu}(\eta_i) \\ &\textit{Subject to } X_{Bu}\in\Omega_{-Bu} \end{aligned}$$

$$\textit{and} \qquad (2.39)$$

$$\begin{aligned} &\textit{Maximize } S'_m\theta_i = \phi_m(\theta_i) \\ &\textit{Subject to } S_m\in\Omega_m(4) \end{aligned}$$

The results are summarized below:

$$\begin{bmatrix} \eta_1=[1\ 0]' & \phi_m(\eta_1)=7 & \phi_{-Bu}(\eta_1)=2 \\ \eta_2=[-1\ 0]' & \phi_m(\eta_2)=0 & \phi_{-Bu}(\eta_2)=0 \\ \eta_3=[0\ 1]' & \phi_m(\eta_3)=12 & \phi_{-Bu}(\eta_3)=2 \\ \eta_4=[0\ -1]' & \phi_m(\eta_4)=0 & \phi_{-Bu}(\eta_4)=2 \\ \theta_1=[1\ 0]' & \phi_m(\theta_1)=7 & \phi_{-Bu}(\theta_1)=2 \\ \theta_2=[-1\ 0]' & \phi_m(\theta_2)=0 & \phi_{-Bu}(\theta_2)=0 \\ \theta_3=[1\ 1]' & \phi_m(\theta_3)=19 & \phi_{-Bu}(\theta_3)=2 \\ \theta_4=[-1\ -1]' & \phi_m(\theta_4)=0 & \phi_{-Bu}(\theta_4)=0 \end{bmatrix}. \tag{2.40}$$

Then, the hyperplanes of Ω_{AS} are

$$\Omega_{AS}$$
$$\begin{bmatrix} X_{AS1}+0X_{AS2}\le 9 \\ -X_{AS1}+0X_{AS2}\le 0 \\ 0X_{AS1}+X_{AS2}\le 14 \\ 0X_{AS1}-X_{AS2}\le 2 \\ X_{AS1}+0X_{AS2}\le 9 \\ -X_{AS1}+0X_{AS2}\le 0 \\ X_{AS1}+X_{AS2}\le 21 \\ -X_{AS1}-X_{AS2}\le 0 \end{bmatrix}. \tag{2.41}$$

It is noted that some of the above hyperplanes may be repetitive. To avoid unnecessary calculations and computer memory overtaxing, one should remove these hyperplanes from Ω_{AS} before proceeding. In this example, two hyperplanes are repetitive because set Ω_{-Bu} and $\Omega_m(4)$ share two common support vectors. After removing these hyperplanes, Ω_{AS} is given by

$$\Omega_{AS}(3)$$

$$\begin{bmatrix} X_{AS1} + 0X_{AS2} \le 9 \\ -X_{AS1} + 0X_{AS2} \le 0 \\ 0X_{AS1} + X_{AS2} \le 14 \\ 0X_{AS1} - X_{AS2} \le 2 \\ X_{AS1} + X_{AS2} \le 21 \\ -X_{AS1} - X_{AS2} \le 0 \end{bmatrix} . \tag{2.42}$$

Computation of $\Omega_o(3)$ from $\Omega_{AS}(3)$

Let $\mathbf{X}_o=[X_{o1} \quad X_{o2}]'$ denote any vector in set $\Omega_o(3)$. Since **A** is an identity matrix in this example, $\Omega_o(3)$ equals $\Omega_{AS}(3)$ according to Eq. (2.20). Namely,

$$\Omega_o(3)$$

$$\begin{bmatrix} X_{o1} + 0X_{o2} \le 9 \\ -X_{o1} + 0X_{o2} \le 0 \\ 0X_{o1} + X_{o2} \le 14 \\ 0X_{o1} - X_{o2} \le 2 \\ X_{o1} + X_{o2} \le 21 \\ -X_{o1} - X_{o2} \le 0 \end{bmatrix} . \tag{2.43}$$

Computation of $\Omega_r(3)$

Let $\mathbf{S}_r=[S_{r1} \quad S_{r2}]'$ denote any vector in set $\Omega_r(3)$. $\Omega_r(3)$ is determined from the intersection of $\Omega_o(3)$ and $\Omega_s(3)$(Eq. 2.21):

$$\begin{aligned} \Omega_r(3)=\{S_r:\ & S_r'\tau_i \le Min[\phi_s(\tau_i),\phi_o(\tau_i)], \quad i=1,\ldots,n_s\ , \\ & S_r'\rho_j \le Min[\phi_s(\rho_j),\phi_o(\rho_j)], \quad j=1,\ldots,n_o\}\ . \end{aligned} \tag{2.44}$$

where τ_i and $\phi_i(\tau_i)$ are the support vectors and function of set $\Omega_s(3)$, while ρ_i and $\phi_j(\rho_j)$ are the support vectors and function of set $\Omega_o(3)$.

Again, $\phi_o(\tau_i)$ and $\phi_s(\rho_j)$ are unknown but can be computed by solving LP problems similar to those formulated earlier. The results are given below

$$\begin{bmatrix}
\tau_1=[1\ 0]' & \phi_s(\tau_1)=10 & \phi_o(\tau_1)=9 \\
\tau_2=[-1\ 0]' & \phi_s(\tau_2)=0 & \phi_o(\tau_2)=0 \\
\tau_3=[0\ 1]' & \phi_s(\tau_3)=15 & \phi_o(\tau_3)=14 \\
\tau_4=[0\ -1]' & \phi_s(\tau_4)=0 & \phi_o(\tau_4)=2 \\
\rho_1=[1\ 0]' & \phi_s(\rho_1)=10 & \phi_o(\rho_1)=9 \\
\rho_2=[-1\ 0]' & \phi_s(\rho_2)=0 & \phi_o(\rho_2)=0 \\
\rho_3=[0\ 1]' & \phi_s(\rho_3)=15 & \phi_o(\rho_3)=14 \\
\rho_4=[0\ -1]' & \phi_s(\rho_4)=0 & \phi_o(\rho_4)=2 \\
\rho_5=[1\ 1]' & \phi_s(\rho_5)=25 & \phi_o(\rho_5)=21 \\
\rho_6=[-1\ -1]' & \phi_s(\rho_6)=0 & \phi_o(\rho_6)=0
\end{bmatrix}. \tag{2.45}$$

The corresponding set $\Omega_r(3)$ is defined by

$$\Omega_r(3)$$

$$\begin{bmatrix}
S_{r1}+0S_{r2} \le 9 \\
-S_{r1}+0S_{r2} \le 0 \\
0S_{r1}+S_{r2} \le 14 \\
0S_{r1}-S_{r2} \le 0 \\
S_{r1}+0S_{r2} \le 9 \\
-S_{r1}+0S_{r2} \le 0 \\
0S_{r1}+S_{r2} \le 14 \\
0s_{r1}-S_{r2} \le 0 \\
S_{r1}+S_{r2} \le 21 \\
-S_{r1}-S_{r2} \le 0
\end{bmatrix}. \tag{2.46}$$

Discarding the repeated hyperplanes, $\Omega_r(3)$ simplifies as follows:

$$\Omega_r(3)$$

$$\begin{bmatrix} S_{r1} + 0S_{r2} \le 9 \\ -S_{r1} + 0S_{r2} \le 0 \\ 0S_{r1} + S_{r2} \le 14 \\ 0S_{r1} - S_{r2} \le 0 \\ S_{r1} + S_{r2} \le 21 \end{bmatrix}. \tag{2.47}$$

The above procedure is repeated to compute sets $\Omega_m(3)$, $\Omega_r(2)$, $\Omega_m(2)$, $\Omega_r(1)$,$\Omega_m(1)$, $\Omega_r(0)$. These sets are summarized in Table 2.1.

Computation of the admissible control set $\Omega_c(0)$

The admissible control set $\Omega_c(0)$ can be computed by the procedure described in Section 2.5.

First, the admissible set $\Omega_{Bu}(0)$ is computed by Eq.(23). Let $X_{Bu} = [X_{Bu1}\ X_{Bu2}]'$ denote any vector in set $\Omega_{Bu}(0)$. Then, $\Omega_{Bu}(0)$ is given by:

$$\Omega_{Bu}(0) = \{X_{Bu}: X_{Bu}'\eta_i \le \phi_m(\eta_i) - S'(0)A'\eta_i,\ i=1,...,4\}, \tag{2.48}$$

where $\phi_m(\eta_i)$, η_i, i = 1,...,4, represent the support function and associated vector set for $\Omega_m(1)$ given in Table 2.1. S(0) = [4,4]′ is the initial state.

Substituting the initial state vector into Eq. (2.23), we have

$$\begin{bmatrix} \eta_1=[1\ 0]' & \phi_m(\eta_1)=4 & S'(0)A'\eta_1=4 \\ \eta_2=[-1\ 0]' & \phi_m(\eta_2)=0 & S'(0)A'\eta_2=-4 \\ \eta_3=[0\ -1]' & \phi_m(\eta_3)=0 & S'(0)A'\eta_3=-4 \\ \eta_4=[1\ 1]' & \phi_m(\eta_4)=7 & S'(0)A'\eta_4=8 \end{bmatrix}. \tag{2.49}$$

Thus, the corresponding admissible set $\Omega_{Bu}(0)$ is

$$\Omega_{Bu}(0)$$
$$\begin{bmatrix} X_{Bu1} + 0X_{Bu2} \le 0 \\ -X_{Bu1} + 0X_{Bu2} \le 4 \\ 0X_{Bu1} - X_{Bu2} \le 4 \\ X_{Bu1} + X_{Bu2} \le -1 \end{bmatrix}. \tag{2.50}$$

Secondly, $\Omega_u(0)$ is computed from $\Omega_{Bu}(0)$. Let $\mathbf{X_u} = [X_{u1}, X_{u2}]'$ denote any vector in set $\Omega_u(0)$. $\Omega_u(0)$ is obtained by Eq.(2.20):

$$\Omega_u(0) = \{X_u : X_u' B' e_i \le \phi_{Bu}(e_i),\ i=1,...,4\}\ , \tag{2.51}$$

where $\mathbf{e_i}$, $\phi_{Bu}(\mathbf{e_i})$ are the support vector and support function of $\Omega_{Bu}(0)$, respectively. After performing the indicated matrix-vector multiplication, one obtains

$$\Omega_u(0)$$
$$\begin{bmatrix} -X_{u1} + 0X_{u2} \le 0 \\ X_{u1} + 0X_{u2} \le 4 \\ -X_{u1} + X_{u2} \le 4 \\ 0X_{u1} - X_{u2} \le -1 \end{bmatrix}. \tag{2.52}$$

Finally, the admissible control set $\Omega_c(0)$ is given by the intersection of $\Omega_u(0)$ and Ω_u. Let $\mathbf{u_c} = [u_{c1}, u_{c2}]'$ denote any vector in set $\Omega_c(0)$. then, $\Omega_c(0)$ is given by (Eq. 2.21):

$$\begin{aligned} \Omega_c(0) = \{u_c:\ & u_c' \eta_i \le Min[\phi_c(\eta_i), \phi_u(\eta_i)], \quad i=1,...,4, \\ & and \quad u_c' v_j \le Min[\phi_c(v_j), \phi_u(v_j)], \quad j=1,...,4\} \end{aligned} \tag{2.53}$$

Vectors η_i and v_j are support vectors of $\Omega_u(0)$ and Ω_u respectively. $\phi_u(\eta_i)$ and $\phi_c(\rho_j)$ are unknown but can be computed by solving the following LP problems:

$$\begin{aligned} &\textit{Maximize } u_c'\eta_i = \phi_u(\eta_i) \\ &\textit{Subject to } \quad u_c \in \Omega_u(0) \\ &\qquad\qquad \textit{and} \\ &\textit{Maximize } u'v_i = \phi_c(v_i) \\ &\textit{Subject to } \quad u \in \Omega_u . \end{aligned} \tag{2.54}$$

The results are summarized below:

$$\begin{bmatrix} \eta_1=[-1\ 0]' & \phi_c(\eta_1)=0 & \phi_u(\eta_1)=0 \\ \eta_2=[1\ 0]' & \phi_c(\eta_2)=4 & \phi_u(\eta_2)=2 \\ \eta_3=[-1\ 1]' & \phi_c(\eta_3)=4 & \phi_u(\eta_3)=2 \\ \eta_4=[0\ -1]' & \phi_c(\eta_4)=-1 & \phi_u(\eta_4)=0 \\ v_1=[1\ 0]' & \phi_c(v_1)=4 & \phi_u(v_1)=2 \\ v_2=[-1\ 0]' & \phi_c(v_2)=0 & \phi_u(v_2)=0 \\ v_3=[0\ 1]' & \phi_c(v_3)=8 & \phi_u(v_3)=2 \\ v_4=[0\ -1]' & \phi_c(v_4)=-1 & \phi_u(v_4)=0 \end{bmatrix} \tag{2.55}$$

The admissible control set $\Omega_c(0)$ is then defined by

$$\Omega_c(0) \begin{bmatrix} -u_{c1} + 0u_{c2} \le 0 \\ u_{c1} + 0u_{c2} \le 2 \\ -u_{c1} + u_{c2} \le 2 \\ 0u_{c1} - u_{c2} \le -1 \\ u_{c1} + 0u_{c2} \le 2 \\ -u_{c1} + 0u_{c2} \le 0 \\ 0u_{c1} + u_{c2} \le 2 \\ 0u_{c1} - u_{c2} \le -1 \end{bmatrix}. \tag{2.56}$$

After discarding the repeated hyperplanes, this set becomes

$$\Omega_c(0) \begin{bmatrix} u_{c1} + 0u_{c2} \le 2 \\ -u_{c1} + 0u_{c2} \le 0 \\ 0u_{c1} + u_{c2} \le 2 \\ 0u_{c1} - u_{c2} \le -1 \end{bmatrix}. \tag{2.57}$$

2.7 COMPARISON OF POLYHEDRAL AND ELLIPSOIDAL SET CONTROL ALGORITHMS

The second computational experiment aims at comparing the polyhedral control algorithm discussed earlier with an ellipsoidal approximation algorithm proposed by *Bertsekas and Rhodes [1971]*. The basis of this approach is to create ellipsoidal approximations of all sets and develop recursive relationships for the ellipsoid centers and principle axes. These relationships are similar to the Ricatti equations encountered in Linear Quadratic Gaussian control problems. Since these equations can be solved recursively, they present computational advantages for large systems.

The system is again described by Equation (2.24) and the state, input, and control sets are as follows:

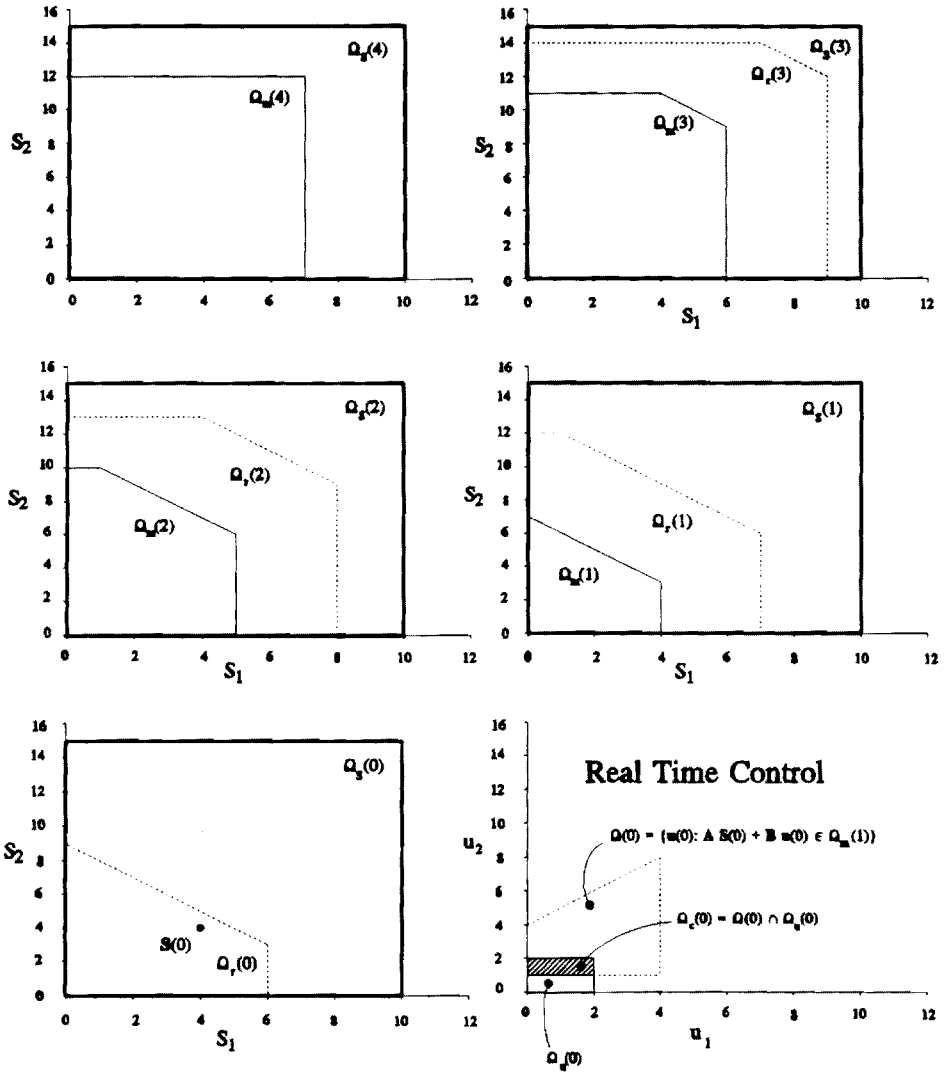

Figure 2.7: State and Control Sets for the Example

$$\Omega_S(k) = \left\{ \begin{matrix} -37.5 \le S_1(k) \le 37.5 \\ -31 \le S_2(k) \le 31 \end{matrix} \right\}, \; k = 0,1,\ldots,15,$$

$$\Omega_w(k) = \left\{ \begin{matrix} -10 \le w_1(k) \le 10 \\ -15 \le w_2(k) \le 15 \end{matrix} \right\}, \; k = 0,1,\ldots,14, \qquad (2.58)$$

$$\Omega_u(k) = \left\{ \begin{matrix} -10 \le u_1(k) \le 10 \\ -22 \le u_2(k) \le 22 \end{matrix} \right\}, \; k = 0,1,\ldots,14.$$

For the ellipsoidal approximation algorithm, the state, input, and control sets are the smallest ellipses enveloping the previous rectangles.

Figure 2.8 portrays the resulting modified and reduced state sets for both set computation approaches at times 15, 14, 13, 12, 1, and 0. Until time 12, both approaches produce feasible results, although the polyhedral modified and reduced sets are significantly larger. At time 11, the ellipsoidal algorithm terminates indicating infeasibility, while the polyhedral approach remains feasible until time 0. This experiment shows that the required ellipsoidal approximations underestimate the feasible regions and cause early algorithm termination. Given that the polyhedral algorithm is fairly efficient (see computational time estimates in companion article), this suboptimality of the ellipsoidal set control approach is a major weakness.

Table 2.1: Modified and Reduced State Sets for the Example

N	$\Omega_m(N)$	$\Omega_r(N)$
4	$1S_{m1} + 0S_{m2} \le 7$ $(-1)S_{m1} + 0S_{m2} \le 0$ $0S_{m1} + 1S_{m2} \le 12$ $0S_{m1} + (-1)S_{m2} \le 0$	
3	$1S_{m1} + 0S_{m2} \le 6$ $(-1)S_{m1} + 0S_{m2} \le 0$ $0S_{m1} + 1S_{m2} \le 11$ $0S_{m1} + (-1)S_{m2} \le 0$ $1S_{m1} + 1S_{m2} \le 15$	$1S_1 + 0S_2 \le 9$ $(-1)S_1 + 0S_2 \le 0$ $0S_1 + 1S_2 \le 14$ $0S_1 + (-1)S_2 \le 0$ $1S_1 + 1S_2 \le 21$
2	$1S_1 + 0S_2 \le 5$ $(-1)S_1 + 0S_2 \le 0$ $0S_1 + 1S_2 \le 10$ $0S_1 + (-1)S_2 \le 0$ $1S_1 + 1S_2 \le 11$	$1S_1 + 0S_2 \le 8$ $(-1)S_1 + 0S_2 \le 0$ $0S_1 + 1S_2 \le 13$ $0S_1 + (-1)S_2 \le 0$ $1S_1 + 1S_2 \le 17$
	$1S_1 + 0S_2 \le 4$ $(-1)S_1 + 0S_2 \le 0$ $0S_1 + (-1)S_2 \le 0$ $1S_1 + 1S_2 \le 7$	$1S_1 + 0S_2 \le 7$ $(-1)S_1 + 0S_2 \le 0$ $0S_1 + 1S_2 \le 12$ $0S_1 + (-1)S_2 \le 0$ $1S_1 + 1S_2 \le 13$
0		$1S_1 + 0S_2 \le 6$ $(-1)S_1 + 0S_2 \le 0$ $0S_1 + (-1)S_2 \le 0$ $1S_1 + 1S_2 \le 9$

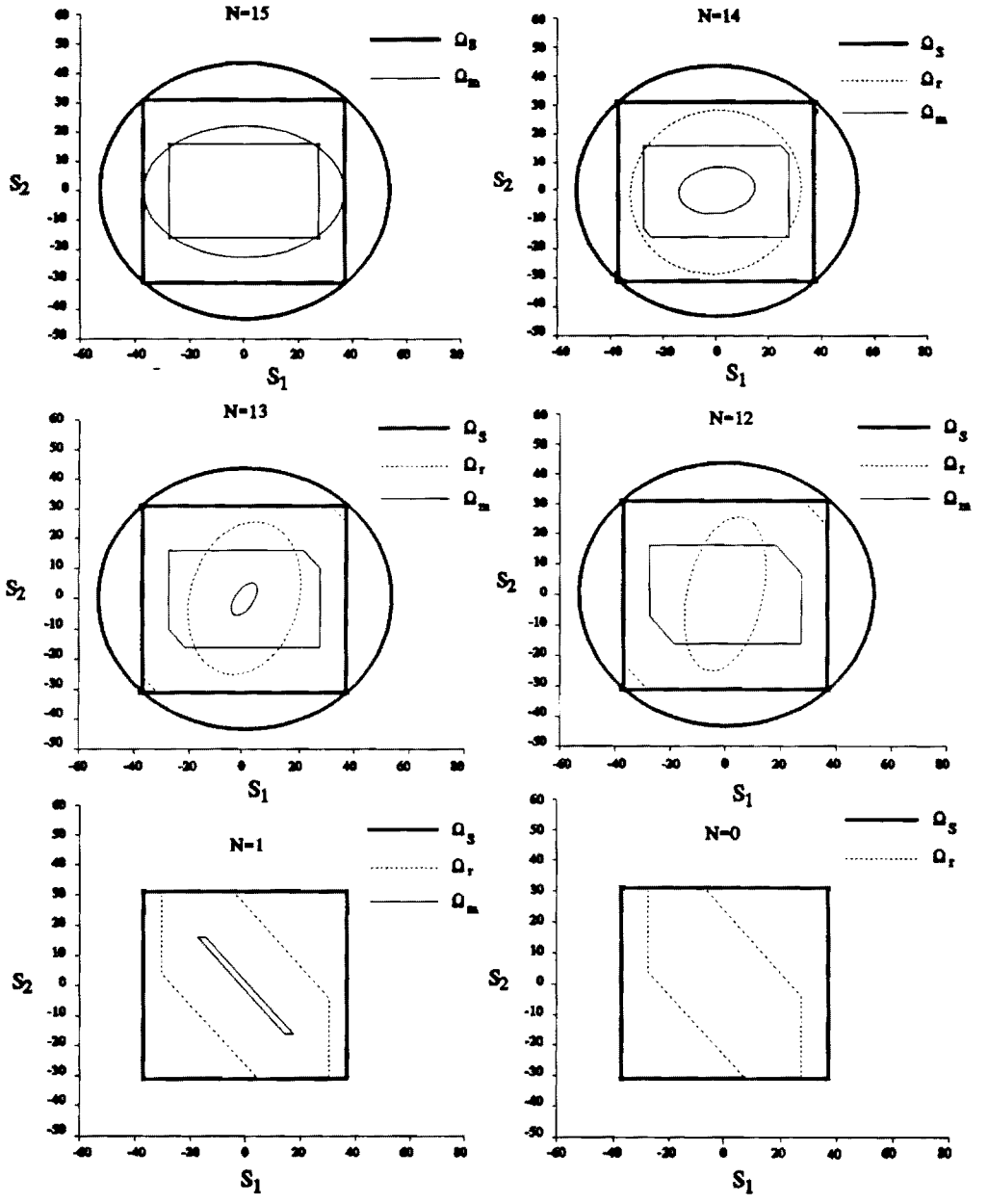

Figure 2.8: A Comparison of Polyhedral and Ellipsoidal Set Algorithms

3. APLLICATION TO RESERVOIR MANAGEMENT

3.1 INTRODUCTION

The need to handle uncertainty in reservoir management is widely recognized by practicing and research professionals and continues to motivate new management approaches [*Foufoula-Georgiou and Kitanidis, 1988, Kelman et al., 1990, Georgakakos, 1989, 1992*]. The common theme is to rely on probability theory to model random quantities and then develop suitable optimization schemes to control the probability distribution of storage, release, energy generation, and other key system variables. The basic suppositions are (**a**) that enough data are available to validate the descriptions of the uncertain elements and (**b**) that the system operator has the ability to balance abstract concepts, such as risks of not meeting certain objectives or expected output levels, among themselves and over time.

Data availability undermines stochastic methods when they are most valuable: during hydrologic extremes. Data deficiencies for extreme floods and droughts usually weaken model predictions and limit management options. What is more, potentially new climatic regimes may totally invalidate existing observation records.

Amidst crises situations, system operators are also faced with nontrivial challenges. At the onset of droughts, they must decide whether to reduce outflow or continue with their normal release schedules. In retrospect, one option is better than the other, but at the time when the decision is made each option involves risks. Anticipating floods, reservoir operators should evacuate enough storage to avoid damage-causing outflows and energy-wasting spillage. Over- or under-estimating this storage again involves risks. Risks are associated with almost every decision in reservoir operations, but it is unclear how reservoir operators should try to appreciate and balance them. Stochastic management methods are useful, but they can only control the probability of extreme events and not their magnitude [*Georgakakos, 1989*]. And, as already mentioned, probability estimates can only be as good as the available data.

As an alternative, in this work we develop operational choices that are easier to understand and offer some guarantees. Using the set control approach, we derive sets of control actions guaranteeing that the system will meet its constraints (satisfy water supplies, maintain outflow below damaging levels, or cover a dependable energy commitment). The guarantees are valid for a certain length of time and for all inflow sequences bounded by specific ranges. The inflow bounds are selected by the operator and should reflect extreme hydrologic circumstances against which the system is to be controlled. This selection affects the size of the admissible control

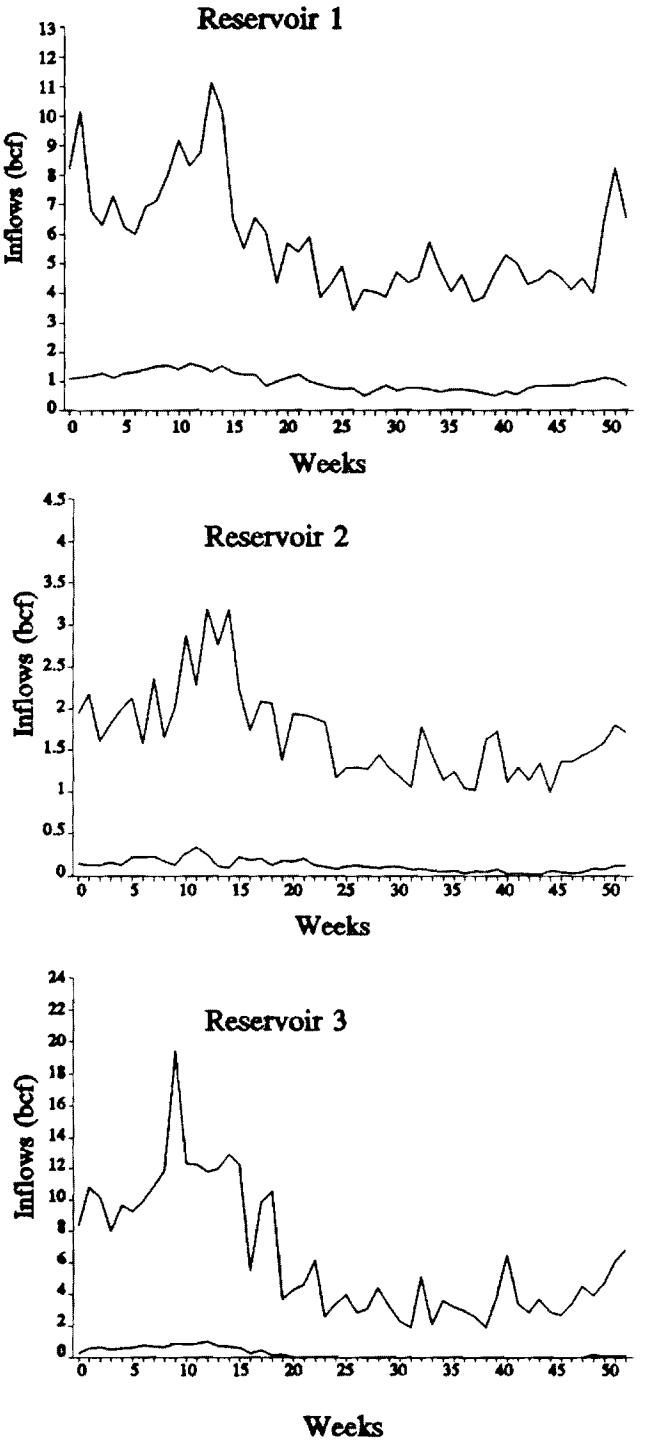

Figure 3.1: Reservoir Inflow Ranges

sets and the length of the operational horizon during which the system can fully meet the stated constraints. Bounds associated with more extreme hydrologies result in shorter guaranteed operational horizons and smaller admissible control sets. Although this judgement involves risks, it is also more meaningful and reassuring, especially during crises. The operators can select any control action within the specified sets and be confident that the system will not violate the stated constraints at least for the duration of the operational horizon.

This article examines this approach as it applies to flood and drought management and hydropower operations and illustrates through examples how some apparent method limitations can be overcome. Potential applications for reservoir design and operational policy determination are also briefly discussed.

3.2 FLOOD AND DROUGHT MANAGEMENT / RESERVOIR DESIGN

The following discussion, although general, will make reference to a three-reservoir cascade as an example and test case study. This system is located on the Savannah River in the southeastern U.S. and is described in *Georgakakos* [*1989, 1992*]. For the purposes of this section (namely, to investigate issues exclusive of hydropower), the system is modelled by the following water balance state equation:

$$\begin{bmatrix} S_1(k+1) \\ S_2(k+1) \\ S_3(k+1) \end{bmatrix} = \begin{bmatrix} 1 & 0 & 0 \\ 0 & 1 & 0 \\ 0 & 0 & 1 \end{bmatrix} \begin{bmatrix} S_1(k) \\ S_2(k) \\ S_3(k) \end{bmatrix} + \begin{bmatrix} -1 & 0 & 0 \\ 1 & -1 & 0 \\ 0 & 1 & -1 \end{bmatrix} \begin{bmatrix} u_1(k) \\ u_2(k) \\ u_3(k) \end{bmatrix} + \begin{bmatrix} 1 & 0 & 0 \\ 0 & 1 & 0 \\ 0 & 0 & 1 \end{bmatrix} \begin{bmatrix} w_1(k) \\ w_2(k) \\ w_3(k) \end{bmatrix}, \quad (3.1)$$

$$k = 0,1,\ldots,N-1,$$

where $S_i(k)$, $u_i(k)$, and $w_i(k)$ respectively represent storage, release, and inflow volumes for reservoir $i=1,2,3$. Table 3.1 reports permissible storage and release ranges reflecting water conservation and flood control objectives, and Figure 3.1 depicts the weekly inflow ranges. These ranges were obtained, somewhat arbitrarily, using the third lowest and third highest inflow values on record (63 years).

The first question is whether the system can control inflows without violating the stated constraints, namely, without effecting water shortages (where $u_3(k) < 2.2$ billion cubic feet/week) or damage-causing outflows (where $u_3(k) > 18$ bcf/week). The answer is far from obvious since system inflow ($w_1(k)+w_2(k)+w_3(k)$) saturates the admissible range of $u_3(k)$ for more than one third of the year (rainy season).

Table 3.1: Reservoir Storage and Release Constraints

	Minimum	Maximum
Reservoir 1		
Storage (bcf)	79.25	123.8
Release (bcf / week)	0.0	18.0
Reservoir 2		
Storage (bcf)	34.2	50.8
Release (bcf/week)	0.0	18.0
Reservoir 3		
Storage (bcf)	69.71	125.95
Release (bcf/week)	2.2	18.0

To provide a partial answer to this question, we ran the set control algorithm with a time horizon of 52 weeks. The algorithm terminated successfully and generated the following reduced state set at time zero:

$$\Omega_r(0) = \left\{ \begin{array}{r} (-0.7071)S_1 + (-0.7071)S_2 + 0S_3 \le -80.2213 \\ 0.5774S_1 + 0.5774S_2 + 0.5774S_3 \le 140.4670 \\ -0.5774)S_1 + (-0.5774)S_2 + (-0.5774)S_3 \le -129.8806 \\ 1S_1 + 0S_2 + 0S_3 \le 123.8 \\ (-1)S_1 + 0S_2 + 0S_3 \le -79.25 \\ 0S_1 + 1S_2 + 0S_3 \le 50.8 \\ 0S_1 + (-1)S_2 + 0S_3 \le -34.2 \\ 0S_1 + 0S_2 + 1S_3 \le 125.93 \\ 0S_1 + 0S_2 + (-1)S_3 \le -69.71 \end{array} \right\}. \qquad (3.2)$$

If this set contains the initial storage values, there exist feasible release sequences that maintain all reservoir storages within their acceptable limits independently of what inflows materialize, provided that they are within the specified bounds. The set of admissible control actions that guarantee feasibility is also determined for initial storage values $S_1(0)=100$, $S_2(0)=45$, and $S_3(0)=95$ bcf:

$$\Omega_c(0) = \left\{ \begin{array}{r} 0.7071u_1 + (-0.7071)u_2 + 0u_3 \le 2.7209 \\ (-0.7071)u_1 + 0.7071u_2 + 0u_3 \le 7.7442 \\ 1u_1 + 0u_2 + 0u_3 \le 18.0 \\ (-1)u_1 + 0u_2 + 0u_3 \le 0.0 \\ 0u_1 + 1u_2 + 0u_3 \le 18.0 \\ 0u_1 + (-1)u_2 + 0u_3 \le 0.0 \\ 0u_1 + 0u_2 + 1u_3 \le 17.2403 \\ 0u_1 + 0u_2 + (-1)u_3 \le -14.7040 \end{array} \right\}. \qquad (3.3)$$

To test the validity of the results, we ran simulation experiments. Each simulation began with the generation of a 52-week, random inflow sequence for each system reservoir. These sequences can be determined in several ways. One approach is to generate inflow values uniformly (equally likely) within each weekly range. The result would be a totally random sequence, but one with very little probability of being consistently high or low (as in wet and dry years). Furthermore, the yearly volume of such sequences usually has a much wider range than actually observed. To avoid these inconsistencies, the inflow sequences were constructed as follows: The yearly inflow ranges for the entire system and each reservoir were first determined using the third lowest and third highest annual inflows on record. A uniform value within each range was then generated. Next, the annual inflow values of each reservoir were appropriately normalized to agree with the system value. Lastly, uniform inflows were obtained within each weekly range and subsequently adjusted to conform to the respective annual inflow values for each reservoir.

At each time period k (week) of the simulation horizon, a control vector was also randomly generated from the corresponding real-time control set $\Omega_c(k)$. The inflow and control vectors were then used in Equation (3.1) to determine the storage values for the next time step $k+1$. Based on these values and the reduced and modified state sets derived by the set control approach for time $k+2$, a new real-time control set $\Omega_c(k+1)$ was determined and the procedure was repeated until the end of the year. The simulation process was applied to 30 different random inflow sequences with the results shown on Figure 3.2. The figure includes the simulated storage and release sequences (solid lines) along with their associated bounds (dashed lines) and indicates that the set control approach accomplishes the objective of maintaining system storages within their limits using only feasible releases. The fact that the reservoirs experience drawdowns is a consequence of the manner in which the applied releases are obtained. Random release selection from the $\Omega_c(k)$ sets leads to reservoir depletion. Note, however, that this does not forewarn that the control

process will become infeasible. What will happen is that sets $\Omega_c(k)$ will shift towards low release regions of the feasible control sets $\Omega_u(k)$.

To see the effect of other selection rules, we ran additional simulation experiments using the release vector associated with the $\Omega_c(k)$ corner point closest to the axis origin (Figure 3.3). The system is again contained within the specified constraints in all simulations, but reservoir storages now tend to be in the proximity of their upper bounds. The applied releases are generally lower than in the previous case, although specific release levels may be higher depending on the seasonal inflow range and the value of storage.

Hence, the selection of applied releases can drastically influence the state of the system, this being a strength and an open question. From the operational point of view and especially during crises, it is comforting to know that any control action from the $\Omega_c(k)$ sets will not force violation of the stated bounds. However, a relevant question is how to establish an appropriate selection mechanism to coerce the system to evolve in a desirable manner. Desirability implies that each possible system sequence has some distinct value to the system users, and this premise is beyond the stated scope of the set control approach which simply aims to guarantee system feasibility. Nevertheless, it is a question of practical interest and will be taken up again in the conclusion section.

The purpose of the above experiments was to see whether the system is controllable in view of the imposed constraints. The answer was positive but partial because the results do not guarantee feasibility beyond the 52-week control horizon. In fact if the control horizon is extended to over 90 weeks, the set control approach terminates identifying empty modified state sets. Infeasibility means that there is no guarantee that the system can be contained within the stated limits so far in advance. The reason is that the minimum required release of 2.2 bcf/week from the 3rd reservoir is higher than the average lower inflow bound ($\sim$1.396 bcf/week). Eventually, this disparity renders the process infeasible. Note, however, that infeasibilities may occur even if average inflow is higher than the required draft. Such is the case when the upper release bound of the third reservoir is reduced below 16 bcf/week, despite an average upper inflow bound of 13.9 bcf/week. The process becomes infeasible due to large seasonal inflow bound fluctuations.

To understand the nature of the solution when no infeasibility is encountered, we ran a 5-year (260-week) control experiment with a lower release bound of 1.39 bcf/week. The results show that after the first year (as the solution proceeds backwards), the modified and reduced state sets exhibit annual periodicity. For the problem stated,

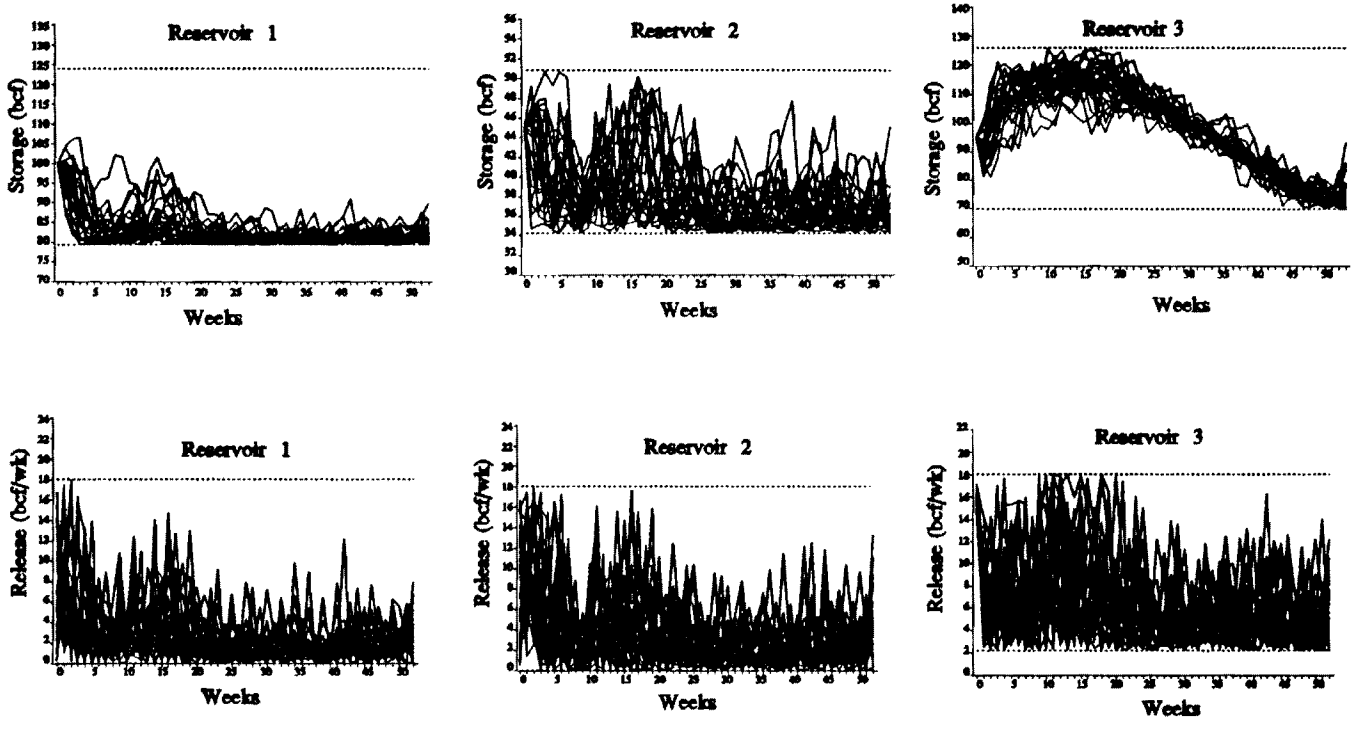

Figure 3.2 Simulation with random release section.

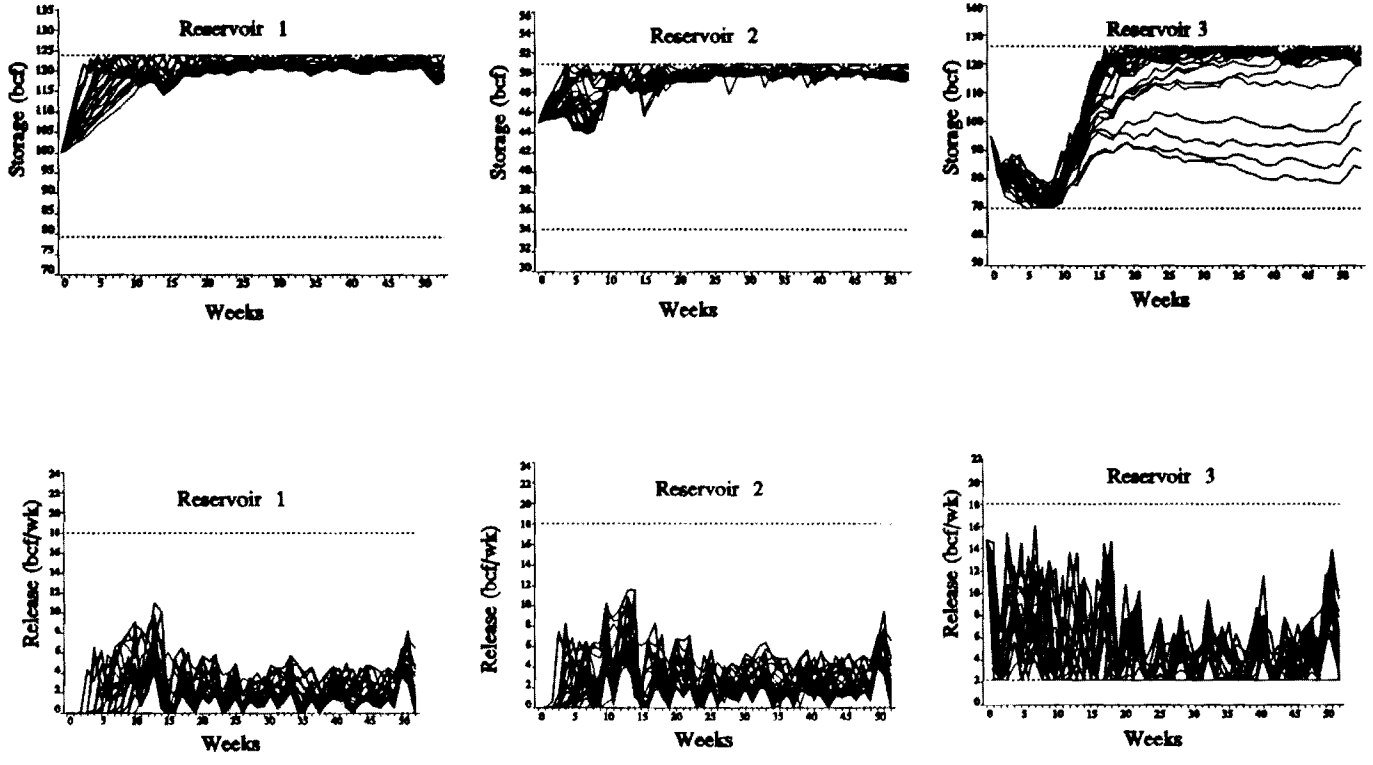

Figure 3.3: Simulation with low release selection.

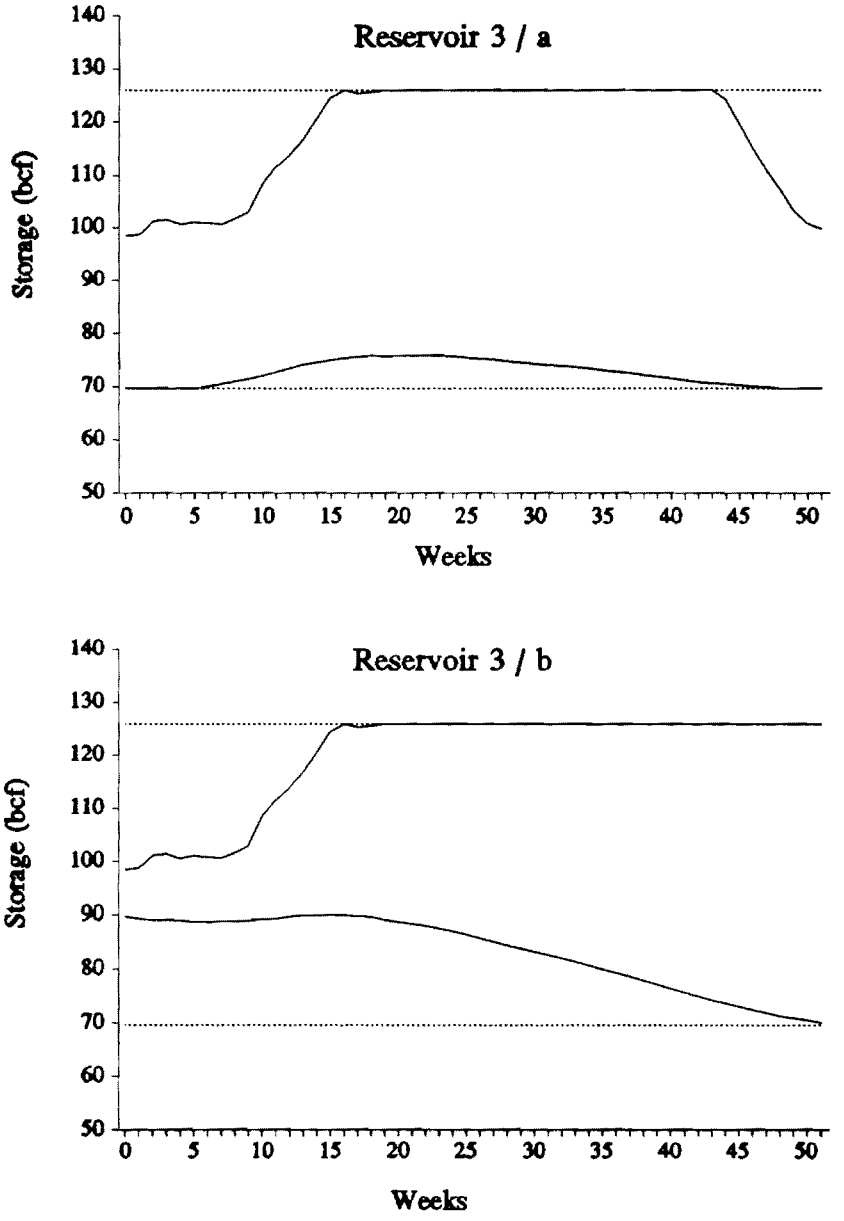

Figure 3.4: Reduced state sets for draft levels: (a) 1.39 billion cubic feet/week (3.93e10 L) and (b) 2.2 billion cubic feet/week (6.23e10 L)

the reduced state sets determine the regions where the storages ought to be located in any given week so that the system can continue its feasible operation independently of inflow realization. In an attempt to visualize these three dimensional sets, Figure 3.4a shows the projection of the minimum set distance on the storage of the 3rd reservoir (solid lines). The shapes for the other reservoirs are identical but contained within the respective bounds. The lower boundary of these regions reflects drought concerns, building up at the beginning of the dry season and easing off as time progresses. During the same period and with no fear of floods, the system can maintain high storages, while the rest of the time, it must make room for high inflows. By contrast, Figure 3.4b gives the same results when the lower bound for u_3 is 2.2 bcf/week. The figure shows how quickly the feasible region contracts as its lower boundary rises to guarantee a higher draft. Eventually the reduced set becomes empty and the procedure is unable to guarantee feasibility so far in advance. The length of the feasible horizon depends on the seasonal and relative variation of inflow, storage, and release constraints and is a measure of system reliability. In particular, if inflows are more predictable (smaller ranges), the reduced state and feasible control sets become larger (available operational options increase) and the system can be guaranteed to meet the operational requirements longer.

The reduced state sets extend the concept of the rule curves commonly used in reservoir operation. A rule curve suggests a target storage sequence that balances various system objectives in an acceptable manner. A reduced state set sequence guarantees that the system will simultaneously meet these objectives at all times. The advantage of thelatter approach is that it considers all system storages simultaneously and guarantees feasibility. A relative disadvantage is that the sets are expressed as a system of inequalities (e.g., Equation 3.2) that storages must satisfy in each period.

Clearly, the set control approach can be used in various reservoir operation and design issues. Three examples of practical interest would be to determine (**a**) the minimum and maximum release levels that can be met given an inflow pattern, (**b**) the maximum inflow range that can be controlled for a given output pattern, or (**c**) the system configuration (reservoir capacities) guaranteeing that the desirable output levels will be met given an inflow pattern. With respect to a procedure for determining minimum and maximum release levels given an inflow range pattern, one would have to use trial an error and explore the tradeoff between release range and length of feasible control horizon. As shown before, a tighter release range implies a shorter feasible control horizon, and the system operator is faced with the dilemma to sustain high demands over a short guaranteed time period or meet lower demand levels longer. Thus, the suggested operational usage of the set control

approach is to quantify the previous tradeoff and let the decision making authority select the most desirable compromise.

A final comment refers to correlated inflows. The effect of inflow correlation (spatial or temporal) is to limit the cumulative inflow range with respect to that corresponding to the individual weekly ranges. Thus, ignoring inflow correlation may limit the length of the feasible control horizon. Both correlation types can be explicitly considered (spatial correlations simply affect the shape of the joint inflow set), but a complete discussion is delegated to a separate publication.

3.3 HYDROPOWER

Hydropower adds nonlinear elements to the reservoir management problem and raises more questions in reference to the set control approach. To include hydropower considerations, we modify the state equation as follows (*Georgakakos, 1992*):

$$\begin{bmatrix} S_1(k+1) \\ S_2(k+1) \\ S_3(k+1) \end{bmatrix} = \begin{bmatrix} 1 & 0 & 0 \\ 0 & 1 & 0 \\ 0 & 0 & 1 \end{bmatrix} \begin{bmatrix} S_1(k) \\ S_2(k) \\ S_3(k) \end{bmatrix} + \begin{bmatrix} -b_1(k) & 0 & 0 \\ b_1(k) & -b_2(k) & 0 \\ 0 & b_2(k) & -b_3(k) \end{bmatrix} \begin{bmatrix} t_1(k) \\ t_2(k) \\ t_3(k) \end{bmatrix} + \begin{bmatrix} 1 & 0 & 0 \\ 0 & 1 & 0 \\ 0 & 0 & 1 \end{bmatrix} \begin{bmatrix} w_1(k) \\ w_2(k) \\ w_3(k) \end{bmatrix}, \quad (3.4)$$

$$k = 0,1,\ldots,N-1,$$

where

$$b_i(k) = \sum_{j=1}^{n_i} u_{ij}(k), \quad i = 1,2,3, \quad (3.5)$$

with $u_{ij}(k)$ being the discharge rate from the j^{th} turbine of the i^{th} reservoir, $t_i(k)$ the generation hours during period k, and n_i the number of turbines at reservoir i.

Turbine discharge depends (nonlinearly) on reservoir storage and power output and complicates the solution process since the matrix multiplying the control vector [t(k)] is now a function of the state. Products of set quantities cannot be explicitly handled in the framework suggested earlier, but one can usually overcome this predicament by following a well-established engineering rule: [*Schweppe, 1973*] "When faced with a nonlinear problem, linearize." In this context, this would imply that coefficients $b_i(k)$ be computed for a particular storage and power level and treated as constants at each time period k. The same approach is usually employed in stochastic control

problems with the linearization performed around the most likely state sequence. The difficulty in this case is that a single most likely sequence does not exist; all sequences with vectors from the reduced state sets are equally likely. Thus, linearization introduces approximations and invalidates the one-time solution approach adopted in the previous section. Instead, a sequential scheme where an N-period set control problem is solved at each decision time has distinct advantages.

In a sequential scheme, linearization can be performed around the initial state vector, which is expected to stay representative for some time. Eventually, the state will digress from the locale of the initial vector and will render the process approximate. However, the error is mitigated by the sequential mode of operation where decisions are always selected from the initial control set $\Omega_c(0)$. However, in some cases the procedure may become infeasible, even though the reduced and modified state sets are nonempty.

The above formulation can also reflect release constraints by specifying lower and upper bounds for the control vector $\mathbf{t}(k)$ such that the products $[b_i(k)\ t_i(k)]$ are within the allowable range. Constraints on energy generation can also be included: Let $P_i(k)$, represent the cumulative power output from all turbines at hydroelectric facility i and time period k. Then, the requirement that energy generation satisfy a minimum commitment $E^{min}(k)$ can be enforced as follows:

$$P_1(k)\,t_1(k) + P_2(k)\,t_2(k) + P_3(k)\,t_3(k) \geq E^{min}(k)\,. \qquad (3.6)$$

This inequality simply defines another bounding hyperplane for the control set $\Omega_u(k)$ and can easily be handled by the set control approach. Thus, the proposed formulation may be used to derive control policies (energy generation schedules) guaranteed to meet a dependable energy sequence, in addition to storage and release constraints.

To gain some insight with the above formulation, we run simulation experiments. The problem is solved with a control horizon of 10 weeks, sequentially at each week of a 10-year simulation horizon. The output of each plant equals its nominal power capacity, 430 MW for Reservoir 1, 375 MW for Reservoir 2, and 350 MW for Reservoir 3. Figure 3.5 shows the dependence of total turbine discharge on reservoir storage at these power levels. The curves take into account tailrace effects and are based on the power-(net hydraulic head)-discharge relationships reported by *Georgakakos [1991, Appendix A]*. The Ω_s and Ω_w sets are as in the previous section. The control set Ω_t reflects the restriction that generation hours be in the (0 to 168)-hour range per week, total system energy exceed a dependable energy commitment

(Eq. 3.6), and weekly average outflow of the third reservoir be greater than 1.4 billion cubic feet. The last requirement is enforced as follows: At the beginning of each week, the discharge, $Q_3(k)$, from Reservoir 3 is determined based on its initial storage and Figure 3.5. Then, the generation hours for Reservoir 3 are constrained by

$$t_3(k) \geq t_3^{\min}(k) = \frac{1.4 \cdot 10^9}{60 \cdot 60 \cdot Q_3(k)}, \quad \text{all } k, \tag{3.7}$$

where $Q_3(k)$ is expressed in cubic feet per second and $t_3^{\min}(k)$ in hours. It is noted that $P_1(k)$, $P_2(k)$, and $P_3(k)$ are herein arbitrarily set equal to nominal plant capacities. Alternatively, they may reflect contracted power outputs necessitating turbine overload or underload conditions. Furthermore, one may determine the power output of each turbine so as to meet the power contracts and additionally maximize plant efficiency [*Georgakakos, 1992*].

Figure 3.6 displays the results from 10 such simulations. Storage and generation sequences are only shown for Reservoir 3. Those of the other two reservoirs are qualitatively similar. Total system energy generation is plotted on the third graph along with the dependable energy requirement (thicker line). Storage stays within the specified bounds and the generation hours are such that the minimum weekly outflow of 1.4 billion cubic feet is always met. Turbine outflow usually suffices to maintain storage within the desirable bounds; however, on four occasions spillways are also activated (generation greater than 168 hours). System energy generation always satisfies the dependable energy commitment. This commitment may be increased but with no guarantee that it will then be met.

For example, the first graph in Figure 3.7 displays the energy generation results for another 10-year simulation series where dependable energy requirements are increased by 25%. The system state and control variables stay within the desirable limits, but energy generation occasionally fails to meet the respective targets. The simulation program is such that when the control algorithm identifies infeasibility (empty reduced and modified state sets), it reduces the dependable energy requirements by a certain percentage and repeats the computations until the problem becomes feasible. The worst violation requires that energy commitment be decreased by 40%.

To explore the effect of the control horizon, we repeated the above simulation series with a control horizon of 20 weeks. The results shown on the second graph in Figure 3.7 indicate that violations of lesser magnitude occur more frequently (the worst

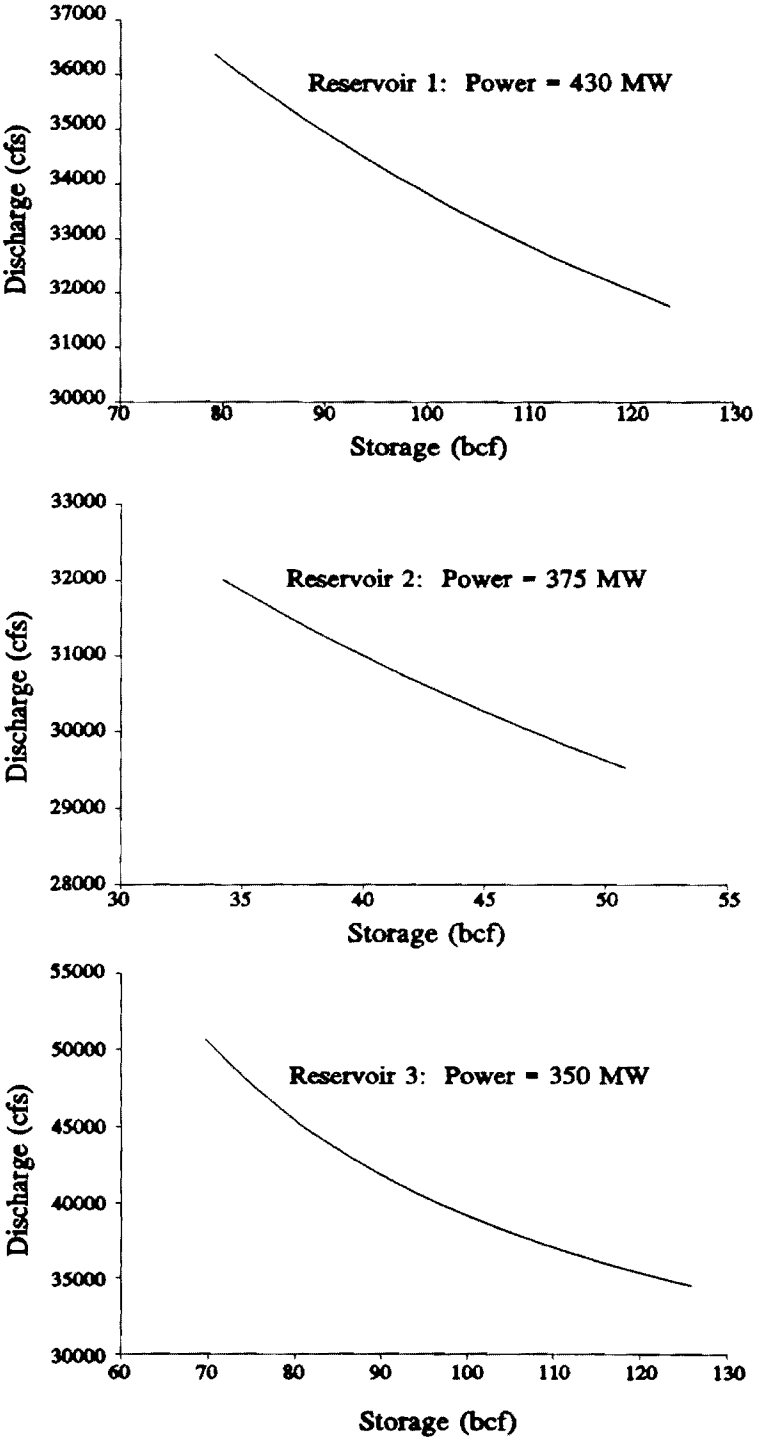

Figure 3.5: Turbine Discharge versus Storage

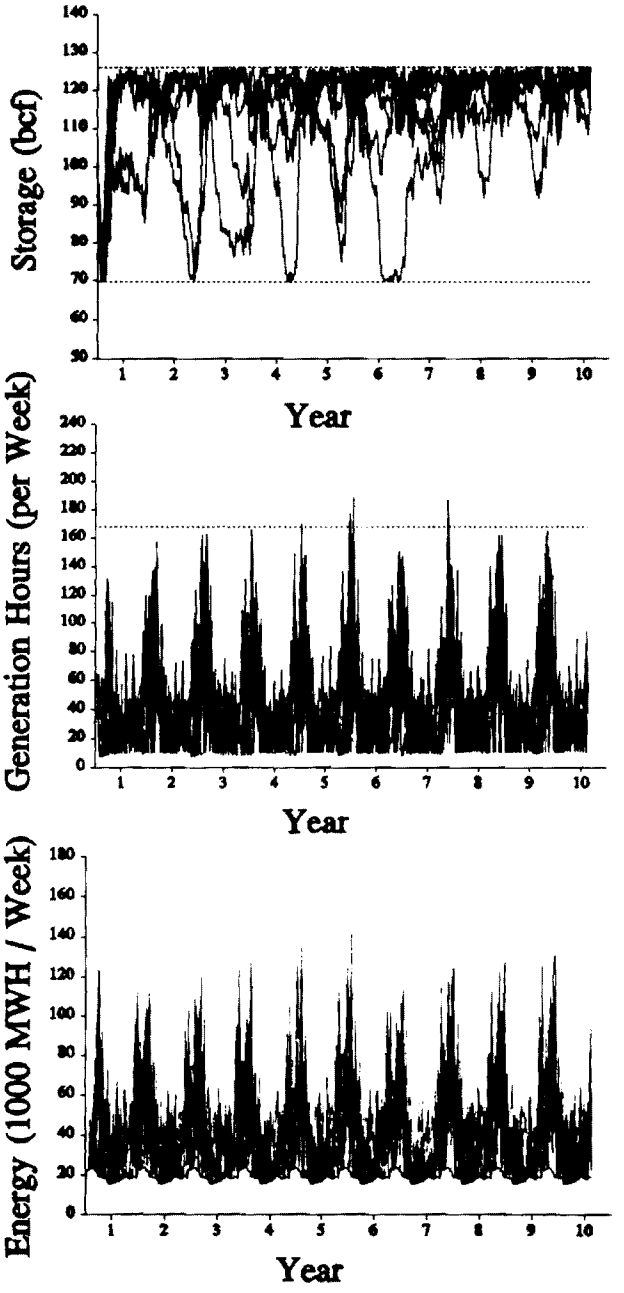

Figure 3.6: Simulation experiments

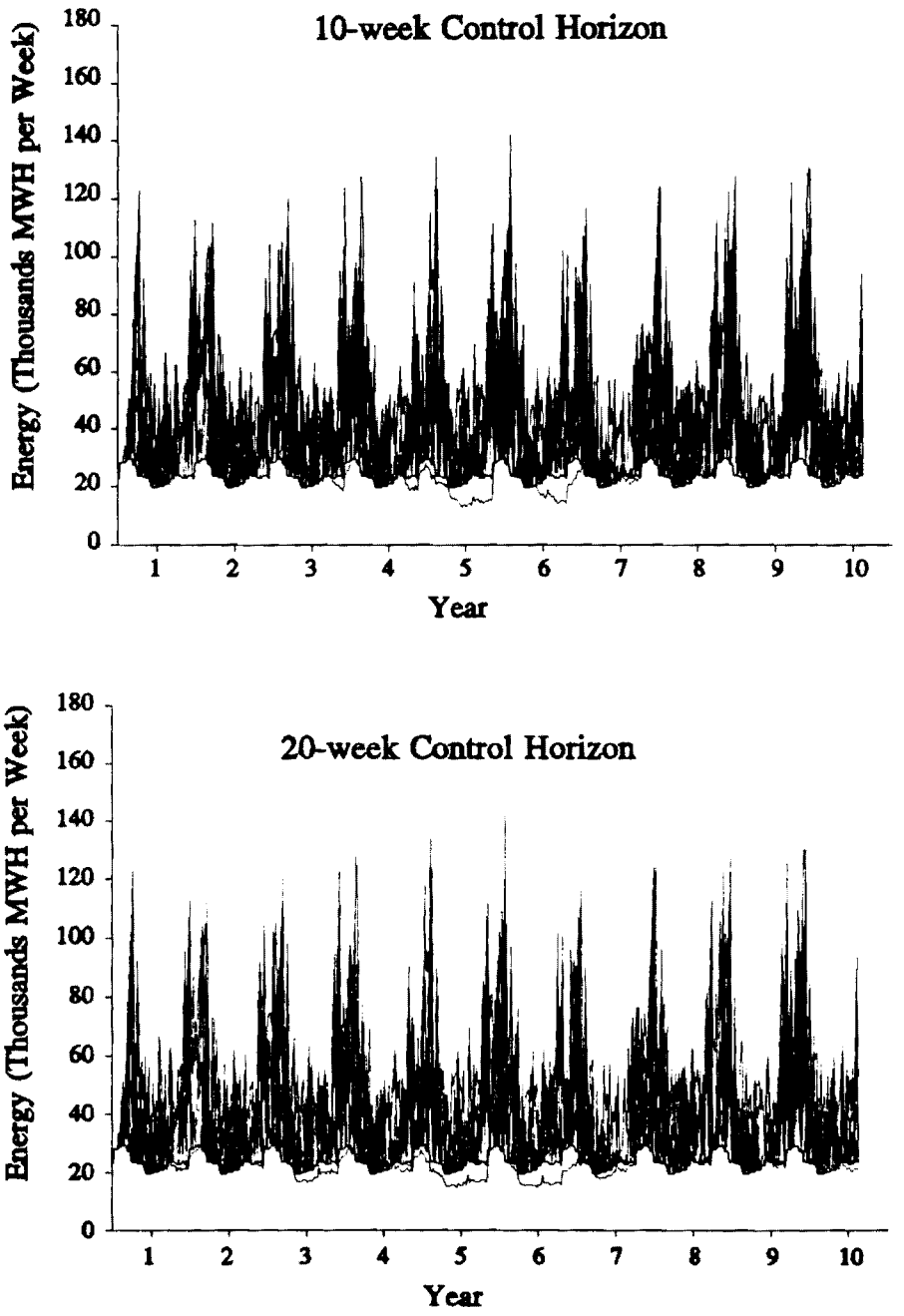

Figure 3.7: Simulation with higher energy commitments and different control horizons.

violation requires 30% reduction of the original target). This happens because the control algorithm anticipates potential infeasibilities further in advance and begins to reduce energy generation early on. When the worst violation actually arrives, it is not as serious as in the 10-week control horizon case.

3.4 ENERGY VALUE

As the power industry moves toward an open market system, hydropower operation focuses on the value of energy. To address some of the related issues, the system model of the previous section can be expanded to include an additional state variable:

$$V(k+1) = V(k) + \lambda(k)\,[P_1(k)\,t_1(k) + P_2(k)\,t_2(k) + P_3(k)\,t_3(k)]\,, \quad V(0) = 0\,, \qquad k = 0,1,\ldots,N-1, \tag{3.8}$$

where V(k) is the cumulative value of energy up to time k, and $\lambda(k)$ is the value of energy at period k, reflecting the avoided cost of alternative energy sources. The power outputs $P_1(k)$, $P_2(k)$ and $P_3(k)$ are fixed as in the previous section, and $t_1(k)$, $t_2(k)$, and $t_3(k)$ are the control variables representing generation hours. A problem of interest would be to develop operational policies that meet the constraints described in the previous section and in addition guarantee that the energy value at time N exceeds a minimum threshold V^{min}:

$$V(N) \geq V^{min}\,. \tag{3.9}$$

As seen by the new system state equation,

$$\begin{bmatrix} S_1(k+1) \\ S_2(k+1) \\ S_3(k+1) \\ V(k+1) \end{bmatrix} = \begin{bmatrix} 1 & 0 & 0 & 0 \\ 0 & 1 & 0 & 0 \\ 0 & 0 & 1 & 0 \\ 0 & 0 & 0 & 1 \end{bmatrix} \begin{bmatrix} S_1(k) \\ S_2(k) \\ S_3(k) \\ V(k) \end{bmatrix} + \begin{bmatrix} -b_1(k) & 0 & 0 \\ b_1(k) & -b_2(k) & 0 \\ 0 & b_2(k) & -b_3(k) \\ \lambda(k)\,P_1(k) & \lambda(k)\,P_2(k) & \lambda(k)\,P_3(k) \end{bmatrix} \begin{bmatrix} t_1(k) \\ t_2(k) \\ t_3(k) \end{bmatrix}$$

$$+ \begin{bmatrix} 1 & 0 & 0 \\ 0 & 1 & 0 \\ 0 & 0 & 1 \end{bmatrix} \begin{bmatrix} w_1(k) \\ w_2(k) \\ w_3(k) \end{bmatrix}, \tag{3.10}$$

$$= \boldsymbol{A}\,\boldsymbol{S}(k) + \boldsymbol{B}(k)\,\boldsymbol{t}(k) + \boldsymbol{G}\,\boldsymbol{w}(k),$$

$$k = 0,1,\ldots,N-1,$$

this problem has more state than control variables and is not directly amenable to the set control approach presented earlier. The problem is that the derivation of the reduced state sets, (lemma (2.17) in Section 2.2) requires that the coefficient matrix **B**(k) is invertible. To overcome this limitation, we can enforce invertibility by including an additional column and a fourth control variable, $t_4(k)$:

$$\boldsymbol{B}(k)\,\boldsymbol{t}(k) = \begin{bmatrix} -b_1(k) & 0 & 0 & 0 \\ b_1(k) & -b_2(k) & 0 & 0 \\ 0 & b_2(k) & -b_3(k) & 0 \\ \lambda(k)\,P_1(k) & \lambda(k)\,P_2(k) & \lambda(k)\,P_3(k) & -1 \end{bmatrix} \begin{bmatrix} t_1(k) \\ t_2(k) \\ t_3(k) \\ t_4(k) \end{bmatrix}. \tag{3.11}$$

The new column vector can have any form as long as it makes **B**(k) invertible. However, the new control variable should have an empty feasible range:

$$0 \le t_4(k) \le 0, \quad k = 0,1,\ldots,N-1. \tag{3.12}$$

The above modification does not alter the character of the original system. (The proof that the two equations essentially describe the same system is trivial.) It only facilitates the application of the set derivation procedures discussed earlier.

In summary, the set control problem amounts to finding feasible control policies for

the system (3.10), (3.11), and (3.5) such that all storage variables remain feasible (see Table 3.1) subject to constraints (3.6), (3.7), (3.9), and (3.12). The λ-values assumed for this computational experiment are shown below and are roughly indicative of the energy generation cost ($/MWH, weekly average) in the southeastern U.S.:

$$\lambda(k) = \begin{cases} 19, & \text{if } 1 \le k \le 13 \\ 24, & \text{if } 14 \le k \le 26 \\ 31, & \text{if } 27 \le k \le 39 \\ 19, & \text{if } 40 \le k \le 52 \end{cases} \qquad (3.13)$$

Annual energy generation is to always exceed 27.3 million dollars ($=V^{min}$), and the dependable energy sequence is 60% of the one reported previously. To determine the system potential to operate under these constraints, we performed the following computational experiment: First, the control model was run with a 52-week planning horizon to determine the reduced state sets. To simplify the procedure, the linearization of the **B**(k) matrices was performed around the initial storage values for all k. Then, the system operation was simulated over 50 weekly sequences of one year duration. Figure 3.8 includes some results related to energy generation. The first graph depicts the value of annual energy from each simulation and shows that it is always greater than the specified minimum. In fact, for V^{min} greater than this value, the control problem becomes infeasible. One can reduce the planning horizon to achieve feasibility but forgo the 52-week operational guarantee. The second graph portrays the energy generation sequences for which the annual energy value is almost equal to V^{min}. Actual energy generation always meets the specified dependable sequence. Storage and generation hour sequences are also feasible but are not shown.

The formulation of this section may also be used to control the system such that annual energy amounts and outflow volumes exceed certain levels. The first case can be analyzed by the same formulation after λ is omitted. The second would require that Equation (3.8) be replaced with one describing the cumulative outflow volume.

3.5 COMPUTATIONAL REQUIREMENTS

As an indication of computational requirements, we report the computer time necessary for three experimental runs. The experiments differ by the number of state variables and the length of the control horizon. All runs were performed on a 486/33 personal computer.

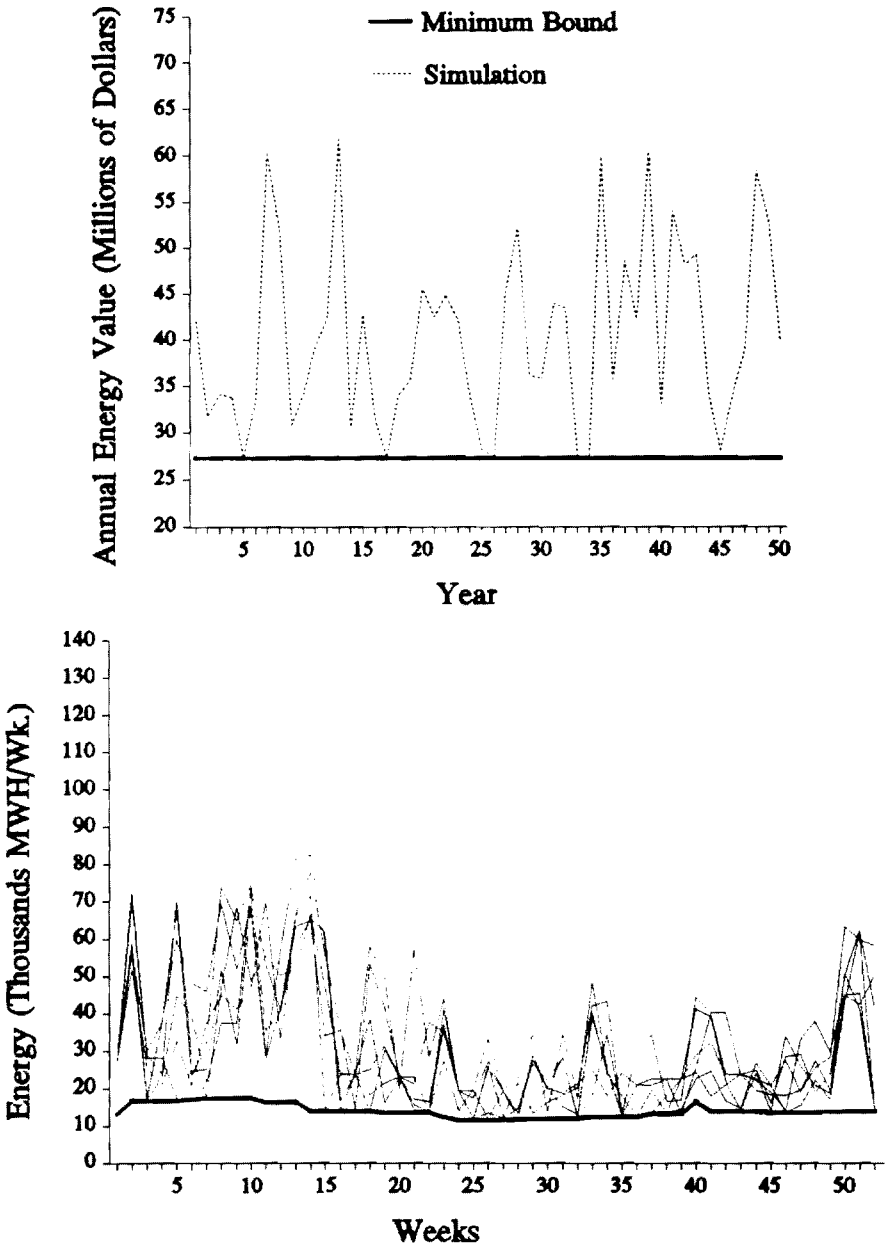

Figure 3.8 : Energy value simulations.

Table 3.2: Computer Time Requirements for Different Set Control Problems

Experiments	System Model Features	486/33 CPU Time (seconds)
I	State Variables: 3 Control Horizon: 52 weeks	29
II	State Variables: 3 Control Horizon: 260 weeks	128
III	State Variables: 4 Control Horizon: 52 weeks	75

A comparison of Experiments I and II, shows that computational requirements increase almost linearly with the length of the control horizon. Experiments I and III indicate that including a fourth state variable more than doubles computer time. Thus, system model size affects computational time more adversely than the length of the control horizon. However, the requirements are generally quite small, and the set control approach can practically handle large systems (including as many as 10 reservoirs) with a reasonable computational effort (70 to 80 minutes). All previous runs were performed under DOS and required less than 640 Kilo-Bytes of random access memory.

3.6 Value of Streamflow Forecasts

Reservoir control schemes with inflow forecasting capabilities are expected to improve flood prevention as well as other reservoir system functions. However, a question often raised is whether the benefits from such systems outweigh their costs. The purpose of this section is to provide a partial answer to this question by demonstrating that reservoir control and inflow forecasting procedures can substantially mitigate flood damage frequency and magnitude. The approach taken is to quantify the improvements for the Savannah reservoir system. While to some extent the actual benefits are expected to be system-specific, some general conclusions can still be drawn.

For the purposes of this section, the time dscretization is one day, and the system is modelled by the following water balance state equation:

$$\begin{bmatrix} S_1(k+1) \\ S_2(k+1) \\ S_3(k+1) \end{bmatrix} = \begin{bmatrix} 1 & 0 & 0 \\ 0 & 1 & 0 \\ 0 & 0 & 1 \end{bmatrix} \begin{bmatrix} S_1(k) \\ S_2(k) \\ S_3(k) \end{bmatrix} + \begin{bmatrix} -b_1(k) & 0 & 0 \\ b_1(k) & -b_2(k) & 0 \\ 0 & b_2(k) & -b_3(k) \end{bmatrix} \begin{bmatrix} t_1(k) \\ t_2(k) \\ t_3(k) \end{bmatrix} + \begin{bmatrix} 1 & 0 & 0 \\ 0 & 1 & 0 \\ 0 & 0 & 1 \end{bmatrix} \begin{bmatrix} w_1(k) \\ w_2(k) \\ w_3(k) \end{bmatrix}, \quad (3.14)$$

$$k = 0,1,\ldots,N-1,$$

$$b_i(k) = \sum_{j=1}^{n_i} u_{ij}(k), \quad i = 1,2,3, \quad (3.15)$$

where as before, $S_i(k)$ and $w_i(k)$ respectively represent storage and inflow volumes for reservoir i = 1,2,3, $u_{ij}(k)$ is the discharge from the j^{th} turbine of the i^{th} reservoir, $t_i(k)$ represents the generation hours during period k, and n_i is the number of turbines at reservoir i. Table 3.3 reports relevant reservoir characteristics including permissible storage and release ranges reflecting water conservation and flood control objectives, and Figure 3.9 depicts extreme daily inflow volume ranges. These ranges represent the lowest and highest inflow values on record (10 years). The dependence of total turbine discharge on reservoir storage at power capacity was shown earlier on Figure 3.5.

Table 3.3: Reservoir Characteristics

	Reservoir 1	**Reservoir 2**	**Reservoir 3**
Min. Storage (bcf)	79.25	34.2	69.71
Max. Storage (bcf)	123.8	50.8	125.95
Min. Release (bcf / day)	0.0	0.0	0.0
Max. Release (bcf / day)	3.0	3.0	3.0
Power Capacity (MW)	430	375	350
Number of Turbines	5	4	7

The purpose of this section is to illustrate the potential benefits of combined inflow forecast - reservoir control schemes. Our approach is to simulate and assess the performance of the Savannah reservoir system over a 10-year period (1972-1981) under the guidance of the Set Control Approach and various inflow forecasting schemes. Inflow forecasts are assumed to restrict the historical inflow ranges (Figure 3.9) as follows: The actually observed inflow sequence over the duration of the

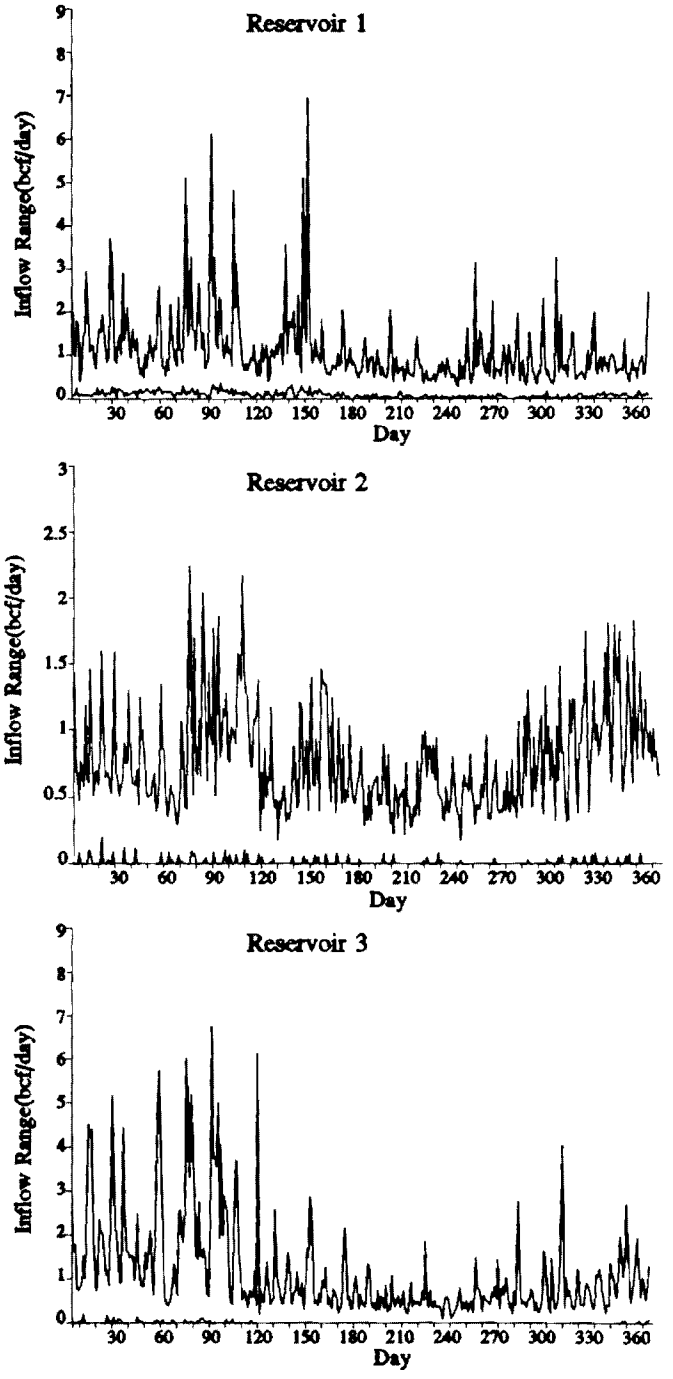

Figure 3.9: Daily inflow bounds

control horizon is first determined along with the corresponding historical ranges from Figure 3.9. The range used in the model for each day is centered around the actually observed value and represents a certain percentage of the historical range. As illustrated on Figure 3.10, these percentages gradually increase from the first to the last day of the control horizon to reflect that forecast quality deteriorates with lead time. The percentages are determined based on the following equation:

$$p(k) = p(1)\,[1.03]^{k-1}, \tag{3.16}$$

where p(k) denotes the percentage of day k. In the computational experiments to follow, this procedure is employed with $p(1)=0.5$ and $p(1)=0.25$. The results are compared with the case where SCA simply uses the historical inflow ranges from Figure 3.9 (no forecasting).

The simulation process is as follows: At each day of the simulation horizon, the forecasting model is first activated to determine the inflow ranges over the control horizon, and then the Set Control Approach is employed to generate the feasible control action set. This set includes all possible decisions guaranteeing that the system variables (storage, generation hours, and releases) will observe the stated constraints over the duration of the control horizon. Next, a decision is selected and the system operation is simulated for one time period. The simulation involves the determination of the next day's storages from Equation 3.14 with $w_i(k)$, $i = 1,2,3$, being equal to their historically observed values. This process is repeated sequentially at each day of a 10-year simulation horizon, and system performance is recorded in terms of energy generation, outflow rates, and reservoir storage levels.

Some features common to all experiments are that the Set Control Approach is implemented with a control horizon of 15 days, the decisions selected correspond to the minimum feasible generation hours, the feasible storage range is restricted to the conservation pools, and the determination of turbine discharge over the 15-day control horizon is based on the current storage values. Experiments with a longer control horizon (30 days) were also conducted, but the results are similar to the ones presented herein. The rational for using the most conservative feasible decision is to conserve water and maintain reservoir pools as high as possible. Turbine discharges are determined based on the current storage because it is the best guess of future storage values. Certainly, the storage will eventually digress from this locale. However, the error is mitigated by the sequential mode of operation forcing continuous updating.

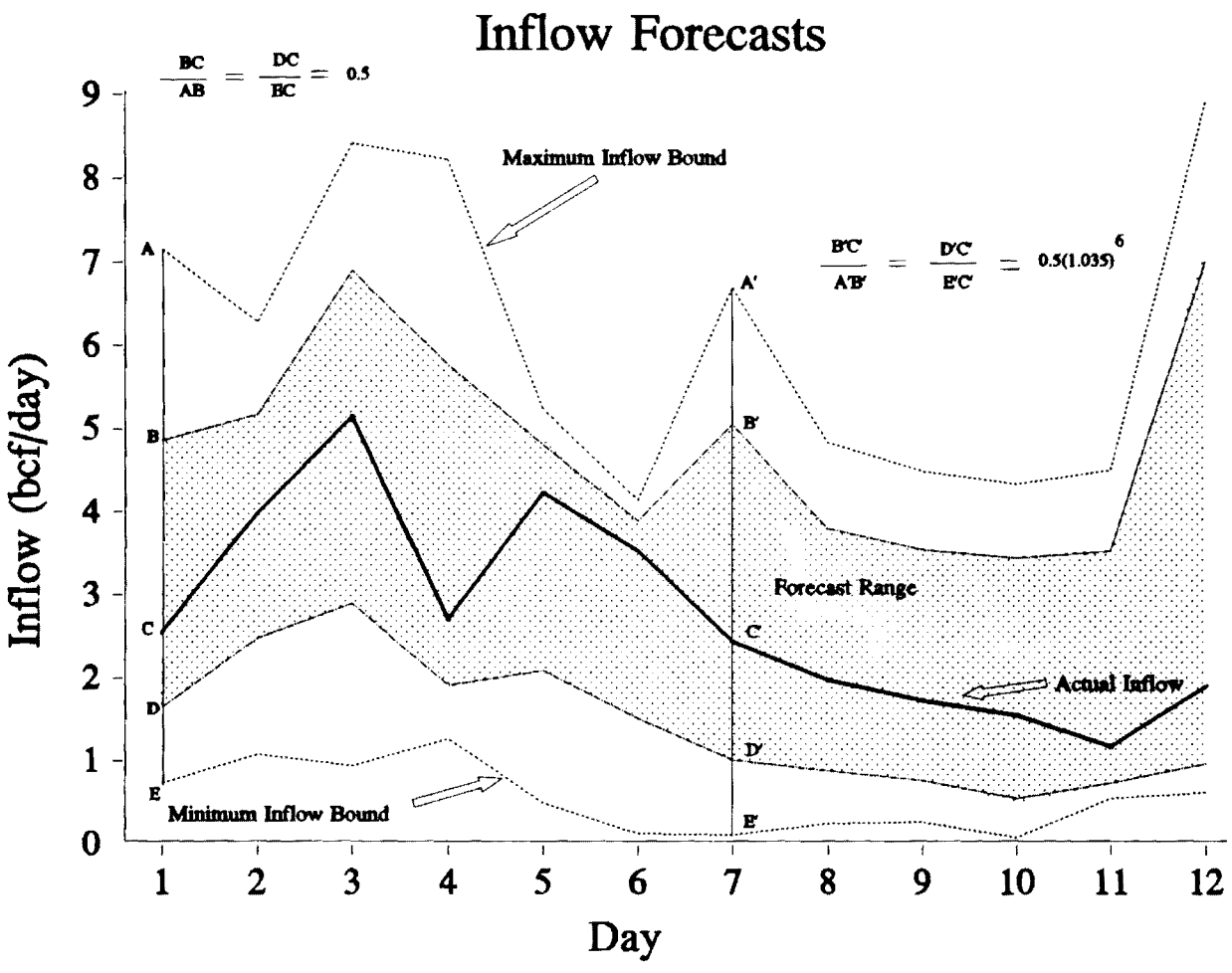

Figure 3.10: Inflow Forecasting Example

Figures 3.11 and 3.12 depict the results for the case where no inflow forecasts are used (base case). The graphs in Figure 3.11 include the storage bounds (dotted lines), the minimum and maximum simulation values for each day (thin solid lines), and the mean simulation storage sequence (thick solid line). The previous statistics were based on 10 simulation storage values for each day of the year. While system storages are maintained within the conservation pools, they tend to fluctuate markedly during the first part of the year (rainy season). Figure 3.12 includes the associated statistics for the control variables (generation hours per day), with dotted lines again representing bounds and solid lines depicting simulation statistics (minimum, maximum, and mean levels). The notable observation is that energy generation hours are often forced to exceed 24 hours per day in order to keep reservoir storages within the conservation pools. This simply implies that turbine conveyance capacity is not enough to control reservoir storage and water must also be released through the dam spillways. To be sure, the higher the exceedance of the 24-hour threshold, the more severe the flooding effects. More specifically, the highest release from the third reservoir in the cascade is about 3 times higher than the acceptable release bound. What is more, the mean generation sequence also violates the constraint threshold.

Figures 3.13 and 3.14 present the simulation results when the Set Control Approach has improved information of the upcoming inflows. This is simulated by using the procedure described previously (Eq. 3.16) with $p(1)=0.5$. The storage sequences (Figure 3.13) are again within the conservation zones, but the fluctuation ranges are now tighter. (The mean storage levels are clearly closer to the upper storage bounds.) The associated generation hours (Figure 3.14) on occasion exceed 24 hours / day, but the magnitude of the violation is much less than in the base case. Better forecasting allows the control model to mitigate flood damage. Nevertheless, the highest outflow is still 1.8 times higher than the acceptable release bound. This trend continues in the third case (Figures 3.15 and 3.16) where inflow forecasting is employed with $p(1)=0.25$. The mean storage sequences have moved even closer to the upper bounds, and the generation hours are for the most part contained within the admissible limits. The magnitude of constraint violations is reduced further, while the distance of the mean generation sequence from the 24-hour bounds indicates that violations occur infrequently.

The previous computational experiments demonstrate that inflow forecasting and reservoir control schemes can usefully assist reservoir operations during extreme hydrologic conditions. In particular, better inflow forecasting allows the control model to minimize flood control storage and, at the same time, avoid damage-causing outflows. While, the actual forecast quality cannot be quantified before the implementation of a forecast system, the potential reduction of flood damage

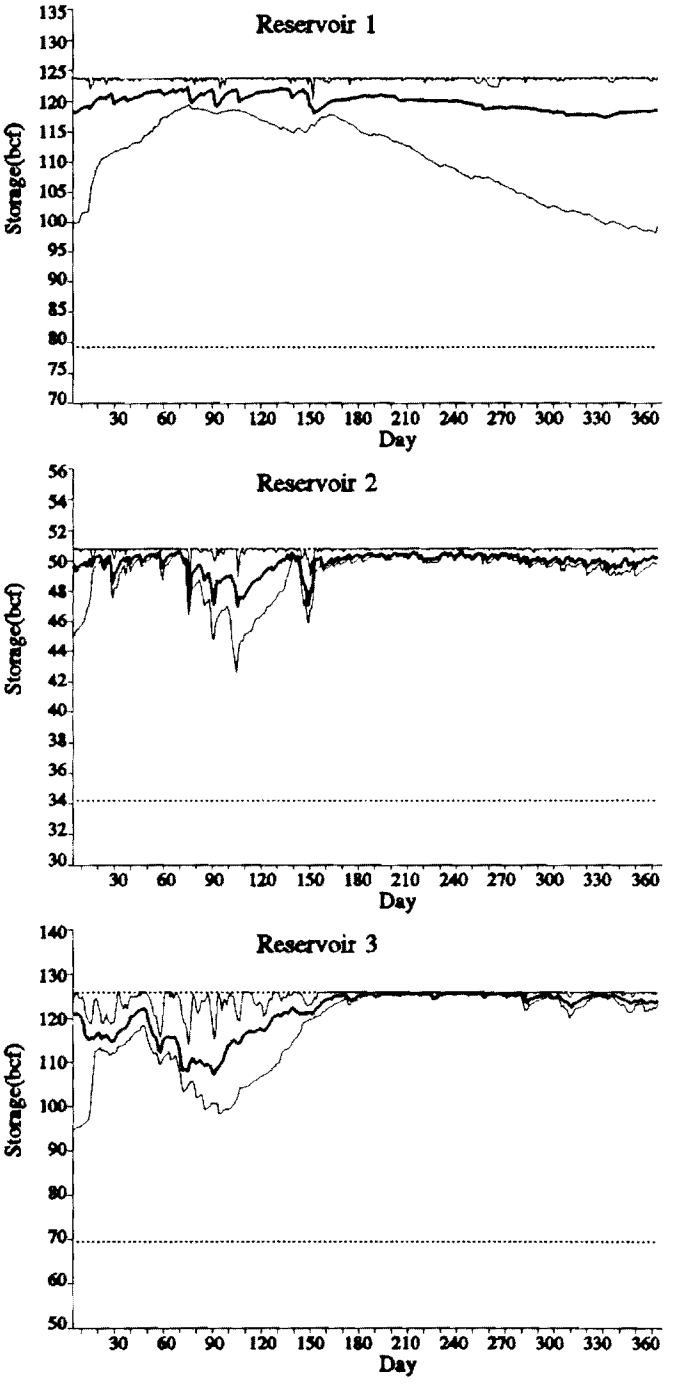

Figure 3.11: Simulation Storage; Base Case

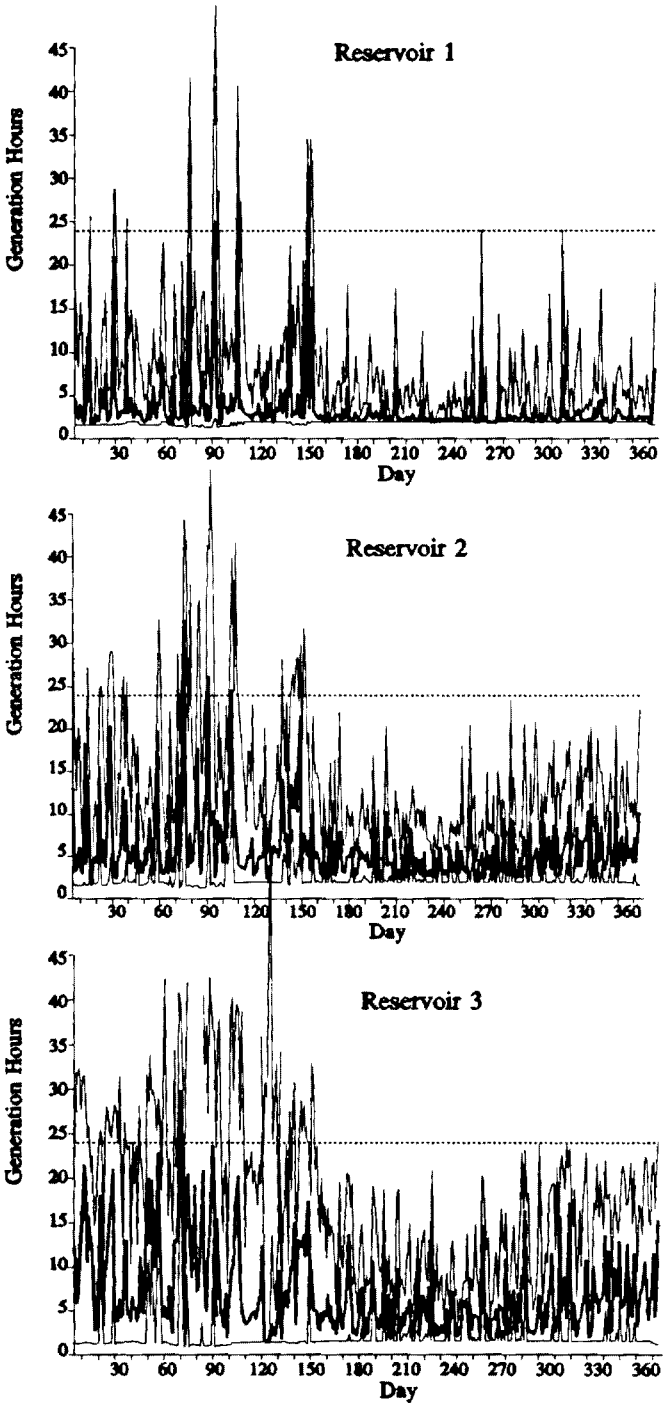

Figure 3.12: Simulation Gen. Hours; Base Case

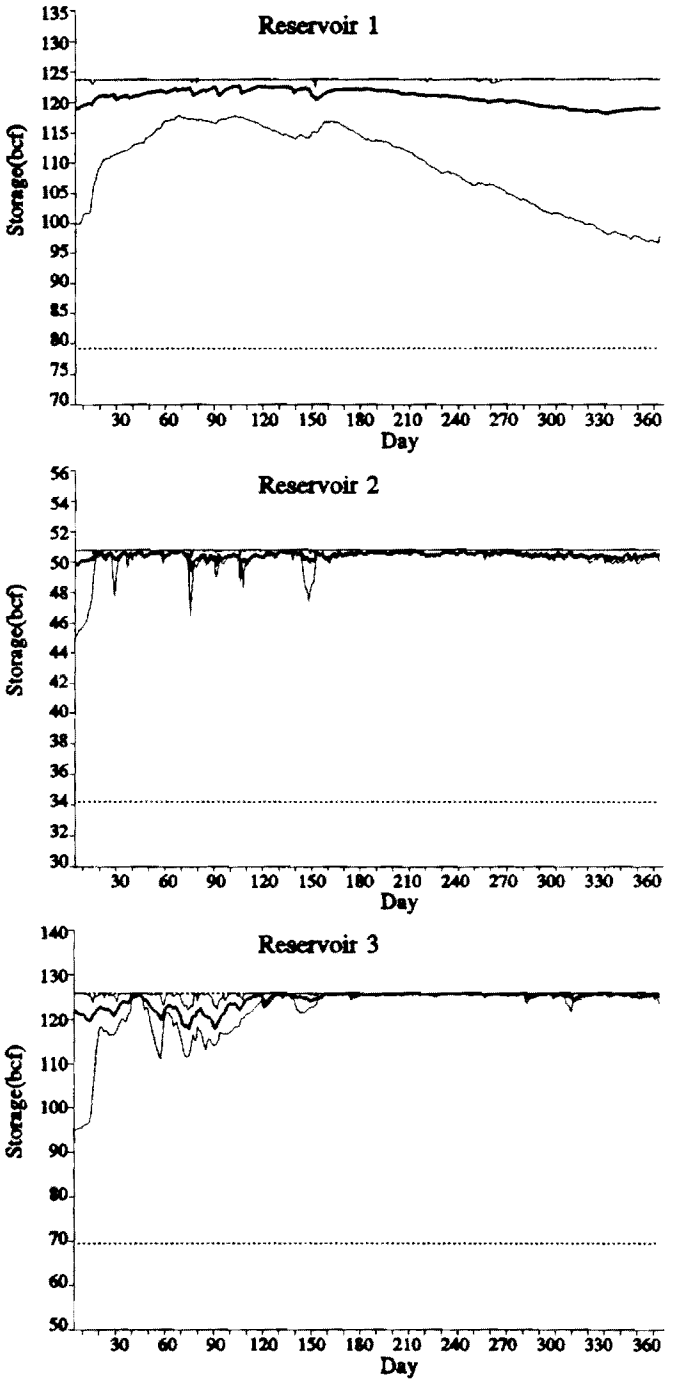

Figure 3.13: Simulation Storage; P(1)=0.5

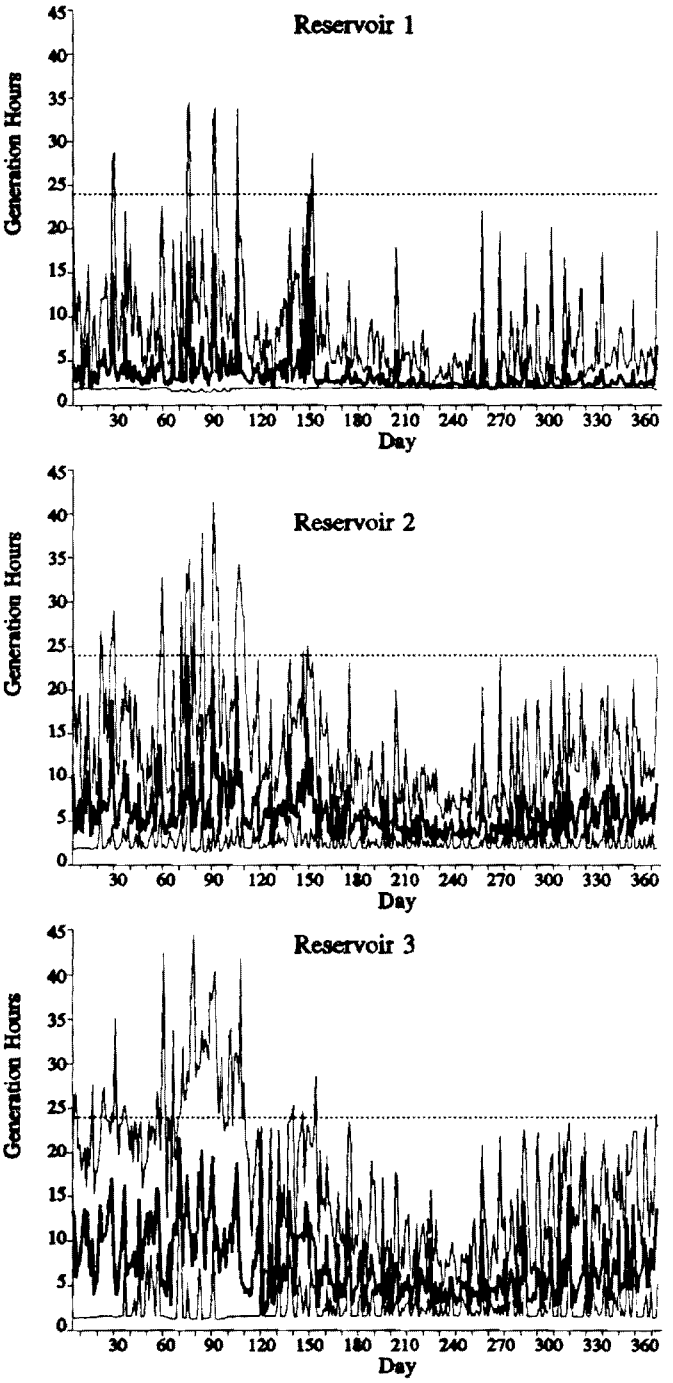

Figure 3.14: Simulation Gen. Hours;P(1)=0.5

frequency and magnitude can be substantial. In addition, benefits accrue from energy generation due to higher hydraulic head and less wasted spillage.

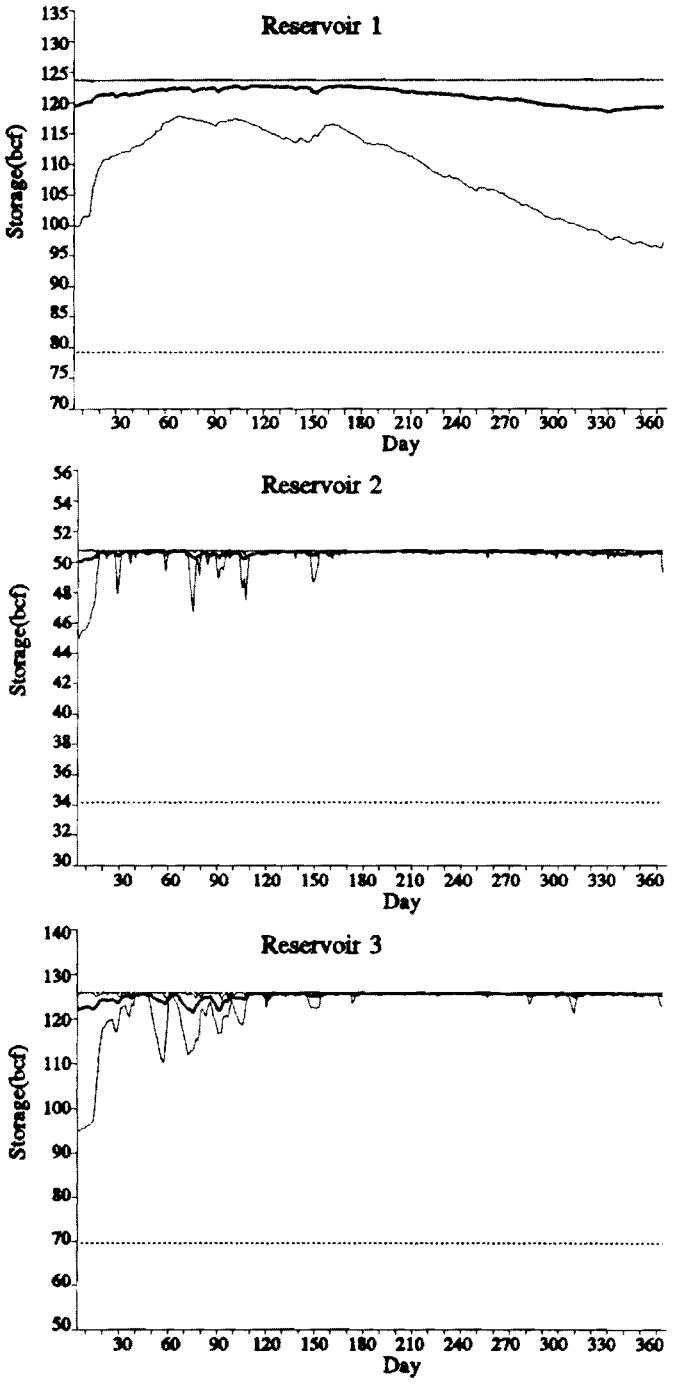

Figure 3.15: Simulation Storage; P(1) = 0.25

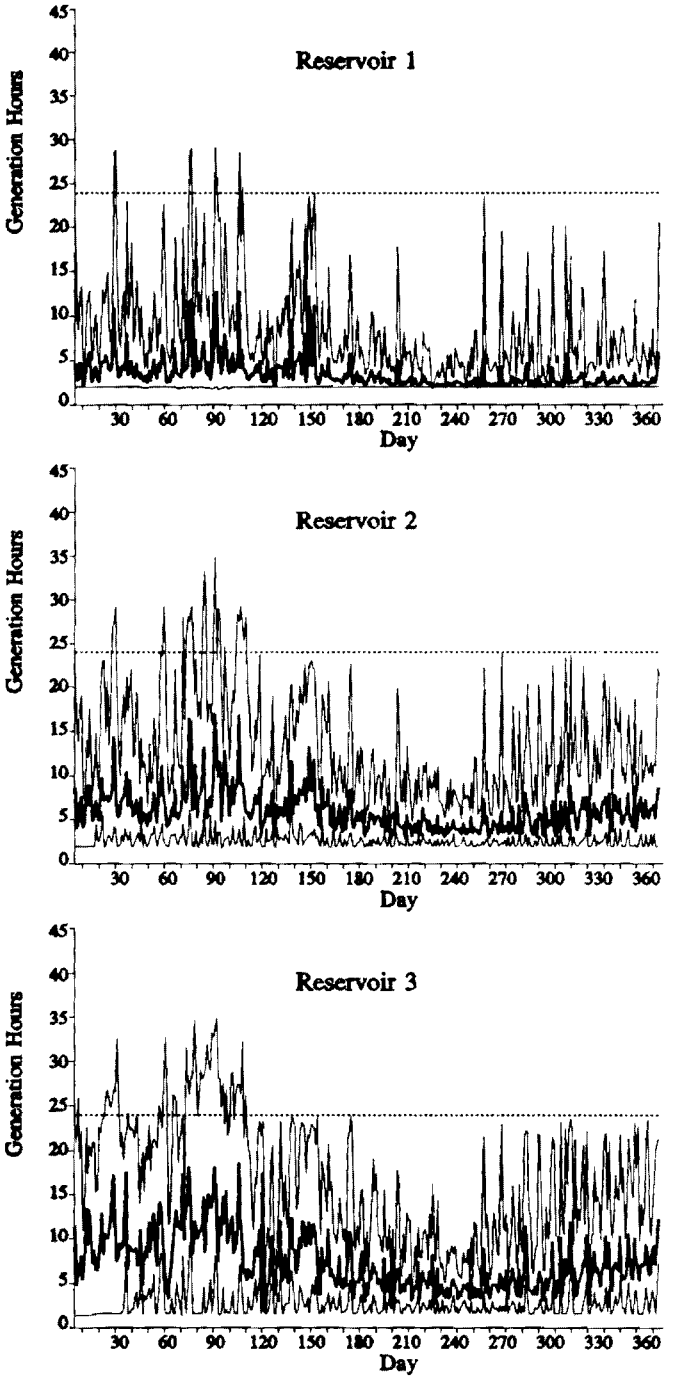

Figure 3.16: Simulation Gen. Hours; P(1) = 0.25

4. COMBINED RIVERFLOW FORECASTING AND RESERVOIR CONTROL – SENSITIVITY OF RESERVOIR SYSTEMS TO CLIMATE CHANGE

In this chapter we focus on two areas. The first is the integration of streamflow forecasting procedures with reservoir control methods, and the second is the sensitivity of reservoir system outputs to climate change. Our objectives are (1) to assess the value of combined forecast-control schemes and (2) to examine whether their use can mitigate the adverse effects of potential climate changes.

The approach we take is depicted on Figure 4.1. It consists of a physically-based streamflow forecasting model and a reservoir control scheme. The forecasting model has been developed by the University of Iowa research team and is described in detail in the companion report (Volume II). The reservoir control scheme is the Set Control Approach developed by the Georgia Tech research team and has been presented in the previous chapters. For continuity, we next include a short overview of the two models.

The streamflow forecasting model is a modified version of the Sacramento model [*Peck, 1976*]. It is a conceptual, spatially lumped parameter model which predicts channel inflow based on estimates of mean areal precipitation, pan evaporation, and temperature [*Georgakakos, 1986*]. The model distinguishes upper and lower soil moisture zones where water is temporarily stored on its way to the stream channel. Each zone stores water in two forms: either as "tension water" or as "free water." Tension water is bound to soil particles and can be depleted only by evapotranspiration (ET). Free water moves through the various zones and eventually appears in the channel. Depletion of the upper zone free water may occur horizontally as channel inflow (interflow), vertically as percolation to the lower zone, or as evapotranspiration. Lower zone free water storage is further subdivided into primary (which sustains channel inflow during long lasting dry weather) and a supplementary (which drains faster). The model also includes a frozen ground component to account for the reduced yield from groundwater storage during winter, and a snow accumulation and ablation model to account for spring snowmelt. Channel inflow is obtained as the sum of five flow components: (**a**) Direct Runoff, resulting from precipitation occurring over the impervious soil surface adjacent to the watershed streams; (**b**) Surface Runoff, resulting when the rainfall rate over the pervious soil surface exceeds the soil infiltration capacity; (**c**) Interflow, draining from the upper zone free water; (**d**) Primary Base Flow, draining from the lower zone primary free water; and (**e**) Supplementary Base Flow, draining from the lower zone supplementary free water. Total channel inflow is routed through the channel system of the watershed via a lumped parameter nonlinear routing scheme. Final model output is the outflow discharge at the watershed outlet.

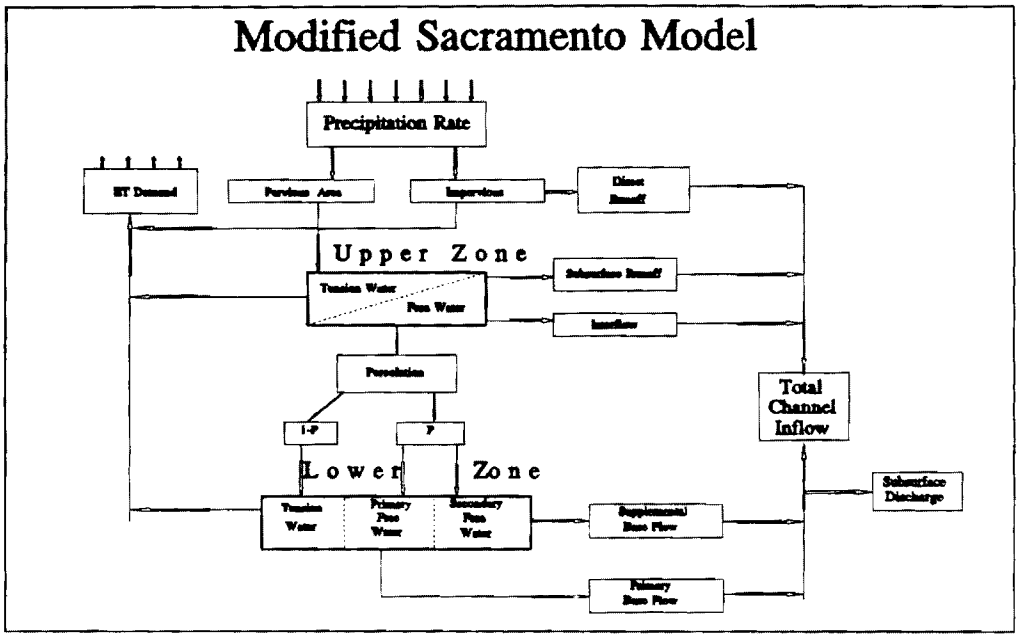

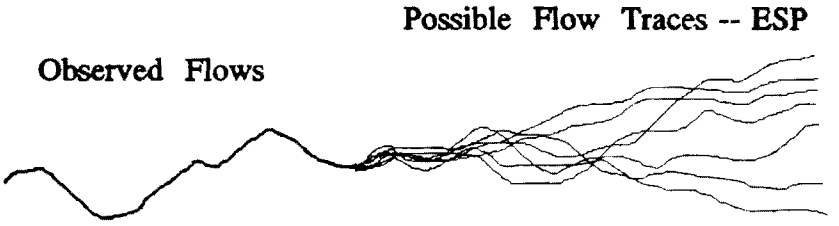

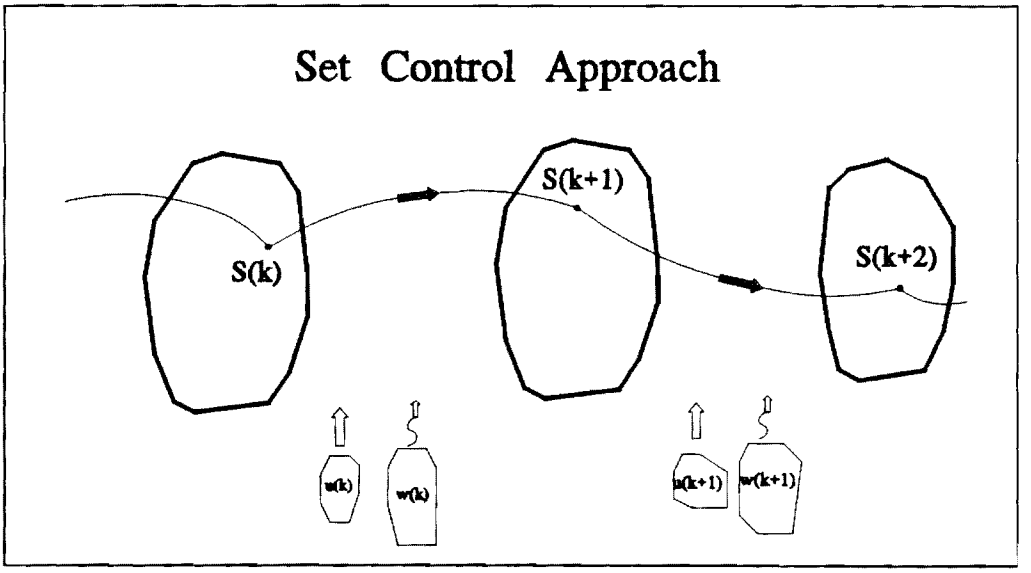

Figure 4.1: Combined Riverflow Forecasting and Reservoir Control

The modified Sacramento model is coupled with a Kalman Filter (state estimator) to utilize system observations up to the present time (streamflow measurements and snowpack thickness) and estimate key system variables (storage of the various surface and subsurface components) with minimal error. The basic concept of the state updating model is to linearize the model equations about the current variable estimates, propagate their uncertainty in time, and update their values when new observations become available. In practical terms, this mechanism enables one to quantify and minimize forecast uncertainty.

Herein, the modified Sacramento model is used to generate equally likely future inflow traces via a technique known as Extended Streamflow Prediction or ESP [*Day, 1985*]. ESP uses (**a**) current soil moisture, snowpack, and channel flow conditions and (**b**) historical data of mean areal precipitation, pan evaporation, and temperature corresponding to the calendar days of the forecast horizon, to generate possible inflow realizations. These realizations represent inflow sequences that would materialize if the historically observed input sequences were repeated again over the forecast horizon. The inflow traces tend to spread out as they "forget" the current watershed conditions and eventually fill up the historically observed inflow range. The ESP results are next used by the control model to define forecasted reservoir inflow ranges over the management horizon.

The control model is based on the Set Control Approach and aims at maintaining all system variables (storages, releases, and possibly other outputs) within acceptable sets. This approach was developed as an alternative to stochastic control methods with the motivation that during extreme hydrologic events (floods and droughts) or climate change circumstances, probabilistic inflow characterizations become unreliable due to the lack of adequate data records.

In the following section, the combined forecast-control procedure will be applied for the management of the Sailorville reservoir in the upper Des Moines river basin.

4.1 APPLICATION TO THE UPPER DES MOINES RIVER (MIDWEST)

4.1.1 The Upper Des Moines River Basin

The upper Des Moines river basin (Figure 4.2) has an area of 14,120 square kilometers (5,452 square miles), two thirds of which is in the state of Iowa and the rest in Minnesota. The river is controlled by Saylorville, a US Army Corps of Engineers reservoir located at the basin outlet. Saylorville has a usable storage of 0.7 billion cubic meters (567,906 acre-ft) and two primary purposes: (1) Provide flood protection for the city of Des Moines and surrounding areas and (2) augment the river low flows for water supply and water quality. In terms of reservoir release rates, these two purposes translate into the requirements shown on Figure 4.3. To avoid flood damage, from December 15 to April 15 maximum reservoir release should not exceed 16,000 cubic feet per second (cfs) , while the rest of the year (farming season) it should be less than 12,000 cfs. The importance of Sayloville's flood control objective cannot be overemphasized in light of the on-going devastating floods of the Mississippi river and its tributaries, one of which is the Des Moines river. (The juncture of the Des Moines with the Mississippi is at the tri-state border between the states of Iowa, Illinois, and Missouri.) The second graph in this figure shows the minimum releases for low flow augmentation. Water supply accounts for 200 cfs, and water quality for an additional, seasonally-varying amount ranging from 30 cfs in January to 110 cfs in July. Saylorville is operated by the Rock Island US Army Corps of Engineers District who also provided all hydrologic and operational data used in this report.

To assess the value of the forecast-control scheme and examine the sensitivity of the case study system to climate changes, we subdivided the historical inflow record into three periods (Figure 4.4). The first extends from 1925 to 1949 and has the warmest annual average temperature and the lowest average streamflow (1,596 cfs). The second (from 1949 to 1974) is cooler by 2° C with respect to the first but has a higher annual average streamflow (2,003 cfs) and markedly higher variability. The third period (from 1965 to 1988) is the coolest and wettest of all three (with an annual inflow mean of 2,686 cfs). Each period herein serves as a historical analogue of a potential climatic scenario and is a first approximation to climate changes of larger magnitude. For a detailed discussion of the hydrologic analysis leading to the selection of these periods, the reader is referred to the companion report (Volume II) by the University of Iowa research team.

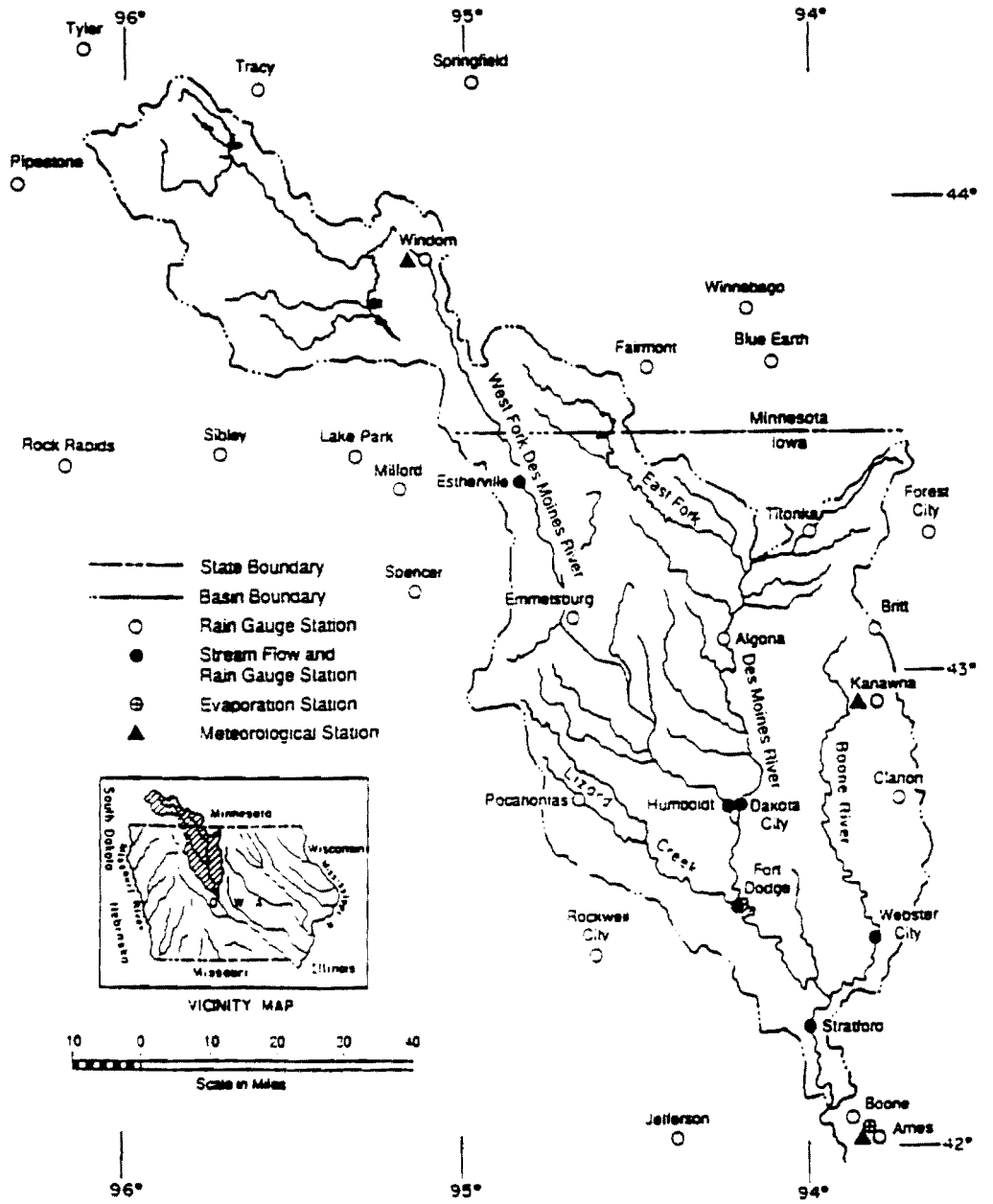

Figure 4.2: The Upper Des Moines River Basin

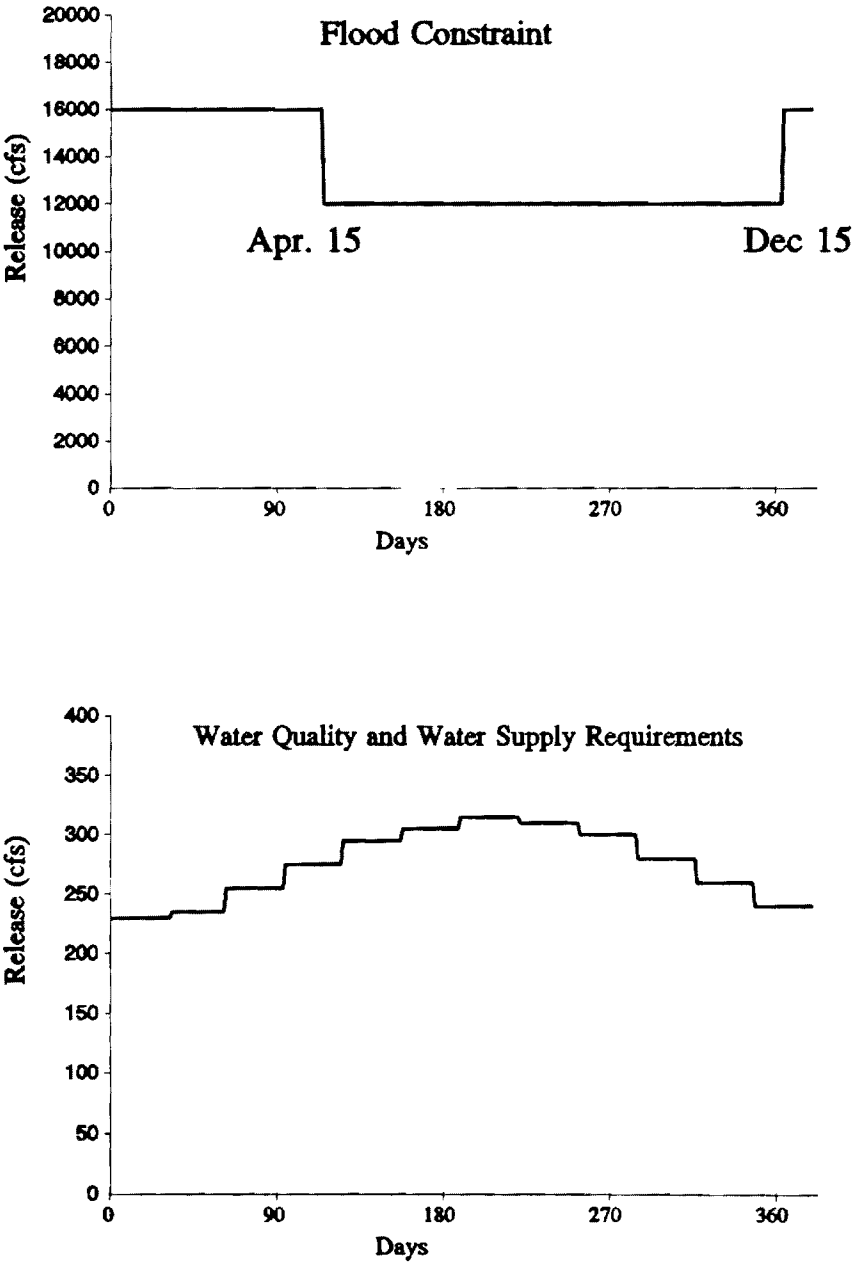

Figure 4.3 Release Requirements for Saylorville

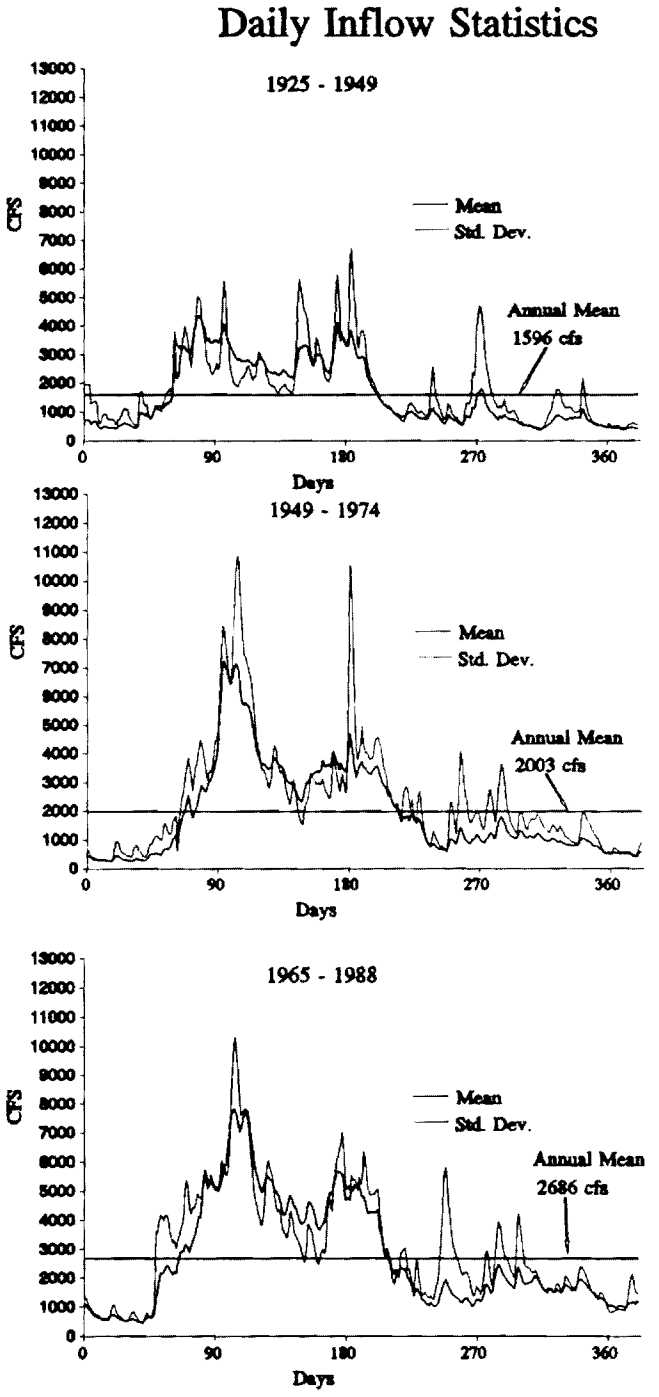

Figure 4.4 Historical Analogues of Potential Climatic Changes

4.1.2 Value of Forecast-Control Scheme -- Sensitivity to Climate Changes

In this section we present the results from several computational experiments intended to assess the performance of Saylorville under the guidance of three different management approaches. The first is a heuristic procedure presently used by the Corps of Engineers (COE), consisting of a simple forecasting scheme and a rule curve [U.S. Army Corps of Engineers, 1983]. The second is the Set Control Approach with knowledge only of the historical inflow bounds (without forecasting), and the third is the combined forecast-control scheme. Each approach is implemented on a daily basis and the performance of the system is simulated over the three hydrologic periods. The second and third approaches are implemented with a forecast-control horizon of 20 days. The simulation experiments are designed to (1) investigate whether formal control schemes such as the Set Control Approach offer any relative advantages over heuristic reservoir management procedures, (2) assess the benefit of streamflow forecasting in reservoir management, and (3) examine the sensitivity of Saylorville to potential climate changes.

Figure 4.5 presents the simulation results for the first hydrologic period (warm-dry scenario). In each of the three graphs, the horizontal axis depicts the days of the year and the vertical is the axis of reservoir release. Namely, the graphs show the release sequences that would have resulted had the operator followed the recommendations of each management approach. The first graph corresponds to the Corps of Engineers management method, the second to the Set Control Approach with only historical inflow information, and the third to the Set Control Approach using forecasted information furnished by the modified Sacramento model and the Extended Streamflow Prediction (ESP) procedure. Each graph includes as many lines as the number of years in the hydrologic sequence.

In reference to flood constraint violations, the important observation is that, unlike the other two approaches, the heuristic management procedure cannot avoid flooding. In fact, several violations of the 12,000 cfs release bound are recorded ranging from 4,000 to 10,000 cfs. Though not clearly shown in the figure, the heuristic procedure also violates the low flow augmentation constraint. By contrast, the other two models meet both requirements almost always, with the exception of one flooding instance by the HIS-SCA model by about 2,000 cfs. Figure 4.6 shows the associated reservoir elevation sequences. The COE graph reflects the heuristic rule-curve procedure attempting to maintain reservoir levels at 836 feet from December 15 to April 15 and 838 feet the rest of the year. This, however, is not always possible and frequent excursions from these targets are noted during wet or dry periods. Under the Set Control Approach, reservoir levels are allowed to vary anywhere within their feasible range. However, without the benefit of forecasting,

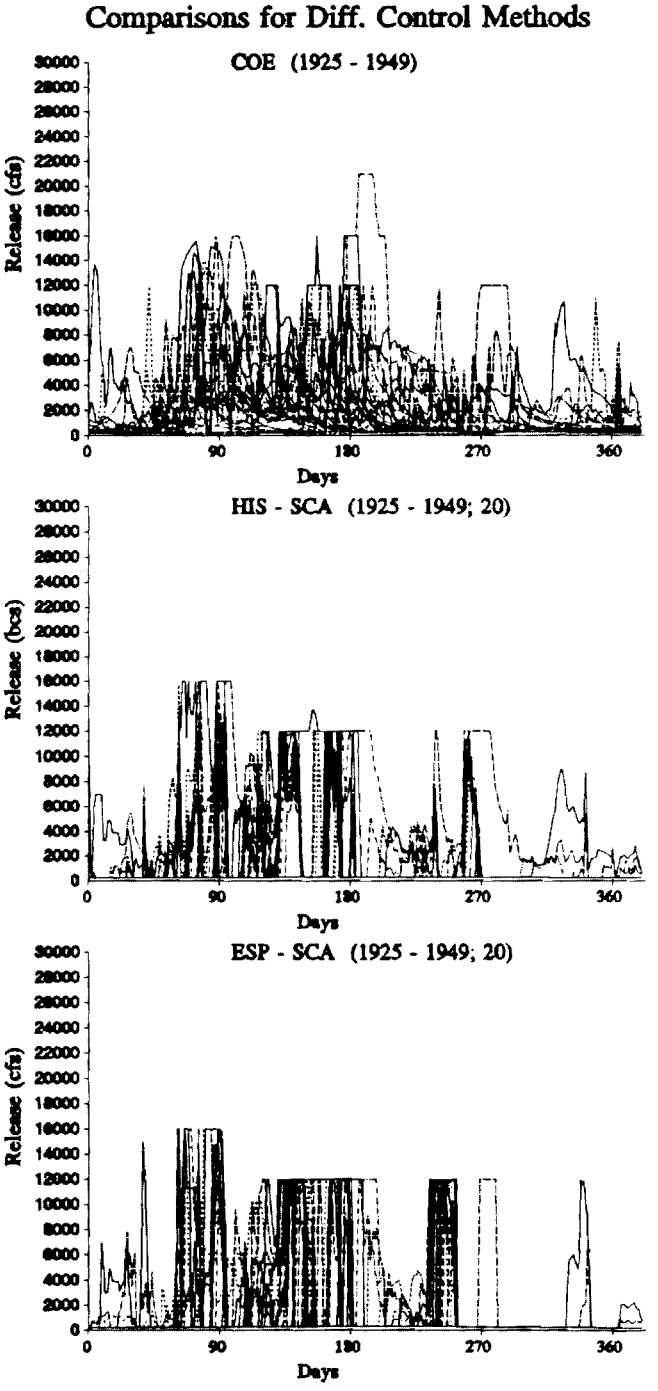

Figure 4.5 Simulated Reservoir Release; First Hydrologic Period

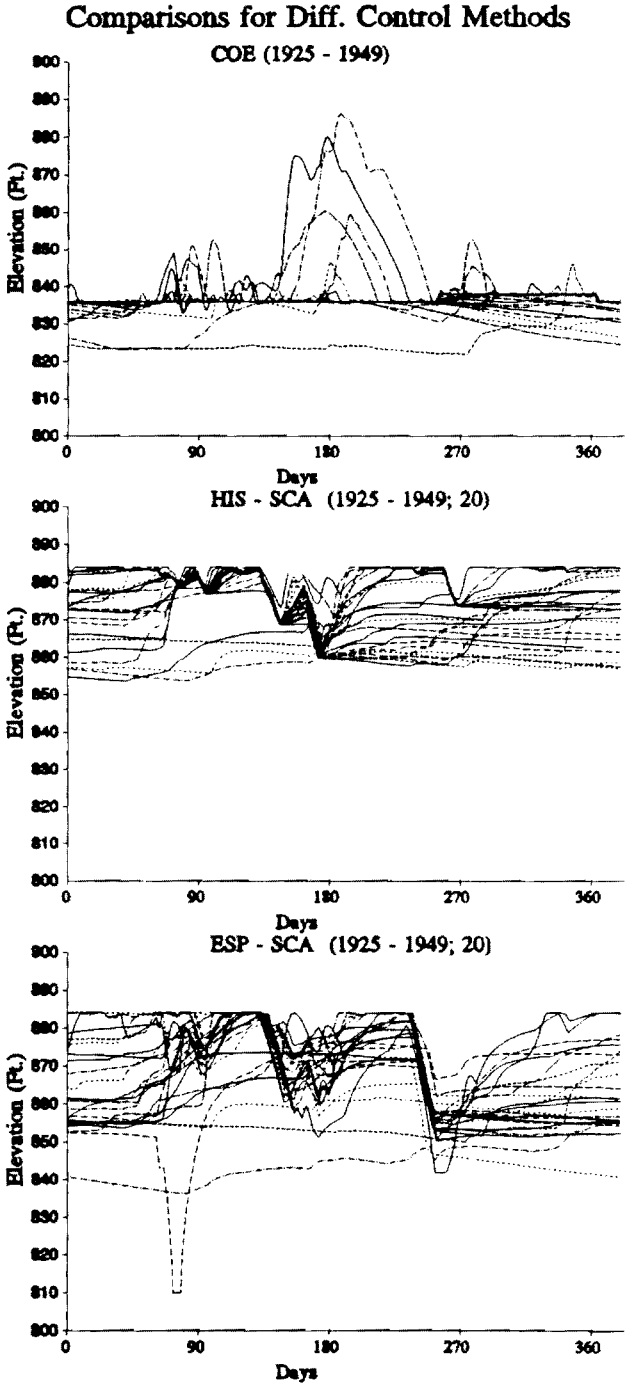

Figure 4.6 Simulated Reservoir Levels; First Hydrologic Period

the HIS-SCA model is conservative, maintaining reservoir levels within a relatively narrow range, while the ESP-SCA model if necessary utilizes the entire feasible range and avoids constraint violations altogether.

Figures 4.7 and 4.8 include the results of the second (wetter) hydrologic period. The release graphs show that both the COE and the HIS-SCA models experience violations of the flood control bound, while the ESP-SCA approach is always feasible. Reservoir levels (Figure 4.8) are forced to fluctuate over a wider range in comparison to the first period (Figure 4.6), with the ESP-SCA levels fluctuating the most. With regard to flooding, the COE model performs better than the HIS-SCA model. However, as will shortly be discussed, HIS-SCA causes far fewer water shortages.

Lastly, Figures 4.9 and 4.10 depict the results of the third hydrologic period, the wettest one of all. All models exhibit violations, but the ESP-SCA model violations are considerably fewer and far less severe than those of the other two.

The previous graphs mainly illustrate the performance of Saylorville with respect to flood control. Table 4.1 summarizes its performance also with respect to drought management (low flow augmentation) and hydropower production. Although hydropower is not a real project purpose (Saylorville does not have hydropower facilities), it was hypothesized as such to examine its sensitivity to the various management methods and hydrologic scenarios. Its power production function was assumed to have the form $P = {}^{n} H_n u$, where P represents power, H_n is the net hydraulic head, u denotes turbine discharge, and ^{n} is an efficiency factor. The discharge capacity of the turbines is assumed to be 16,000 cfs. For the flood and drought management, system performance is characterized by the magnitudes of the maximum and mean violations as well as the violation frequency, while for hydropower the comparison is based on the yearly average production. To examine the effect of the forecast lead time, we run two additional simulation experiments using the ESP-SCA approach with 10 and 30 days forecast/control horizon.

Comparing the performance of the original methods (COE, HIS-SCA(20), and ESP-SCA(20)), we observe that also with respect to droughts the forecast-control scheme is better than the other two. For all three periods, ESP-SCA(20) recorded zero low flow constraint violations. By comparison, the heuristic procedure (COE) experiences frequent water shortages in all periods, while the control approach without forecasting (HIS-SCA(20)) reports violations only in the second and third periods. At first glance, it would seem odd that the HIS-SCA model does not incur low flow violations during the first (dry) period while having such instances during the second and third (wetter) periods. This happens because mean inflow is but one hydrologic parameter influencing reservoir operation and outputs, with inflow

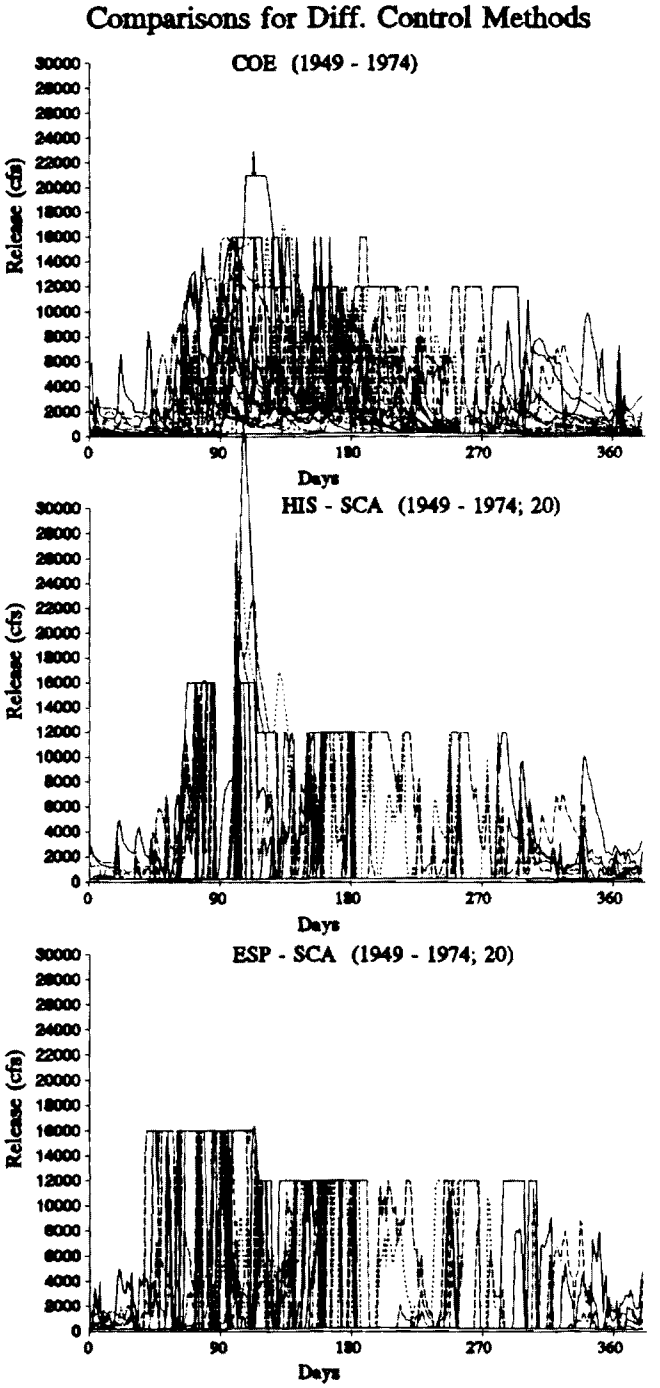

Figure 4.7 Simulated Reservoir Release; Second Hydrologic Period

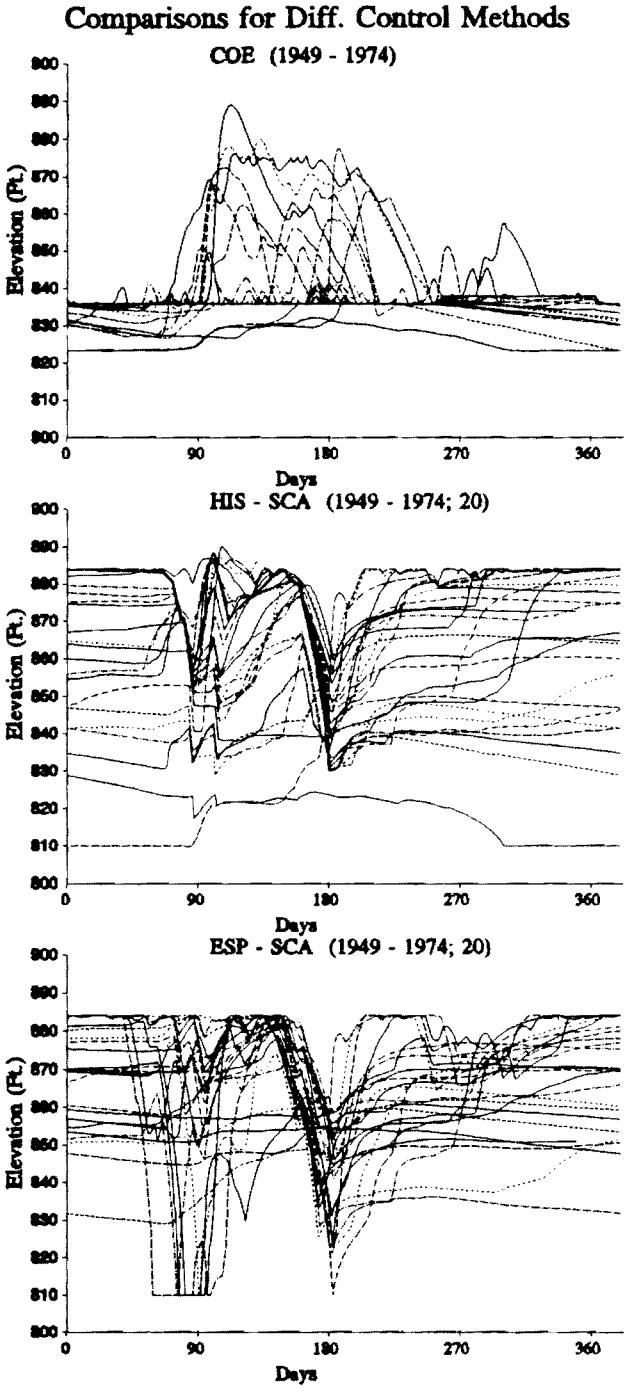

Figure 4.8 Simulated Reservoir Levels; Second Hydrologic Period

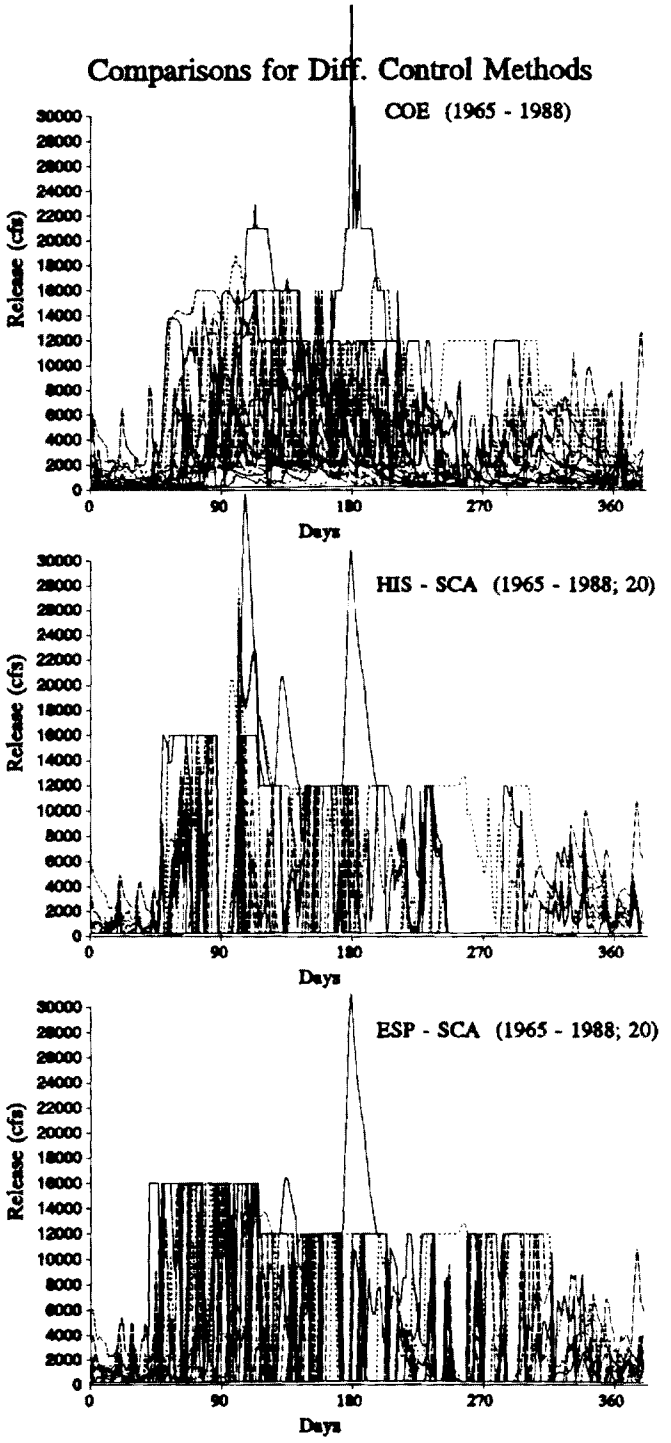

Figure 4.9 Simulated Reservoir Release; Third Hydrologic Period

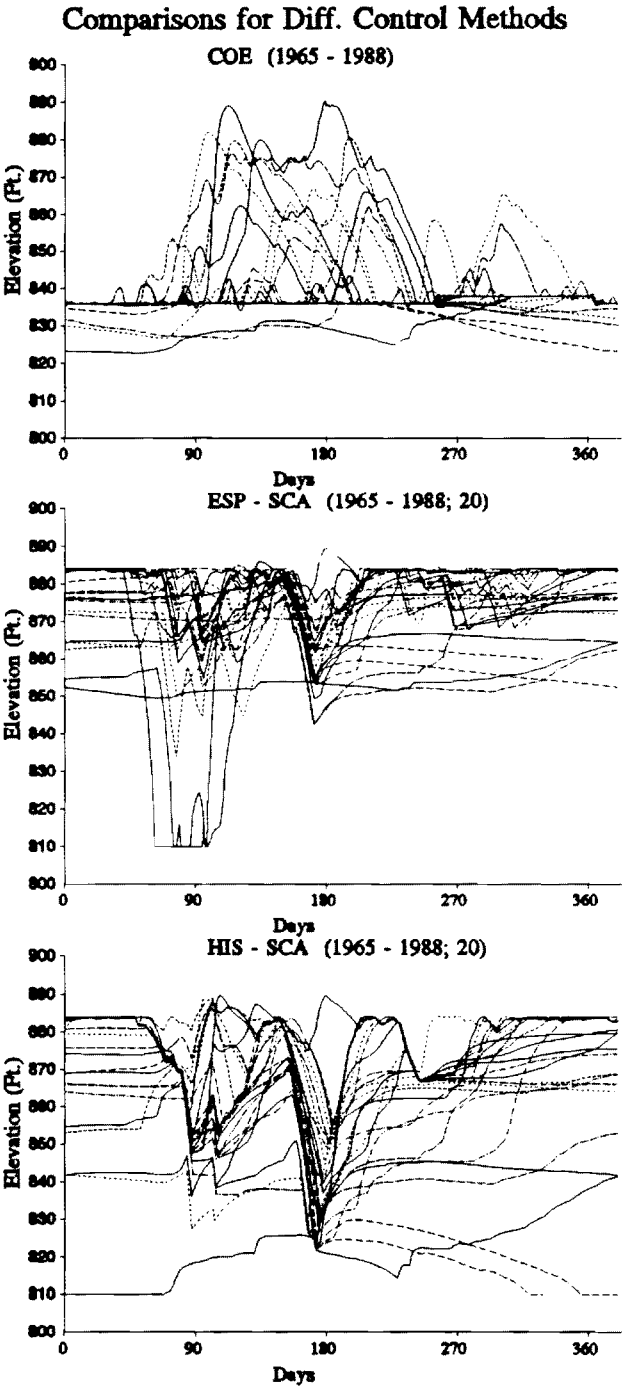

Figure 4.10 Simulated Reservoir Levels; Third Hydrologic Period

Table 4.1 Summary of Simulation Results

Performance Statistics for Period 1925-1949

Cases	Flood Constraint Violation			Water Qual. & Supply Violations			Yearly Avg. Power Production (x8760 KWH)
	Max Viol. (cfs)	Mean Viol. (cfs)	Viol. Times	Max. Viol. (cfs)	Mean Viol. (cfs)	Viol. Times	
COE	9000.	5275	40	205	37	1384	2613.56
HIS/SCA(20)	1728	1088	6	0	0	0	3987.76
ESP/SCA(10)	7232	3240	30	0	0	0	3960.00
ESP/SCA(20)	0	0	0	0	0	0	3729.60
ESP/SCA(30)	0	0	0	0	0	0	3563.54

Performance Statistics for Period 1949-1974

Cases	Flood Constraint Violation			Water Qual. & Supply Violations			Yearly Avg. Power Production (x8760 KWH)
	Max. Viol. (cfs)	Mean Viol. (cfs)	Viol. Times	Max Viol. (cfs)	Mean Viol. (cfs)	Viol. Times	
COE	9000	4145	75	200	36	1250	3473.10
HIS/SCA(20)	20957	5045	77	237	163	155	4345.41
ESP/SCA(10)	11446	5804	9	0	0	0	4615.00
ESP/SCA(20)	436	436	1	0	0	0	4084.56
ESP/SCA(30)	0	0	0	237	158	209	3639.04

Performance Statistics for Period 1965-1988

Cases	Flood Constraint Violation			Water Qual. & Supply Violations			Yearly Avg. Power Production (x8760 KWH)
	Max. Viol. (cfs)	Mean Viol. (cfs)	Viol. Times	Max Viol. (cfs)	Mean Viol. (cfs)	Viol. Times	
COE	32422	5000	136	250	25	954	4555.42
HIS/SCA(20)	19480	5518	122	219	178	102	5912.50
ESP/SCA(10)	20166	4869	114	0	0	0	6721.00
ESP/SCA(20)	19064	5296	46	0	0	0	6189.12
ESP/SCA(30)	14186	7604	19	0	0	0	5601.93

variability being another. To guard against high flows during the wet periods, the controller draws the reservoir down. If a dry spell then occurs, reservoir storage is not enough to meet low flow requirements and the reservoir defaults. Thus, wetter hydrologic climates may not necessarily provide more insurance against droughts. With regard to power generation, the heuristic procedure falls short of the other two in all cases (by about 20 to 30 percent). In the first two periods, HIS-SCA(20) maintains higher storage levels (and net hydraulic heads) than ESP-SCA(20) and generates more energy (by about 5 percent). In the third period, spillage becomes the limiting factor, and this trend is reversed. As a general rule, energy generation is higher in wetter climates.

In reference to the forecast lead time, it can generally be stated that the longer the lead time the better the system performance. However, these benefits extend up to the time when the forecasted ranges are smaller than the historical bounds. For the upper Des Moines river basin and the Sayloville reservoir, this time is about 20 to 30 days.

As a final remark, we note that the forecast-control model ESP-SCA(20) manages to mitigate the adverse effects of climatic change. It experiences zero low flow violations for all hydrologic periods and zero flooding violations for the first and second periods. By contrast, the effectiveness of the heuristic management procedure is low as is its ability to adapt to potential climatic changes.

4.2 APPLICATION TO THE CHATTAHOOCHEE RIVER (SOUTHEAST)

4.2.1 System Description

Lake Lanier is a man-made reservoir (Figure 4.11) located on the upper reaches of the Chattahoochee River in the State of Georgia (about 35 miles northeast of Atlanta). This reservoir extends up the Chattahoochee and Chestatee River and has a 1,040 square miles drainage area. The Dam at the Lake's outlet (at Buford) was constructed by the U.S. Army Corps of Engineers (COE) in 1957, and, along with three other federal storage projects in the Apalachicola-Chattahoochee-Flint (ACF) River basin, its operation falls under the jurisdiction of the Mobile COE District.

The project has several operational objectives including flood protection as far downstream as West Point (150 miles below Buford), navigation in the Apalachicola River below Woodruff Dam, industrial and domestic water supply for Atlanta and environs, recreation, and hydroelectric energy generation. The reservoir has a conservation storage of 1.342 billion cubic meters (1,088,065 acre-ft) between the elevations of 1035 and 1071 feet. Hydropower is produced by two main turbines each with an installed capacity of 49.5 MW and a small 6 MW unit. Buford releases are especially critical during low flow periods.

Appendix B describes various reservoir characteristics such as the elevation vs. storage curve, tailwater function, and power generation relationships of the Dam's three turbines. These curves were developed using data from the reservoir regulation manual (US. Army Corps of Engineers, 1959).

Buford is primarily operated to satisfy peak power and minimum flow requirements. These requirements are presently met by "running" the two main turbines at 49.5 MW for two hours each day except weekends (for a total of 43.5 hours per month) and the smaller turbine at 6 MW continuously. Additional releases and energy generation are scheduled based on SEPA's (South-Eastern Power Administration) energy commitments and the condition of the other federal hydropower facilities in the southeastern U.S. region.

Figure 4.12 portrays the monthly statistics (mean, 75th and 2th percentiles, maximum and minimum) of Lake Lanier inflow.

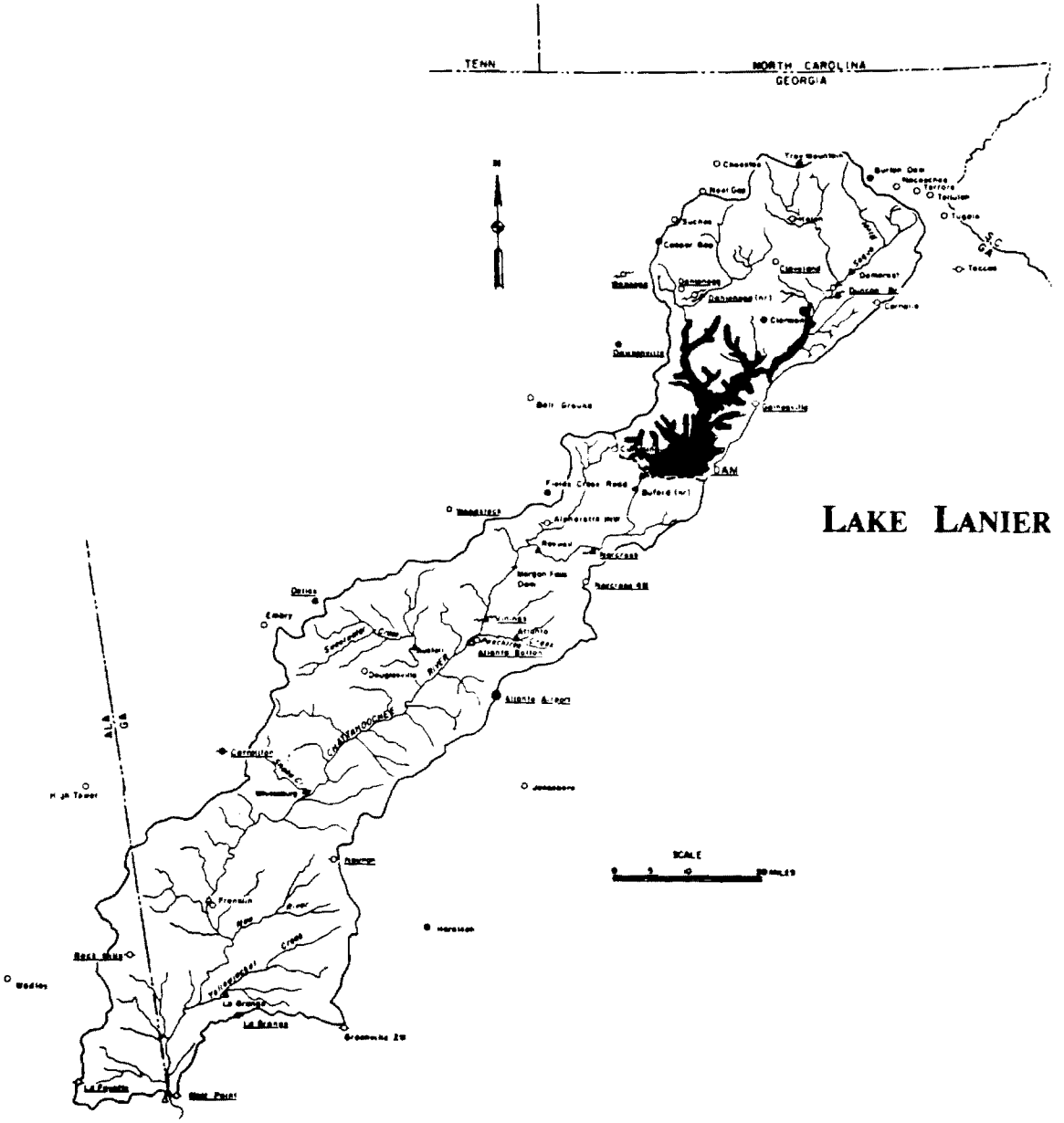

Figure 4.11: Hydrological Map of Lake Lanier-Bufford Dam

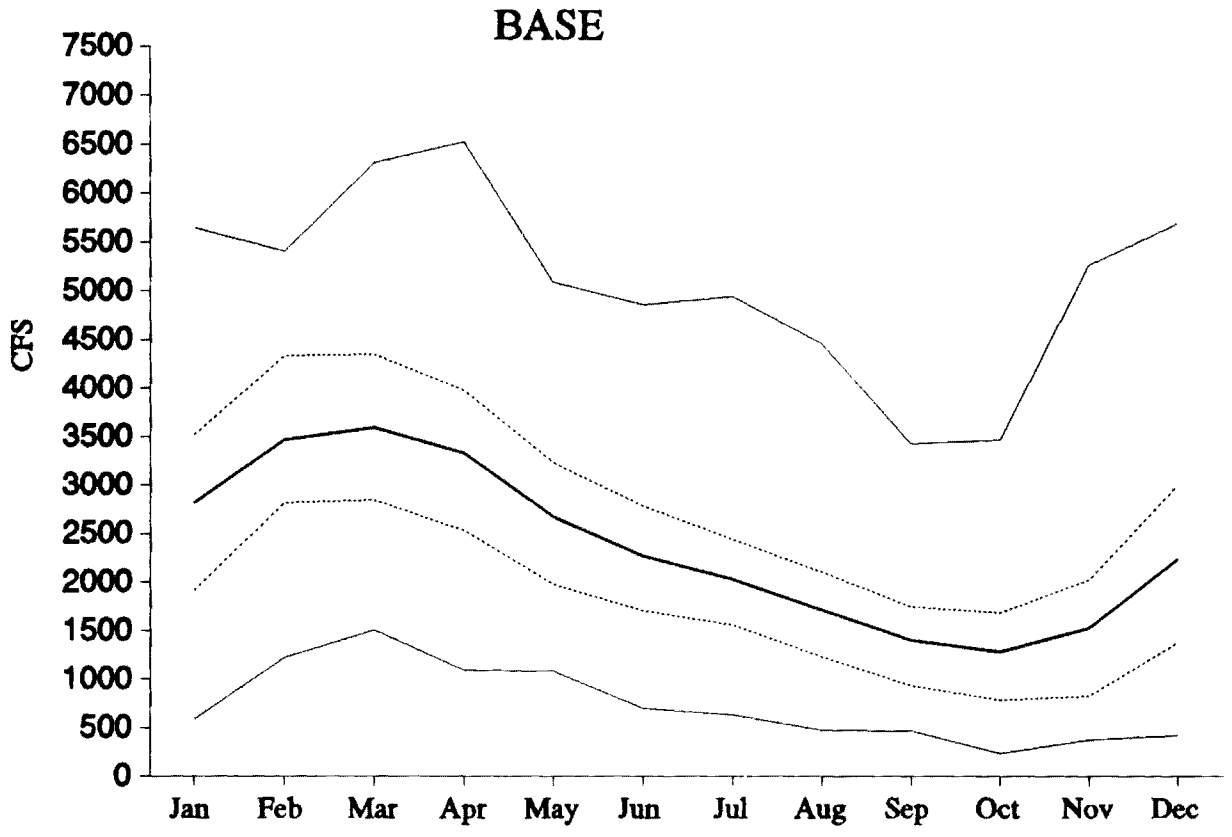

Figure 4.12 Lake Lanier Inflow Statistics (mean, 75th and 25th percentiles, maximum and minimum)

4.2.2 Lake Lanier Sensitivity to Climatic Changes

The purpose of this section is to investigate the operational sensitivity of Lake Lanier under various hydrologic and operational scenarios. This investigation is based on simulation experiments similar to the ones conducted in the previous section, but with a monthly time step. All runs utilize the Set Control Approach with a control horizon of 12 months. Streamflow forecasting is simulated in the same manner as in Section 3 (Savannah River case study). The simulations are performed using four 94-year long inflow traces that reflect present and potentially different climatic circumstances. These traces have been kindly provided to us by G. D. Tasker of the Reston USGS office. Their derivation is briefly explained next. [See also, *Tasker, 1993.*]

General circulation models (GCMs) show that further accumulation of green-house gases in the atmosphere may substantially change the prevailing temperature and precipitation patterns. In the case of the southeastern United States, three GCMs (Geophysical Fluid Dynamics Lab -- GFDL, Goddard Institute for Space Studies -- GISS, and the Oregon State University -- OSU models) indicate that doubling of atmospheric CO_2 would lead to an increase in annual temperature by several degrees and a substantial decrease of precipitation. More specifically, GFDL predicts a 5.3 °C annual temperature increase and a 88.9% precipitation reduction, GISS similarly predicts a 5.2 °C temperature increase and a 100.5% precipitation reduction, and OSU a 3.7 °C temperature increase and a 99.8% precipitation reduction. Monthly percentages are also available [*Tasker, 1993*] indicating strong seasonality. Although the predictive accuracy of GCMs is questionable [*Gleick,1989*], their results are herein used to establish plausible future climatic scenarios.

To convert this information to inflow traces, Tasker [*1993*] first generates random temperature and precipitation deviations from the historical monthly means using a multi-site Markov model. These estimates are next adjusted by a percentage determined by the GCM-predicted monthly increment or reduction. Finally, a physically-based rainfall-runoff model is used to translate the resulting temperature and precipitation traces to inflow sequences.

To compare with the base case (Figure 4.12), monthly inflow statistics for the GFDL, GISS, and OSU inflow sequences are also plotted on Figures 4.13, 4.14, and 4.15. While the figures show a clear reduction of mean monthly inflow relative to the base case, extreme inflow values are in some cases outside the base case range.

The first simulation experiment is the base case where the generation hours may range from 43.5 to 730 hours per month and the inflow sequence corresponds to the

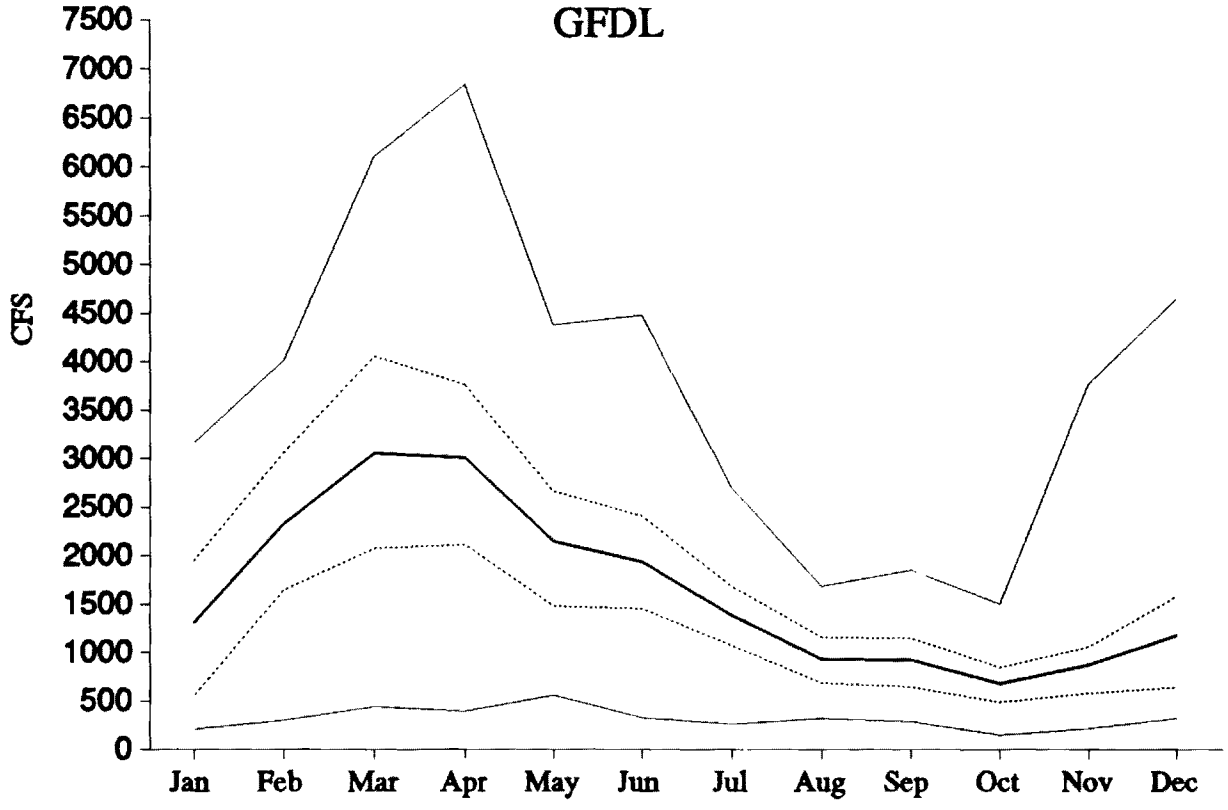

Figure 4.13 GFDL Inflow Trace Statistics (mean, 75th and 25th percentiles, maximum and minimum)

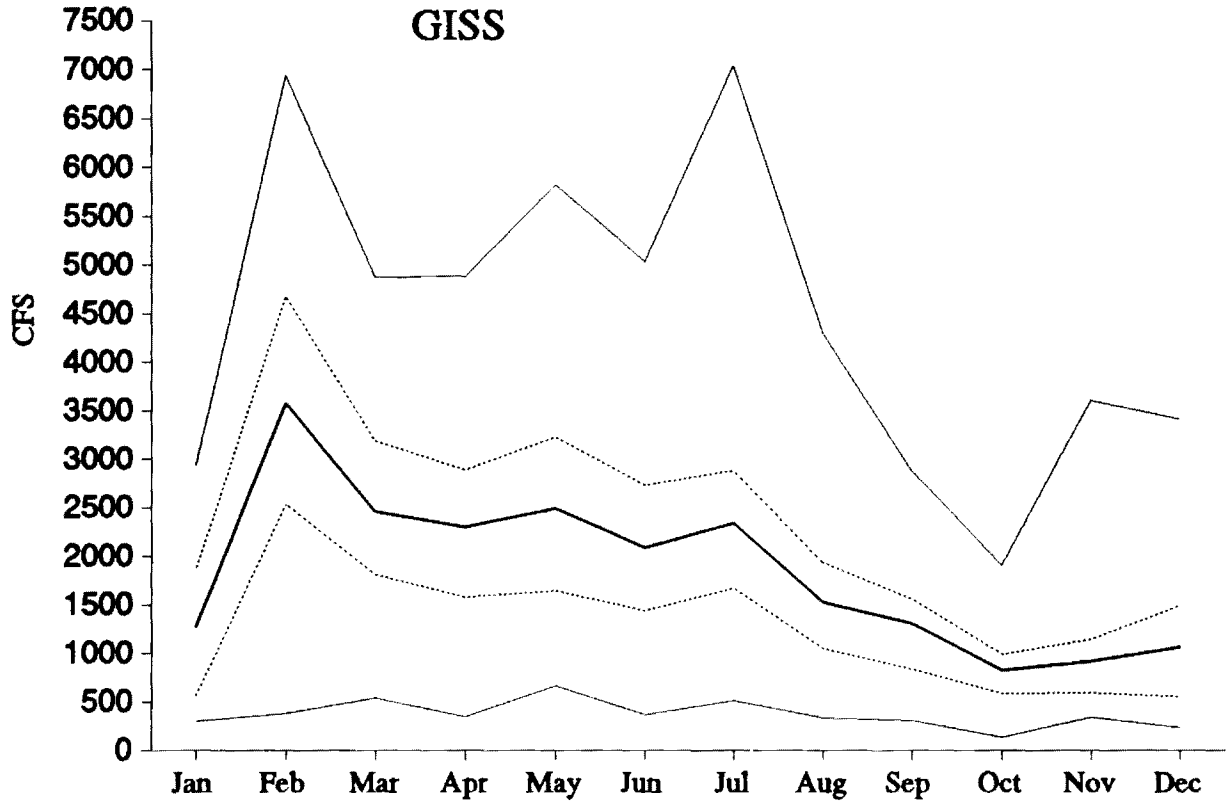

Figure 4.14 GISS Inflow Trace Statistics (mean, 75th and 25th percentiles, maximum and minimum)

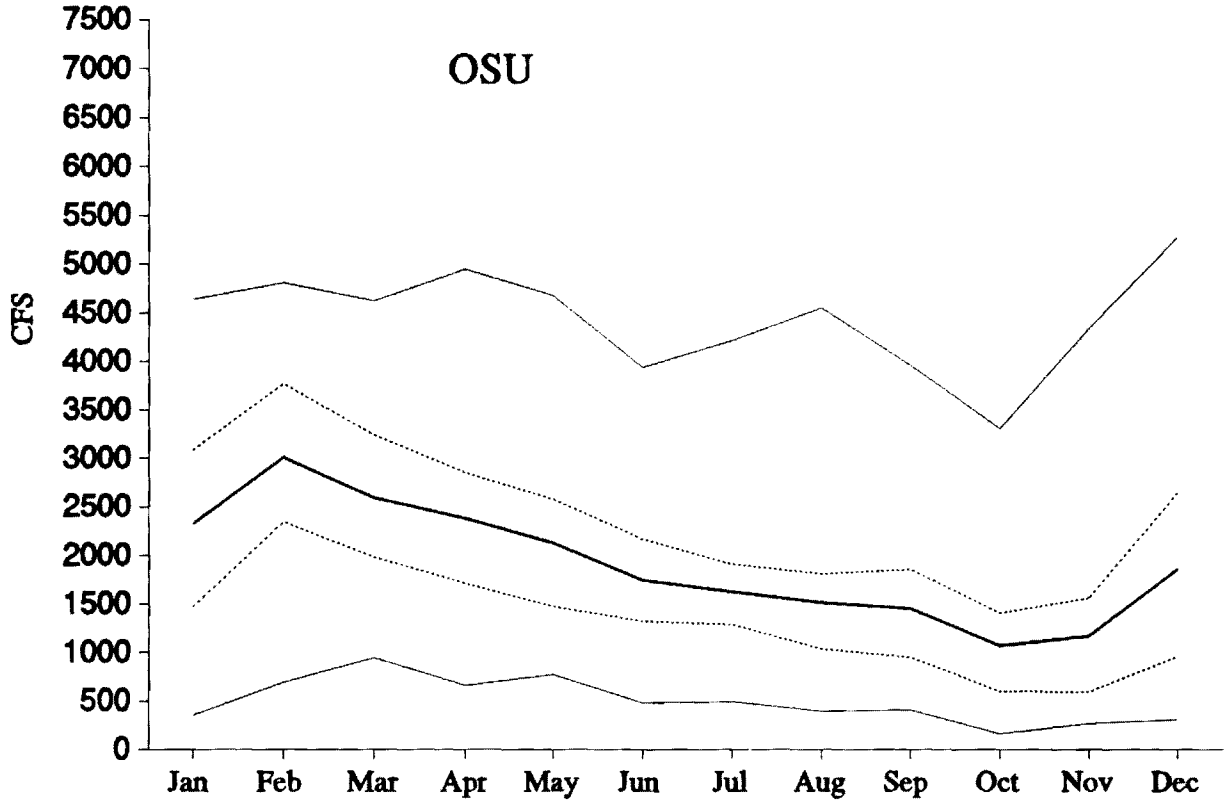

Figure 4.15 OSU Inflow Trace Statistics (mean, 75th and 25th percentiles, maximum and minimum)

to the present climatic conditions. In lieu of inflow forecasts, the SCA control model has access only to maximum and minimum monthly inflows. The results are summarized in three graphs shown on Figure 4.16. The first graph includes the simulated monthly reservoir elevation sequence along with the conservation pool boundaries, the second delineates the monthly energy generation, and the third shows the associated release. On the outflow graph, the solid line in the neighborhood of 1000 cfs indicates the outflow level corresponding to the 43.5 minimum generation hours per month. This level fluctuates in response to the fluctuation of the reservoir level (and the net hydraulic head). The figure shows that the reservoir stays within the conservation pool and the generation hours satisfy the minimum constraint. Due to the uncertainty of future inflows, the controller keeps the average reservoir level at about 1060 feet, and manages to avoid water shortages or excessive releases. Reservoir levels have a fluctuation range of about 16 to 17 feet.

The following three figures (4.17, 4.18, and 4.19) summarize the results for the GFDL, GISS, and OSU inflow scenarios (CO_2 doubling). Concentrating on the GFDL simulation run, one sees that reservoir levels now fluctuate much more than before and droughts are much more frequent and severe. The worst drought is toward the end of the simulation period when reservoir storage is entirely depleted and the model actually fails to meet the minimum generation/water supply requirements almost for the last four years. The results of the GISS run are similar, with a major operational failure occurring at about the same time. By contrast, the OSU simulation run is different than the previous two, with the reservoir being able to satisfy its operational objectives throughout the simulation period. A closer examination of the inflow statistics for the three sequences (Figures 4.13, 4.14. and 4.15) can explain this difference. Relative to the base case, the GFDL and GISS inflow reduction is uneven for different months of the year. Especially during the low flow months of August, September, October and November, GFDL and GISS inflow deficits are higher than those of OSU. Thus in the first two cases, droughts are more likely and end-up causing severe water shortages.

Thus, the previous results indicate that the operational reliability of Lake Lanier will be at risk under the GFDL and GISS climatic scenarios. In the following experiments, we are interested to investigate whether improved streamflow forecasting can mitigate this effect. Better forecasting is simulated via the procedure described in Chapter 3, the forecast parameter p(1) being equal to 0.5 or 0.25. The new simulation runs are shown on Figures 4.20 through 4.27 in the familiar format.

Examination of the $p(1)=0.5$ case results shows that better streamflow forecasting makes a distinct difference. For the base case scenario, the improvement is clearly

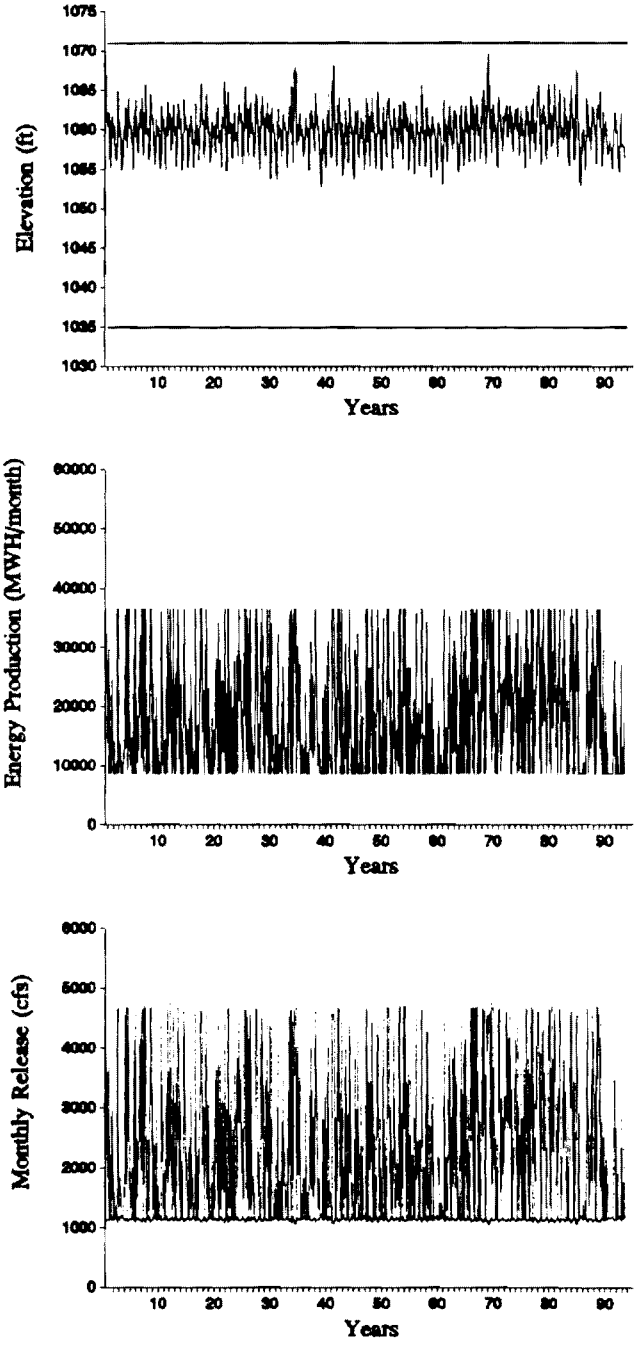

Figure 4.16 Simulation Results for Base Scenario

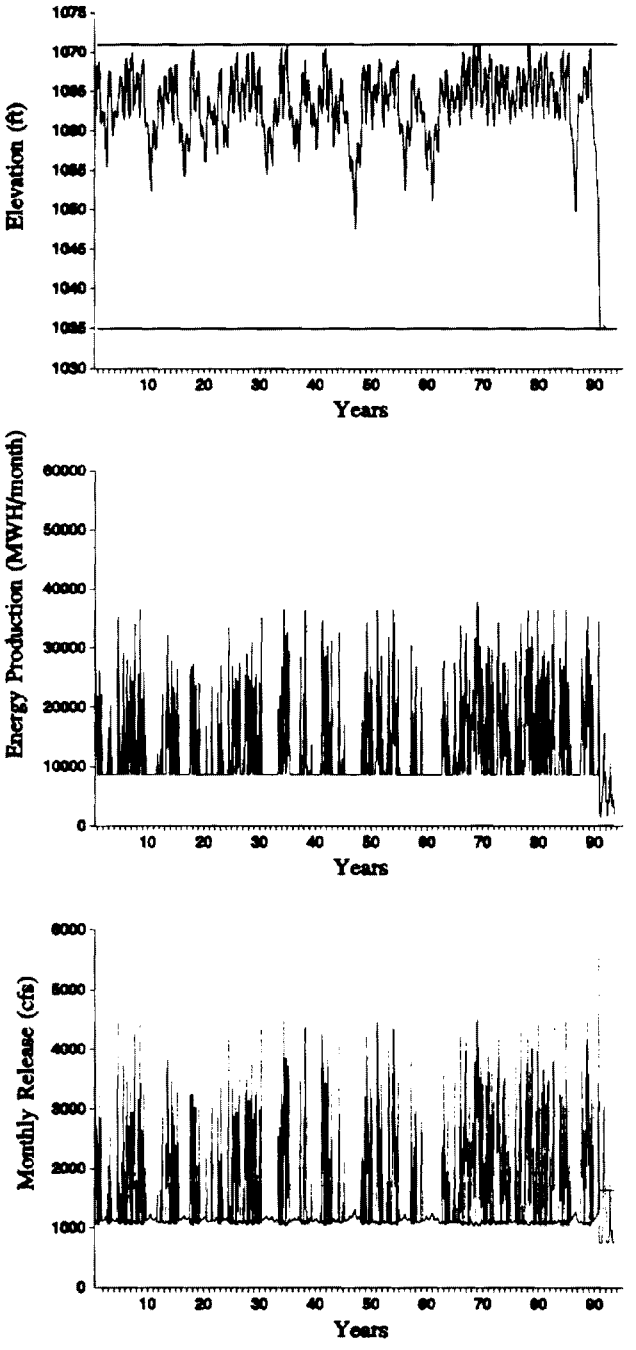

Figure 4.17 Simulation Results for GFDL Scenario

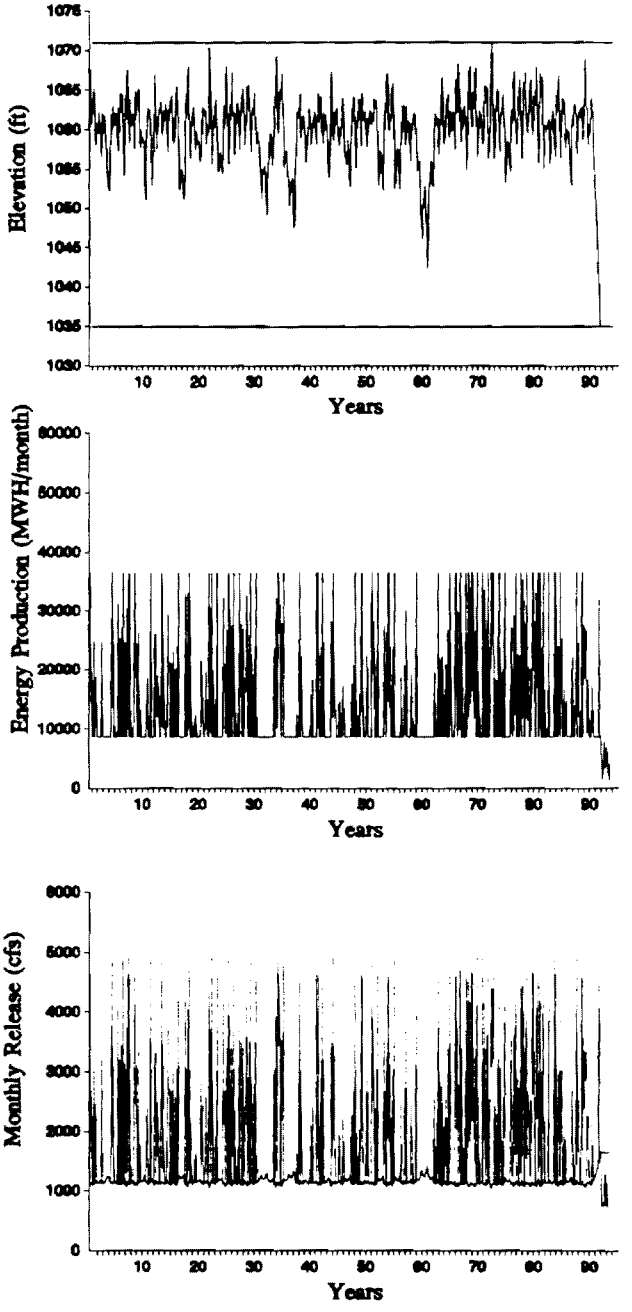

Figure 4.18 Simulation Results for GISS Scenario

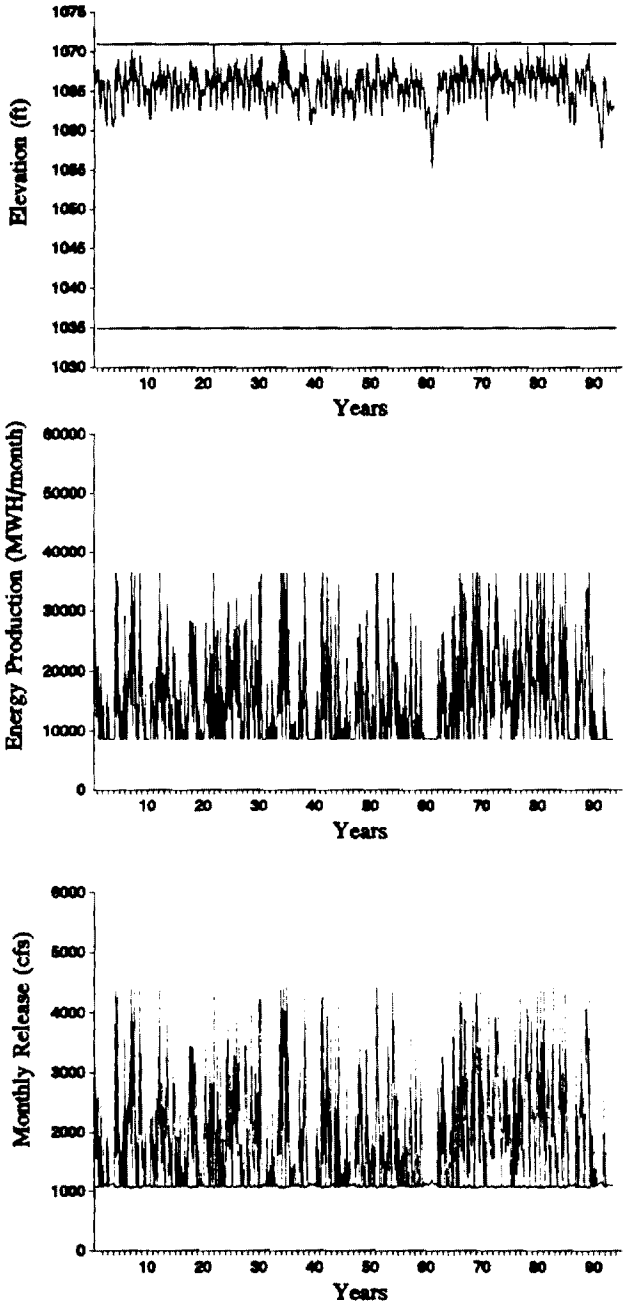

Figure 4.19 Simulation Results for OSU Scenario

evident in the first graph of Figure 4.20 where reservoir levels are substantially higher than those of Figure 4.16 and fluctuate much less. Having more accurate information of the upcoming inflows, the controller maintains higher reservoir levels without causing spillage. With the reservoir almost always full, the drought risk is now smaller. This is better seen in the GFDL and GISS scenarios where droughts are almost entirely avoided except in the last GFDL simulation year. This drought is finally averted in the $p(1)=0.25$ forecast case.

Table 4.2 summarizes all simulation runs recording frequency and magnitude of violations and total energy generation. Relative to present conditions, energy generation is expected to decline by about 30 (GFDL) to 15 (OSU) percent. On the other hand, forecasting tends to secure 2 to 7 percent more energy.

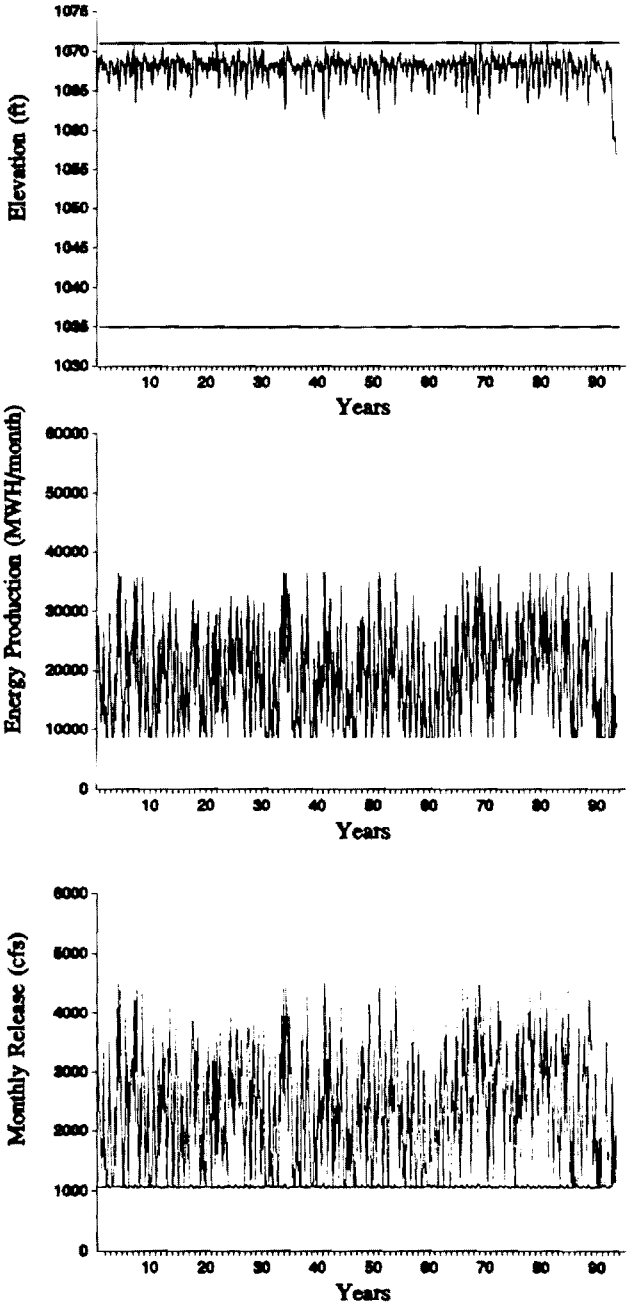

Figure 4.20 Simulation Results for BASE Scenario; P(1) = 0.5

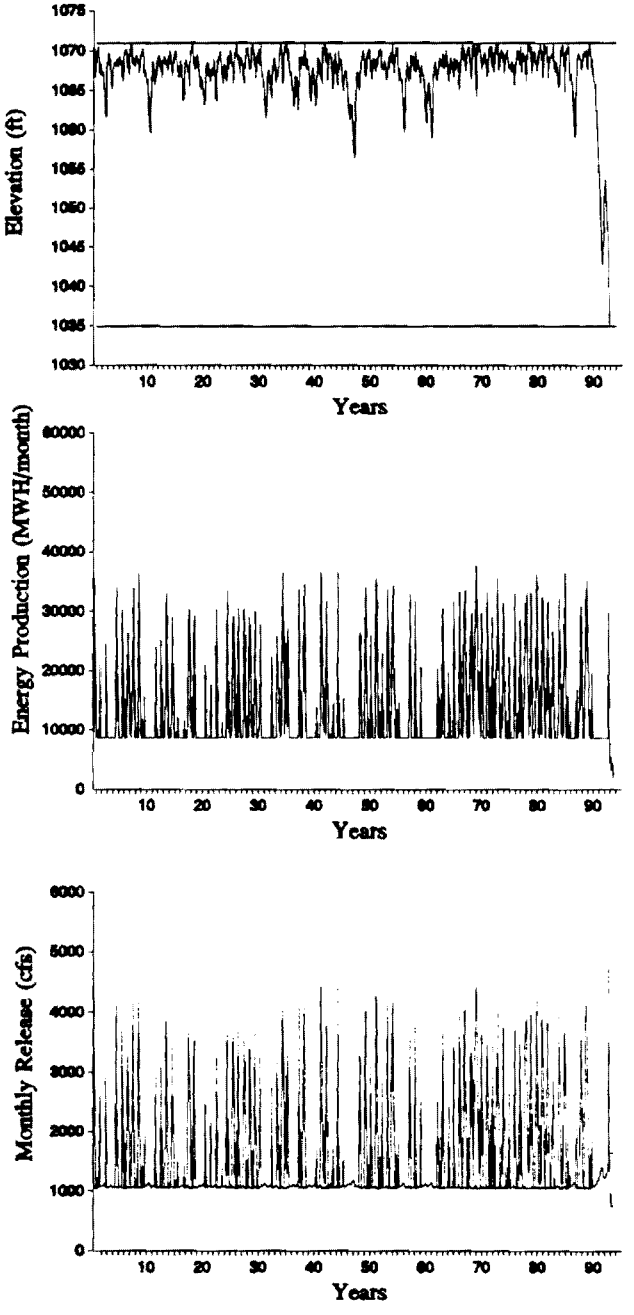

Figure 4.21 Simulation Results for GFDL Scenario; P(1)=0.5

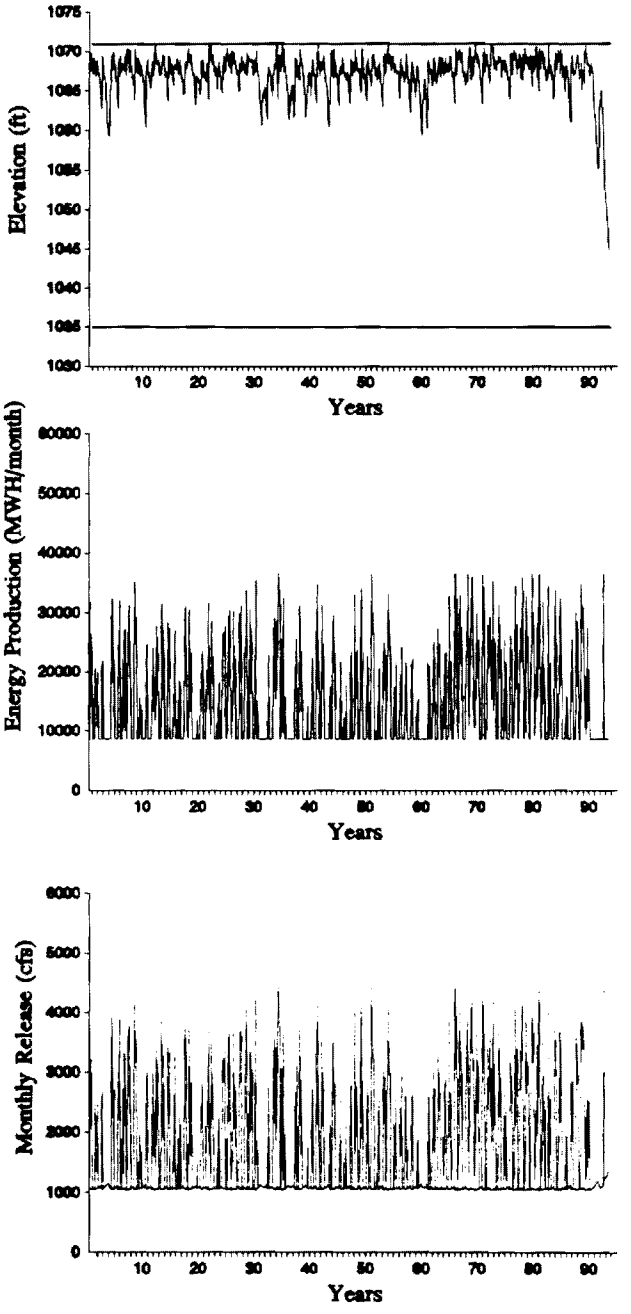

Figure 4.22 Simulation Results for GISS Scenario; P(1) = 0.5

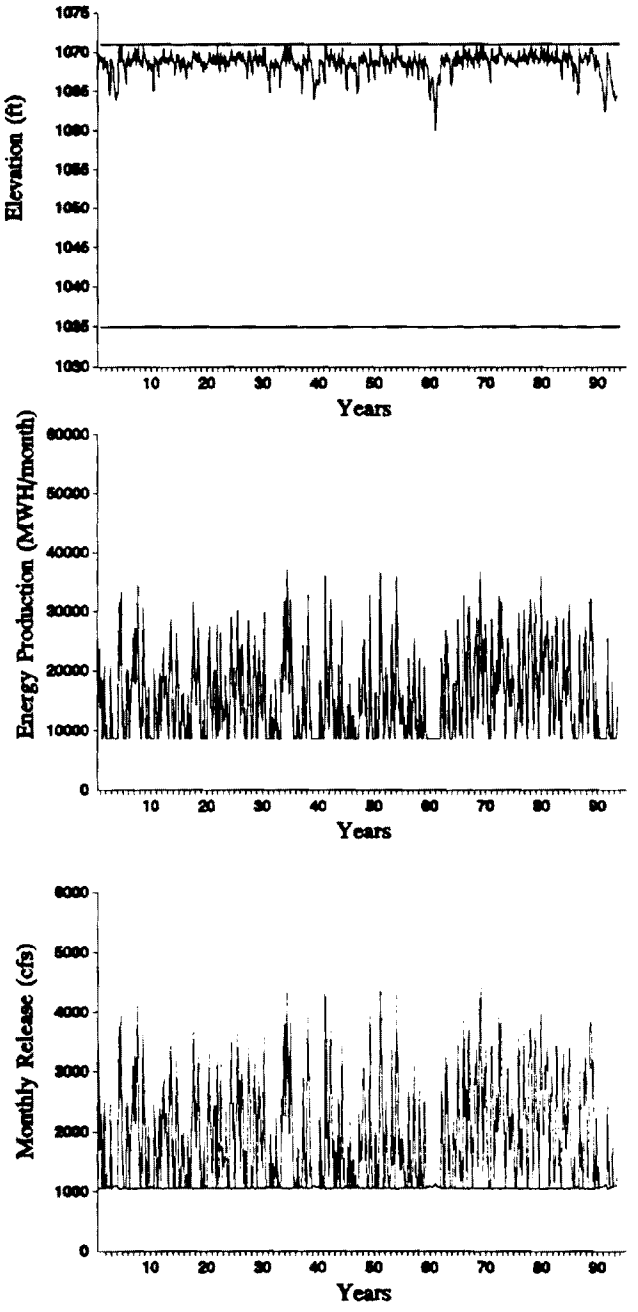

Figure 4.23 Simulation Results for OSU Scenario; P(1) = 0.5

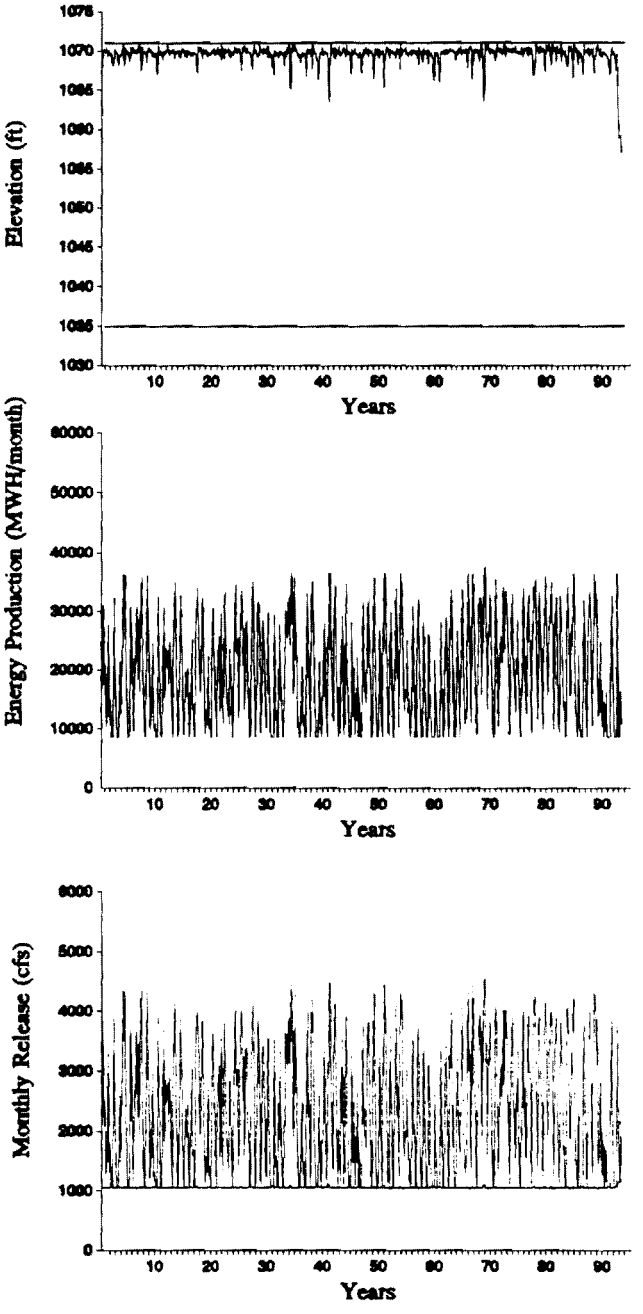

Figure 4.24 Simulation Results for BASE Scenario; P(1)=0.25

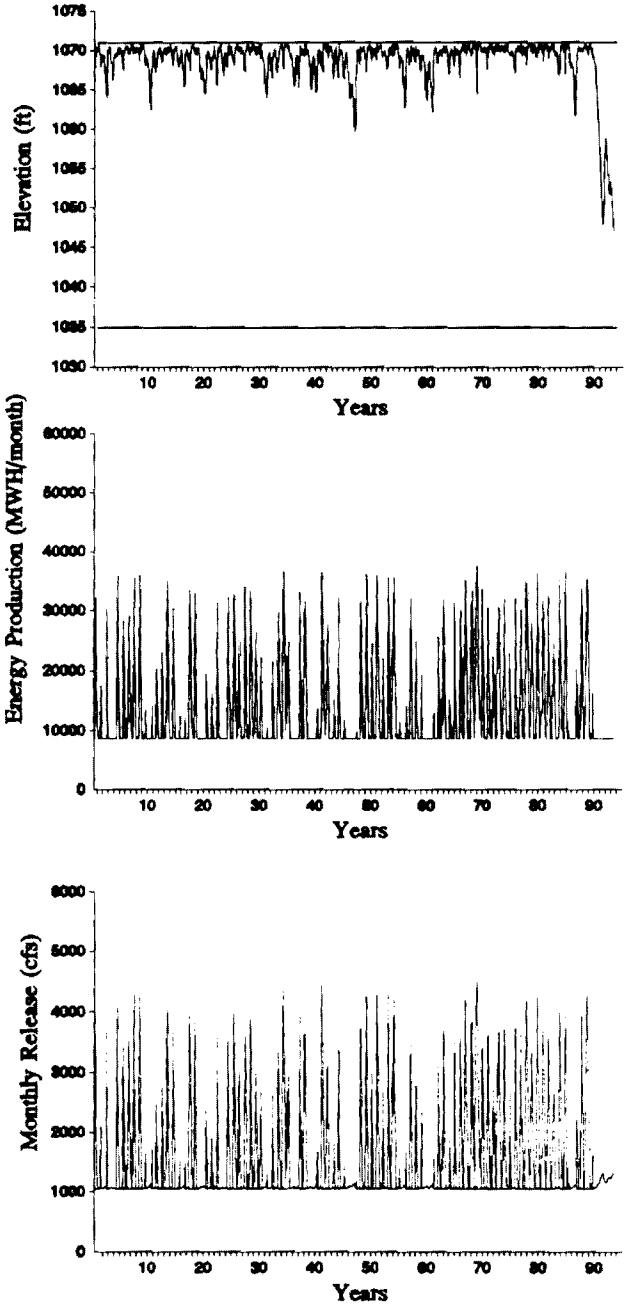

Figure 4.25 Simulation Results for GFDL Sceanrio; P(1) = 0.25

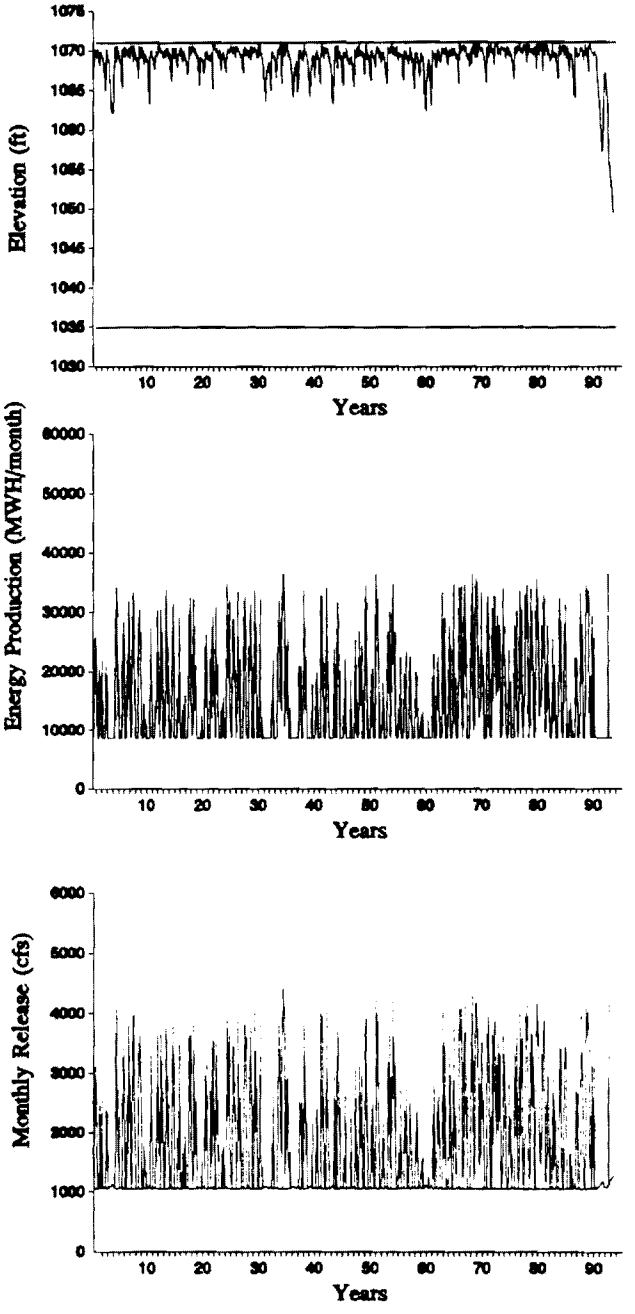

Figure 4.26 Simulation Results for GISS Scenario; P(1) = 0.25

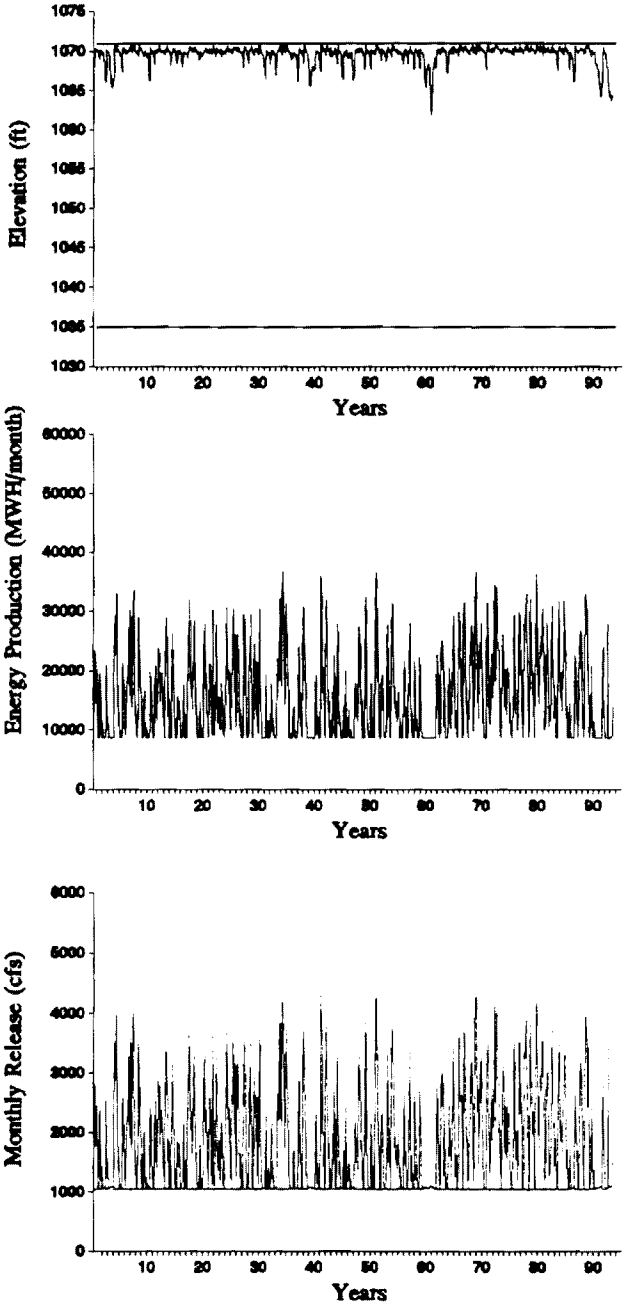

Figure 4.27 Simulation Results for OSU Scenario; P(1) = 0.25

Table 4.2 Violation Tables

No Forecasting

	BASE	GFDL	GISS	OSU
Viol. Number	0	28	20	0
Max. Powr. Viol. (MWH/month)	0	7150	7315	0
Total Powr. Viol. (MWH/month)	0	122914	77408	0
Total. Energy(MWH)	2.0373e7	1.4625e7	1.5916e7	1.7296e7

Forecasting with p(1) = 0.5

	BASE	GFDL	GISS	OSU
Viol. Number	0	8	0	0
Max. Powr. Viol. (MHW/month)	0	6567	0	0
Total Powr. Viol. (MHW/month)	0	34432	0	0
Total. Energy(MWH)	2.1725e7	1.5153e7	1.6987e7	1.767e7

Forecasting with p(1) = 0.25

	BASE	GFDL	GISS	OSU
Viol. Number	0	0	0	0
Max. Powr. Viol. (MHW/month)	0	0	0	0
Total Powr. Viol. (MHW/month)	0	0	0	0
Total. Energy(MWH)	2.2032e7	1.5306e7	1.7187e7	1.7797e7

5. SUMMARY, CONCLUSIONS, AND FURTHER RESEARCH RECOMMENDATIONS

The scope of this research project was to investigate the effects of global warming on reservoir system outputs. This investigation was carried out in four phases:

(1) A general control method suitable for the management of uncertain dynamical systems was first developed (Chapter 2). This new control approach was motivated by the need to guide the operation of water resources systems under extreme or relatively unknown input circumstances (as in the case of long-lasting climatic changes). Rather than using statistical input descriptions, this approach was based on set characterization of uncertainty. The resulting control problem calls for finding the set of admissible actions that ensures that the system stays within its bounds for the duration of the operational horizon. The solution is derived using Dynamic Programming and is efficiently implemented for the case where all sets are convex polyhedra.

(2) In the second phase (Chapter 3), the Set Control Approach was applied to common reservoir operation problems including flood and drought management and hydropower scheduling. Common to all applications is the premise that reservoir operators wish to have a set of policies guaranteed to meet all system constraints, rather than optimize specific objectives. We feel that this mode of operation is more meaningful under crises situations (floods and droughts) and climate change circumstances. Several computational experiments with the Savannah River system in the southeast (three reservoirs) showed that accurate inflow forecasting together with the Set Control Approach improves reservoir operations in that it minimizes flood control storage and avoids damage-causing outflows. In addition, benefits accrue from energy generation due to higher hydraulic head and less wasted spillage.

Reservoir systems usually operate under normal hydrologic conditions and only occasionally experience extreme events. During the former, stochastic methods are appropriate and can effectively guide system operations. One potentially useful research contribution would be to develop a hybrid control model which uses stochastic methods during normal circumstances but switches to the set control approach at the onset of critical periods.

(3) In the third phase (Chapter 4.2), the Set Control Approach was coupled with the Modified Sacramento Model developed by the University of Iowa research team (Volume II). The combined forecast-control procedure was tested in the operation of the Saylorville reservoir in the upper Des Moines river basin (midwest). Side-by-side simulation experiments of this model with (a) heuristic management practices

and (b) the Set Control Approach with no forecasting showed that the forecast-control procedure significantly improved reservoir operations entirely avoiding droughts and effectively controlling floods.

The impacts of a potential global warming scenario were examined using historical analogues of low, intermediate, and high streamflow periods. It was shown that reservoirs can be operated to mitigate the adverse effects of climatic change with the aid of effective forecast-control procedures. It is noted that the heuristic management practices could not readily adapt to changing hydrologic circumstances, causing frequent flooding and water shortages. Thus in climate change impact studies, reservoir optimization procedures such as the ones developed herein are essential. Failure to incorporate them will lead to overly pessimistic results and exaggerate real impacts.

(4) In the fourth phase of the research (Chapter 4.3), we used results from three General Circulation Models (GCMs) to establish plausible inflow scenarios for Lake Lanier (southeast) under the assumption of doubled atmospheric CO_2. The scenarios generally indicate that inflow volumes will be reduced significantly, causing the lake to experience frequent and severe droughts. However, the use of effective streamflow forecasting and reservoir control procedures can ease these consequences. These results, however, should be viewed as only "what if" scenarios as GCM predictions and their processing to watershed scale are presently rather inexact -- an area needing further research.

6. REFERENCES

Barnett, T. P., Long-term changes in precipitation patterns, *Technical Report* to the U.S. Dept. of Energy by Lawrence Livermore National Laboratory under contract no. W-7405-ENG-48, in Detecting the Climate Effects of Increasing Carbon Dioxide, 151-162, 1986.

Bertsekas, D.P. and I.B. Rhodes, On the minimax reachability of target sets and target tubes, *Automatica*, Vol. 7, 233-247, 1971.

Bishop, E. and Phelps, The support functionals of a convex set," *Proc.* of Symp. in Pure Math., 7, AMS, 1963

Bradley, R. S., H. F. Diaz, J.K. Eischeid, P.D. Jones, P.M. Kelly, C. M. Goodess, precipitation fluctuations over the Northern Hemisphere land areas since the mid-19th century, *Science*, 237, 171-175, 1987.

Foufoula-Georgiou, E., and P. K. Kitanidis, Gradient dynamic programming for stochastic control of multidimensional water resources systems, *Water Resources Research*, 24(8), 1345-1359, 1988.

Georgakakos, A.P., Extended Linear Quadratic Gaussian (ELQG) control: Further extensions, *Water Resources Research*, 25(2), 191-201, 1989.

Georgakakos, A. P., Optimal regulation of the Savannah River system, *Technical Report* for U.S. Army Corps of Engineers Research Contract No. DACW21-88-C-0043, School of Civil Engineering, Georgia Tech, May 1991.

Georgakakos, A. P., Operational tradeoffs in reservoir control, *Water Resources Research*, in press, 1993.

Georgakakos, A.P., and D.A. Vlatsa, Stochastic control of groundwater systems, *Water Resources Research*, 27(8), 2077-2090, 1991.

Glover, J.D., and F.C. Schweppe, Control of linear dynamic systems with set-constrained disturbances, IEEE Transactions of Automatic Control, 16(5), 411-423, 1971.

Grygier, J.C., and J.R. Stedinger, Algorithms for optimizing hydropower system operation, *Water Resources Research*, 21(1), 1-10, 1985.

Harris, C.J., Modelling and adaptive control of urban wastewater treatment plants, in *Environmental Systems Planning, Design, and Control*, Proceedings IFAC Symposium, Kyoto, Japan, 1977.

Kabouris , J.C., and A.P. Georgakakos, Optimal control of the activated sludge process, *Water Research*, 24(10), 1197-1208, 1990.

Kelman, J., J. R. Stedinger, L. A. Cooper, E. Hsu, and S.-Q. Yuan, Sampling stochastic dynamic programming applied to reservoir operation, *Water Resources Research*, 26(3), 447-454, 1990.

Loucks, D.P., J. R. Stedinger, and D. A. Haith, *Water resource systems planning and analysis*, Prentice Hall, 1981.

Ramanathan, V., The greenhouse theory of climatic change: a test by an inadvertent global experiment, *Science*, 240, 293-299, 1988.

Schneider, S. H., The greenhouse effect: science and policy, *Science*, 243, 771-781, 1989.

Schweppe, F.C., *Uncertain Dynamic Systems*, Prentice Hall, 1973.

Street-Perrott, F. A., and S. P. Harrison, Temporal variations in lake levels since 30,000 yr bp -- an index of the blobal hydrological change, in Climate Processes and Climate Sensitivity, eds. J. E. Hansen and T. Takahashi, American Geophysical Union *Monograph* 29, Washington D.C., 118-129, 1984.

Tasker, G. D., Some hydrological effects of cliamte change for the Apalachicola, Chattahoochee, and Flint river basins, *Proceedings* of the 1993 Georgia Water Resources Conference, at the Un. of Georgia, Athens, pg. 61-64, April 20 and 21, 1993.

Tennesee Valley Authority, Sensitivity of the Tennessee Valley Authority reservoir system to global climate change, *Technical Report* WR28-1-680-101, prepared by B. A. Miller and W.G. Brock, Norris Eng. Lab., 131p, 1988.

Trezos, T., and W.W-G. Yeh, Use of stochastic dynamic programming for reservoir management, *Water Resources Research*, 23(6), 983-996, 1987.

U.S. Army Corps of Engineers, Saylorville Lake: master reservoir regulation manual, Rock Island District, September 1983.

Wasimi, S.A., and P.K. Kitanidis, Real-time forecast and daily operation of a multireservoir system during floods by Linear Quadratic Gaussian Control, *Water Resources Research*, 19(6), 1511-1522, 1983.

Willis, R., and B.A. Finney, Optimal control of nonlinear groundwater hydraulics: Theoretical development and numerical experiments, *Water Resources Research*, 21(10), 1476-1482, 1985.

APPENDIX A

Lemma: Let Ω_x be a set characterized by

$$\Omega_x = \{X: X'\eta_i \le \phi_x(\eta_i),\ i = 1,\ldots,n_x\} \tag{A.1}$$

and **B** an invertible matrix. Then, the set Ω_y of all vectors **Y** such that **Y** = **B X** is defined by

$$\Omega_y = \{Y: Y'\theta_i \le \phi_x(\eta_i),\ i = 1,\ldots,n_x\},$$
$$\text{where } \theta_i = (B')^{-1}\eta_i,\ i = 1,\ldots,n_x. \tag{A.2}$$

Proof: Let (ABCDE) and (abcde) (Figure A.1) represent sets Ω_x and Ω_y respectively, and let vectors η_i and θ_i be perpendicular to hyperplanes AB and ab. To establish a relationship between η_i and θ_i, we start from the implications of orthogonality between these vectors and any other vector on the corresponding hyperplanes:

$$(\overline{ab})'\theta_i = 0 = (\overline{Ob} - \overline{Oa})'\theta_i = [B(\overline{OB}) - B(\overline{OA})]'\theta_i = (\overline{AB})'B'\theta_i$$
$$\textit{and} \tag{A.3}$$
$$(\overline{AB})'\eta_i = 0.$$

The above relationships suggest that vectors η_i and $\mathbf{B}'\theta_i$ are collinear (parallel) and consequently, a set of θ_i vectors perpendicular to the hyperplanes of Ω_y can be obtained from

$$B'\theta_i = \eta_i \rightarrow \theta_i = (B')^{-1}\eta_i. \tag{A.4}$$

To fully characterize Ω_y, we additionally need the support function values $\phi_m(\theta_i)$, θ_i, $i=1,\ldots,n_x$. Using the definition and the previous result, we obtain

$$\begin{aligned}
\phi_y(\theta_i) &= \underset{Y \in \Omega_y}{\textit{maximum}}\, Y'\theta_i = \underset{X \in \Omega_x}{\textit{maximum}}\, X'B'\theta_i \\
&= \underset{X \in \Omega_x}{\textit{maximum}}\, X'B'(B')^{-1}\eta_i = \underset{X \in \Omega_x}{\textit{maximum}}\, X'\eta_i \\
&= \phi_x(\eta_i)\,.
\end{aligned} \tag{A.5}$$

Even though η_i may be unit vectors, vectors θ_i may not have unit length. However, one can easily normalize them and scale the support function values accordingly:

$$\begin{aligned}
e_i &= \theta_i / |\theta_i| \\
\phi_y(e_i) &= \phi_y(\theta_i) / |\theta_i|\,,
\end{aligned} \tag{A.6}$$

where $\|\cdot\|$ represents vector norm.

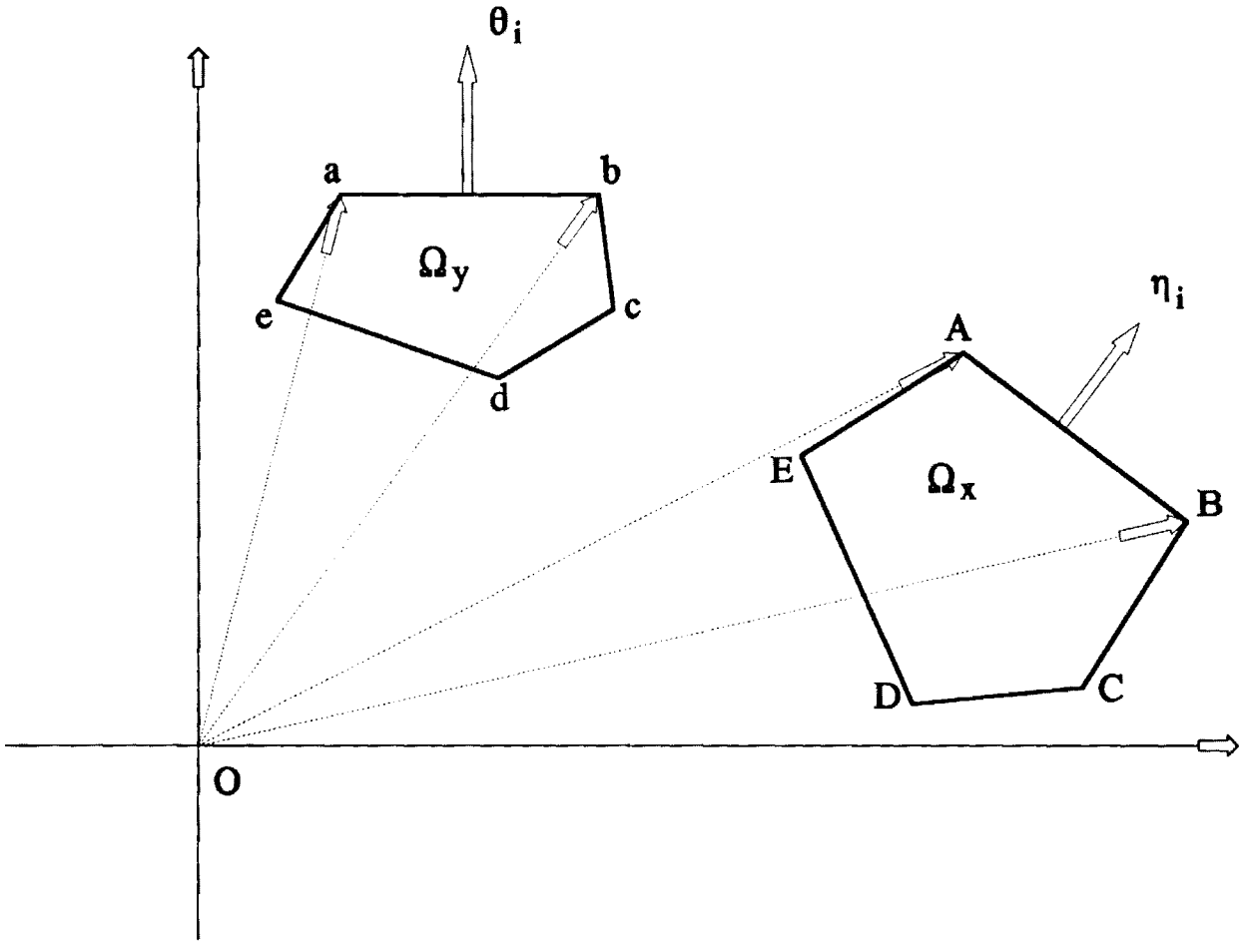

Figure A.1: Linear Set Transformations

APPENDIX B

B.1 ELEVATION (H) VERSE STORAGE (S) CURVE

Curve	$H=a\ln(S)+b(\ln(S))^2+c(\ln(S))^3+d(\ln(S))$
Units	H: feet S: acre-feet
Coefficient Values	a = -229.88257 b = 30.690016 c = -1.8662148 d = 0.046550048 e = 1584.045
Validity Range	H: 1035-1085 feet S: 867,984-2,551,667 acre-feet
Residual Error St. Dev.	0.0251 feet

B.2 TAILWATER ELEVATION (T) VS. OUTFLOW (Q) CURVE

Curve	*If* $0 \le Q < 4{,}000$ $t=dQ+e$ *If* $4{,}000 \le Q \le 14{,}000$ $t=a+b\ \ln(Q)+c\ (\ln(Q))^2$
Units	t: feet Q: cfs
Coefficient Values	a = 1,065.17688 b = -39.85679 c = 2.66528 d = 0.00175 e = 911.

Validity Range	t: 911-926 feet Q: 0-14,000 cfs
Residual Error St.Dev.	0.17 feet

B.3 POWER GENERATION CURVE FOR THE MAIN TURBINES

Curve	$Q=\exp(a+b\frac{P}{H}+c(\frac{P}{H})^2+d\ Ln(P)+e(Ln($ $+f\ Ln(H)+g(Ln(H))^2)$
Units	H: feet P: MW Q: cfs
Coefficients	a = 23.8732 b = 3.012357 c = 0.5261176 d = 1.1328914 e = -0.14784776 f = -7.4528786 g = 0.74083598
Validity Range	H: 103-170 feet P: 9.8-64.8 MW Q: 1600-5200 cfs
Residual Error St. Dev.	130 cfs

B.4 POWER GENERATION CURVE FOR THE SMALL TURBINE

Curve	$Q=\exp(a+b(\frac{P}{H})+c(\frac{P}{H})^2+dLn(P)+e(Ln($ $+f(Ln(H))+g(Ln(H))^2)$
Units	Q: cfs H: feet P: 10^5 KW
Coefficients	a = 17.7903784 b = 0.97088472 c = 0.53824066 d = 0.74410177 e = -0.0482565 f = -5.510093 g = 0.53260768
Validity Range	H: 102-172 feet P: 2.28-7.54 MW Q: 300-600 cfs
Residual Error St. Dev.	11.25 cfs

E-20-686
Del. No. 6

Georgia Tech

School of Civil Engineering

(404) 894-2240
(404) 894-2278

Georgia Institute of Technology
Atlanta, Georgia 30332-0355
USA
404•894•2201
404•894•2278 FAX

11 November 1993

Mary Wolf
Research Support Coordinator
CRB 17A
Campus Mail Code 0420

Dear Mary:

Enclosed please find (**1**) a copy of the final report submitted to the US Geological Survey for project E-20-686, and (**2**) a copy of the progress report submitted to the Atlanta Regional Commission for project E-20-X74. Please take my name off the deliverables-due list.

Sincerely,

Aris P. Georgakakos
Associate Professor -- Water Resources

IMPACTS OF GLOBAL WARMING ON RESERVOIR SYSTEMS

by

ARIS P. GEORGAKAKOS AND HUAMING YAO

FINAL REPORT: VOLUME I

United States Geological Survey
Award No. 14-08-0001-G1886

August 1993

School of Civil Engineering
Georgia Institute of Technology
Atlanta, Georgia 30332

FOREWORD

The research work described herein was primarily supported by the United States Geological Survey, Department of the Interior, under USGS award number 14-08-0001-G1886. Additional funding was provided by the United States Geological Survey, Water Resources Institute Program, as authorized by the Water Resources Research Act of 1984 (P.L. 98-242), under Project G-2013(02).

The views and conclusions contained in this document are those of the authors and should not be interpreted as necessarily representing the official policies, either expressed or implied, of the U.S. Government.

We would like to thank Professor Konstantine P. Georgakakos and Ms. Mary G. Mullusky for making the Modified Sacramento forecasting model available to our research. Their cooperative spirit and technical input made our work more meaningful. We are also grateful to Dr. Gary Tasker for expeditiously providing inflow traces reflecting GCM predictions for the Lake Lanier case study. Finally, we are indebted to Mr. William L. Pollock, USGS contracting officer, for kindly accommodating our research needs and reviewing the final reports.

CONTENTS

LIST OF FIGURES

Caption — Page No.

LIST OF TABLES

Caption Page No.

1. INTRODUCTION AND OVERVIEW

Climate change is an integral part of Earth's history. (For evidence of long-term changes in regional and global precipitation patterns, the reader is referred to *Bradley, et al., [1987]*, and *Barnett [1986]*; for evidence of change in lake levels, to *Street-Perrott and Harrison [1984]*; and for evidence of trends in global surface temperature, to *Schneider [1989]*. Recent models simulating the global circulation in the atmosphere and oceans predict substantial warming of the Earth's climate if current emission trends of CO_2, methane, and CFCs (Chlorofluorocarbons) continue throughout the world [*Ramanathan, 1988, and Schneider, 1989*]. While state-of-the-science general circulation models are far from being complete, and regional predictions are uncertain [*Bradley, et al., 1987, and Ramanathan, 1988*], there are two compelling reasons for studying the effects of climate change on water resources systems: The first is to determine the robustness of water resources to potential climatic change, and the second is to establish defensive measures for systems that are not resilient to such changes. This information is also useful to basin planners and policy makers who may have to reexamine existing water laws and reevaluate the potential of regional water resources.

Climate changes will undoubtedly impact reservoir system outputs. Wetter climates would potentially enhance energy generation and water availability but increase spillage and flooding. Conversely, drier climates would reduce energy generation and flooding and would strain water supplies and minimum flow requirements. The severity of the impact, however, would depend not just on the volumetric inflow increase or reduction but also on its variability and predictability.

Existing reservoir operation practices are largely based on rule-curves derived via simulation experiments on historical reservoir inflows. Such rules define reservoir zones for flood control and water conservation, and specify seasonal reservoir target levels. However, the validity of these rules is tied to historical weather patterns and can be challenged in the event of major climatic changes. A more appropriate procedure would be to use formal reservoir optimization models reflecting system objective priorities and operational constraints [*TVA, 1988*].

The scope of this research project is (1) to investigate the sensitivity of reservoir systems to potential climate changes and (2) to evaluate whether modern streamflow forecasting and reservoir control methods can be used to mitigate their adverse effects. This research was carried out jointly by two teams, one at Georgia Tech and another at the University of Iowa. The research tasks of both teams are summarized below:

(i) Development and testing of a reservoir control model suitable for a changing hydrologic environment;
(ii) Development and calibration of a physically-based rainfall-runoff model;
(iii) Streamflow forecasting by the rainfall-runoff model and the Extended Streamflow Prediction (ESP) method;
(iv) Coupling of the ESP forecasts with the control model;
(v) Development of historical analogues of potential climatic scenarios;
(vi) Development of inflow traces using General Circulation Model results;
(vii) Evaluation of the forecast-control procedure against current management practices in real-world case studies;
(viii) Comparative assessment of the above procedures in mitigating the effects of climatic changes.

The research procedures and findings of each task are described in the final project report which consists of two volumes. This report is Volume I emphasizing the work performed by the Georgia Tech project team, mainly involved with Tasks (i), (iv), (vi), (vii), and (viii). Volume II emphasizes the work performed by the University of Iowa research team and focuses on the remaining tasks. For continuity, each report reviews or contains elements of the other.

This report is organized as follows: In Chapter 2, we introduce a new control method for the management of uncertain dynamic systems. This method describes system uncertainty using sets rather than statistical methods and derives policies guarantying that the system will remain within its physical and operational constraints. This approach is named Set Control Approach (SCA) and is motivated by the possibility of climatic shifts which are incompatible with historical inflow records and, thus, statistical characterizations. In Chapter 3, we apply the Set Control Approach to common reservoir operation problems such as flood and drought management and energy generation, using the Savannah reservoir system as a case study. We argue that this approach is especially useful during critical hydrologic periods when the objective is not so much to optimize reservoir functions as it is to avoid system failure. In Chapter 4, we describe the coupled forecast-control procedure and evaluate its performance against typical operational practices in side-by-side simulation experiments. This application involves the upper Des Moines river basin and the Saylorville reservoir. The results favor the forecast-control model which proves to be much more effective in avoiding droughts and controlling floods. Using historical analogues of low, intermediate, and high streamflow periods, we also examine the impact of potential climate changes, and conclude that effective forecast-control procedures can mitigate their consequences. In the same chapter, we examine the sensitivity of Lake Lanier to inflow scenarios generated using available GCM results. Our analysis shows that the lake can be

drastically impacted by the potential changes, experiencing frequent and more severe droughts. A key issue, however, is predictability. If inflows are accurately predictable, lake operation can be robust even in adverse climatic conditions. We conclude in Chapter 5 with a summary of our contributions and findings and a short reference to areas needing further research.

2. THE SET CONTROL APPROACH

2.1 INTRODUCTION

Many water resources systems can be represented by difference equations describing the evolution of a pivotal quantity, called state, in response to controllable and uncontrollable inputs:

$$S(k+1) = A(k)\,S(k) + B(k)\,u(k) + G(k)\,w(k), \quad k=0,1,...,N-1, \tag{2.1}$$

where S(k) is the n_s-dimensional state vector; u(k) is the n_u-dimensional control vector, w(k) is the n_w-dimensional input vector; and A(k), B(k), and G(k) are $(n_s x n_s)$-, $(n_s x n_u)$-, and $(n_s x n_w)$-dimensional matrix coefficients respectively encoding the system layout and the interaction among its constituent elements. Examples include reservoir systems where state variables (states) represent reservoir storages, control variables (controls) represent releases or power generation hours, and input variables (inputs) represent reservoir inflows [*Loucks et al., 1980, Wasimi and Kitanidis, 1983, Trezos and Yeh, 1987, Georgakakos, 1989, and others*]; groundwater systems where states may represent hydraulic heads and/or pollutant concentrations, controls may represent pumping rates, and inputs may represent boundary conditions [see, among others, *Willis and Finney, 1985, Georgakakos and Vlatsa, 1991*]; and wastewater treatment processes where states are organic and inorganic constituent concentrations, controls are recycling rates, and inputs are wastewater loading characteristics [*Harris, 1977, Kabouris and Georgakakos, 1990, and others*]. Typically, the state and control vectors are restricted within certain acceptable ranges,

$$\begin{aligned} S^{\min}(k) \le S(k) \le S^{\max}(k), \quad k=0,1,...,N, \\ u^{\min}(k) \le u(k) \le u^{\max}(k), \quad k=0,1,...,N-1, \end{aligned} \tag{2.2}$$

where the upper and lower bounds may represent physical capacities or operational requirements.

The purpose of a control scheme is to determine control vector sequences able to guide the system to meet its objectives over an operational horizon. The control process is seriously complicated, however, by the fact that future system inputs are typically unknown. The traditional approach is to develop probabilistic input descriptions and optimize system performance in some average sense. However, this may not always be possible or sound.

In many cases, existing data records are simply not long enough to establish

probabilistic models, and we are forced to make assumptions which in the end cannot be corroborated. Even if sufficient data records exist, probabilistic input models and, consequently the associated control policies, become inadequate for extreme events where observations are sparse. In yet other circumstances, existing data records are atypical of future input realizations due to natural or anthropogenic causes (e.g., global climate changes). On such occasions, probabilistic input characterizations are inappropriate even in the average sense.

Lastly, stochastic control policies can at best guarantee that the system will not violate its bounds with certain probability. They cannot explicitly control the magnitude of the violation. During extreme input episodes, however, the operational goal becomes just that: Take permissible actions guaranteeing that system states stay within acceptable limits. Namely, during crises system operators are not at all concerned with optimizing system performance; they only wish to avoid actions that may endanger or damage the system.

To address the previous concerns, in this work we take a different tact. Rather than relying on probabilistic characterizations, we assume that future inputs are only restricted to belong in certain sets. The boundaries of these sets may represent minimum and maximum input estimates or other extreme levels, against which a sound operational policy is to be developed. In this framework, the purpose of the control process is to determine admissible controls such that system states remain within their acceptable limits as long as system inputs take on values from the specified input sets.

2.2 DYNAMIC PROGRAMMING SOLUTION

Glover and Schweppe [1971] and *Bertsekas and Rhodes [1971]* proposed a general solution for the previous problem using dynamic programming. The solution process is illustrated in Figure 2.1 and explained below:

In what follows, $\{\Omega_s(k), k=0,1,...,N\}$ denotes the sequence of acceptable state sets, $\{\Omega_u(k), k=0,1,...,N-1\}$ the sequence of admissible control sets, and $\{\Omega_w(k), k=0,1,...,N-1\}$ the input set sequence.

Define the modified state set $\Omega_m(N)$ as follows:

$$\Omega_m(N) = \{S \in R^n: [S + G(N-1)\, w(N-1)] \in \Omega_s(N), \quad \forall\, w(N-1) \in \Omega_w(N-1)\}. \tag{2.3}$$

Namely, $\Omega_m(N)$ contains all vectors S such that [S + G(N-1) w(N-1)] belongs to the

state set Ω_s(N) for any input vector in Ω_w(N-1).

Define the reduced state set Ω_r(N-1) as follows:

$$\Omega_r(N-1) = \{S \in \Omega_s(N-1) : \exists\, u(N-1) \in \Omega_u(N-1) : \quad [A(N-1)\, S + B(N-1)\, u(N-1)] \in \Omega_m(N) \}\,. \tag{2.4}$$

Namely, Ω_r(N-1) includes all acceptable state vectors S for which there exists an admissible control vector u(N-1) such that [A(N-1) S + B(N-1) u(N-1)] belongs to the modified state set Ω_m(N). The significance of the previous sets is that if the system state S(N-1) reaches set Ω_r(N-1), there exists an admissible control vector that can transfer it to an acceptable terminal state S(N) for any input vector in Ω_w(N-1).

One can proceed similarly to define the modified and reduced state sets for the previous time:

$$\Omega_m(N-1) = \{S \in R^n : [S + G(N-2)\, w(N-2)] \in \Omega_r(N-1)\,, \quad \forall\, w(N-2) \in \Omega_w(N-2) \}\,, \tag{2.5}$$

(Note that Ω_m(N-1) is defined based on Ω_r(N-1), not Ω_s(N-1).)

$$\Omega_r(N-2) = \{S \in \Omega_s(N-2) : \exists\, u(N-2) \in \Omega_u(N-2) : \quad [A(N-2)\, S + B(N-2)\, u(N-2)] \in \Omega_m(N-1) \}\,. \tag{2.6}$$

Thus, if the system reaches set Ω_m(N-2), there exist control vectors u(N-2) and u(N-1) such that states S(N-1) and S(N) remain within the acceptable limits for any input realizations {w(N-2), w(N-1)} from the specified input sets.

The previous considerations can recursively be repeated in the reverse time direction, k = N-3, N-4, ... , 0. The problem has a feasible solution (i.e., there exist a control sequence able to keep the state vectors within their acceptable sets) if the sets thus derived are nonempty and the reduced state set Ω_r(0) includes the initial state vector S(0). Note, however, that the previous solution process does not determine which controls to use. Specific control vectors can be selected only as the system evolves and the state variable values become known. This and other related issues will further be discussed in Section 2.5.

As usual, dynamic programming leads to a theoretically elegant solution. The practical implementation of this solution, however, presents an equally elegant

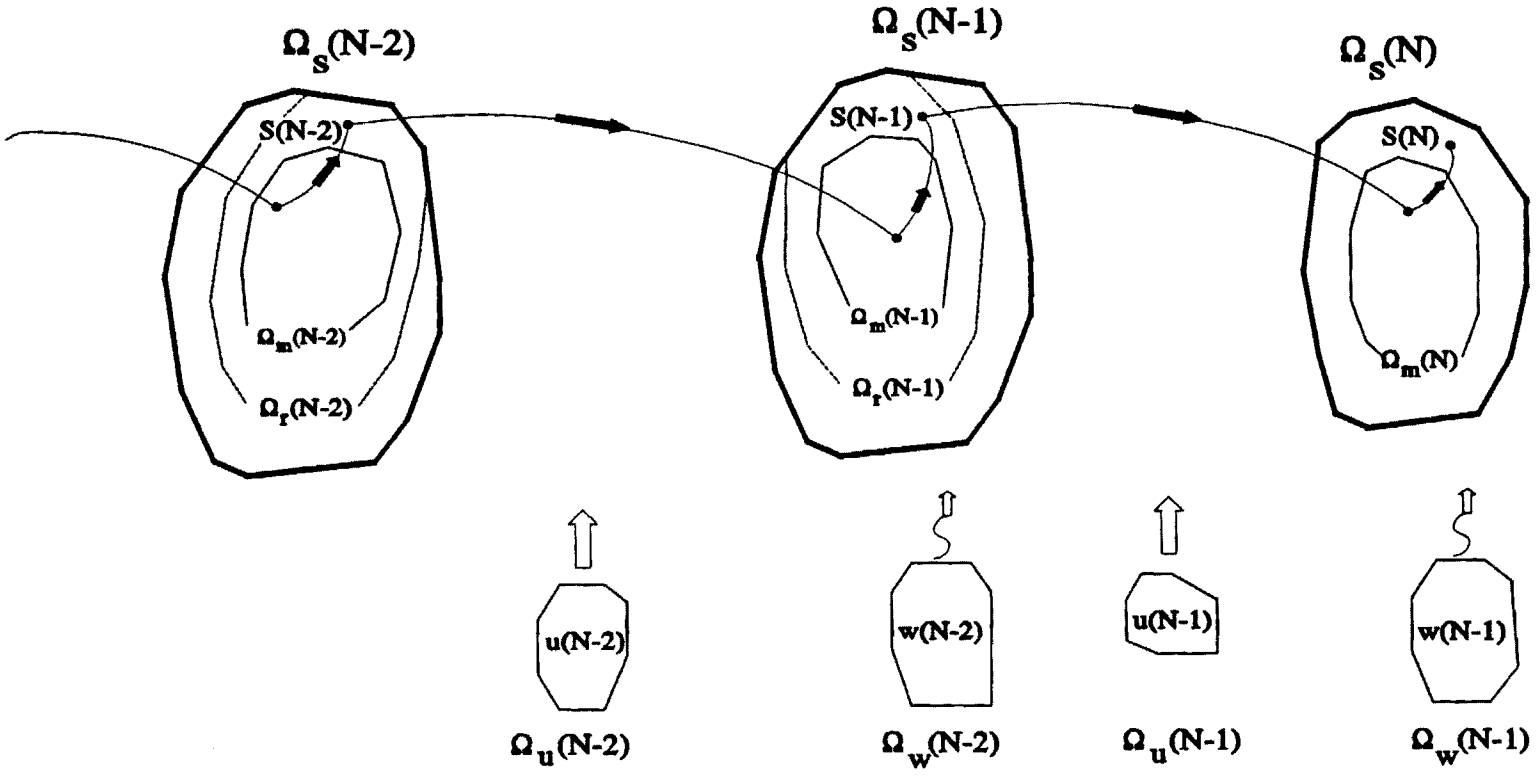

Figure 2.1: Dynamic Programming Solution of the Set Control Problem

challenge. *Glover and Schweppe [1971]* and *Bertsekas and Rhodes [1971]* proposed ellipsoidal approximation algorithms based on Schweppe's bounding ellipsoidalapproximation theory [*Schweppe, 1973*]. The idea is to approximate all sets by bounding ellipsoids and develop recursive relationships for the computation of the modified and reduced state sets. Since ellipsoids are characterized by their center vector and principal axes, the set computation is reduced to a recursive computation of these attributes. However, the required approximations quickly result in empty modified and reduced state sets, and the algorithms falsely indicate infeasibility.

Another approach is to define state, control, and input sets as convex polyhedra and develop efficient procedures to compute the modified and reduced state sets. The modified and reduced state sets then are also convex polyhedra defined by their perpendicular vectors and support functions. This is the approach we adopt herein because it is exact and naturally suitable for water resources systems.

Our work follows that of *Bertsekas and Rhodes [1971]* but also contains several extensions and refinements. A significant extension is the applicability to systems with unequal number of state and control variables, a case that arises frequently in water resources systems especially in the management of groundwater aquifers and wastewater treatment plants. Other new contributions include procedures for the computation of the reduced state set, the identification of set infeasibility and hyperplane redundancy, and the determination of the admissible control set in real time. Furthermore, the proofs included in this article are original and are based on the support function concept for convex sets presented by *Schweppe [1973]*. Finally, a comparison of the polyhedral and ellipsoidal approaches quantifies the suboptimality of the latter and illustrates how quickly it becomes infeasible.

2.3 DERIVATION OF THE MODIFIED STATE SET $\Omega_m(k)$

The modified state set $\Omega_m(k)$, k=N, N-1, ..., 1, is defined by Equation (2.5). $\Omega_m(k)$ includes all state vectors $\mathbf{X}$ such that vectors $[\mathbf{X} + \mathbf{G}(k-1)\mathbf{w}(k-1)]$ belong to the reduced state set $\Omega_r(k)$ for any (or all) $\mathbf{w}(k-1)$ in $\Omega_w(k-1)$. Let $\Omega_r(k)$ be a convex polyhedron in the n_s-dimensional space $\mathbf{R}^{n_s}$ of the state vector elements S_1, S_2, ..., and S_{n_s}. (A polyhedron is a set bounded by hyperplanes. A hyperplane is a straight line in $\mathbf{R}^2$ and a two-dimensional plane in $\mathbf{R}^3$. A set Ω is convex if the line segment joining any two points in Ω also belongs in Ω.) Furthermore, let the reduced state set $\Omega_r(k)$ be known by its support function $\phi_r(\eta)$. (This information is available by the computations of the following section.) Namely, let $\Omega_r(k)$ be the following set (*Schweppe, 1973*; *Bishop and Phelps, 1963*)

$$\Omega_r(k) = \{S:\ S'\eta \le \phi_r(\eta),\ \textit{for all}\ \eta,\ \eta'\eta = 1\},$$
$$\text{where } \phi_r(\eta) = \underset{\text{all } S \in \Omega_r(k)}{\text{maximum}}\{S'\eta\}. \tag{2.7}$$

Figure 2.2 provides a graphical interpretation of the support function in two dimensions and demonstrates that a convex polyhedron can be completely defined by the support function values at only a finite number of vectors η: the vectors η_i perpendicular to its bounding hyperplanes. Thus, we will assume that $\Omega_r(k)$ is defined as follows:

$$\Omega_r(k) = \{S:\ S'\eta_i \le \phi_r(\eta_i),\ i = 1,\ldots,n_r\}, \tag{2.8}$$

where n_r is the number of bounding hyperplanes. The use of unit vectors is only a matter of convenience and, especially in the case of polyhedra, non-unit vectors will also serve our purpose as long as the support function $\phi()$ is defined accordingly.

By our earlier definitions, the reduced state set $\Omega_r(k)$, the modified state set $\Omega_m(k)$, and the input set $\Omega_w(k-1)$ are related as follows:

$$\Omega_r(k) = \{S:\ S = X + G(k-1)w(k-1),\ \text{for any } X \in \Omega_m(k) \text{ and any } w(k-1) \in \Omega_w(k-1)\}. \tag{2.9}$$

The modified state set $\Omega_m(k)$ will be completely defined if its support function value can be computed for any vector η. Let $\phi_m()$ and $\phi_w()$ represent the support functions of the modified state and input sets respectively. Then,

$$\begin{aligned}\phi_r(\eta) &= \underset{\substack{X \in \Omega_m(k)\\ w(k-1) \in \Omega_w(k-1)}}{\text{maximum}}\ [X + G(k-1)w(k-1)]'\eta \\ &= \underset{X \in \Omega_r(k)}{\text{maximum}}\ X'\eta + \underset{w(k-1) \in \Omega_w(k-1)}{\text{maximum}}\ w'(k-1)G'(k-1)\eta \\ &= \phi_m(\eta) + \phi_w[G'(k-1)\eta], \\ &\text{all } \eta'\eta = 1,\end{aligned} \tag{2.10}$$

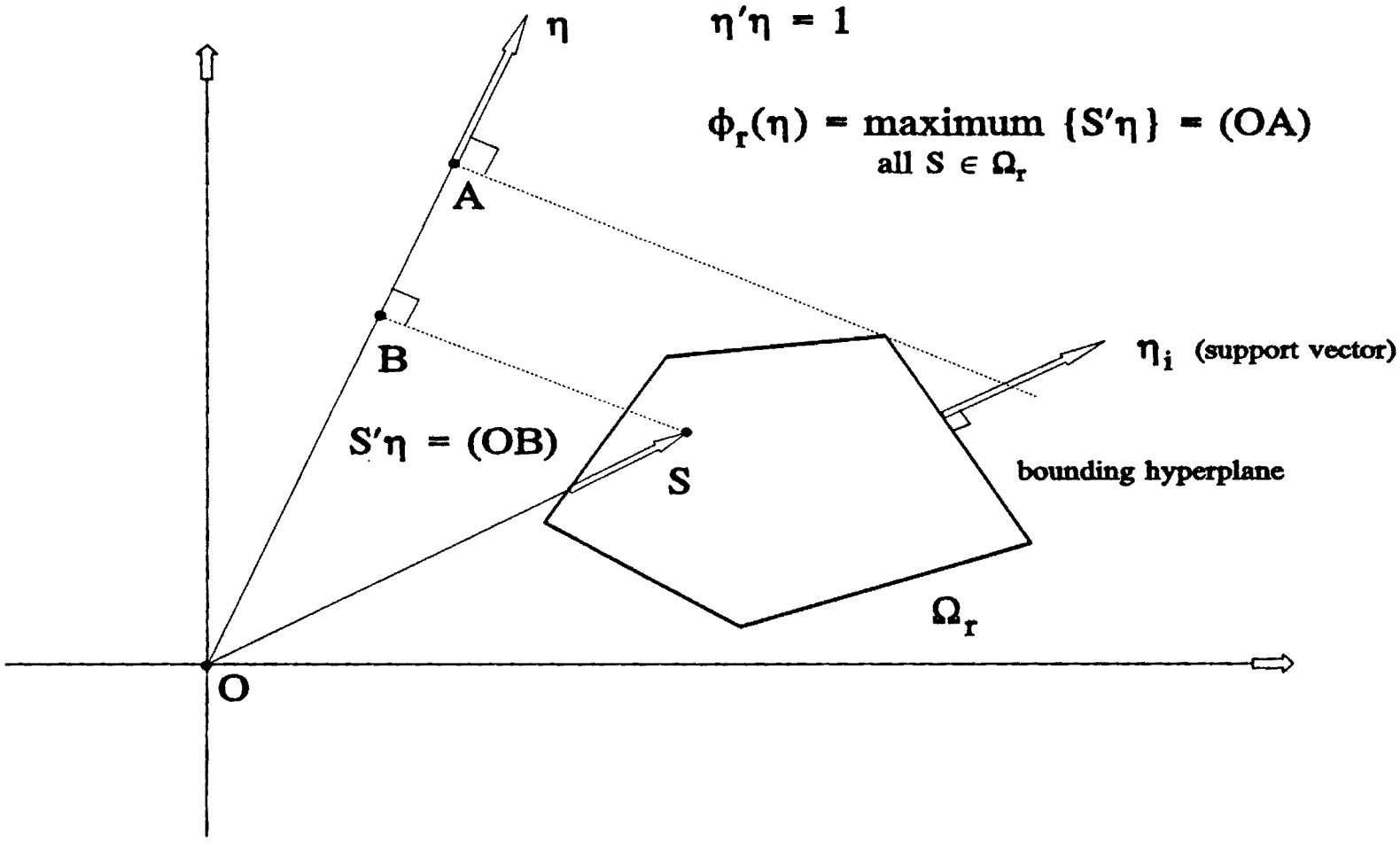

Figure 2.2: The Support Function of a Convex Polyhedron

and therefore,

$$\phi_m(\eta) = \phi_r(\eta) - \phi_w[G'(k-1)\eta], \text{ for all } \eta'\eta = 1. \quad (2.11)$$

Although $\Omega_m(k)$ is now fully defined, it would be computationally more economical to restrict Equation (2.11) to vectors η perpendicular to its bounding hyperplanes. The hyperplanes of $\Omega_m(k)$ are parallel to those of $\Omega_r(k)$, and consequently vectors $\{\eta_i, i=1, ..., n_r\}$ associated with Equation (2.8) are sufficient for the definition of $\phi_m()$ and $\Omega_m(k)$.

Figure 2.3 provides a graphical proof of this fact by deriving set $\Omega_m(k)$ from $\Omega_r(k)$ and $\Omega_{Gw}(k-1)$ in two dimensions. ($\Omega_{Gw}(k-1)$ is the set including all vectors Gw(k-1).) Points (vectors) A, B, C, D, and E are on the boundary hyperplanes of $\Omega_r(k)$. The dashed polygons originating from each point are obtained by subtracting the vectors defining the $\Omega_{Gw}(k-1)$ corner points. Set $\Omega_m(k)$ is the polygon circumscribed by the interior corner points of the dashed polygons, as A, B, C, D, and E trace the periphery of $\Omega_r(k)$. By construction, if a point (vector) belongs to $\Omega_m(k)$, adding any vector within $\Omega_{Gw}(k-1)$ generates points (vectors) inside $\Omega_r(k)$.

In summary, the modified state set $\Omega_m(k)$ can be determined as follows:

$$\Omega_m(k) = \{X: X'\eta_i \le \phi_m(\eta_i) = \phi_r(\eta_i) - \phi_w[G'(k-1)\eta_i],\ i = 1,...,n_r\},$$

where η_i, $i = 1,...,n_r$, are perpendicular to the bounding hyperplanes of $\Omega_r(k)$. (2.12)

$\phi_w[G'(k-1)\eta_i]$ can be specified by solving the following linear programming (LP) problem:

$$\underset{\text{all } w}{\text{Maximize}}\ J = w'G'(k-1)\eta_i$$

$$\text{subject to} \quad (2.13)$$

$$w'e_j \le \phi_w(e_j),\ j = 1,...,n_w,$$

where e_j, $j=1,...,n_w$, represent unit vectors perpendicular to the bounding hyperplanes of $\Omega_w(k-1)$. $\phi_w[G'(k-1)\eta_i)$ is equal to the optimum value of J.

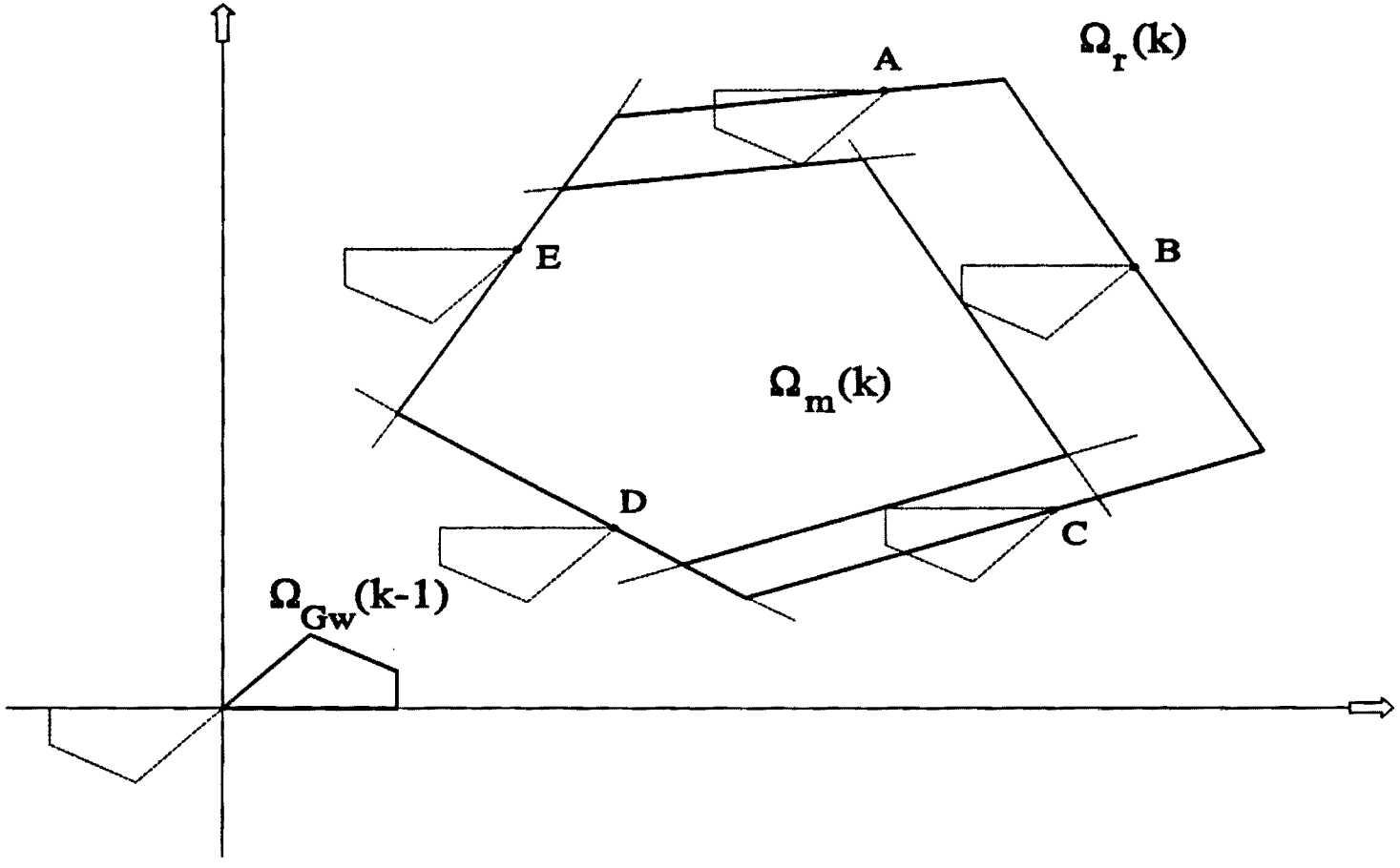

Figure 2.3: Derivation of $\Omega_m(k)$

It is finally possible that set $\Omega_m(k)$ is empty or has fewer bounding hyperplanes than $\Omega_r(k)$. Namely depending on the shape of $\Omega_{Ow}(k-1)$, the previous operations may result in an empty $\Omega_m(k)$ set or cause some hyperplanes to vanish. (One can easily envision this possibility with the aid of Figure 2.3.) If set $\Omega_m(k)$ is empty, then the procedure stops at time k indicating that there does not exist an admissible control sequence that can meet the specified constraints. If $\Omega_m(k)$ is nonempty, discarding unnecessary hyperplanes is generally desirable to reduce the computational overhead. To test for these two conditions, let $\zeta(\zeta_1, \zeta_2,..., \zeta_{n_z})$ be any fixed unit vector and $X(X_1, X_2,..., X_{n_z})$ be any vector in $\Omega_m(k)$. The projection of X on ζ is given by the inner product

$$J = X'\zeta = X_1\zeta_1 + X_2\zeta_2 + \cdots + X_{n_z}\zeta_{n_z}. \tag{2.14}$$

The vector X^* whose coordinates maximize (or minimize) J is a corner point of $\Omega_m(k)$. (For example, (OC') in Figure 2.4 is the maximum projection length of all points in $\Omega_m(k)$.) Thus, a corner point can be found by solving the following LP problem: Find $X(X_1, X_2,..., X_{n_z})$ which maximize/minimize J given by Equation (2.14) subject to inequalities (2.12). If this problem has no feasible solution, set $\Omega_m(k)$ is empty. Furthermore, if any single inequality is replaced by a strict equality, the solution of this Linear Program will provide a corner point on the associated hyperplane. However, if the hyperplane is redundant, LP will indicate infeasibility. The corresponding inequality and hyperplane can then be discarded. This procedure should be repeated n_r times to test the redundancy of all hyperplanes. One can avoid multiple LP solutions by selecting a vector ζ which is not perpendicular to any hyperplane. To guarantee this fact, ζ should not be collinear with any vector η_i, $i=1,...,n_r$.

The previous procedure identifies hyperplanes which are completely outside the set $\Omega_m(k)$. However, redundant hyperplanes are also those that pass through a single corner point of this set. To discard these hyperplanes, one can repeat the above procedure using two unit vectors that are negative of one another. If both problems are feasible and have the same solution, the associated hyperplane should be discarded.

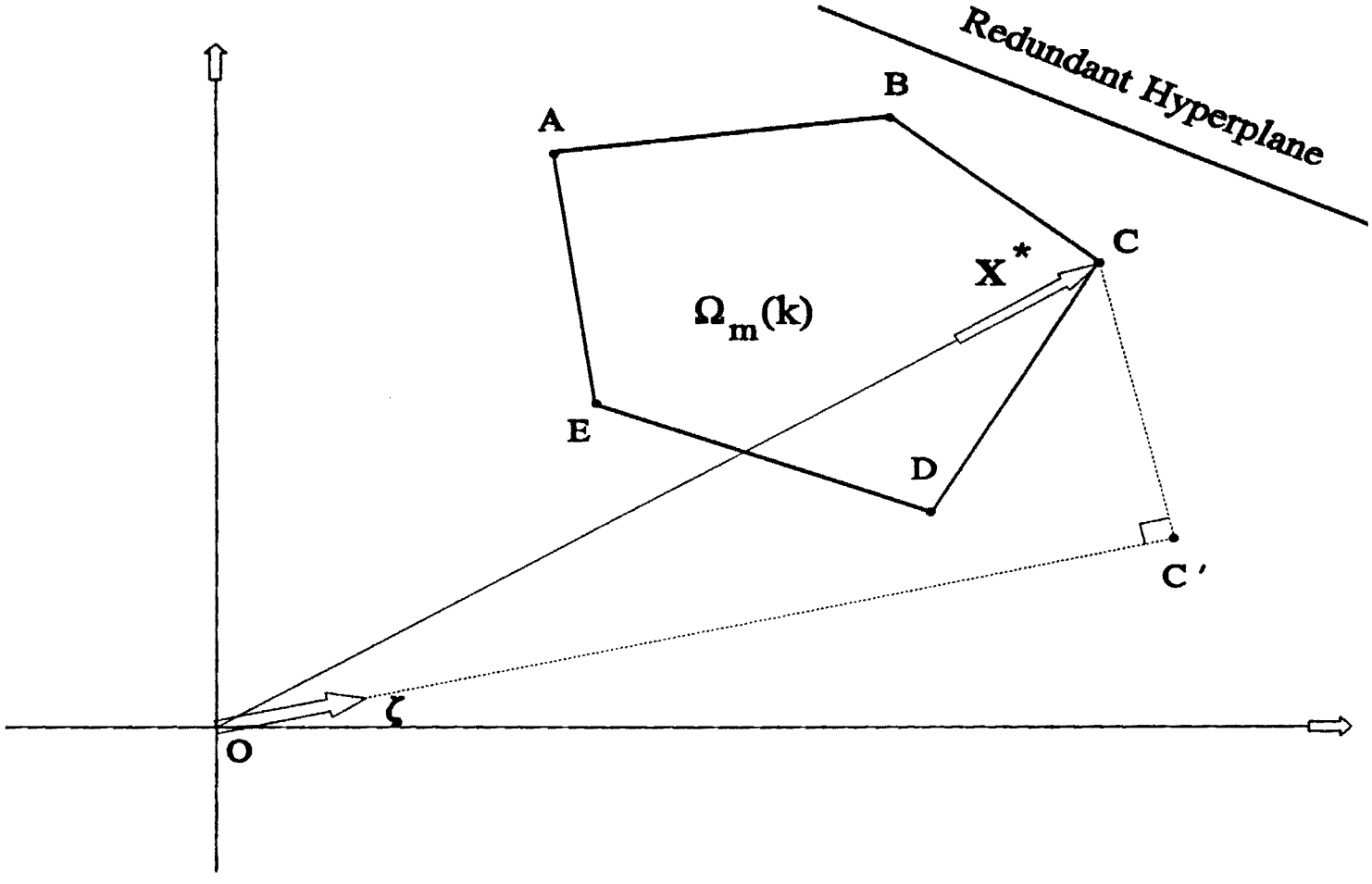

Figure 2.4: Determining the Corner Points of $\Omega_m(k)$

2.4 DERIVATION OF THE REDUCED STATE SETS $\Omega_r(k)$

The reduced state set $\Omega_r(k)$, k=N-1, N-2, ..., 0, was defined as follows (cf. Equation (2.6)):

$$\Omega_r(k) = \{S \in \Omega_s(k) : \exists\, u(k) \in \Omega_u(k) : [A(k)\,S + B(k)\,u(k)] \in \Omega_m(k+1)\}\,. \tag{2.15}$$

The derivation of $\Omega_r(k)$ involves the following set operations: (1) Derivation of set $\Omega_{Bu}(k)$ including all vectors $\mathbf{B}(k)\mathbf{u}(k)$ such that $\mathbf{u}(k) \in \Omega_u(k)$; (2) Derivation of set $\Omega_{AS}(k)$ with all vectors $\mathbf{X}$ such that there exist vectors (at least one) in $\Omega_{Bu}(k)$ that transfer $[\mathbf{X} + \mathbf{B}(k)\mathbf{u}(k)]$ in $\Omega_m(k+1)$; (3) Derivation of set $\Omega_s(k)$ including all vectors $\mathbf{S}$ such that $\mathbf{A}(k)\mathbf{S} \in \Omega_{AS}(k)$; and (4) Derivation of $\Omega_r(k) = \Omega_s(k) \cap \Omega_S(k)$ (set intersection), where $\Omega_S(k)$ denotes the admissible state set (depicted in Figure 2.1).

For the first set operation, the problem is as follows: Given that $\Omega_u(k)$ is defined by

$$\Omega_u(k) = \{u:\ u'\mathbf{v}_i \le \phi_u(\mathbf{v}_i),\ i = 1,\ldots,n_u\}\,, \tag{2.16}$$

namely, by the values of its support function at the vectors perpendicular to its bounding hyperplanes, find the vectors perpendicular to the hyperplanes of $\Omega_{Bu}(k)$ and the associated support function values. The following result holds for the case where $\mathbf{B}(k)$ is an invertible matrix (see appendix for a proof):

$$\begin{gathered}\Omega_{Bu}(k) = \{X:\ X'\theta_i \le \phi_u(\mathbf{v}_i),\ i = 1,\ldots,n_u\}\,,\\ \text{where } \theta_i = (B'(k))^{-1}\mathbf{v}_i,\ i = 1,\ldots,n_u\,.\end{gathered} \tag{2.17}$$

If there are more $\mathbf{B}(k)$ rows than columns (most usual case when $\mathbf{B}(k)$ is not invertible), one can still use the previous result by augmenting $\mathbf{B}(k)$ (and the state equations) to include columns corresponding to fictitious control variables with empty feasible ranges. This technique is further discussed and illustrated in the companion article. If the rank of $\mathbf{B}(k)$ is less than the dimension of its rows or columns, in all likelihood the state equations are ill-posed and some may be redundant.

The second set operation calls for the derivation of set $\Omega_{AS}(k)$ with all vectors $\mathbf{X}$ such that there exist vectors in $\Omega_{Bu}(k)$ which transfer $[\mathbf{X} + \mathbf{B}(k)\mathbf{u}(k)]$ in $\Omega_m(k+1)$. The above is equivalent to finding a set $\Omega_{AS}(k)$ such that for all vectors $\mathbf{Z} \in \Omega_m(k+1)$ and $\mathbf{Y} \in \Omega_{-Bu}(k)$, there holds $\mathbf{Z} + \mathbf{Y} = \mathbf{X} \in \Omega_{AS}(k)$. The equivalence of these two

statements can be easily demonstrated by showing that the set $\Omega_{AS}(k)$ corresponding to the first statement is a subset of the set corresponding to the second and vice-versa. Thus, $\Omega_{AS}(k)$ is the vector sum of $\Omega_m(k+1)$ and $\Omega_{-Bu}(k)$, where $\Omega_{-Bu}(k)$ is the set including all vectors $[-\mathbf{B}(k)\mathbf{u}(k)]$. As shown in the previous section (Equation 2.10), the support function of $\Omega_{AS}(k)$ can then be computed from the support functions of $\Omega_m(k+1)$ and $\Omega_{-Bu}(k)$ as follows:

$$\begin{aligned}
\phi_{AS}(\eta) &= \max_{\substack{Z \in \Omega_m(k+1) \\ Y \in \Omega_{-Bu}(k)}} [Z + Y]'\eta \\
&= \max_{Z \in \Omega_m(k+1)} Z'\eta + \max_{Y \in \Omega_{-Bu}(k)} Y'\eta \\
&= \phi_m(\eta) + \phi_{-Bu}(\eta), \\
&\text{all } \eta'\eta = 1 .
\end{aligned} \tag{2.18}$$

In the above equation, the support vectors and function of $\Omega_{-Bu}(k)$ have not been defined. However, using the support function definition (2.7), one can easily show that the support vectors of $\Omega_{-Bu}(k)$ are negatives of the $\Omega_{Bu}(k)$ support vectors, while the support function values remain the same.

The minimal set of vectors η where the support function has to be evaluated includes all vectors perpendicular to the hyperplanes of both $\Omega_m(k+1)$ and $\Omega_{-Bu}(k)$. Thus, $\Omega_{AS}(k)$ is defined by

$$\begin{aligned}
\Omega_{AS}(k) = \{X:\ & X'\eta_i \le \phi_m(\eta_i) + \phi_{-Bu}(\eta_i),\ i = 1,\ldots,n_m,\ \textit{and} \\
& X'(-\theta_j) \le \phi_m(-\theta_j) + \phi_{-Bu}(-\theta_j),\ j = 1,\ldots,n_u\} ,
\end{aligned} \tag{2.19}$$

where $\phi_m(\eta_i)$, $i=1,\ldots,n_m$, are provided by the computations of the previous section (Equation 2.12 and discussion thereafter) and $\phi_{-Bu}(-\theta_j)$, $j=1,\ldots,n_u$, are equal to $\phi_{Bu}(\theta_j)$, $j=1,\ldots,n_u$ as explained earlier. Figure 2.5 illustrates how $\Omega_{AS}(k)$ is graphically constructed in two dimensions. Let ABCD represent set $\Omega_m(k+1)$. Hyperplanes A′D′, D′C′, C′B′, and A′B′ (solid lines) of $\Omega_{AS}(k)$ are respectively parallel to hyperplanes AD, DC, CB, and AB of $\Omega_m(k+1)$ and include points which can be transferred to $\Omega_m(k+1)$ only by a single corner point of $\Omega_{Bu}(k)$. The additional hyperplanes needed to define $\Omega_{AS}(k)$, namely, A′A′, A′A′, C′C′, and B′B′, are parallel to those of $\Omega_{Bu}(k)$ which is the set symmetric to $\Omega_{Bu}(k)$ about the origin. The sets resulting by subtracting the corner point vectors of $\Omega_{Bu}(k)$ from each corner point

of $\Omega_m(k+1)$ (dashed line polygons in Figure 2.5) are simply parallel translations of $\Omega_{Bu}(k)$ as though each corner point of $\Omega_m(k+1)$ were the origin of the axes. Namely, $\Omega_{AS}(k)$ is the polyhedron circumscribed by the exterior corner points of $\Omega'_{Bu}(k)$ as it traces the periphery of $\Omega_m(k+1)$.

The third set operation calls for determining set $\Omega_o(k)$ from $\Omega_{AS}(k)$. By noting that $\mathbf{S} = \mathbf{A}^{-1}(\mathbf{A}\,\mathbf{S})$ and applying the lemma associated with Equation (2.17), set $\Omega_o(k)$ can be determined by

$$\Omega_o(k) = \{X:\ X'\rho_i \le \phi_{AS}(e_i),\ i = 1,\ldots,n_{AS}\},$$
$$\text{where } \rho_i = A'(k)\,e_i,\ i = 1,\ldots,n_{AS}, \tag{2.20}$$

and e_i, $i=1,\ldots,n_{AS}$, includes all vectors η_i, $i=1,\ldots,n_m$, and θ_j, $j=1,\ldots,n_u$, associated with Equation (2.19) ($n_{AS}=n_m+n_u$).

Finally, set $\Omega_r(k)$ can be derived as the intersection of $\Omega_o(k)$ and $\Omega_S(k)$. In mathematical form, this intersection is determined by

$$\Omega_r(k) = \{X: X'\tau_i \le \text{minimum}[\phi_S(\tau_i), \phi_o(\tau_i)],\ i = 1,\ldots,n_S, \text{ and}$$
$$X'\rho_j \le \text{minimum}[\phi_S(\rho_j), \phi_o(\rho_j)],\ j = 1,\ldots,n_o\}, \tag{2.21}$$

where $\phi_S()$, τ_i, $i=1,\ldots,n_S$, represent the support function and associated vector set for $\Omega_S(k)$, and $\phi_o()$, ρ_j, $j=1,\ldots,n_o$, represent the support function and associated vector set for $\Omega_o(k)$. The validity of the above statement is illustrated in Figure 2.6.

As with the modified state set, some of the hyperplanes associated with the reduced state set computed above may be redundant and should be discarded using the procedure outlined at the end of the previous section.

2.5. Real-Time Implementation

The computation of the modified and reduced state sets can thus proceed from the terminal time N to the initial time 0. The problem has a solution (namely, there exists a feasible control sequence that guarantees that the state variables will remain within their admissible limits for any input realization within the specified input sets) if the reduced state set $\Omega_r(0)$ at time 0 is nonempty and includes the initial state vector S(0). The determination of these solutions has yet to be discussed.

Assuming that S(0) is known, the state equation describes the transition to state S(1)

by

$$S(1) = A(0)\,S(0) + B(0)\,u(0) + G(0)\,w(0)\,. \tag{2.22}$$

The issue here is to determine an admissible control subset whose vectors guarantee that whatever the input w(0), the state S(1) will be within the reduced state set $\Omega_r(1)$. Equivalently, this subset should be such that vector [A(0)S(0)+B(0)u(0)] always belongs in the modified state set $\Omega_m(1)$. The set $\Omega_{Bu}(0)$ that satisfies this requirement is obviously a parallel translation of $\Omega_m(1)$ by the vector A(0)S(0). More formally, $\Omega_{Bu}(0)$ can be defined by

$$\Omega_{Bu}(0) = \{X:\ X'\eta_i \le \phi_m(\eta_i) - S'(0)\,A'(0)\,\eta_i,\ i = 1,\ldots,n_m\}\,, \tag{2.23}$$

where $\phi_m()$, η_i, i=1,...,n_m, represent the support function and associated vector set for $\Omega_m(1)$ already determined by the DP procedure.

The admissible control set $\Omega_c(0)$ can finally be obtained from the lemma associated with Equation (2.17) and an intersection with $\Omega_u(0)$ (Equation 2.21). Any control vector in the set $\Omega_c(0)$ guarantees that (**a**) state S(1) will be feasible and (**b**) there will exist **u**(k), k=1,2,...,N-1, vector sequences which will produce feasible states all through the control horizon. Subsequent sets $\Omega_c(k)$, k=1,2,...,N-1, can be obtained by similar considerations as the system evolves and the state values S(k), k=1,2,...,N-1, become known.

2.6. AN EXAMPLE

To provide some computational insight for the theory presented earlier, we first solve a two-dimensional problem with four time steps. The state equation is as follows:

$$\begin{bmatrix} S_1(k+1) \\ S_2(k+1) \end{bmatrix} = \begin{bmatrix} 1 & 0 \\ 0 & 1 \end{bmatrix}\begin{bmatrix} S_1(k) \\ S_2(k) \end{bmatrix} + \begin{bmatrix} -1 & 0 \\ 1 & -1 \end{bmatrix}\begin{bmatrix} u_1(k) \\ u_2(k) \end{bmatrix} + \begin{bmatrix} 1 & 0 \\ 0 & 1 \end{bmatrix}\begin{bmatrix} w_1(k) \\ w_2(k) \end{bmatrix},$$
$$k = 0,1,2,3\,, \quad \begin{bmatrix} S_1(0) = 4 \\ S_2(0) = 4 \end{bmatrix}, \tag{2.24}$$

where the state, input, and control sets are shown below:

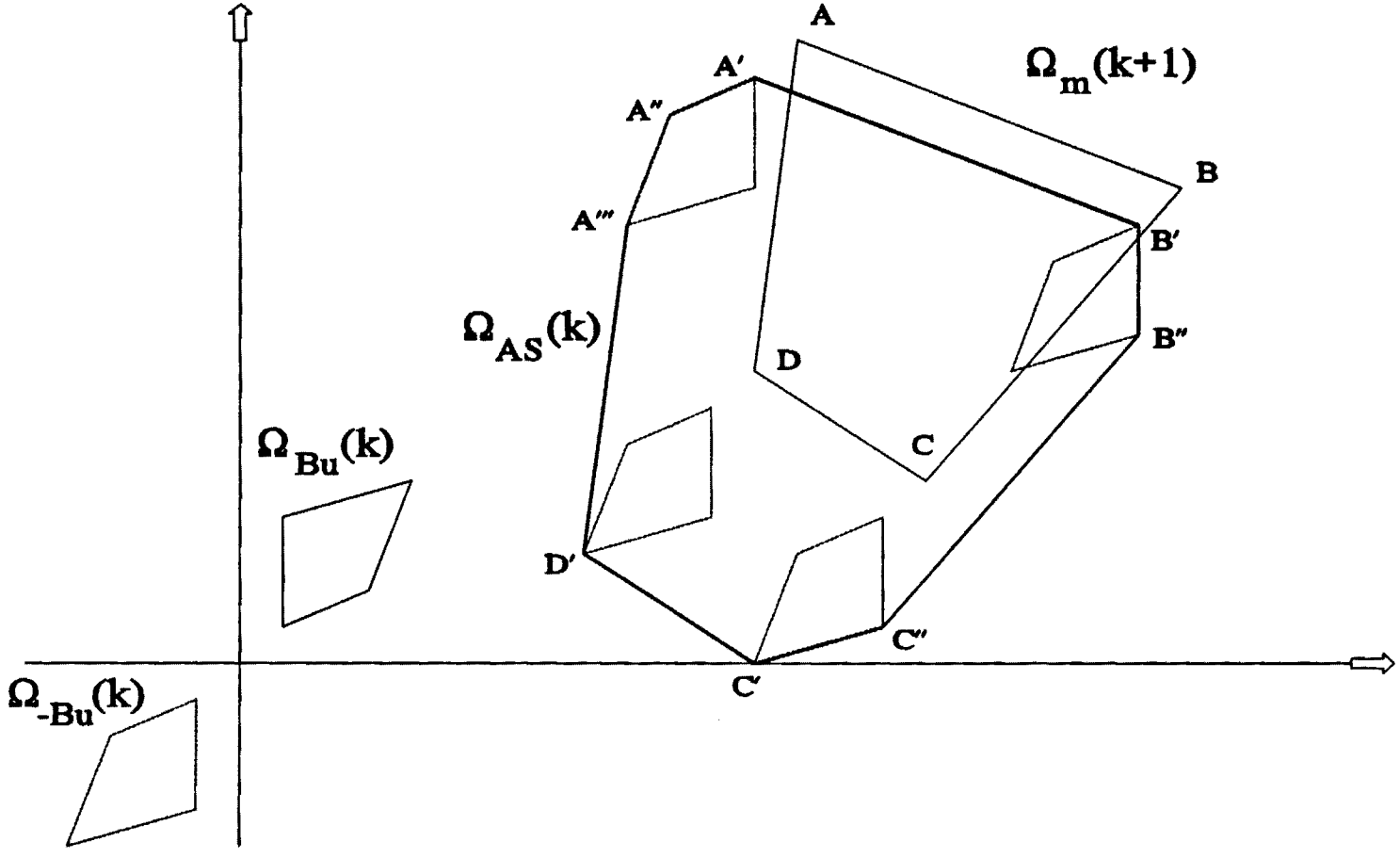

Figure 2.5: Derivation of $\Omega_{AS}(k)$

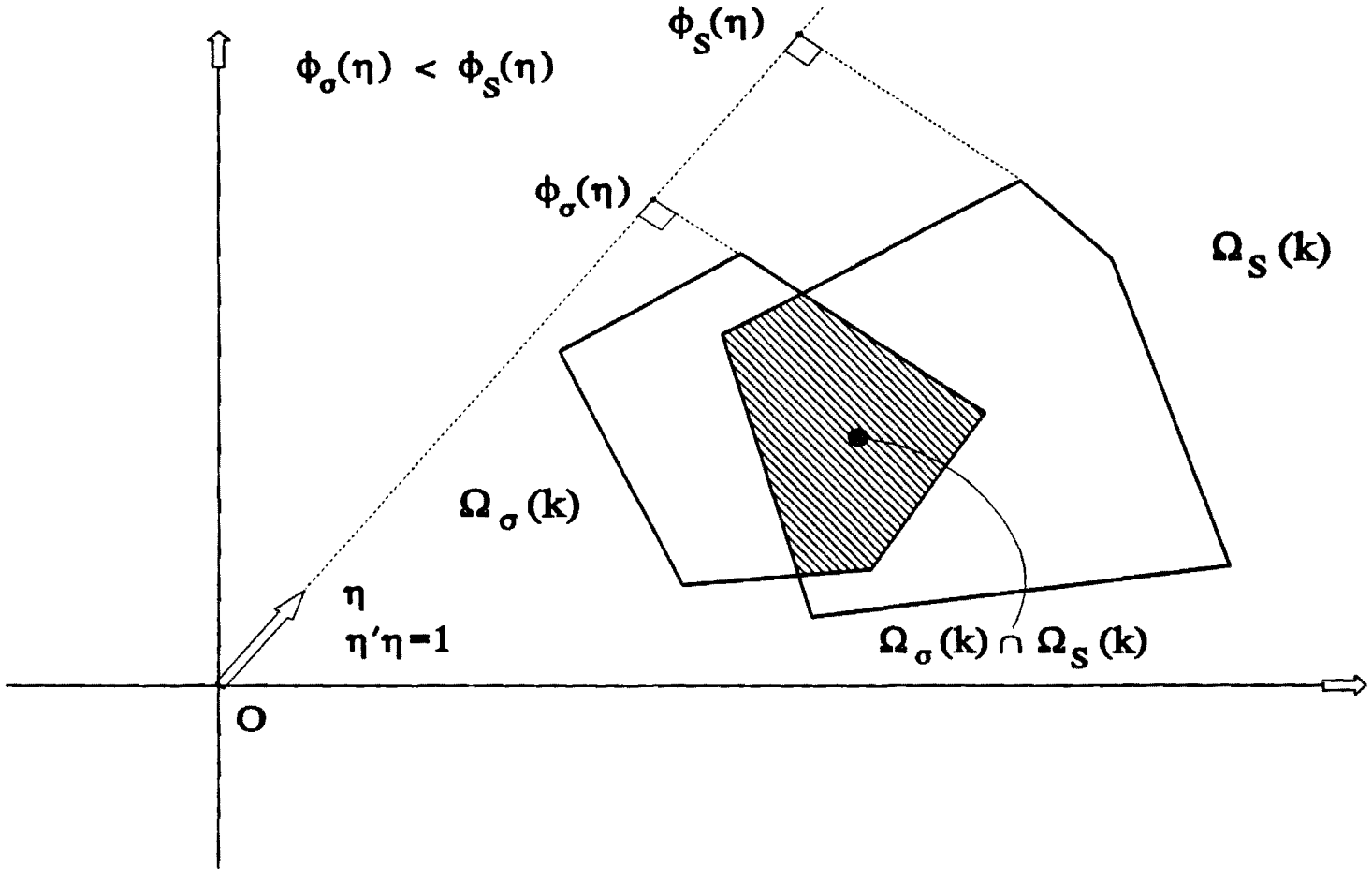

Figure 2.6: Set Intersection

$$\Omega_S(k) = \begin{Bmatrix} 0 \le S_1(k) \le 10 \\ 0 \le S_2(k) \le 15 \end{Bmatrix}, \; k = 0,1,2,3,4,$$

$$\Omega_w(k) = \begin{Bmatrix} 0 \le w_1(k) \le 3 \\ 0 \le w_2(k) \le 3 \end{Bmatrix}, \; k = 0,1,2,3, \tag{2.25}$$

$$\Omega_u(k) = \begin{Bmatrix} 0 \le u_1(k) \le 2 \\ 0 \le u_2(k) \le 2 \end{Bmatrix}, \; k = 0,1,2,3.$$

It is noted that the above formulation could represent a two-reservoir cascade. In hyperplane form, the constraints become

$$\underset{\Omega_S}{\begin{bmatrix} 1\,S_1(k) + 0\,S_2(k) \le 10 \\ (-1)\,S_1(k) + 0\,S_2(k) \le 0 \\ 0\,S_1(k) + 1\,S_2(k) \le 15 \\ 0\,S_1(k) + (-1)\,S_2(k) \le 0 \end{bmatrix}}, \quad \underset{\Omega_w}{\begin{bmatrix} 1\,w_1(k) + 0\,w_2(k) \le 3 \\ (-1)\,w_1(k) + 0\,w_2(k) \le 0 \\ 0\,w_1(k) + 1\,w_2(k) \le 3 \\ 0\,w_1(k) + (-1)\,w_2(k) \le 0 \end{bmatrix}}, \quad \underset{\Omega_u}{\begin{bmatrix} 1\,u_1(k) + 0\,u_2(k) \le 2 \\ (-1)\,u_1(k) + 0\,u_2(k) \le 0 \\ 0\,u_1(k) + 1\,u_2(k) \le 2 \\ 0\,u_1(k) + (-1)\,u_2(k) \le 0 \end{bmatrix}}, \tag{2.26}$$

where the support function ($\phi(\eta)$) values are given by the right-hand side of the above inequalities, and the coordinates of the associated vectors (η) are the coefficients on the left-hand side. In this example, the constraint sets and matrices **A**, **B**, and **G** are time-invariant.

Computation of Sets Ω_{Bu} and Ω_{-Bu}

Let $\mathbf{X}_{Bu}=[X_{Bu1}\ X_{Bu2}]'$ denote any vector in set Ω_{Bu}. Then, the support function and vectors of this set are given by (Eq.2.17):

$$\Omega_{Bu}=\{X_{Bu} : X'_{Bu}(B')^{-1}\mathbf{v}_i \le \phi_u(\mathbf{v}_i), i=1,...,4\} \tag{2.27}$$

where $\mathbf{v}_i$ and $\phi_u(\mathbf{v}_i)$ are the support vector and support function value of set Ω_u respectively,

$$(B')^{-1}=\begin{bmatrix}-1 & -1\\ 0 & -1\end{bmatrix}, \tag{2.28}$$

$$\begin{bmatrix} v_1=[1\ 0]' & \phi_u(v_1)=2\\ v_2=[-1\ 0]' & \phi_u(v_2)=0\\ v_3=[0\ 1]' & \phi_u(v_3)=2\\ v_4=[0\ -1]' & \phi_u(v_4)=0\end{bmatrix}. \tag{2.29}$$

After performing the indicated matrix-vector multiplication, one obtains

$$\Omega_{Bu}\begin{bmatrix} -X_{Bu1}+0X_{Bu2}\le 2\\ X_{Bu1}+0X_{Bu2}\le 0\\ -X_{Bu1}-X_{Bu2}\le 2\\ X_{Bu1}+X_{Bu2}\le 0\end{bmatrix}. \tag{2.30}$$

By changing the sign of the left-hand side coefficients, we get set Ω_{-Bu}. Namely,

$$\Omega_{-Bu}\begin{bmatrix} X_{Bu1}+0X_{Bu2}\le 2\\ -X_{Bu1}+0X_{Bu2}\le 0\\ X_{Bu1}+X_{Bu2}\le 2\\ -X_{Bu1}-X_{Bu2}\le 0\end{bmatrix}. \tag{2.31}$$

Computation of $\Omega_m(4)$

Reduced state set $\Omega_r(4)$ is the same as $\Omega_S(4)$, and therefore its support function vectors are known. Let $S_m=[S_{m1}\ S_{m2}]'$ denote any vector in set $\Omega_m(4)$. Then, set $\Omega_m(4)$

is given by Equation (2.12):

$$\Omega_m(4)=\{S_m: S_m'\eta_i \le \phi_m(\eta_i) = \phi_r(\eta_i) - \phi_w(G'\eta_i),\ i=1,...,4\}, \tag{2.32}$$

where η_i are the support vectors of $\Omega_r(4)$ as follows (Eq. 2.26):

$$\begin{bmatrix} \eta_1=[1\ 0]' & \phi_r(\eta_1)=10 \\ \eta_2=[-1\ 0]' & \phi_r(\eta_2)=0 \\ \eta_3=[0\ 1]' & \phi_r(\eta_3)=15 \\ \eta_4=[0\ -1]' & \phi_r(\eta_4)=0 \end{bmatrix}. \tag{2.33}$$

$\phi_w[G'\eta_i]$ can be generally computed by solving the following LP problem:

$$\begin{aligned} &\textit{Maximize}\ w'G'\eta_i \\ &\textit{Subject to}\quad w\in\Omega_w, \end{aligned} \tag{2.34}$$

where Ω_w is given by (2.26). The optimal value of $w'G'\eta_i$ represents $\phi_w[G'\eta_i]$.

In this example, this optimization problem has a simple solution as illustrated for their support vector η_1:

$$\begin{bmatrix} \textit{Maximize}\ w'G'\eta_1 = \phi_w[G'\eta_1] \\ \textit{Subject to}\quad w\in\Omega_w \end{bmatrix} = \begin{bmatrix} \textit{Maximize}\ w_1 \\ \textit{Subject to}\quad w\in\Omega_w \end{bmatrix} = 3 \tag{2.35}$$

Thus, the $\Omega_m(4)$ hyperplane associated with η_1 is

$$S_m' \begin{bmatrix} 1 \\ 0 \end{bmatrix} \le 10-3 = 7. \tag{2.36}$$

Similarly, we can compute the other three hyperplanes and specify $\Omega_m(4)$:

$$\Omega_m(4)$$
$$\begin{bmatrix} S_{m1}+0S_{m2} \le 7 \\ -S_{m1}+0S_{m2} \le 0 \\ 0S_{m1}+1S_{m2} \le 12 \\ 0S_{m1}-1S_{m2} \le 0 \end{bmatrix}. \qquad (2.37)$$

After the specification of all relevant hyperplanes, one should check whether the Ω_m set is nonempty and whether it includes redundant hyperplanes. Redundant hyperplanes should be discarded because they unnecessarily increase computational requirement. Procedures for performing these tasks have been outlined in Section 2.3. In this cases, the set is nonempty and does not include redundant hyperplanes.

Computation of set Ω_{AS}

Let $X_{AS}=[X_{AS1}\ X_{AS2}]'$ denote any vector in set Ω_{AS}. Then, Ω_{AS} is given by (Eq. 2.19):

$$\Omega_{AS}(3)=\{X_{AS}:\ X'_{AS}\eta_i \le \phi_m(\eta_i)+\phi_{-BU}(\eta_i),\ i=1,...,4, \qquad (2.38)$$
$$X'_{AS}\theta_j \le \phi_m(\theta_j)+\phi_{-BU}(\theta_j),\ j=1,...,4\}$$

where η_i are the support vectors of set $\Omega_m(4)$, and θ_j are the support vectors of set Ω_{-Bu}. For each η_i and θ_j, $\phi_m(\eta_i)$ and $\phi_{-Bu}(\theta_j)$ are known. To compute $\phi_{-Bu}(\eta_i)$ and $\phi_m(\theta_j)$, one needs to solve the following LP problems:

$$\textit{Maximize } X'_{Bu}\eta_i = \phi_{-Bu}(\eta_i)$$
$$\textit{Subject to } X_{Bu}\in\Omega_{-Bu}$$

$$\textit{and} \qquad (2.39)$$

$$\textit{Maximize } S'_m\theta_i = \phi_m(\theta_i)$$
$$\textit{Subject to } S_m\in\Omega_m(4)$$

The results are summarized below:

$$\begin{bmatrix} \eta_1=[1\ 0]' & \phi_m(\eta_1)=7 & \phi_{-Bu}(\eta_1)=2 \\ \eta_2=[-1\ 0]' & \phi_m(\eta_2)=0 & \phi_{-Bu}(\eta_2)=0 \\ \eta_3=[0\ 1]' & \phi_m(\eta_3)=12 & \phi_{-Bu}(\eta_3)=2 \\ \eta_4=[0\ -1]' & \phi_m(\eta_4)=0 & \phi_{-Bu}(\eta_4)=2 \\ \theta_1=[1\ 0]' & \phi_m(\theta_1)=7 & \phi_{-Bu}(\theta_1)=2 \\ \theta_2=[-1\ 0]' & \phi_m(\theta_2)=0 & \phi_{-Bu}(\theta_2)=0 \\ \theta_3=[1\ 1]' & \phi_m(\theta_3)=19 & \phi_{-Bu}(\theta_3)=2 \\ \theta_4=[-1\ -1]' & \phi_m(\theta_4)=0 & \phi_{-Bu}(\theta_4)=0 \end{bmatrix}. \quad (2.40)$$

Then, the hyperplanes of Ω_{AS} are

$$\Omega_{AS} \begin{bmatrix} X_{AS1}+0X_{AS2}\le 9 \\ -X_{AS1}+0X_{AS2}\le 0 \\ 0X_{AS1}+X_{AS2}\le 14 \\ 0X_{AS1}-X_{AS2}\le 2 \\ X_{AS1}+0X_{AS2}\le 9 \\ -X_{AS1}+0X_{AS2}\le 0 \\ X_{AS1}+X_{AS2}\le 21 \\ -X_{AS1}-X_{AS2}\le 0 \end{bmatrix}. \quad (2.41)$$

It is noted that some of the above hyperplanes may be repetitive. To avoid unnecessary calculations and computer memory overtaxing, one should remove these hyperplanes from Ω_{AS} before proceeding. In this example, two hyperplanes are repetitive because set Ω_{-Bu} and $\Omega_m(4)$ share two common support vectors. After removing these hyperplanes, Ω_{AS} is given by

$$\Omega_{AS}(3)$$
$$\begin{bmatrix} X_{AS1} + 0X_{AS2} \le 9 \\ -X_{AS1} + 0X_{AS2} \le 0 \\ 0X_{AS1} + X_{AS2} \le 14 \\ 0X_{AS1} - X_{AS2} \le 2 \\ X_{AS1} + X_{AS2} \le 21 \\ -X_{AS1} - X_{AS2} \le 0 \end{bmatrix}. \qquad (2.42)$$

Computation of $\Omega_o(3)$ from $\Omega_{AS}(3)$

Let $\mathbf{X}_o=[X_{o1} \quad X_{o2}]'$ denote any vector in set $\Omega_o(3)$. Since **A** is an identity matrix in this example, $\Omega_o(3)$ equals $\Omega_{AS}(3)$ according to Eq. (2.20). Namely,

$$\Omega_o(3)$$
$$\begin{bmatrix} X_{o1} + 0X_{o2} \le 9 \\ -X_{o1} + 0X_{o2} \le 0 \\ 0X_{o1} + X_{o2} \le 14 \\ 0X_{o1} - X_{o2} \le 2 \\ X_{o1} + X_{o2} \le 21 \\ -X_{o1} - X_{o2} \le 0 \end{bmatrix}. \qquad (2.43)$$

Computation of $\Omega_r(3)$

Let $\mathbf{S}_r=[S_{r1} \quad S_{r2}]'$ denote any vector in set $\Omega_r(3)$. $\Omega_r(3)$ is determined from the intersection of $\Omega_o(3)$ and $\Omega_s(3)$(Eq. 2.21):

$$\Omega_r(3)=\{S_r;\ S_r'\tau_i \le Min[\phi_s(\tau_i),\phi_o(\tau_i)], \quad i=1,...,n_s\ , \\ S_r'\rho_j \le Min[\phi_s(\rho_j),\phi_o(\rho_j)], \quad j=1,...,n_o\}\ . \qquad (2.44)$$

where τ_i and $\phi_i(\tau_i)$ are the support vectors and function of set $\Omega_s(3)$, while ρ_i and $\phi_j(\rho_j)$ are the support vectors and function of set $\Omega_o(3)$.

Again, $\phi_o(\tau_i)$ and $\phi_s(\rho_j)$ are unknown but can be computed by solving LP problems similar to those formulated earlier. The results are given below

$$\begin{bmatrix} \tau_1=[1\ 0]' & \phi_s(\tau_1)=10 & \phi_o(\tau_1)=9 \\ \tau_2=[-1\ 0]' & \phi_s(\tau_2)=0 & \phi_o(\tau_2)=0 \\ \tau_3=[0\ 1]' & \phi_s(\tau_3)=15 & \phi_o(\tau_3)=14 \\ \tau_4=[0\ -1]' & \phi_s(\tau_4)=0 & \phi_o(\tau_4)=2 \\ \rho_1=[1\ 0]' & \phi_s(\rho_1)=10 & \phi_o(\rho_1)=9 \\ \rho_2=[-1\ 0]' & \phi_s(\rho_2)=0 & \phi_o(\rho_2)=0 \\ \rho_3=[0\ 1]' & \phi_s(\rho_3)=15 & \phi_o(\rho_3)=14 \\ \rho_4=[0\ -1]' & \phi_s(\rho_4)=0 & \phi_o(\rho_4)=2 \\ \rho_5=[1\ 1]' & \phi_s(\rho_5)=25 & \phi_o(\rho_5)=21 \\ \rho_6=[-1\ -1]' & \phi_s(\rho_6)=0 & \phi_o(\rho_6)=0 \end{bmatrix}. \tag{2.45}$$

The corresponding set $\Omega_r(3)$ is defined by

$$\Omega_r(3)$$

$$\begin{bmatrix} S_{r1}+0S_{r2} \le 9 \\ -S_{r1}+0S_{r2} \le 0 \\ 0S_{r1}+S_{r2} \le 14 \\ 0S_{r1}-S_{r2} \le 0 \\ S_{r1}+0S_{r2} \le 9 \\ -S_{r1}+0S_{r2} \le 0 \\ 0S_{r1}+S_{r2} \le 14 \\ 0s_{r1}-S_{r2} \le 0 \\ S_{r1}+S_{r2} \le 21 \\ -S_{r1}-S_{r2} \le 0 \end{bmatrix}. \tag{2.46}$$

Discarding the repeated hyperplanes, $\Omega_r(3)$ simplifies as follows:

$$\Omega_r(3)$$

$$\begin{bmatrix} S_{r1} + 0S_{r2} \le 9 \\ -S_{r1} + 0S_{r2} \le 0 \\ 0S_{r1} + S_{r2} \le 14 \\ 0S_{r1} - S_{r2} \le 0 \\ S_{r1} + S_{r2} \le 21 \end{bmatrix}. \tag{2.47}$$

The above procedure is repeated to compute sets $\Omega_m(3)$, $\Omega_r(2)$, $\Omega_m(2)$, $\Omega_r(1)$,$\Omega_m(1)$, $\Omega_r(0)$. These sets are summarized in Table 2.1.

Computation of the admissible control set $\Omega_c(0)$

The admissible control set $\Omega_c(0)$ can be computed by the procedure described in Section 2.5.

First, the admissible set $\Omega_{Bu}(0)$ is computed by Eq.(23). Let $X_{Bu} = [X_{Bu1}\ X_{Bu2}]'$ denote any vector in set $\Omega_{Bu}(0)$. Then, $\Omega_{Bu}(0)$ is given by:

$$\Omega_{Bu}(0) = \{X_{Bu}: X_{Bu}'\eta_i \le \phi_m(\eta_i) - S'(0)A'\eta_i,\ i=1,...,4\}, \tag{2.48}$$

where $\phi_m(\eta_i)$, η_i, i = 1,...,4, represent the support function and associated vector set for $\Omega_m(1)$ given in Table 2.1. S(0) = [4,4]′ is the initial state.

Substituting the initial state vector into Eq. (2.23), we have

$$\begin{bmatrix} \eta_1=[1\ 0]' & \phi_m(\eta_1)=4 & S'(0)A'\eta_1=4 \\ \eta_2=[-1\ 0]' & \phi_m(\eta_2)=0 & S'(0)A'\eta_2=-4 \\ \eta_3=[0\ -1]' & \phi_m(\eta_3)=0 & S'(0)A'\eta_3=-4 \\ \eta_4=[1\ 1]' & \phi_m(\eta_4)=7 & S'(0)A'\eta_4=8 \end{bmatrix}. \tag{2.49}$$

Thus, the corresponding admissible set $\Omega_{Bu}(0)$ is

$$\Omega_{Bu}(0)$$
$$\begin{bmatrix} X_{Bu1} + 0X_{Bu2} \le 0 \\ -X_{Bu1} + 0X_{Bu2} \le 4 \\ 0X_{Bu1} - X_{Bu2} \le 4 \\ X_{Bu1} + X_{Bu2} \le -1 \end{bmatrix}. \tag{2.50}$$

Secondly, $\Omega_u(0)$ is computed from $\Omega_{Bu}(0)$. Let $\mathbf{X_u}=[X_{u1},X_{u2}]'$ denote any vector in set $\Omega_u(0)$. $\Omega_u(0)$ is obtained by Eq.(2.20):

$$\Omega_u(0)=\{X_u : X_u' B' e_i \le \phi_{Bu}(e_i),\ i=1,...,4\}\ , \tag{2.51}$$

where $\mathbf{e_i}$, $\phi_{Bu}(\mathbf{e_i})$ are the support vector and support function of $\Omega_{Bu}(0)$, respectively. After performing the indicated matrix-vector multiplication, one obtains

$$\Omega_u(0)$$
$$\begin{bmatrix} -X_{u1} + 0X_{u2} \le 0 \\ X_{u1} + 0X_{u2} \le 4 \\ -X_{u1} + X_{u2} \le 4 \\ 0X_{u1} - X_{u2} \le -1 \end{bmatrix}. \tag{2.52}$$

Finally, the admissible control set $\Omega_c(0)$ is given by the intersection of $\Omega_u(0)$ and Ω_u. Let $\mathbf{u_c}=[u_{c1},u_{c2}]'$ denote any vector in set $\Omega_c(0)$. then, $\Omega_c(0)$ is given by (Eq. 2.21):

$$\begin{aligned} \Omega_c(0)=\{u_c:\ & u_c'\eta_i \le Min[\phi_c(\eta_i),\phi_u(\eta_i)], \quad i=1,...,4, \\ & and \quad u_c'v_j \le Min[\phi_c(v_j),\phi_u(v_j)], \quad j=1,...,4\} \end{aligned} \tag{2.53}$$

Vectors η_i and v_j are support vectors of $\Omega_u(0)$ and Ω_u respectively. $\phi_u(\eta_i)$ and $\phi_c(\rho_j)$ are unknown but can be computed by solving the following LP problems:

$$\begin{aligned} &\textit{Maximize } u_c'\eta_i = \phi_u(\eta_i) \\ &\textit{Subject to } \quad u_c \in \Omega_u(0) \\ &\qquad\qquad \textit{and} \\ &\textit{Maximize } u'v_i = \phi_c(v_i) \\ &\textit{Subject to } \quad u \in \Omega_u . \end{aligned} \tag{2.54}$$

The results are summarized below:

$$\begin{bmatrix} \eta_1=[-1\ 0]' & \phi_c(\eta_1)=0 & \phi_u(\eta_1)=0 \\ \eta_2=[1\ 0]' & \phi_c(\eta_2)=4 & \phi_u(\eta_2)=2 \\ \eta_3=[-1\ 1]' & \phi_c(\eta_3)=4 & \phi_u(\eta_3)=2 \\ \eta_4=[0\ -1]' & \phi_c(\eta_4)=-1 & \phi_u(\eta_4)=0 \\ v_1=[1\ 0]' & \phi_c(v_1)=4 & \phi_u(v_1)=2 \\ v_2=[-1\ 0]' & \phi_c(v_2)=0 & \phi_u(v_2)=0 \\ v_3=[0\ 1]' & \phi_c(v_3)=8 & \phi_u(v_3)=2 \\ v_4=[0\ -1]' & \phi_c(v_4)=-1 & \phi_u(v_4)=0 \end{bmatrix} \tag{2.55}$$

The admissible control set $\Omega_c(0)$ is then defined by

$$\Omega_c(0) \begin{bmatrix} -u_{c1} + 0u_{c2} \le 0 \\ u_{c1} + 0u_{c2} \le 2 \\ -u_{c1} + u_{c2} \le 2 \\ 0u_{c1} - u_{c2} \le -1 \\ u_{c1} + 0u_{c2} \le 2 \\ -u_{c1} + 0u_{c2} \le 0 \\ 0u_{c1} + u_{c2} \le 2 \\ 0u_{c1} - u_{c2} \le -1 \end{bmatrix} . \tag{2.56}$$

After discarding the repeated hyperplanes, this set becomes

$$\Omega_c(0) \begin{bmatrix} u_{c1} + 0u_{c2} \le 2 \\ -u_{c1} + 0u_{c2} \le 0 \\ 0u_{c1} + u_{c2} \le 2 \\ 0u_{c1} - u_{c2} \le -1 \end{bmatrix} . \tag{2.57}$$

2.7 Comparison of Polyhedral and Ellipsoidal Set Control Algorithms

The second computational experiment aims at comparing the polyhedral control algorithm discussed earlier with an ellipsoidal approximation algorithm proposed by *Bertsekas and Rhodes [1971]*. The basis of this approach is to create ellipsoidal approximations of all sets and develop recursive relationships for the ellipsoid centers and principle axes. These relationships are similar to the Ricatti equations encountered in Linear Quadratic Gaussian control problems. Since these equations can be solved recursively, they present computational advantages for large systems.

The system is again described by Equation (2.24) and the state, input, and control sets are as follows:

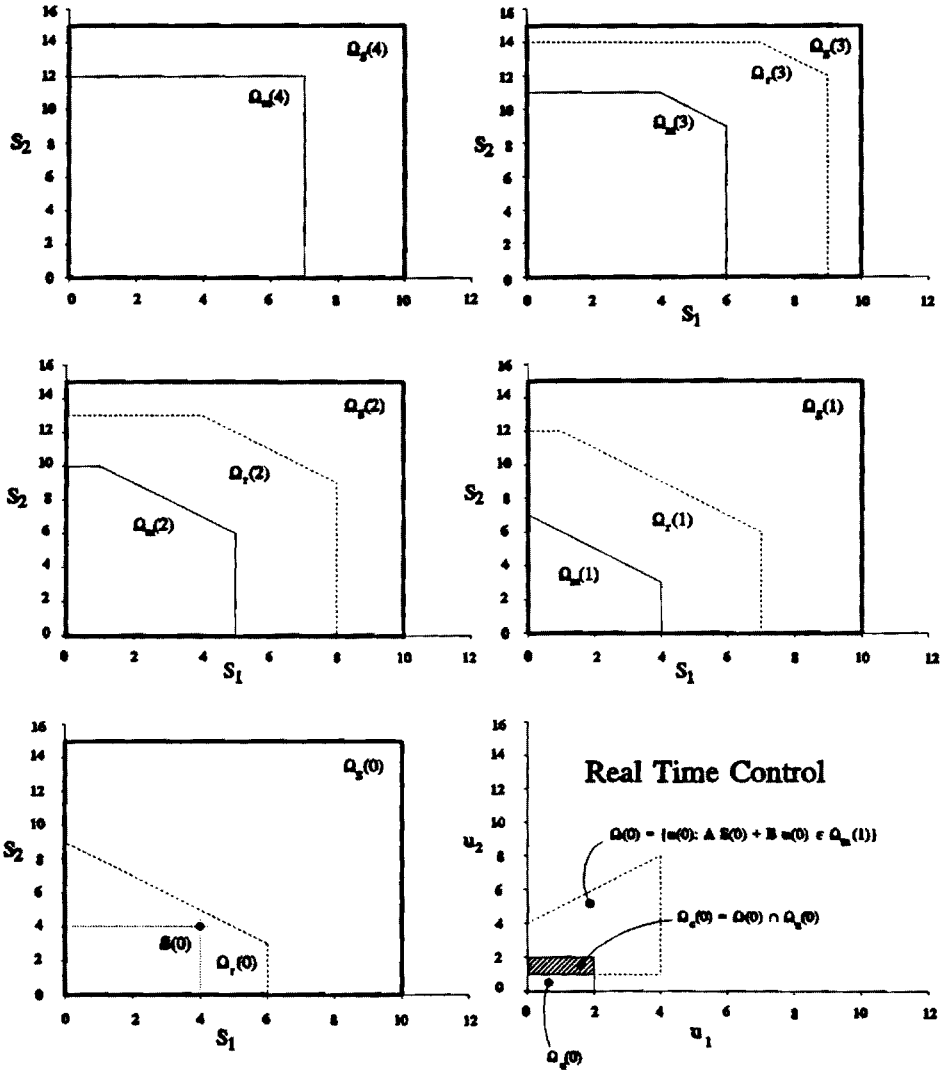

Figure 2.7: State and Control Sets for the Example

$$\Omega_S(k) = \left\{ \begin{matrix} -37.5 \le S_1(k) \le 37.5 \\ -31 \le S_2(k) \le 31 \end{matrix} \right\}, \; k = 0,1,\ldots,15,$$

$$\Omega_w(k) = \left\{ \begin{matrix} -10 \le w_1(k) \le 10 \\ -15 \le w_2(k) \le 15 \end{matrix} \right\}, \; k = 0,1,\ldots,14, \qquad (2.58)$$

$$\Omega_u(k) = \left\{ \begin{matrix} -10 \le u_1(k) \le 10 \\ -22 \le u_2(k) \le 22 \end{matrix} \right\}, \; k = 0,1,\ldots,14.$$

For the ellipsoidal approximation algorithm, the state, input, and control sets are the smallest ellipses enveloping the previous rectangles.

Figure 2.8 portrays the resulting modified and reduced state sets for both set computation approaches at times 15, 14, 13, 12, 1, and 0. Until time 12, both approaches produce feasible results, although the polyhedral modified and reduced sets are significantly larger. At time 11, the ellipsoidal algorithm terminates indicating infeasibility, while the polyhedral approach remains feasible until time 0. This experiment shows that the required ellipsoidal approximations underestimate the feasible regions and cause early algorithm termination. Given that the polyhedral algorithm is fairly efficient (see computational time estimates in companion article), this suboptimality of the ellipsoidal set control approach is a major weakness.

Table 2.1: Modified and Reduced State Sets for the Example

N	$\Omega_m(N)$	$\Omega_r(N)$
4	$1S_{m1} + 0S_{m2} \le 7$ $(-1)S_{m1} + 0S_{m2} \le 0$ $0S_{m1} + 1S_{m2} \le 12$ $0S_{m1} + (-1)S_{m2} \le 0$	
3	$1S_{m1} + 0S_{m2} \le 6$ $(-1)S_{m1} + 0S_{m2} \le 0$ $0S_{m1} + 1S_{m2} \le 11$ $0S_{m1} + (-1)S_{m2} \le 0$ $1S_{m1} + 1S_{m2} \le 15$	$1S_1 + 0S_2 \le 9$ $(-1)S_1 + 0S_2 \le 0$ $0S_1 + 1S_2 \le 14$ $0S_1 + (-1)S_2 \le 0$ $1S_1 + 1S_2 \le 21$
2	$1S_1 + 0S_2 \le 5$ $(-1)S_1 + 0S_2 \le 0$ $0S_1 + 1S_2 \le 10$ $0S_1 + (-1)S_2 \le 0$ $1S_1 + 1S_2 \le 11$	$1S_1 + 0S_2 \le 8$ $(-1)S_1 + 0S_2 \le 0$ $0S_1 + 1S_2 \le 13$ $0S_1 + (-1)S_2 \le 0$ $1S_1 + 1S_2 \le 17$
	$1S_1 + 0S_2 \le 4$ $(-1)S_1 + 0S_2 \le 0$ $0S_1 + (-1)S_2 \le 0$ $1S_1 + 1S_2 \le 7$	$1S_1 + 0S_2 \le 7$ $(-1)S_1 + 0S_2 \le 0$ $0S_1 + 1S_2 \le 12$ $0S_1 + (-1)S_2 \le 0$ $1S_1 + 1S_2 \le 13$
0		$1S_1 + 0S_2 \le 6$ $(-1)S_1 + 0S_2 \le 0$ $0S_1 + (-1)S_2 \le 0$ $1S_1 + 1S_2 \le 9$

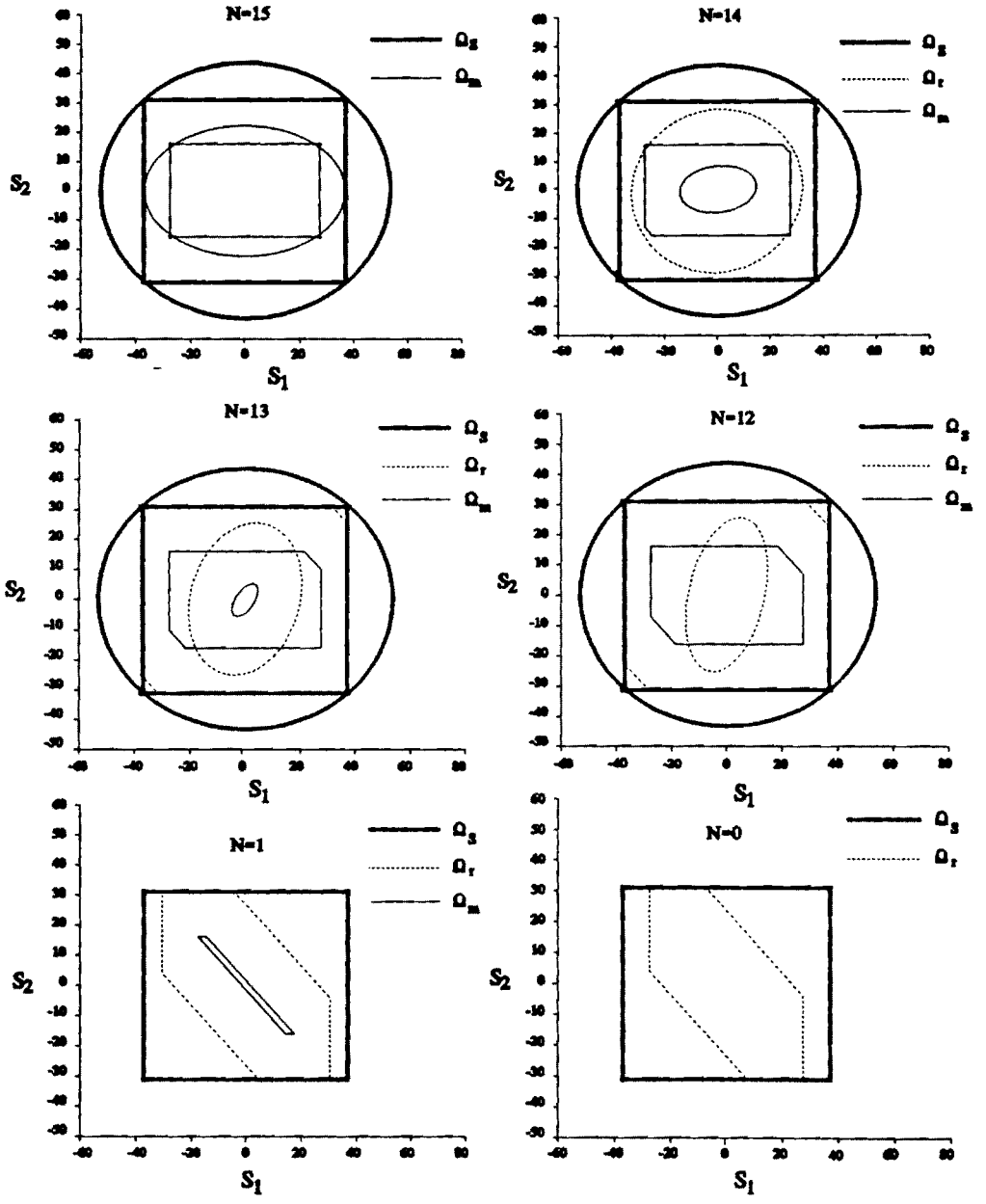

Figure 2.8: A Comparison of Polyhedral and Ellipsoidal Set Algorithms

3. APLLICATION TO RESERVOIR MANAGEMENT

3.1 INTRODUCTION

The need to handle uncertainty in reservoir management is widely recognized by practicing and research professionals and continues to motivate new management approaches [*Foufoula-Georgiou and Kitanidis, 1988, Kelman et al., 1990, Georgakakos, 1989, 1992*]. The common theme is to rely on probability theory to model random quantities and then develop suitable optimization schemes to control the probability distribution of storage, release, energy generation, and other key system variables. The basic suppositions are (**a**) that enough data are available to validate the descriptions of the uncertain elements and (**b**) that the system operator has the ability to balance abstract concepts, such as risks of not meeting certain objectives or expected output levels, among themselves and over time.

Data availability undermines stochastic methods when they are most valuable: during hydrologic extremes. Data deficiencies for extreme floods and droughts usually weaken model predictions and limit management options. What is more, potentially new climatic regimes may totally invalidate existing observation records.

Amidst crises situations, system operators are also faced with nontrivial challenges. At the onset of droughts, they must decide whether to reduce outflow or continue with their normal release schedules. In retrospect, one option is better than the other, but at the time when the decision is made each option involves risks. Anticipating floods, reservoir operators should evacuate enough storage to avoid damage-causing outflows and energy-wasting spillage. Over- or under-estimating this storage again involves risks. Risks are associated with almost every decision in reservoir operations, but it is unclear how reservoir operators should try to appreciate and balance them. Stochastic management methods are useful, but they can only control the probability of extreme events and not their magnitude [*Georgakakos, 1989*]. And, as already mentioned, probability estimates can only be as good as the available data.

As an alternative, in this work we develop operational choices that are easier to understand and offer some guarantees. Using the set control approach, we derive sets of control actions guaranteeing that the system will meet its constraints (satisfy water supplies, maintain outflow below damaging levels, or cover a dependable energy commitment). The guarantees are valid for a certain length of time and for all inflow sequences bounded by specific ranges. The inflow bounds are selected by the operator and should reflect extreme hydrologic circumstances against which the system is to be controlled. This selection affects the size of the admissible control

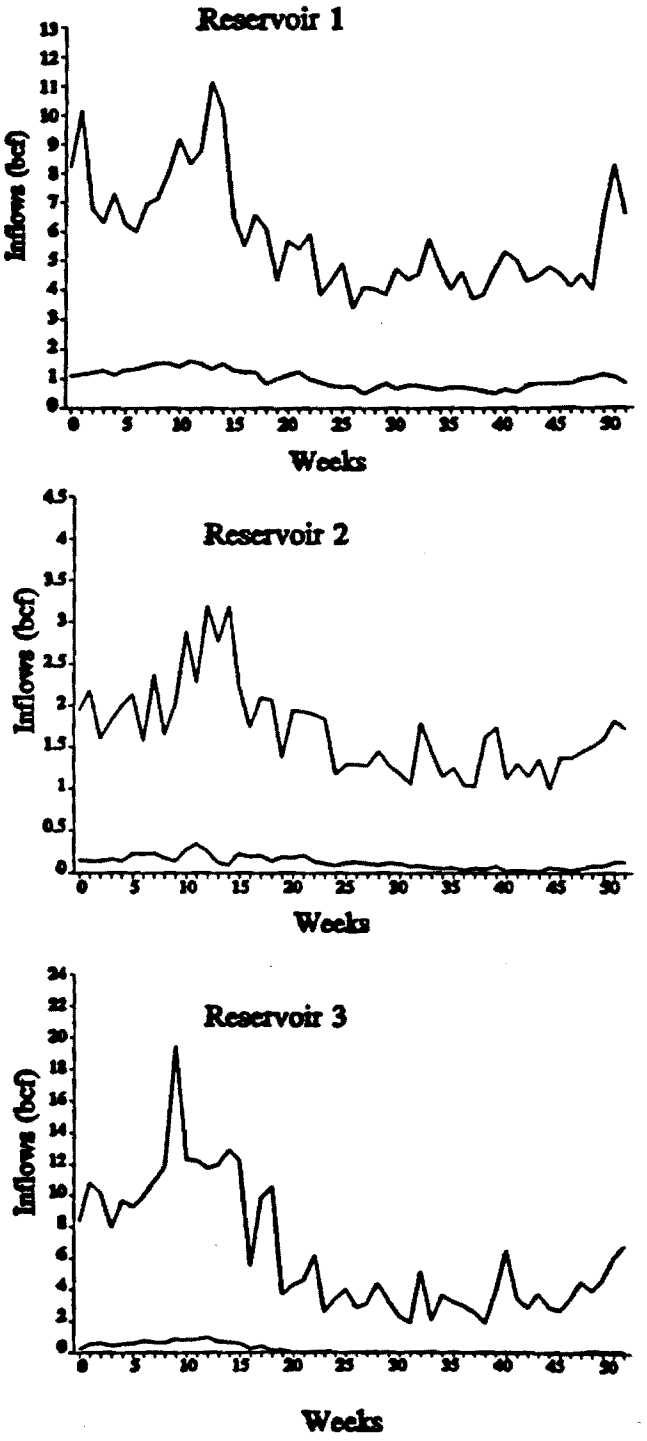

Figure 3.1: Reservoir Inflow Ranges

sets and the length of the operational horizon during which the system can fully meet the stated constraints. Bounds associated with more extreme hydrologies result in shorter guaranteed operational horizons and smaller admissible control sets. Although this judgement involves risks, it is also more meaningful and reassuring, especially during crises. The operators can select any control action within the specified sets and be confident that the system will not violate the stated constraints at least for the duration of the operational horizon.

This article examines this approach as it applies to flood and drought management and hydropower operations and illustrates through examples how some apparent method limitations can be overcome. Potential applications for reservoir design and operational policy determination are also briefly discussed.

3.2 FLOOD AND DROUGHT MANAGEMENT / RESERVOIR DESIGN

The following discussion, although general, will make reference to a three-reservoir cascade as an example and test case study. This system is located on the Savannah River in the southeastern U.S. and is described in *Georgakakos [1989, 1992]*. For the purposes of this section (namely, to investigate issues exclusive of hydropower), the system is modelled by the following water balance state equation:

$$\begin{bmatrix} S_1(k+1) \\ S_2(k+1) \\ S_3(k+1) \end{bmatrix} = \begin{bmatrix} 1 & 0 & 0 \\ 0 & 1 & 0 \\ 0 & 0 & 1 \end{bmatrix} \begin{bmatrix} S_1(k) \\ S_2(k) \\ S_3(k) \end{bmatrix} + \begin{bmatrix} -1 & 0 & 0 \\ 1 & -1 & 0 \\ 0 & 1 & -1 \end{bmatrix} \begin{bmatrix} u_1(k) \\ u_2(k) \\ u_3(k) \end{bmatrix} + \begin{bmatrix} 1 & 0 & 0 \\ 0 & 1 & 0 \\ 0 & 0 & 1 \end{bmatrix} \begin{bmatrix} w_1(k) \\ w_2(k) \\ w_3(k) \end{bmatrix}, \quad (3.1)$$

$$k = 0,1,\ldots,N-1,$$

where $S_i(k)$, $u_i(k)$, and $w_i(k)$ respectively represent storage, release, and inflow volumes for reservoir i=1,2,3. Table 3.1 reports permissible storage and release ranges reflecting water conservation and flood control objectives, and Figure 3.1 depicts the weekly inflow ranges. These ranges were obtained, somewhat arbitrarily, using the third lowest and third highest inflow values on record (63 years).

The first question is whether the system can control inflows without violating the stated constraints, namely, without effecting water shortages (where $u_3(k) < 2.2$ billion cubic feet/week) or damage-causing outflows (where $u_3(k) > 18$ bcf/week). The answer is far from obvious since system inflow ($w_1(k)+w_2(k)+w_3(k)$) saturates the admissible range of $u_3(k)$ for more than one third of the year (rainy season).

Table 3.1: Reservoir Storage and Release Constraints

	Minimum	Maximum
Reservoir 1		
Storage (bcf)	79.25	123.8
Release (bcf / week)	0.0	18.0
Reservoir 2		
Storage (bcf)	34.2	50.8
Release (bcf/week)	0.0	18.0
Reservoir 3		
Storage (bcf)	69.71	125.95
Release (bcf/week)	2.2	18.0

To provide a partial answer to this question, we ran the set control algorithm with a time horizon of 52 weeks. The algorithm terminated successfully and generated the following reduced state set at time zero:

$$\Omega_r(0) = \left\{ \begin{array}{r} (-0.7071)S_1 + (-0.7071)S_2 + 0S_3 \le -80.2213 \\ 0.5774S_1 + 0.5774S_2 + 0.5774S_3 \le 140.4670 \\ -0.5774)S_1 + (-0.5774)S_2 + (-0.5774)S_3 \le -129.8806 \\ 1S_1 + 0S_2 + 0S_3 \le 123.8 \\ (-1)S_1 + 0S_2 + 0S_3 \le -79.25 \\ 0S_1 + 1S_2 + 0S_3 \le 50.8 \\ 0S_1 + (-1)S_2 + 0S_3 \le -34.2 \\ 0S_1 + 0S_2 + 1S_3 \le 125.93 \\ 0S_1 + 0S_2 + (-1)S_3 \le -69.71 \end{array} \right\}. \qquad (3.2)$$

If this set contains the initial storage values, there exist feasible release sequences that maintain all reservoir storages within their acceptable limits independently of what inflows materialize, provided that they are within the specified bounds. The set of admissible control actions that guarantee feasibility is also determined for initial storage values $S_1(0)=100$, $S_2(0)=45$, and $S_3(0)=95$ bcf:

$$\Omega_c(0) = \left\{ \begin{array}{r} 0.7071u_1 + (-0.7071)u_2 + 0u_3 \le 2.7209 \\ (-0.7071)u_1 + 0.7071u_2 + 0u_3 \le 7.7442 \\ 1u_1 + 0u_2 + 0u_3 \le 18.0 \\ (-1)u_1 + 0u_2 + 0u_3 \le 0.0 \\ 0u_1 + 1u_2 + 0u_3 \le 18.0 \\ 0u_1 + (-1)u_2 + 0u_3 \le 0.0 \\ 0u_1 + 0u_2 + 1u_3 \le 17.2403 \\ 0u_1 + 0u_2 + (-1)u_3 \le -14.7040 \end{array} \right\}. \qquad (3.3)$$

To test the validity of the results, we ran simulation experiments. Each simulation began with the generation of a 52-week, random inflow sequence for each system reservoir. These sequences can be determined in several ways. One approach is to generate inflow values uniformly (equally likely) within each weekly range. The result would be a totally random sequence, but one with very little probability of being consistently high or low (as in wet and dry years). Furthermore, the yearly volume of such sequences usually has a much wider range than actually observed. To avoid these inconsistencies, the inflow sequences were constructed as follows: The yearly inflow ranges for the entire system and each reservoir were first determined using the third lowest and third highest annual inflows on record. A uniform value within each range was then generated. Next, the annual inflow values of each reservoir were appropriately normalized to agree with the system value. Lastly, uniform inflows were obtained within each weekly range and subsequently adjusted to conform to the respective annual inflow values for each reservoir.

At each time period k (week) of the simulation horizon, a control vector was also randomly generated from the corresponding real-time control set $\Omega_c(k)$. The inflow and control vectors were then used in Equation (3.1) to determine the storage values for the next time step k+1. Based on these values and the reduced and modified state sets derived by the set control approach for time k+2, a new real-time control set $\Omega_c(k+1)$ was determined and the procedure was repeated until the end of the year. The simulation process was applied to 30 different random inflow sequences with the results shown on Figure 3.2. The figure includes the simulated storage and release sequences (solid lines) along with their associated bounds (dashed lines) and indicates that the set control approach accomplishes the objective of maintaining system storages within their limits using only feasible releases. The fact that the reservoirs experience drawdowns is a consequence of the manner in which the applied releases are obtained. Random release selection from the $\Omega_c(k)$ sets leads to reservoir depletion. Note, however, that this does not forewarn that the control

process will become infeasible. What will happen is that sets $\Omega_c(k)$ will shift towards low release regions of the feasible control sets $\Omega_u(k)$.

To see the effect of other selection rules, we ran additional simulation experiments using the release vector associated with the $\Omega_c(k)$ corner point closest to the axis origin (Figure 3.3). The system is again contained within the specified constraints in all simulations, but reservoir storages now tend to be in the proximity of their upper bounds. The applied releases are generally lower than in the previous case, although specific release levels may be higher depending on the seasonal inflow range and the value of storage.

Hence, the selection of applied releases can drastically influence the state of the system, this being a strength and an open question. From the operational point of view and especially during crises, it is comforting to know that any control action from the $\Omega_c(k)$ sets will not force violation of the stated bounds. However, a relevant question is how to establish an appropriate selection mechanism to coerce the system to evolve in a desirable manner. Desirability implies that each possible system sequence has some distinct value to the system users, and this premise is beyond the stated scope of the set control approach which simply aims to guarantee system feasibility. Nevertheless, it is a question of practical interest and will be taken up again in the conclusion section.

The purpose of the above experiments was to see whether the system is controllable in view of the imposed constraints. The answer was positive but partial because the results do not guarantee feasibility beyond the 52-week control horizon. In fact if the control horizon is extended to over 90 weeks, the set control approach terminates identifying empty modified state sets. Infeasibility means that there is no guarantee that the system can be contained within the stated limits so far in advance. The reason is that the minimum required release of 2.2 bcf/week from the 3rd reservoir is higher than the average lower inflow bound (~1.396 bcf/week). Eventually, this disparity renders the process infeasible. Note, however, that infeasibilities may occur even if average inflow is higher than the required draft. Such is the case when the upper release bound of the third reservoir is reduced below 16 bcf/week, despite an average upper inflow bound of 13.9 bcf/week. The process becomes infeasible due to large seasonal inflow bound fluctuations.

To understand the nature of the solution when no infeasibility is encountered, we ran a 5-year (260-week) control experiment with a lower release bound of 1.39 bcf/week. The results show that after the first year (as the solution proceeds backwards), the modified and reduced state sets exhibit annual periodicity. For the problem stated,

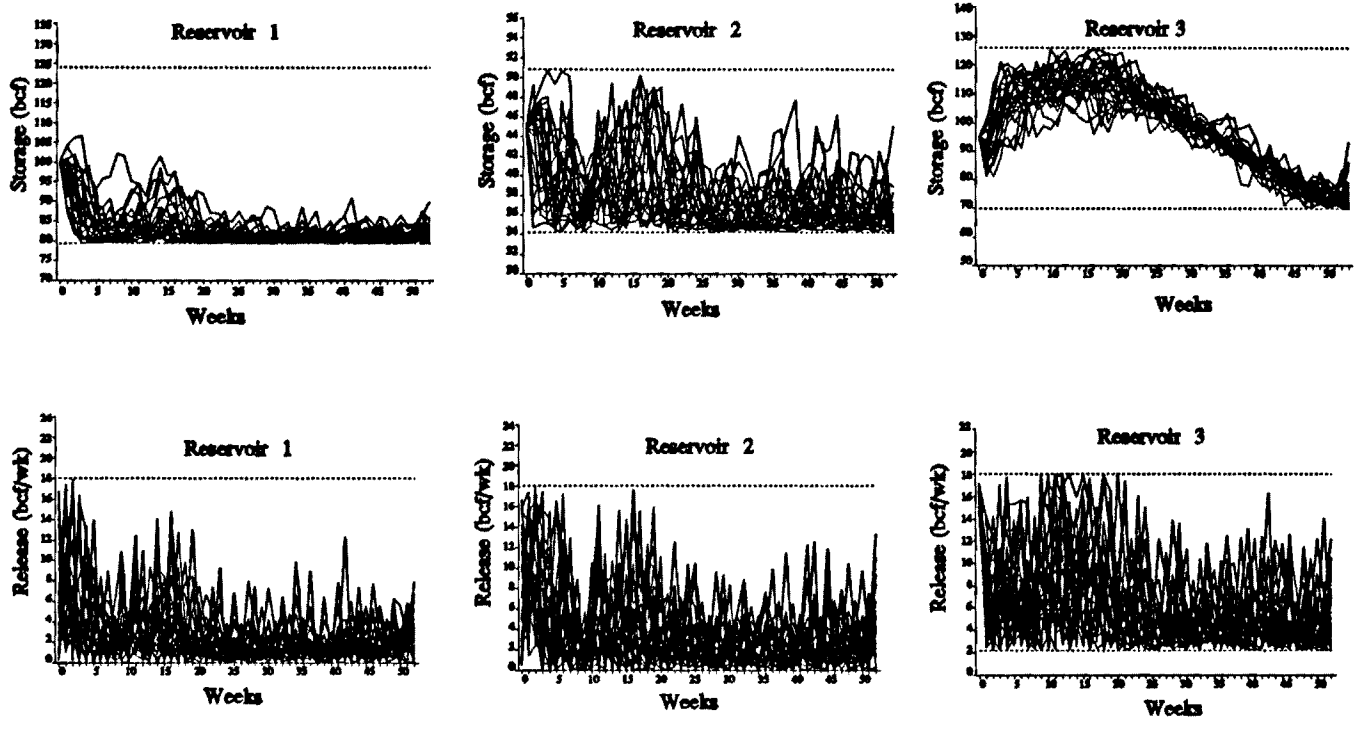

Figure 3.2 Simulation with random release section.

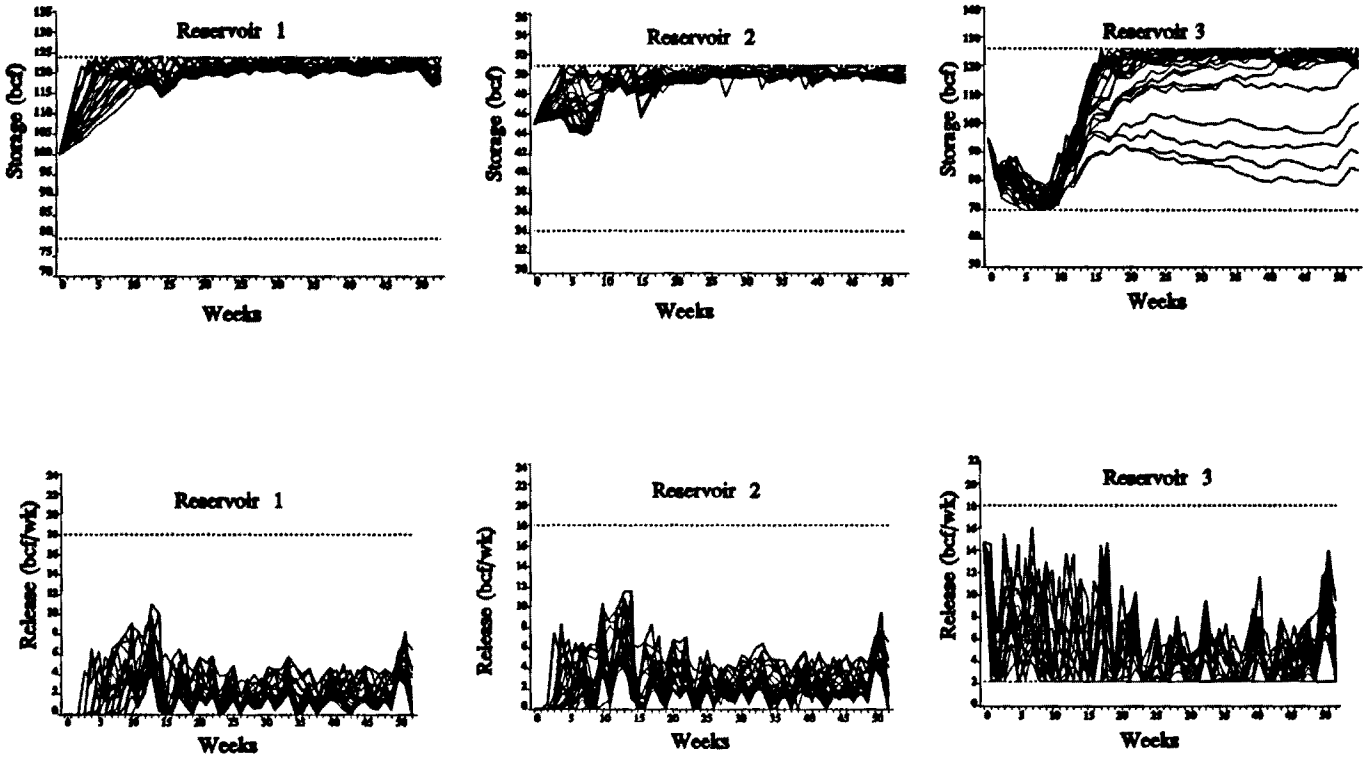

Figure 3.3: Simulation with low release selection.

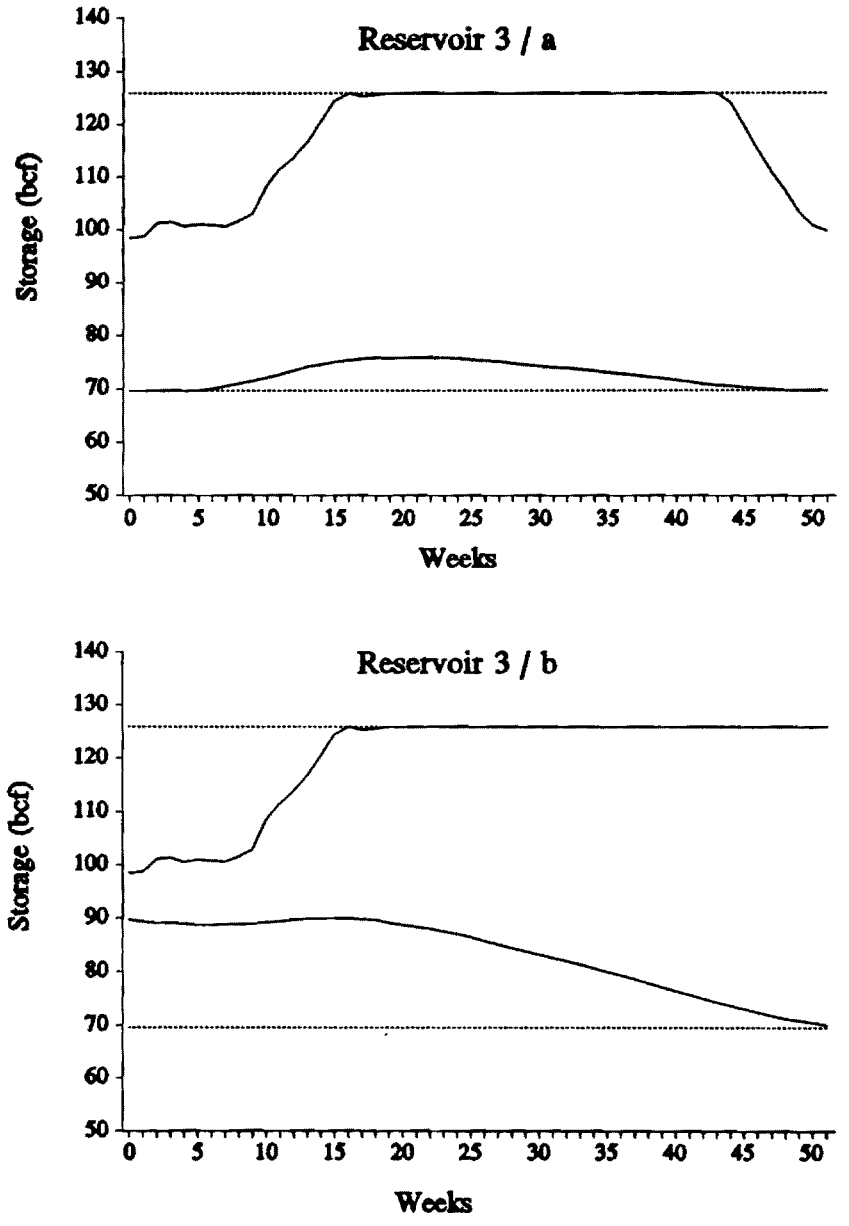

Figure 3.4: Reduced state sets for draft levels: (a) 1.39 billion cubic feet/week (3.93e10 L) and (b) 2.2 billion cubic feet/week (6.23e10 L)

the reduced state sets determine the regions where the storages ought to be located in any given week so that the system can continue its feasible operation independently of inflow realization. In an attempt to visualize these three dimensional sets, Figure 3.4a shows the projection of the minimum set distance on the storage of the 3rd reservoir (solid lines). The shapes for the other reservoirs are identical but contained within the respective bounds. The lower boundary of these regions reflects drought concerns, building up at the beginning of the dry season and easing off as time progresses. During the same period and with no fear of floods, the system can maintain high storages, while the rest of the time, it must make room for high inflows. By contrast, Figure 3.4b gives the same results when the lower bound for u_3 is 2.2 bcf/week. The figure shows how quickly the feasible region contracts as its lower boundary rises to guarantee a higher draft. Eventually the reduced set becomes empty and the procedure is unable to guarantee feasibility so far in advance. The length of the feasible horizon depends on the seasonal and relative variation of inflow, storage, and release constraints and is a measure of system reliability. In particular, if inflows are more predictable (smaller ranges), the reduced state and feasible control sets become larger (available operational options increase) and the system can be guaranteed to meet the operational requirements longer.

The reduced state sets extend the concept of the rule curves commonly used in reservoir operation. A rule curve suggests a target storage sequence that balances various system objectives in an acceptable manner. A reduced state set sequence guarantees that the system will simultaneously meet these objectives at all times. The advantage of thelatter approach is that it considers all system storages simultaneously and guarantees feasibility. A relative disadvantage is that the sets are expressed as a system of inequalities (e.g., Equation 3.2) that storages must satisfy in each period.

Clearly, the set control approach can be used in various reservoir operation and design issues. Three examples of practical interest would be to determine (**a**) the minimum and maximum release levels that can be met given an inflow pattern, (**b**) the maximum inflow range that can be controlled for a given output pattern, or (**c**) the system configuration (reservoir capacities) guaranteeing that the desirable output levels will be met given an inflow pattern. With respect to a procedure for determining minimum and maximum release levels given an inflow range pattern, one would have to use trial an error and explore the tradeoff between release range and length of feasible control horizon. As shown before, a tighter release range implies a shorter feasible control horizon, and the system operator is faced with the dilemma to sustain high demands over a short guaranteed time period or meet lower demand levels longer. Thus, the suggested operational usage of the set control

approach is to quantify the previous tradeoff and let the decision making authority select the most desirable compromise.

A final comment refers to correlated inflows. The effect of inflow correlation (spatial or temporal) is to limit the cumulative inflow range with respect to that corresponding to the individual weekly ranges. Thus, ignoring inflow correlation may limit the length of the feasible control horizon. Both correlation types can be explicitly considered (spatial correlations simply affect the shape of the joint inflow set), but a complete discussion is delegated to a separate publication.

3.3 HYDROPOWER

Hydropower adds nonlinear elements to the reservoir management problem and raises more questions in reference to the set control approach. To include hydropower considerations, we modify the state equation as follows (*Georgakakos, 1992*):

$$\begin{bmatrix} S_1(k+1) \\ S_2(k+1) \\ S_3(k+1) \end{bmatrix} = \begin{bmatrix} 1 & 0 & 0 \\ 0 & 1 & 0 \\ 0 & 0 & 1 \end{bmatrix} \begin{bmatrix} S_1(k) \\ S_2(k) \\ S_3(k) \end{bmatrix} + \begin{bmatrix} -b_1(k) & 0 & 0 \\ b_1(k) & -b_2(k) & 0 \\ 0 & b_2(k) & -b_3(k) \end{bmatrix} \begin{bmatrix} t_1(k) \\ t_2(k) \\ t_3(k) \end{bmatrix} + \begin{bmatrix} 1 & 0 & 0 \\ 0 & 1 & 0 \\ 0 & 0 & 1 \end{bmatrix} \begin{bmatrix} w_1(k) \\ w_2(k) \\ w_3(k) \end{bmatrix}, \quad (3.4)$$

$$k = 0,1,\ldots,N-1,$$

where

$$b_i(k) = \sum_{j=1}^{n_i} u_{ij}(k), \quad i = 1,2,3, \quad (3.5)$$

with $u_{ij}(k)$ being the discharge rate from the j^{th} turbine of the i^{th} reservoir, $t_i(k)$ the generation hours during period k, and n_i the number of turbines at reservoir i.

Turbine discharge depends (nonlinearly) on reservoir storage and power output and complicates the solution process since the matrix multiplying the control vector [t(k)] is now a function of the state. Products of set quantities cannot be explicitly handled in the framework suggested earlier, but one can usually overcome this predicament by following a well-established engineering rule: [*Schweppe, 1973*] "When faced with a nonlinear problem, linearize." In this context, this would imply that coefficients $b_i(k)$ be computed for a particular storage and power level and treated as constants at each time period k. The same approach is usually employed in stochastic control

problems with the linearization performed around the most likely state sequence. The difficulty in this case is that a single most likely sequence does not exist; all sequences with vectors from the reduced state sets are equally likely. Thus, linearization introduces approximations and invalidates the one-time solution approach adopted in the previous section. Instead, a sequential scheme where an N-period set control problem is solved at each decision time has distinct advantages.

In a sequential scheme, linearization can be performed around the initial state vector, which is expected to stay representative for some time. Eventually, the state will digress from the locale of the initial vector and will render the process approximate. However, the error is mitigated by the sequential mode of operation where decisions are always selected from the initial control set $\Omega_c(0)$. However, in some cases the procedure may become infeasible, even though the reduced and modified state sets are nonempty.

The above formulation can also reflect release constraints by specifying lower and upper bounds for the control vector $\mathbf{t}(k)$ such that the products $[b_i(k)\ t_i(k)]$ are within the allowable range. Constraints on energy generation can also be included: Let $P_i(k)$, represent the cumulative power output from all turbines at hydroelectric facility i and time period k. Then, the requirement that energy generation satisfy a minimum commitment $E^{min}(k)$ can be enforced as follows:

$$P_1(k)\,t_1(k) + P_2(k)\,t_2(k) + P_3(k)\,t_3(k) \geq E^{min}(k)\,. \qquad (3.6)$$

This inequality simply defines another bounding hyperplane for the control set $\Omega_u(k)$ and can easily be handled by the set control approach. Thus, the proposed formulation may be used to derive control policies (energy generation schedules) guaranteed to meet a dependable energy sequence, in addition to storage and release constraints.

To gain some insight with the above formulation, we run simulation experiments. The problem is solved with a control horizon of 10 weeks, sequentially at each week of a 10-year simulation horizon. The output of each plant equals its nominal power capacity, 430 MW for Reservoir 1, 375 MW for Reservoir 2, and 350 MW for Reservoir 3. Figure 3.5 shows the dependence of total turbine discharge on reservoir storage at these power levels. The curves take into account tailrace effects and are based on the power-(net hydraulic head)-discharge relationships reported by *Georgakakos [1991, Appendix A]*. The Ω_s and Ω_w sets are as in the previous section. The control set Ω_t reflects the restriction that generation hours be in the (0 to 168)-hour range per week, total system energy exceed a dependable energy commitment

(Eq. 3.6), and weekly average outflow of the third reservoir be greater than 1.4 billion cubic feet. The last requirement is enforced as follows: At the beginning of each week, the discharge, $Q_3(k)$, from Reservoir 3 is determined based on its initial storage and Figure 3.5. Then, the generation hours for Reservoir 3 are constrained by

$$t_3(k) \geq t_3^{\min}(k) = \frac{1.4 \cdot 10^9}{60 \cdot 60 \cdot Q_3(k)}, \quad \text{all } k, \tag{3.7}$$

where $Q_3(k)$ is expressed in cubic feet per second and $t_3^{\min}(k)$ in hours. It is noted that $P_1(k)$, $P_2(k)$, and $P_3(k)$ are herein arbitrarily set equal to nominal plant capacities. Alternatively, they may reflect contracted power outputs necessitating turbine overload or underload conditions. Furthermore, one may determine the power output of each turbine so as to meet the power contracts and additionally maximize plant efficiency [*Georgakakos, 1992*].

Figure 3.6 displays the results from 10 such simulations. Storage and generation sequences are only shown for Reservoir 3. Those of the other two reservoirs are qualitatively similar. Total system energy generation is plotted on the third graph along with the dependable energy requirement (thicker line). Storage stays within the specified bounds and the generation hours are such that the minimum weekly outflow of 1.4 billion cubic feet is always met. Turbine outflow usually suffices to maintain storage within the desirable bounds; however, on four occasions spillways are also activated (generation greater than 168 hours). System energy generation always satisfies the dependable energy commitment. This commitment may be increased but with no guarantee that it will then be met.

For example, the first graph in Figure 3.7 displays the energy generation results for another 10-year simulation series where dependable energy requirements are increased by 25%. The system state and control variables stay within the desirable limits, but energy generation occasionally fails to meet the respective targets. The simulation program is such that when the control algorithm identifies infeasibility (empty reduced and modified state sets), it reduces the dependable energy requirements by a certain percentage and repeats the computations until the problem becomes feasible. The worst violation requires that energy commitment be decreased by 40%.

To explore the effect of the control horizon, we repeated the above simulation series with a control horizon of 20 weeks. The results shown on the second graph in Figure 3.7 indicate that violations of lesser magnitude occur more frequently (the worst

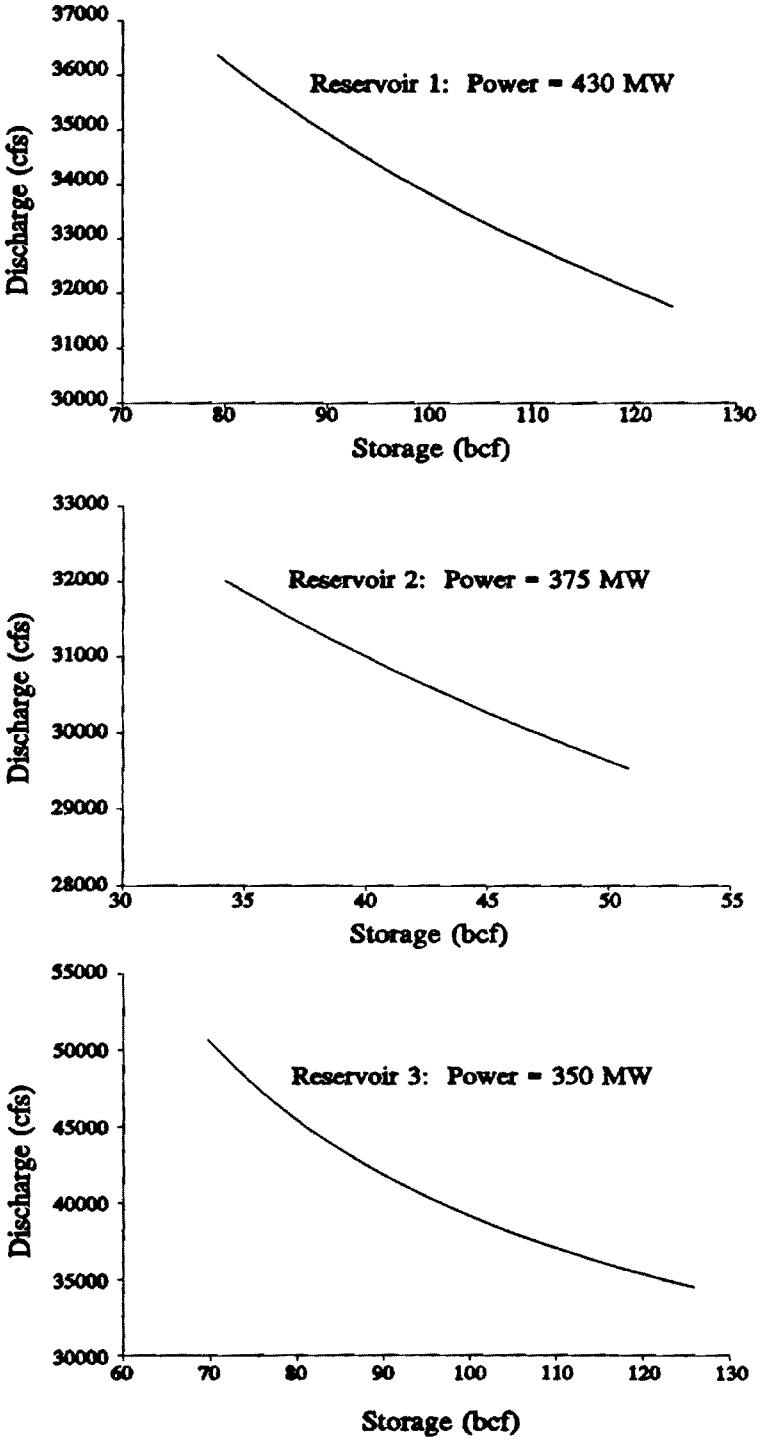

Figure 3.5: Turbine Discharge versus Storage

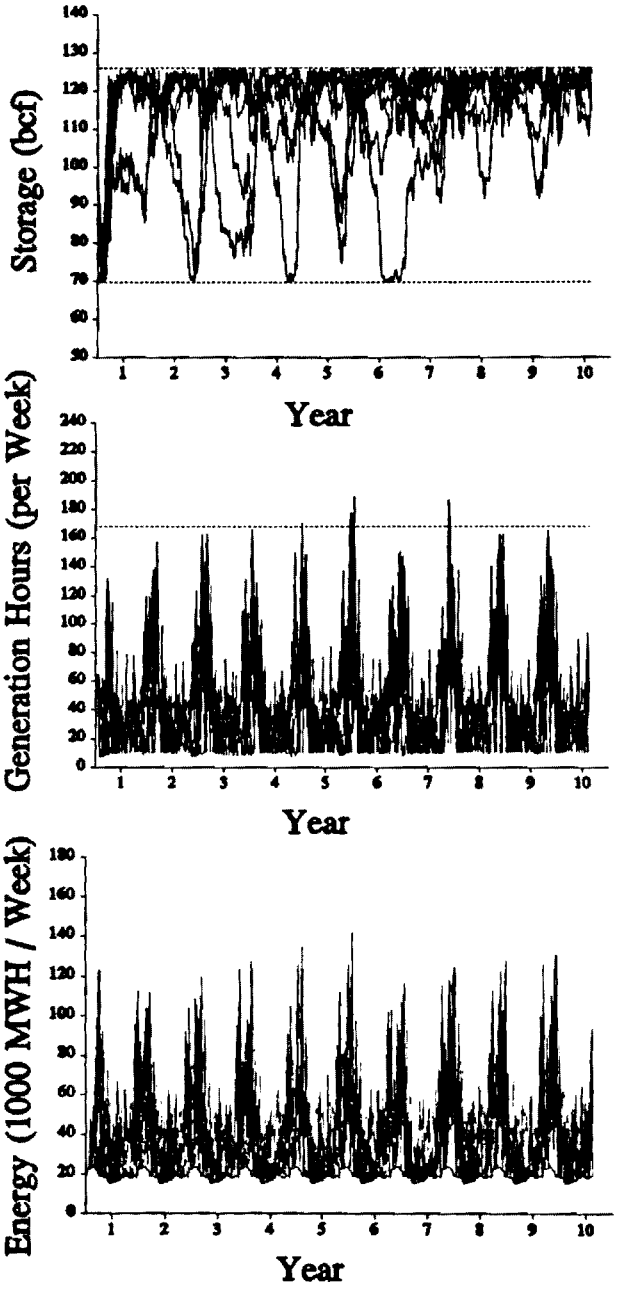

Figure 3.6: Simulation experiments

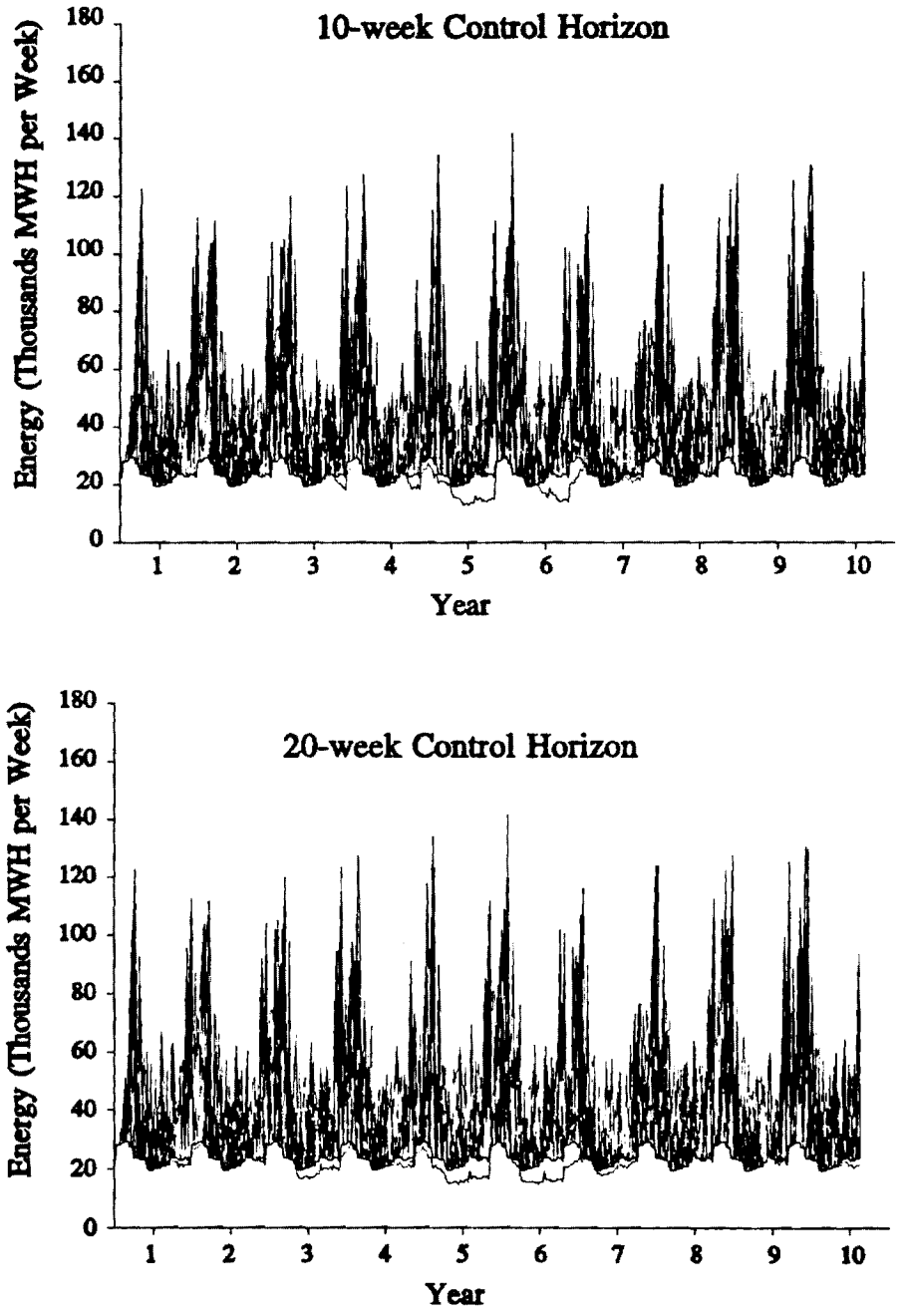

Figure 3.7: Simulation with higher energy commitments and different control horizons.

violation requires 30% reduction of the original target). This happens because the control algorithm anticipates potential infeasibilities further in advance and begins to reduce energy generation early on. When the worst violation actually arrives, it is not as serious as in the 10-week control horizon case.

3.4 ENERGY VALUE

As the power industry moves toward an open market system, hydropower operation focuses on the value of energy. To address some of the related issues, the system model of the previous section can be expanded to include an additional state variable:

$$V(k+1) = V(k) + \lambda(k)\,[P_1(k)\,t_1(k) + P_2(k)\,t_2(k) + P_3(k)\,t_3(k)]\,, \quad V(0) = 0\,, \qquad k = 0,1,\ldots,N-1\,, \tag{3.8}$$

where V(k) is the cumulative value of energy up to time k, and $\lambda(k)$ is the value of energy at period k, reflecting the avoided cost of alternative energy sources. The power outputs $P_1(k)$, $P_2(k)$ and $P_3(k)$ are fixed as in the previous section, and $t_1(k)$, $t_2(k)$, and $t_3(k)$ are the control variables representing generation hours. A problem of interest would be to develop operational policies that meet the constraints described in the previous section and in addition guarantee that the energy value at time N exceeds a minimum threshold V^{min}:

$$V(N) \geq V^{min}\,. \tag{3.9}$$

As seen by the new system state equation,

$$\begin{bmatrix} S_1(k+1) \\ S_2(k+1) \\ S_3(k+1) \\ V(k+1) \end{bmatrix} = \begin{bmatrix} 1 & 0 & 0 & 0 \\ 0 & 1 & 0 & 0 \\ 0 & 0 & 1 & 0 \\ 0 & 0 & 0 & 1 \end{bmatrix} \begin{bmatrix} S_1(k) \\ S_2(k) \\ S_3(k) \\ V(k) \end{bmatrix} + \begin{bmatrix} -b_1(k) & 0 & 0 \\ b_1(k) & -b_2(k) & 0 \\ 0 & b_2(k) & -b_3(k) \\ \lambda(k)\,P_1(k) & \lambda(k)\,P_2(k) & \lambda(k)\,P_3(k) \end{bmatrix} \begin{bmatrix} t_1(k) \\ t_2(k) \\ t_3(k) \end{bmatrix}$$

$$+ \begin{bmatrix} 1 & 0 & 0 \\ 0 & 1 & 0 \\ 0 & 0 & 1 \end{bmatrix} \begin{bmatrix} w_1(k) \\ w_2(k) \\ w_3(k) \end{bmatrix}, \tag{3.10}$$

$$= A\,S(k) + B(k)\,t(k) + G\,w(k),$$

$$k = 0,1,\ldots,N-1,$$

this problem has more state than control variables and is not directly amenable to the set control approach presented earlier. The problem is that the derivation of the reduced state sets, (lemma (2.17) in Section 2.2) requires that the coefficient matrix **B**(k) is invertible. To overcome this limitation, we can enforce invertibility by including an additional column and a fourth control variable, $t_4(k)$:

$$B(k)\,t(k) = \begin{bmatrix} -b_1(k) & 0 & 0 & 0 \\ b_1(k) & -b_2(k) & 0 & 0 \\ 0 & b_2(k) & -b_3(k) & 0 \\ \lambda(k)\,P_1(k) & \lambda(k)\,P_2(k) & \lambda(k)\,P_3(k) & -1 \end{bmatrix} \begin{bmatrix} t_1(k) \\ t_2(k) \\ t_3(k) \\ t_4(k) \end{bmatrix}. \tag{3.11}$$

The new column vector can have any form as long as it makes **B**(k) invertible. However, the new control variable should have an empty feasible range:

$$0 \le t_4(k) \le 0, \quad k = 0,1,\ldots,N-1. \tag{3.12}$$

The above modification does not alter the character of the original system. (The proof that the two equations essentially describe the same system is trivial.) It only facilitates the application of the set derivation procedures discussed earlier.

In summary, the set control problem amounts to finding feasible control policies for

the system (3.10), (3.11), and (3.5) such that all storage variables remain feasible (see Table 3.1) subject to constraints (3.6), (3.7), (3.9), and (3.12). The λ-values assumed for this computational experiment are shown below and are roughly indicative of the energy generation cost ($/MWH, weekly average) in the southeastern U.S.:

$$\lambda(k) = \begin{cases} 19, & \text{if } 1 \le k \le 13 \\ 24, & \text{if } 14 \le k \le 26 \\ 31, & \text{if } 27 \le k \le 39 \\ 19, & \text{if } 40 \le k \le 52 \end{cases} \qquad (3.13)$$

Annual energy generation is to always exceed 27.3 million dollars ($=V^{min}$), and the dependable energy sequence is 60% of the one reported previously. To determine the system potential to operate under these constraints, we performed the following computational experiment: First, the control model was run with a 52-week planning horizon to determine the reduced state sets. To simplify the procedure, the linearization of the B(k) matrices was performed around the initial storage values for all k. Then, the system operation was simulated over 50 weekly sequences of one year duration. Figure 3.8 includes some results related to energy generation. The first graph depicts the value of annual energy from each simulation and shows that it is always greater than the specified minimum. In fact, for V^{min} greater than this value, the control problem becomes infeasible. One can reduce the planning horizon to achieve feasibility but forgo the 52-week operational guarantee. The second graph portrays the energy generation sequences for which the annual energy value is almost equal to V^{min}. Actual energy generation always meets the specified dependable sequence. Storage and generation hour sequences are also feasible but are not shown.

The formulation of this section may also be used to control the system such that annual energy amounts and outflow volumes exceed certain levels. The first case can be analyzed by the same formulation after λ is omitted. The second would require that Equation (3.8) be replaced with one describing the cumulative outflow volume.

3.5 COMPUTATIONAL REQUIREMENTS

As an indication of computational requirements, we report the computer time necessary for three experimental runs. The experiments differ by the number of state variables and the length of the control horizon. All runs were performed on a 486/33 personal computer.

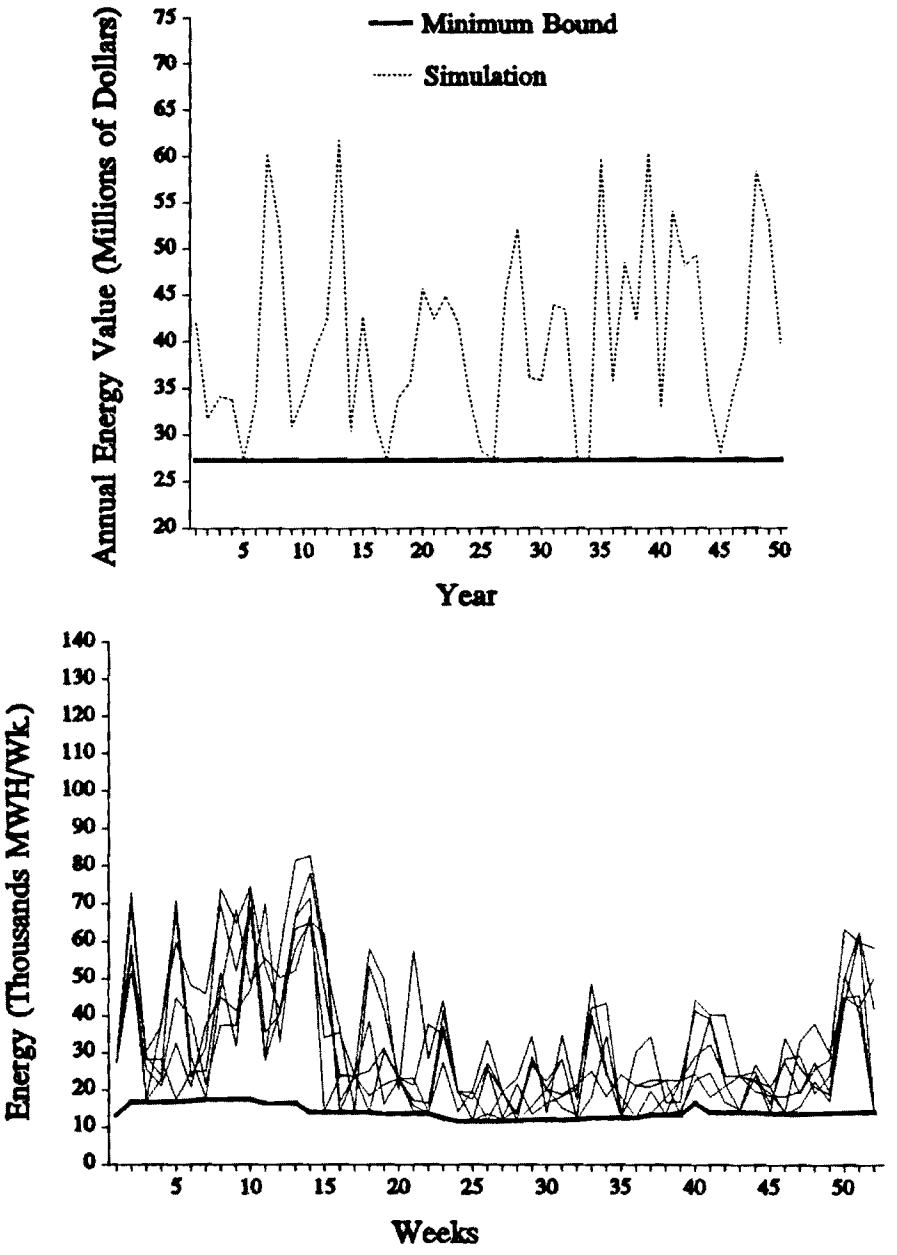

Figure 3.8 : Energy value simulations.

Table 3.2: Computer Time Requirements for Different Set Control Problems

Experiments	System Model Features	486/33 CPU Time (seconds)
I	State Variables: 3 Control Horizon: 52 weeks	29
II	State Variables: 3 Control Horizon: 260 weeks	128
III	State Variables: 4 Control Horizon: 52 weeks	75

A comparison of Experiments I and II, shows that computational requirements increase almost linearly with the length of the control horizon. Experiments I and III indicate that including a fourth state variable more than doubles computer time. Thus, system model size affects computational time more adversely than the length of the control horizon. However, the requirements are generally quite small, and the set control approach can practically handle large systems (including as many as 10 reservoirs) with a reasonable computational effort (70 to 80 minutes). All previous runs were performed under DOS and required less than 640 Kilo-Bytes of random access memory.

3.6 Value of Streamflow Forecasts

Reservoir control schemes with inflow forecasting capabilities are expected to improve flood prevention as well as other reservoir system functions. However, a question often raised is whether the benefits from such systems outweigh their costs. The purpose of this section is to provide a partial answer to this question by demonstrating that reservoir control and inflow forecasting procedures can substantially mitigate flood damage frequency and magnitude. The approach taken is to quantify the improvements for the Savannah reservoir system. While to some extent the actual benefits are expected to be system-specific, some general conclusions can still be drawn.

For the purposes of this section, the time dscretization is one day, and the system is modelled by the following water balance state equation:

$$\begin{bmatrix} S_1(k+1) \\ S_2(k+1) \\ S_3(k+1) \end{bmatrix} = \begin{bmatrix} 1 & 0 & 0 \\ 0 & 1 & 0 \\ 0 & 0 & 1 \end{bmatrix} \begin{bmatrix} S_1(k) \\ S_2(k) \\ S_3(k) \end{bmatrix} + \begin{bmatrix} -b_1(k) & 0 & 0 \\ b_1(k) & -b_2(k) & 0 \\ 0 & b_2(k) & -b_3(k) \end{bmatrix} \begin{bmatrix} t_1(k) \\ t_2(k) \\ t_3(k) \end{bmatrix} + \begin{bmatrix} 1 & 0 & 0 \\ 0 & 1 & 0 \\ 0 & 0 & 1 \end{bmatrix} \begin{bmatrix} w_1(k) \\ w_2(k) \\ w_3(k) \end{bmatrix}, \quad (3.14)$$

$$k = 0,1,\ldots,N-1,$$

$$b_i(k) = \sum_{j=1}^{n_i} u_{ij}(k), \quad i = 1,2,3, \quad (3.15)$$

where as before, $S_i(k)$ and $w_i(k)$ respectively represent storage and inflow volumes for reservoir i=1,2,3, $u_{ij}(k)$ is the discharge from the j^{th} turbine of the i^{th} reservoir, $t_i(k)$ represents the generation hours during period k, and n_i is the number of turbines at reservoir i. Table 3.3 reports relevant reservoir characteristics including permissible storage and release ranges reflecting water conservation and flood control objectives, and Figure 3.9 depicts extreme daily inflow volume ranges. These ranges represent the lowest and highest inflow values on record (10 years). The dependence of total turbine discharge on reservoir storage at power capacity was shown earlier on Figure 3.5.

Table 3.3: Reservoir Characteristics

	Reservoir 1	Reservoir 2	Reservoir 3
Min. Storage (bcf)	79.25	34.2	69.71
Max. Storage (bcf)	123.8	50.8	125.95
Min. Release (bcf / day)	0.0	0.0	0.0
Max. Release (bcf / day)	3.0	3.0	3.0
Power Capacity (MW)	430	375	350
Number of Turbines	5	4	7

The purpose of this section is to illustrate the potential benefits of combined inflow forecast - reservoir control schemes. Our approach is to simulate and assess the performance of the Savannah reservoir system over a 10-year period (1972-1981) under the guidance of the Set Control Approach and various inflow forecasting schemes. Inflow forecasts are assumed to restrict the historical inflow ranges (Figure 3.9) as follows: The actually observed inflow sequence over the duration of the

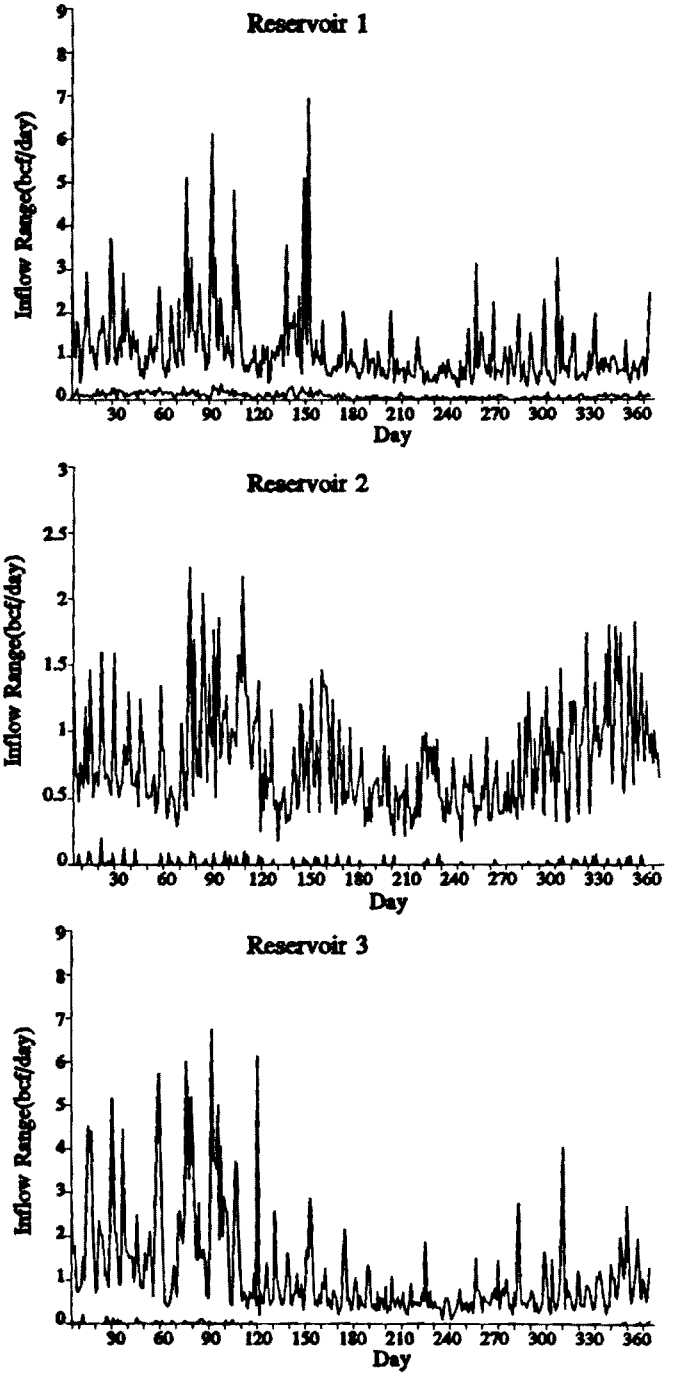

Figure 3.9: Daily inflow bounds

control horizon is first determined along with the corresponding historical ranges from Figure 3.9. The range used in the model for each day is centered around the actually observed value and represents a certain percentage of the historical range. As illustrated on Figure 3.10, these percentages gradually increase from the first to the last day of the control horizon to reflect that forecast quality deteriorates with lead time. The percentages are determined based on the following equation:

$$p(k) = p(1)\,[1.03]^{k-1}, \tag{3.16}$$

where p(k) denotes the percentage of day k. In the computational experiments to follow, this procedure is employed with $p(1)=0.5$ and $p(1)=0.25$. The results are compared with the case where SCA simply uses the historical inflow ranges from Figure 3.9 (no forecasting).

The simulation process is as follows: At each day of the simulation horizon, the forecasting model is first activated to determine the inflow ranges over the control horizon, and then the Set Control Approach is employed to generate the feasible control action set. This set includes all possible decisions guaranteeing that the system variables (storage, generation hours, and releases) will observe the stated constraints over the duration of the control horizon. Next, a decision is selected and the system operation is simulated for one time period. The simulation involves the determination of the next day's storages from Equation 3.14 with $w_i(k)$, $i=1,2,3$, being equal to their historically observed values. This process is repeated sequentially at each day of a 10-year simulation horizon, and system performance is recorded in terms of energy generation, outflow rates, and reservoir storage levels.

Some features common to all experiments are that the Set Control Approach is implemented with a control horizon of 15 days, the decisions selected correspond to the minimum feasible generation hours, the feasible storage range is restricted to the conservation pools, and the determination of turbine discharge over the 15-day control horizon is based on the current storage values. Experiments with a longer control horizon (30 days) were also conducted, but the results are similar to the ones presented herein. The rational for using the most conservative feasible decision is to conserve water and maintain reservoir pools as high as possible. Turbine discharges are determined based on the current storage because it is the best guess of future storage values. Certainly, the storage will eventually digress from this locale. However, the error is mitigated by the sequential mode of operation forcing continuous updating.

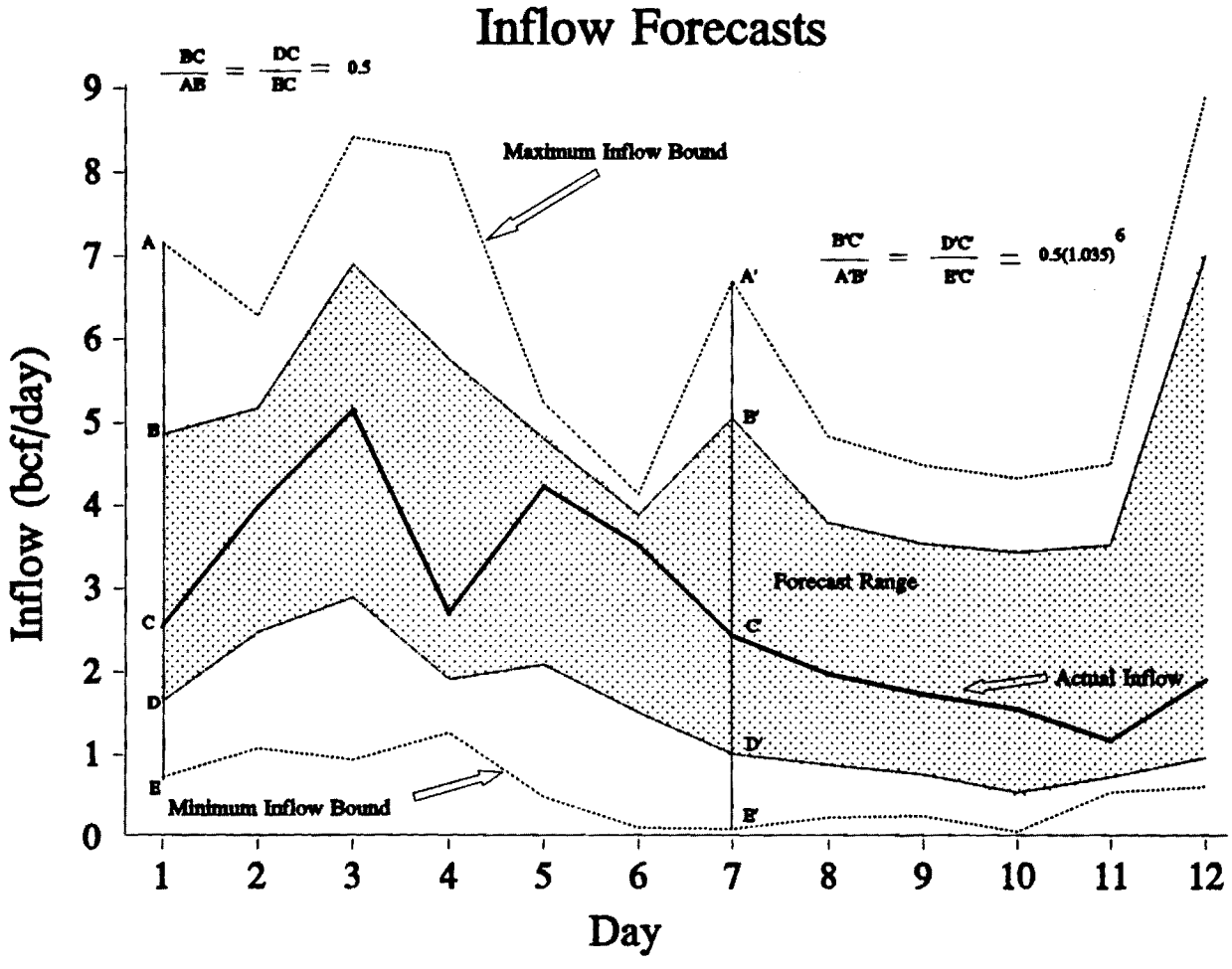

Figure 3.10: Inflow Forecasting Example

Figures 3.11 and 3.12 depict the results for the case where no inflow forecasts are used (base case). The graphs in Figure 3.11 include the storage bounds (dotted lines), the minimum and maximum simulation values for each day (thin solid lines), and the mean simulation storage sequence (thick solid line). The previous statistics were based on 10 simulation storage values for each day of the year. While system storages are maintained within the conservation pools, they tend to fluctuate markedly during the first part of the year (rainy season). Figure 3.12 includes the associated statistics for the control variables (generation hours per day), with dotted lines again representing bounds and solid lines depicting simulation statistics (minimum, maximum, and mean levels). The notable observation is that energy generation hours are often forced to exceed 24 hours per day in order to keep reservoir storages within the conservation pools. This simply implies that turbine conveyance capacity is not enough to control reservoir storage and water must also be released through the dam spillways. To be sure, the higher the exceedance of the 24-hour threshold, the more severe the flooding effects. More specifically, the highest release from the third reservoir in the cascade is about 3 times higher than the acceptable release bound. What is more, the mean generation sequence also violates the constraint threshold.

Figures 3.13 and 3.14 present the simulation results when the Set Control Approach has improved information of the upcoming inflows. This is simulated by using the procedure described previously (Eq. 3.16) with $p(1)=0.5$. The storage sequences (Figure 3.13) are again within the conservation zones, but the fluctuation ranges are now tighter. (The mean storage levels are clearly closer to the upper storage bounds.) The associated generation hours (Figure 3.14) on occasion exceed 24 hours / day, but the magnitude of the violation is much less than in the base case. Better forecasting allows the control model to mitigate flood damage. Nevertheless, the highest outflow is still 1.8 times higher than the acceptable release bound. This trend continues in the third case (Figures 3.15 and 3.16) where inflow forecasting is employed with $p(1)=0.25$. The mean storage sequences have moved even closer to the upper bounds, and the generation hours are for the most part contained within the admissible limits. The magnitude of constraint violations is reduced further, while the distance of the mean generation sequence from the 24-hour bounds indicates that violations occur infrequently.

The previous computational experiments demonstrate that inflow forecasting and reservoir control schemes can usefully assist reservoir operations during extreme hydrologic conditions. In particular, better inflow forecasting allows the control model to minimize flood control storage and, at the same time, avoid damage-causing outflows. While, the actual forecast quality cannot be quantified before the implementation of a forecast system, the potential reduction of flood damage

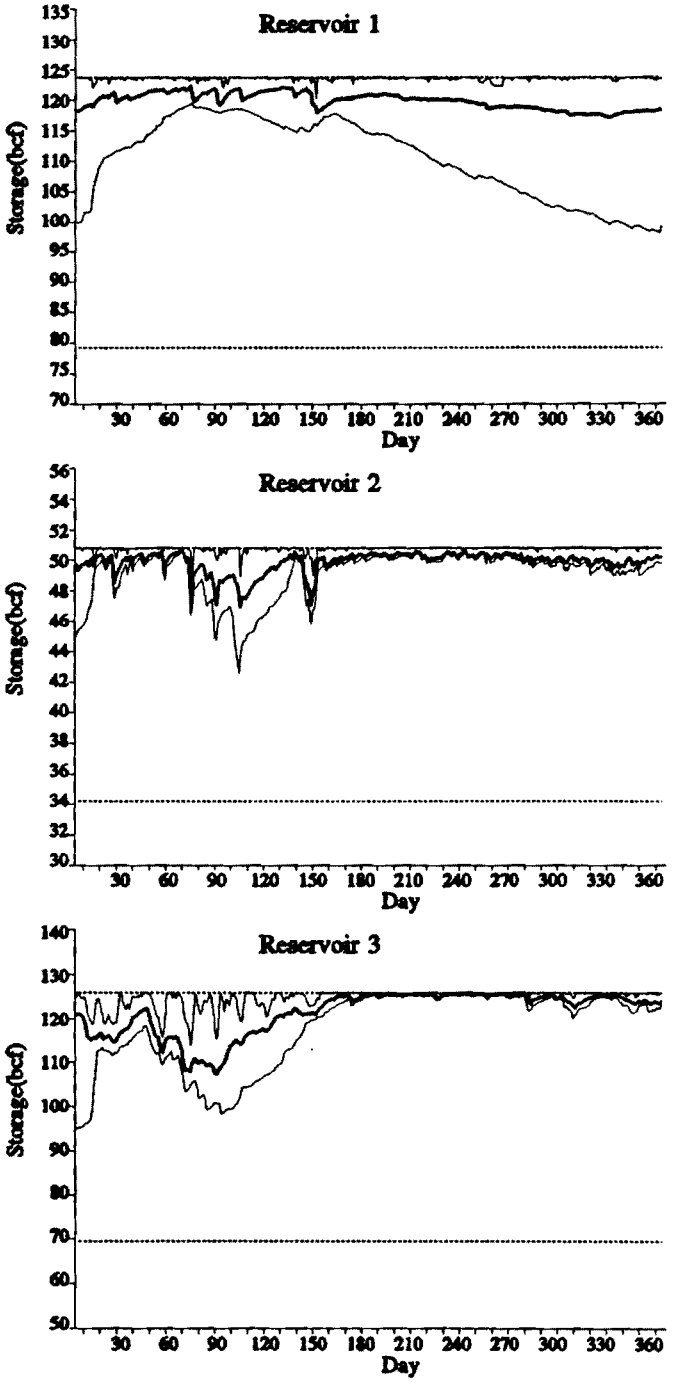

Figure 3.11: Simulation Storage; Base Case

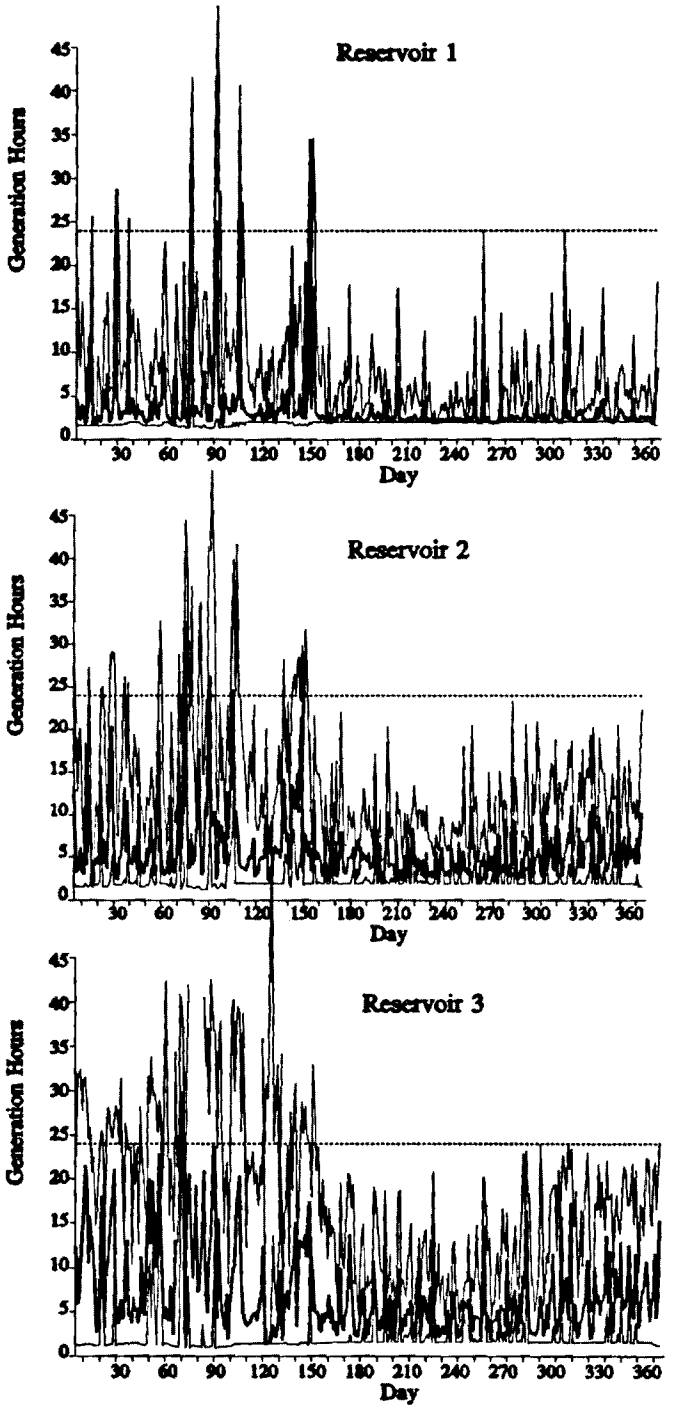

Figure 3.12: Simulation Gen. Hours; Base Case

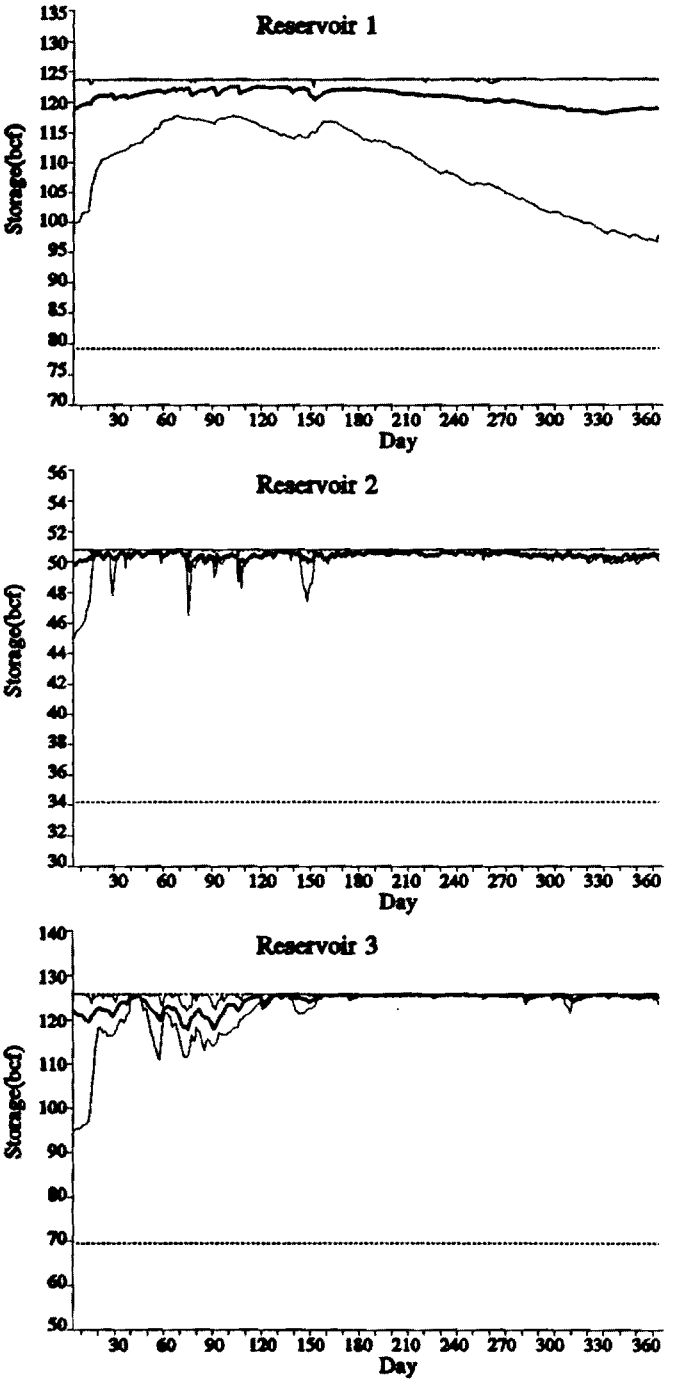

Figure 3.13: Simulation Storage; P(1)=0.5

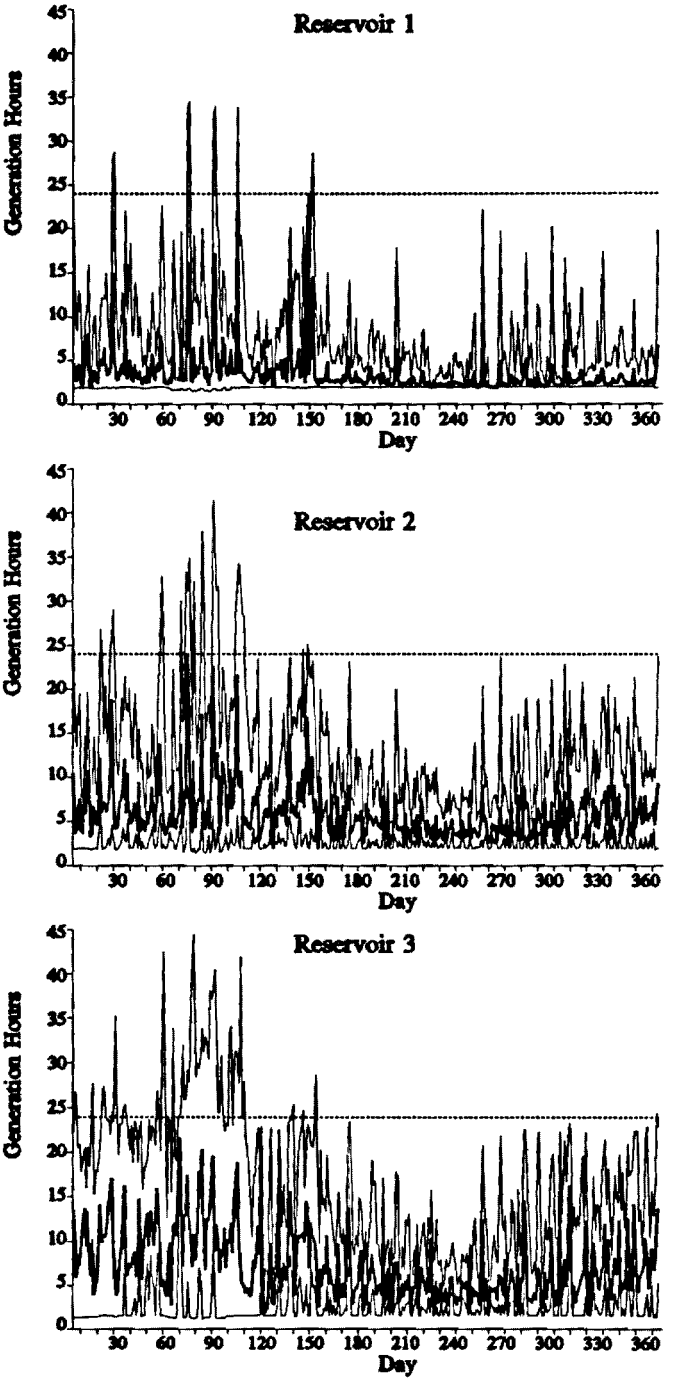

Figure 3.14: Simulation Gen. Hours;P(1)=0.5

frequency and magnitude can be substantial. In addition, benefits accrue from energy generation due to higher hydraulic head and less wasted spillage.

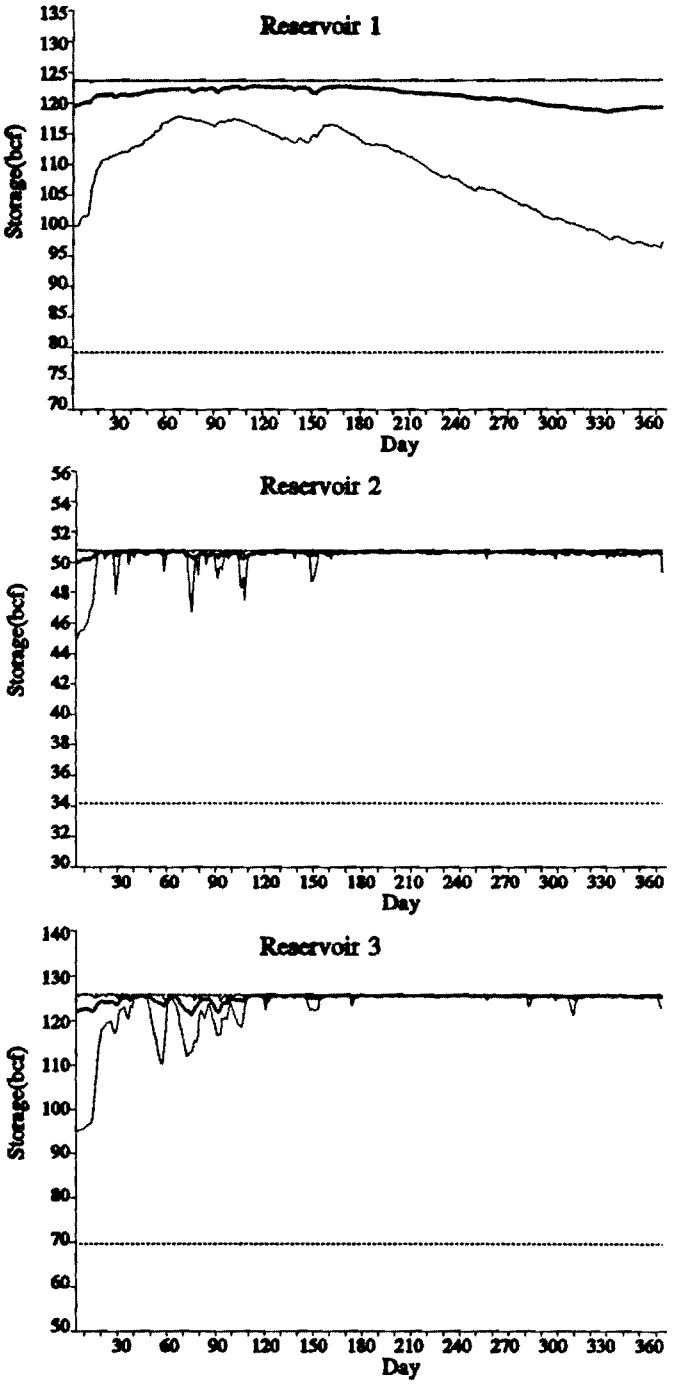

Figure 3.15: Simulation Storage; P(1)=0.25

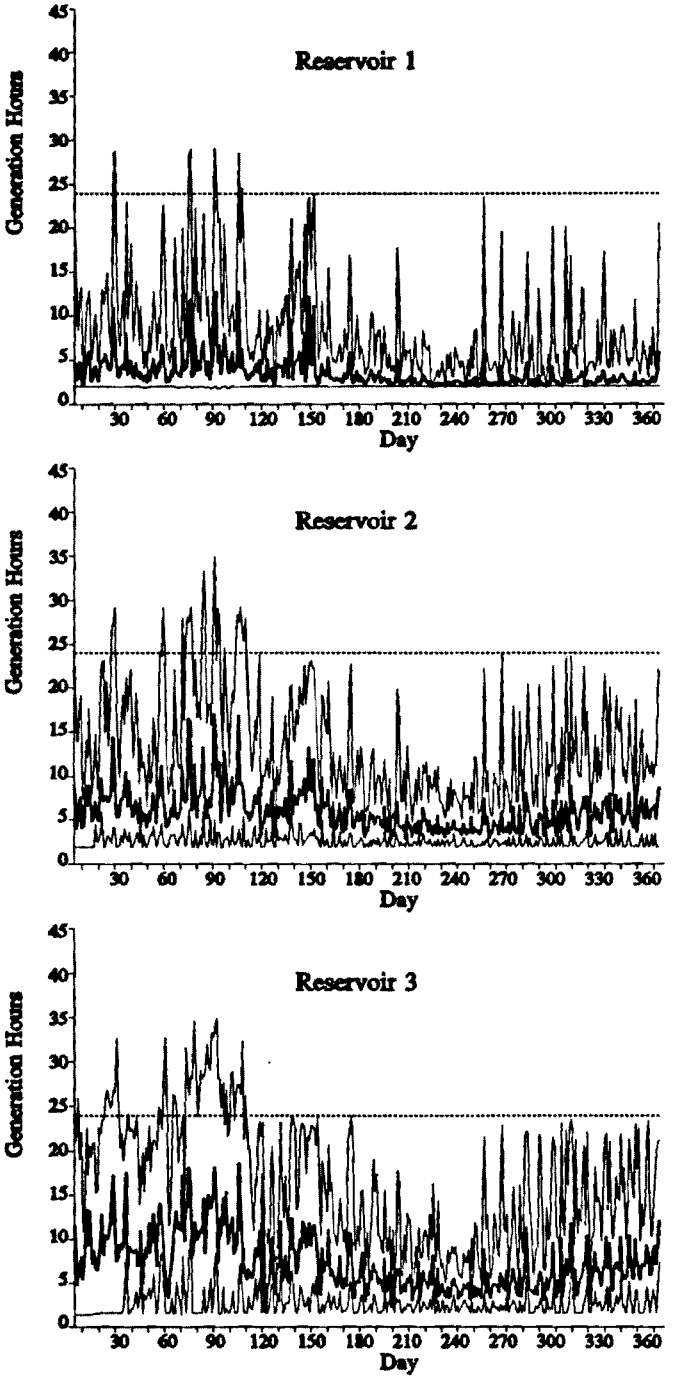

Figure 3.16: Simulation Gen. Hours; P(1)=0.25

4. COMBINED RIVERFLOW FORECASTING AND RESERVOIR CONTROL – SENSITIVITY OF RESERVOIR SYSTEMS TO CLIMATE CHANGE

In this chapter we focus on two areas. The first is the integration of streamflow forecasting procedures with reservoir control methods, and the second is the sensitivity of reservoir system outputs to climate change. Our objectives are (1) to assess the value of combined forecast-control schemes and (2) to examine whether their use can mitigate the adverse effects of potential climate changes.

The approach we take is depicted on Figure 4.1. It consists of a physically-based streamflow forecasting model and a reservoir control scheme. The forecasting model has been developed by the University of Iowa research team and is described in detail in the companion report (Volume II). The reservoir control scheme is the Set Control Approach developed by the Georgia Tech research team and has been presented in the previous chapters. For continuity, we next include a short overview of the two models.

The streamflow forecasting model is a modified version of the Sacramento model [*Peck, 1976*]. It is a conceptual, spatially lumped parameter model which predicts channel inflow based on estimates of mean areal precipitation, pan evaporation, and temperature [*Georgakakos, 1986*]. The model distinguishes upper and lower soil moisture zones where water is temporarily stored on its way to the stream channel. Each zone stores water in two forms: either as "tension water" or as "free water." Tension water is bound to soil particles and can be depleted only by evapotranspiration (ET). Free water moves through the various zones and eventually appears in the channel. Depletion of the upper zone free water may occur horizontally as channel inflow (interflow), vertically as percolation to the lower zone, or as evapotranspiration. Lower zone free water storage is further subdivided into primary (which sustains channel inflow during long lasting dry weather) and a supplementary (which drains faster). The model also includes a frozen ground component to account for the reduced yield from groundwater storage during winter, and a snow accumulation and ablation model to account for spring snowmelt. Channel inflow is obtained as the sum of five flow components: (**a**) Direct Runoff, resulting from precipitation occurring over the impervious soil surface adjacent to the watershed streams; (**b**) Surface Runoff, resulting when the rainfall rate over the pervious soil surface exceeds the soil infiltration capacity; (**c**) Interflow, draining from the upper zone free water; (**d**) Primary Base Flow, draining from the lower zone primary free water; and (**e**) Supplementary Base Flow, draining from the lower zone supplementary free water. Total channel inflow is routed through the channel system of the watershed via a lumped parameter nonlinear routing scheme. Final model output is the outflow discharge at the watershed outlet.

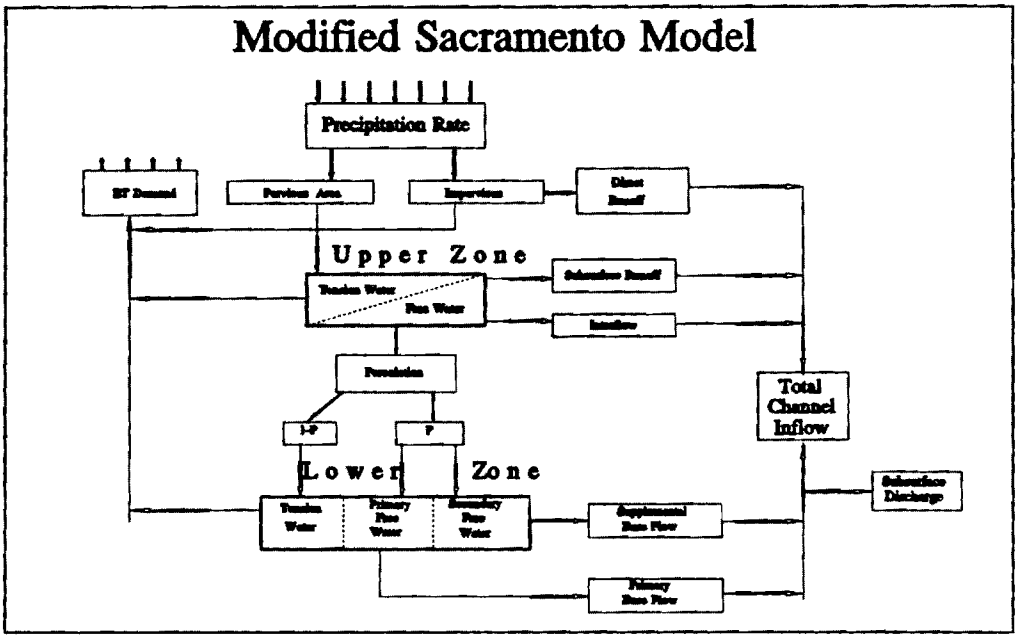

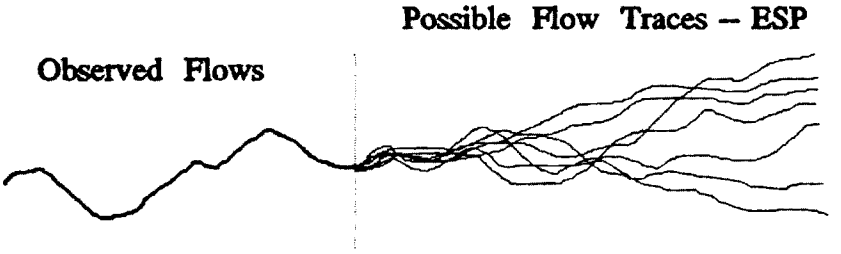

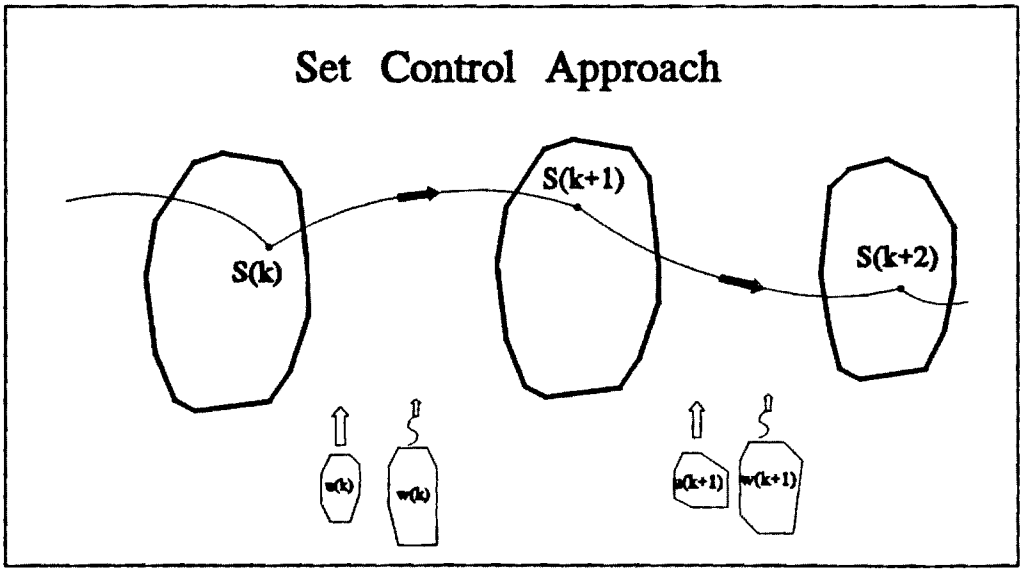

Figure 4.1: Combined Riverflow Forecasting and Reservoir Control

The modified Sacramento model is coupled with a Kalman Filter (state estimator) to utilize system observations up to the present time (streamflow measurements and snowpack thickness) and estimate key system variables (storage of the various surface and subsurface components) with minimal error. The basic concept of the state updating model is to linearize the model equations about the current variable estimates, propagate their uncertainty in time, and update their values when new observations become available. In practical terms, this mechanism enables one to quantify and minimize forecast uncertainty.

Herein, the modified Sacramento model is used to generate equally likely future inflow traces via a technique known as Extended Streamflow Prediction or ESP [*Day, 1985*]. ESP uses (**a**) current soil moisture, snowpack, and channel flow conditions and (**b**) historical data of mean areal precipitation, pan evaporation, and temperature corresponding to the calendar days of the forecast horizon, to generate possible inflow realizations. These realizations represent inflow sequences that would materialize if the historically observed input sequences were repeated again over the forecast horizon. The inflow traces tend to spread out as they "forget" the current watershed conditions and eventually fill up the historically observed inflow range. The ESP results are next used by the control model to define forecasted reservoir inflow ranges over the management horizon.

The control model is based on the Set Control Approach and aims at maintaining all system variables (storages, releases, and possibly other outputs) within acceptable sets. This approach was developed as an alternative to stochastic control methods with the motivation that during extreme hydrologic events (floods and droughts) or climate change circumstances, probabilistic inflow characterizations become unreliable due to the lack of adequate data records.

In the following section, the combined forecast-control procedure will be applied for the management of the Sailorville reservoir in the upper Des Moines river basin.

4.1 APPLICATION TO THE UPPER DES MOINES RIVER (MIDWEST)

4.1.1 The Upper Des Moines River Basin

The upper Des Moines river basin (Figure 4.2) has an area of 14,120 square kilometers (5,452 square miles), two thirds of which is in the state of Iowa and the rest in Minnesota. The river is controlled by Saylorville, a US Army Corps of Engineers reservoir located at the basin outlet. Saylorville has a usable storage of 0.7 billion cubic meters (567,906 acre-ft) and two primary purposes: (1) Provide flood protection for the city of Des Moines and surrounding areas and (2) augment the river low flows for water supply and water quality. In terms of reservoir release rates, these two purposes translate into the requirements shown on Figure 4.3. To avoid flood damage, from December 15 to April 15 maximum reservoir release should not exceed 16,000 cubic feet per second (cfs) , while the rest of the year (farming season) it should be less than 12,000 cfs. The importance of Sayloville's flood control objective cannot be overemphasized in light of the on-going devastating floods of the Mississippi river and its tributaries, one of which is the Des Moines river. (The juncture of the Des Moines with the Mississippi is at the tri-state border between the states of Iowa, Illinois, and Missouri.) The second graph in this figure shows the minimum releases for low flow augmentation. Water supply accounts for 200 cfs, and water quality for an additional, seasonally-varying amount ranging from 30 cfs in January to 110 cfs in July. Saylorville is operated by the Rock Island US Army Corps of Engineers District who also provided all hydrologic and operational data used in this report.

To assess the value of the forecast-control scheme and examine the sensitivity of the case study system to climate changes, we subdivided the historical inflow record into three periods (Figure 4.4). The first extends from 1925 to 1949 and has the warmest annual average temperature and the lowest average streamflow (1,596 cfs). The second (from 1949 to 1974) is cooler by 2° C with respect to the first but has a higher annual average streamflow (2,003 cfs) and markedly higher variability. The third period (from 1965 to 1988) is the coolest and wettest of all three (with an annual inflow mean of 2,686 cfs). Each period herein serves as a historical analogue of a potential climatic scenario and is a first approximation to climate changes of larger magnitude. For a detailed discussion of the hydrologic analysis leading to the selection of these periods, the reader is referred to the companion report (Volume II) by the University of Iowa research team.

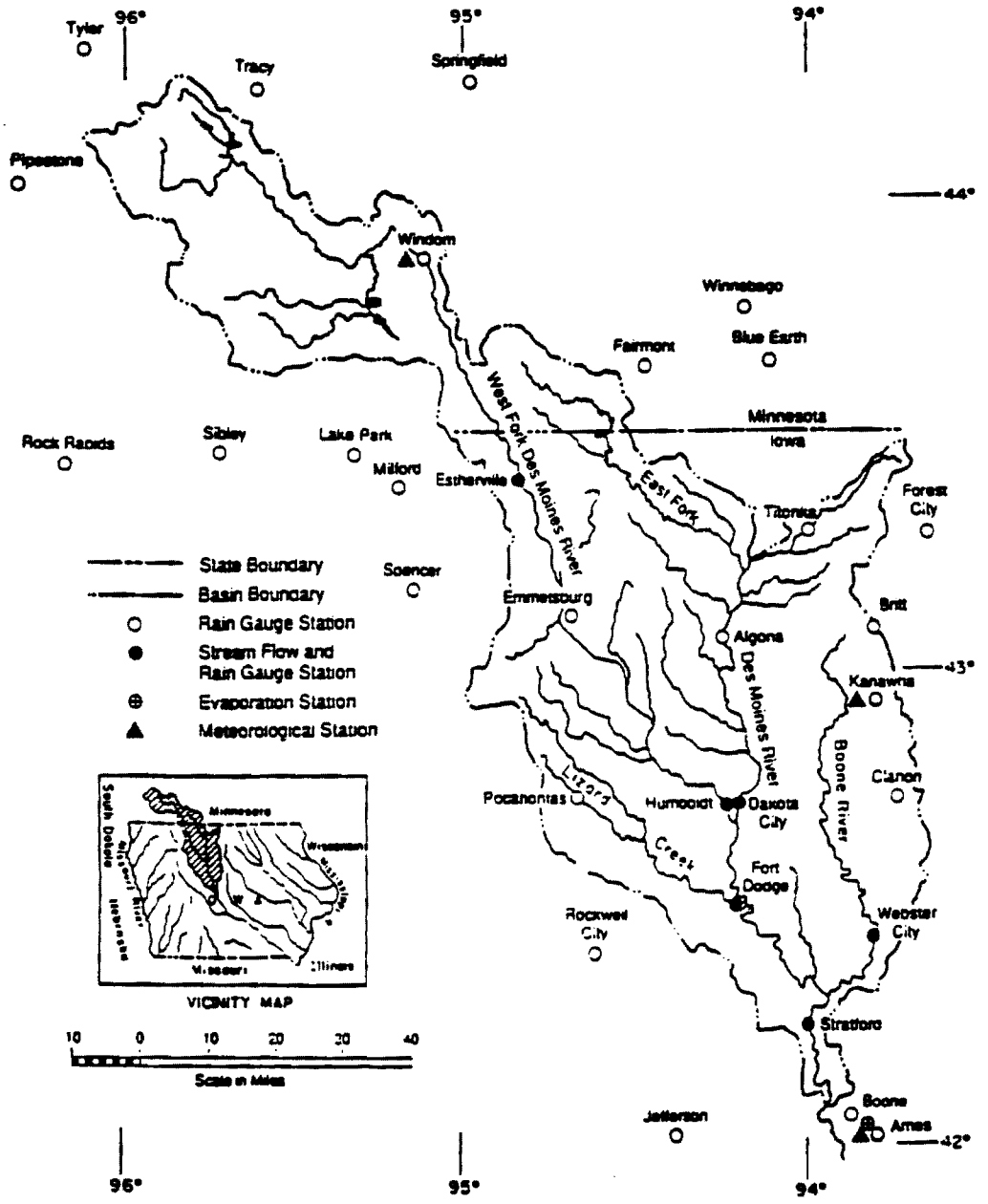

Figure 4.2: The Upper Des Moines River Basin

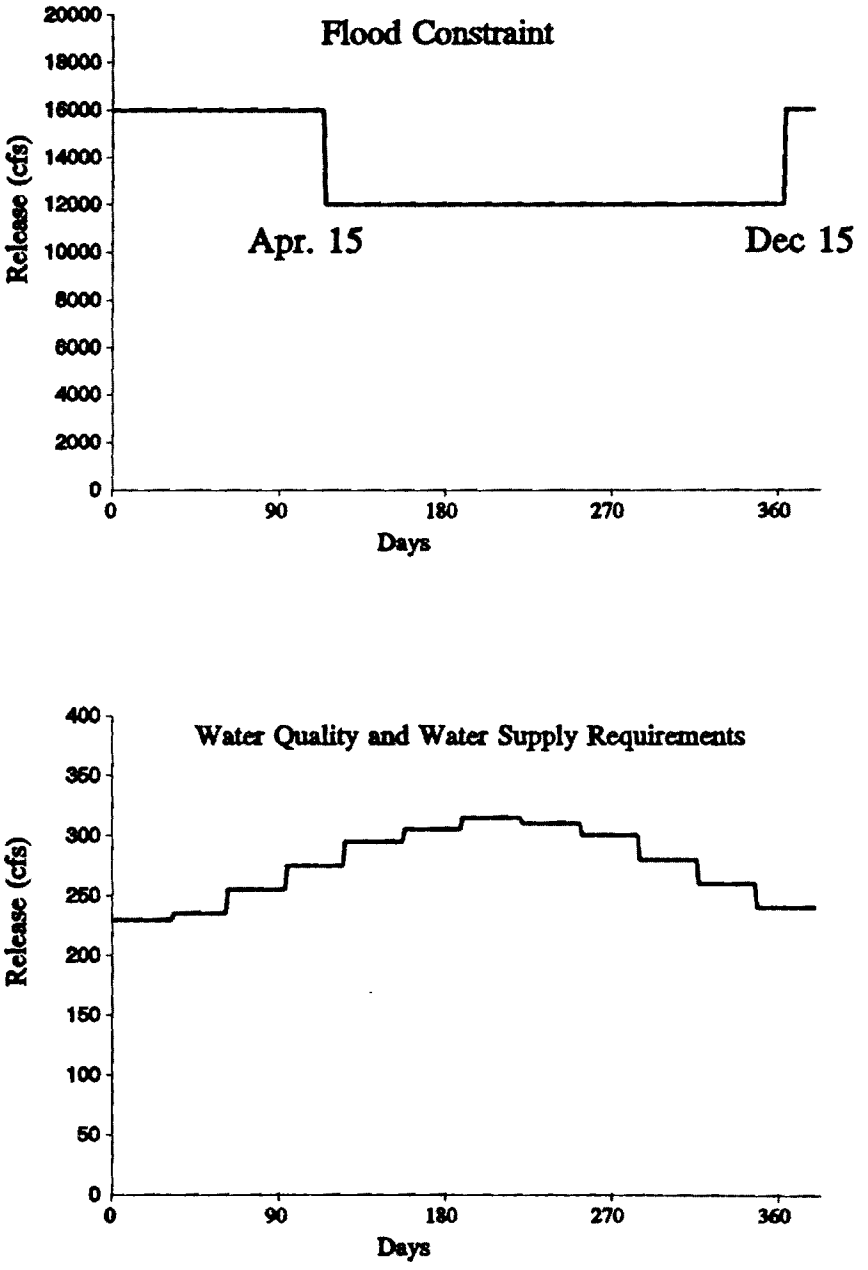

Figure 4.3 Release Requirements for Saylorville

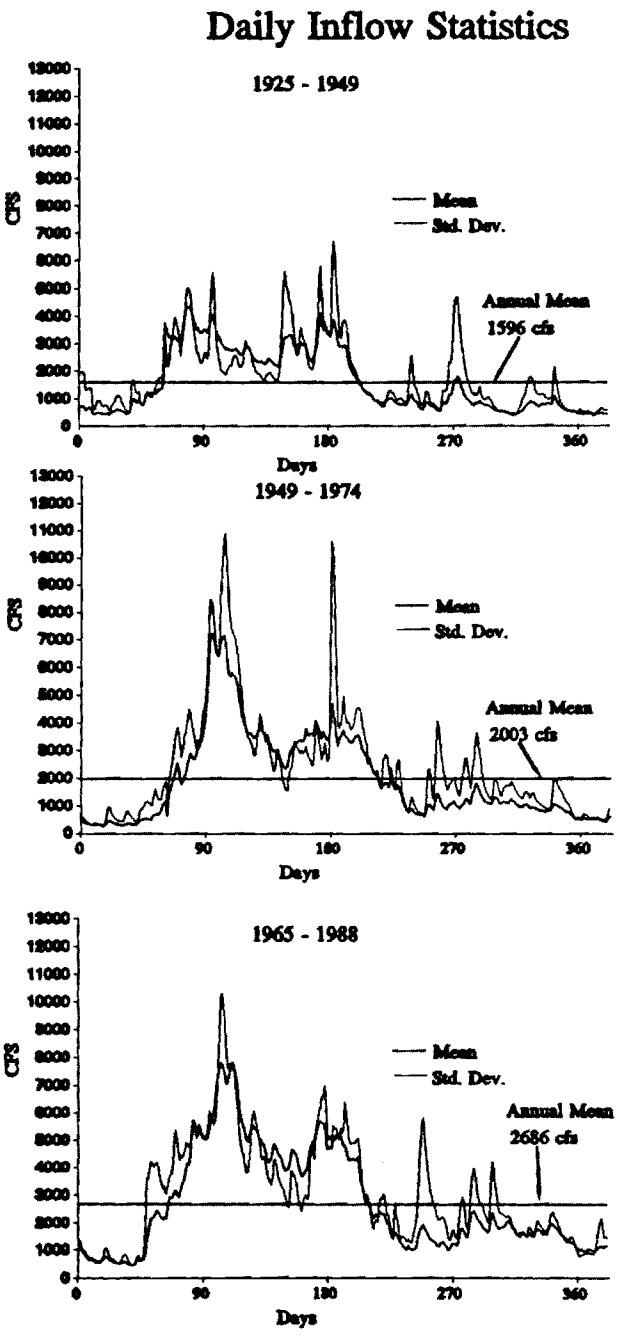

Figure 4.4 Historical Analogues of Potential Climatic Changes

4.1.2 Value of Forecast-Control Scheme -- Sensitivity to Climate Changes

In this section we present the results from several computational experiments intended to assess the performance of Saylorville under the guidance of three different management approaches. The first is a heuristic procedure presently used by the Corps of Engineers (COE), consisting of a simple forecasting scheme and a rule curve [U.S. Army Corps of Engineers, 1983]. The second is the Set Control Approach with knowledge only of the historical inflow bounds (without forecasting), and the third is the combined forecast-control scheme. Each approach is implemented on a daily basis and the performance of the system is simulated over the three hydrologic periods. The second and third approaches are implemented with a forecast-control horizon of 20 days. The simulation experiments are designed to (1) investigate whether formal control schemes such as the Set Control Approach offer any relative advantages over heuristic reservoir management procedures, (2) assess the benefit of streamflow forecasting in reservoir management, and (3) examine the sensitivity of Saylorville to potential climate changes.

Figure 4.5 presents the simulation results for the first hydrologic period (warm-dry scenario). In each of the three graphs, the horizontal axis depicts the days of the year and the vertical is the axis of reservoir release. Namely, the graphs show the release sequences that would have resulted had the operator followed the recommendations of each management approach. The first graph corresponds to the Corps of Engineers management method, the second to the Set Control Approach with only historical inflow information, and the third to the Set Control Approach using forecasted information furnished by the modified Sacramento model and the Extended Streamflow Prediction (ESP) procedure. Each graph includes as many lines as the number of years in the hydrologic sequence.

In reference to flood constraint violations, the important observation is that, unlike the other two approaches, the heuristic management procedure cannot avoid flooding. In fact, several violations of the 12,000 cfs release bound are recorded ranging from 4,000 to 10,000 cfs. Though not clearly shown in the figure, the heuristic procedure also violates the low flow augmentation constraint. By contrast, the other two models meet both requirements almost always, with the exception of one flooding instance by the HIS-SCA model by about 2,000 cfs. Figure 4.6 shows the associated reservoir elevation sequences. The COE graph reflects the heuristic rule-curve procedure attempting to maintain reservoir levels at 836 feet from December 15 to April 15 and 838 feet the rest of the year. This, however, is not always possible and frequent excursions from these targets are noted during wet or dry periods. Under the Set Control Approach, reservoir levels are allowed to vary anywhere within their feasible range. However, without the benefit of forecasting,

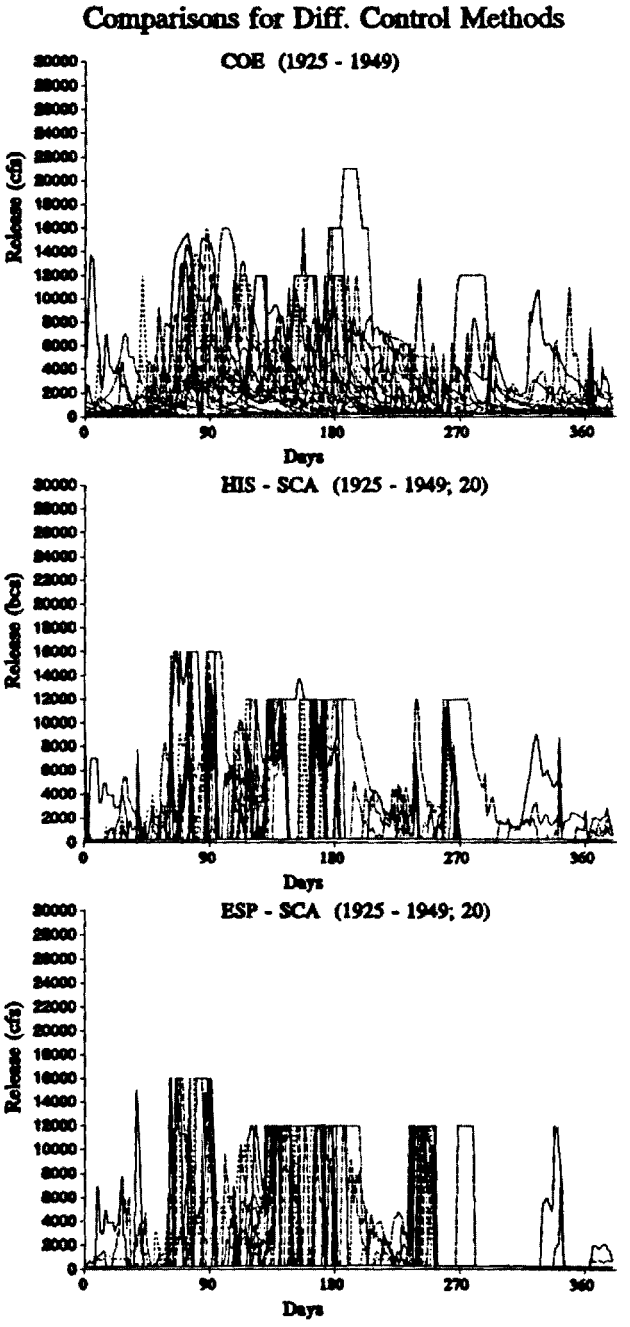

Figure 4.5 Simulated Reservoir Release; First Hydrologic Period

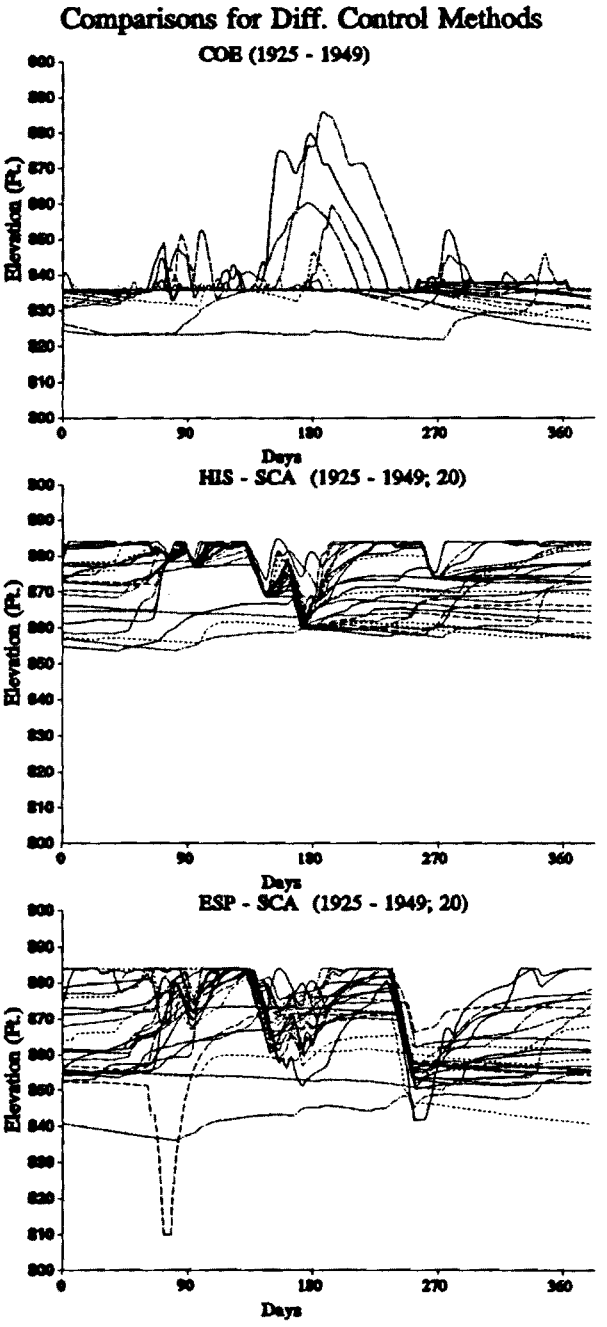

Figure 4.6 Simulated Reservoir Levels; First Hydrologic Period

the HIS-SCA model is conservative, maintaining reservoir levels within a relatively narrow range, while the ESP-SCA model if necessary utilizes the entire feasible range and avoids constraint violations altogether.

Figures 4.7 and 4.8 include the results of the second (wetter) hydrologic period. The release graphs show that both the COE and the HIS-SCA models experience violations of the flood control bound, while the ESP-SCA approach is always feasible. Reservoir levels (Figure 4.8) are forced to fluctuate over a wider range in comparison to the first period (Figure 4.6), with the ESP-SCA levels fluctuating the most. With regard to flooding, the COE model performs better than the HIS-SCA model. However, as will shortly be discussed, HIS-SCA causes far fewer water shortages.

Lastly, Figures 4.9 and 4.10 depict the results of the third hydrologic period, the wettest one of all. All models exhibit violations, but the ESP-SCA model violations are considerably fewer and far less severe than those of the other two.

The previous graphs mainly illustrate the performance of Saylorville with respect to flood control. Table 4.1 summarizes its performance also with respect to drought management (low flow augmentation) and hydropower production. Although hydropower is not a real project purpose (Saylorville does not have hydropower facilities), it was hypothesized as such to examine its sensitivity to the various management methods and hydrologic scenarios. Its power production function was assumed to have the form $P = \eta H_n u$, where P represents power, H_n is the net hydraulic head, u denotes turbine discharge, and η is an efficiency factor. The discharge capacity of the turbines is assumed to be 16,000 cfs. For the flood and drought management, system performance is characterized by the magnitudes of the maximum and mean violations as well as the violation frequency, while for hydropower the comparison is based on the yearly average production. To examine the effect of the forecast lead time, we run two additional simulation experiments using the ESP-SCA approach with 10 and 30 days forecast/control horizon.

Comparing the performance of the original methods (COE, HIS-SCA(20), and ESP-SCA(20)), we observe that also with respect to droughts the forecast-control scheme is better than the other two. For all three periods, ESP-SCA(20) recorded zero low flow constraint violations. By comparison, the heuristic procedure (COE) experiences frequent water shortages in all periods, while the control approach without forecasting (HIS-SCA(20)) reports violations only in the second and third periods. At first glance, it would seem odd that the HIS-SCA model does not incur low flow violations during the first (dry) period while having such instances during the second and third (wetter) periods. This happens because mean inflow is but one hydrologic parameter influencing reservoir operation and outputs, with inflow

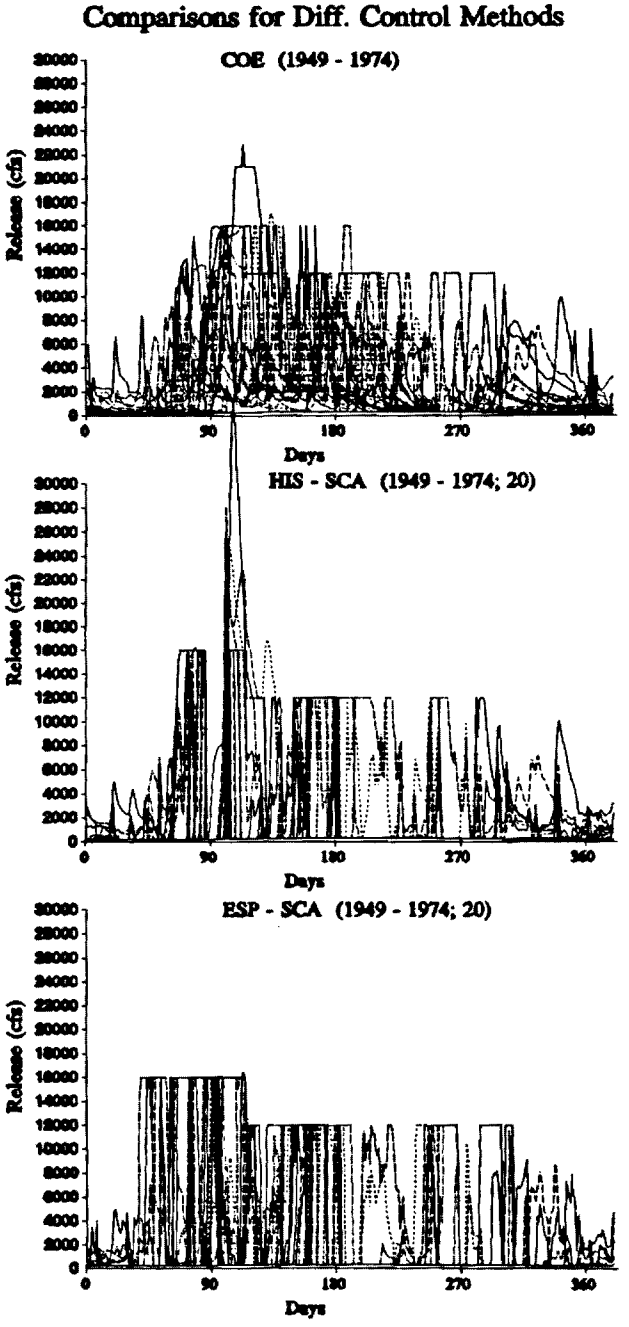

Figure 4.7 Simulated Reservoir Release; Second Hydrologic Period

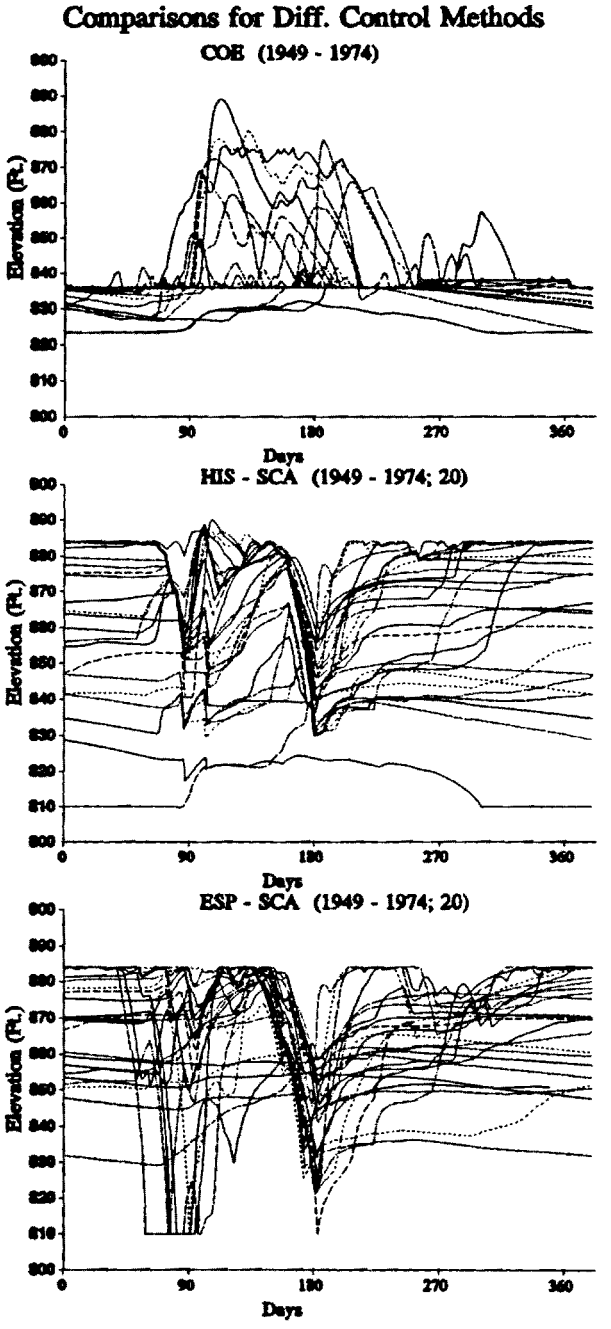

Figure 4.8 Simulated Reservoir Levels; Second Hydrologic Period

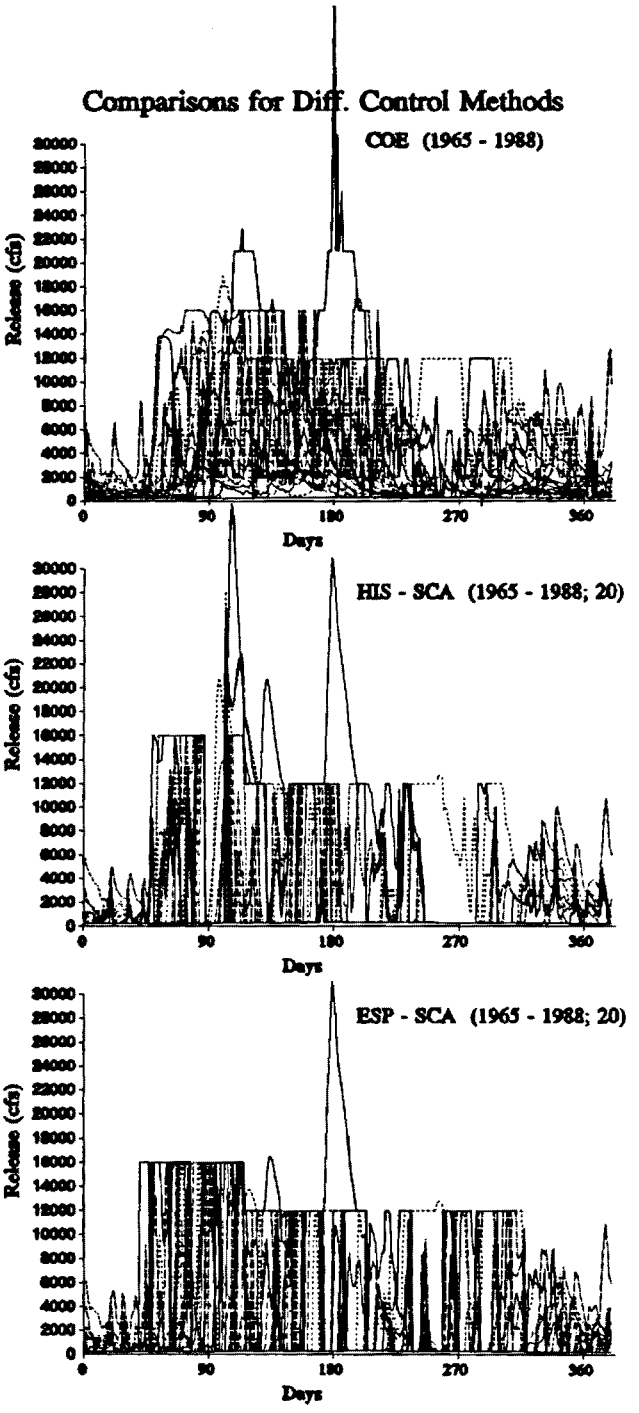

Figure 4.9 Simulated Reservoir Release; Third Hydrologic Period

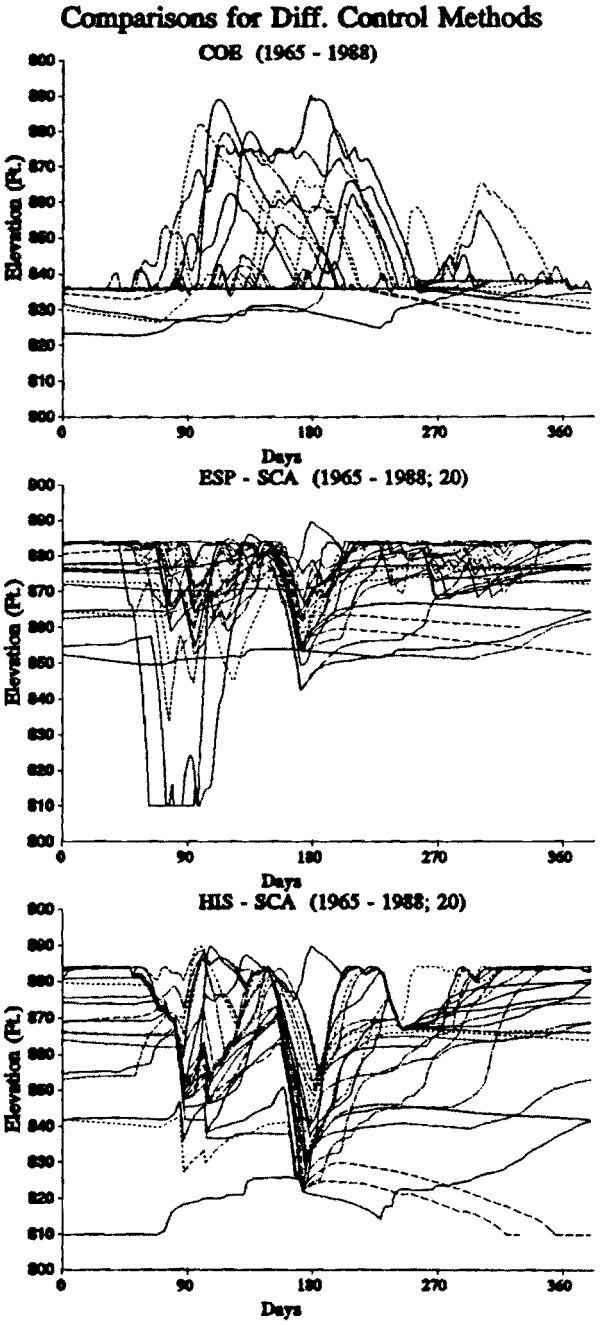

Figure 4.10 Simulated Reservoir Levels; Third Hydrologic Period

Table 4.1 Summary of Simulation Results

Performance Statistics for Period 1925-1949

Cases	Flood Constraint Violation			Water Qual. & Supply Violations			Yearly Avg. Power Production (x8760 KWH)
	Max Viol. (cfs)	Mean Viol. (cfs)	Viol. Times	Max. Viol. (cfs)	Mean Viol. (cfs)	Viol. Times	
COE	9000.	5275	40	205	37	1384	2613.56
HIS/SCA(20)	1728	1088	6	0	0	0	3987.76
ESP/SCA(10)	7232	3240	30	0	0	0	3960.00
ESP/SCA(20)	0	0	0	0	0	0	3729.60
ESP/SCA(30)	0	0	0	0	0	0	3563.54

Performance Statistics for Period 1949-1974

Cases	Flood Constraint Violation			Water Qual. & Supply Violations			Yearly Avg. Power Production (x8760 KWH)
	Max. Viol. (cfs)	Mean Viol. (cfs)	Viol. Times	Max Viol. (cfs)	Mean Viol. (cfs)	Viol. Times	
COE	9000	4145	75	200	36	1250	3473.10
HIS/SCA(20)	20957	5045	77	237	163	155	4345.41
ESP/SCA(10)	11446	5804	9	0	0	0	4615.00
ESP/SCA(20)	436	436	1	0	0	0	4084.56
ESP/SCA(30)	0	0	0	237	158	209	3639.04

Performance Statistics for Period 1965-1988

Cases	Flood Constraint Violation			Water Qual. & Supply Violations			Yearly Avg. Power Production (x8760 KWH)
	Max. Viol. (cfs)	Mean Viol. (cfs)	Viol. Times	Max Viol. (cfs)	Mean Viol. (cfs)	Viol. Times	
COE	32422	5000	136	250	25	954	4555.42
HIS/SCA(20)	19480	5518	122	219	178	102	5912.50
ESP/SCA(10)	20166	4869	114	0	0	0	6721.00
ESP/SCA(20)	19064	5296	46	0	0	0	6189.12
ESP/SCA(30)	14186	7604	19	0	0	0	5601.93

variability being another. To guard against high flows during the wet periods, the controller draws the reservoir down. If a dry spell then occurs, reservoir storage is not enough to meet low flow requirements and the reservoir defaults. Thus, wetter hydrologic climates may not necessarily provide more insurance against droughts. With regard to power generation, the heuristic procedure falls short of the other two in all cases (by about 20 to 30 percent). In the first two periods, HIS-SCA(20) maintains higher storage levels (and net hydraulic heads) than ESP-SCA(20) and generates more energy (by about 5 percent). In the third period, spillage becomes the limiting factor, and this trend is reversed. As a general rule, energy generation is higher in wetter climates.

In reference to the forecast lead time, it can generally be stated that the longer the lead time the better the system performance. However, these benefits extend up to the time when the forecasted ranges are smaller than the historical bounds. For the upper Des Moines river basin and the Sayloville reservoir, this time is about 20 to 30 days.

As a final remark, we note that the forecast-control model ESP-SCA(20) manages to mitigate the adverse effects of climatic change. It experiences zero low flow violations for all hydrologic periods and zero flooding violations for the first and second periods. By contrast, the effectiveness of the heuristic management procedure is low as is its ability to adapt to potential climatic changes.

4.2 APPLICATION TO THE CHATTAHOOCHEE RIVER (SOUTHEAST)

4.2.1 System Description

Lake Lanier is a man-made reservoir (Figure 4.11) located on the upper reaches of the Chattahoochee River in the State of Georgia (about 35 miles northeast of Atlanta). This reservoir extends up the Chattahoochee and Chestatee River and has a 1,040 square miles drainage area. The Dam at the Lake's outlet (at Buford) was constructed by the U.S. Army Corps of Engineers (COE) in 1957, and, along with three other federal storage projects in the Apalachicola-Chattahoochee-Flint (ACF) River basin, its operation falls under the jurisdiction of the Mobile COE District.

The project has several operational objectives including flood protection as far downstream as West Point (150 miles below Buford), navigation in the Apalachicola River below Woodruff Dam, industrial and domestic water supply for Atlanta and environs, recreation, and hydroelectric energy generation. The reservoir has a conservation storage of 1.342 billion cubic meters (1,088,065 acre-ft) between the elevations of 1035 and 1071 feet. Hydropower is produced by two main turbines each with an installed capacity of 49.5 MW and a small 6 MW unit. Buford releases are especially critical during low flow periods.

Appendix B describes various reservoir characteristics such as the elevation vs. storage curve, tailwater function, and power generation relationships of the Dam's three turbines. These curves were developed using data from the reservoir regulation manual (US. Army Corps of Engineers, 1959).

Buford is primarily operated to satisfy peak power and minimum flow requirements. These requirements are presently met by "running" the two main turbines at 49.5 MW for two hours each day except weekends (for a total of 43.5 hours per month) and the smaller turbine at 6 MW continuously. Additional releases and energy generation are scheduled based on SEPA's (South-Eastern Power Administration) energy commitments and the condition of the other federal hydropower facilities in the southeastern U.S. region.

Figure 4.12 portrays the monthly statistics (mean, 75th and 2th percentiles, maximum and minimum) of Lake Lanier inflow.

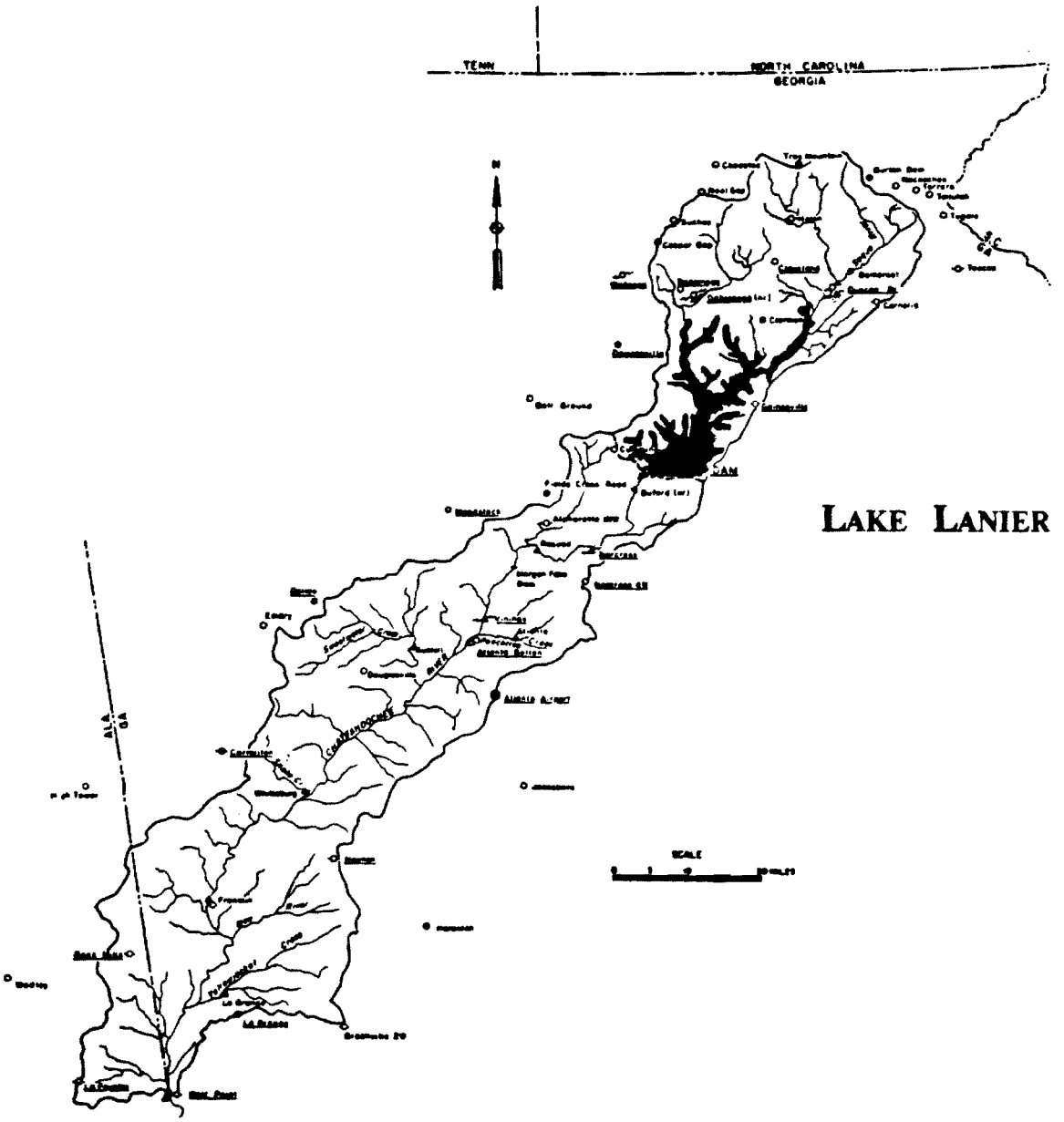

Figure 4.11: Hydrological Map of Lake Lanier-Bufford Dam

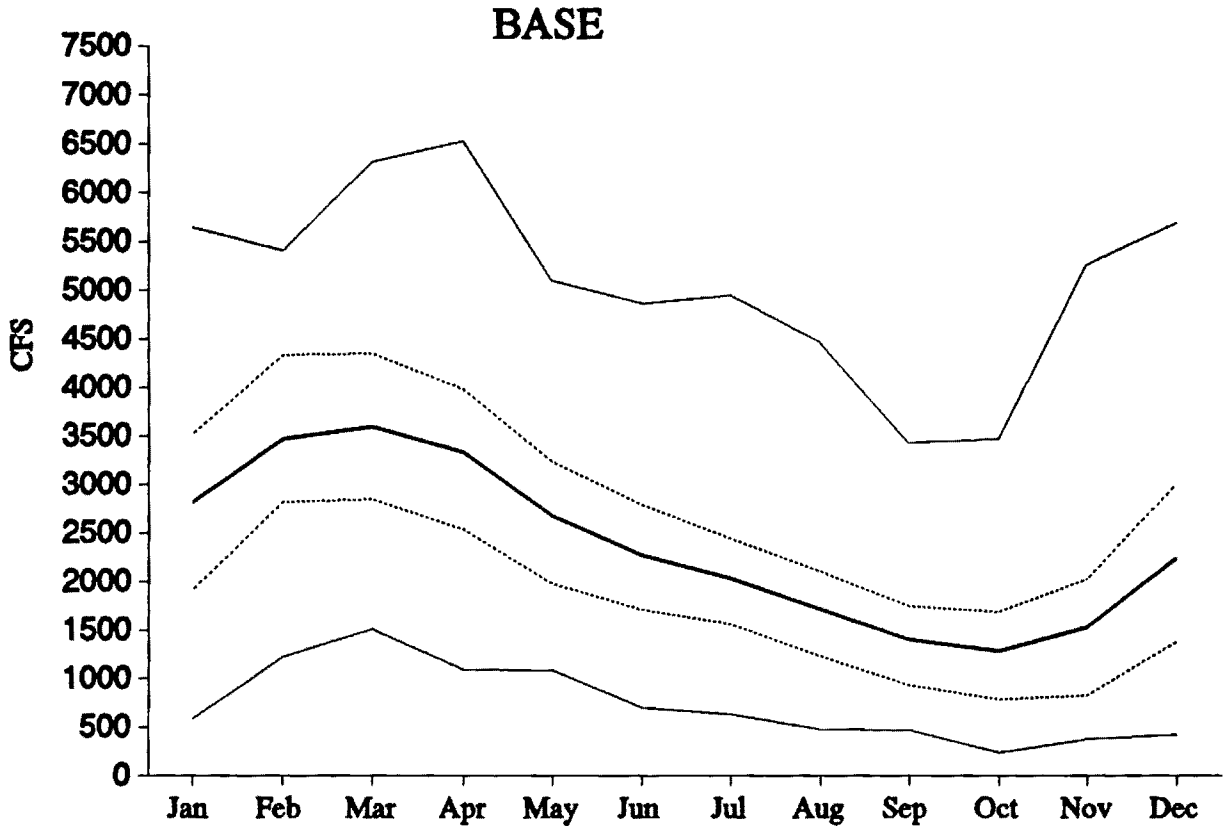

Figure 4.12 Lake Lanier Inflow Statistics (mean, 75th and 25th percentiles, maximum and minimum)

4.2.2 Lake Lanier Sensitivity to Climatic Changes

The purpose of this section is to investigate the operational sensitivity of Lake Lanier under various hydrologic and operational scenarios. This investigation is based on simulation experiments similar to the ones conducted in the previous section, but with a monthly time step. All runs utilize the Set Control Approach with a control horizon of 12 months. Streamflow forecasting is simulated in the same manner as in Section 3 (Savannah River case study). The simulations are performed using four 94-year long inflow traces that reflect present and potentially different climatic circumstances. These traces have been kindly provided to us by G. D. Tasker of the Reston USGS office. Their derivation is briefly explained next. [See also, *Tasker, 1993.*]

General circulation models (GCMs) show that further accumulation of green-house gases in the atmosphere may substantially change the prevailing temperature and precipitation patterns. In the case of the southeastern United States, three GCMs (Geophysical Fluid Dynamics Lab -- GFDL, Goddard Institute for Space Studies -- GISS, and the Oregon State University -- OSU models) indicate that doubling of atmospheric CO_2 would lead to an increase in annual temperature by several degrees and a substantial decrease of precipitation. More specifically, GFDL predicts a 5.3 °C annual temperature increase and a 88.9% precipitation reduction, GISS similarly predicts a 5.2 °C temperature increase and a 100.5% precipitation reduction, and OSU a 3.7 °C temperature increase and a 99.8% precipitation reduction. Monthly percentages are also available [*Tasker, 1993*] indicating strong seasonality. Although the predictive accuracy of GCMs is questionable [*Gleick,1989*], their results are herein used to establish plausible future climatic scenarios.

To convert this information to inflow traces, Tasker [*1993*] first generates random temperature and precipitation deviations from the historical monthly means using a multi-site Markov model. These estimates are next adjusted by a percentage determined by the GCM-predicted monthly increment or reduction. Finally, a physically-based rainfall-runoff model is used to translate the resulting temperature and precipitation traces to inflow sequences.

To compare with the base case (Figure 4.12), monthly inflow statistics for the GFDL, GISS, and OSU inflow sequences are also plotted on Figures 4.13, 4.14, and 4.15. While the figures show a clear reduction of mean monthly inflow relative to the base case, extreme inflow values are in some cases outside the base case range.

The first simulation experiment is the base case where the generation hours may range from 43.5 to 730 hours per month and the inflow sequence corresponds to the

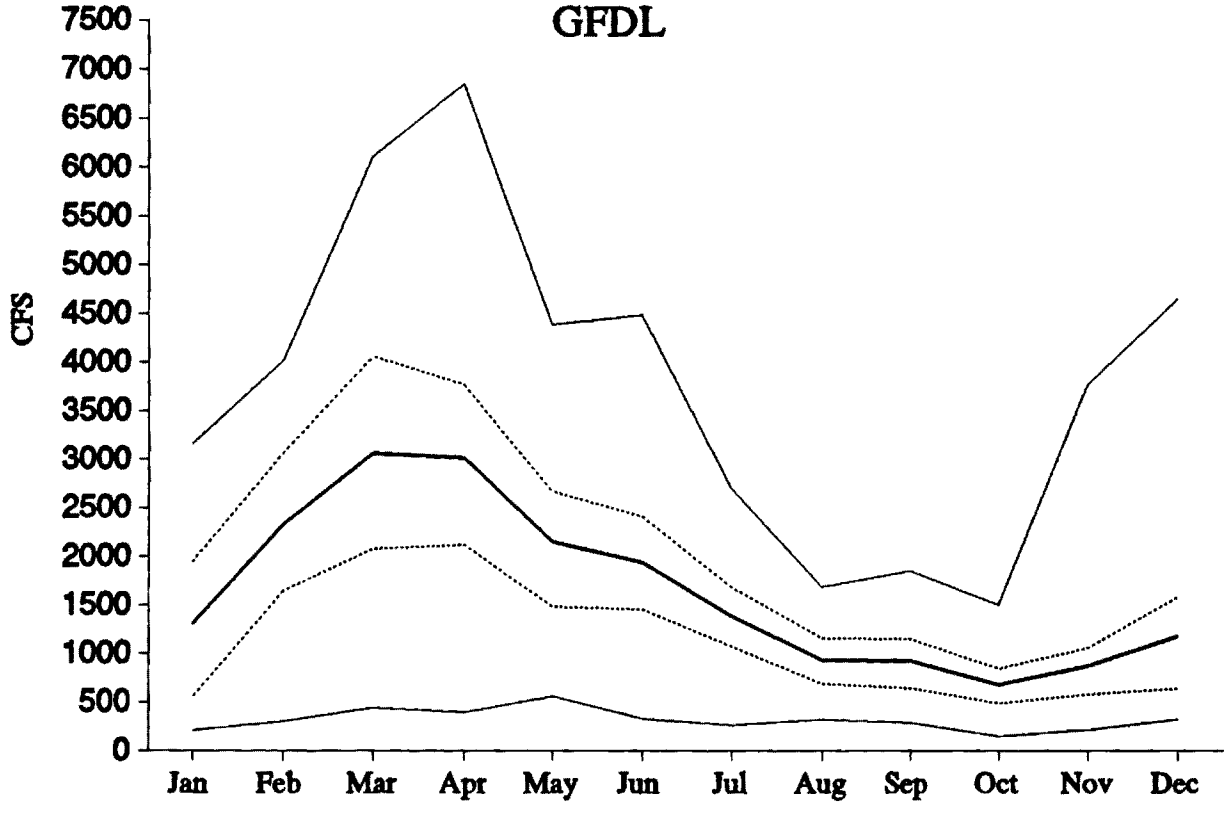

Figure 4.13 GFDL Inflow Trace Statistics (mean, 75th and 25th percentiles, maximum and minimum)

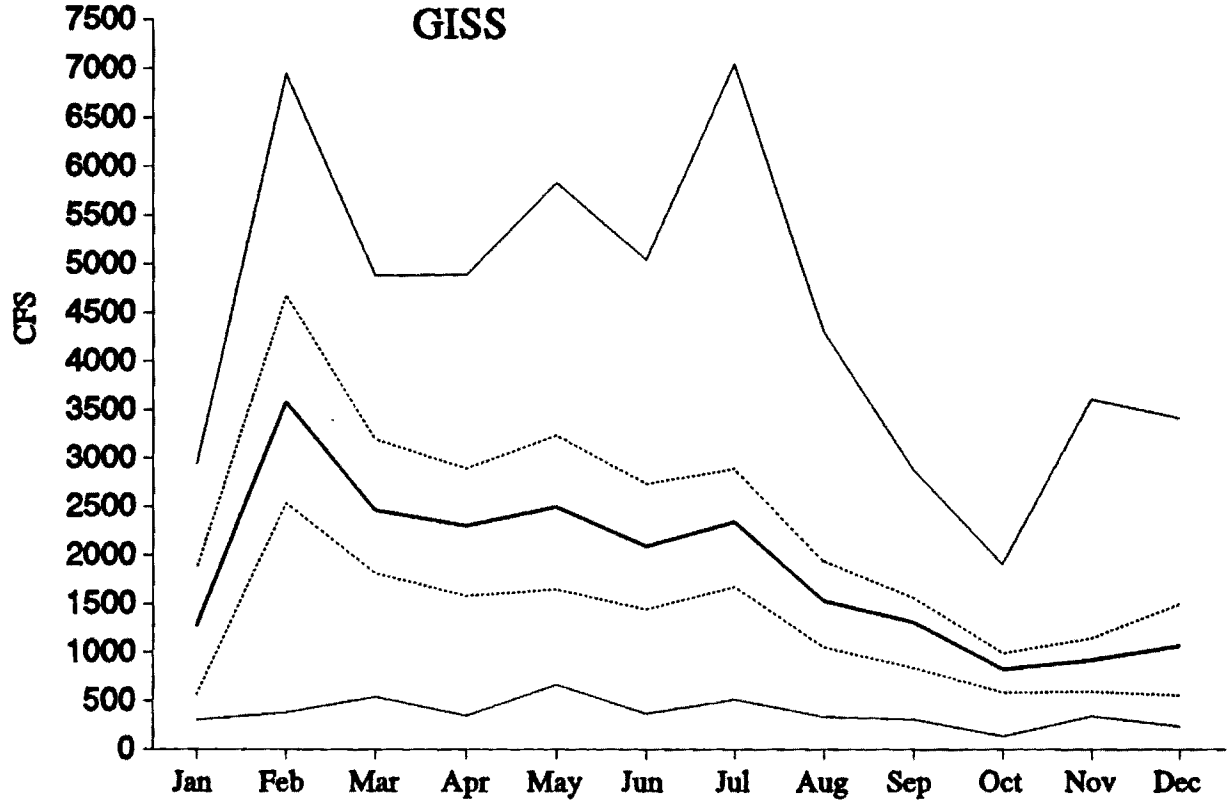

Figure 4.14 GISS Inflow Trace Statistics (mean, 75th and 25th percentiles, maximum and minimum)

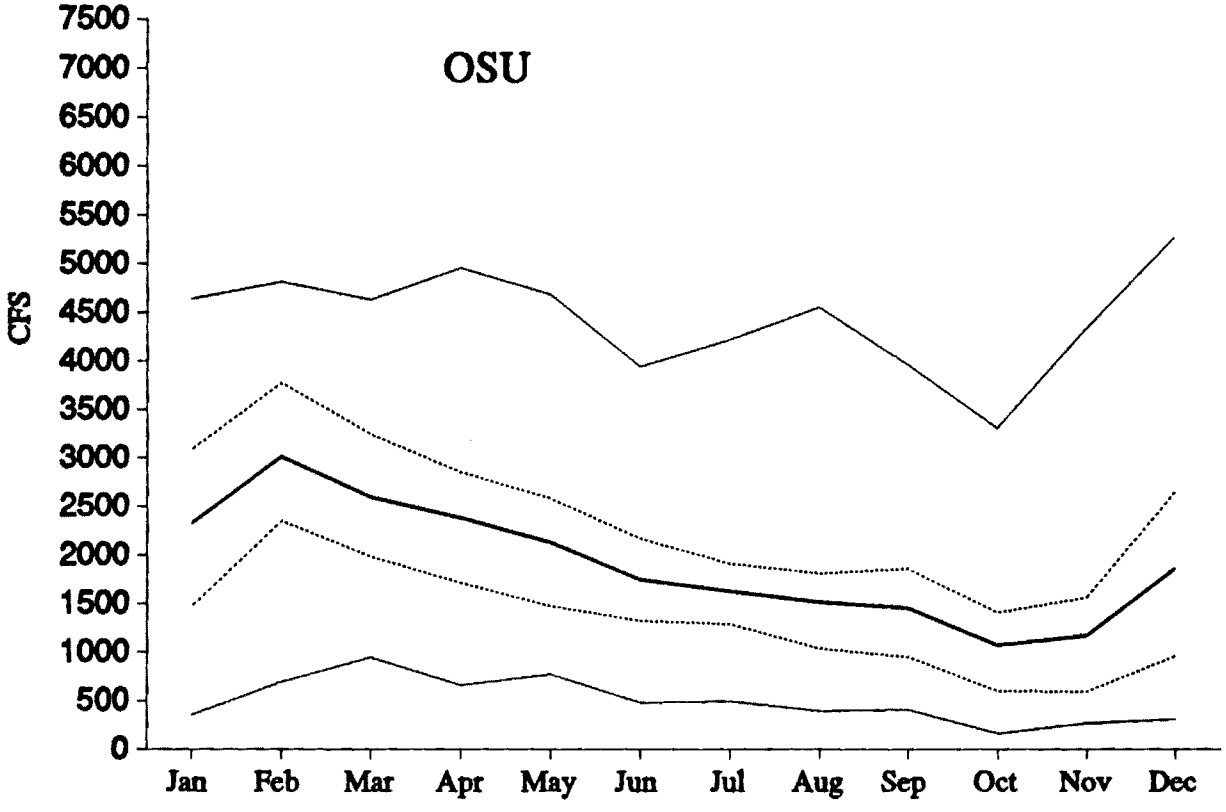

Figure 4.15 OSU Inflow Trace Statistics (mean, 75th and 25th percentiles, maximum and minimum)

to the present climatic conditions. In lieu of inflow forecasts, the SCA control model has access only to maximum and minimum monthly inflows. The results are summarized in three graphs shown on Figure 4.16. The first graph includes the simulated monthly reservoir elevation sequence along with the conservation pool boundaries, the second delineates the monthly energy generation, and the third shows the associated release. On the outflow graph, the solid line in the neighborhood of 1000 cfs indicates the outflow level corresponding to the 43.5 minimum generation hours per month. This level fluctuates in response to the fluctuation of the reservoir level (and the net hydraulic head). The figure shows that the reservoir stays within the conservation pool and the generation hours satisfy the minimum constraint. Due to the uncertainty of future inflows, the controller keeps the average reservoir level at about 1060 feet, and manages to avoid water shortages or excessive releases. Reservoir levels have a fluctuation range of about 16 to 17 feet.

The following three figures (4.17, 4.18, and 4.19) summarize the results for the GFDL, GISS, and OSU inflow scenarios (CO_2 doubling). Concentrating on the GFDL simulation run, one sees that reservoir levels now fluctuate much more than before and droughts are much more frequent and severe. The worst drought is toward the end of the simulation period when reservoir storage is entirely depleted and the model actually fails to meet the minimum generation/water supply requirements almost for the last four years. The results of the GISS run are similar, with a major operational failure occurring at about the same time. By contrast, the OSU simulation run is different than the previous two, with the reservoir being able to satisfy its operational objectives throughout the simulation period. A closer examination of the inflow statistics for the three sequences (Figures 4.13, 4.14. and 4.15) can explain this difference. Relative to the base case, the GFDL and GISS inflow reduction is uneven for different months of the year. Especially during the low flow months of August, September, October and November, GFDL and GISS inflow deficits are higher than those of OSU. Thus in the first two cases, droughts are more likely and end-up causing severe water shortages.

Thus, the previous results indicate that the operational reliability of Lake Lanier will be at risk under the GFDL and GISS climatic scenarios. In the following experiments, we are interested to investigate whether improved streamflow forecasting can mitigate this effect. Better forecasting is simulated via the procedure described in Chapter 3, the forecast parameter p(1) being equal to 0.5 or 0.25. The new simulation runs are shown on Figures 4.20 through 4.27 in the familiar format.

Examination of the p(1)=0.5 case results shows that better streamflow forecasting makes a distinct difference. For the base case scenario, the improvement is clearly

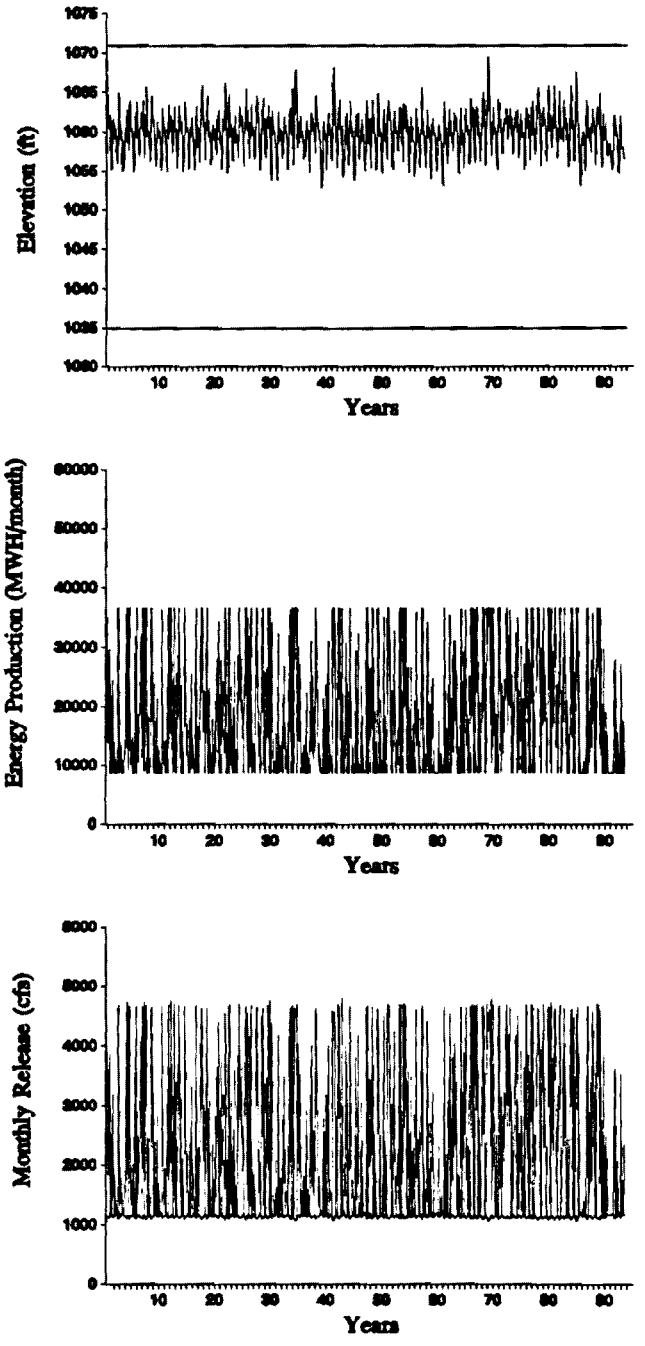

Figure 4.16 Simulation Results for Base Scenario

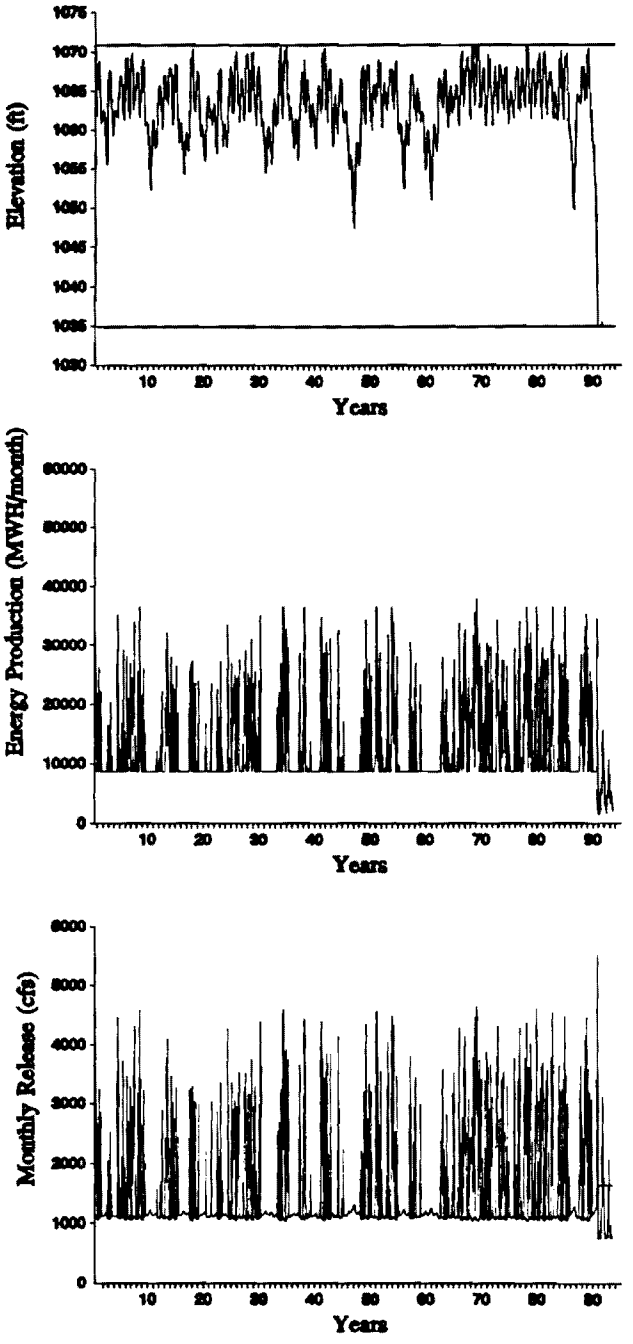

Figure 4.17 Simulation Results for GFDL Scenario

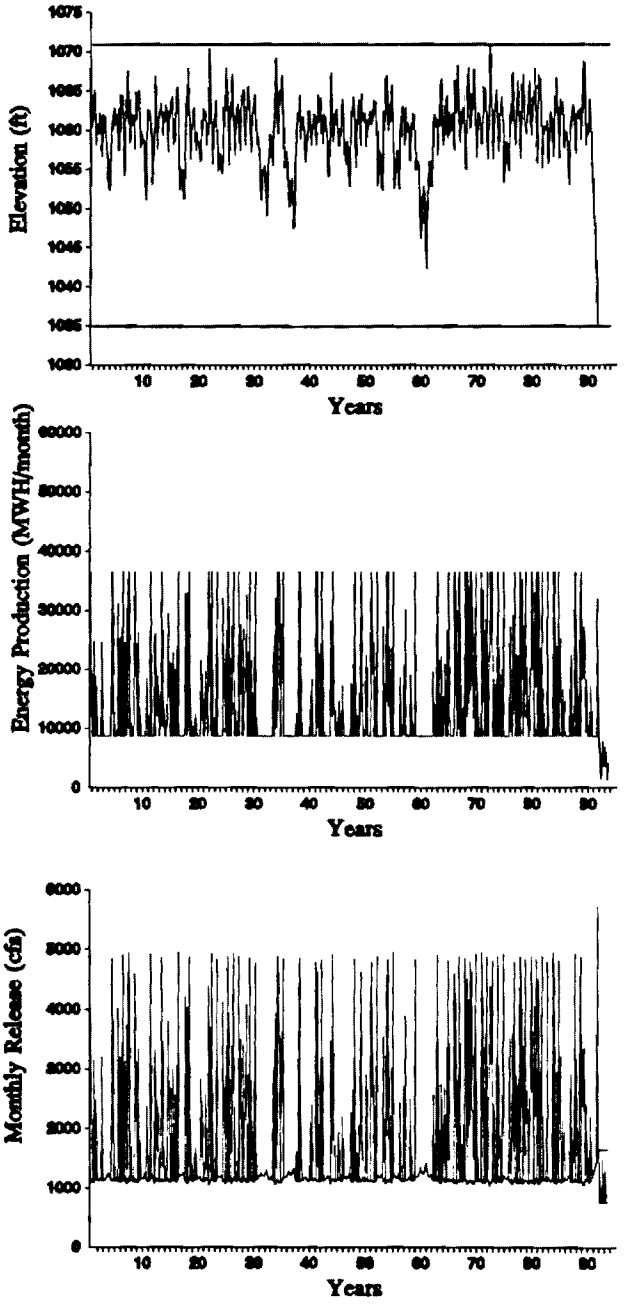

Figure 4.18 Simulation Results for GISS Scenario

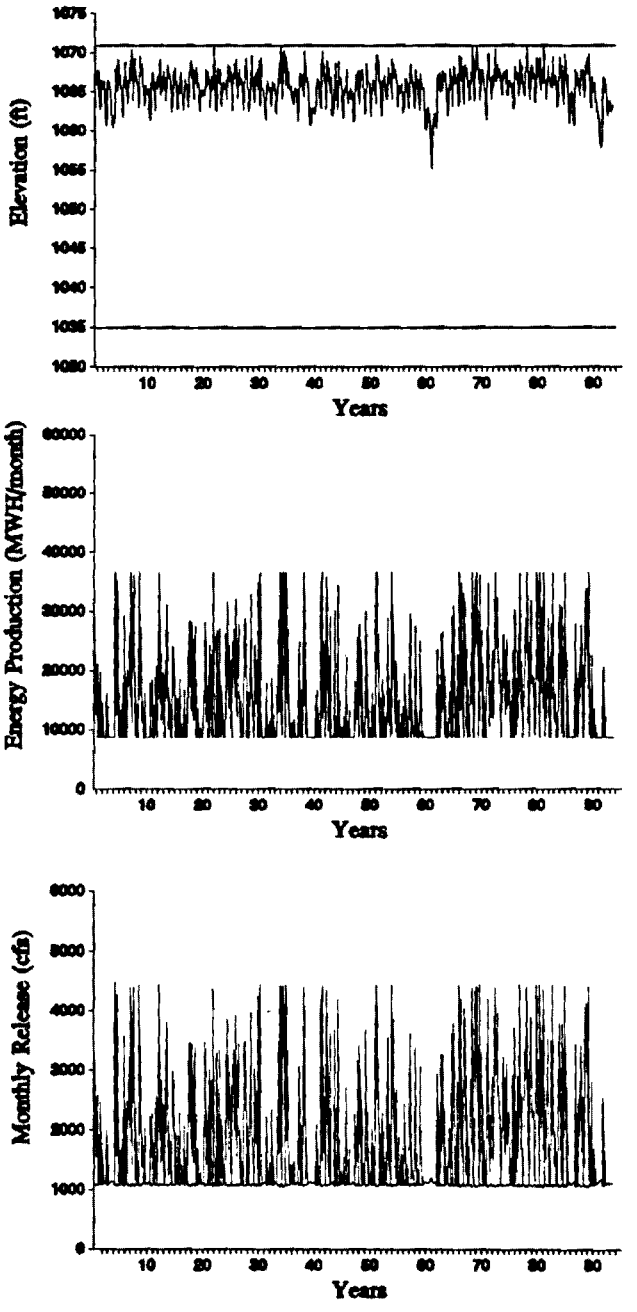

Figure 4.19 Simulation Results for OSU Scenario

evident in the first graph of Figure 4.20 where reservoir levels are substantially higher than those of Figure 4.16 and fluctuate much less. Having more accurate information of the upcoming inflows, the controller maintains higher reservoir levels without causing spillage. With the reservoir almost always full, the drought risk is now smaller. This is better seen in the GFDL and GISS scenarios where droughts are almost entirely avoided except in the last GFDL simulation year. This drought is finally averted in the $p(1)=0.25$ forecast case.

Table 4.2 summarizes all simulation runs recording frequency and magnitude of violations and total energy generation. Relative to present conditions, energy generation is expected to decline by about 30 (GFDL) to 15 (OSU) percent. On the other hand, forecasting tends to secure 2 to 7 percent more energy.

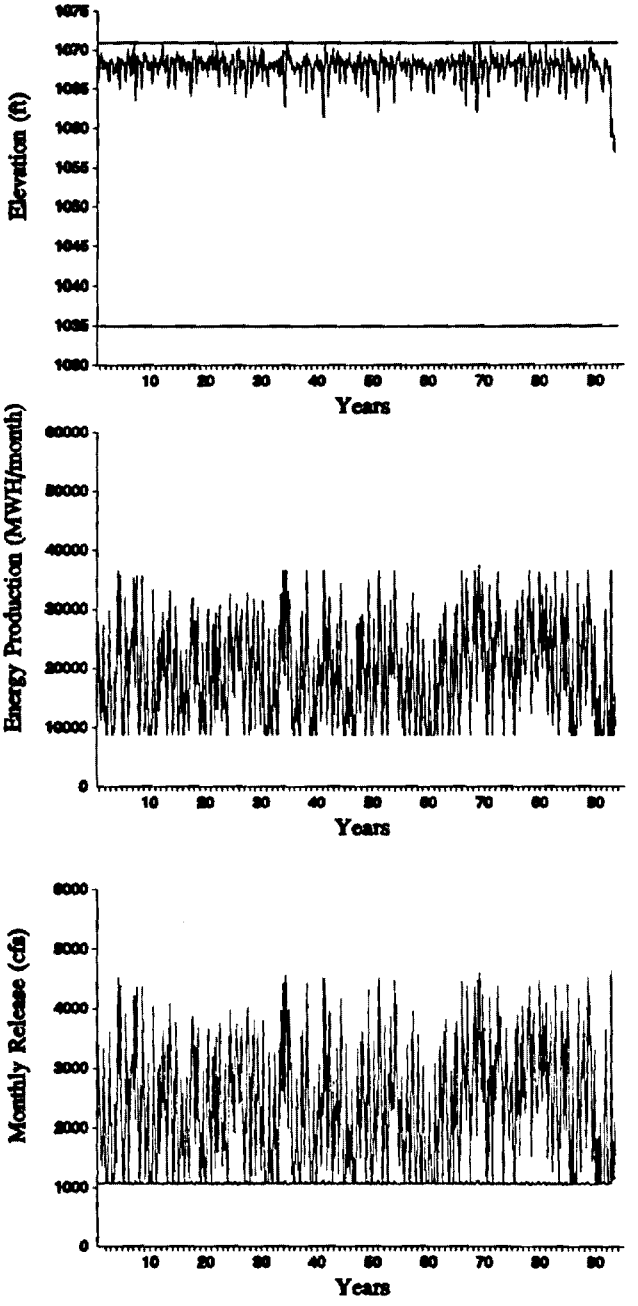

Figure 4.20 Simulation Results for BASE Scenario; P(1)=0.5

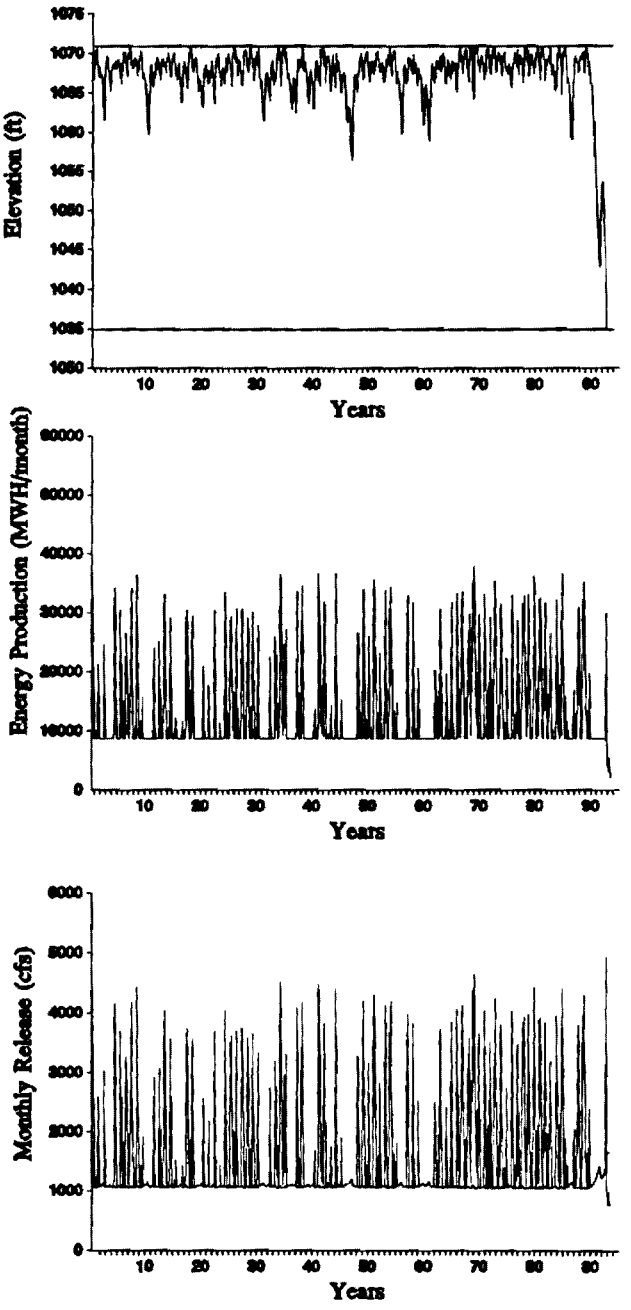

Figure 4.21 Simulation Results for GFDL Scenario; P(1)=0.5

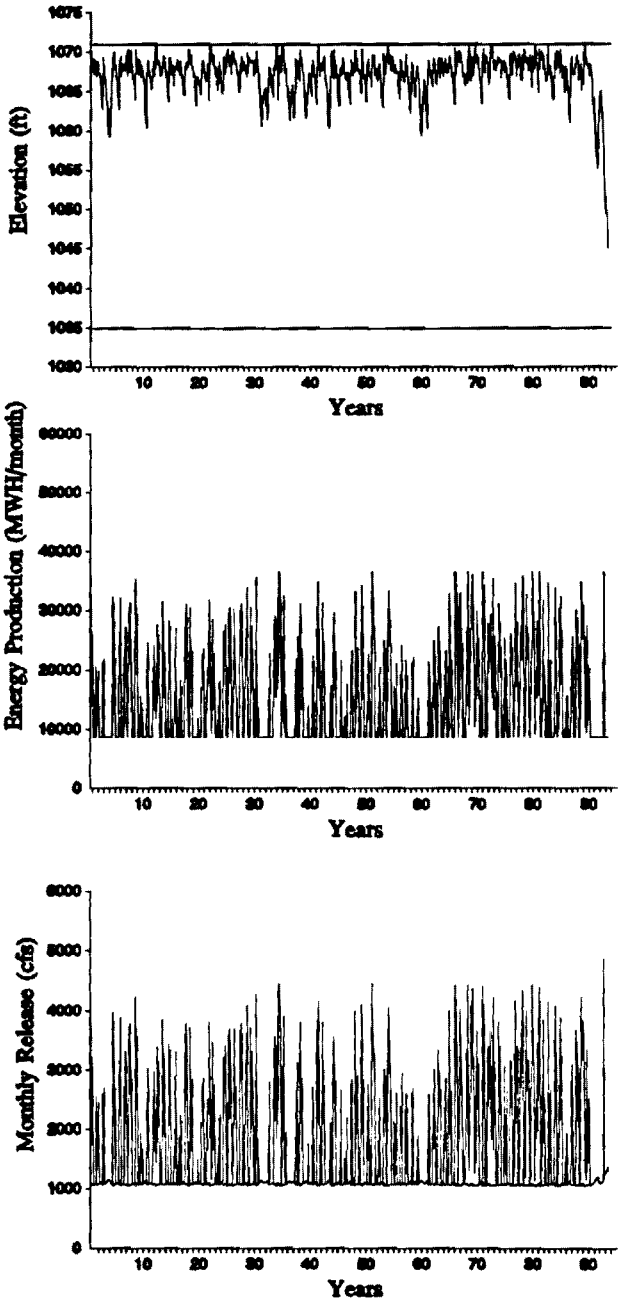

Figure 4.22 Simulation Results for GISS Scenario; P(1)=0.5

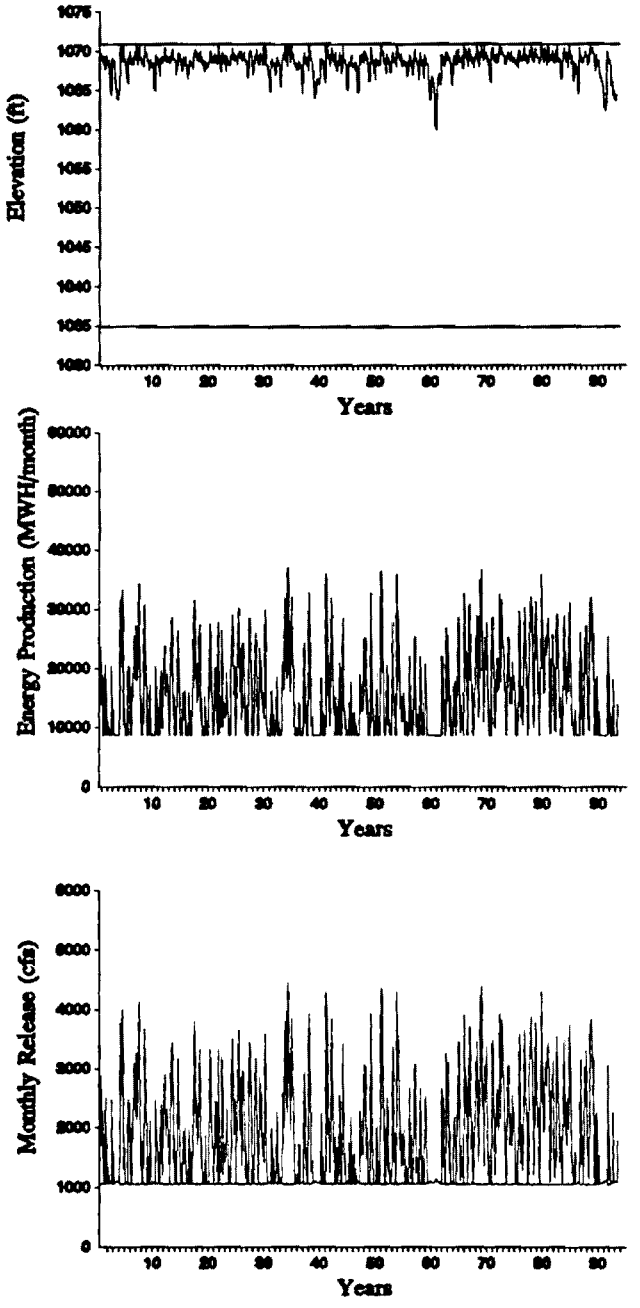

Figure 4.23 Simulation Results for OSU Scenario; P(1)=0.5

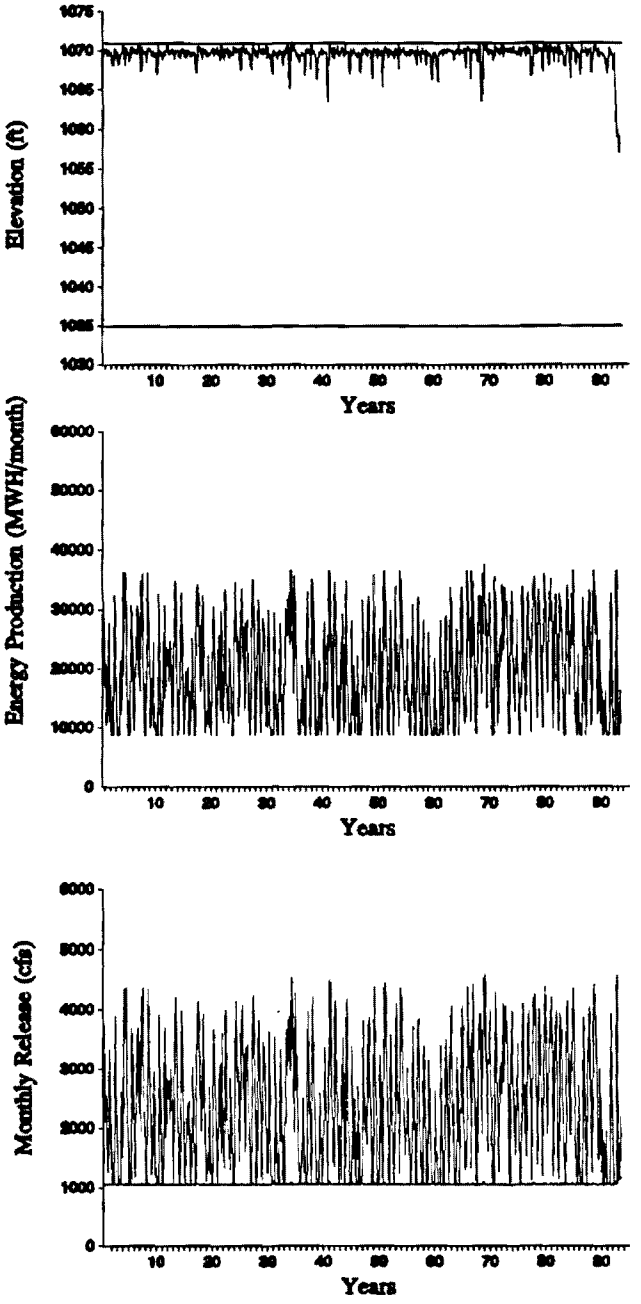

Figure 4.24 Simulation Results for BASE Scenario; P(1)=0.25

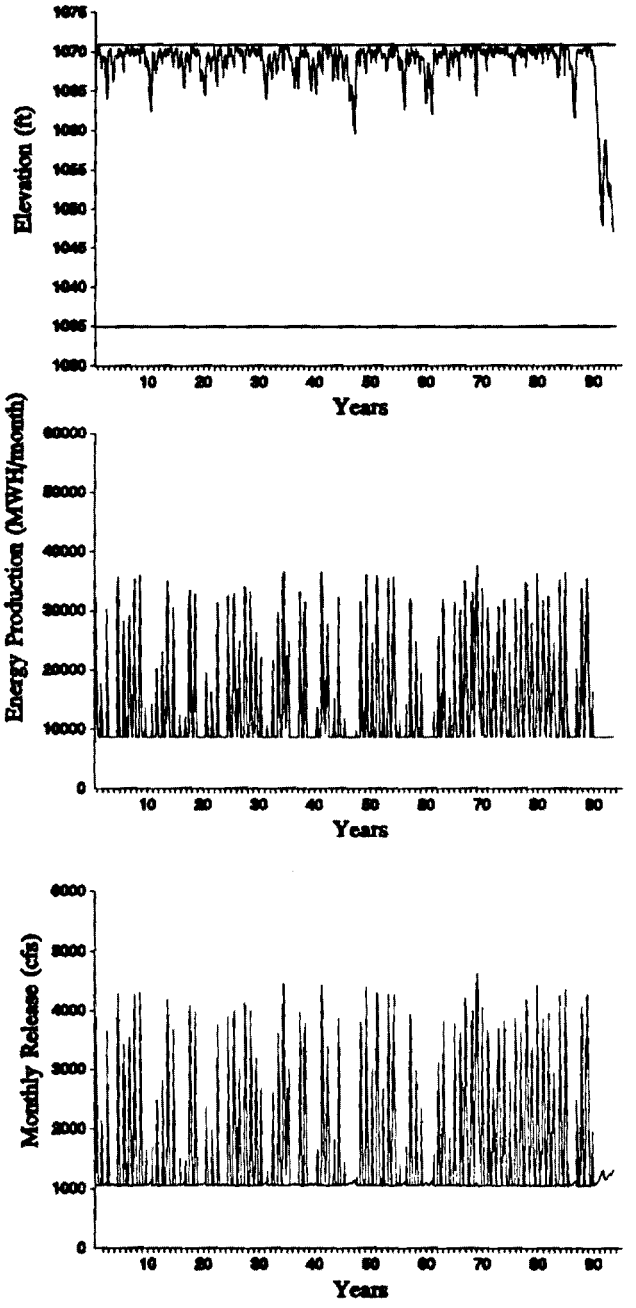

Figure 4.25 Simulation Results for GFDL Sceanrio; P(1)=0.25

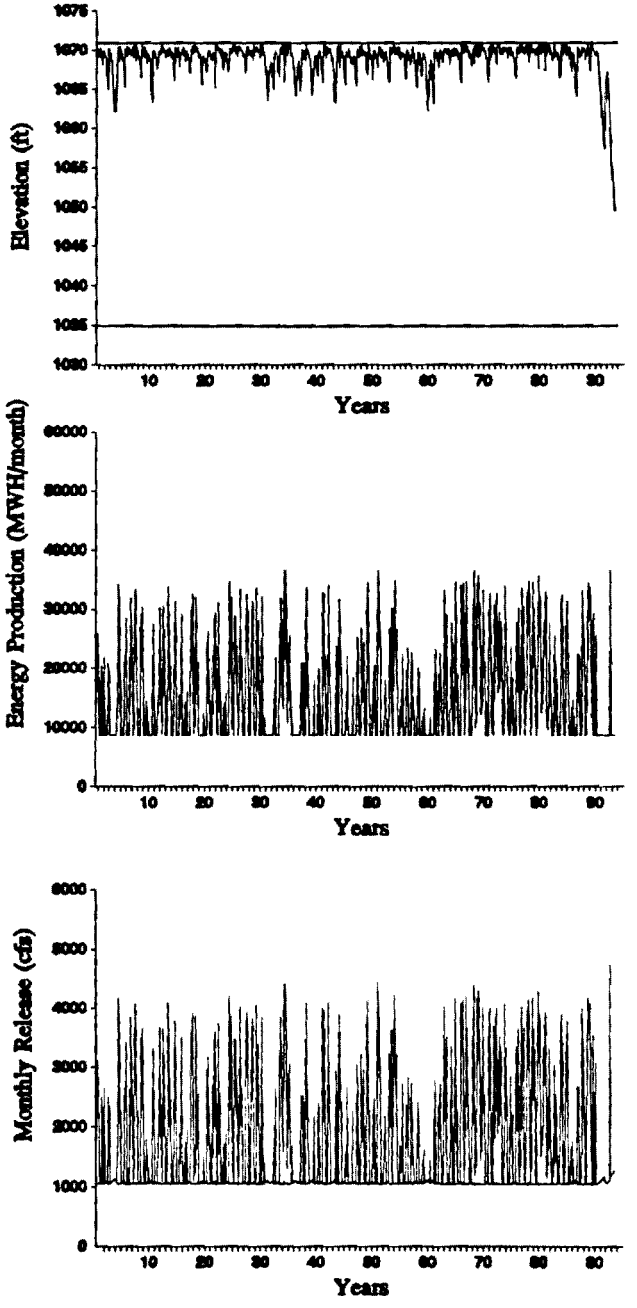

Figure 4.26 Simulation Results for GISS Scenario; P(1)=0.25

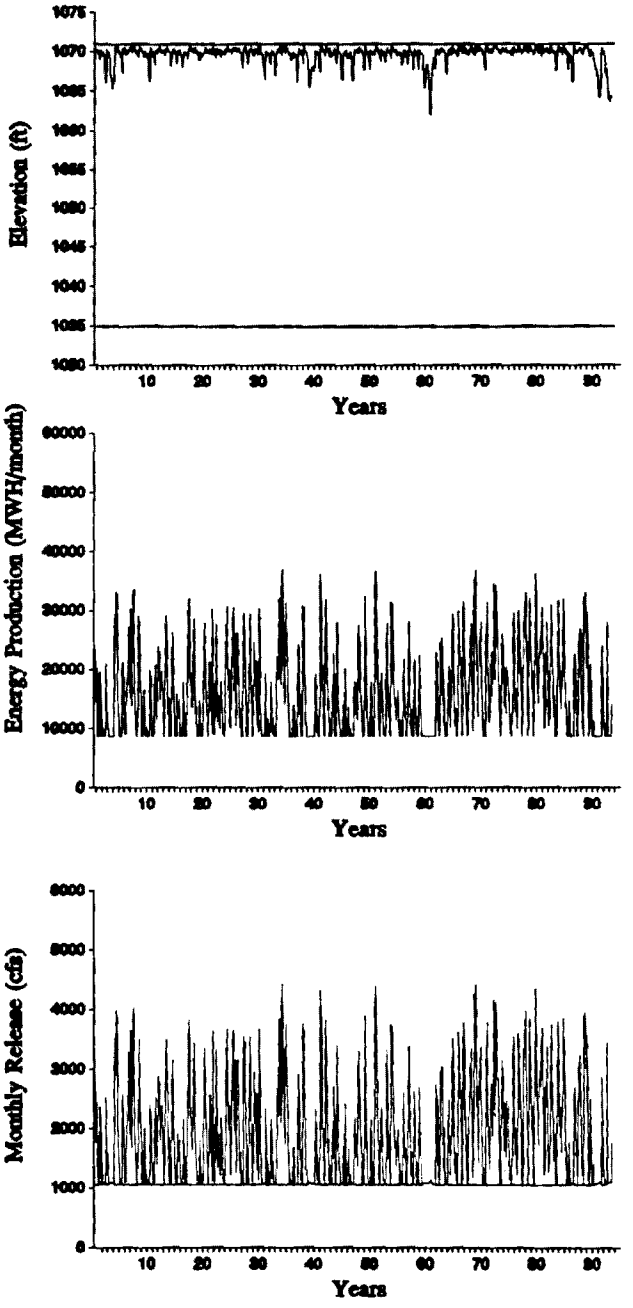

Figure 4.27 Simulation Results for OSU Scenario; P(1)=0.25

Table 4.2 Violation Tables

No Forecasting

	BASE	GFDL	GISS	OSU
Viol. Number	0	28	20	0
Max. Powr. Viol. (MWH/month)	0	7150	7315	0
Total Powr. Viol. (MWH/month)	0	122914	77408	0
Total. Energy(MWH)	2.0373e7	1.4625e7	1.5916e7	1.7296e7

Forecasting with p(1)=0.5

	BASE	GFDL	GISS	OSU
Viol. Number	0	8	0	0
Max. Powr. Viol. (MHW/month)	0	6567	0	0
Total Powr. Viol. (MHW/month)	0	34432	0	0
Total. Energy(MWH)	2.1725e7	1.5153e7	1.6987e7	1.767e7

Forecasting with p(1)=0.25

	BASE	GFDL	GISS	OSU
Viol. Number	0	0	0	0
Max. Powr. Viol. (MHW/month)	0	0	0	0
Total Powr. Viol. (MHW/month)	0	0	0	0
Total. Energy(MWH)	2.2032e7	1.5306e7	1.7187e7	1.7797e7

5. SUMMARY, CONCLUSIONS, AND FURTHER RESEARCH RECOMMENDATIONS

The scope of this research project was to investigate the effects of global warming on reservoir system outputs. This investigation was carried out in four phases:

(1) A general control method suitable for the management of uncertain dynamical systems was first developed (Chapter 2). This new control approach was motivated by the need to guide the operation of water resources systems under extreme or relatively unknown input circumstances (as in the case of long-lasting climatic changes). Rather than using statistical input descriptions, this approach was based on set characterization of uncertainty. The resulting control problem calls for finding the set of admissible actions that ensures that the system stays within its bounds for the duration of the operational horizon. The solution is derived using Dynamic Programming and is efficiently implemented for the case where all sets are convex polyhedra.

(2) In the second phase (Chapter 3), the Set Control Approach was applied to common reservoir operation problems including flood and drought management and hydropower scheduling. Common to all applications is the premise that reservoir operators wish to have a set of policies guaranteed to meet all system constraints, rather than optimize specific objectives. We feel that this mode of operation is more meaningful under crises situations (floods and droughts) and climate change circumstances. Several computational experiments with the Savannah River system in the southeast (three reservoirs) showed that accurate inflow forecasting together with the Set Control Approach improves reservoir operations in that it minimizes flood control storage and avoids damage-causing outflows. In addition, benefits accrue from energy generation due to higher hydraulic head and less wasted spillage.

Reservoir systems usually operate under normal hydrologic conditions and only occasionally experience extreme events. During the former, stochastic methods are appropriate and can effectively guide system operations. One potentially useful research contribution would be to develop a hybrid control model which uses stochastic methods during normal circumstances but switches to the set control approach at the onset of critical periods.

(3) In the third phase (Chapter 4.2), the Set Control Approach was coupled with the Modified Sacramento Model developed by the University of Iowa research team (Volume II). The combined forecast-control procedure was tested in the operation of the Saylorville reservoir in the upper Des Moines river basin (midwest). Side-by-side simulation experiments of this model with (a) heuristic management practices

and (b) the Set Control Approach with no forecasting showed that the forecast-control procedure significantly improved reservoir operations entirely avoiding droughts and effectively controlling floods.

The impacts of a potential global warming scenario were examined using historical analogues of low, intermediate, and high streamflow periods. It was shown that reservoirs can be operated to mitigate the adverse effects of climatic change with the aid of effective forecast-control procedures. It is noted that the heuristic management practices could not readily adapt to changing hydrologic circumstances, causing frequent flooding and water shortages. Thus in climate change impact studies, reservoir optimization procedures such as the ones developed herein are essential. Failure to incorporate them will lead to overly pessimistic results and exaggerate real impacts.

(4) In the fourth phase of the research (Chapter 4.3), we used results from three General Circulation Models (GCMs) to establish plausible inflow scenarios for Lake Lanier (southeast) under the assumption of doubled atmospheric CO_2. The scenarios generally indicate that inflow volumes will be reduced significantly, causing the lake to experience frequent and severe droughts. However, the use of effective streamflow forecasting and reservoir control procedures can ease these consequences. These results, however, should be viewed as only "what if" scenarios as GCM predictions and their processing to watershed scale are presently rather inexact -- an area needing further research.

6. REFERENCES

Barnett, T. P., Long-term changes in precipitation patterns, *Technical Report* to the U.S. Dept. of Energy by Lawrence Livermore National Laboratory under contract no. W-7405-ENG-48, in Detecting the Climate Effects of Increasing Carbon Dioxide, 151-162, 1986.

Bertsekas, D.P. and I.B. Rhodes, On the minimax reachability of target sets and target tubes, *Automatica*, Vol. 7, 233-247, 1971.

Bishop, E. and Phelps, The support functionals of a convex set," *Proc.* of Symp. in Pure Math., 7, AMS, 1963

Bradley, R. S., H. F. Diaz, J.K. Eischeid, P.D. Jones, P.M. Kelly, C. M. Goodess, precipitation fluctuations over the Northern Hemisphere land areas since the mid-19th century, *Science*, 237, 171-175, 1987.

Foufoula-Georgiou, E., and P. K. Kitanidis, Gradient dynamic programming for stochastic control of multidimensional water resources systems, *Water Resources Research*, 24(8), 1345-1359, 1988.

Georgakakos, A.P., Extended Linear Quadratic Gaussian (ELQG) control: Further extensions, *Water Resources Research*, 25(2), 191-201, 1989.

Georgakakos, A. P., Optimal regulation of the Savannah River system, *Technical Report* for U.S. Army Corps of Engineers Research Contract No. DACW21-88-C-0043, School of Civil Engineering, Georgia Tech, May 1991.

Georgakakos, A. P., Operational tradeoffs in reservoir control, *Water Resources Research*, in press, 1993.

Georgakakos, A.P., and D.A. Vlatsa, Stochastic control of groundwater systems, *Water Resources Research*, 27(8), 2077-2090, 1991.

Glover, J.D., and F.C. Schweppe, Control of linear dynamic systems with set-constrained disturbances, IEEE Transactions of Automatic Control, 16(5), 411-423, 1971.

Grygier, J.C., and J.R. Stedinger, Algorithms for optimizing hydropower system operation, *Water Resources Research*, 21(1), 1-10, 1985.

Harris, C.J., Modelling and adaptive control of urban wastewater treatment plants, in *Environmental Systems Planning, Design, and Control*, Proceedings IFAC Symposium, Kyoto, Japan, 1977.

Kabouris , J.C., and A.P. Georgakakos, Optimal control of the activated sludge process, *Water Research*, 24(10), 1197-1208, 1990.

Kelman, J., J. R. Stedinger, L. A. Cooper, E. Hsu, and S.-Q. Yuan, Sampling stochastic dynamic programming applied to reservoir operation, *Water Resources Research*, 26(3), 447-454, 1990.

Loucks, D.P., J. R. Stedinger, and D. A. Haith, *Water resource systems planning and analysis*, Prentice Hall, 1981.

Ramanathan, V., The greenhouse theory of climatic change: a test by an inadvertent global experiment, *Science*, 240, 293-299, 1988.

Schneider, S. H., The greenhouse effect: science and policy, *Science*, 243, 771-781, 1989.

Schweppe, F.C., *Uncertain Dynamic Systems*, Prentice Hall, 1973.

Street-Perrott, F. A., and S. P. Harrison, Temporal variations in lake levels since 30,000 yr bp -- an index of the blobal hydrological change, in Climate Processes and Climate Sensitivity, eds. J. E. Hansen and T. Takahashi, American Geophysical Union *Monograph* 29, Washington D.C., 118-129, 1984.

Tasker, G. D., Some hydrological effects of cliamte change for the Apalachicola, Chattahoochee, and Flint river basins, *Proceedings* of the 1993 Georgia Water Resources Conference, at the Un. of Georgia, Athens, pg. 61-64, April 20 and 21, 1993.

Tennesee Valley Authority, Sensitivity of the Tennessee Valley Authority reservoir system to global climate change, *Technical Report* WR28-1-680-101, prepared by B. A. Miller and W.G. Brock, Norris Eng. Lab., 131p, 1988.

Trezos, T., and W.W-G. Yeh, Use of stochastic dynamic programming for reservoir management, *Water Resources Research*, 23(6), 983-996, 1987.

U.S. Army Corps of Engineers, Saylorville Lake: master reservoir regulation manual, Rock Island District, September 1983.

Wasimi, S.A., and P.K. Kitanidis, Real-time forecast and daily operation of a multireservoir system during floods by Linear Quadratic Gaussian Control, *Water Resources Research*, 19(6), 1511-1522, 1983.

Willis, R., and B.A. Finney, Optimal control of nonlinear groundwater hydraulics: Theoretical development and numerical experiments, *Water Resources Research*, 21(10), 1476-1482, 1985.

APPENDIX A

Lemma: Let Ω_x be a set characterized by

$$\Omega_x = \{X: X'\eta_i \le \phi_x(\eta_i),\ i = 1,...,n_x\} \tag{A.1}$$

and **B** an invertible matrix. Then, the set Ω_y of all vectors **Y** such that **Y = B X** is defined by

$$\Omega_y = \{Y: Y'\theta_i \le \phi_x(\eta_i),\ i = 1,...,n_x\},$$
$$\text{where } \theta_i = (B')^{-1}\eta_i,\ i = 1,...,n_x. \tag{A.2}$$

Proof: Let (ABCDE) and (abcde) (Figure A.1) represent sets Ω_x and Ω_y respectively, and let vectors η_i and θ_i be perpendicular to hyperplanes AB and ab. To establish a relationship between η_i and θ_i, we start from the implications of orthogonality between these vectors and any other vector on the corresponding hyperplanes:

$$(\overline{ab})'\theta_i = 0 = (\overline{Ob} - \overline{Oa})'\theta_i = [B(\overline{OB}) - B(\overline{OA})]'\theta_i = (\overline{AB})'B'\theta_i$$
$$\textit{and} \tag{A.3}$$
$$(\overline{AB})'\eta_i = 0.$$

The above relationships suggest that vectors η_i and $B'\theta_i$ are collinear (parallel) and consequently, a set of θ_i vectors perpendicular to the hyperplanes of Ω_y can be obtained from

$$B'\theta_i = \eta_i \rightarrow \theta_i = (B')^{-1}\eta_i. \tag{A.4}$$

To fully characterize Ω_y, we additionally need the support function values $\phi_m(\theta_i)$, θ_i, $i=1,...,n_x$. Using the definition and the previous result, we obtain

$$\begin{aligned}\phi_y(\theta_i) &= \underset{Y\epsilon\Omega_y}{maximum}\, Y'\theta_i = \underset{X\epsilon\Omega_x}{maximum}\, X'B'\theta_i \\ &= \underset{X\epsilon\Omega_x}{maximum}\, X'B'(B')^{-1}\eta_i = \underset{X\epsilon\Omega_x}{maximum}\, X'\eta_i \\ &= \phi_x(\eta_i)\,.\end{aligned} \tag{A.5}$$

Even though η_i may be unit vectors, vectors θ_i may not have unit length. However, one can easily normalize them and scale the support function values accordingly:

$$\begin{aligned}e_i &= \theta_i / |\theta_i| \\ \phi_y(e_i) &= \phi_y(\theta_i) / |\theta_i|\,,\end{aligned} \tag{A.6}$$

where $|\cdot|$ represents vector norm.

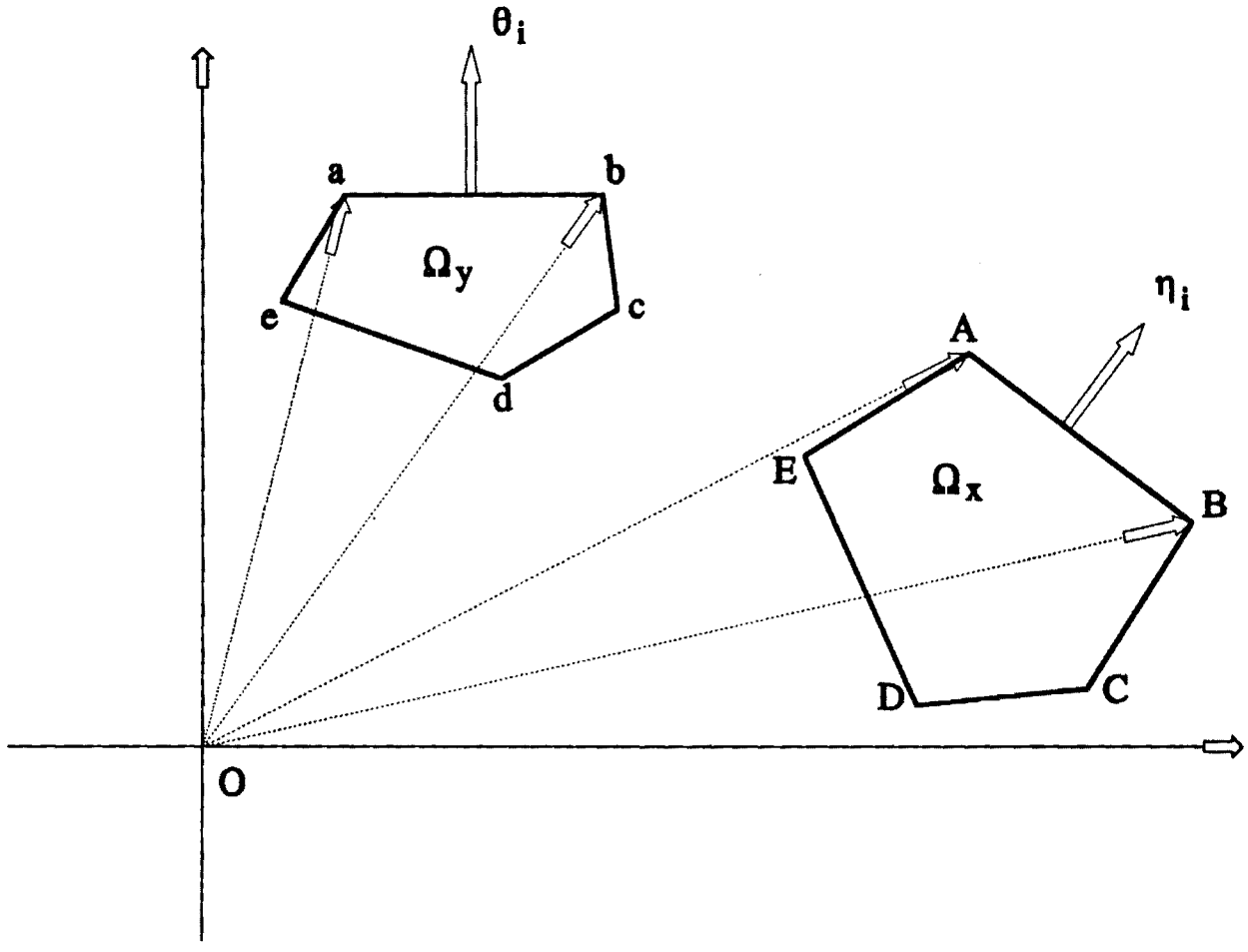

Figure A.1: Linear Set Transformations

APPENDIX B

B.1 ELEVATION (H) VERSE STORAGE (S) CURVE

Curve	$H=a\ln(S)+b(\ln(S))^2+c(\ln(S))^3+d(\ln(S))$
Units	H: feet S: acre-feet
Coefficient Values	a = -229.88257 b = 30.690016 c = -1.8662148 d = 0.046550048 e = 1584.045
Validity Range	H: 1035-1085 feet S: 867,984-2,551,667 acre-feet
Residual Error St. Dev.	0.0251 feet

B.2 TAILWATER ELEVATION (T) VS. OUTFLOW (Q) CURVE

Curve	*If* $0 \le Q < 4{,}000$ $t=dQ+e$ *If* $4{,}000 \le Q \le 14{,}000$ $t=a+b\ \ln(Q)+c\ (\ln(Q))^2$
Units	t: feet Q: cfs
Coefficient Values	a = 1,065.17688 b = -39.85679 c = 2.66528 d = 0.00175 e = 911.

Validity Range	t: 911-926 feet Q: 0-14,000 cfs
Residual Error St.Dev.	0.17 feet

B.3 POWER GENERATION CURVE FOR THE MAIN TURBINES

Curve	$Q=\exp(a+b\frac{P}{H}+c(\frac{P}{H})^2+d\ Ln(P)+e(Ln($ $+f\ Ln(H)+g(Ln(H))^2)$
Units	H: feet P: MW Q: cfs
Coefficients	a = 23.8732 b = 3.012357 c = 0.5261176 d = 1.1328914 e = -0.14784776 f = -7.4528786 g = 0.74083598
Validity Range	H: 103-170 feet P: 9.8-64.8 MW Q: 1600-5200 cfs
Residual Error St. Dev.	130 cfs

B.4 POWER GENERATION CURVE FOR THE SMALL TURBINE

Curve	$Q=\exp(a+b(\frac{P}{H})+c(\frac{P}{H})^2+dLn(P)+e(Ln($ $+f(Ln(H))+g(Ln(H))^2)$
Units	Q: cfs H: feet P: 10^5 KW
Coefficients	a = 17.7903784 b = 0.97088472 c = 0.53824066 d = 0.74410177 e = -0.0482565 f = -5.510093 g = 0.53260768
Validity Range	H: 102-172 feet P: 2.28-7.54 MW Q: 300-600 cfs
Residual Error St. Dev.	11.25 cfs

SENSITIVITY OF LARGE-BASIN HYDROLOGY, FORECASTS AND MANAGEMENT TO HISTORICAL CLIMATIC FORCING

By

Mary G. Mullusky
and
Konstantine P. Georgakakos

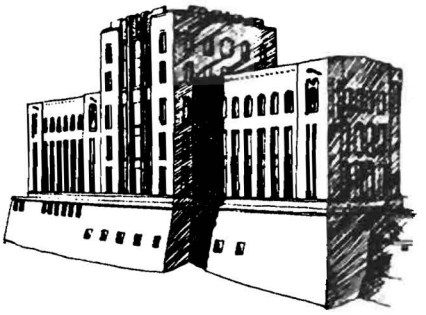

IIHR Report No. 364

Iowa Institute of Hydraulic Research
The University of Iowa
Iowa City IA 52242-1585

September 1993

SENSITIVITY OF LARGE-BASIN HYDROLOGY, FORECASTS AND MANAGEMENT TO HISTORICAL CLIMATIC FORCING

By

Mary G. Mullusky
and
Konstantine P. Georgakakos

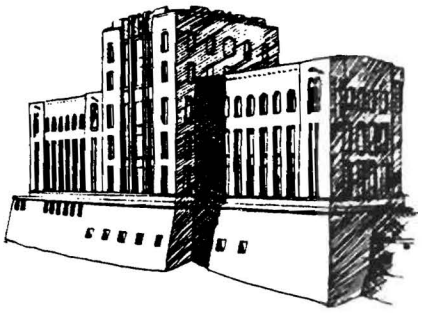

IIHR Report No. 364

Iowa Institute of Hydraulic Research
The University of Iowa
Iowa City IA 52242-1585

September 1993

ACKNOWLEDGEMENTS

This research work was sponsored in part by the U.S. Geological Survey Award No. E-20-686-S1 (subcontract to a Georgia Institute of Technology USGS contract). Additional support was provided by the Center for Global and Regional Environmental Research (CGRER) of The University of Iowa under Seed Grant QK96 and by the Iowa Institute of Hydraulic Research through the EPRIa Program, funded by a consortium of the mid-western Power Utilities. The computational work was performed at the Hydromet Lab of The University of Iowa. This report essentially constitutes the M.S. Thesis of Mary Mullusky.

Special thanks go to Dr. Deg Hyo Bae for his assistance and guidance in modifying the UIFS model to generate ESP and to Dr. Aris P. Georgakakos for providing the reservoir set controller method and his review of the final draft. Also, the comments and suggestions of Dr. G.R. Carmichael, Dr. W.F. Krajewski, T.M. Carpenter and A.K. Guetter are gratefully appreciated.

The views and conclusions contained in this document are those of the authors and should not be interpreted as necessarily representing the official policies, either expressed or implied, of the U.S. Government.

EXECUTIVE SUMMARY

Examined is the sensitivity of reservoir hydrosystems to changes in their climatic forcing. The study is based on hydrometeorological data and models of the Upper Des Moines River basin, which drains 14,000 km^2 in the midwestern United States. Historical data for the period from 1925 through 1988 have been used. Coupled forecast-control procedures simulate operational flow forecasting and reservoir management. These procedures involve large-scale operational hydrologic/ hydraulic models (i.e., the UIFS model), probabilistic schemes for extended flow forecasts based on conditional ensemble flow forecasting (i.e., the National Weather Service ESP scheme), and operational optimal reservoir control models (i.e., a set constrained controller). Sensitivity of the subject reservoir hydrosystems was determined by dividing the historical record into three climatic periods. Differences were detected in temperature and precipitation among the three climatic periods. Model-generated soil water features were obtained and compared among the periods. The study shows that large differences among the average extended streamflow predictions corresponding to warm/cool and wet/dry initial conditions occur in the spring and late summer. This suggests that streamflow forecasts are most sensitive to climatic change during the aforementioned seasons. Climatic forcing with either the warm/cool or the wet/dry historical model input realizations increases these differences. Results obtained for the historical record using the current reservoir operating policies indicate the inadequacy of the existing release operations to accommodate the observed natural variability of streamflow. The set control procedure successfully accommodates the observed climatic forcing variability. Thus, for climate-change impact studies concerning reservoir hydrosystems, an optimal forecast-control procedure should be used, otherwise pronounced sensitivity may result. Alternatively, substantial gain in resilience to changes in climatic forcing would result if existing reservoirs were operated in an optimal fashion that involves coupled forecast-control schemes.

TABLE OF CONTENTS

LIST OF TABLES

LIST OF FIGURES

I. INTRODUCTION

1.1 Background and Scope of Study

There has been much concern and research in the area of anthropogenic influence on the global environment. Many concerns have been raised about the increasing rates of CO_2 and other trace gases, and, consequently, the increasing "greenhouse effect" (e.g., Houghton, et al., 1990). This has lead to the development of several General Circulation Models (GCM) used to predict global climatic features under the scenario of a doubling of CO_2. These models produce results that are in general agreement one with another as regards certain global climate indices (i.e. most predict an increase in global temperature in the range of 2-5°C). It is very difficult, however to infer from these models the potential climate change effects on a more regional level, e.g., over the 14,000 km^2 Upper Des Moines River basin in the Midwest. There have been estimates of regional change in weather and climate indices such as temperature and precipitation, but these estimates are subjective and uncertain (Schneider, et al., 1990).

Efforts are in progress to evaluate the regional implications of a potential climate change. These efforts have included using hydrologic/hydraulic regional models and historical or generated data, or feeding hydrologic models with the regional predictions of a GCM. The use of either historical data or generated data requires the compiling of climate change scenarios for the region under consideration, (i.e., increase in temperature with an increase in precipitation, increase in temperature with a decrease in precipitation, etc...), (Gleick, 1987).

The scope of the subject study is to determine the sensitivity of a coupled operational flow-forecast/control procedure to changes in the climatic forcing over a large basin in the Midwest. The sensitivity study presented here uses historical data and a hydrologic/hydraulic model coupled with a probabilistic forecast procedure. The method used is suitable for studying the effects of past climatic variability on the hydrologic regimes of large basins and on the regional water resources development practices (e.g., operation of large rainfed reservoirs). This study differs from previous impact studies, in that it: (a) provides detailed hydrology of a 14,000 km^2 midwestern U.S. region, down to scales of order 10^3 km^2, and (b) it uses a probabilistic forecast/control procedure, simulating optimal real time reservoir management practices. The latter procedure allows the user to study the effects of the variability of climate and of climate change, on the real-time flow forecasts and on the resultant reservoir control actions, that are crucial for the operation of large reservoirs.

The results of studies of the sensitivity of reservoir operations to a potential regional climate change are highly significant for water resources planners. A sensitivity in reservoir operations to such a change will impact all facets of reservoir water resources management, such as water supply, flood prevention, water quality and hydroelectric power generation. Presently, existing laws and policies are tailored to the current climate conditions. These policies may need be reevaluated to account for changes in streamflow due to a changing environment. The subject study is particularly relevant to evaluating the impacts of a potential climate change in a region that is in the focus area of the GEWEX Continental-scale International Project (GCIP) (WMO, 1990). The Upper Des Moines River is a tributary to the Mississippi River system identified as a target area for GCIP.

1.2. Methodology

The application basin is the 14,000 km^2 Upper Des Moines River basin in Minnesota and Iowa. The basin was discretized into six smaller tributary sub-basins. The three headwater (no upstream inflow) tributary basins are: the 2160 km^2 Boone River with outlet at Webster City, the 3540 km^2 West Fork Des Moines River with outlet at Estherville and the 3380 km^2 East Fork Des Moines River with outlet at Dakota City. All flow into the Upper Des Moines River, and the large-basin outlet is at Stratford. Stratford is the inlet for the 676,000 acre-feet Saylorville Reservoir in central Iowa, which is the reservoir of interest in this work. The primary function of the Saylorville Reservoir is flood control to protect the city of Des Moines, which is south of the reservoir. Secondary objectives are water supply, recreation and low-flow augmentation.

The purpose of this work is to determine the sensitivity of the hydrology, of the hydrologic forecasts and of the operational water management practices to historical climatic forcing in the Upper Des Moines River basin. To the extent that historical climatic periods resemble projected future climatic periods of enhanced greenhouse forcing, the results of this work can be used to assess the sensitivity of forecast/control practices in the basin to a potential climatic change. The mathematical/numerical tool for the sensitivity study consists of three main components: a large scale hydrologic/hydraulic model of the basin with a daily temporal and a 2,000 km^2 spatial resolution, an operational probabilistic forecast procedure with a forecast horizon of a few months, and an operational reservoir management procedure. These components are briefly described next.

The hydrologic/hydraulic model used is the University of Iowa Forecast System (UIFS), which has been developed and calibrated for the Upper Des Moines River basin with outlet at Stratford, Iowa (Bae and Georgakakos, 1992). UIFS uses an adaptation of

the NWS operational Sacramento rainfall-runoff model and the NWS snow accumulation and frozen ground components to compute the detailed hydrology of the six tributary sub-basins. The UIFS model accepts inputs of mean areal precipitation, temperature, and evapotranspiration for each of the six sub-basins and predicts outflows for each sub-basin. To route the flows between sub-basins and to the outflow point, UIFS incorporates a Muskingum-Cunge hydraulic routing scheme, well suited for the mild slope of the channels in the Upper Des Moines River basin. The model forecasts the streamflow at eleven forecast points within the basin and captures many of its hydrologic features.

For use with reservoir operation practices, probabilistic forecasts were generated by the Extended Streamflow Prediction (ESP) scheme of the NWS (Day, 1985). This scheme coupled with the UIFS invokes the use of historical climate indices to create future realizations of flow forecasts up to the maximum forecast lead time. The UIFS model is started with the current soil moisture, snow depth, frozen ground state, and streamflow for each forecast preparation time. Daily mean areal precipitation, temperature, and evapotranspiration for each of the historical years in the climatic period of interest are fed into the UIFS, beginning at the month and day of the forecast preparation time and extending to the maximum forecast lead time. Thus, each historical year creates a trace of flow forecasts that are dependent on the current soil moisture conditions.

The probabilistic forecasts are fed into a reservoir set control approach (Georgakakos and Yao, 1993). The set control method starts with the current reservoir storage and allows for hydrologic inputs and controllable inputs. The hydrologic inputs are taken from the set of forecast realizations generated by the UIFS model using the ESP procedure. The controllable inputs represent the reservoir releases which are defined based on the systems limitations and operational requirements. The set control approach then determines operational decisions, such that the reservoir storage level, does not violate the operational constraints for each of the possible streamflow traces. A set of operational decisions is determined for each forecast preparation time that guarantees that the reservoir system will perform within the desirable bounds for the duration of the forecast horizon up to the maximum forecast lead time.

Sensitivity studies were performed on the ESP probabilistic forecasts and reservoir operations for forecast preparation times in three climatic periods. A second-moment statistical analysis was performed on the ESP ensemble of forecasts for each forecast preparation time in the wettest, driest, coolest and warmest year of each climatic period. A similar analysis was performed when climatic forcing was imposed by using only wet/dry or the warm/cool historical model input realizations.

1.3. Review of Literature

Various methods have been developed and used to simulate regional climate change. These methods include: the direct use of a GCM, semi-empirical methods of hypothetical climate scenarios loosely based on the results of a GCM, and an empirical use of historical climate analogues both from the recent measurements or paleoclimatic analogues. Reviews of these methods can be found in Gleick, 1989, Mearns et al., 1990, and Giorgi and Mearns, 1991.

Direct output of a GCM can be used to simulate regional climate change. Although GCMs represent the main characteristics of the general circulation reasonably well, their performance in reproducing regional climatic detail is rather poor, mainly due to their resolution and cloud and land-surface parameterizations. Regardless, attempts have been made using GCM output in hydrologic studies. In one such study, Gleick, 1987 compares the climate change scenarios of three GCMs for a basin in Northern California. The Tennessee Valley Authority, 1988 uses two scenarios of the GISS GCM to examine the range of effects to a reservoir system. Lettenmaier and Gan, 1990 examine the hydrologic sensitivities of four basins in California to the scenarios generated by four different GCMs. Presently, the nesting of a regional hydrologic model in a GCM is being researched for climate studies (Giorgi and Mearns, 1991).

There have been many regional studies using the semi-empirical method of creating scenarios, loosely based on the estimates of a GCM, and combining the scenarios with regional hydrologic models. Revelle and Waggoner, 1983 use an empirical relationship between precipitation, temperature and runoff to determine the effects of warmer air temperature and a slight decrease in precipitation on water supplies in the Western United States. Gleick, 1987 uses a water balance modeling technique for a watershed in Northern California to compare different scenarios of temperature and precipitation. The limitation with using these types of scenarios is that there is a large subjective component in the selection of scenarios that does not lead to generalizations.

The underlying assumption of empirical methods is that, independent of the nature of the forcing, the general circulation internally adjusts itself to give similar responses to different forcings. Several limitations have been identified in the use of paleoclimatic scenarios for evaluating the impacts of future climate changes to water resources. The causes of climatic shifts over geological time may differ considerably from the anthropogenic influences now anticipated. In addition, because this time predates recorded human activity there has been no evidence of how they might affect society. Therefore, it has been argued that there has been no paleoclimatic time period that is a satisfactory analogue for future

climate (Crowley, 1990). Because of this, attention has lately turned to the use of the more recent instrumental record.

The historical analogue method basically consists of selecting a series of warm years and cold years from the instrument record, and then mapping the differences of temperature, pressure, or precipitation between the periods. One example of this use is the study performed by Lough et al., 1983 that compares temperature, pressure, and precipitation of the warmest and coolest 20 year periods in order to analyze the effect of global warming on energy consumption and agriculture. It is believed that consecutive blocks of historical analogues that preserve the sequence of years are more realistic in that a transient response can be observed. This method is limited in that regional results obtained from the analysis of this historical time period may not apply for global climate changes of larger magnitudes. However, such results can reveal important effects and can be used to provide qualitative estimates of the direction and changes of possible regional climate variations. In addition, they are invaluable in assessing the resilience of operational management practices.

The study presented in this work uses recent consecutive blocks of historical analogues with the UIFS model to predict streamflow. This study differs from previous studies in the area of focus and in that it also uses a probabilistic forecast procedure to forecast flows and a set controller approach to examine the sensitivity of reservoir operations.

1.4. Report Outline

Chapter II describes the application basin, the Upper Des Moines River basin. The first part is a physical description of the area including the land use and land cover properties as well as the geology and soil types. A physical description and release requirements of the Saylorville Reservoir are also presented. The last part of this chapter describes relevant hydroclimatic features of the basin. The climatic studies are based on a statistical analysis of the recorded temperature, pan evaporation, precipitation and flow over the entire basin as well as a comparison of hydroclimatological features of two tributary headwater basins.

Chapter III gives a detailed description of the forecast-control procedure. First, a description of the components of hydrologic/hydraulic model, the University of Iowa Forecast System (UIFS) is given. The components include a modified version of the NWS Sacramento model, a frozen ground component, a snow ablation component, and a Muskingum-Cunge component for routing flows. The performance of the UIFS model with the available historical data is presented in this section. Secondly, the ESP scheme and

its coupling with the UIFS to create probabilistic flow forecasts is outlined. In this chapter, the real time reservoir operation procedure is also described, explaining the system objectives and the characteristics of the controller.

Chapter IV presents a sensitivity analysis with the historical data. This chapter includes a comparative study of the data availability, atmospheric forcing variables, model soil water, and temporal analyses in each of the three climatic periods. Chapter V presents the results and discussion pertaining to the forecast-control scheme applied to the Saylorville Reservoir. The first part contains an analysis of the performance of the probabilistic flow forecasts. The second part examines the sensitivity of the probabilistic flow forecasts to initial conditions and climatic forcing. The final part presents the results of the set-controller for the three climatic periods. Conclusions and recommendations are presented in Chapter VI. The Appendix contains various auxiliary figures.

II. THE UPPER DES MOINES RIVER BASIN

2.1. Description of the Upper Des Moines River Basin

The Upper Des Moines River basin is located in Minnesota and north-central Iowa. The basin has an elongated shape and it is about 170 miles long from northwest to south-east and up to 50 miles wide as shown in Figure III.1. It is bounded approximately by 42° N to 44.3° N in latitude and 93.7° W to 96° W in longitude. The drainage area of the basin is about 14,120 km^2 (5,452 mi^2) with outlet at Stratford, Iowa. Agriculture is the principle industry of this region. The land cover predominantly supports rural crops of corn and beans.

The Upper Des Moines River Basin is drained by three main tributaries: the West Fork Des Moines River, the East Fork Des Moines River, and Boone River. The West Fork Des Moines River starts from the area of Pipestone, Lyon and Murray Counties, Minnesota. It flows southeasterly to the junction with the East Fork. The source of the East Fork is in Jackson County, Minnesota from which it flows southeasterly and then south to join the West Fork, approximately 14 miles upstream from Fort Dodge. The Upper Des Moines River is then joined by the Boone River north of Stratford, Iowa. The Boone River has its source in Hancock County, Iowa and flows south and then southwesterly to join the Upper Des Moines River. The basin outlet is at Stratford, Iowa which is considered the inflow point for the Saylorville Reservoir. The Saylorville Reservoir is located approximately 11 miles north of Des Moines, Iowa.

The topography of the Upper Des Moines River basin is predominantly a result of the deposits from three glacial periods: the Nebraskan, the Kansan and the Wisconsin (U.S. Army Corps of Engineers, 1968). Above the junction of the East and West Forks the area is flat and natural drainage is not fully developed. The stream bed is cut only a few feet below the surrounding plain. The stream gradually cuts deeper in the vicinity of Humboldt and the stream valley is well defined. As the river approaches Boone, Iowa, hard ledge-rock outcrops and the stream valley becomes more narrow.

The soils found in the Upper Des Moines River basin are related to the several glaciations and associated deposits. The surficial material covering the area of the basin was deposited by the Wisconsin Glacier and is made up of loamy alluvium, sand and silt. The predominant soil types in this region are Webster-Clarion-Nicollet and Webster-Nicollet-Canisteo. These soils are rich in carbon, remain moist and are ideal for agriculture.

For the purpose of streamflow prediction, the Upper Des Moines River basin has been divided into six sub-basins, (Bae and Georgakakos, 1992): the Boone River basin

with outlet at Webster City, the East Fork Des Moines River basin with outlet at Dakota City, the West Fork Des Moines River basin with outlet at Estherville, the West Fork Des Moines River basin with outlet at Humboldt, the Des Moines River basin with inlet at the junction of the East and West Forks and outlet at Fort Dodge, and the Des Moines River basin with inlet at Fort Dodge and outlet at Stratford. The subdivision was based on the channel network and the location of the discharge measurement stations. Each sub-basin contains several raingauge stations and one USGS stream gauging station located at the downstream end.

2.2. Description of the Saylorville Reservoir

The Saylorville Reservoir is located approximately 11 miles north of Des Moines, Iowa (U.S. Army Corps of Engineers, 1983). The principle reservoir purpose is to store flood waters and provide a high degree of protection to the urban area of Des Moines. Secondary purposes of the reservoir are low-flow augmentation to improve water quality and recreation. At maximum flood capacity, the pool elevation is 890 feet. The reservoir area is about 16,700 acres and extends 54 miles upstream. It contains approximately 676,000 acre-feet of water. For minimum flow water quality requirements, the pool elevation is 833 feet. The reservoir area is 5,400 acres an extends 17 miles upstream.

The regulation plan is based on flood control and low flow augmentation. The area downstream of the reservoir has a channel capacity of 16,000 cfs from January through April and 12,000 cfs from May through December. The reservoir will be operated to release flows between 1,000 and 12,000/16,000 cfs at the reservoir elevation of 875 feet until forecasts indicate that the spillway crest elevation of 884 feet will be exceeded. When these forecasts of exceedence are made, the reservoir releases will increase progressively from 12,000/16,000 cfs at a reservoir elevation of 875 feet to 21,000 cfs at an elevation of 884 feet. Thereafter, the operation plan provides for the use of the remaining six feet of reservoir pool elevation to the elevation of 890 feet to limit the outflow to 21,000 cfs insofar as possible. The low flow operation plan is to release as required to provide a minimum flow of 200 cfs in the Des Moines River for the city of Des Moines and to provide a minimum flow of 300 cfs for the city of Ottumwa. Damage downstream is a nonlinear convex function of releases with disproportionally high damage at high release rates.

2.3. Hydroclimatology of the Upper Des Moines River Basin

The hydroclimatic features of the Upper Des Moines River basin are revealed through precipitation, pan evaporation, discharge and temperature data. The data used in this study was obtained from CD-ROM disks distributed by "EarthInfo, Inc.". The precipitation, discharge, and temperature data spans 64 years, 1925-1988. The pan evaporation data spans 40 years, 1949-1988. A complete listing of the location of the recording stations used for each hydroclimatic index, and the corresponding data availability is given in Table II.1.

Table II.1 Location of recording stations and period of record.

Data	Station	Latitude	Longitude	Period
Precipitation:				
	Algona	43:04:00	94:18:00	1925-1988
	Ames	42:00:00	93:39:00	1925-1988
	Hampton	42:45:00	93:12:00	1925-1988
	Mason City	43:09:00	93:14:00	1925-1988
	Rockwell City	42:24:00	94:37:00	1925-1988
	Spencer	43:10:00	95:09:00	1925-1988
	Storm Lake	42:38:00	95:11:00	1925-1988
	Webster City	42:28:00	93:48:00	1925-1988
	Worthington	43:37:00	95:36:00	1925-1988
Maximum Temperature				
	Ames	42:00:00	93:39:00	1925-1988
	Worthington	43:37:00	95:36:00	1925-1988
Minimum Temperature				
	Ames	42:00:00	93:39:00	1925-1988
	Worthington	43:37:00	95:36:00	1925-1988
Streamflow				
	Stratford	42:15:00	94:00:00	1925-1988
Pan Evaporation				
	Ames	42:00:00	93:39:00	1949-1988

The analysis of the hydroclimatological features is based on monthly average values and monthly auto-correlations as obtained from the daily mean areal values of each index. The mean areal precipitation was computed by the NWS weighted average method (Larson and VanDemark, 1979) using all of the precipitation stations listed in Table II.1. The selection of these stations was based on available data and for the period of record for stations in the proximity of or within the Upper Des Moines River basin. The mean areal temperature was computed by averaging data from the two temperature stations, Ames and Worthington. The analysis was based on maximum and minimum daily temperatures. One streamflow station at Stratford, Iowa and one pan evaporation station at Ames, Iowa with a shorter period of record (1949-1988) were also used. It is noted that pan evaporation has been shown (Pruitt, 1966) to bear a strong relationship to evapotranspiration from well-watered vegetated areas (potential evapotranspiration).

Figure II.2 represents the seasonal cycles of the monthly means and standard deviations of each of the hydroclimatic indices. Months are represented by the numbers from 1 through 12, with 1 corresponding to January. The means and standard deviations presented were computed by averaging the daily observations for each month of the period of record and then computing the mean and standard deviation over that period for all the same months.

All indices show pronounced monthly cycles. Figure II.2a represents the monthly cycle for mean areal precipitation determined from the period 1925-1988. Approximately 10% of the annual total precipitation is snowfall, mainly occurring during the winter months (December-February). The mean areal precipitation has a maximum in June of 4.0 mm/day and a second peak in August of 3.4 mm/day. Figure II.2b shows the monthly cycle of pan evaporation calculated from daily measurements taken during the period 1949-1988. The seasonal cycle of pan evaporation shows very little pan evaporation in the winter months. The cycle shows a steep increase in the spring months of April and May to a maximum pan evaporation in the summer of almost 5 mm/day. The cycle then decreases sharply in the fall months to the small amounts recorded in the winter. It should be noted, however, that pan evaporation observations during the winter months are few and with significant uncertainty as the process of sublimation from snow covered areas is a subject of research. The monthly cycle of streamflow observed at Stratford, Iowa is shown in Figure II.2c. The streamflow cycle shows two peaks; the maximum peak of 0.8 mm/day in April is due to snowmelt, and the later peak of 0.6 mm/day occurs in June in response to maximum rainfall (see Figure II.2a). The monthly cycle of the average temperature over the basin is shown in Figure II.2d. This cycle shows a minimum in January of -10°C and

increasing to a maximum of 23°C in July. The influence of air temperature to pan evaporation measurements becomes apparent by comparing Figures II.2b and II.2d.

The monthly cycles of standard deviation in all cases but temperature show similar shapes to those of the monthly means. The coefficients of variation in months of high values (spring and summer) are: 0.5 for mean areal precipitation, 0.20 for pan evaporation, 1.0 for flow and less than 0.15 for temperature. In the spring, approximately 50% of the variability of precipitation translates to variability in streamflow. In the summer, approximately 25% of precipitation variability becomes streamflow variability. The storage effect of the soil in reducing the variability is evident.

Standardized monthly anomalies were determined by calculating the average daily records of a month, subtracting out the long-term mean for that month for each average, and then, standardizing the resulting anomaly by dividing by the long-term standard deviation for that particular month. This was done for each month since January 1925 for mean areal precipitation, streamflow at Stratford, and temperature. The time series are shown in Figures II.3a, 3b, and 3c, respectively. Months of higher than average values have positive anomalies and months of lower than average values have negative anomalies. Standardized anomalies that are greater than 2 in absolute value are very significant.

From the standardized anomalies of mean areal precipitation shown in Figure II.3a the natural variability of mean areal precipitation can be detected. Periods of low precipitation are noted in months 364-410, which correspond to April 1954 through March 1958, and in months 615-628, which correspond to the period from April 1975 through May 1976. High precipitation can be found in months 566-586, which correspond to the period from February 1971 through December 1972, and 684-714, which correspond to the period from January 1981 through July 1983. The early period of record is characterized by the lowest precipitation anomalies on record, while the latter period of record by the highest anomalies on record. The period from 150 to 400 (from June 1937 to April 1958) is characterized by the absence of very large positive anomalies.

The standardized monthly anomalies of the streamflow at Stratford shown in Figure II.3b show extended periods of low flows and high flows. Extended periods of low flow are seen from April 1954 (364) through April 1958 (424). Extended periods of high flows are detected from April 1970 (556) through October 1973 (596). The record flow around month 85 is associated with a precipitation anomaly that exceeds 3 standard deviations. The second highest flow anomaly around month 655, however, is not associated with a particularly high precipitation anomaly. This is an example of the nonlinear response of the catchment to precipitation input, and the importance of antecedent precipitation.

Figure II.3c shows the standardized monthly anomalies for temperature. In this figure a negative slope (temperature decreasing with time) is detected. The monthly anomalies in the 1920s are positive, while those of 1980s are negative. Notice that the highest negative temperature anomalies are near the end of the record. This is an example of the unpredictable relationship that regional values of temperature (and other hydroclimatic indices) have with the global values (that have been documented to show an increasing trend (e.g., Schneider et al., 1990)).

Monthly auto-correlations were computed from daily values at lag times from 0-30 days for the period from 1925-1988. The auto-correlations are shown for various months for mean areal precipitation, streamflow at Stratford and temperature in Figures II.4, 5 and 6 respectively. The auto-correlations for mean areal precipitation drop to very low values even at a lag of 1 day with values near 0.3 for the months of March, September and December as shown in Figure II.4. June shows a value less than 0.2 reflecting the summer convective natures of storms in the area. Thus, for all months and on the scales of the analysis, the precipitation may be taken as an uncorrelated sequence for all practical purposes.

The auto-correlation of streamflow at Stratford is shown for March, June, September and December in Figure II.5. The significant lag time of the auto-correlations of streamflow varies depending on the month. In March an auto-correlation of 0.6 can be found for a lag of 5 days, in June for a lag of 7 days, in September for a lag of 8 days and in December for a lag of more than 10 days. Significant persistence of the time series is present for all months, with the shortest persistence in months of excessive rainfall.

Figure II.6 represents the sample auto-correlation function of temperature for various months. For all the months shown, the auto-correlation of 0.6 has a lag between 1 and two days.

The data that spanned 64 years was split in half representing two separate climatic periods which were used to further analyze the hydroclimatological features of the basin. The first climatic period of 31 years contains data from 1925-1956 and the second period contains the data from 1957-1988. The analysis was performed based on monthly average values computed from daily mean areal values for each climatic period and for each index.

Figure II.7 shows the monthly cycle of means and standard deviations for each climatic period for a) mean areal precipitation, b) temperature and c) streamflow at Stratford. Figure II.7a shows the differences and similarities between the two climatic periods in the monthly means of mean areal precipitation. Both the mean and standard deviation cycles are very similar between the two periods. The first climatic period, 1925-1956, shows two peaks one in June and the second in August, whereas the second climatic period is more rounded and shows a maximum of 3.8 mm/day spanning from May through September.

On the average, there was more rainfall for the second climatic period in spring, summer and fall and less rainfall in winter. Such behavior is probably associated with large scale shifts in the seasonal character of the causative circulation. Significant differences in both means and standard deviations are observed in July with higher such quantities observed for the more recent historical period. The seasonal differences in temperature between the two climatic periods are shown in Figure II.7b. It can be seen that the first climatic period is slightly warmer then the second period for all months of the year, but especially for the winter months. It is interesting to note that in winter higher temperatures are associated with higher precipitation, while in summer and fall the opposite is true for this region of the mid-continental U.S.

Significant seasonal differences in streamflow at Stratford are shown in Figure II.7c. The Figure shows consistently lower flows in the first climatic period for the months March through December with the greatest difference occurring in April (0.4 mm/day). In fact, the early historical period shows maximum flows in June, while the recent historical period shows a pronounced peak in April, presumably due to snowmelt. Such differences are most likely due to the corresponding differences in mean areal precipitation shown in Figure II.7a and to a lesser degree due to the temperature differences of Figure II.7b. Temperature differences may account, however, for the early high flows in March during the early climatic period, as higher temperatures would melt the snowpack earlier. The fraction of precipitation that becomes flow ranges from about 10% to 40% with the maximum in the spring months.

It is clear from the plots of Figure II.7 that small relative difference in the forcing produce large differences in the hydrologic response of the large catchment. Understanding such behavior through modeling on the large scale is a necessary prerequisite to further impact analysis. The hydrologic/hydraulic models used toward that goal are described in the next chapter.

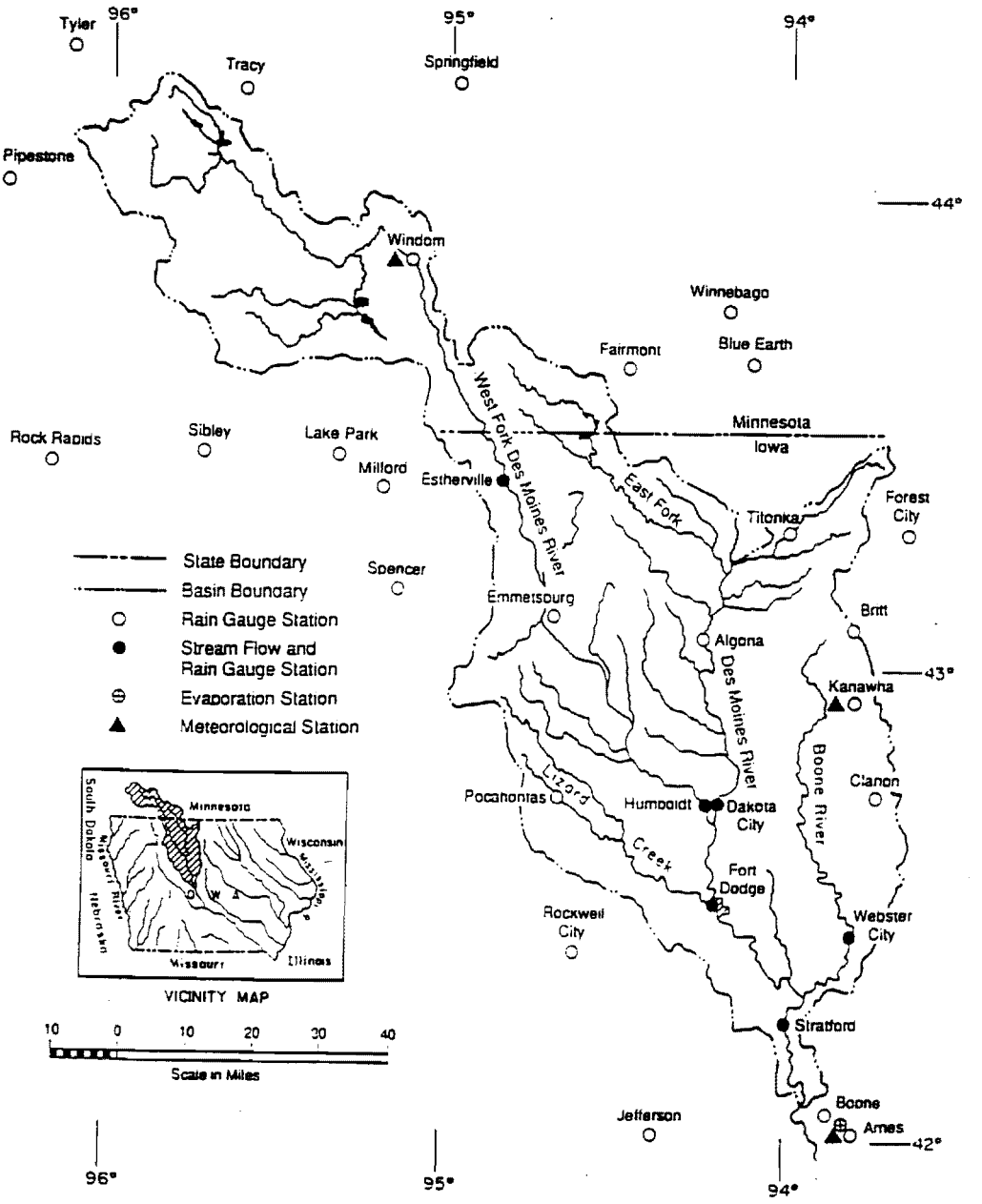

Figure II.1 Map of the Upper Des Moines River basin. (Adopted from Bae and Georgakakos, 1992.)

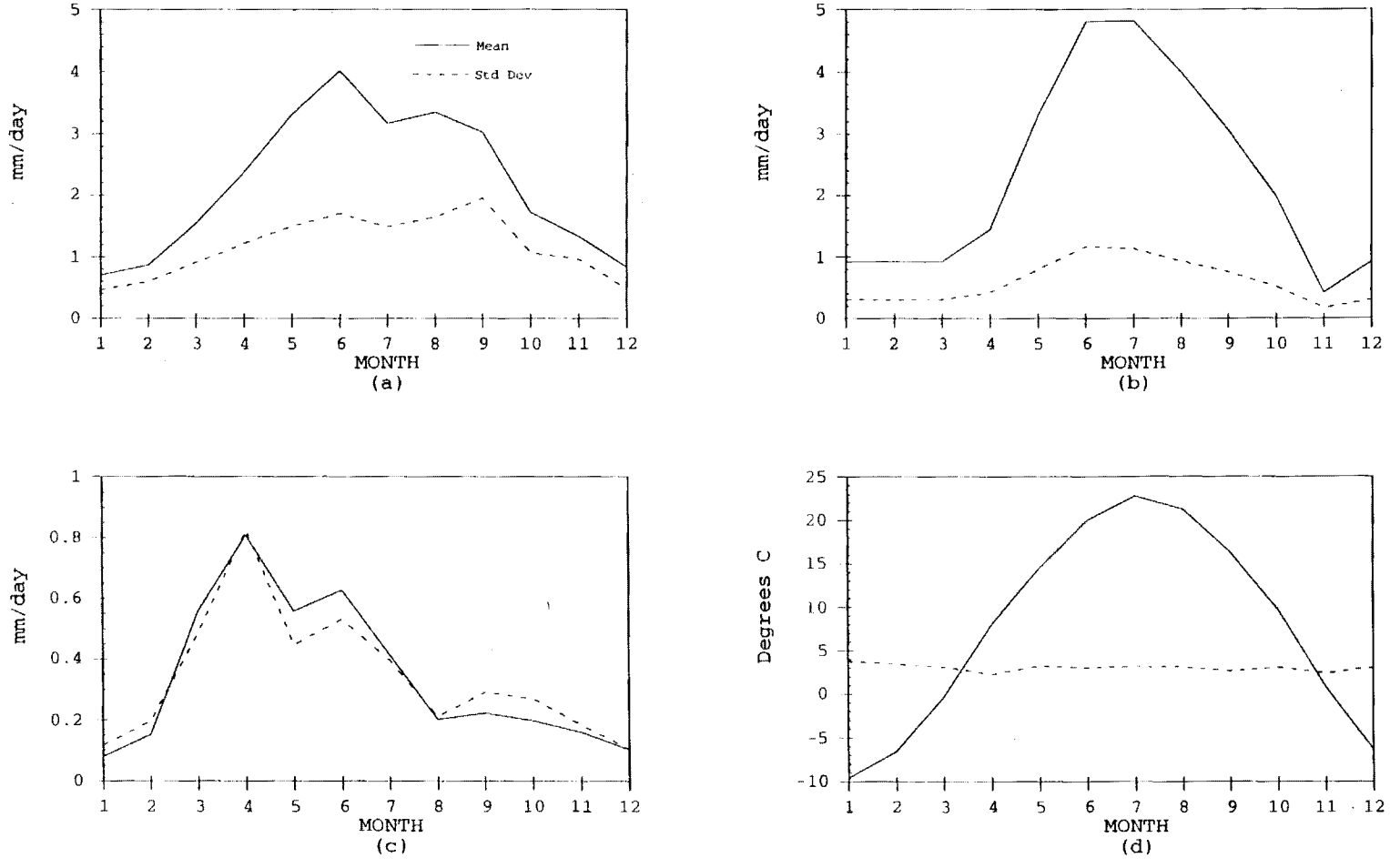

Figure II.2 Seasonal cycles of monthly means and standard deviations for a) mean areal precipitation (1925-1988), b) pan evaporation (1949-1988), c) streamflow at Stratford (1925-1988), and d) temperature(1925-1988).

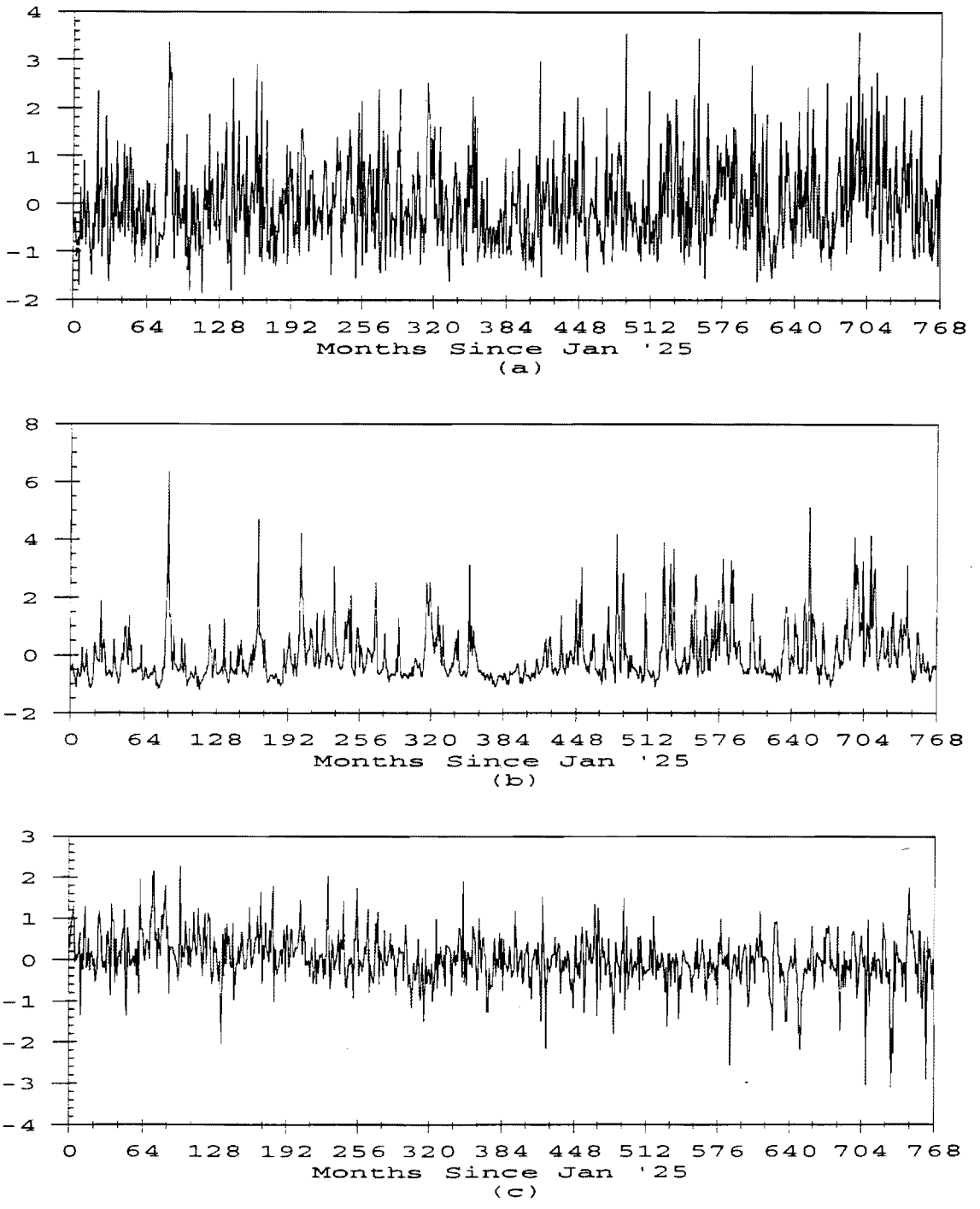

Figure II.3 Standardized monthly anomalies from January 1925 for a) mean areal precipitation b) streamflow at Stratford and c) temperature.

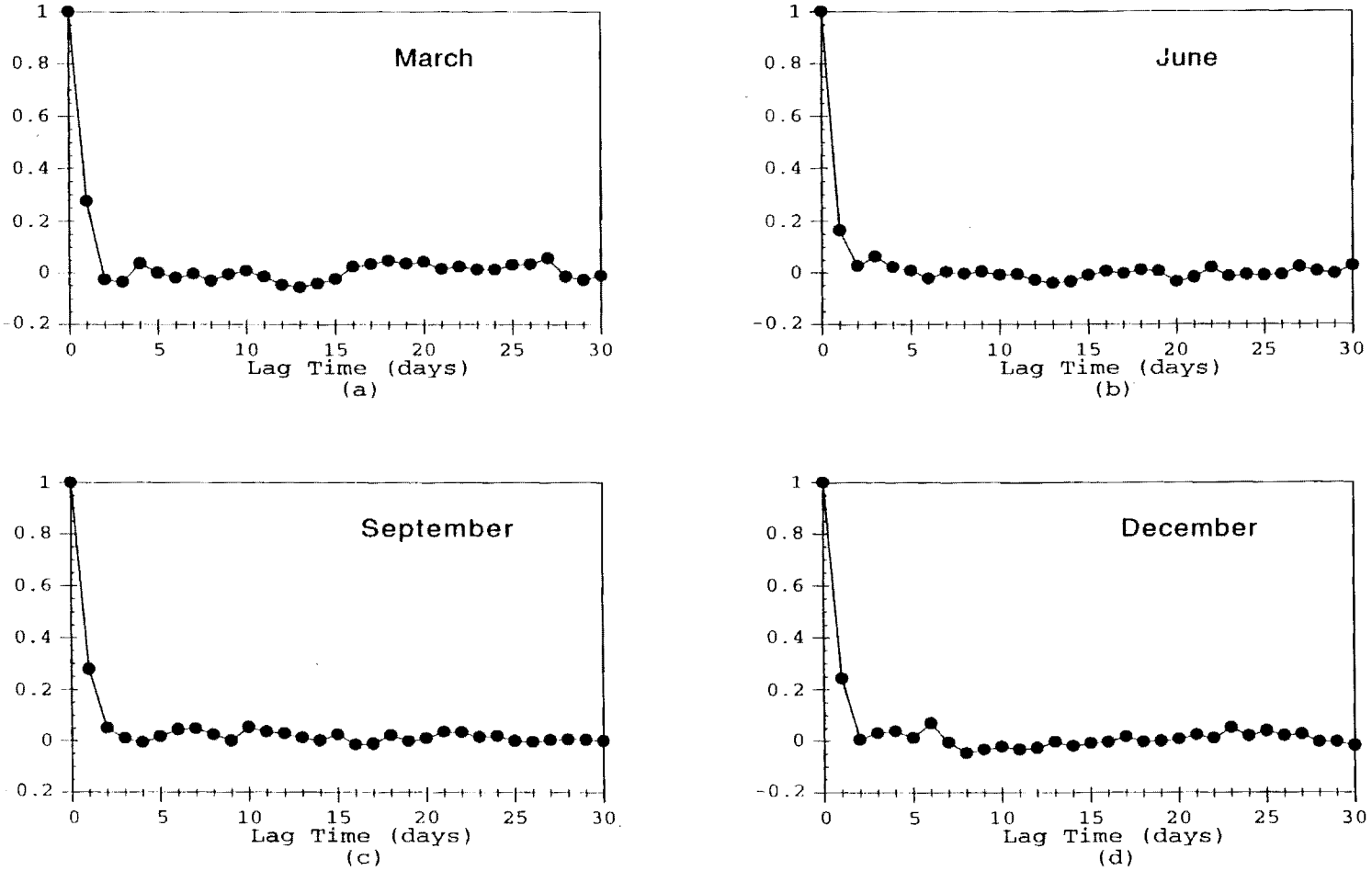

Figure II.4 Auto-correlations of mean areal precipitation in a) March, b) June, c) September, and d) December.

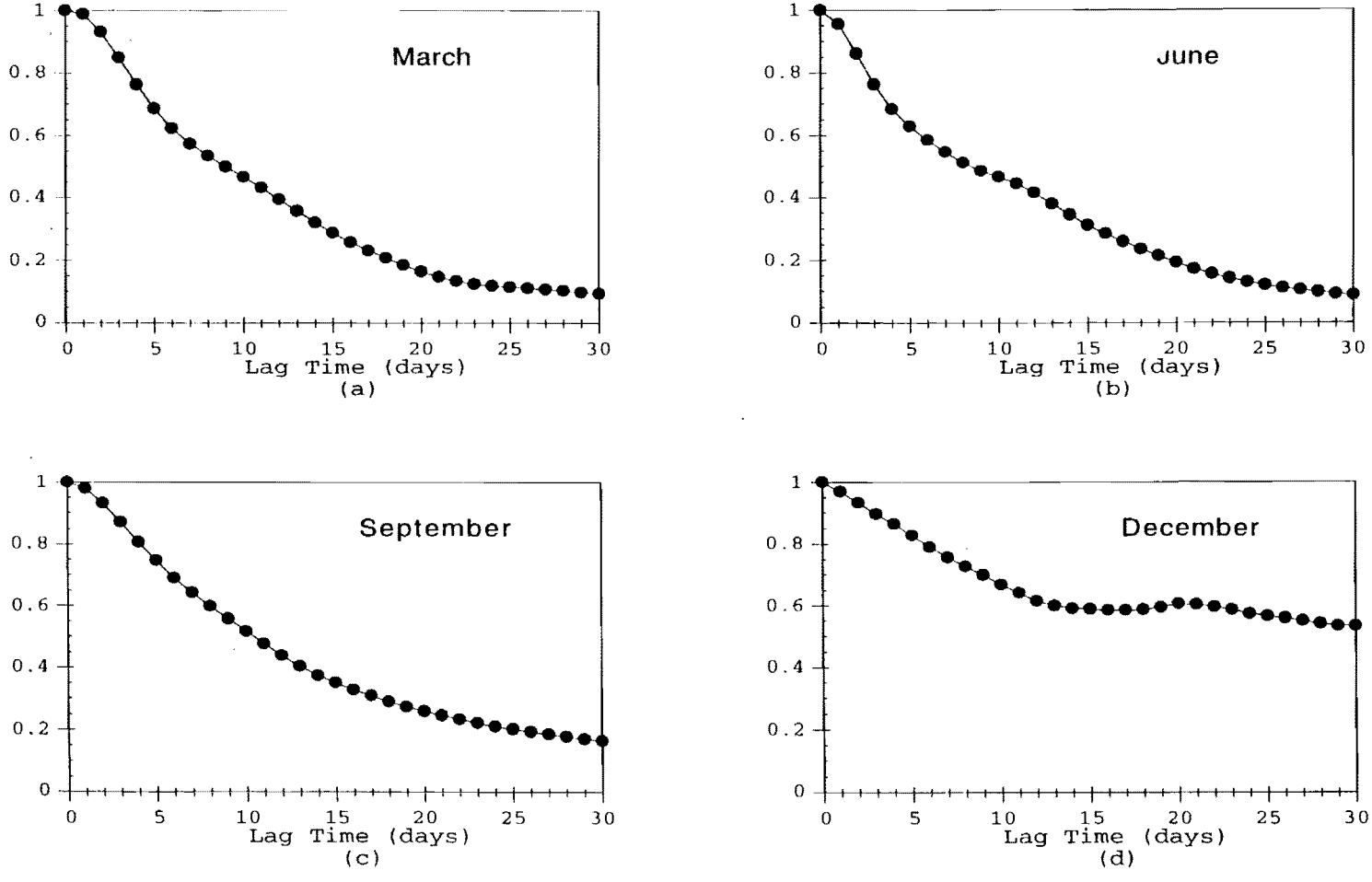

Figure II.5 Auto-correlations of streamflow at Stratford for a) March, b) June, c) September, and d) December.

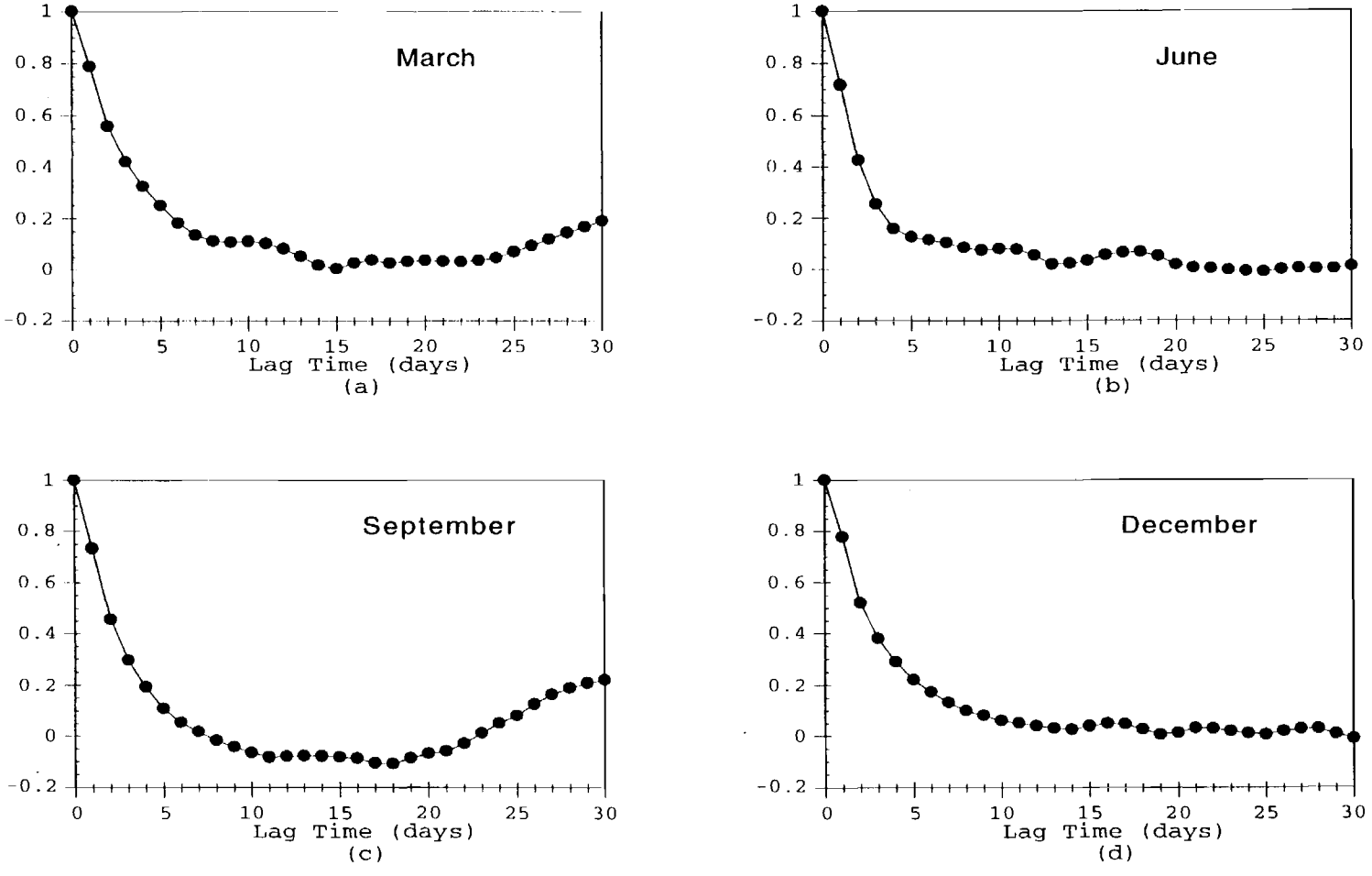

Figure II.6 Auto-correlations of temperature for a) March, b) June, c) September, and d) December.

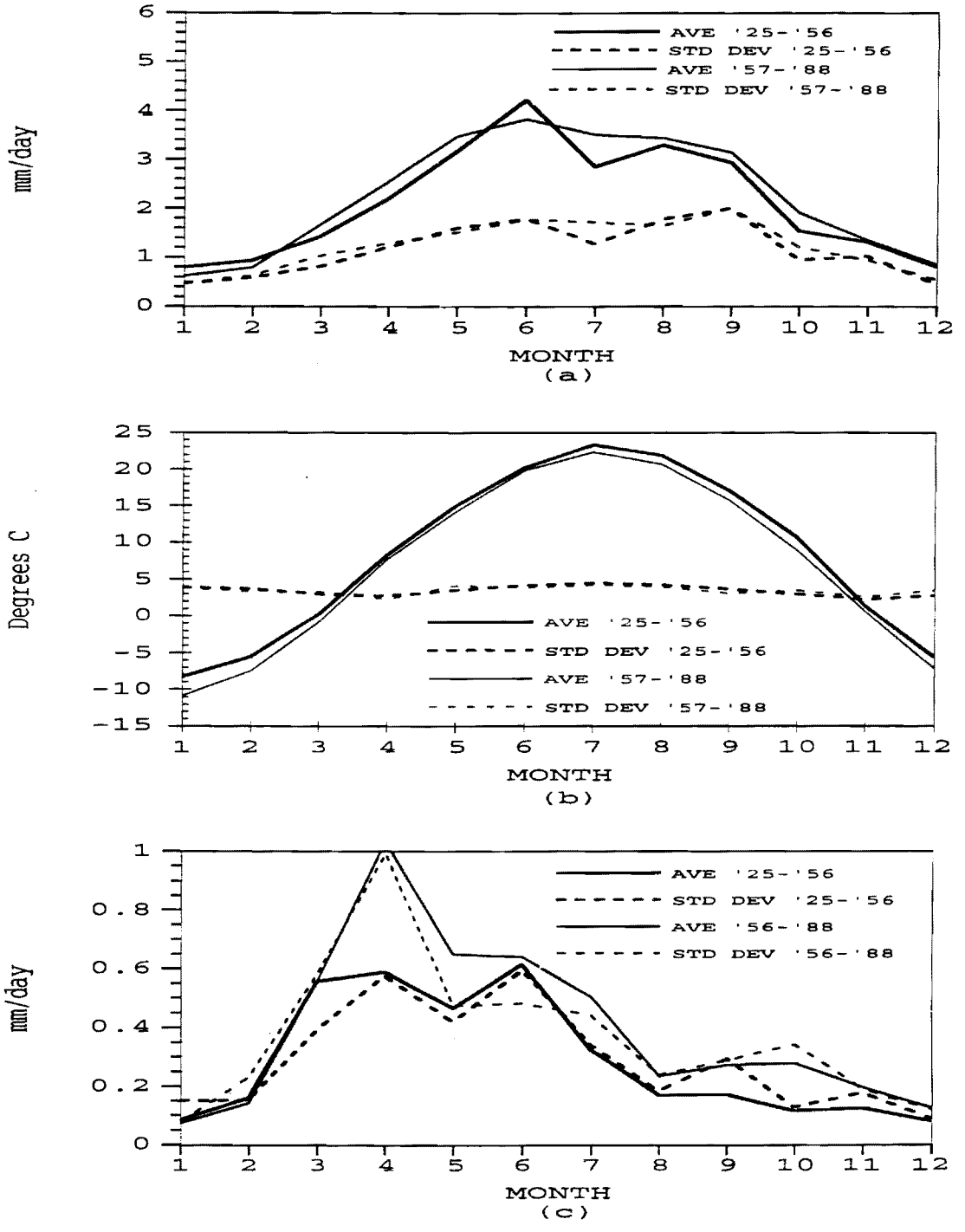

Figure II.7 Seasonal cycles of monthly averages and standard deviations for the periods of 1925-1956 and 1957-1988 for a) mean areal precipitation, b) temperature and c) streamflow at Stratford.

III. THE FORECAST-CONTROL PROCEDURE

The forecast procedure uses the University of Iowa Forecast System (UIFS) with an Extended Streamflow Prediction (ESP) procedure to produce conditional inflow forecasts for the Saylorville reservoir. Three different scenarios of climatic forcing based on historical daily data that span 64 years were determined. The conditional inflow forecasts using such scenarios were then fed to an operational reservoir control scheme to study the resilience of the reservoir operating policies to climate variability. This chapter gives a detailed description of the models that constitute the forecast-control procedure.

3.1. The University of Iowa Forecast System (UIFS)

3.1.1. Description

Bae and Georgakakos (1992) developed, calibrated and tested the UIFS model for the Upper Des Moines River basin. It is based on a modified version of the operational National Weather Service Sacramento model with a frozen ground component. It also utilizes the NWS snow accumulation and ablation model, and a Muskingum-Cunge hydraulic routing scheme. Figure III.1 shows a schematic diagram for the real time application of UIFS on the Upper Des Moines River Basin. The flows in the tributary basins are computed from the modified Sacramento and snowmelt models (depicted as QI for each tributary basin). The tributary flows are routed through the river channels between tributary outlets and to the large-basin outlet at Stratford using the hydraulic routing component (depicted as QC). The details of the model formulation and the mathematical equations for UIFS are in Bae and Georgakakos, 1992, and will not be repeated here. The following, outlines some important features of the model.

3.1.1.1. Modified Sacramento Model

The modified Sacramento model is a spatially-lumped conceptual model that is based on the conservation of water mass equations for the hydrologic catchment. It is a lumped-input lumped-parameter model, and, therefore, it does not account for spatial variability of the input over the basin. It does allow for a variable impervious area which accounts for spatial soil saturation effects. The model has been applied successfully to basins of various sizes and is currently used by the NWS for operational flow forecasting. A typical basin size is of the order of 10^3 km^2.

Several modifications of the original NWS Sacramento model have been made. The original version (Burnash, Ferral and McGuire, 1973) was a discrete time model. Kitanidis and Bras (1978) presented a simplified state space form of the discrete-time version, thus,

allowing the propagation of uncertainty from the model input to the model output via a state estimator. Georgakakos (1986) presented and tested successfully a continuous-time state-space form of the model differential equations that closely approximates the original discrete-time version. The Georgakakos version of the modified Sacramento model equations is used in UIFS, and it is referred to as the modified Sacramento model in the following.

The modified Sacramento model accepts mean areal precipitation, pan evaporation and temperature as input for each sub-catchment, and produces the resultant hydrologic channel inflow. The flow components contributing to the estimated channel inflow are direct runoff from impervious areas, surface runoff in cases of excessive rainfall rates, interflow through the upper soil layers, and groundwater flow that appears in the channels as baseflow.

The model structure, shown in Figure III.2, divides the drainage basin into two zones, an upper and a lower zone. The upper zone represents the upper soil layer and interception storage while the lower zone represents the bulk of the soil moisture and longer groundwater storage. Both zones have tension-water and free-water elements. The former simulates water which can be extracted only be evapotranspiration, while the later simulates water that is "free" to move under the action of gravity. The upper soil zone contains one tension and one free water element, while the lower zone contains one tension and two free water elements in order to capture the observed nonlinear baseflow.

The basic mechanics are that the moisture entering a zone is first stored as tension water until the tension water capacity is filled. Once tension water is filled, then additional water is stored as free water. Free water elements are depleted by percolation from upper zone to lower zone, horizontal channel inflow, non-channel groundwater outflow, or evapotranspiration. The percolation rate is modeled as a nonlinear function of the lower zone deficiency ratio. It is a nonlinear absorber of the type identified by Dooge (1973). An additional impervious area storage element accounts for the temporal changes of the saturated soil area during flooding events. The continuous-time, state-space form of the Sacramento model equations (Georgakakos et al., 1988) model the movement of the moisture through the zones. The movement is governed by these equations and parameters that are unique for each catchment and require long records for their calibration.

Due to the cold weather experienced in the Upper Des Moines River basin, a frozen ground component was added to the modified Sacramento model. Cold temperature, shallow snow cover, and lack of vegetation during the winter months produce the best conditions for deep frost penetration. This results in the reduction of the contribution of groundwater to streamflow. The effects of frozen ground are determined as a reduction factor that

is used to modify the percolation function and the interflow function in the modified Sacramento model equations. The reduction factor is dependent on a frost index, temperature and soil water content.

3.1.1.2 Snow Accumulation and Ablation Models

Snowmelt is the primary source of streamflow in early spring in the Upper Des Moines River basin. It affects many facets of flow prediction (such as flood forecasting) and reservoir operation. The UIFS incorporates a snow accumulation and ablation model to account for such effects. The lumped conceptual temperature index model developed by Anderson (1973) is used. This model is used operationally by the NWS for snowmelt estimation.

The snowpack is modeled as having a snow-water equivalent storage (w_S), liquid water content (w_l), and negative heat storage (w_{nS}). The properties of the snowpack continuously change due to new snowfall and temperature differences between the air and snow surface. Snowmelt occurs when the snowpack gains heat due to warm air. The energy exchange in the snowpack can be expressed from the energy budget. The Anderson air-temperature index model accounts for the energy exchange under different meteorological conditions and calculates a snowmelt rate. There are different indices for snowmelt during rain periods and snowmelt during no-rain periods as well as snowmelt at the soil-snow interface. The model also calculates the heat exchange during no melt periods. It includes an empirical equation for the time lag of snowpack to producing meltwater.

Bae and Georgakakos (1992) present overall sensitivity studies of the snowmelt component in the Upper Des Moines River basin. It was found that the snow component was particularly useful for the northernmost basin of the West Fork with outlet at Estherville.

3.1.1.3. Channel Routing Model

The modified Sacramento model and a snow accumulation and ablation model are used to predict the channel inflow in each tributary sub-catchment of the Upper Des Moines River basin. A Muskingum-Cunge routing scheme (e.g. Georgakakos, et al., 1990) is used to route the flows between the basins and down the Upper Des Moines River to the basin outlet at Stratford, Iowa. The Muskingum-Cunge diffusive-wave model ignores inertia effects on the streamflow, and only accounts for pressure, gravity and bed friction in the momentum equation for channel flow. This type of routing is well suited for steep as well as for mild slopes and flows with a Froude number less than one. Bae and Georgakakos (1992) describe the estimation of the model parameters for the stream network of the Upper Des Moines River based on geometric and geomorphologic channel data.

3.1.2. Tests

The UIFS model performance was tested for forecast reliability by Bae and Georgakakos, 1992, in the Upper Des Moines River basin during the period of 1965 through 1988. Similar results are shown here for easy reference and to ascertain model validity. The model input of daily mean areal precipitation for each sub-catchment was computed by a weighted-average method (developed by the NWS - Larson and VanDemark, 1979) of all the available raingauge station data in or near the sub-catchment of interest. The daily temperature input was determined by an average of the daily maximum and minimum temperature at Ames, Iowa.

Potential evapotranspiration was determined using the monthly average pan evaporation times a monthly correction factor. The correction factor is to adjust the pan values to represent the soil potential evaporation and the plant transpiration. Bae and Georgakakos (1992) give the monthly correction values by basin. The monthly average pan evaporation was calculated from daily pan evaporation data from 1965 through 1988 at Ames, Iowa. It is noted that the station is located in the southernmost region of the basin and, thus, the correction coefficients also account for any biases associated with the representativeness of this station.

The forecast reliability was determined by examining the observed versus the UIFS predicted streamflows at the two head water basins; Boone River at Webster City and West Fork Des Moines River at Estherville, and at the large-basin outlet at Stratford.

The observed versus predicted flows at Stratford, the basin outlet, have a daily cross-correlation of 0.79. It is noted that this value is less than the daily cross-correlation of 0.85 found by Bae and Georgakakos. This is attributed to the use of monthly average values of pan evaporation in this study rather than the daily values used in the work by Bae and Georgakakos. The mean predicted daily flow at Stratford was 0.44 mm/day with a standard deviation of 0.70 mm/day. The corresponding mean observed flow was 0.47 mm/day with a standard deviation of 0.70 mm/day.

Figure III.3a shows the monthly cycle of the means and standard deviations of the observed and the predicted flows based on 24 years of data (1965-1988). This figure shows that the model accurately captures the first flow peak due to snowmelt in April and does a reasonable job in reproducing the later flow peak observed in June. The model also reproduces the monthly variability of the observed record. In the summer, model-predicted flows have a deficit in variability. Such a bias might be due to the lack of daily potential evapotranspiration values, which are highest in summer.

Figure III.3b shows the observed and predicted average monthly flows at Stratford starting from January 1965. From this figure it is seen that the model does reproduce the monthly flow averages at Stratford over a period of record that includes both high flows (e.g., months 252-261) and low flows (e.g., months 18-27). Notable exceptions are the overestimates of flow after month 45 and for months 144-162.

Figures III.4a and III.4b analyze the model performance for two separate headwater sub-catchments that differ in hydroclimatological features of the temperature, precipitation and snowmelt records (see Bae and Georgakakos, 1992). Figure III.4a shows 5-day seasonal cycles of mean and standard deviations of the observed and predicted flows of the 2160 km^2 Boone River at Webster City, Iowa using 24 years of data. Figure III.4b shows similar statistics for the observed and predicted flows of the 3513 km^2 West Fork Des Moines River with outlet at Estherville, Iowa. These figures show that even on the smaller spatial scale of a sub-catchment and the smaller time-scale of 5 days, the model-predicted flows still capture the means and variabilities of the observed flow. It is, then, reasonable to use the model estimated (but not recorded) soil water content as a surrogate measure of field soil moisture on 10^3 km^2 scales. In addition, the model forecasts appear reliable for use in operational forecast procedures.

3.2 Extended Streamflow Prediction

Day (1985) presented the theory, capabilities, and potential application of the ESP methodology. Smith, et al. (1991) generalized the procedure to a nonparametric statistical framework for long-range streamflow forecasting with hydrologic models. The ESP procedure assumes that meteorological events that occurred in the past are representative of events that may occur in the future. Each year of historical meteorological data is assumed to be a possible representation of the future, and is used in a conceptual hydrologic model to simulate a possible future streamflow trace (i.e., a realization). One streamflow trace is simulated for each historical year using the current basin conditions (e.g., snowpack, soil moisture and channel flow) as initial conditions for each simulation. Thus, if N years of historical data are available, N traces of possible future streamflow are simulated. The ensemble of realizations is conditional on the current basin conditions. From the ensemble, moments of the conditional flow-forecast distribution can be constructed and analyzed. The ESP procedure provides an objective means of using conceptual models for medium and long-range forecasting with the capability of assessing forecast uncertainty. It does assume, however, that the variability of the historical input record is representative of the future variability.

Conditional probabilistic forecasts were created by using the ESP procedure with UIFS. Figure III.5 is a schematic for the use of ESP with the UIFS. The UIFS model is started with the current initial soil water and snow accumulation conditions at the forecast preparation time (t_C). Each past year of historical surface meteorological data (i.e., mean areal precipitation, temperature and potential evapotranspiration), starting from t_C and extending to a maximum forecast lead time (*tfld*) with a daily resolution, is then input into UIFS. For each historical year of meteorological data, UIFS predicts a streamflow trace that is conditional on the soil moisture and snow accumulation of the forecast preparation time. Because of limited computer resources and because of the rather substantial size of the reservoir, ensembles of probabilistic forecasts are generated only for the first and fifteenth of every month for each of the three 25-year long periods of study (see Chapter IV).

3.3 The Real Time Reservoir Operating Procedure

The real time reservoir operating procedure used in this work follows a set control approach. The theory and mathematical formulation of the set control approach is presented in Georgakakos and Yao, 1993 and the application of it to reservoir management in Yao and Georgakakos, 1993. The purpose of the set control scheme is to determine control vector sequences able to guide the system to meet its objectives over an operational horizon. The method accounts explicitly for the hydrologic input uncertainty as it is based on set descriptions of such uncertainty.

The set control approach assumes that the future inputs belong in certain sets. The boundaries of these sets may represent minimum and maximum input estimates or other extreme levels, against which a sound operational policy is to be developed. The control process determines admissible controls such that system states (i.e., reservoir levels and storage) remain within their acceptable limits as long as the inputs take on values from the specified input sets.

For the purpose of this study, the set control method starts with the current reservoir storage and allows for hydrologic inputs and controllable inputs. The hydrologic inputs are taken from the set of forecast realizations generated by the UIFS model using the ESP procedure. The controllable inputs represent the reservoir releases which are defined based on the systems limitations and operational requirements. The set control approach then determines sets of operational decisions such that the reservoir storage does not violate the operational constraints for the boundaries determined by the maximum and minimum inflow levels expected to materialize over the control horizon. These boundaries are determined from the streamflow traces generated by UIFS with the ESP procedure. A set of

operational decisions are determined for each forecast preparation time that guarantee that the reservoir system will perform within the desirable bounds for the duration of the forecast horizon up to the maximum forecast lead time.

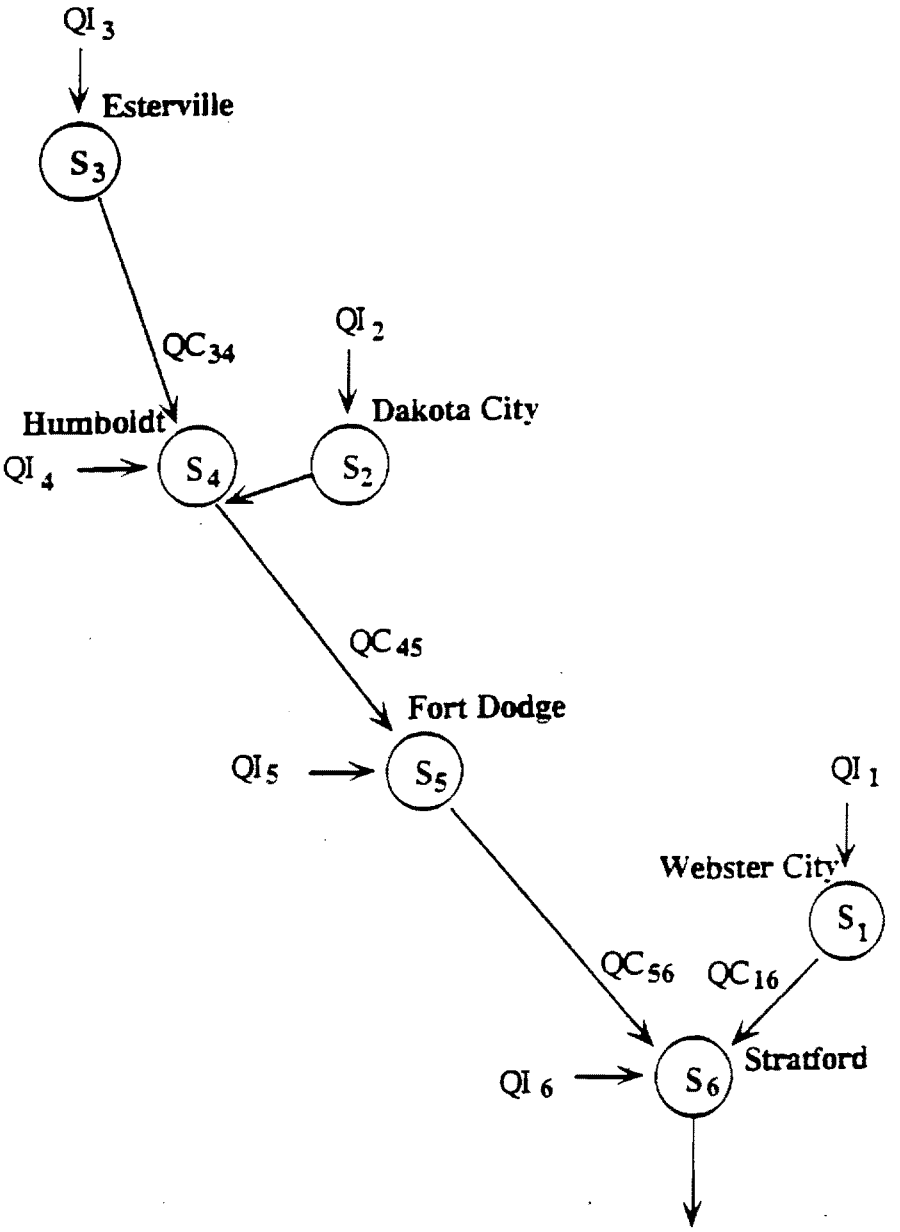

Figure III.1 Schematic of UIFS model. (Adopted from Bae and Georgakakos, 1993)

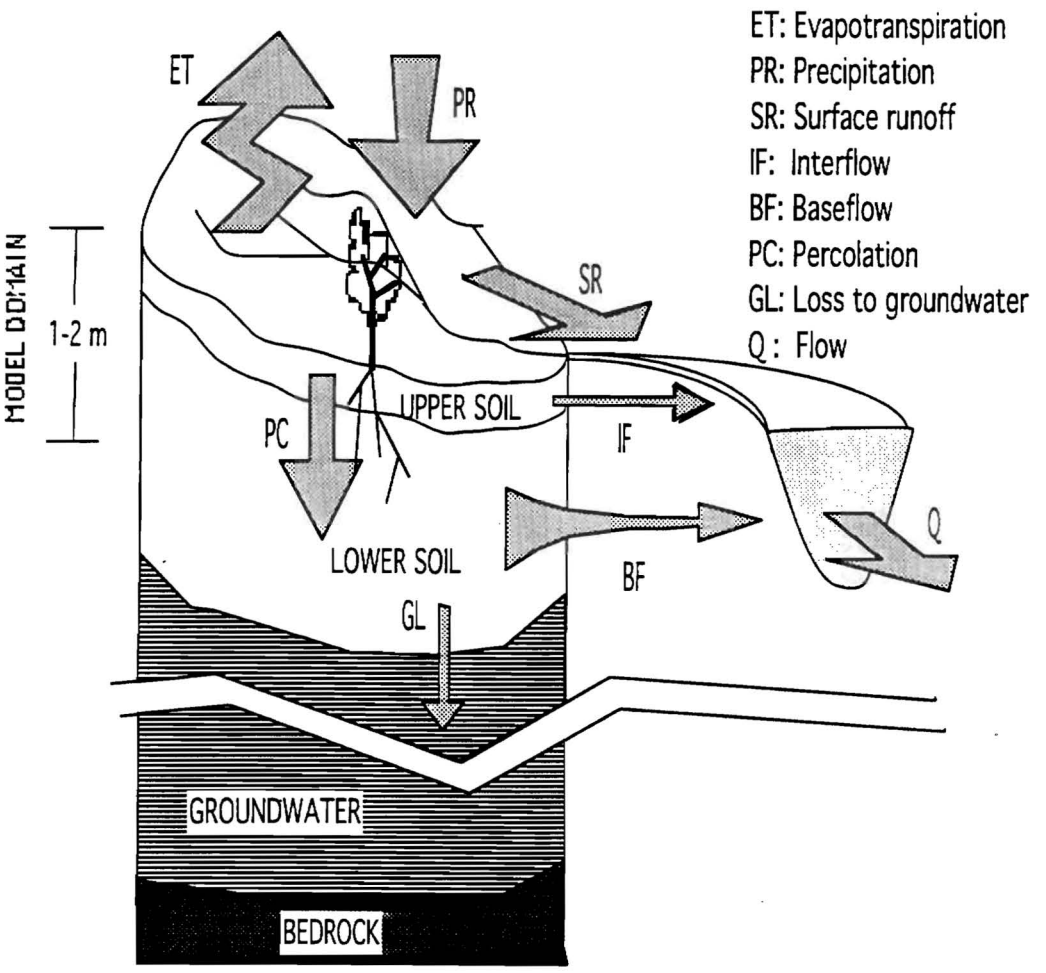

Figure III.2 Schematic of the modified Sacramento Model.

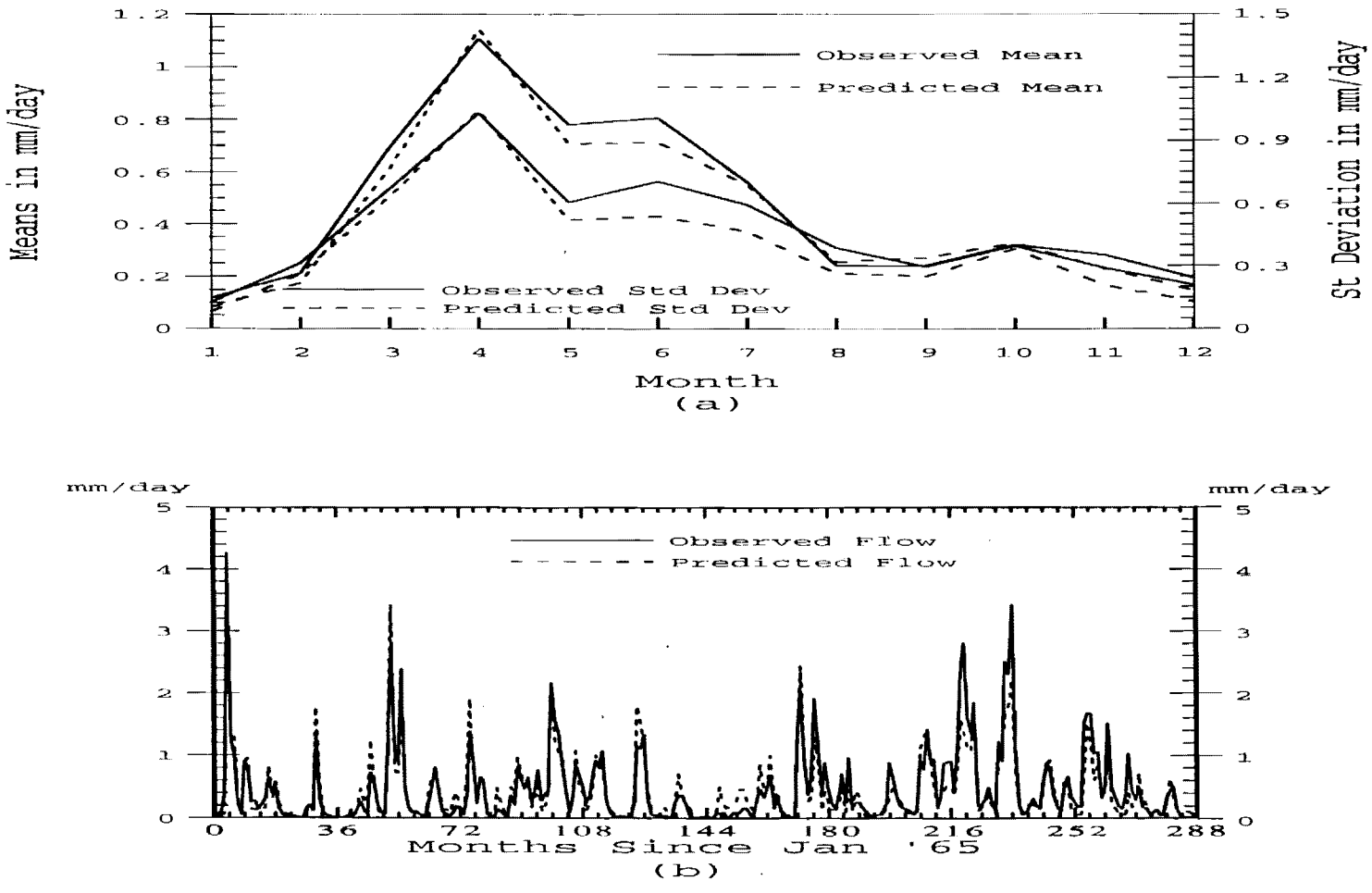

Figure III.3 Observed and predicted streamflows at Stratford, Iowa for a) seasonal monthly flow cycles mean and standard deviation, and b) average monthly flows since Jan, 1965.

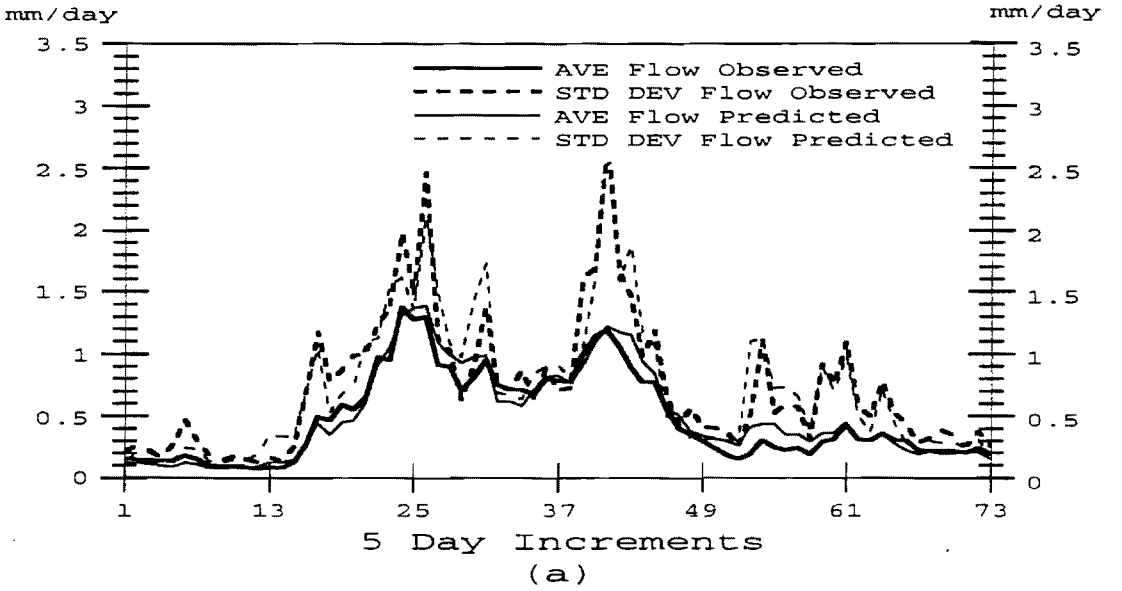

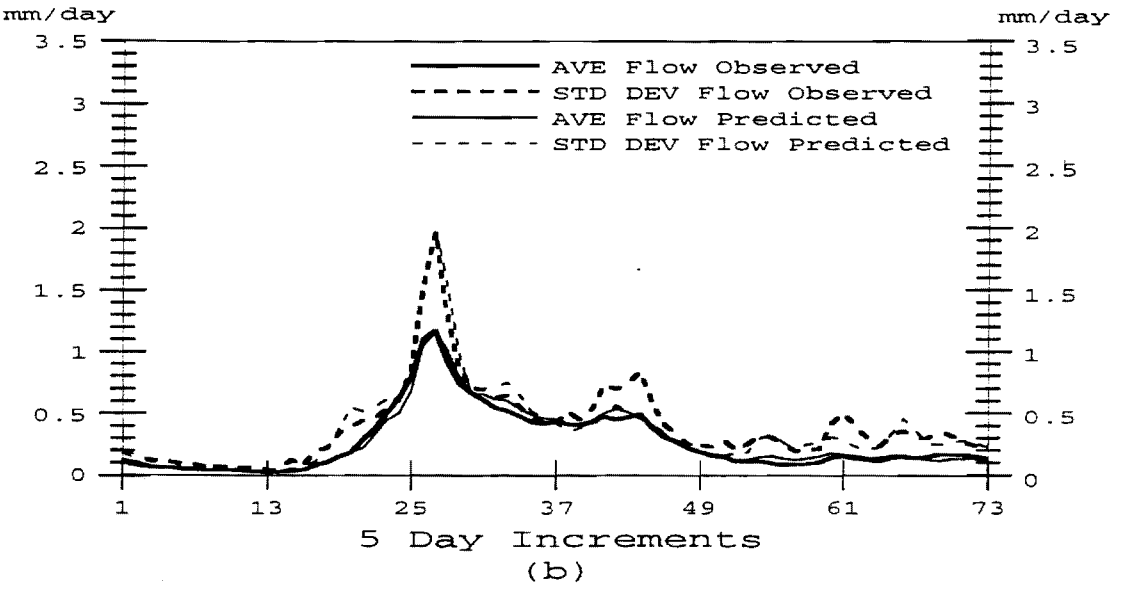

Figure III.4 Five-day seasonal means and standard deviations of the observed and predicted flows for a) the Boone River at Webster City, Iowa, and b) the West Fork Des Moines River at Estherville

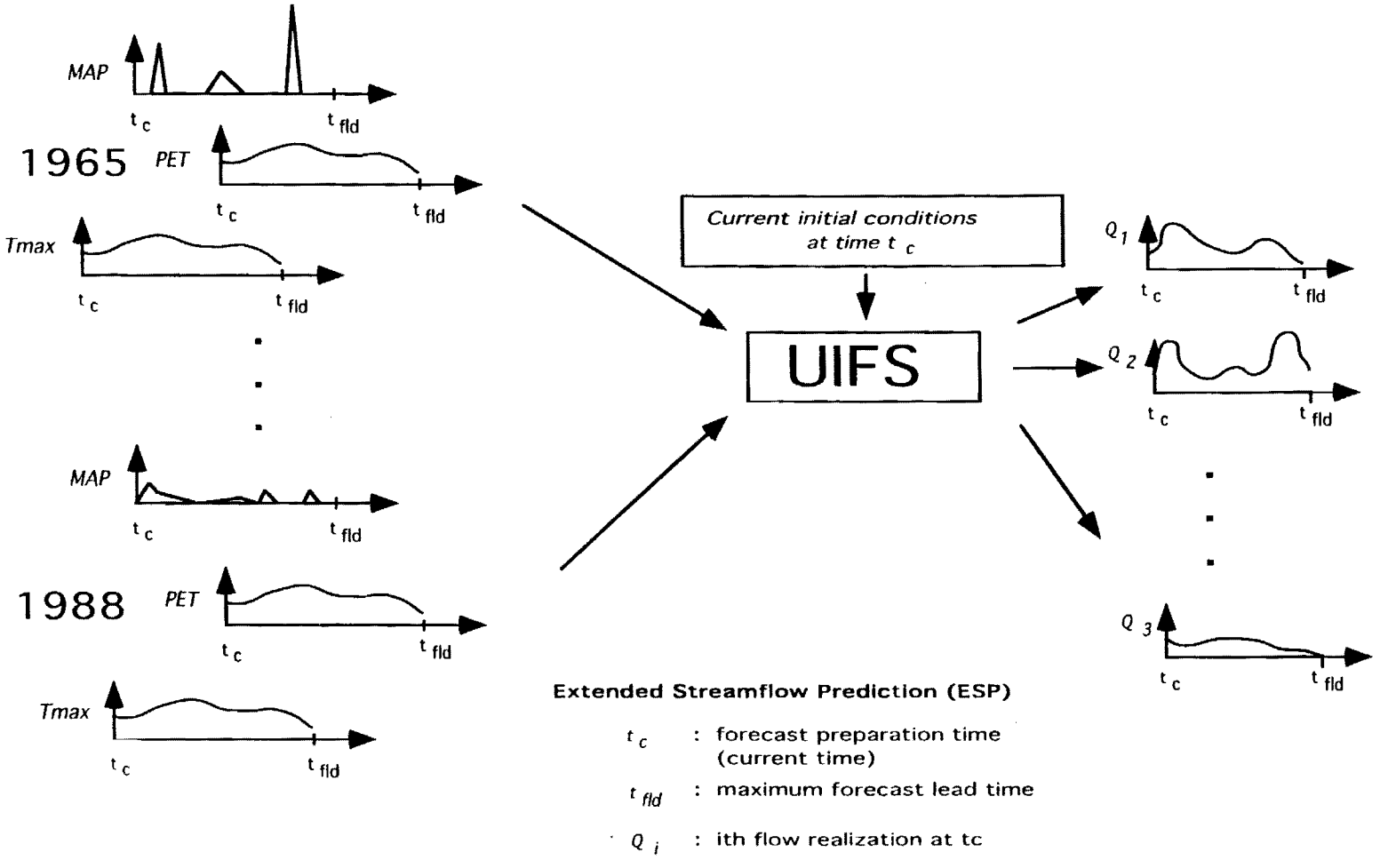

Figure III.5 Schematic of the UIFS-ESP forecast procedure.

IV. SENSITIVITY ANALYSIS WITH HISTORICAL DATA

4.1 The Three Climatic Periods

Available data of precipitation and temperature spanning the period from 1925-1988 were divided into three climatic periods; a) 1925-1949, b) 1949-1974 and c) 1965-1988, and used in the forecast-control procedure. Considerations for the definition of the individual periods were a) approximately similar lengths, b) 1965-1988 is a period with data from all recording stations in the area and was, thus, defined as one of the periods because it is the best observed period of record, c) period lengths should be at least 20 years long and as close to a climatic period (30 years) as possible. The three climatic periods differed in data availability, seasonal cycles of the model forcing parameters (temperature, precipitation and potential evapotranspiration), and seasonal cycles of the model estimated parameters (soil water content). This section examines the similarities and differences of the large-basin hydrology between the three climatic periods before the assessment of the sensitivity of the forecasts and management to such differences (Chapter V).

4.2 Data Availability

The UIFS model requires inputs of mean areal precipitation, mean areal temperature and potential evapotranspiration for each of the six sub-basins to forecast flows. Observed streamflow at a gauging station for each sub-basin outlet may also be needed if the updating option is used. The inputs are calculated from available station data obtained from CD-ROM disks distributed by "EarthInfo, Inc." Tables IV.1-3 describe the data type and location of all the available stations in the Upper Des Moines River basin for each of the climatic periods studied. Many precipitation stations span the period from 1949 to present and few date back to the early 1900s. One temperature station at Ames, Iowa recorded both maximum and minimum temperature from the early 1900s to present. Pan evaporation data was recorded at Ames, Iowa from 1965 to present. Complete observed streamflow data for all six sub-basin outlets was found for the 1965-1988 period.

For the latter two climatic periods, 1949-1974 and 1965-1988, mean areal precipitation was calculated by the NWS weighted average technique (Larson, 1975, and Larson and VanDemark, 1979) for each sub-basin. Sets consisting of stations from the 29 available were determined for each sub-basin based on the location and distribution of raingauge stations in and around the sub-basin. By sub-basin, the selected raingauge stations are; the 11 stations 2, 3, 5, 6, 7, 9, 10, 11, 12, 15, and 16 for the Boone River basin with

Table IV.1. Station data for 1925-1949

Data	Station	Latitude	Longitude
Precipitation:			
1	Ames	42:02:00	93:39:00
2	Rockwell City	42:24:00	94:37:00
3	Webster City	42:28:00	93:48:00
4	Storm Lake	42:38:00	95:11:00
5	Hampton	42:45:00	93:12:00
6	Algona	43:04:00	94:18:00
7	Mason City	43:09:00	93:14:00
8	Spencer	43:10:00	95:09:00
9	Worthington	43:37:00	95:36:00
Maximum Temperature			
	Ames	42:02:00	93:39:00
Minimum Temperature			
	Ames	42:02:00	93:39:00
Streamflow			
	Stratford	42:15:04	93:52:52

Table IV.2. Station data for 1949-1974

Data	Station	Latitude	Longitude
Precipitation			
1	Jefferson	42:01:00	94:23:00
2	Ames	42:02:00	93:48:00
3	Boone	42:03:00	93:53:00
4	Rockwell City	42:24:00	94:37:00
5	Webster City	42:28:00	93:48:00
6	Fort Dodge	42:30:00	94:10:00
7	Humboldt	42:41:00	94:12:00
8	Pocahontas	42:42:00	94:40:00
9	Clarion	42:44:00	93:44:00
10	Kanawha	42:56:00	93:48:00
11	Algona	43:04:00	94:18:00
12	Britt	43:05:00	93:48:00
13	Emmetsburg	43:06:00	94:41:00
14	Spencer	43:10:00	95:09:00
15	Forest City	43:17:00	93:38:00
16	Titonka	43:17:00	93:59:00
17	Milford	43:23:00	95:11:00
18	Estherville	43:25:00	94:50:00
19	Rock Rapids	43:26:00	96:10:00
20	Lake Park	43:27:00	95:19:00
21	Sibley	43:27:00	95:43:00
22	Fairmont	43:38:00	94:28:00
23	Blue Earth	43:39:00	94:06:00
24	Winnebago	43:46:00	94:10:00
25	Windom	43:52:00	95:06:00
26	Pipestone	44:01:00	96:19:00
27	Tracy	44:14:00	95:37:00
28	Springfield	44:15:00	94:59:00
29	Tyler	44:19:00	96:08:00
Maximum Temperature			
	Ames	42:02:00	93:48:00
Minimum Temperature			
	Ames	42:02:00	93:48:00
Streamflow			
	Stratford	42:15:04	93:52:52

Table IV.3. Station data for 1965-1988

Data	Station	Latitude	Longitude
Precipitation			
1	Jefferson	42:01:00	94:23:00
2	Ames	42:02:00	93:48:00
3	Boone	42:03:00	93:53:00
4	Rockwell City	42:24:00	94:37:00
5	Webster City	42:28:00	93:48:00
6	Fort Dodge	42:30:00	94:10:00
7	Humboldt	42:41:00	94:12:00
8	Pocahontas	42:42:00	94:40:00
9	Clarion	42:44:00	93:44:00
10	Kanawha	42:56:00	93:48:00
11	Algona	43:04:00	94:18:00
12	Britt	43:05:00	93:48:00
13	Emmetsburg	43:06:00	94:41:00
14	Spencer	43:10:00	95:09:00
15	Forest City	43:17:00	93:38:00
16	Titonka	43:17:00	93:59:00
17	Milford	43:23:00	95:11:00
18	Estherville	43:25:00	94:50:00
19	Rock Rapids	43:26:00	96:10:00
20	Lake Park	43:27:00	95:19:00
21	Sibley	43:27:00	95:43:00
22	Fairmont	43:38:00	94:28:00
23	Blue Earth	43:39:00	94:06:00
24	Winnebago	43:46:00	94:10:00
25	Windom	43:52:00	95:06:00
26	Pipestone	44:01:00	96:19:00
27	Tracy	44:14:00	95:37:00
28	Springfield	44:15:00	94:59:00
29	Tyler	44:19:00	96:08:00
Maximum Temperature			
	Ames	42:02:00	93:48:00
Minimum Temperature			
	Ames	42:02:00	93:48:00
Pan Evaporation			
	Ames	42:02:00	93:48:00
Streamflow			
	Webster City	42:26:01	93:48:12
	Dakota City	42:43:26	94:11:30
	Estherville	43:23:51	94:50:38
	Humboldt	42:43:12	94:13:06
	Fort Dodge	42:30:22	94:12:04
	Stratford	42:15:04	93:52:52

outlet at Webster City, the 11 stations 6, 7, 8, 11, 12, 13, 16, 18, 22, 23, and 24 for the East Fork Des Moines River basin with outlet at Dakota City, the 9 stations 18, 19, 20, 21, 25, 26, 27, 28, and 29 for the West Fork Des Moines River basin with outlet at Estherville, the 7 stations 7, 8, 11, 13, 14, 17, and 18 for the Des Moines River Basin with outlet at Humboldt, the 5 stations 4, 5, 6, 7, and 8 for the Des Moines River basin with outlet at Fort Dodge, and the 5 stations 1, 3, 4, 5, and 6 for the Des Moines River basin with outlet at Stratford. (The station numbers correspond to the station numbers on Tables IV.2 and IV.3.)

Due to the presence of few precipitation data stations in the first climatic period, 1925-1949, linear regression was used to determine mean areal precipitation for each sub-basin and for that period. The regression coefficients were determined using data from the well-observed 1965-1988 period. The mean areal precipitation for each sub-basin determined by the NWS weighted average method was used as the dependent variable and the 9 precipitation stations available in the 1925-1949 period were used as the predictor random variables. A regression analysis using MINITAB software (MINITAB, Inc, 1989) was performed, and the best model was chosen for each sub-basin.

Table IV.4 shows the regression coefficients of each raingauge station for the sub-basin models. In Table IV.4 the subscript b_0 indicates the regression constant and the subscripts b_1-b_9 indicate the coefficient corresponding to the raingauge station as numbered in Table IV.1. The daily cross-correlation between the regression model chosen and the mean areal precipitation determined by the NWS weighted average method is listed in the table as r_o. All of the models have a daily cross-correlation greater than 0.84. The percent of variation in the response data that is explained by the model is identified as R^2. For each sub-basin model the R^2 value is greater than 70%. The standard deviation of each model is indicated by s where the worst case is 2.98 mm/day for the sub-basin with the outlet at Estherville.

Selection criteria for determining which raingauge stations to use for each sub-basin were based on overall F-tests, R^2 values, standard deviations, and the sequential sum-of-squares values. The variable selection procedure was based on forward selection which adds into the model the regressor variable with the largest t-ratio. Regressor variables were added until there was no significant addition to the sequential sum-of-squares term (sequential sum-of- squares less than 2). The other values of the overall F-test, R^2 value and standard deviation were then examined to determine if the addition of any other regressor variable significantly improved the model. An alternative selection procedure that eliminates regressor variables with a t-ratio less than 2 was also tested and showed similar

Table IV.4 Regression Coefficients

Subbasin	b_0	b_1	b_2	b_3	b_4	b_5	b_6	b_7	b_8	b_9	ρ_0	R^2	s (mm/day)
Webster City	0.17	0.18	0.13	0.18	0.00	0.09	0.24	0.13	0.07	0.00	0.95	90.6	1.69
Dakota City	0.21	0.00	0.14	0.00	0.00	0.07	0.26	0.09	0.12	0.13	0.90	81.4	1.89
Estherville	0.42	0.00	0.00	0.00	0.07	0.00	0.08	0.00	0.16	0.52	0.84	70.4	2.81
Humboldt	0.21	0.00	0.08	0.00	0.08	0.06	0.27	0.07	0.25	0.14	0.87	75.2	2.62
Fort Dodge	0.35	0.00	0.40	0.15	0.12	0.09	0.00	0.00	0.11	0.00	0.86	73.1	2.98
Stratford	0.13	0.07	0.58	0.33	0.00	0.00	0.00	0.00	0.00	0.00	0.98	95.7	1.32

results to the models found by the sequential sum-of-squares method. The models presented here were determined by the sequential sum-of-squares method.

Figure IV.1a shows a comparison of the monthly means and standard deviations, averaged over the 1965-1988 period, of the mean areal precipitation computed by the NWS weighted average method to the regression model for the Boone River basin with outlet at Webster City. The regression model captures the seasonal cycle of both the mean and standard deviation of mean areal precipitation with a large peak in June and a second peak in September. Figure IV.1b shows the monthly means for each month since January 1965 for both the NWS mean areal precipitation and the regression model. A comparison of the other sub-basins regression models with the corresponding sub-basins NWS mean areal precipitation can be seen in Appendix Figures A.1-5. In general, the regression model predictions have a smaller variance than the all raingauge cases of the NWS method. The regression model for the sub-basin with outlet at Estherville (Appendix Figure A.2) slightly underestimates the mean rainfall during the summer months and early fall months and over estimates it during the winter months. Similar behavior is seen in the sub-basin with outlet at Fort Dodge (Appendix Figure A.4).

The mean areal temperature was computed identically for all three climatic periods. In each case mean areal temperature was determined as the average of the maximum and minimum daily temperature measured at Ames, Iowa. This value was used for each sub-basin.

Daily observations of pan evaporation were only taken in the 1965-1988 period. Therefore monthly values of potential evapotranspiration needed for model input were determined by multiplying the monthly average pan evaporation (computed from the 1965-1988 period) by an evaporation correction factor. Table IV.5 shows the monthly evaporation correction factors for all six sub-basins in each of the climatic periods. The twelve correction factors were estimated based on published regional estimates (e.g., Farnsworth, et al., 1982, and Georgakakos, et al., 1988), then adjusted by running the UIFS model for the full climatic period and comparing the observed flows to the model forecasted flows. In most cases, the correction factors for the two more recent periods were smaller than those for the earlier period, making for reduced potential evapotranspiration. Notable exceptions are the correction factors for April in the period 1949-1974.

4.3 Atmospheric Forcing Variables

The hydrologic/hydraulic model forcing parameters of temperature, precipitation and potential evapotranspiration show many similarities and differences between the three

climatic periods. Comparisons were made based on monthly average values and monthly standard deviations obtained from summing the daily observations for all the same months within the respective climatic period. Further analysis was performed by studying the monthly standardized anomalies of each index for each climatic period. Standardized anomalies were determined by averaging the daily values of a certain month, subtracting the long term mean value of that month, and then standardizing by dividing the anomaly by the standard deviation. The analysis methods are similar to those employed in Chapter II for the climatological study of the observed record.

Figures IV.2a, 2b and 2c show the seasonal cycle of the means and standard deviations of mean areal precipitation over the entire basin for each climatic period. Also indicated is the average total annual rainfall for each period. The basin average was determined by a weighted area method of the contributing sub-basins. It is noted that these estimates are different in character from those discussed in Chapter II in that they are tuned to the hydrologic basins, rather than the station locations alone. From the average total annual rainfall it is clear that the the first climatic period had on average almost 20 mm less precipitation per year then the other two climatic periods. Such a deficit is largely due to the reduced average rainfall in mid-summer. The 1925-1949 climatic period shows an increase from it's January precipitation to the first peak of 3.8 mm/day in June. This is followed by a slight decrease and then a second peak of 3.2 mm/day in September which then decreases in the winter months. The 1949-1974 period differs in that it shows an increase of precipitation from January to one peak of 4 mm/day in June. The precipitation gradually decreases between June and September and, then, sharply decreases between September and December. The third climatic period shows precipitation to increase from January to the first peak in June of 3.6 mm/day and then drops to about 3.0 mm/day for July through September. After September, precipitation decreases through December. The seasonal cycle of standard deviation for each climatic period generally follows the cycle of the means. A notable exception is the large value of standard deviation seen in September indicating a high variability of precipitation at this time. Months with high amount of precipitation show a coefficient of variation to be about 0.50 for all climatic periods.

The seasonal cycle of the mean and standard deviation of temperature in °C for each climatic period is shown in Figures IV.3a, 3b, and 3c. The climatic period 1925-1949 shows a minimum temperature of -7°C in January increasing to a maximum temperature of 24°C in July and decreasing to -4°C in December. The second climatic period's seasonal cycle is cooler by almost 2°C. The minimum in January is -9°C which then increases to the maximum seen in July of 22°C followed by a decreases to -6°C in December. The most

Table IV.5 Evaporation Correction Factors

Period/ Subbasin	Monthly Correction Factors											
	Jan	Feb	Mar	Apr	May	Jun	Jul	Aug	Sep	Oct	Nov	Dec
1925-1949												
Webster City	0.70	0.70	0.88	1.10	0.72	0.72	1.20	1.20	1.20	0.80	0.80	0.70
Dakota City	0.70	0.70	0.88	1.10	0.72	0.72	1.08	1.08	1.08	0.75	0.75	0.70
Estherville	0.70	0.70	0.77	1.10	0.84	0.84	1.20	1.20	1.20	0.80	0.80	0.70
Humboldt	0.70	0.70	0.88	1.10	0.72	0.72	1.08	1.08	1.08	0.75	0.75	0.70
Fort Dodge	0.70	0.70	0.88	1.10	0.72	0.72	1.20	1.20	1.20	0.80	0.80	0.70
Stratford	0.70	0.70	0.88	1.10	0.72	0.72	1.20	1.20	1.20	0.80	0.80	0.70
1949-1974												
Webster City	0.70	0.70	0.80	1.35	0.69	0.72	1.15	1.15	1.00	0.80	0.80	0.70
Dakota City	0.70	0.70	0.80	1.35	0.69	0.72	1.04	1.04	0.90	0.75	0.75	0.70
Estherville	0.70	0.70	0.70	1.35	0.81	0.84	1.15	1.15	1.00	0.80	0.80	0.70
Humboldt	0.70	0.70	0.80	1.35	0.69	0.72	1.04	1.04	0.90	0.75	0.75	0.70
Fort Dodge	0.70	0.70	0.80	1.35	0.69	0.72	1.15	1.15	1.00	0.80	0.80	0.70
Stratford	0.70	0.70	0.80	1.35	0.69	0.72	1.15	1.15	1.00	0.80	0.80	0.70
1965-1988												
Webster City	0.70	0.70	0.80	1.00	0.60	0.60	1.00	1.00	1.00	0.80	0.80	0.70
Dakota City	0.70	0.70	0.80	1.00	0.60	0.60	0.90	0.90	0.90	0.75	0.75	0.70
Estherville	0.70	0.70	0.70	1.00	0.70	0.70	1.00	1.00	1.00	0.80	0.80	0.70
Humboldt	0.70	0.70	0.80	1.00	0.60	0.60	0.90	0.90	0.90	0.75	0.75	0.70
Fort Dodge	0.70	0.70	0.80	1.00	0.60	0.60	1.00	1.00	1.00	0.80	0.80	0.70
Stratford	0.70	0.70	0.80	1.00	0.60	0.60	1.00	1.00	1.00	0.80	0.80	0.70

recent climatic period has a seasonal temperature cycle that is cooler in winter by almost 1°C than the previous period. The minimum temperature for this period occurs again in January at -10°C then increases to the maximum temperature of 23°C in July decreasing to -7°C in December. The results of Figures IV.2-3 show that there is no clear relationship between average regional temperature and precipitation. The first and second periods support the relationship high-rainfall/cool- temperature while the second and third do not. The seasonal cycle for the standard deviation of temperature is generally between 2-4°C for each climatic period with small within-year variability. Certainly, interannual variability is larger than the differences in monthly average temperatures experienced by the region during the three climatic periods.

Figures IV.4a, 4b, and 4c show the seasonal cycle of the mean potential evapotranspiration of the entire basin for each climatic period. The monthly values were computed from the monthly average of pan evaporation measured in 1965-1988 multiplied by the appropriate correction factor for each sub-basin within each climatic period. The overall basin average was determined by a weighted area method of the sub-basins. All three climatic periods show similar potential evapotranspiration seasonal cycles that follow the temperature seasonal cycle. All have low potential evapotranspiration in January through March and then begin to increase to a peak in July. Following the July peak, potential evapotranspiration decreases to it's low winter values. A comparison of the three climatic periods shows that the first period, 1925-1949, has the highest potential evapotranspiration and the third period has the lowest potential evapotranspiration. This corresponds to the warmer temperatures being found in the first climatic period and the cooler temperatures being found in the latter period.

Standardized anomalies of precipitation for each of the climatic periods can be found in Figures IV.5a, 5b, and 5c. The thin line represents the monthly anomaly standardized by the long term standard deviation for a particular month. The thick line is a smoothing curve of the anomalies using a sliding thirteen-month averaging window. The smoothing curve allows an easier view of extended periods of above average or below average anomalies (low frequency variation). Positive anomalies indicate higher than average precipitation and negative anomalies indicate lower than average precipitation.

A first observation is that the frequency of occurrence of positive precipitation extremes has increased with time. This is evident by the spread of anomalies from -1.5 to +2 units of standard deviation in the first climatic period compared to the spread of anomalies from -1.5 to +3 units of standard deviation in the second climatic period. Anomalies in the third climatic period range between -1.5 to +3 units of standard deviation with one anomaly almost reaching +4 units of standard deviation. This conclusion is also evident by

the variability of the smoothing curve. In the first climatic period the smoothing curve only slightly deviates from zero for more than half the record. In the second climatic period the smoothing curve deviates from zero by almost one unit of standard deviation (positive and negative) and continues this trend for an extended number of months. The third climatic period also shows large departures of the smoothing curve from zero for an extended length of time. An interesting feature of the most recent period is the decreasing regional precipitation trend in the 80s. Such a trend is also depicted in Figure II.3a.

The standardized anomalies for temperature are shown in Figures IV.6a, 6b, and 6c for each climatic period. The anomalies within the first climatic period have a rather consistent spread of -2 to +2 units of standard deviation. The second climatic period shows a larger spread of anomalies until about August 1965 (month 200 on Figure IV.6b) and then smaller departures from zero for the remaining months. The third climatic period of course shows the small departures of the anomalies from zero until June 1967 (month 150 on Figure IV.6c) after, which the anomalies increase dramatically, especially in the 80s. It is interesting to note that no consistent relationship exists between precipitation and temperature during the 80s when precipitation shows a decreasing trend. This points to the subjective nature of regional climate change scenarios based on an increase or decrease of the variables (see discussion in section 1.3).

4.4 Model Soil Water

The observed versus predicted flows presented in Section 3.1.2 indicate that the model predicts flows well, even when the atmospheric forcing is weak. It is therefore reasonable to assume that the model estimates water content reliably. The soil water content estimates have similarities and differences in the three climatic periods studied. An analysis comparing the three climatic periods includes studying the seasonal cycle of upper soil water content and total soil water content for each climatic period. Study of upper soil water is warranted given its important role in the atmospheric/land-surface hydrologic interaction. Also studied was the time series of the standardized anomalies of the two soil states for each climatic period. The sample frequency distribution of total soil water content for various months was also computed and inter-compared for the three climatic periods.

The monthly cycle of the means and standard deviations of both total soil water and upper soil water in mm is shown in Figures IV.7a, 7b, and 7c for each climatic period. The basin average values were computed from the six sub-basins using an area-weighted method. In the first climatic period, total soil water content varies by almost 100 mm in the course of the year. The cycle increases until it reaches a maximum of 460 mm in June,

decreases to the minimum of 360 mm in September then begins the increasing trend again. The upper soil water content varies from 110 mm to 160 mm in the course of the cycle. The second climatic period has less of a fluctuation in the total soil water content. The total soil water content varies by almost 80 mm from the maximum in June of 460 mm to the minimum in September of 380 mm. The upper soil water cycle changes by 40 mm from the maximum of 160 mm in the spring to the minimum of 120 mm in late summer. The third climatic period shows a higher content of total soil water but the same 80 mm difference between the maximum of 500 mm in June and the minimum 420 mm in September. The upper soil water content shows the same maximum and minimum as that found in the second climatic period which varies 40 mm from the maximum of 160 mm in the spring to the minimum of 120 mm in August. Small within-year variability is displayed by the standard deviation monthly cycles for all cases. Comparison of Figures IV.2, IV.4, and IV.7 reveals that the total soil water content maximum in June coincides with the maximum rainfall while potential evapotranspiration has been substantially lower than maximum. These conditions allow soil water to accumulate. In September, however, in spite of the high rainfall rates, potential evapotranspiration has been dominant during the summer (especially July) and the soil water attains a minimum.

The standardized anomalies for the total soil water content are presented in Figures IV.8a, 8b, and 8c for each climatic period. The thin line represents the monthly anomalies standardized by the long term standard deviation of the representative month. The thick line represents a smooth curve of the anomalies using a thirteen-month sliding averaging window. It appears that for the latter two climatic periods, negative anomalies are more extreme and more persistent than the positive ones. Significant negative anomalies extend through the late 50s and mid 70s. Significant positive anomalies are in the late 60s/early 70s and in the early 80s. It is also evident that the temporal scale of soil water fluctuations is significantly longer than that of the forcing variables (i.e., precipitation and temperature).

The standardized anomalies for the upper zone soil water content are shown in Figures IV.9a, 9b, and 9c for each of the climatic periods. Here it is seen that the anomalies vary more rapidly than the total soil water content anomalies. The smoothing curve in the first climatic period stays close to zero with mild fluctuations. In the second climatic period these fluctuations become more pronounced and tend to persist for a longer period of time. This is especially noted with negative fluctuations. This is also true through the third climatic period. It is noted that the upper soil water content resembles the total soil water during the more recent two periods. The earliest climatic period is an exception to that, reflecting the less variable time series of precipitation during this period.

The sample frequency distributions of the total soil water content anomalies for various months were analyzed for the three climatic periods. The anomalies were determined by the daily values of total soil water content minus the long term monthly average from the respective climatic period. The total soil water content anomaly distribution for March is shown in Figures IV.10a, 10b, and 10c for each climatic period. It is seen that in all cases the distribution has a high number of samples of slightly positive anomalies but a longer tail of negative anomalies (negatively skewed). There is a suggestion in the plots the frequency distribution may be multi-modal.

Figures IV.11a, 11b, and 11c show the distribution of the total soil water content anomalies in June for each climatic period. The first climatic period shows the June distribution of anomalies to be nearly uniform. The second climatic period distribution appears to be negatively skewed, such the number of samples of large negative anomalies is evident. The third climatic period also shows a distribution that is skewed with negative anomalies. The distributions for September and December can be found in Appendix Figures A.6-7. Comparing the distributions in different months, in all but the earliest climatic period, anomalies tend to be less extreme in June than in March.

4.5 Temporal Analyses

The following section examines the temporal scales of soil water content as well as the temporal relationship between total soil water content with precipitation and total soil water content with temperature. In all cases in order to remove the seasonality from the time series daily anomalies were used. To assess the temporal scales of total soil water content and upper zone water content the auto-correlation function for various months was determined for each climatic period. The temporal relationship between total soil water content with either precipitation or temperature was determined by the cross-correlation function computed for various months in each climatic period.

4.5.1 Soil Water Temporal Scales

The auto-correlation function of total soil water content and upper zone soil water content for March is shown in Figures IV.12a, 12b, and 12c for each climatic period. In the first climatic period total soil water content has a auto-correlation coefficient of 0.8 or higher for a lag of 18 days. The upper zone soil water content has an auto-correlation coefficient of 0.8 up to a 6-day lag. In the second climatic period the auto-correlation coefficient for total soil water remains above 0.8 for lag time of 24 days. The upper zone soil water content auto-correlation function is above 0.8 for a lag of 6 days. In the most recent cli-

matic period the auto-correlation function for the total soil water content is above 0.8 for a lag of 22 days. In this period the upper zone soil water content auto-correlation function remains above 0.8 for a lag of 8 days. The upper soil water is more susceptible to the forcing of the low-correlation rainfall than the total soil water and, thus, it shows lower temporal coherence. The high auto-correlation values for lags of a week or so for the upper soil water make for enhanced interaction with the regional atmosphere.

Figures IV.13a, 13b, and 13c show for each climatic period the auto-correlation functions of total soil water content and upper zone soil water content for June. For an auto-correlation coefficient greater than 0.8 total soil water content has a lag time of over 30 days in the first, 10 days in the second and 12 days in the third climatic periods. For the same auto-correlation coefficient the upper zone soil water content has a lag of 2 days in the first two climatic periods and 3 days in the most recent climatic period. In all cases, but for the total soil water during the first climatic period the June soil water exhibits shorter time scales than the March soil water.

From Figures IV.14a, 14b, and 14c of the auto-correlation functions in September of the two soil states it is seen that the auto-correlation function for both soil states increases with each climatic period. In the first climatic period an auto-correlation coefficient greater than 0.8 occurs at a 12 day lag for total soil water and a 4 day lag for upper zone soil water content. In the second climatic period the auto-correlation function of total soil water content is above 0.8 for over a 30 day lag. The upper zone soil water content auto-correlation coefficient of 0.8 occurs at a lag of 15 days. In the most recent climatic period the auto-correlation of total soil water again is well above 0.8 for over a 30 day lag. The upper zone soil water content auto-correlation coefficient occurs at a lag of 21 days. Such long persistence for upper soil water is a pre-requisite for soil water feedbacks to the atmosphere due to evaporation.

The auto-correlations for both soil states are also shown for December in Appendix Figure A.8. Here the auto-correlation functions for both soil states in all three climatic periods remain above the 0.8 coefficient for over a 30 day lag. Presumably this is due to the frozen ground at this time of the year and the relative immobility of the frozen soil water.

It is interesting to contrast the seasonal behavior of soil water temporal scales for the different climatic periods. The more recent two periods show a decrease in temporal scales of total soil water from March to June and an increase after September. The opposite trend is observed during the earliest period (1925-1949). The temporal scales of upper soil water, however, show the same trend in all climatic periods. It can be concluded that the lower soil zone seasonal behavior has changed from the first to the second and third climatic periods. Since lower soil water is associated with long term hydrologic behavior of

the catchments, such a change is attributed to changes in the low frequency components of the atmospheric forcing.

4.5.2 Precipitation vs. Upper Soil Water

The temporal scales of the interaction between precipitation and upper zone soil water content were analyzed by daily cross-correlations for various months in each climatic period. For the cross-correlation plots a positive lag indicates precipitation leading upper zone soil water content (cases of atmospheric forcing) and a negative lag corresponds to the upper zone soil water leading precipitation (cases of hydrologic feedback). Positive values of cross-correlation indicate that a high value of the leading parameter corresponds to a high value in the lagging parameter or a low value of the leading parameter corresponds to a low value of the lagging parameter. A negative cross-correlation coefficient indicates that a high value of the leading parameter corresponds to a low value in the lagging parameter or a low value in the leading parameter corresponds to a high value of the lagging parameter. In each figure, a measure of the sampling error (Wei, 1990) is also shown. The sampling error was determined as $\sqrt{1/N}$ were N represents the number of samples of a certain lag within the specified month.

Figures IV.15a, 15b, and 15c show the cross-correlation of precipitation with upper zone soil water content in March for each climatic period. In March cross-correlations are small and there is very little difference among the cross-correlation functions of the three climatic periods. All show a slightly positive correlation for positive lags and a slightly negative correlation for negative lags, all being very small. It is indicative of the fact that during this time of the year snowmelt is a significant contributor to soil water variability and masks precipitation dependence.

The greatest cross-correlation between precipitation and upper zone soil water content is in June, here shown in Figures IV.16a, 16b, and 16c for each climatic period. A slight difference of the correlation coefficient can be detected between the climatic periods. In the first climatic period the cross-correlation has a maximum of 0.35 at a lag of one day and remains above the coefficient of 0.20 for a lag of 10 days. The negative lags have a correlation coefficient that only slightly deviates from zero. The second climatic period has a maximum correlation coefficient of 0.45 at a lag of 2 days and remains above 0.20 for a lag of 10 days. The negative lags deviate from zero to a correlation coefficient of -0.10 for a lag of -6 days. The third climatic period has a maximum correlation coefficient of 0.45 at a lag of 2 days and remains above the correlation coefficient of 0.20 for a lag of 18 days. The negative lag times reach a maximum correlation coefficient of -0.10 between the lags of

-16 to -22 days. The role of the atmosphere in forcing the regional soil water by precipitation is evident by the asymmetry of the cross-correlations. Significant forcing persists for up to a month or so. Only weak feedback if any from the soil water to the atmosphere and precipitation is evident (negative lags).

The cross-correlation between precipitation and upper zone soil water content in September is shown in Figures IV.17a, 17b, and 17c for each climatic period. For the first climatic period a maximum correlation coefficient is 0.30 at a lag of 2 days. The coefficient remains above 0.20 up to a lag of 16 days. The negative lags generally have a correlation coefficient of -0.05. The second climatic period has a maximum correlation coefficient of 0.35 at a lag of 4 days. The coefficient remains above 0.20 for all positive lags of 30 days studied. The negative lags show a positive correlation coefficient of 0.10 for a lag of 6 days and then drops to about 0.05 for the remaining lags studied. The third climatic period has a maximum correlation coefficient of 0.35 at a lag of 2 days and remain above a coefficient of 0.20 beyond the 30 day lags studied. The negative lags have a positive correlation of 0.10 for a lag up to -8 days. The forcing of the atmosphere through precipitation is much more persistent in September than in earlier months, being significant for more than a month.

The cross-correlation of precipitation with upper zone soil water content for December for each climatic period can be found in Appendix Figure A.9. Cross-correlations return to very small levels for all cases with no direct evidence of significant atmospheric forcing by precipitation.

4.5.3 Temperature vs. Upper Soil Water

The cross-correlation between temperature and upper zone soil water content for various months in each climatic period was also studied. In these cross-correlation plots, a positive lag indicates that temperature leads the upper zone soil water content and a negative lag indicates that upper zone soil water content leads temperature. The cross-correlation for March is shown in Figures IV.18a, 18b, and 18c for each climatic period. The first climatic period shows a positive correlation of about 0.05 from a -12 day lag to +4 day lag. For the longer lag periods between -15 day lag to -30 day lags and +15 day lags to +30 day lags the correlation is negative and reaches a maximum of -0.10. The second climatic period has a larger negative correlation coefficient than the previous climatic period for the longer lag times. The absolute maximum cross-correlation coefficient of -0.25 occurs at a +30 day lag. The third climatic period also shows larger negative correlation coefficients with local maximums of -0.20 at +18 day lag and -14 day lag. Although the correlation coefficient function shows similar cycles for the three climatic periods the correlation is more pro-

nounced in the latter two climatic periods as indicated by the higher values of the correlation coefficient. Also, evidence of feedback (albeit small) by the soil water to the atmosphere is seen for the negative lags; i.e., high soil water leads to a low temperature following, and vice versa. The plots show a period of two weeks as the time necessary for such feedback to occur.

Figures IV.19a, 19b, and 19c show the cross-correlation of temperature with the upper zone soil water content in June for each climatic period. All three climatic periods show a local absolute maximum at zero lag. The local absolute maximums for zero lags are -0.30, -0.25, and -0.25 respectively. Other similar features are the increasingly negative correlation for large positive lags. This would indicate that, with a larger positive lag, higher values of temperature correspond to low values of upper zone soil water or low temperatures correspond to high values of the upper zone soil water. The second climatic period appears to have a steeper increase of negative correlation. Again, there is evidence of regional soil water feedback for negative lags of a few days duration. Such feedback appears stronger during the first climatic period.

Cross-correlations for September and December are shown in Appendix Figures A.10 and A.11. Apart from the cross-correlations of the first period in September, which reaches a maximum of -0.3 for a zero lag, all other cases show negligible values.

To eliminate the noise present in daily values of temperature and upper zone soil water content we have also computed cross-correlation between precipitation and upper zone soil water, and maximum temperature and upper zone soil water, for 5-day aggregation intervals. The results for maximum temperature and upper zone soil water are shown in Appendix Figures A.12 and A.13. The results for the 5-day data show stronger cross-correlation (e.g., compare Figure IV.19 and A.12). In summary, the results of association of upper soil water content and surface air temperature indicate higher associations for summer and for warmer periods.

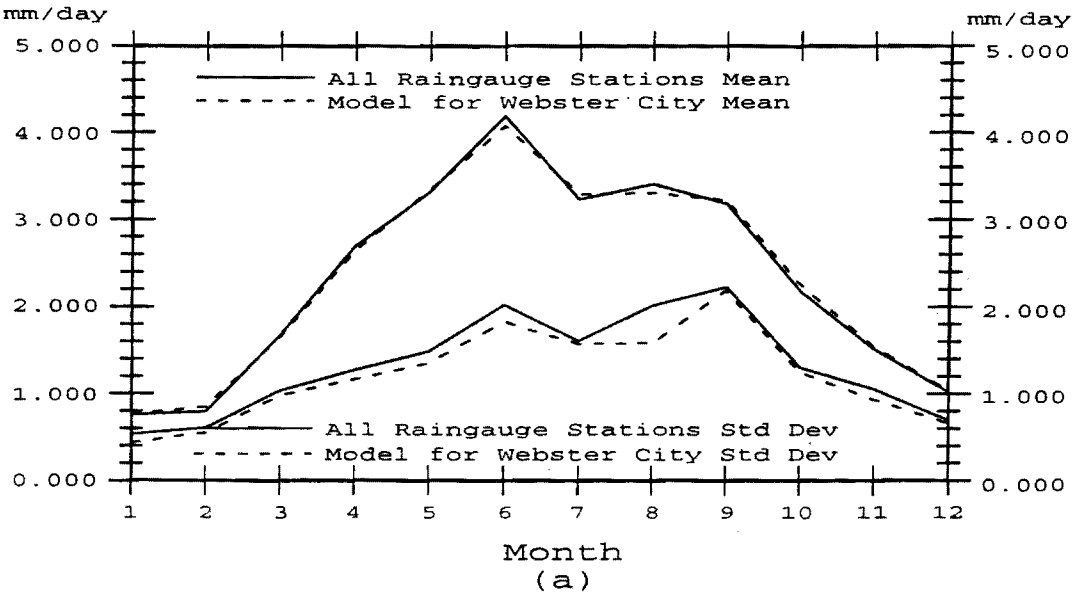

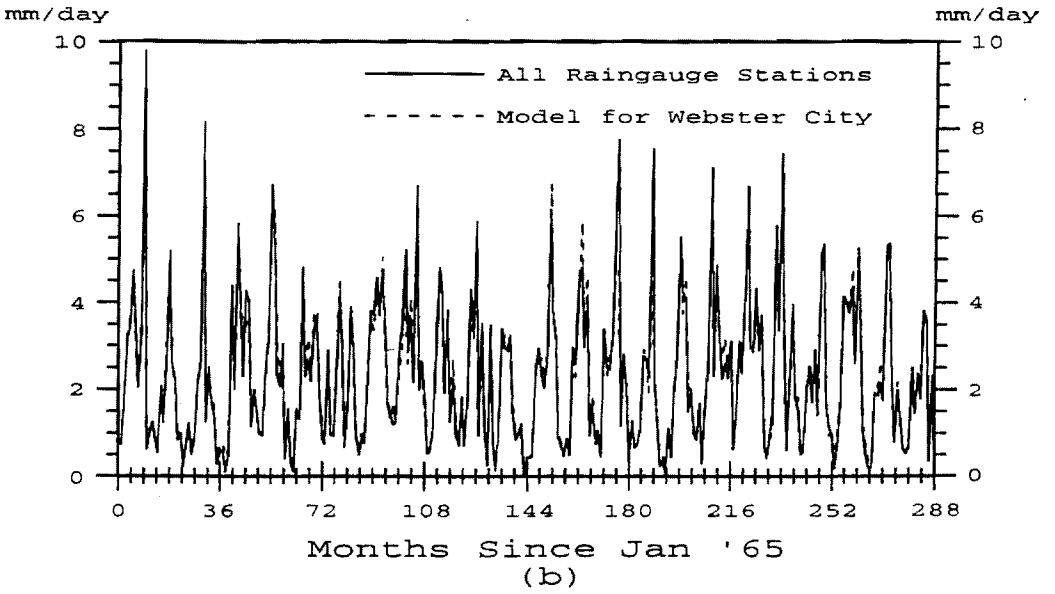

Figure IV.1 Monthly precipitation determined by the NWS weighted average method using all described stations (solid) and the regression model (dashed) for Webster City a) seasonal cycle of means and standard deviations averaged from 1965-1988 and b) monthly means since January 1965.

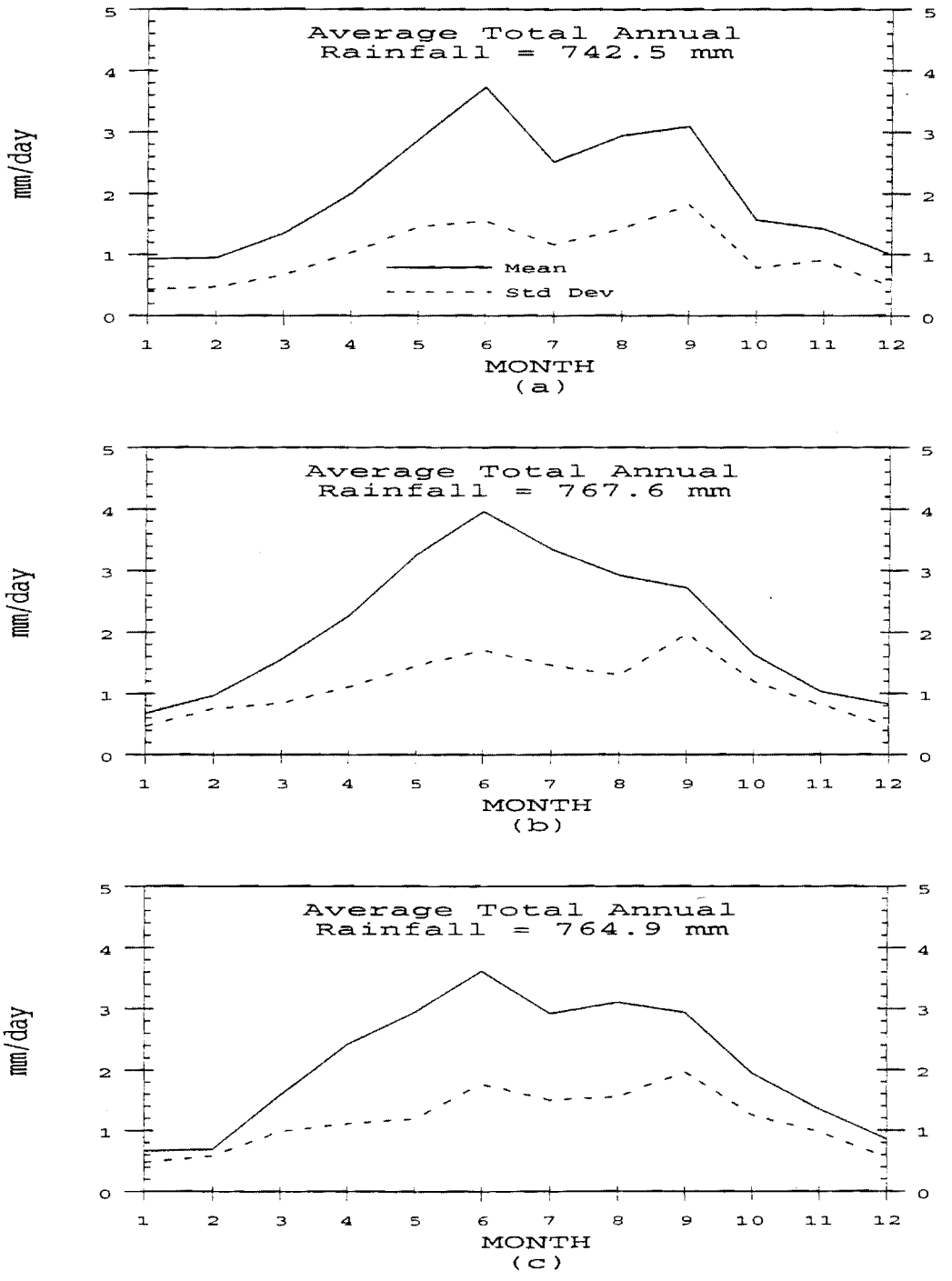

Figure IV.2 Monthly cycle of mean areal precipitation means and standard deviations computed from a) 1925-1949 b) 1949-1974 and c) 1965-1988.

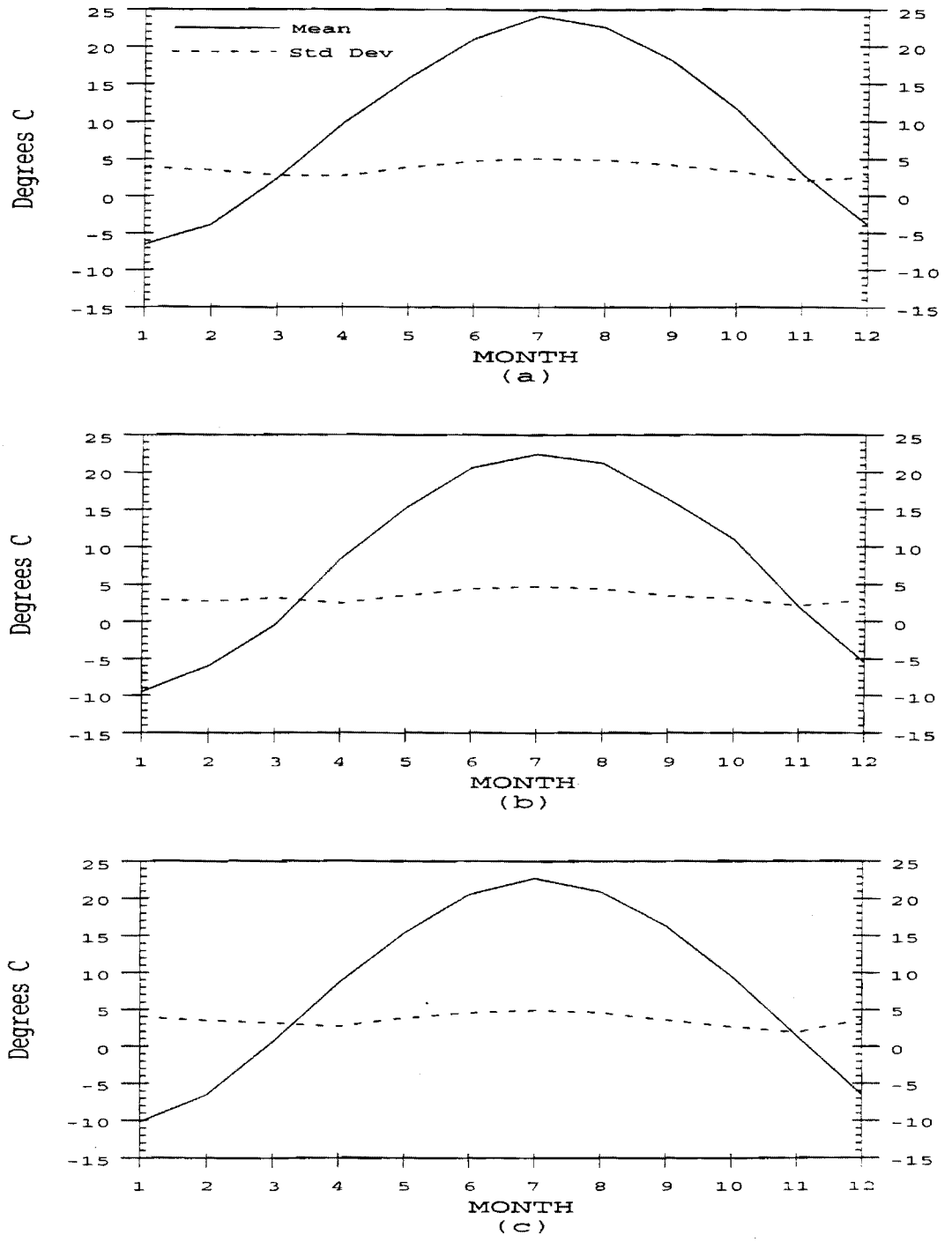

Figure IV.3 Monthly cycle of temperature means and standard deviations computed from a) 1925-1949, b) 1949-1974 and c) 1965-1988.

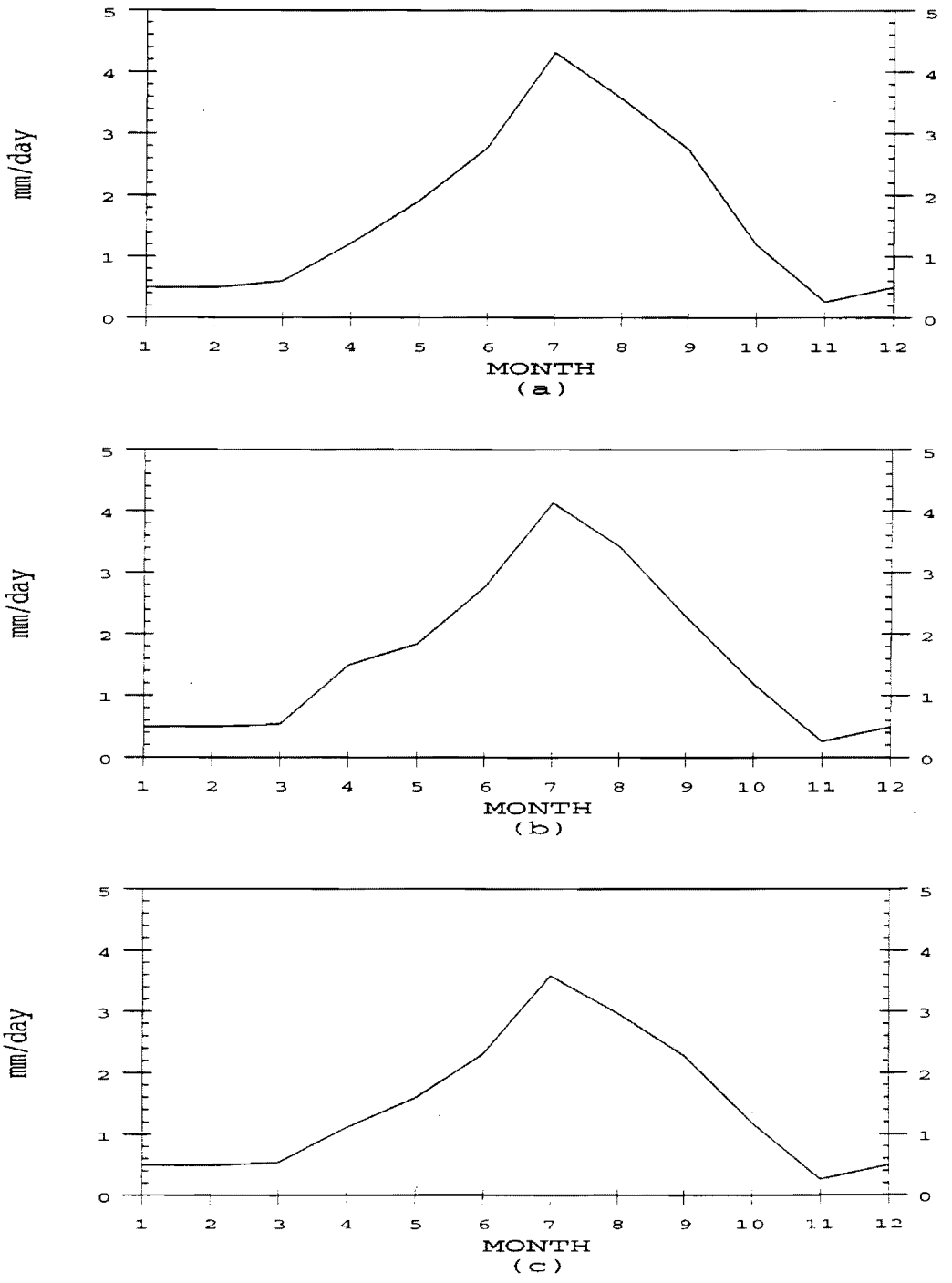

Figure IV.4 Monthly cycle of potential evapotranspiration means computed from a)1925-1949, b) 1949-1974 and c)1965-1988

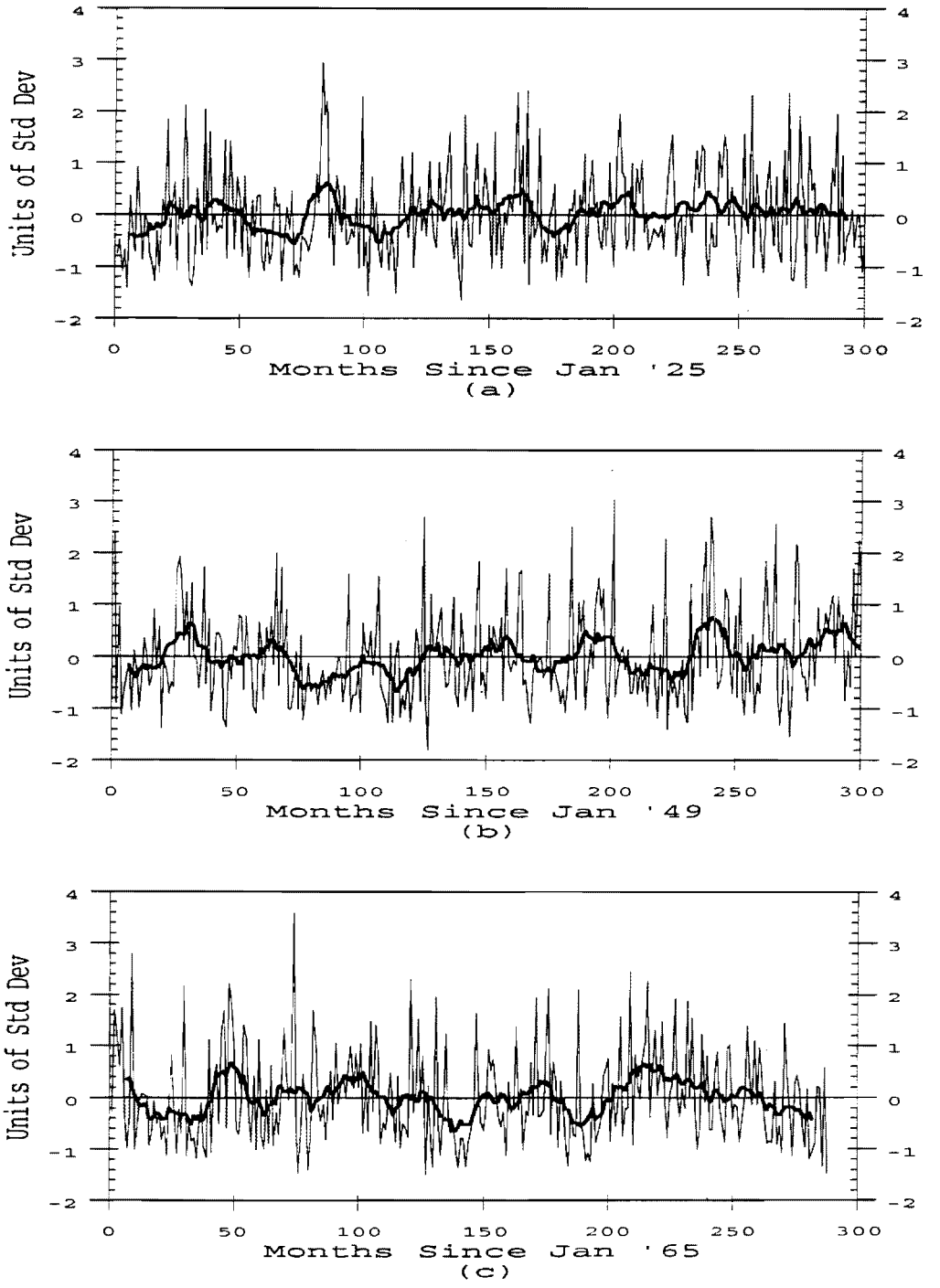

Figure IV.5 Mean areal precipitation monthly standardized anomalies (thin line) and smoothed curve (thick line) for months since a) January 1925, b) January 1949 and c) January 1965.

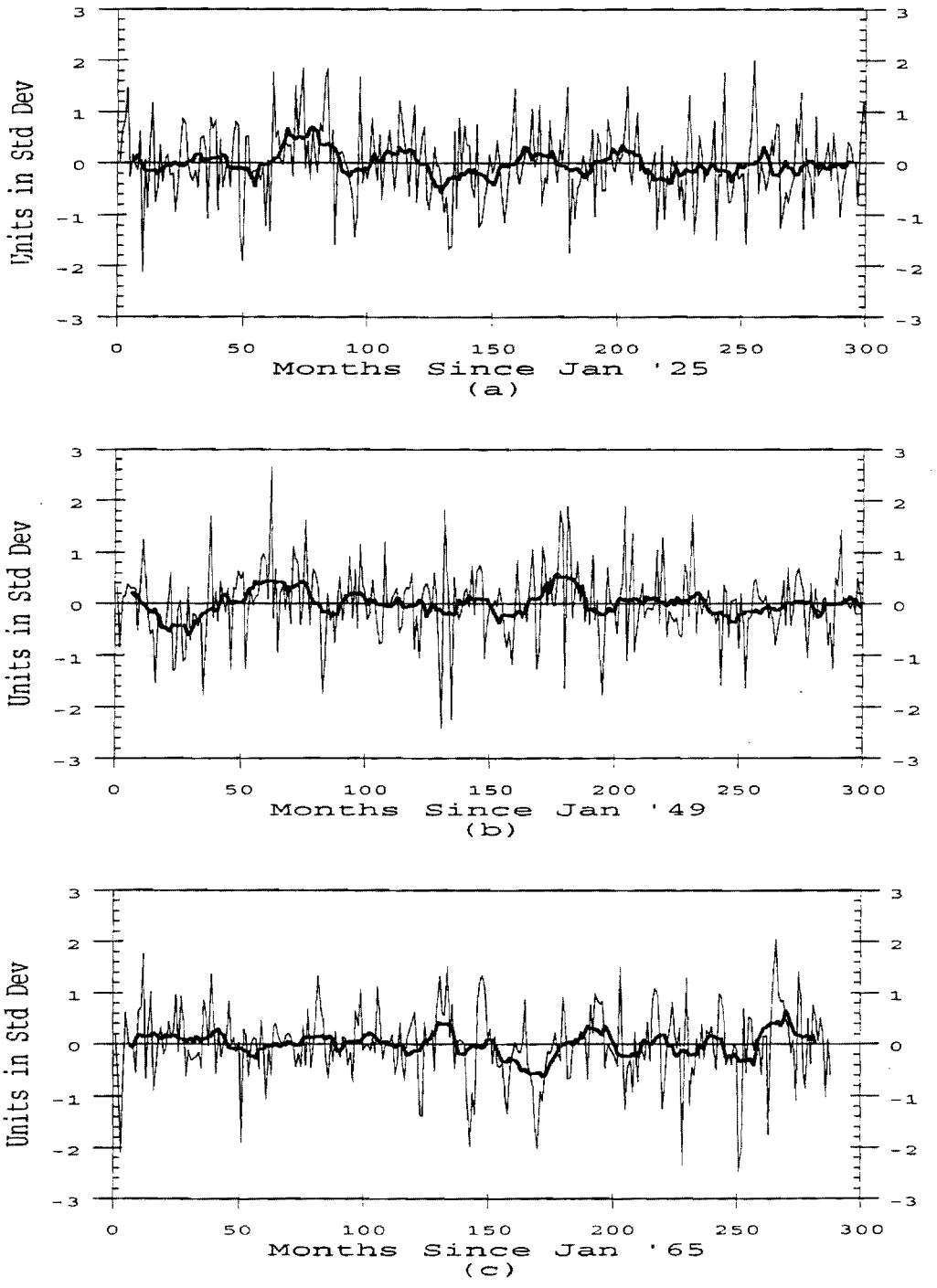

Figure IV.6 Temperature monthly standardized anomalies (thin line) and smoothing curve (thick line) for months since a) January 1925, b) January 1949 and c) January 1965.

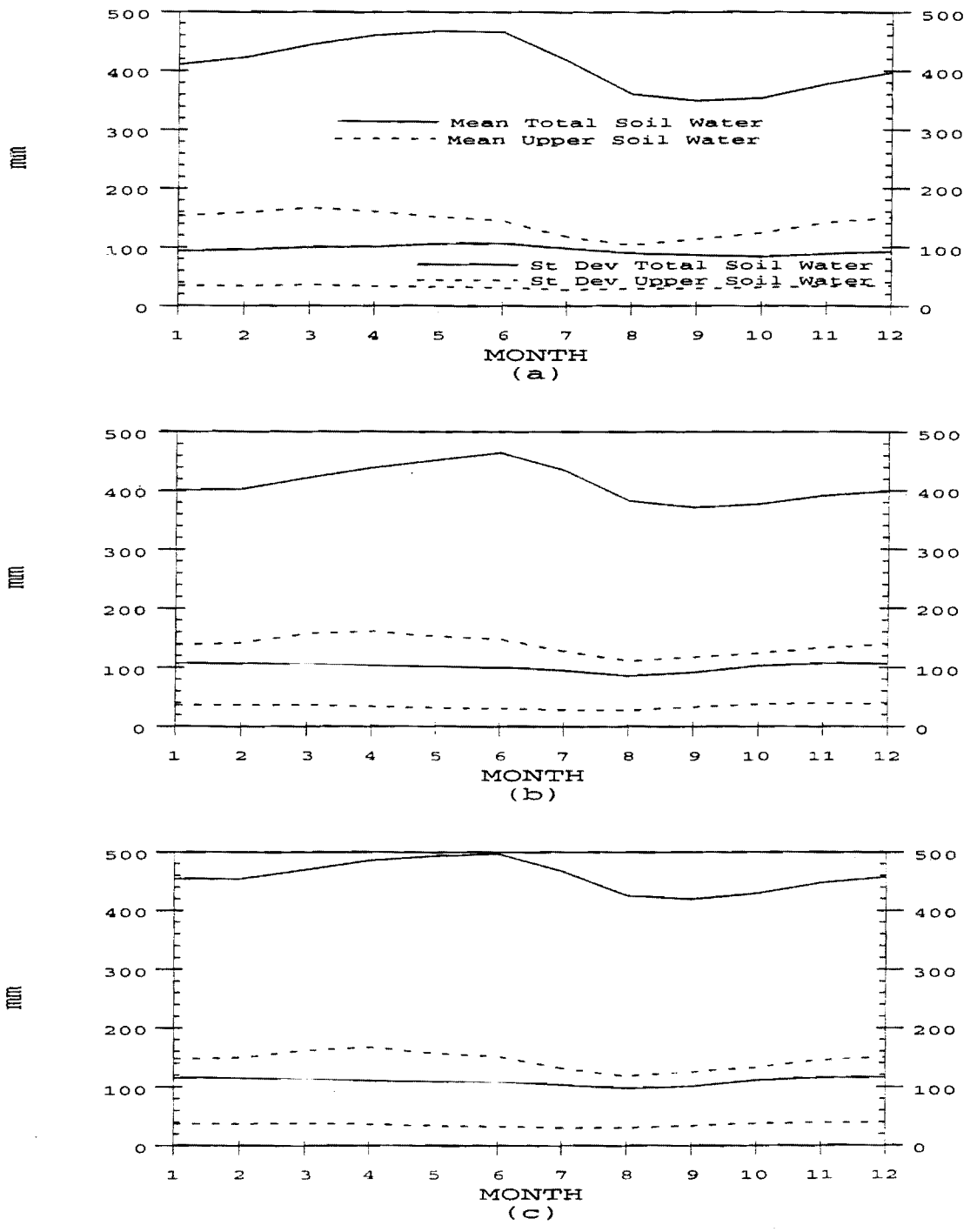

Figure IV.7 Total soil water content and upper zone soil water content mean and standard deviation monthly cycles computed from a) 1925-1949, b) 1949-1974 and c) 1965-1988.

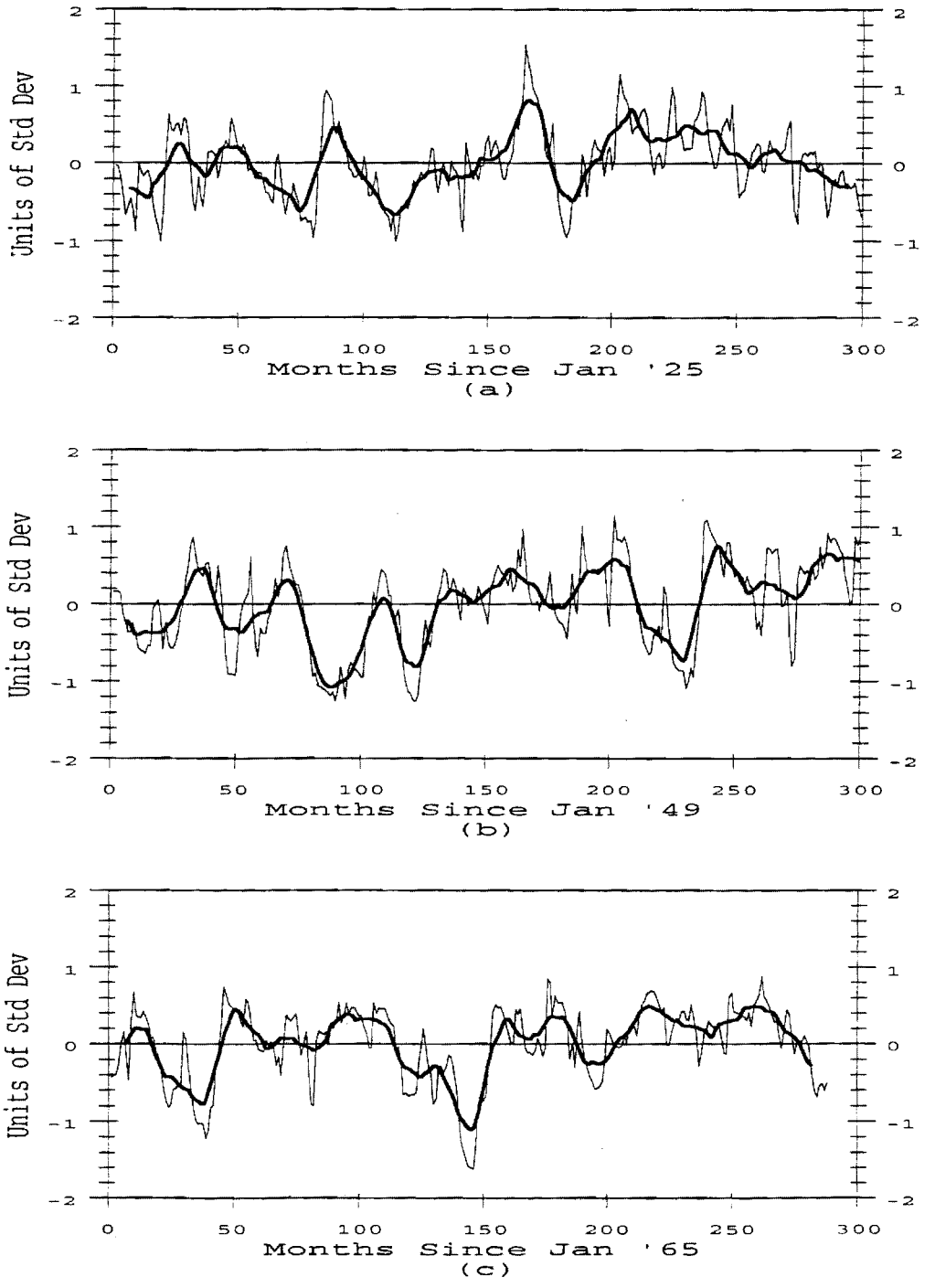

Figure IV.8 Total soil water content monthly standardized anomalies (thin line) and smoothing curve (thick line) for months since a) January 1925, b) January 1949 and c) January 1965.

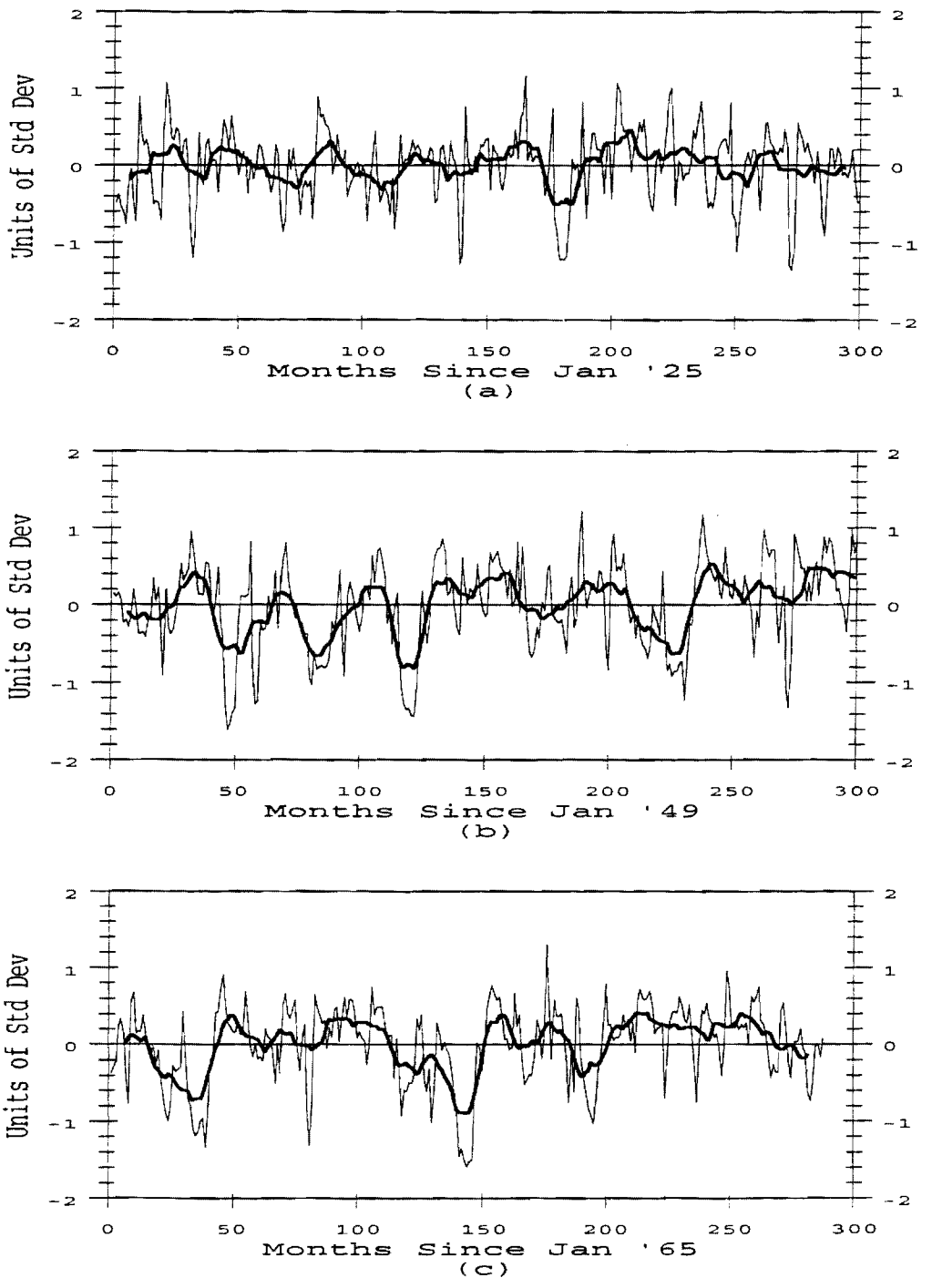

Figure IV.9 Upper zone soil water content monthly standardized anomalies (thin line) and smoothing curve (thick line) for months since a) January 1925, b) January 1949 and c) January 1965.

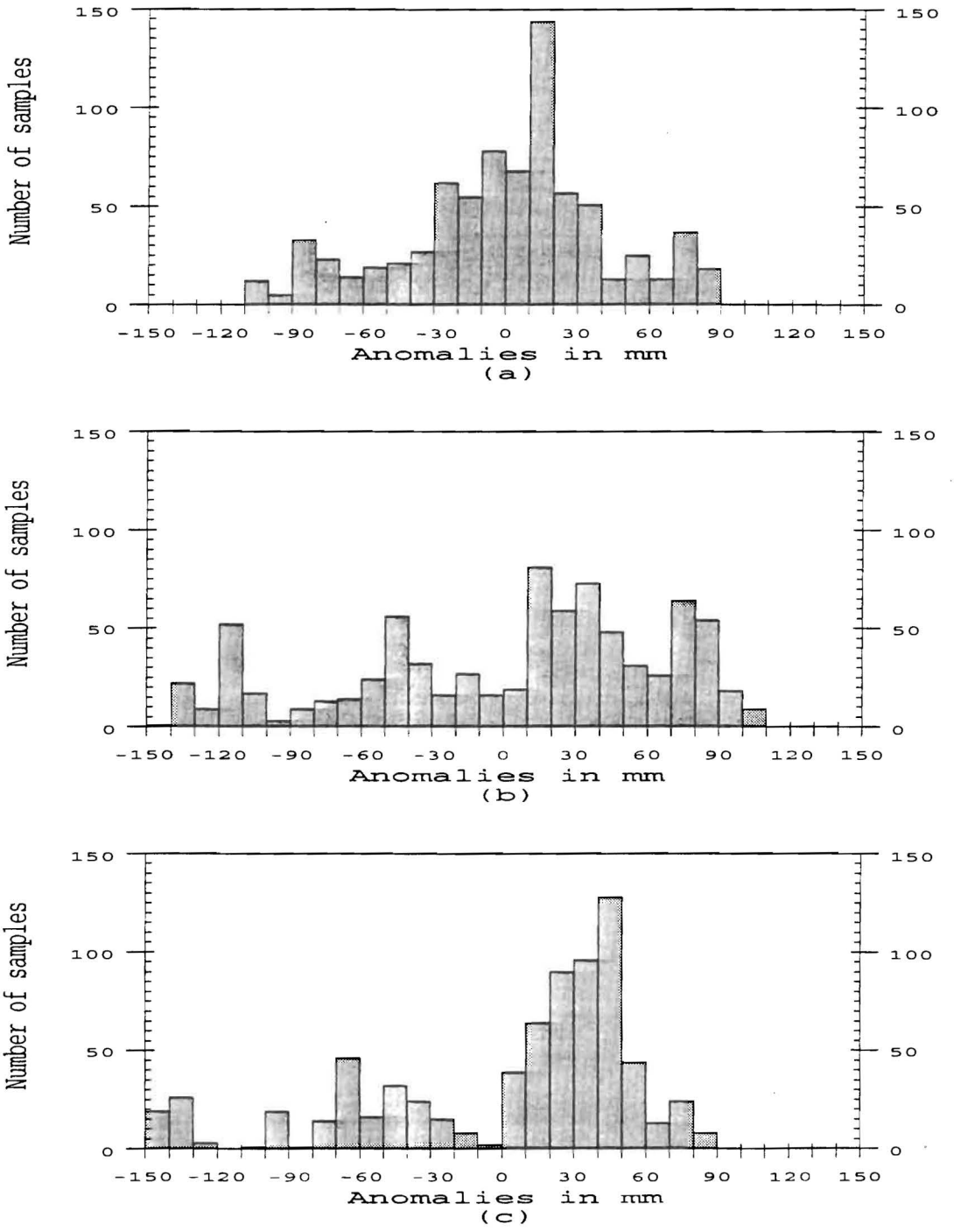

Figure IV.10 Total soil water content daily anomaly distribution in March for a) 1925-1949, b) 1949-1974 and c) 1965-1988.

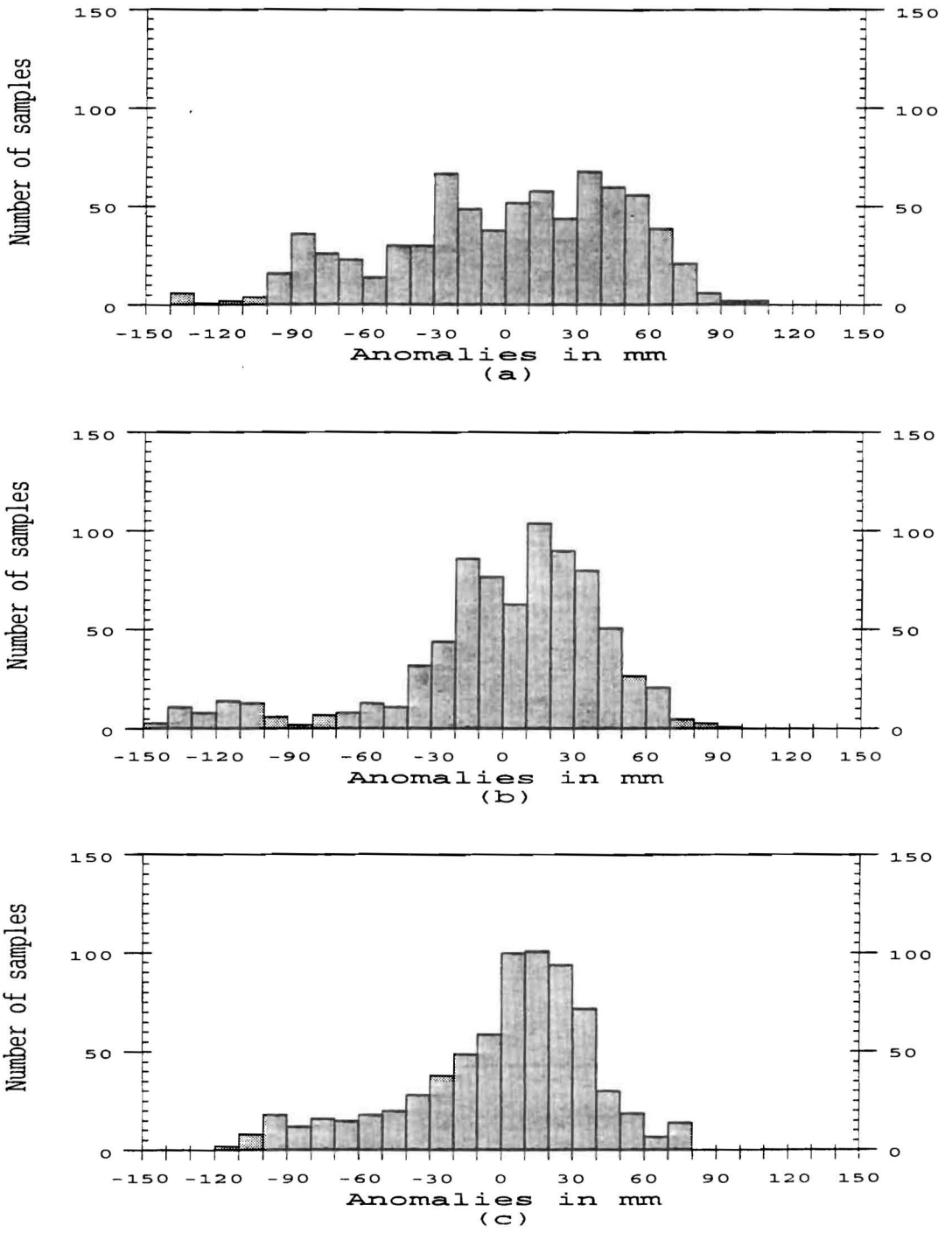

Figure IV.11 Total soil water content daily anomaly distribution in June for a) 1925-1949, b) 1949-1974 and c) 1965-1988.

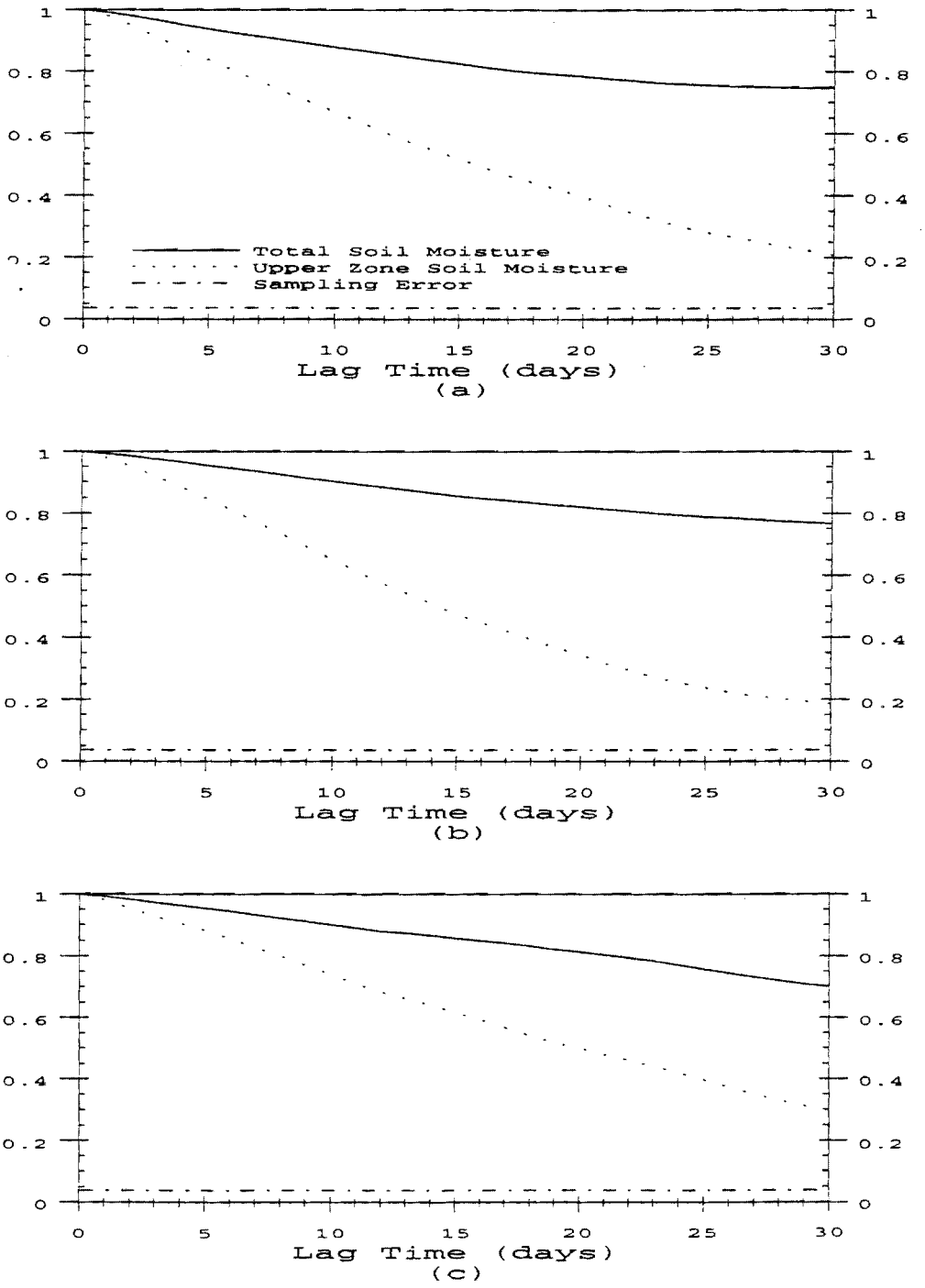

Figure IV.12 Auto-correlation of total soil water content (solid line) and upper zone soil water content (dashed line) in March for a) 1925-1949, b) 1949-1974 and c)1965-1988.

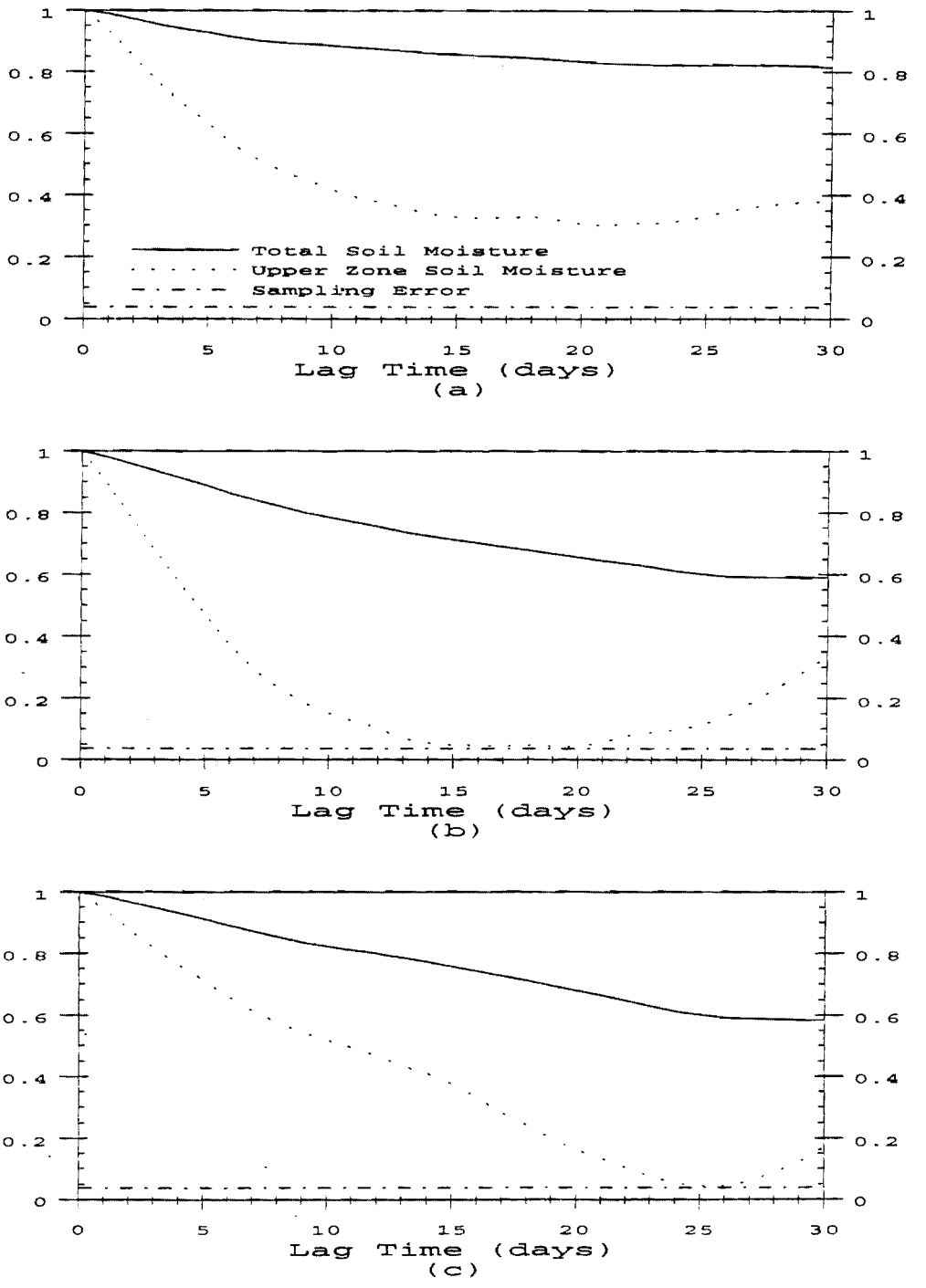

Figure IV.13 Auto-correlation of total soil water content (solid line) and upper zone soil water content (dashed line) in June for a) 1925-1949, b) 1949-1974 and c)1965-1988.

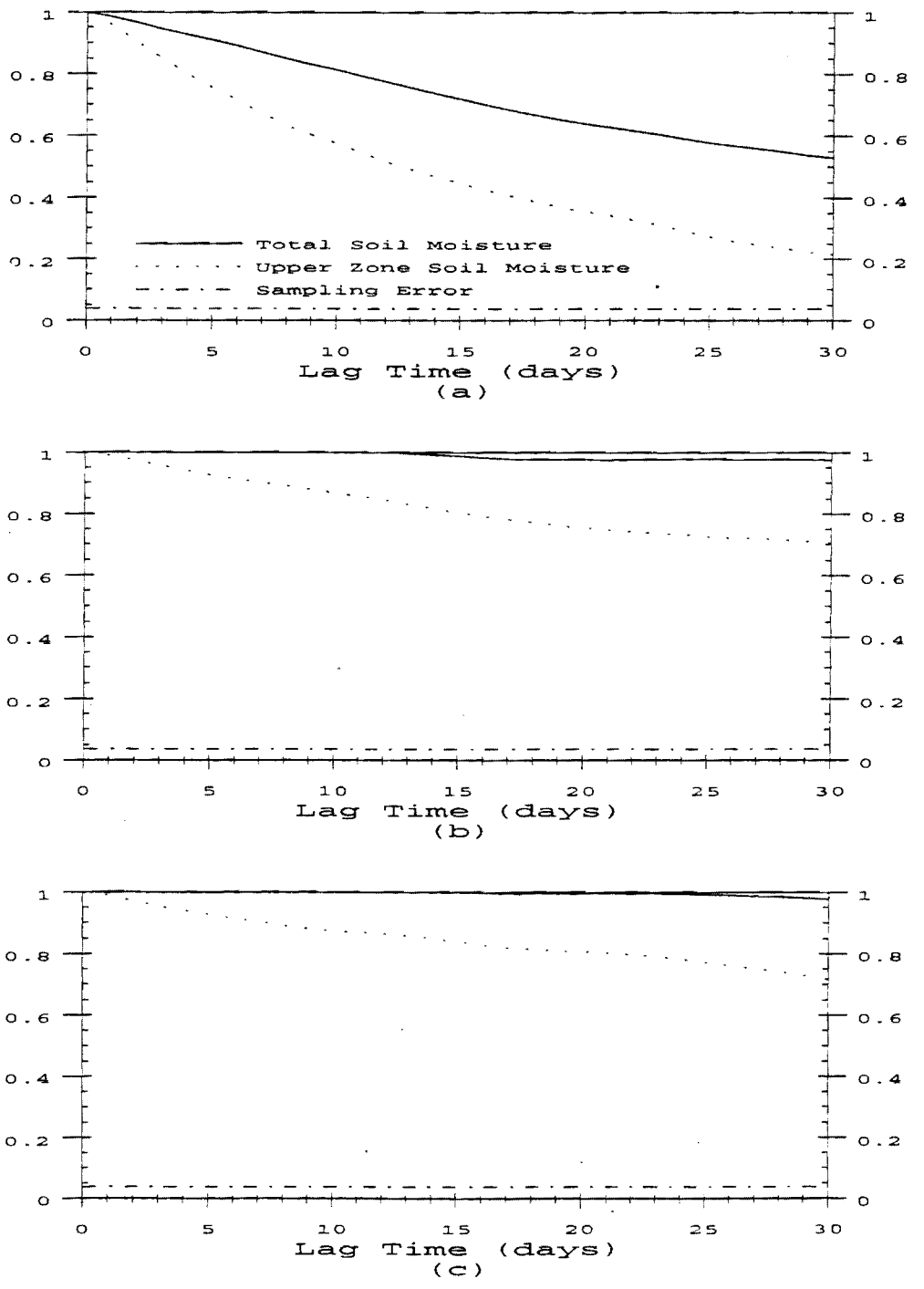

Figure IV.14 Auto-correlation of total soil water content (solid line) and upper zone soil water content (dashed line) in September for a) 1925-1949, b) 1949-1974 and c)1965-1988.

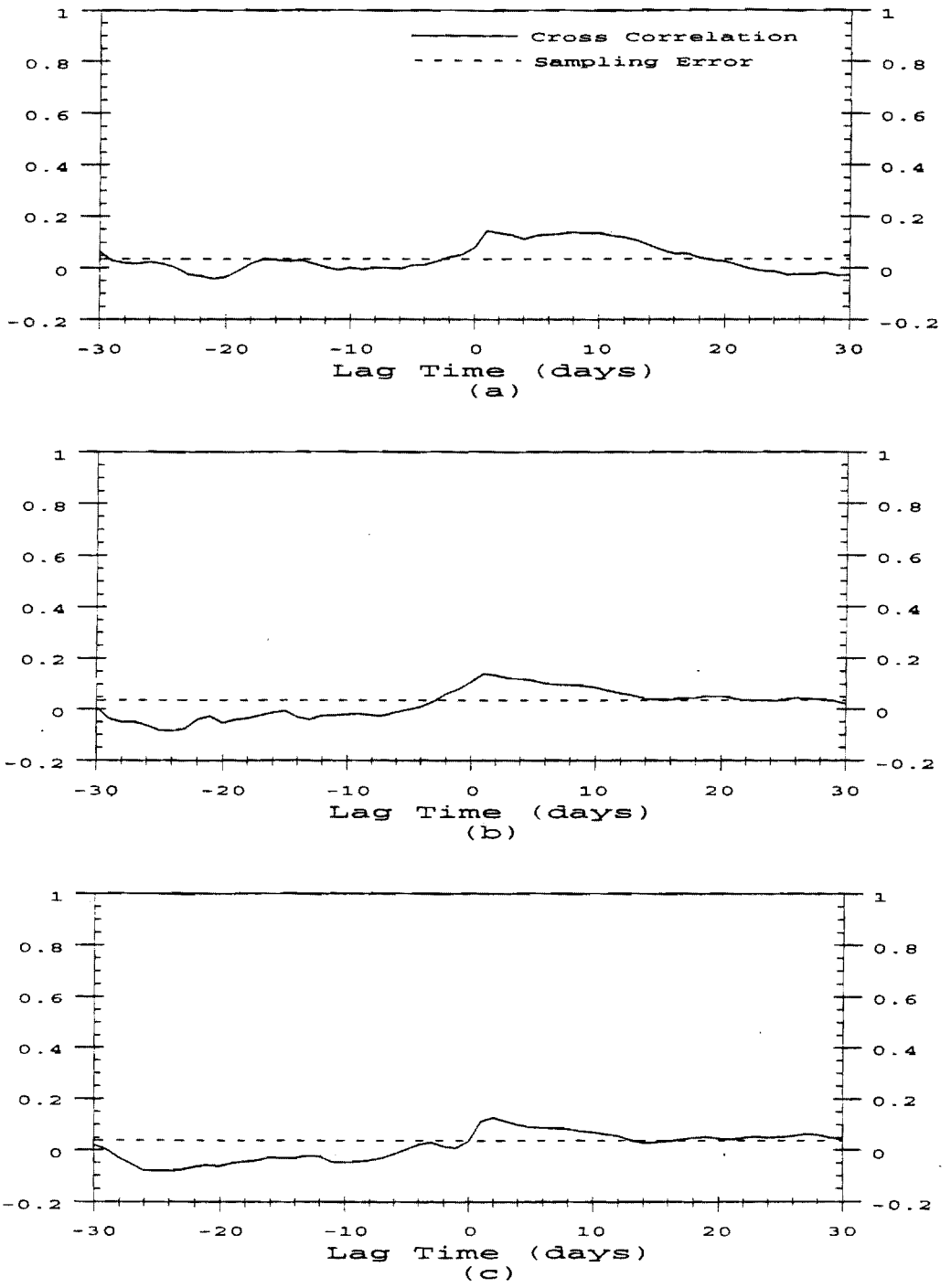

Figure IV.15 Cross-correlation of precipitation and upper zone soil water content in March for a) 1925-1949, b) 1949-1974 and c)1965-1988.

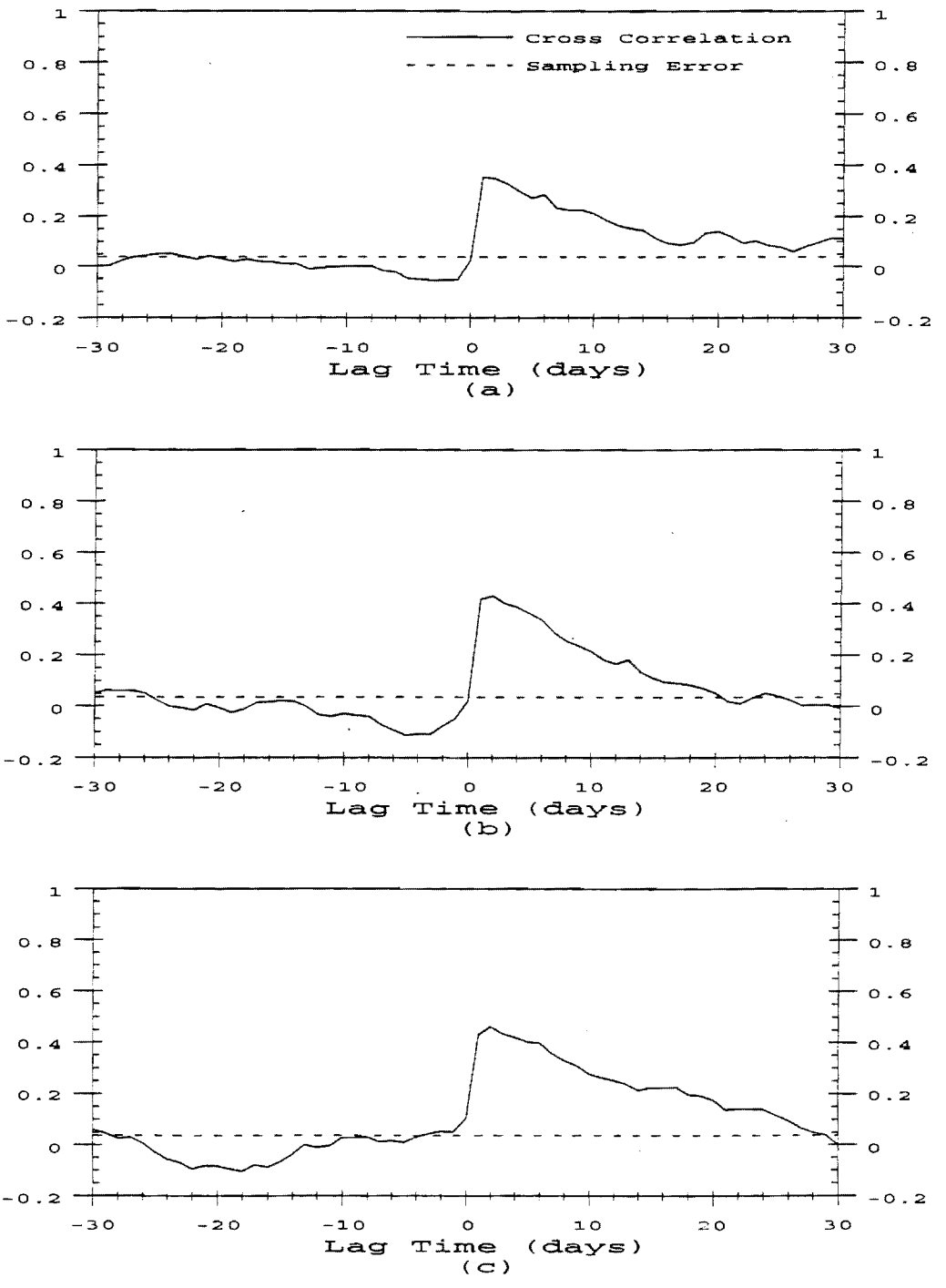

Figure IV.16 Cross-correlation of precipitation and upper zone soil water content in June for a) 1925-1949, b) 1949-1974 and c)1965-1988.

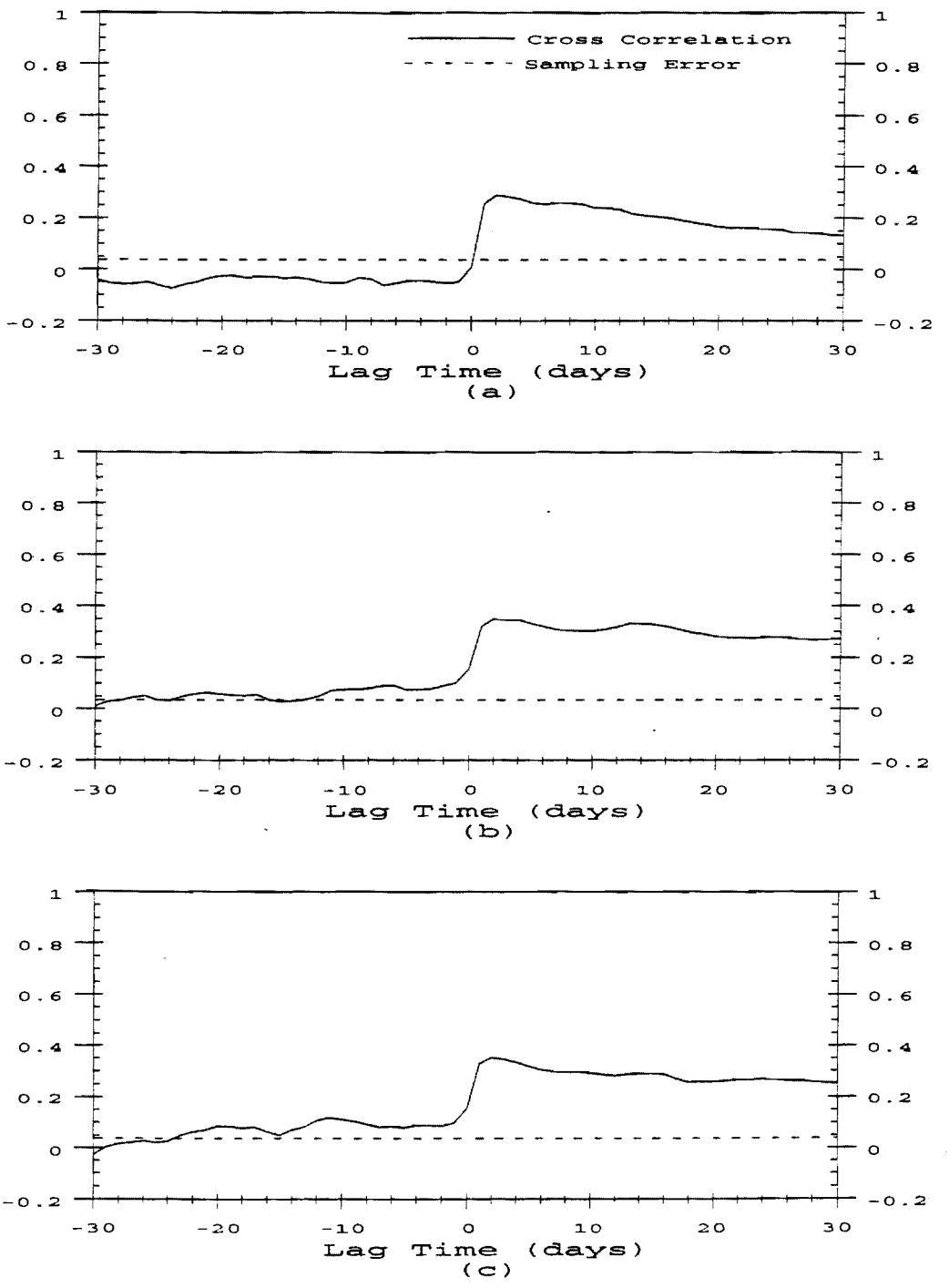

Figure IV.17 Cross-correlation of precipitation and upper zone soil water content in September for a) 1925-1949, b) 1949-1974 and c)1965-1988.

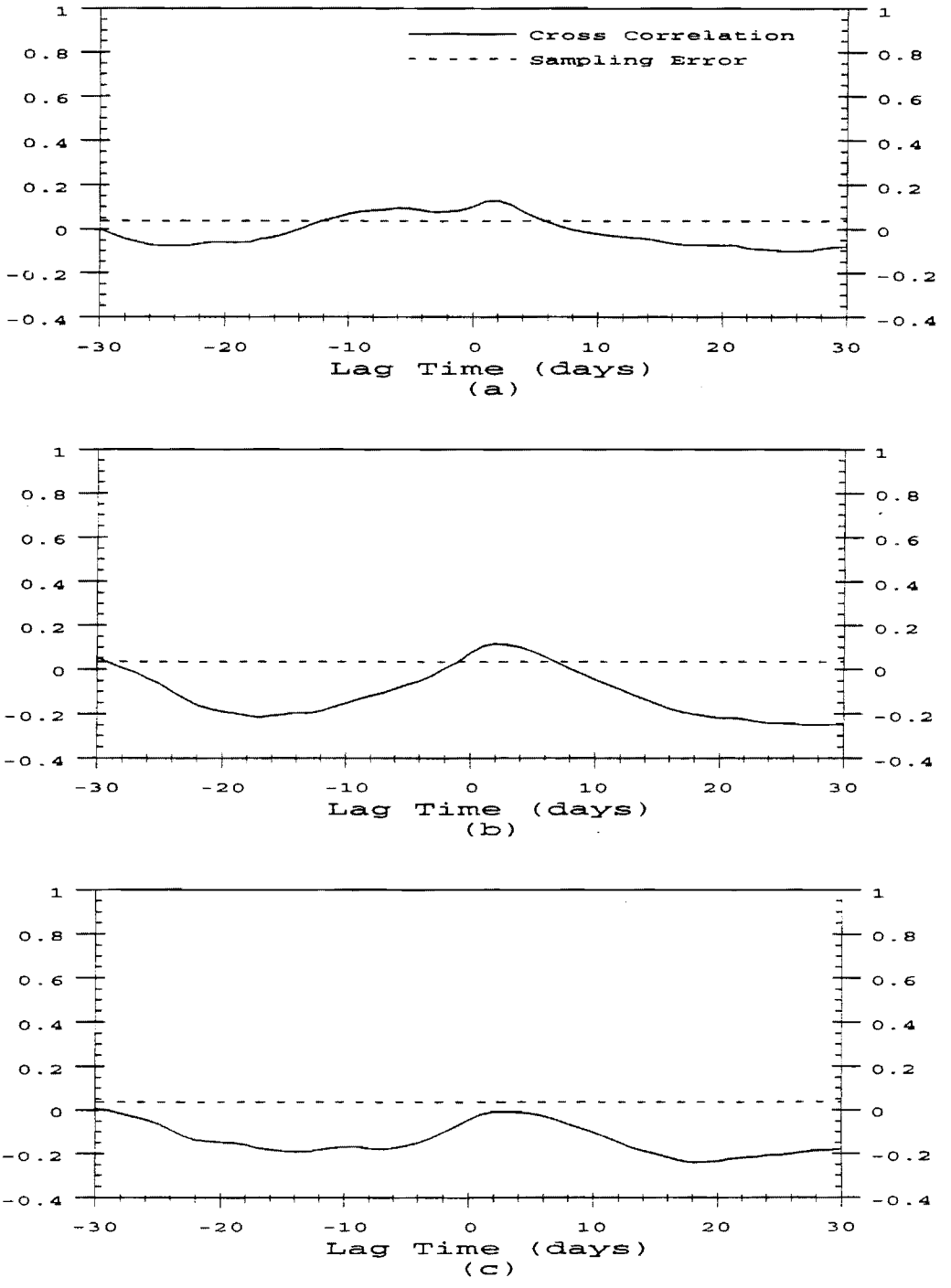

Figure IV.18 Cross-correlation of temperature and upper zone soil water content in March for a) 1925-1949, b) 1949-1974 and c)1965-1988.

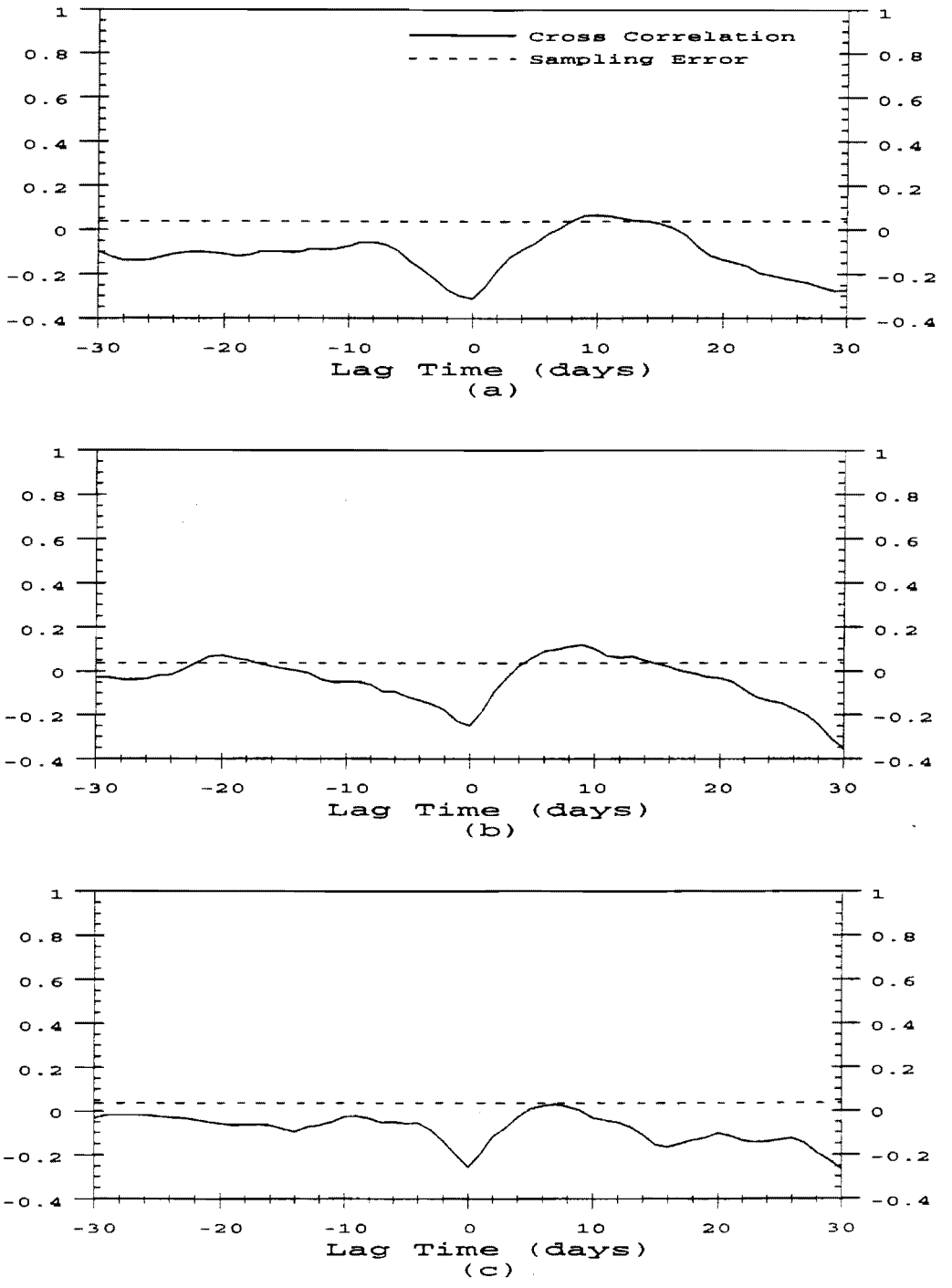

Figure IV.19 Cross-correlation of temperature and upper zone soil water content in June for a) 1925-1949, b) 1949-1974 and c)1965-1988.

V. FORECAST-CONTROL RESULTS AND SENSITIVITY

The forecast-control procedure was followed using the initial conditions of the first and fifteenth of every month in each climatic period. The UIFS model is started with the soil moisture, snow depth, frozen ground state and streamflow from the initial condition date. Daily values of the forcing parameters for each of the historical years in the climatic period of interest are fed into the UIFS, beginning at the month and day of the initial condition date and extending to the maximum forecast lead time. Thus, each historical year creates a trace of flow forecasts that are dependent on the initial conditions. The set of flow traces for a certain initial condition are referred to as Extended Streamflow Predictions (ESP). The probabilistic forecasts for each initial condition are fed into a reservoir set control approach. The set control approach determines a set of decision actions guaranteeing that the system will stay within the desirable bounds for the duration of the control horizon.

The first part of this chapter examines the ESP performance. The average and bounds of standard deviation of the ESP realizations generated from initial conditions for various dates in the wettest, driest, coolest and warmest years in each climatic period are compared to the historical streamflow trace of that initial condition. The second section is an analysis of the sensitivity of the streamflow traces to different initial conditions. In each climatic period the average ESPs using all historical realizations are compared between dates with wet and dry initial conditions and cool and warm initial conditions. These results are then compared for the various climatic periods. Further analysis was performed for each climatic period by averaging the ESP using forcing realizations of extreme conditions for dates with wet and dry initial conditions and cool and warm initial conditions. A comparison of the sensitivity of the predictions due to extreme forcing is also made between the climatic periods. The third section compares the decision sets generated by the set control approach for the different climatic periods.

5.1 ESP Performance

The ESP performance is analyzed in the framework of comparing the average and bounds of standard deviation of the ESP realizations for the forecast horizon generated from the initial conditions of certain dates to the corresponding observed flow. Initial condition dates were chosen to represent each season in the wettest, driest, coolest and warmest years in each climatic period. The wettest and driest years were determined by computing an annual average of daily mean areal precipitation over the Boone River basin

with outlet at Webster City. An annual average of daily temperature at Ames, Iowa was also computed to determine the coolest and warmest years in each climatic period.

Figure V.1 shows the average and bounds of standard deviation of ESP at the basin outlet, Stratford, for the forecast horizon beginning with the initial conditions of a) March 15, b) June 15, c) September 15, and d) December 15 for the wettest year in the first climatic period, 1938. Also shown is the historical observed flow at Stratford for the same period. The average ESP and the forecast uncertainty indicated by the bounds of standard deviation differ depending on the seasonal initial condition of the wet year. Occasional large observed flow departures from the ESP average are detected in September (days 85 to 120 in Figure V.1b and days 1 thru 10 in Figure V.1c). Such behavior attests to the positively skewed nature of streamflows.

Analogous results for initial conditions in the driest year of the first climatic period, 1933, are seen in Figures V.2a, 2b, 2c, and 2d. With the dry initial conditions of 1933 again it is seen that the average ESP and the forecast uncertainty differs depending on the season. There appears to be only one large departure of the observed flow from the average ESP in late March (days 15-30 in Figure V.2a). For the remaining forecast horizons of each initial condition the observed flow is within the bounds of one standard deviation of the average ESP.

The results for initial condition dates in the coolest year of the first climatic period, 1929, are shown in Figures V.3a, 3b, 3c, and 3d. The bounds of standard deviation are wider for the forecast horizon beginning with March 15 and are more narrow for the other forecast horizons. Additionally, there appear to be large departures of the observed flow from the average ESP only in the forecast horizon beginning March 15.

The initial conditions chosen from the warmest year in the first climatic period, 1931 produce the results shown in Figures V.4a, 4b, 4c, and 4d. Again the average ESP and the forecast uncertainty is different in each forecast horizon indicating the dependency of the forecasts on the season. Departures of the observed flow from the average ESP occur in mid November (days 70 thru 80 in Figure V.4c), late December (days 100 through 120 in Figure V.4c and days 15 thru 40 in Figure V.4d) and late February (days 70 to 90 in Figure V.4d).

A comparison between the initial conditions of wet, dry, cool and warm initial conditions show that the average ESP and the forecast uncertainty are not only dependent on the season but also on the characteristics of the initial conditions. For example, the forecast uncertainty of the forecast horizon beginning with the initial condition of September 15, 1938 in the wettest year (Figure V.1c) is much larger than the forecast uncertainty of all other cases beginning with a September 15 initial condition (Figures V.2c, 3c, and 4c).

Also, ESP reproduced the observed high variability of the flows in Spring. That is, the standard deviation of the forecasts was higher during periods of higher flows in accordance with the observed behavior (see Figure II.2).

An identical analysis was performed for the wettest, driest, coldest and warmest years in the second climatic period. In the second climatic period, 1951 ranked as the wettest and the coldest year. The average ESP and bounds of standard deviation along with the observed flow is shown in Figures V.5a, 5b, 5c, and 5d for the forecast horizons beginning with the initial condition of March 15, June 15, September 15, and December 15, 1951, respectively. In this plot the dependence of the average ESP and forecast uncertainty on the season is evident. The highest uncertainty is seen in the spring months. Observed flow departures from the average ESP are evident in the spring and summer forecast horizons (Figure V.5a and 5b) due to the skewed flow distributions.

Analogous results for the initial conditions of the dry year, 1958 are presented in Figures V.6a, 6b, 6c, and 6d. Here, the forecast uncertainty is larger in the spring forecast horizon with the initial condition of March 15 and is seen to decrease through the remaining forecast horizons. There is little uncertainty in the winter months until it again increases as the forecast horizon extends into the spring months. No large departures of the observed flow from the average ESP are detected in the horizons for dry conditions.

The observed flow, average ESP and bounds of standard deviation for the forecast horizons with initial conditions in the warm year, 1964 are presented in Figures V.7a, 7b, 7c, and 7d. The forecast horizons shown have different average ESP and forecast uncertainty trends depending on the season of the initial condition. One large departure of the observed flow from the average ESP is evident in the winter forecast horizon (Figure V.7d) and occurs in mid March (day 110 thru 120).

It has been shown that the average ESP and bounds of standard deviation for a forecast horizon are dependent on the season of the initial condition date in the second climatic period. It can also be shown that the second moment statistics are dependent on the characteristics of the initial condition. For example, the forecast uncertainty in the coldest, wettest year 1951, with the initial condition of March 15 (Figure V.5a) is much greater than that seen in the forecast uncertainty in the initial condition of March 15 in the dry or warm year (Figures V.6a and V.7a). Similarly, the large uncertainty seen in September of the warm year (Figure V.7c) is not detected in Septembers of other years (Figures V.5c and V.6c). Greater departures of the observed flow from the average ESP occur with the cold and wet initial conditions.

An identical analysis was performed for the third climatic period. The results for initial conditions representative of each season in each of the extreme years are presented in

Figures V.8-11 for the wettest, driest, coolest and warmest years, respectively. Each set of Figures indicates the dependence of the average ESP and the bounds of standard deviation on the season of the initial condition. By comparing the Figures it can be seen that the forecast uncertainty for the March 15 initial condition is greater in the wet and cool years (Figures V.8a and V.10a) than in the warm and dry years (Figures V.9a and V.11a). It is also evident that for these initial conditions, there are a greater number of large departures of the observed flow from the average ESP in the wettest and coolest years then in the driest and warmest years.

A comparison between the climatic periods for the wettest years reveals the greatest difference is in the forecast horizons with the initial condition of March 15. The forecast uncertainty of the first climatic period for this date (Figure V.1a) is much narrower than the forecast uncertainty in the other two climatic periods (Figures V.5a and V.8a). The second climatic period appears to have its maximum uncertainty in April (day 15 of Figure V.5a) with the maximum average ESP. For the third climatic period the maximum average ESP occurs March 15 (day 1 of Figure V.8a) and then decreases. In general, the initial conditions from the wettest year in the first climatic period have narrower bounds of standard deviation than the wettest initial conditions of the other two climatic periods. This is probably a direct result of the smaller variability exhibited by the forcing during the first climatic period (see Figure IV.5). Another feature apparent in comparing the wettest initial conditions of the three climatic periods, is the large value of average ESP in September of the first climatic period (Figure V.1c) that is not evident in September of the other two climatic periods (Figures V.5c and V.8c). Again, this is in accordance with the previously discussed observed behavior (e.g., see Figure IV.2).

A comparison of the driest initial conditions between the three climatic periods displays only a slight difference in the forecast horizons with the initial conditions of March 15 and June 15. The uncertainty bounds of the driest year in the first climatic period for these two initial conditions (Figures V.2a and 2b) are more narrow than the corresponding bounds in the other two climatic periods (Figures V.6a, 6b, 9a, and 9b). No major differences between the climatic periods are noted for the fall and winter forecast horizons with initial conditions from the driest years.

Initial conditions from the coolest year of each climatic period (Figures V.3, V.5, and V.8) show a more narrow forecast uncertainty in the first climatic period then in the other periods. This difference is especially noted by the large bounds of standard deviations for the forecast horizons with initial condition of March 15 for the latter two climatic periods (Figures V.5a and V.10a).

The forecast horizons generated from the initial conditions of the warmest years for each climatic period (Figures V.4, V.7, and V.11) do not differ greatly. A notable exception is the large value of the average ESP in September of the second climatic period (Figure V.7c) that is not evident in the other September 15 initial conditions forecast horizons.

5.1.1 ESP Reliability

The overall forecast reliability of the ESP realizations was determined by comparing the observed flow with the average and bounds of standard deviation of the ESP realizations for the forecast horizons previously presented. In general, the observed flow was within 2 standard deviation bounds of the ESP realizations. For most dry initial conditions, ESP performed even better, with the observed flow within 1 bound of standard deviation. Occasional large departures of the observed flow from the average ESP were also shown to occur. These large departures generally exceeded the average ESP by approximately 7 bounds of standard deviation with one exceeding 14 bounds (Figure V.2a). It is thus, concluded that for the utilization of the ESP for the subject basin, care should be taken to account for the skewed nature of flows, because the assumption of normality does not apply to both flow observations and forecasts. In addition, warm and dry trends in climate increase the reliability of the ESP forecasts.

5.2 Analysis of ESP Realizations

ESP realizations were analyzed by averaging all possible realizations for the climatic period and comparing the average ESP for the wettest/driest and coolest/warmest initial conditions. Further comparisons were made of the initial conditions by imposing a climatic forcing. Climatic forcing was imposed by ranking the realizations according to precipitation and temperature and averaging those forcing realizations for a certain initial condition. For example, if the initial condition of a wet year is chosen, only those realizations generated by the top 50% of the wettest years in that climatic period were used to compute the average ESP.

Figure V.12 compares the average ESP computed from all possible realizations in the 1925-1949 climatic period for initial condition dates from the wettest (1938) and driest (1933) years. The initial condition dates chosen are a) March 15, b) June 15, c) September 15, and d) December 15, and have forecast horizons representative of the four seasons. The largest difference of the average ESP occurs in the forecast horizon with the initial condition date of September 15 (Figure V.12c). The average ESP, dependent on the wet or

dry initial condition, has a maximum difference of about 2.5 mm/day and an extended difference of over 1 mm/day for almost 20 days. Smaller differences are detected in other initial condition dates.

The average of all possible realizations from the second climatic period are shown for initial condition dates from the wettest (1951) and driest (1958) years in Figure V.13. The maximum difference between the average ESP for the wet/dry initial conditions is seen in the forecast horizon with the starting date of March 15 (Figure V.13a). The maximum difference of almost 2.5 mm/day occurs in early April (day 20 of Figure V.13a). A large difference persists between the average ESP for almost 40 days. A small difference of almost 0.5 mm/day persists for 20 days in the forecast horizon with the starting date of September 15. A significant difference also persists as the forecast horizon with the starting date of December 15 extends into the spring months.

Figure V.14 presents the average ESP for various initial conditions from the wettest (1973) and driest (1976) conditions of the third climatic period. A maximum difference of 2.5 mm/day is seen in the forecast horizon with the starting date of March 15 (Figure V.14a). The difference decreases rapidly but then persists at 0.5 mm/day for close to 40 days. A significant difference is also seen in the winter forecast horizon (Figure V.14d) as it extends into the spring months.

The features of the differences between wet and dry initial conditions can also be compared between the three climatic periods. The first climatic period does not show any significant differences of average ESP with the March 15 initial condition whereas the second and third climatic period show the largest difference in this forecast horizon. The second climatic period has the largest difference in this forecast horizon in early April and the third climatic period has the largest difference in mid March. These differences are presumably due to the less precipitation and the low variability of precipitation detected in the first climatic period (see Figures IV.2 and IV.5). Thus, the uncertainty bounds and the means of the first climatic period are expected to be lower.

There is a large difference in the September 15 forecast horizon of the first climatic period that is only slightly evident in the second climatic period and non-existent in the third climatic period. It shows that even for climatic periods with less overall precipitation, fall high flows may still be significant in terms of flood prediction and control. As the forecast horizon with the starting date of December 15 extends into the spring months a slight difference of average ESP is detected in the first climatic period. This difference is slightly larger in the second climatic period and even more so in the third climatic period.

Average ESP with climatic forcing was computed by averaging the realizations generated by inputs of the 50% wettest years for the wet initial conditions and the 50% driest

years for the dry initial conditions in each climatic period. Figure V.15 shows the average ESP with climatic forcing for the wettest (1938) and driest (1933) initial conditions in the first climatic period. Significant differences of greater than 0.5 mm/day occur in the summer forecast horizon (Figure V.15b) and persist for 20 days. A maximum difference of 2.6 mm/day occurs in September of the fall forecast horizon (Figure V.15c). The difference of 1 mm/day persists for almost 20 days. The winter forecast horizon (Figure V.15d) shows a significant difference as the horizon extends into the spring months. A difference greater than 0.5 mm/day persists for almost 30 days.

The average ESP with climatic forcing for the second climatic period's wettest (1951) and driest (1958) initial conditions is shown in Figure V.16. Large differences greater than 2 mm/day are evident in the spring forecast horizon (Figure V.16a). Differences greater than 0.5 mm/day persist for over 60 days. Significant differences greater than 0.5 mm/day are also evident in the fall forecast horizon (Figure V.16c) and persist up to 40 days. The winter forecast horizon (Figure V.16d) shows little difference until the horizon extends into the spring months. The difference then expands to a maximum of 2.4 mm/day.

Figure V.17 shows the average ESP with climatic forcing for the wettest (1973) and driest (1976) initial conditions of the third climatic period. A maximum difference of 2.4 mm/day occurs on March 15 of the spring forecast horizon (Figure V.17a). Differences greater than 0.5 mm/day in this horizon extend up to 80 days. Another significant difference occurs in the winter horizon (Figure V.17d) as it extends into the spring months. This difference persists from March 15 to April 15 (day 90 to day 120).

A comparison of the average ESP with climatic forcing between the climatic periods for wet and dry initial conditions reveals similar features to the average ESP with all realizations. For example, no difference is detected in the average ESP with forcing in the spring realization of the first climatic period, whereas the difference in this horizon in the latter two climatic periods is a maximum. Similarly, a large difference is detected in the fall realization of the first climatic period that is small in the second climatic period and is hardly evident in the third climatic period. The main effect of imposing climatic forcing on the average ESP is that the difference between wet and dry initial conditions appears to persist for a longer forecast time. The differences found when climatic forcing is imposed appear to be slightly larger than the average ESP using all of the realizations. It is also noted that the wet vs. dry condition differences are comparable in magnitude to the forecast standard deviation of the ESP (compare Figures V.1 and V.2 to Figures V.12 and V.15). Thus, the event-to-event variability is as important as the differences in forecasting wet and dry trends.

A similar analysis was conducted comparing the average ESP with initial conditions of the coolest and warmest years of each climatic period. The first comparison uses all possible realizations to compute the average ESP. For the second comparison, the average ESP are computed with climatic forcing by averaging the realizations generated by 50% of the warmest years with the warm initial conditions and 50% of the coolest years with the cool initial conditions.

Figure V.18 shows the average ESP of all possible realizations for various initial condition dates from the coolest (1929) and warmest (1931) years from the first climatic period. A significant difference between the average ESP from wet or dry initial conditions appears only in the spring forecast horizon (Figure V.18a). In this horizon a difference of greater than 0.5 mm/day persists for almost 40 days. No other significant differences are detected in the other forecast horizons.

The average ESP computed from all realizations from the initial conditions of various dates in the coolest (1951) and the warmest (1964) years of the second climatic period are shown in Figure V.19. A maximum difference between the average ESP predicted by wet or dry initial conditions occurs in the forecast horizon with the initial date of March 15 (Figure V.19a). A maximum difference of 3 mm/day occurs at day 20 in this horizon and a large difference persists up to 40 days. The summer forecast horizon does not show any significant differences. A maximum difference of 2 mm/day is detected in the beginning of the fall horizon (Figure V.19c) and only persists for about 10 days.

The results for the third climatic period are shown in Figure V.20. The average ESP is computed from all possible realizations from various initial condition dates from the coolest (1979) and the warmest (1987) years. The largest difference occurs in the forecast horizon with the initial condition date of March 15 (Figure V.20a). The maximum difference of 2 mm/day occurs around day 25 and a significant difference of over 0.5 mm/day persists for over 50 days. A smaller difference is seen to persist for 10 days in late September of the fall forecast horizon (Figure V.20c)

Similarities and differences of the average ESP for cool and warm initial conditions exist between the three climatic periods. A major difference between the climatic periods is the average ESP in the spring forecast horizon. In the first climatic period the spring has a small difference between the two initial conditions. In the second and third climatic periods this difference is attenuated. The summer forecast horizon is similar for all three climatic periods. The fall forecast horizons differ. The second climatic period has a large difference in average ESP for about 10 days whereas the first climatic period shows no difference and the third climatic period shows only a slight difference for 10 days. In the winter forecast horizons no major differences occur between the cool and warm initial conditions, however

a difference does exist between the climatic periods. In the first climatic period the average ESP (note: not the difference between the two initial conditions average ESP but the actual average ESP) increases in the spring months to 0.6 mm/day. The second climatic period maximum average ESP is 1.6 mm/day and the third climatic period maximum average ESP is 1.4 mm/day.

The average ESP prediction with climatic forcing for the dates with the coolest and warmest initial conditions are shown in Figures V.21, 22, and 23 for each climatic period. Climatic forcing imposed on the average ESP causes the differences between the average ESP to increase and persist for a longer forecast lead time. This is especially true in the spring horizons and occasionally in September of the fall horizons. Differences are also increased by climatic forcing in the winter forecast horizon as it extends to the spring months.

5.3 Set Control Results

The set control method uses the inflow traces forecast by the UIFS model using the ESP procedure as maximum and minimum inflow levels expected to materialize over the forecast horizon. From these inflow bounds a set of decision actions is determined guaranteeing that the system will stay within the desirable bounds for the duration of the control horizon. More specifically, from the inflow bounds a suitable reservoir release was determined. For the Saylorville Reservoir releases of less than 16,000 cfs in January through April and less than 12,000 cfs for the remaining months are considered suitable maximum releases. Releases below 200 cfs are considered deficit releases. The release was applied to the system with the historically observed inflow as input. The resulting storage and release values were recorded and the procedure was repeated over the entire simulation horizon.

Decision actions were generated for the decision time of the first and fifteenth of each month of every year for the simulation horizon of a climatic period by the team at Georgia Institute of Technology headed by Dr. A.P. Georgakakos. Their results of simulated set control release sequences are shown here in Figures V.24-26 for each climatic period. The plots illustrate that the reservoir performance differs from period to period. The first hydrologic period is controlled reasonably well with no excessive releases and relatively few violations (85 days) of the lower release bound. The second climatic period is also handled effectively with only one release of 20,300 cfs (4,300 cfs excessive violation) and 188 days of release deficits. Lastly, the third hydrologic period exhibited 35 days of excessive releases (one release of 36,000 cfs) and 25 days of release deficits. For contrast, simulation of the current operational practices of the Army Corps of Engineers, Rock

Island District for the Saylorville Reservoir are shown in Figures V.27-30 in twenty year periods. For the set controller excessive release of 36,000 cfs the current operational practices show that the release would reach 45,000 cfs. Given the incremental damage cost of excessive releases increase significantly with magnitude of release, the reduction from 45,000 cfs to the 36,000 cfs level represents considerable savings. For the same time periods the total days of release deficits of the simulated current operational practices would be comparable to the results obtained using the forecast-control scheme.

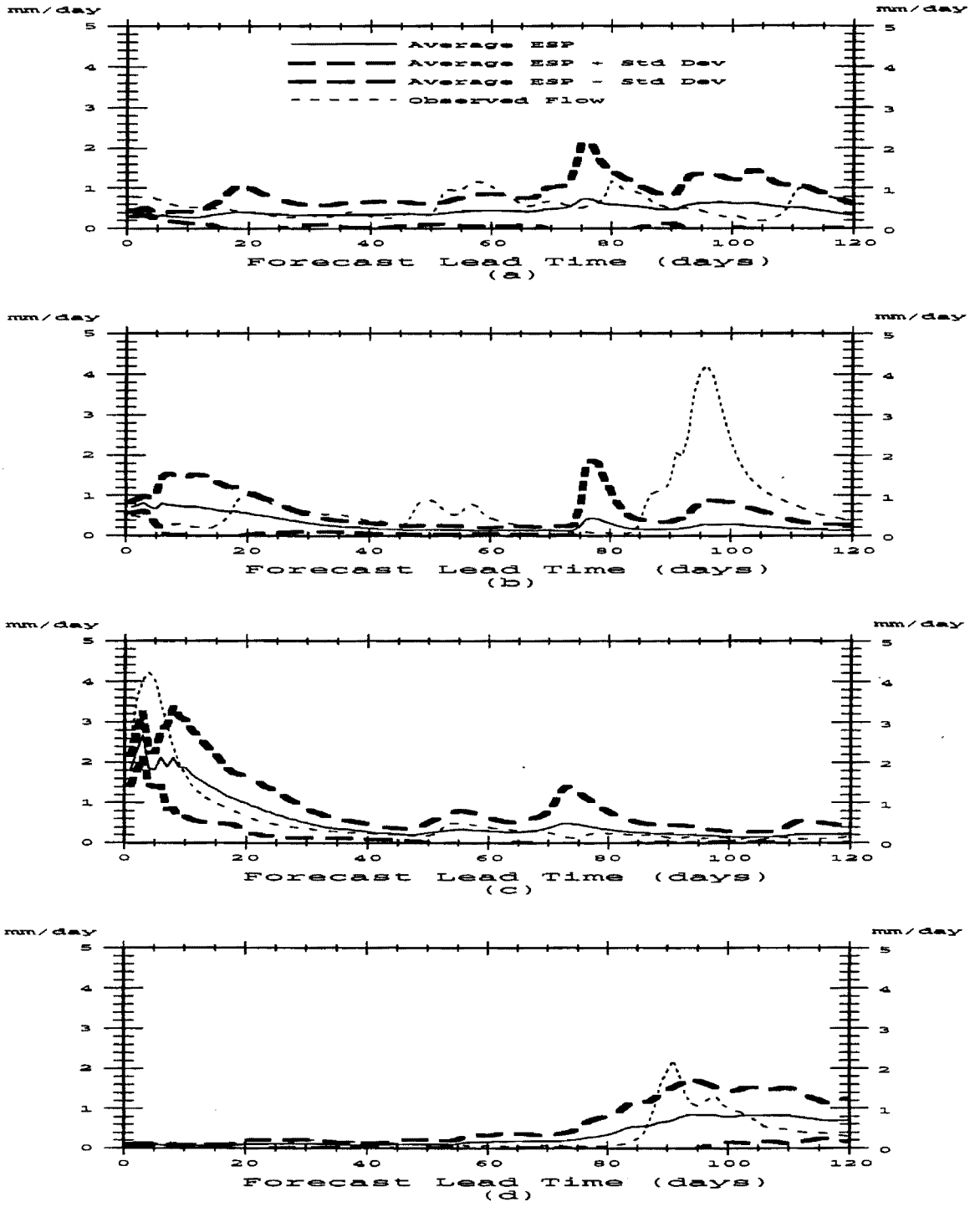

Figure V.1 Average ESP and bounds of standard deviation with observed flows for forecast horizons beginning a)March 15, b) June 15, c) September 15 and d) December 15 for the wettest year in the first climatic period, 1938.

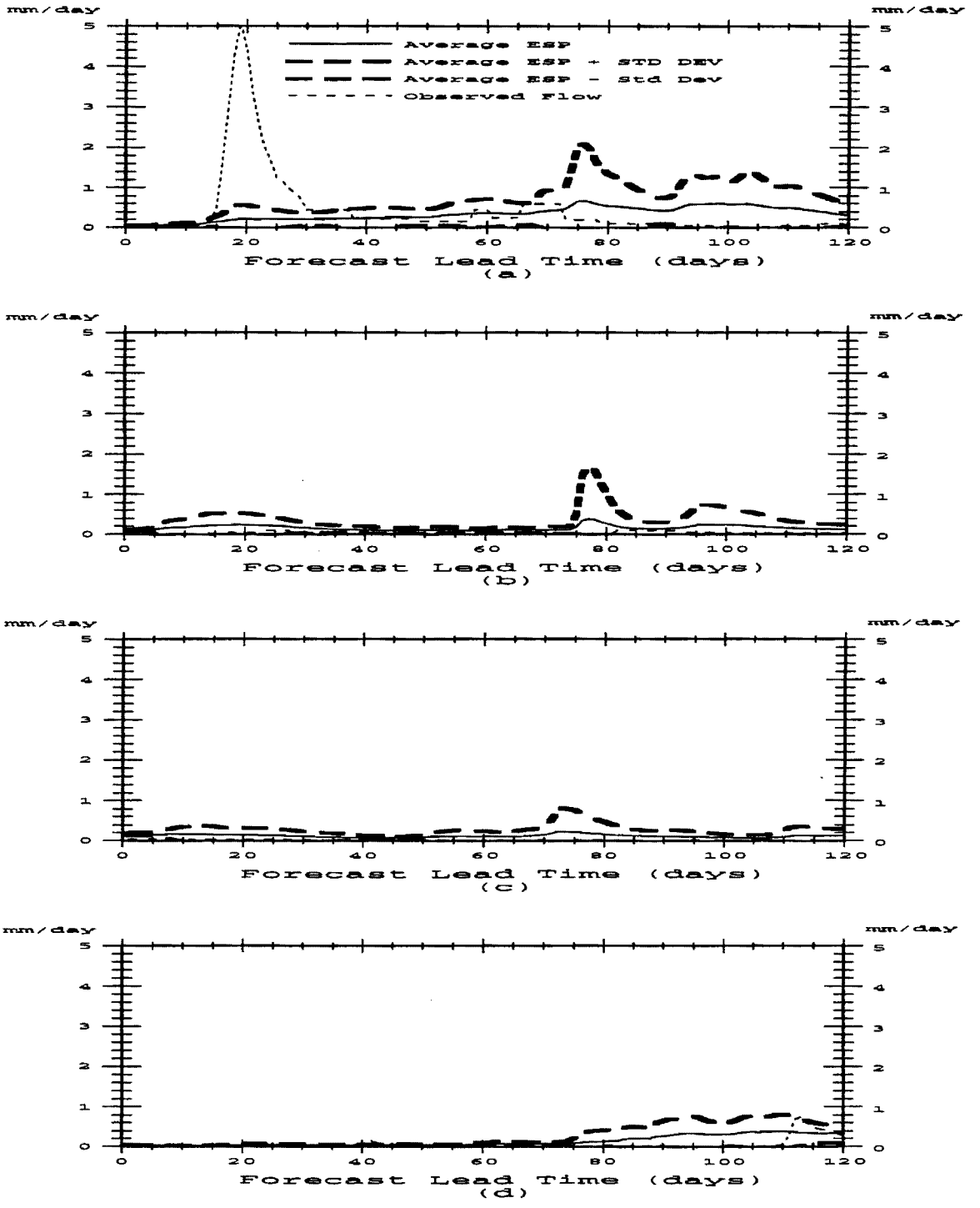

Figure V.2 Average ESP and bounds of standard deviation with observed flows for forecast horizons beginning a)March 15, b) June 15, c) September 15 and d) December 15 for the driest year in the first climatic period, 1933.

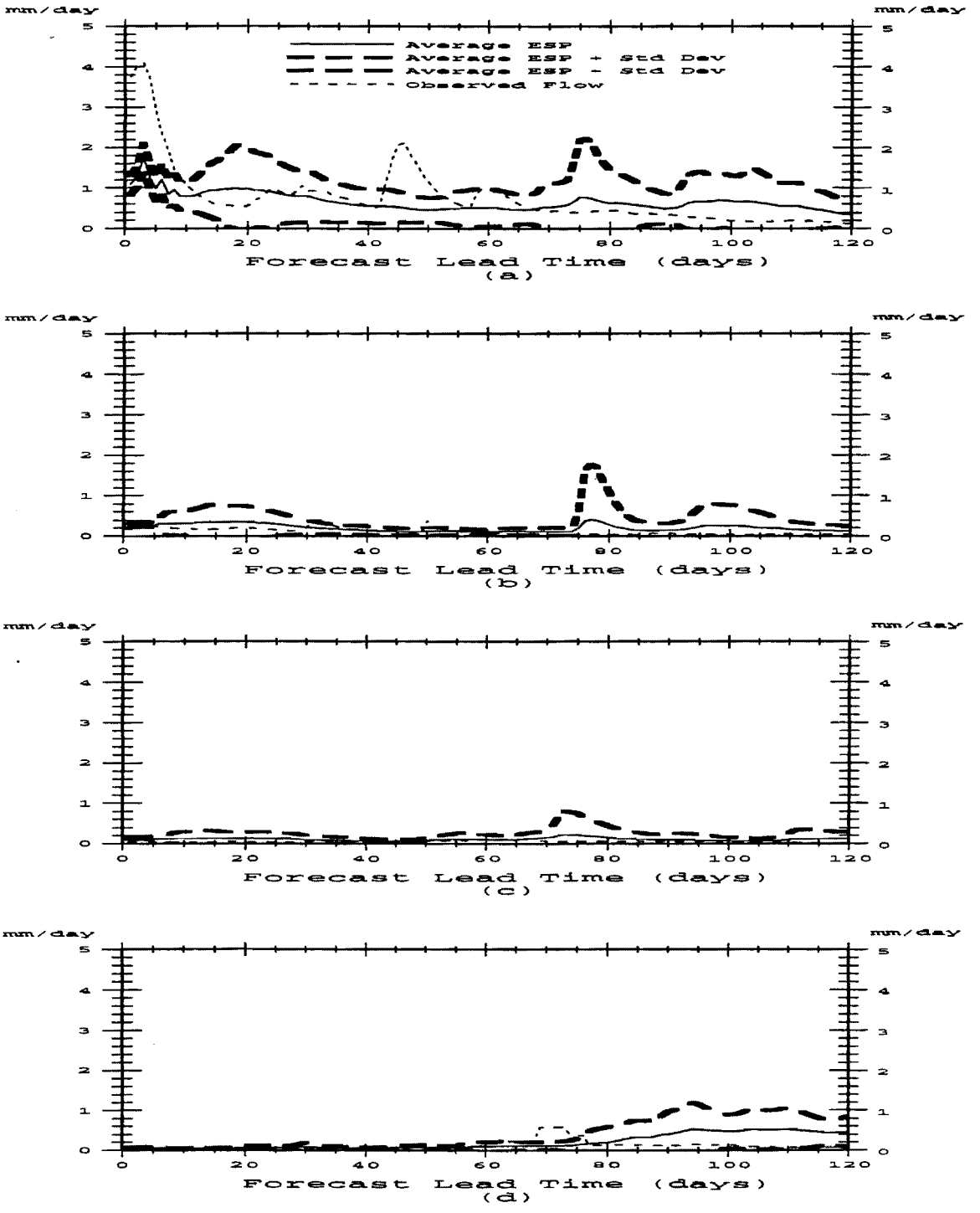

Figure V.3 Average ESP and bounds of standard deviation with observed flows for forecast horizons beginning a)March 15, b) June 15, c) September 15 and d) December 15 for the coolest year in the first climatic period, 1929.

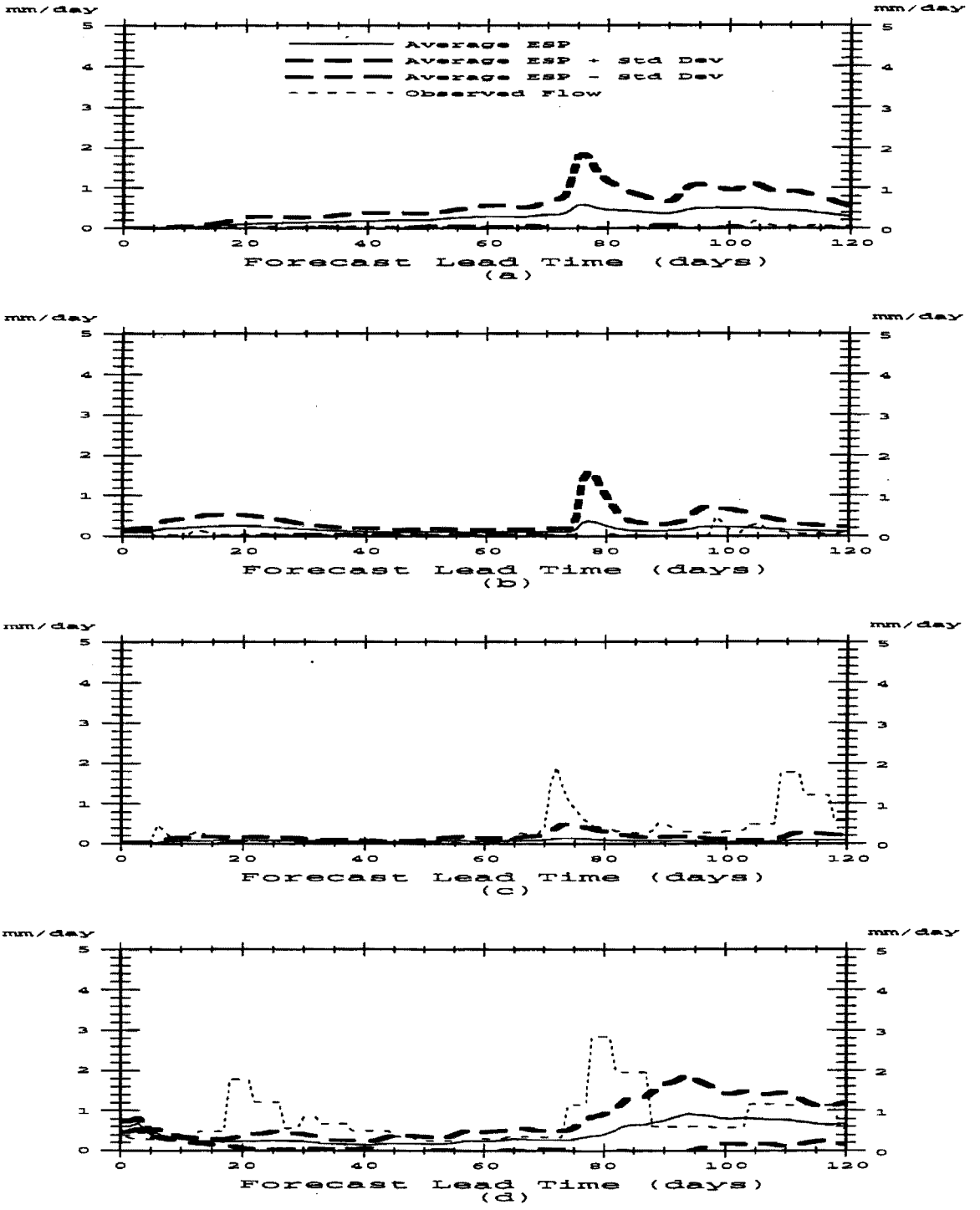

Figure V.4 Average ESP and bounds of standard deviation with observed flows for forecast horizons beginning a)March 15, b) June 15, c) September 15 and d) December 15 for the warmest year in the first climatic period, 1931.

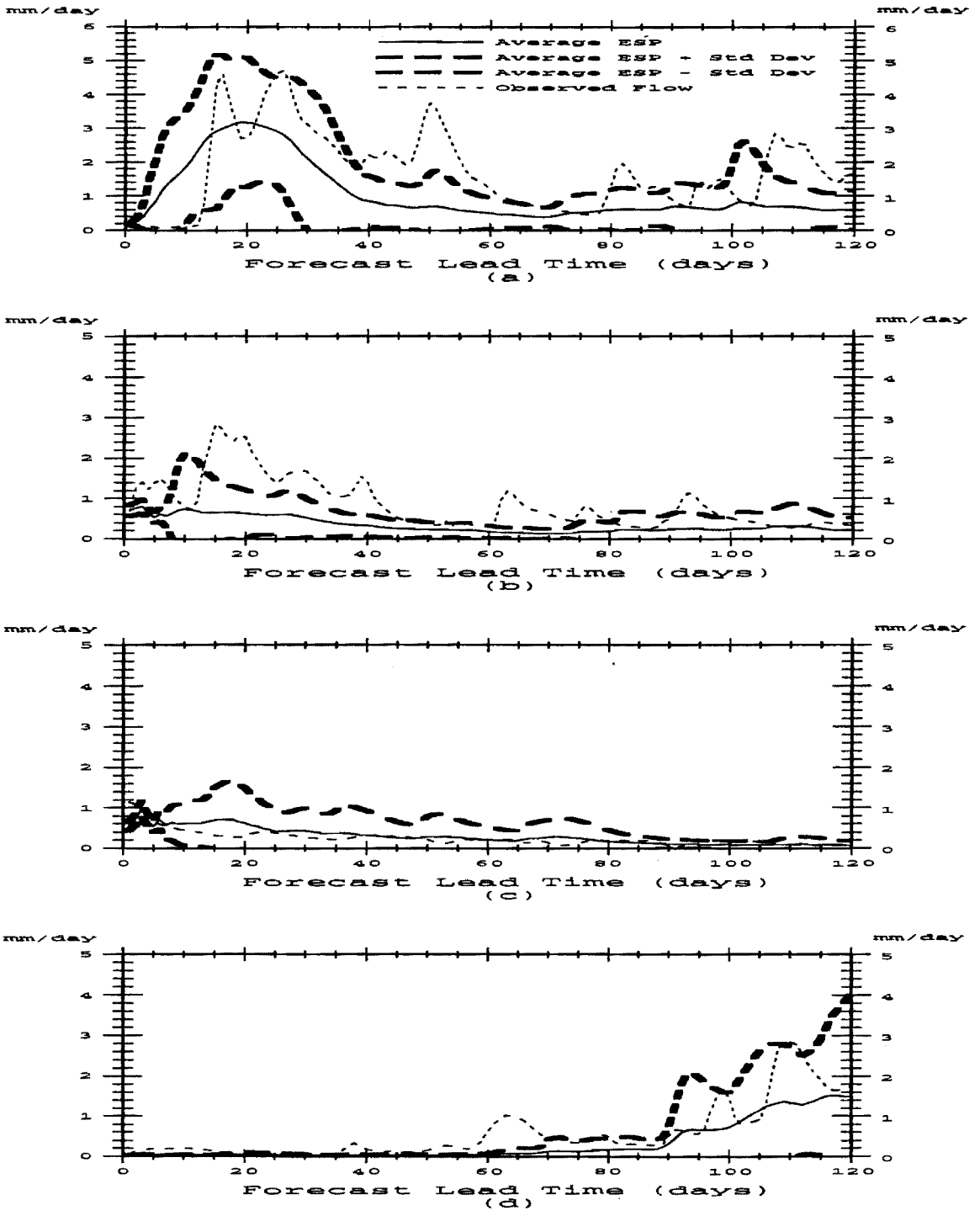

Figure V.5 Average ESP and bounds of standard deviation with observed flows for forecast horizons beginning a)March 15, b) June 15, c) September 15 and d) December 15 for the coldest/wettest year in the second climatic period, 1951.

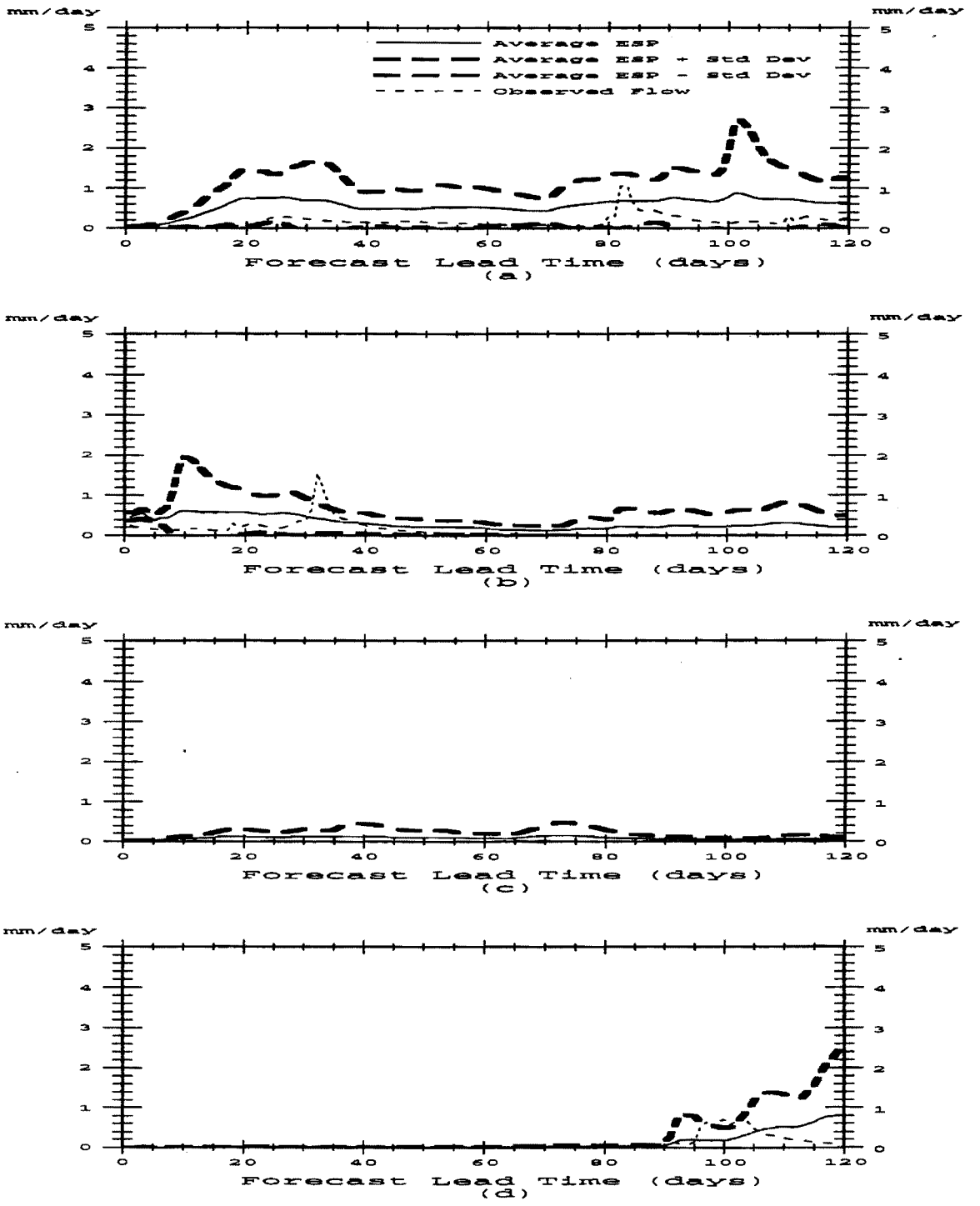

Figure V.6 Average ESP and bounds of standard deviation with observed flows for forecast horizons beginning a)March 15, b) June 15, c) September 15 and d) December 15 for the driest year in the second climatic period, 1958.

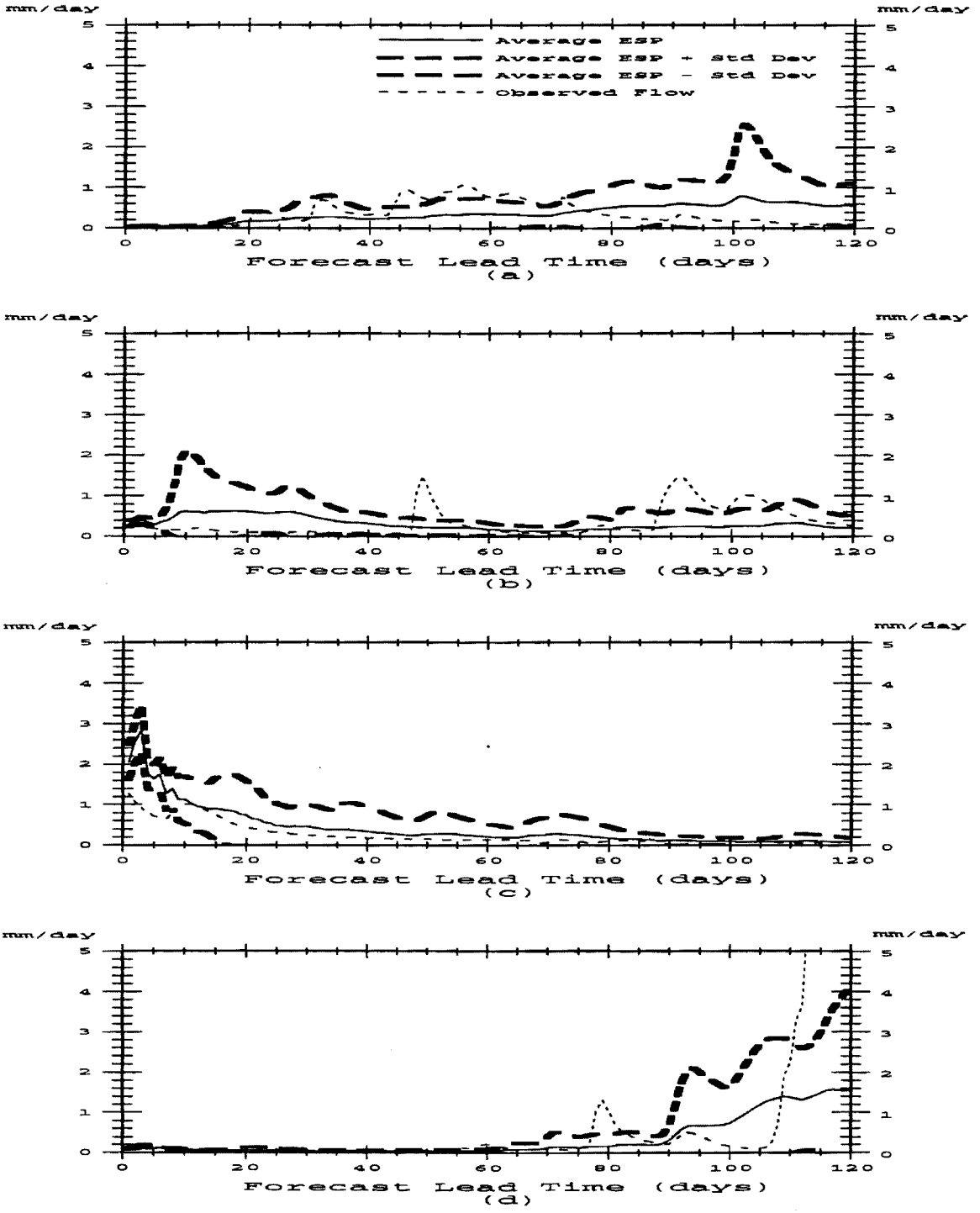

Figure V.7 Average ESP and bounds of standard deviation with observed flows for forecast horizons beginning a)March 15, b) June 15, c) September 15 and d) December 15 for the warmest year in the second climatic period, 1964.

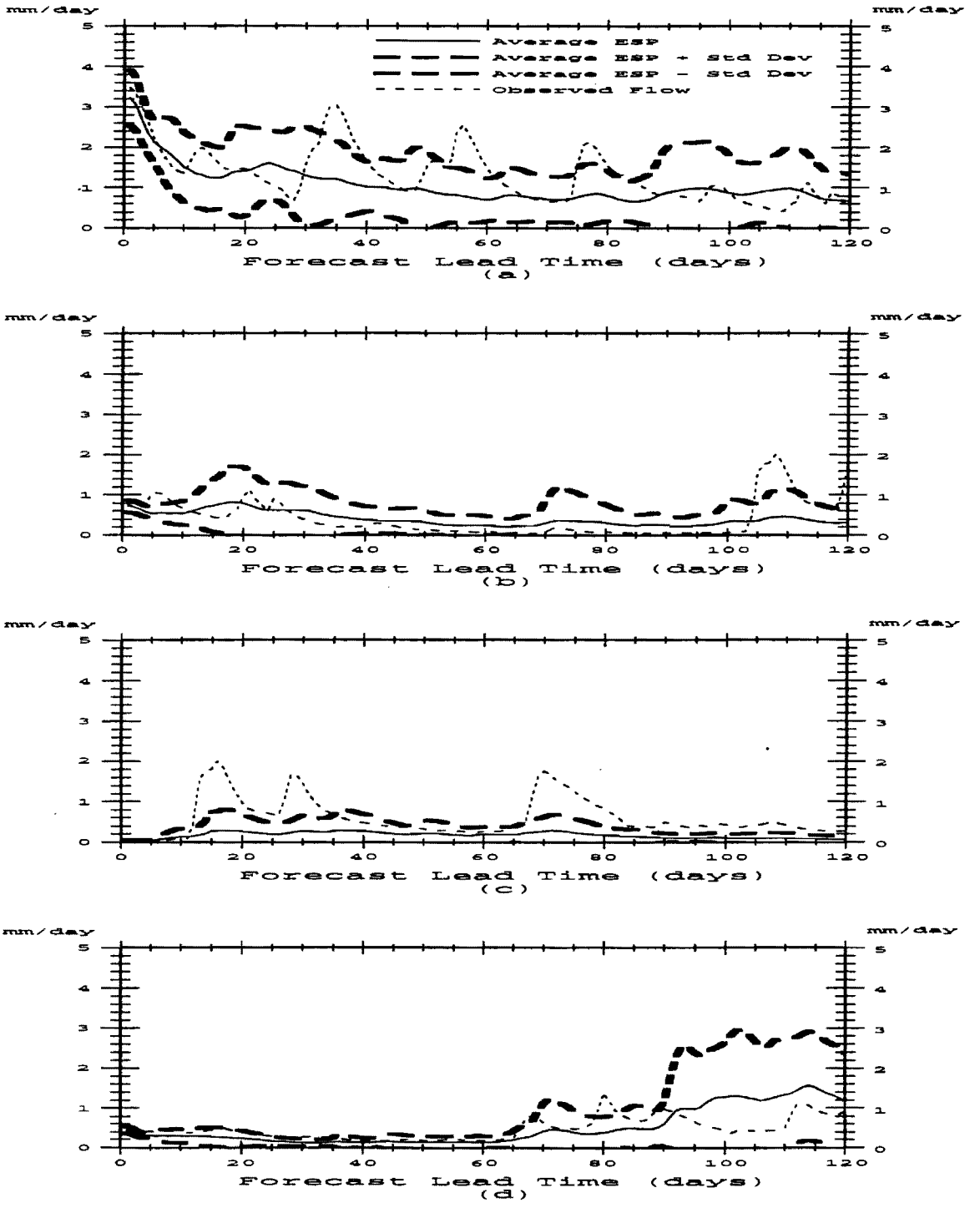

Figure V.8 Average ESP and bounds of standard deviation with observed flows for forecast horizons beginning a)March 15, b) June 15, c) September 15 and d) December 15 for the wettest year in the third climatic period, 1973.

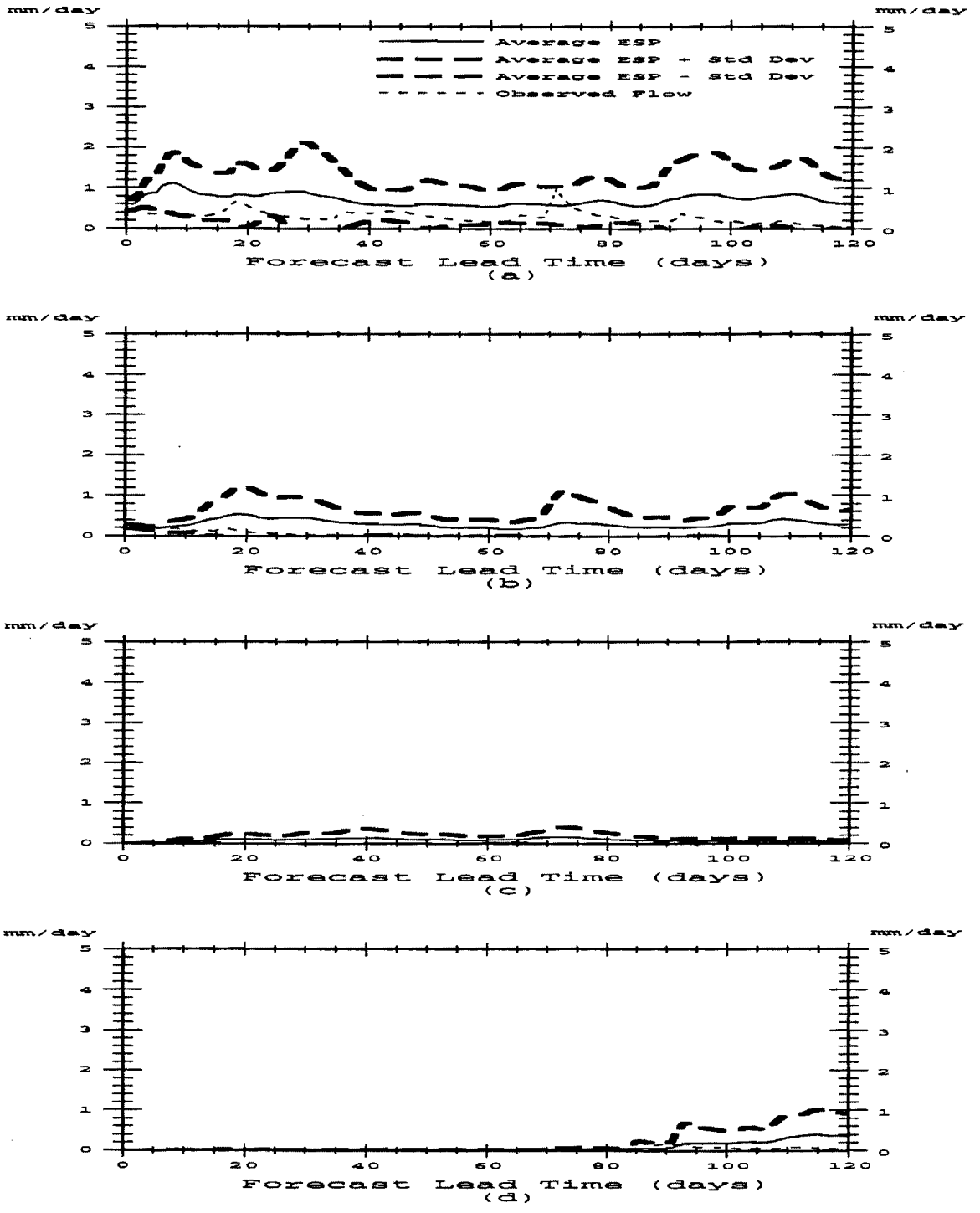

Figure V.9 Average ESP and bounds of standard deviation with observed flows for forecast horizons beginning a)March 15, b) June 15, c) September 15 and d) December 15 for the driest year in the third climatic period, 1976.

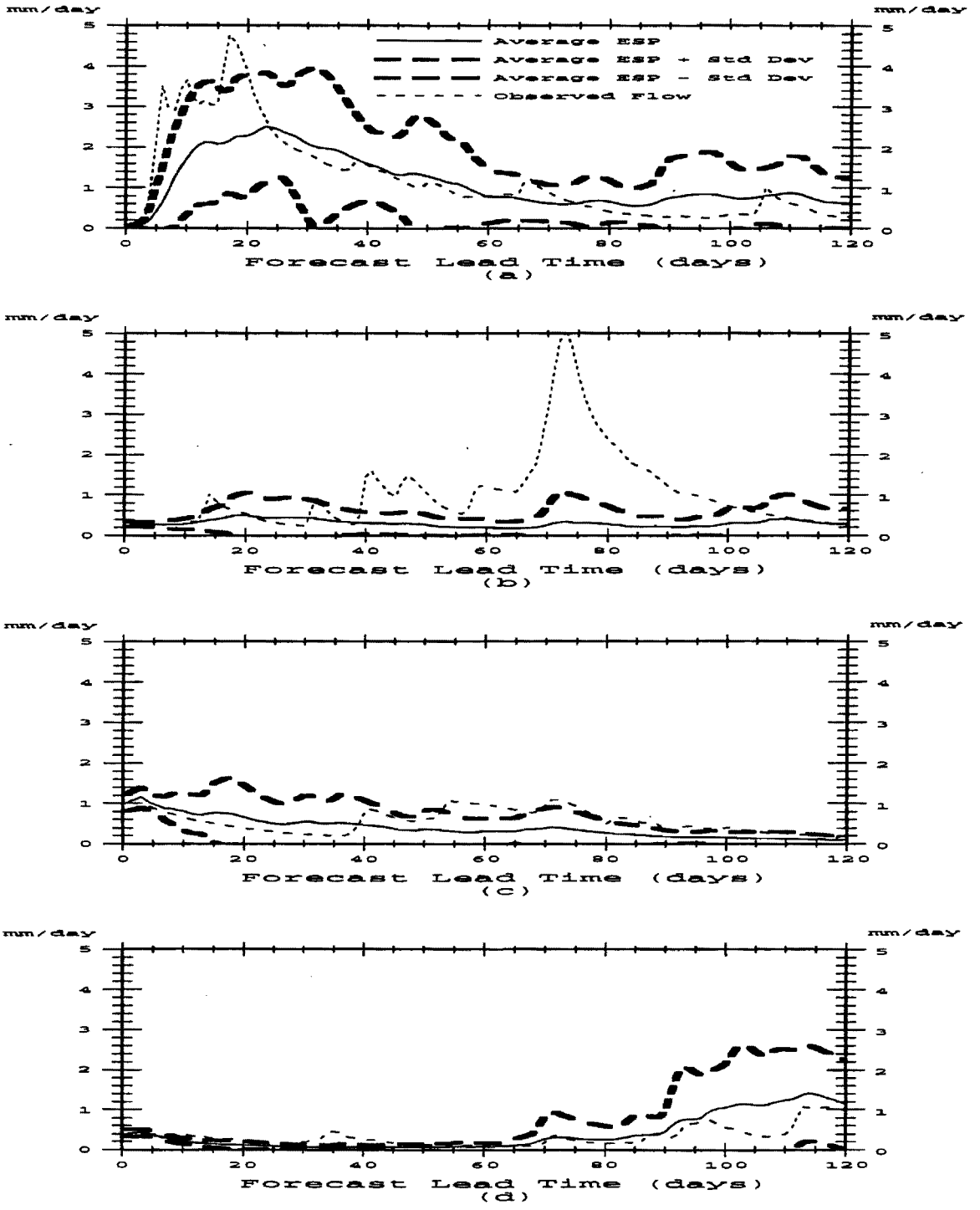

Figure V.10 Average ESP and bounds of standard deviation with observed flows for forecast horizons beginning a)March 15, b) June 15, c) September 15 and d) December 15 for the coolest year in the third climatic period, 1979.

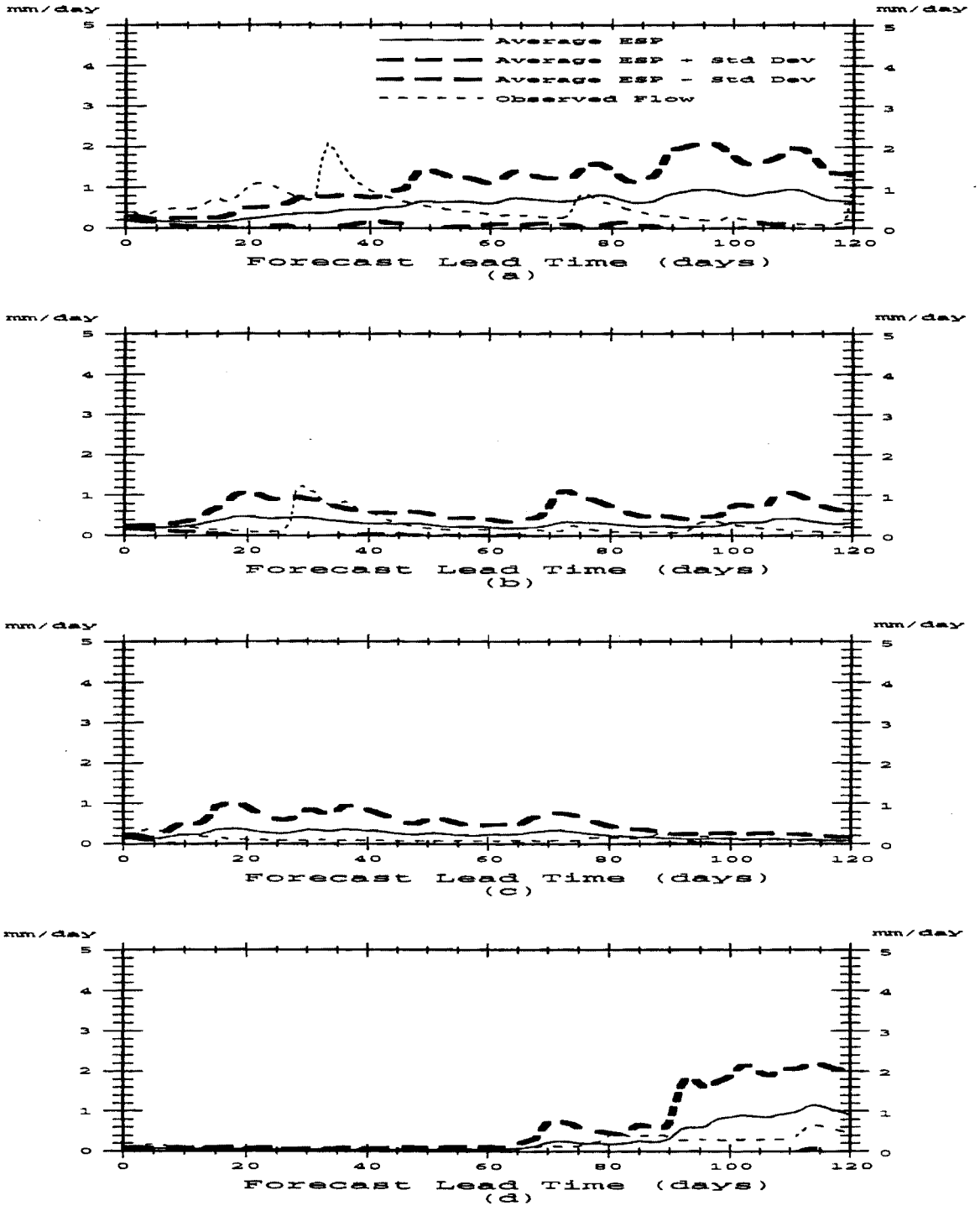

Figure V.11 Average ESP and bounds of standard deviation with observed flows for forecast horizons beginning a)March 15, b) June 15, c) September 15 and d) December 15 for the warmest year in the third climatic period, 1987.

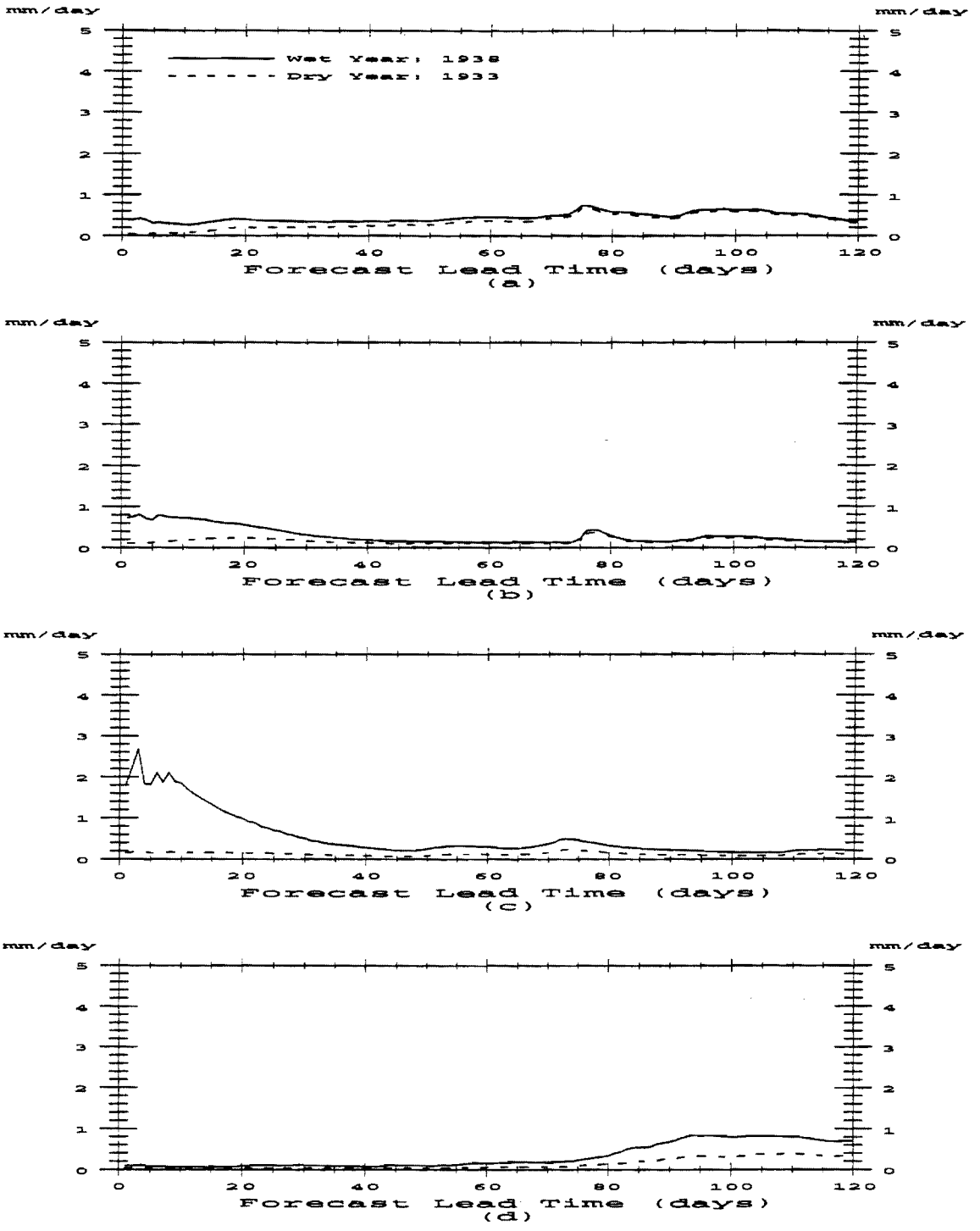

Figure V.12 Average ESP of all possible realizations for the forecast horizons beginning a) March 15, b) June 15, c) September 15 and d) December 15 of the wettest (1938) and driest (1933) years of the first climatic period.

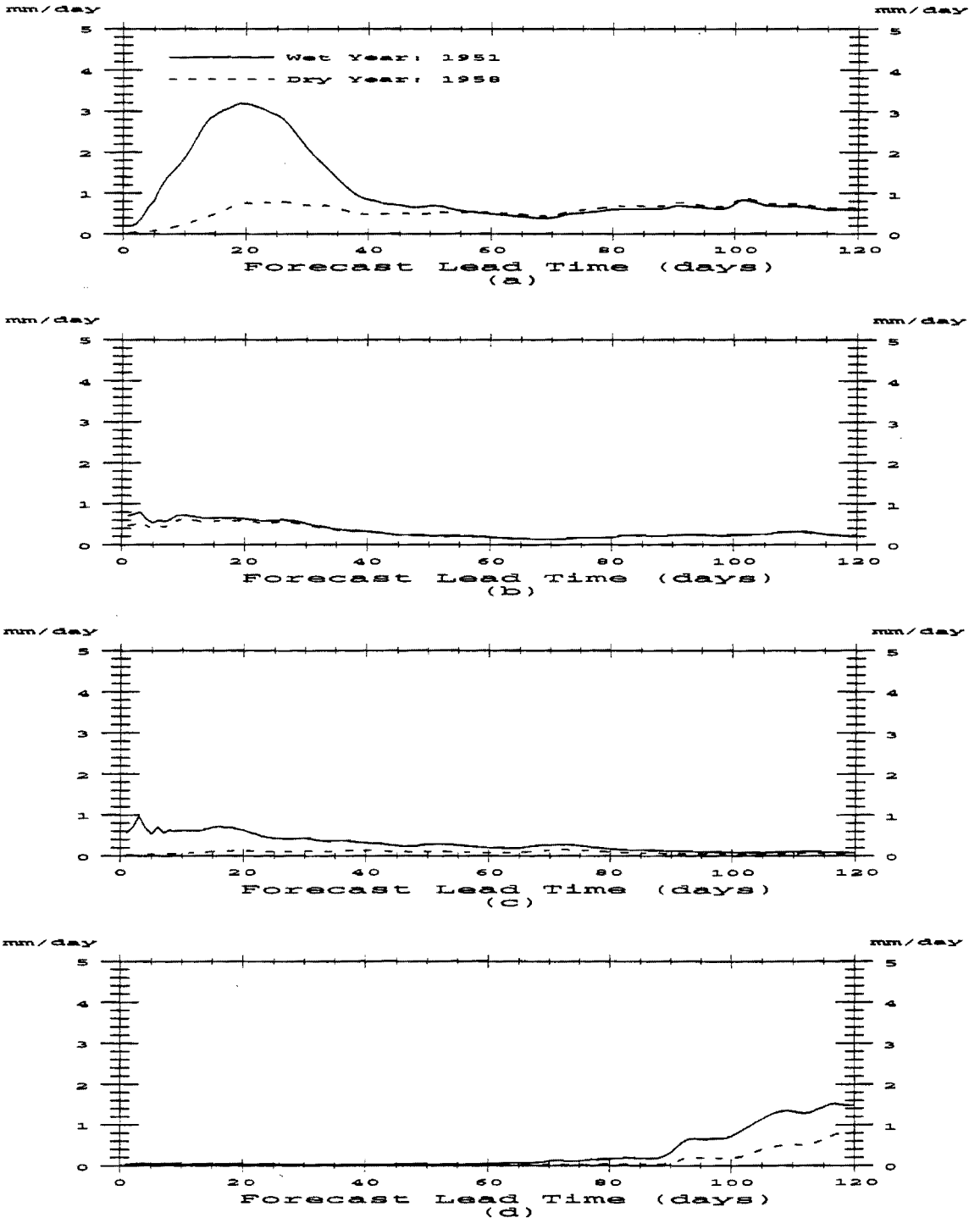

Figure V.13 Average ESP of all possible realizations for the forecast horizons beginning a) March 15, b) June 15, c) September 15 and d) December 15 of the wettest (1951) and driest (1958) years of the second climatic period.

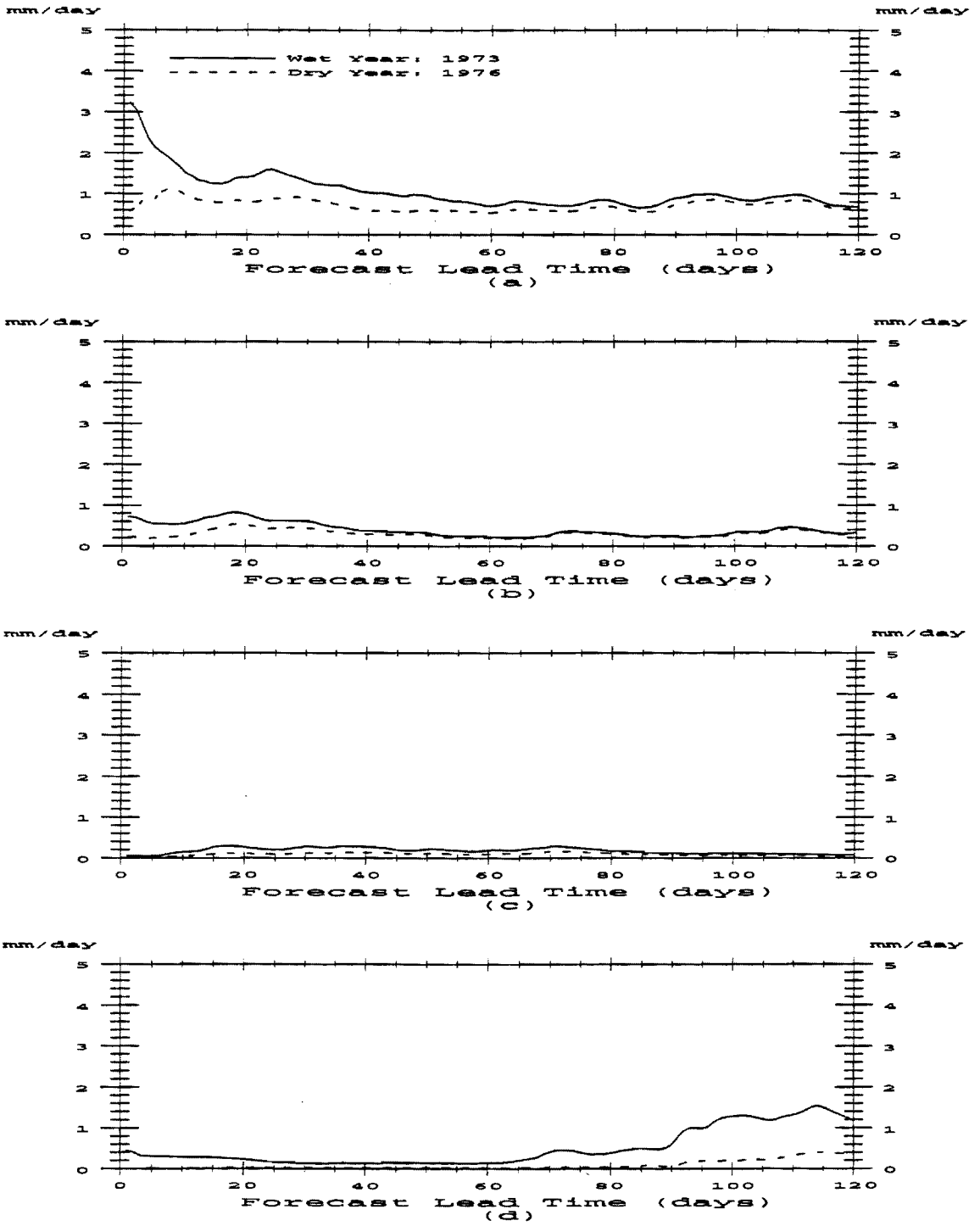

Figure V.14 Average ESP of all possible realizations for the forecast horizons beginning a) March 15, b) June 15, c) September 15 and d) December 15 of the wettest (1973) and driest (1976) years of the third climatic period.

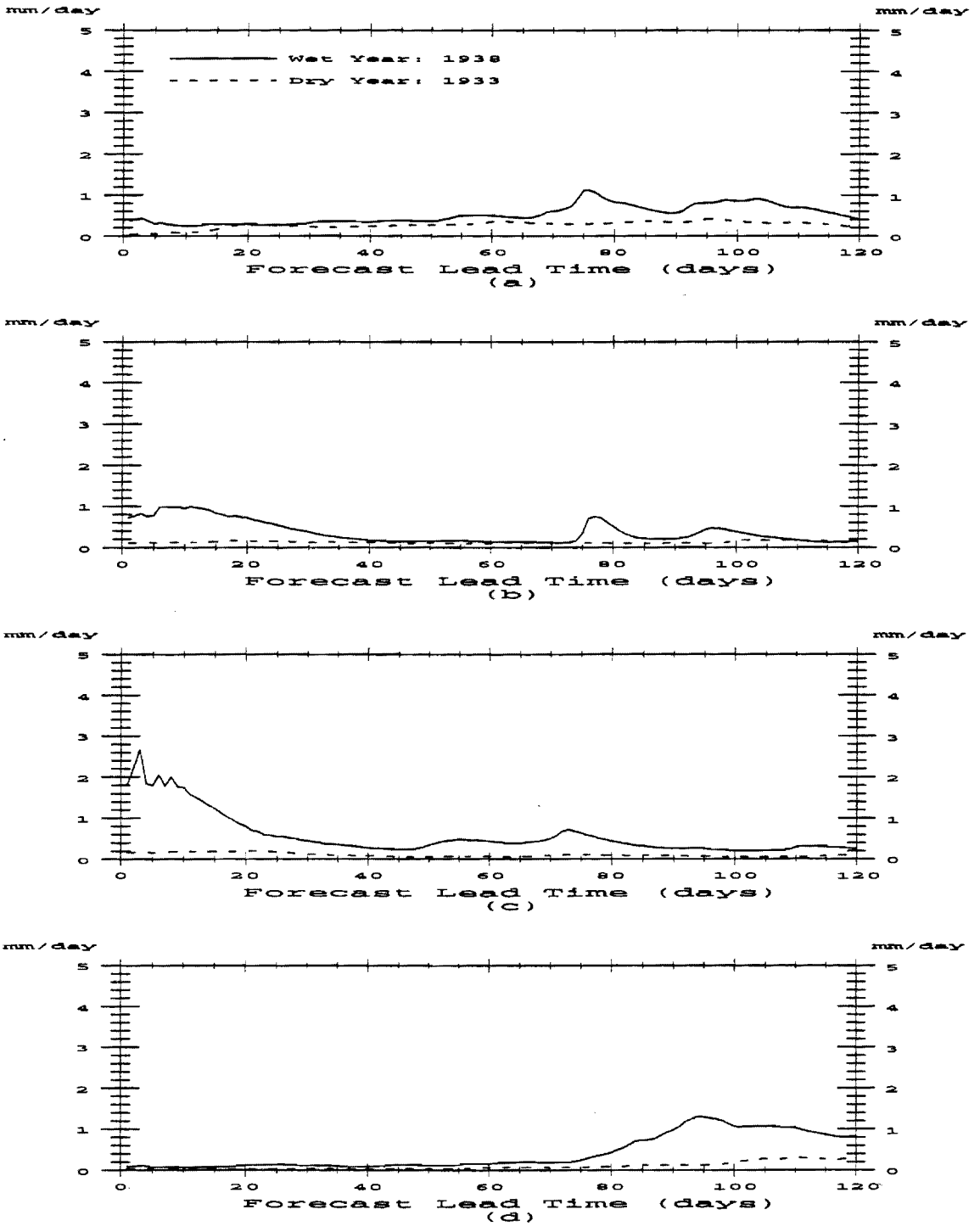

Figure V.15 Average ESP of wet/dry climatic forcing for the forecast horizons beginning a) March 15, b) June 15, c) September 15 and d) December 15 of the wettest (1938) and driest (1933) years of the first climatic period.

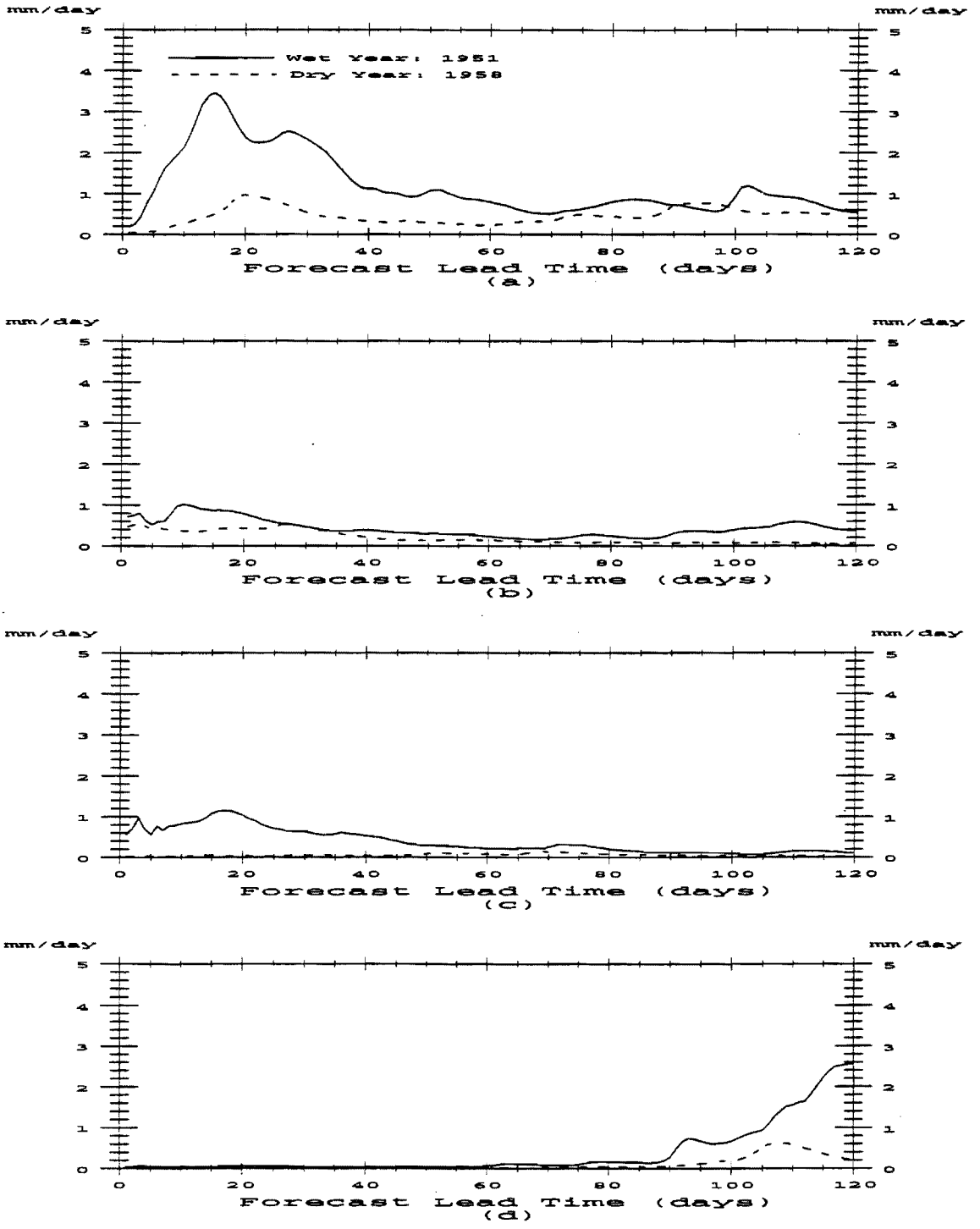

Figure V.16 Average ESP of wet/dry climatic forcing for the forecast horizons beginning a) March 15, b) June 15, c) September 15 and d) December 15 of the wettest (1951) and driest (1958) years of the second climatic period.

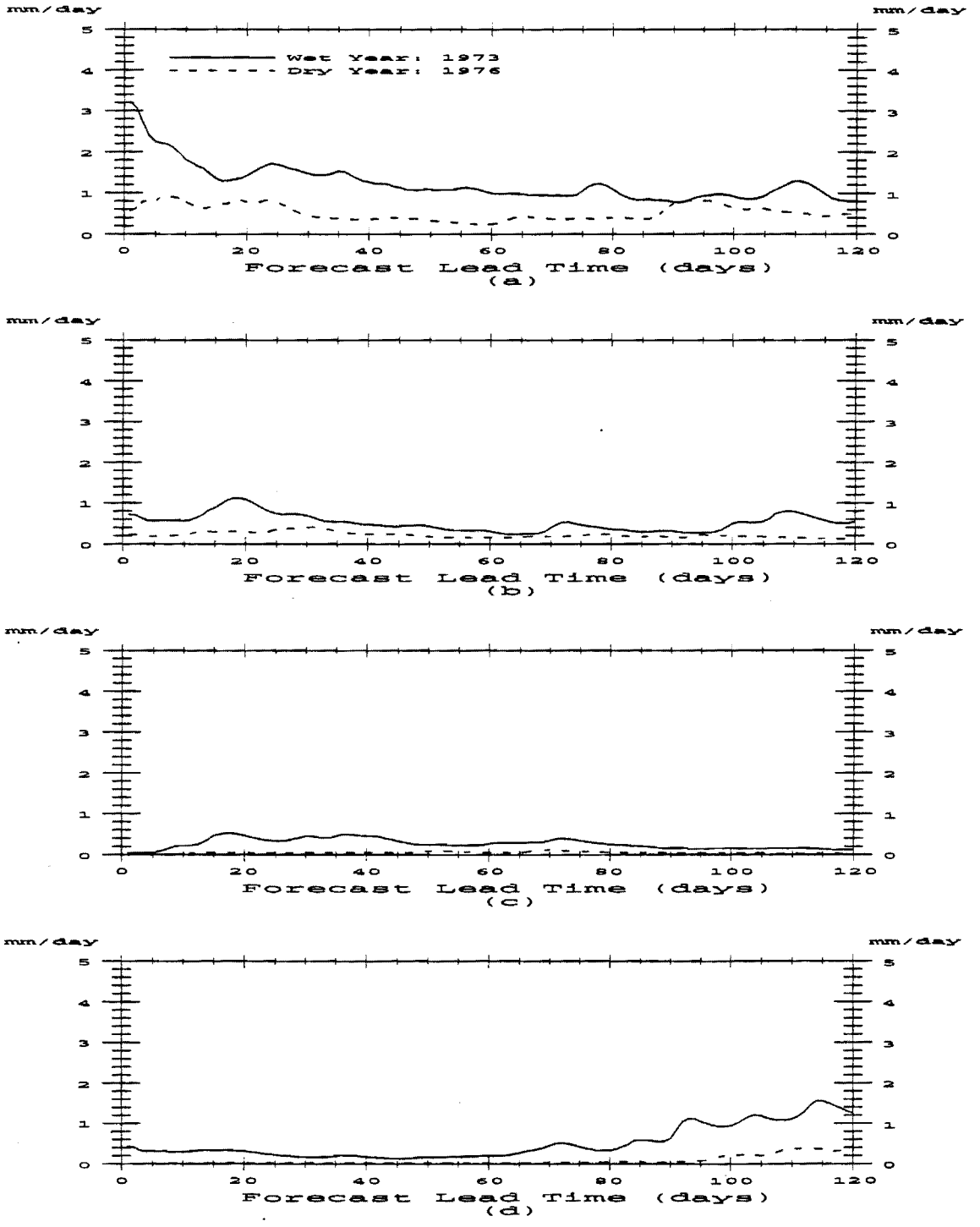

Figure V.17 Average ESP of wet/dry climatic forcing for the forecast horizons beginning a) March 15, b) June 15, c) September 15 and d) December 15 of the wettest (1973) and driest (1976) years of the third climatic period.

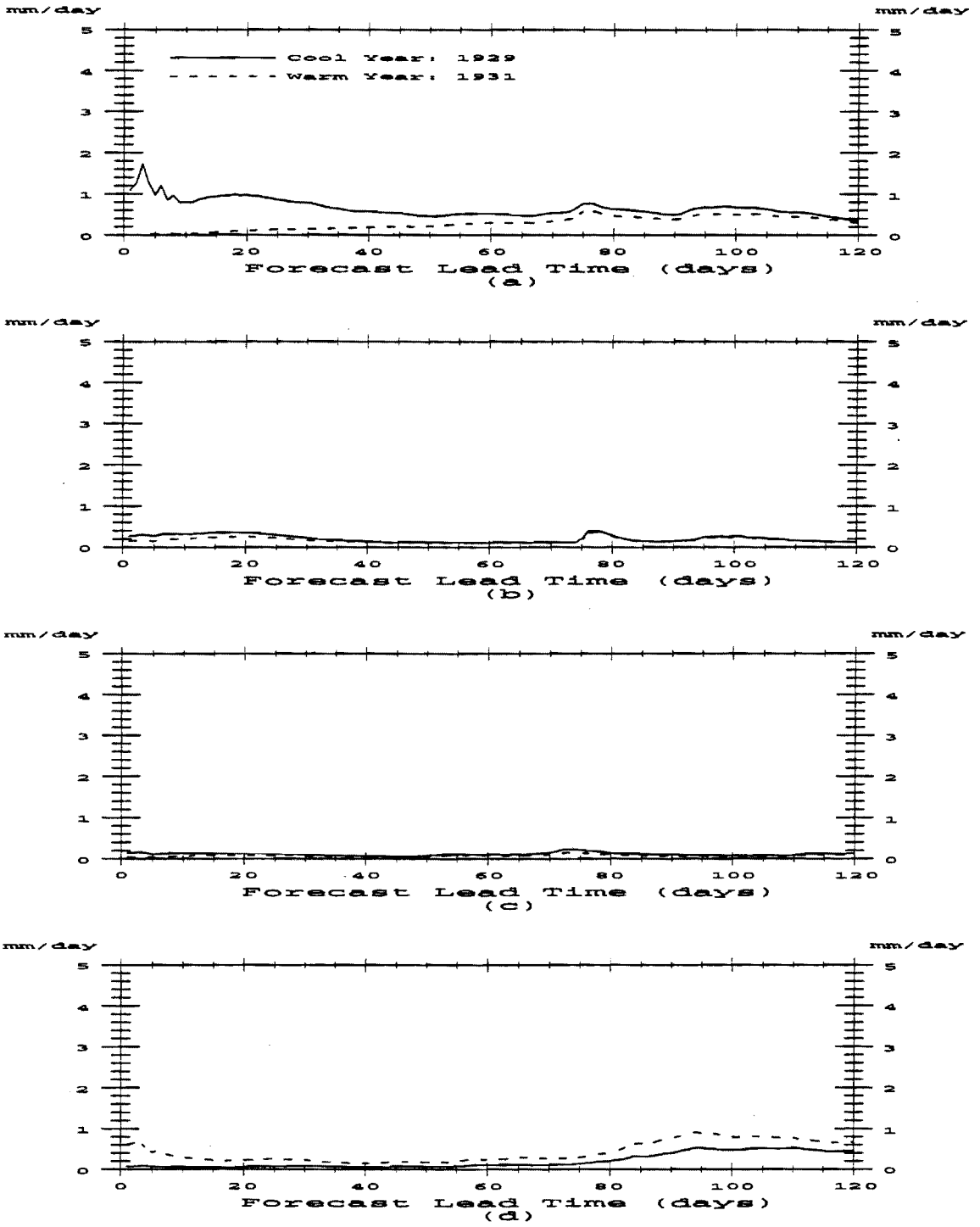

Figure V.18 Average ESP of all possible realizations for the forecast horizons beginning a) March 15, b) June 15, c) September 15 and d) December 15 of the coolest (1929) and warmest (1931) years of the first climatic period.

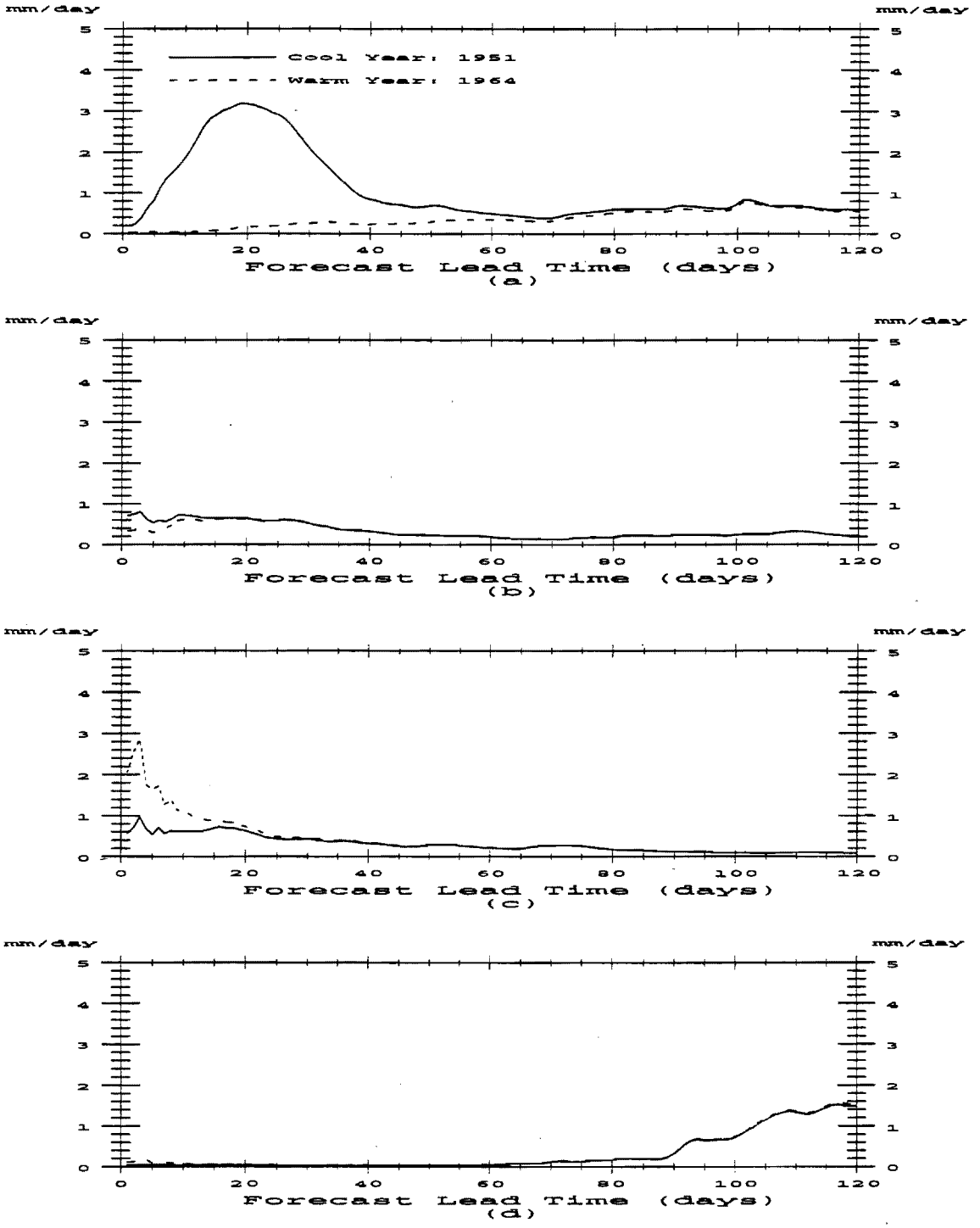

Figure V.19 Average ESP of all possible realizations for the forecast horizons beginning a) March 15, b) June 15, c) September 15 and d) December 15 of the coolest (1951) and warmest (1964) years of the second climatic period.

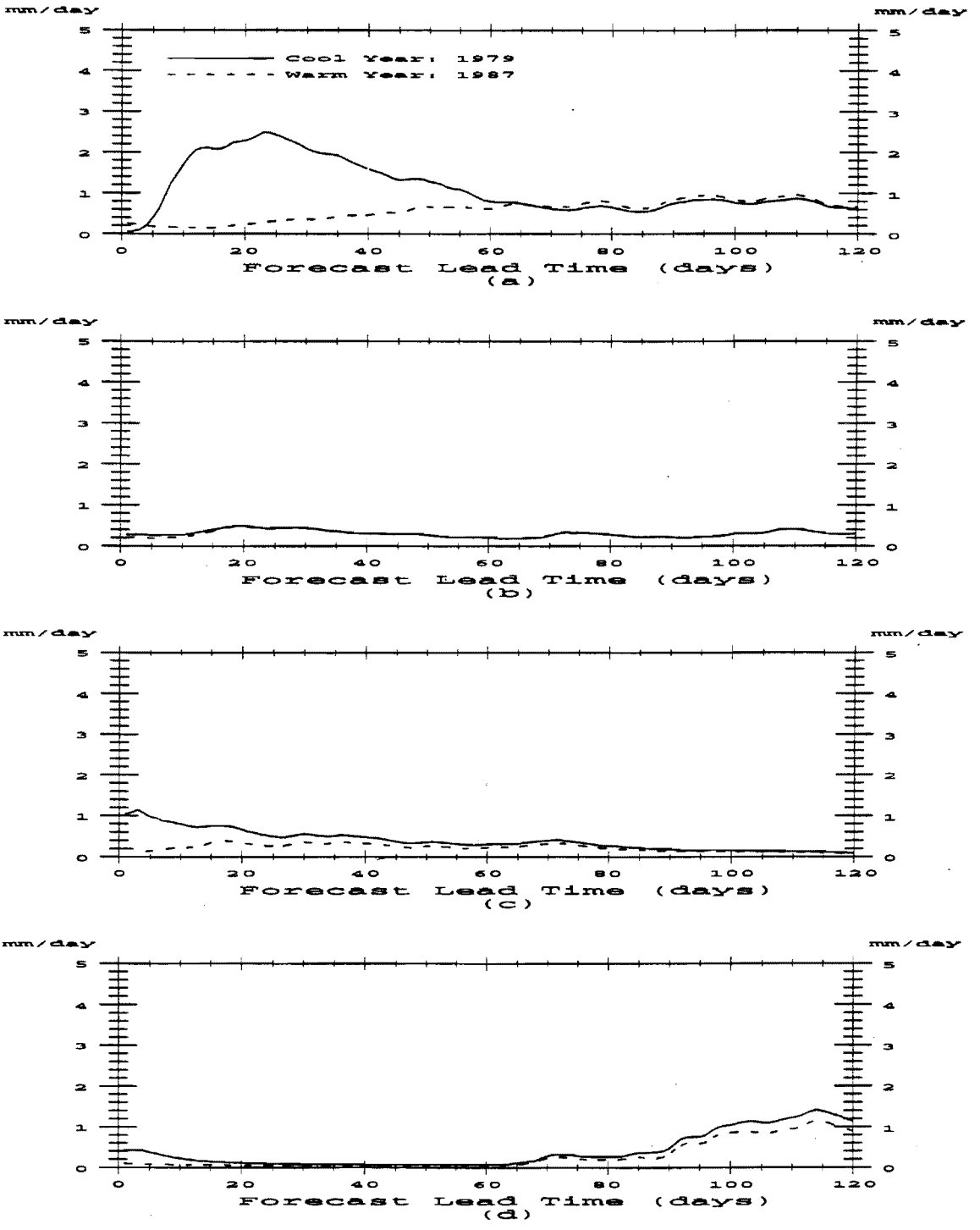

Figure V.20 Average ESP of all possible realizations for the forecast horizons beginning a) March 15, b) June 15, c) September 15 and d) December 15 of the coolest (1979) and warmest (1987) years of the third climatic period.

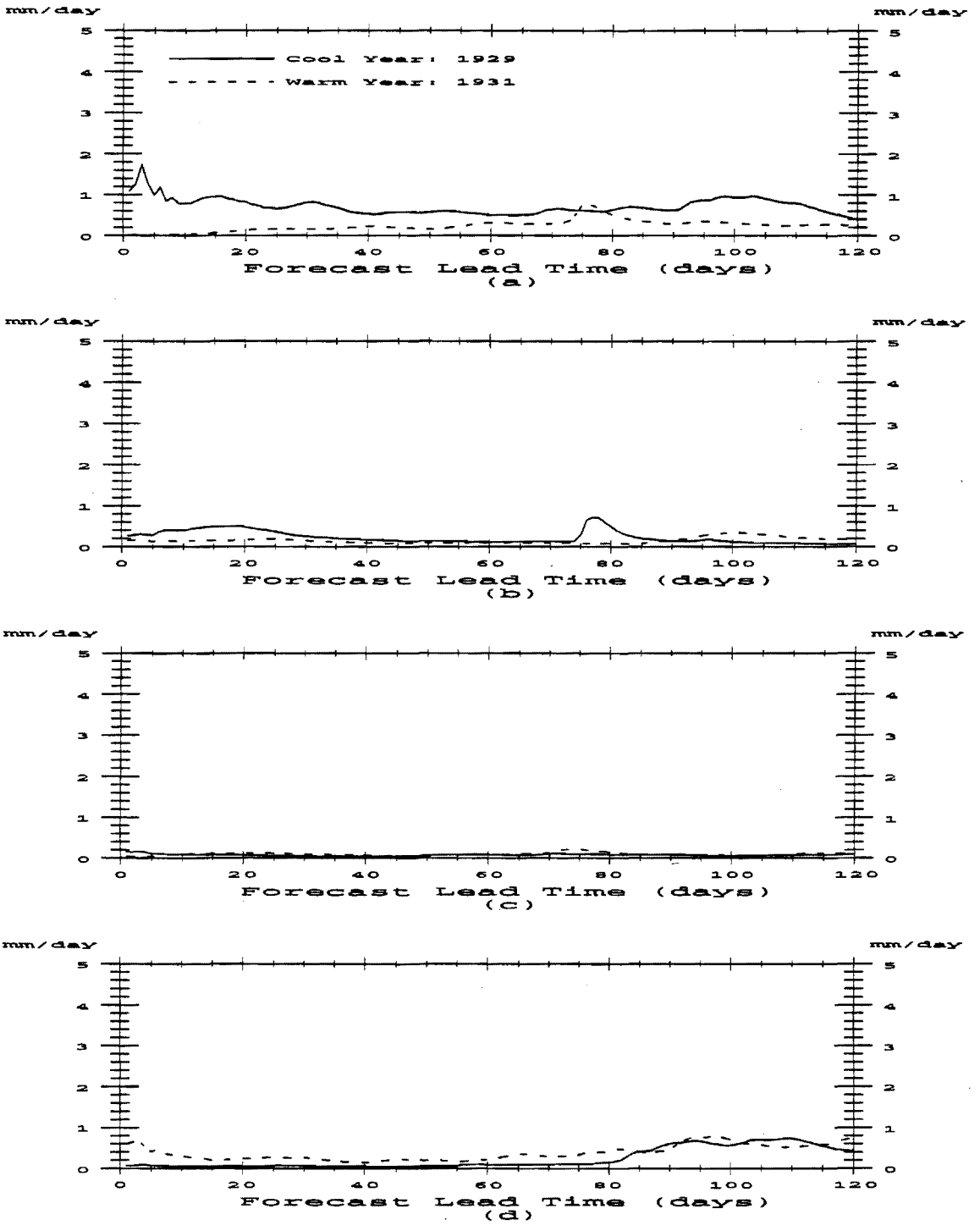

Figure V.21 Average ESP of cool/warm climatic forcing for the forecast horizons beginning a) March 15, b) June 15, c) September 15 and d) December 15 of the coolest (1929) and warmest (1931) years of the first climatic period.

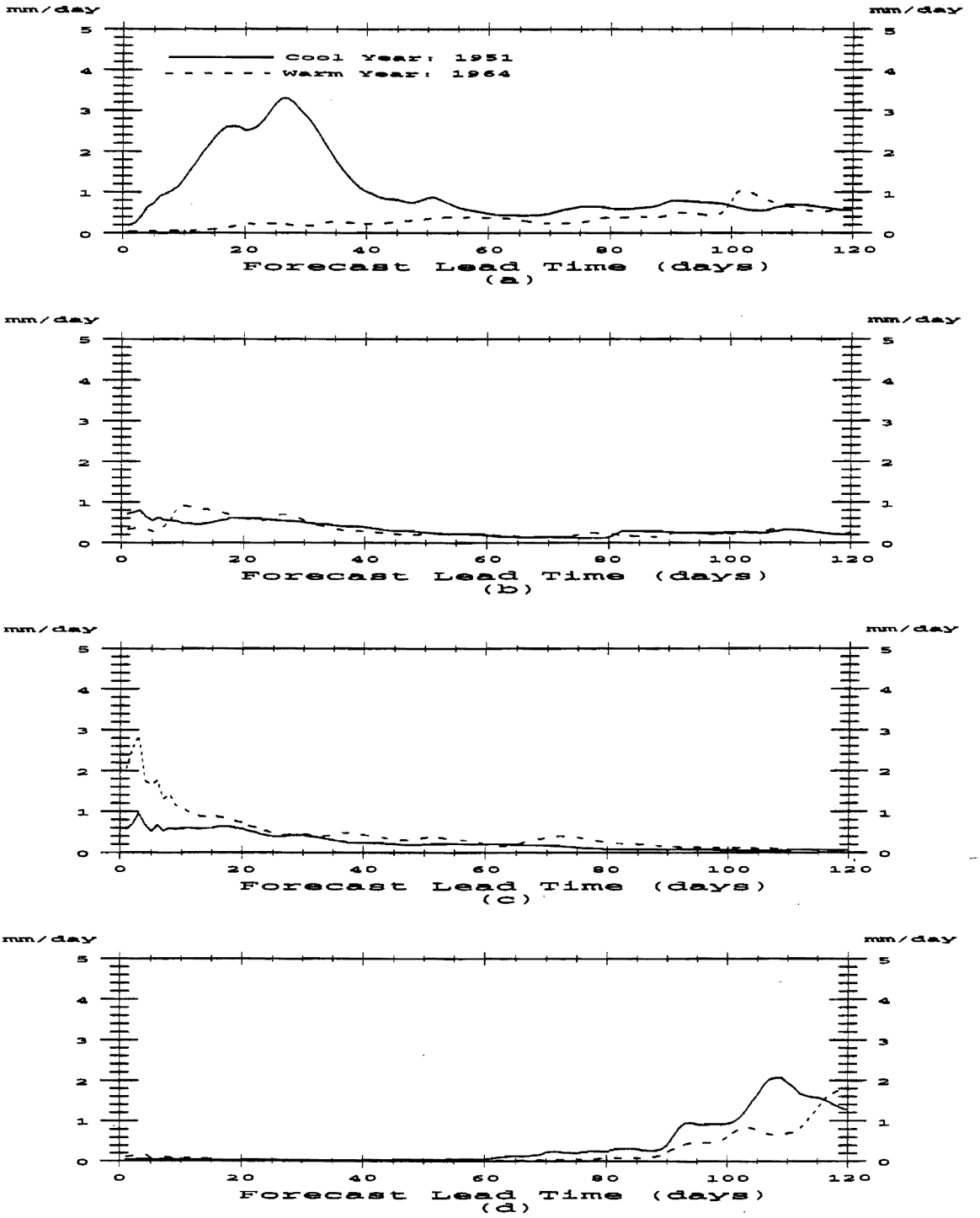

Figure V.22 Average ESP of cool/warm climatic forcing for the forecast horizons beginning a) March 15, b) June 15, c) September 15 and d) December 15 of the coolest (1951) and warmest (1964) years of the second climatic period.

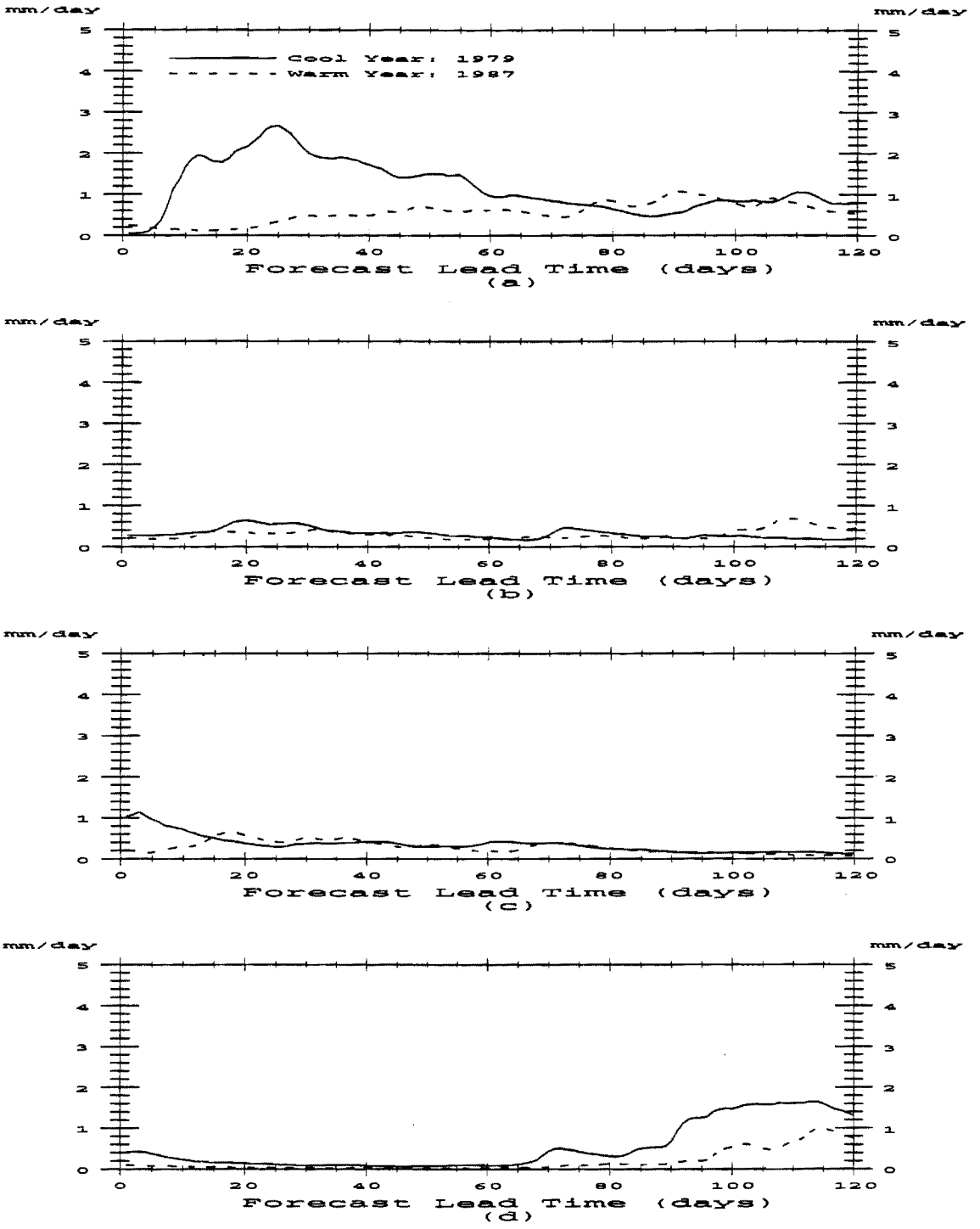

Figure V.23 Average ESP of cool/warm climatic forcing for the forecast horizons beginning a) March 15, b) June 15, c) September 15 and d) December 15 of the coolest (1979) and warmest (1987) years of the third climatic period.

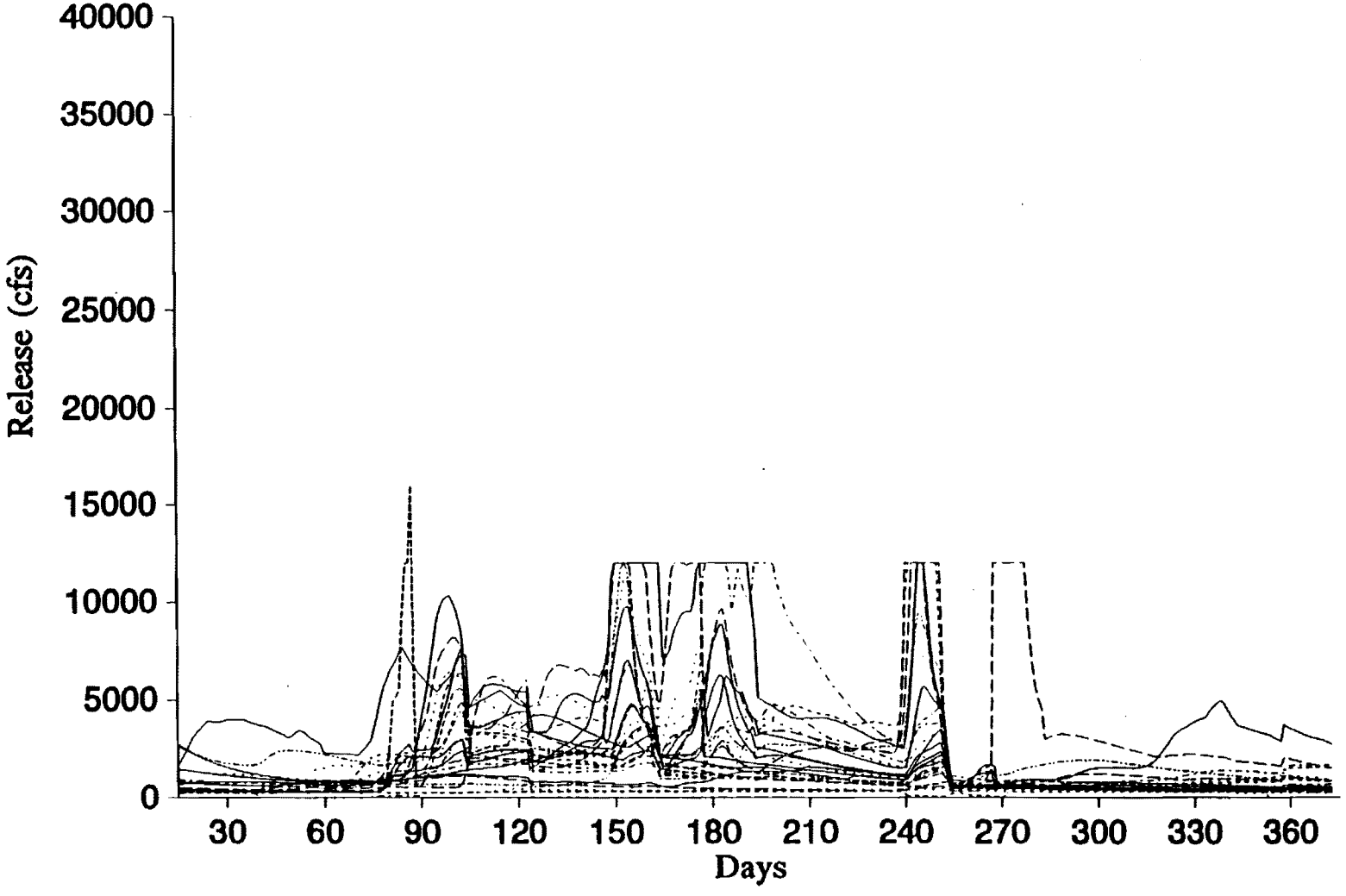

Figure V.24 Forecast-control simulated release sequences, 1925-1949.

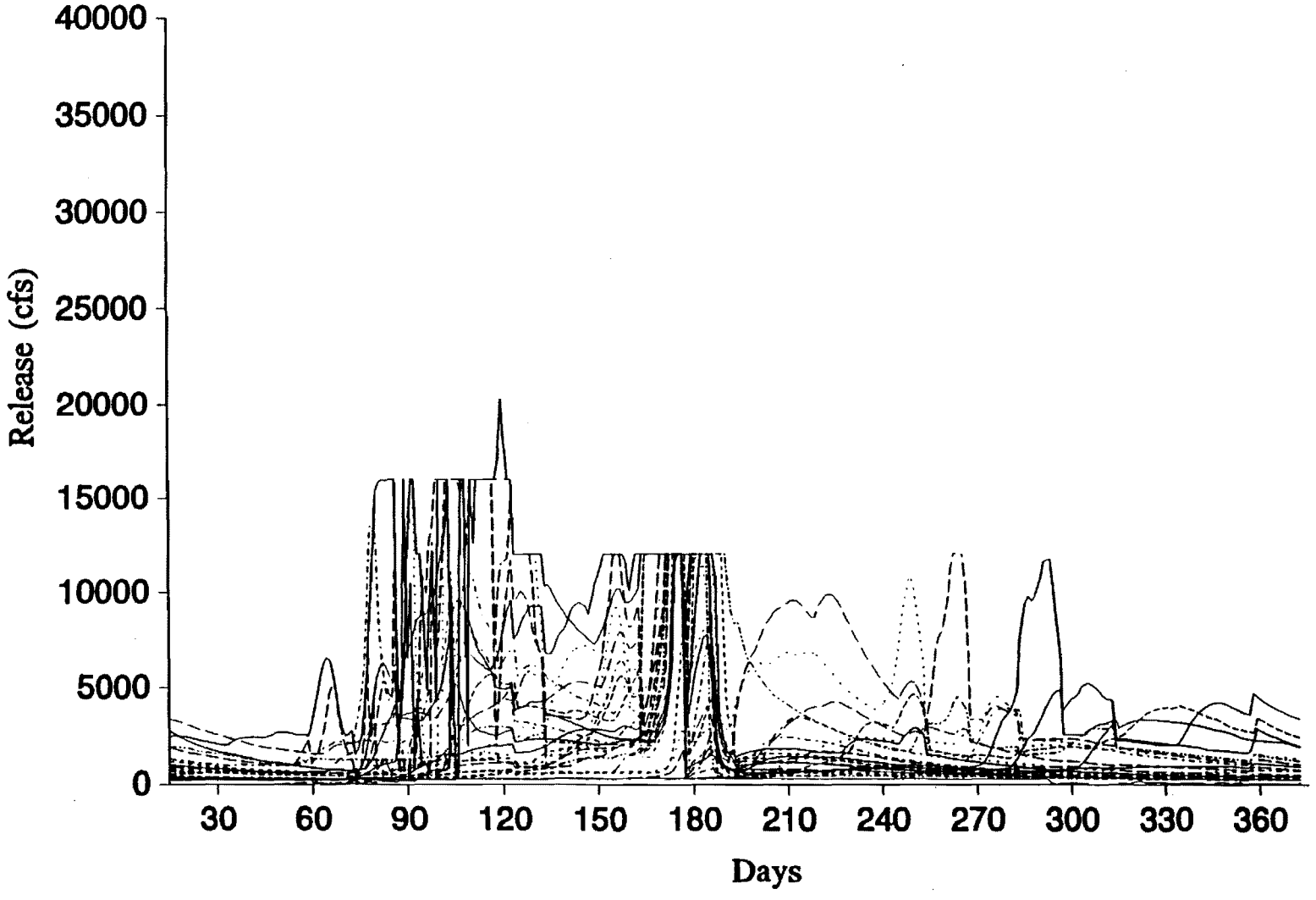

Figure V.25 Forecast-control simulated release sequences, 1949-1974.

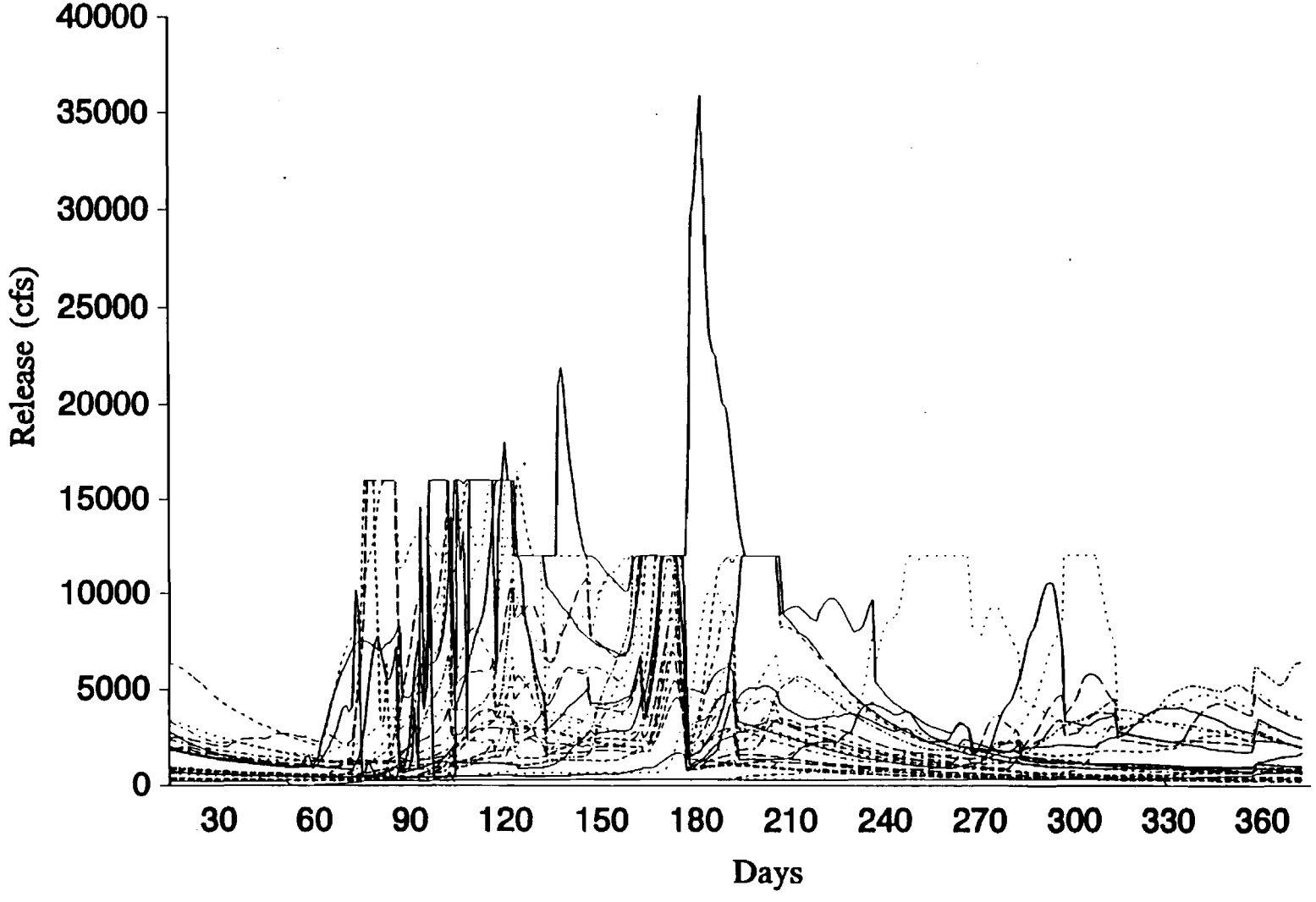

Figure V.26 Forecast-control simulated release sequences, 1965-1988.

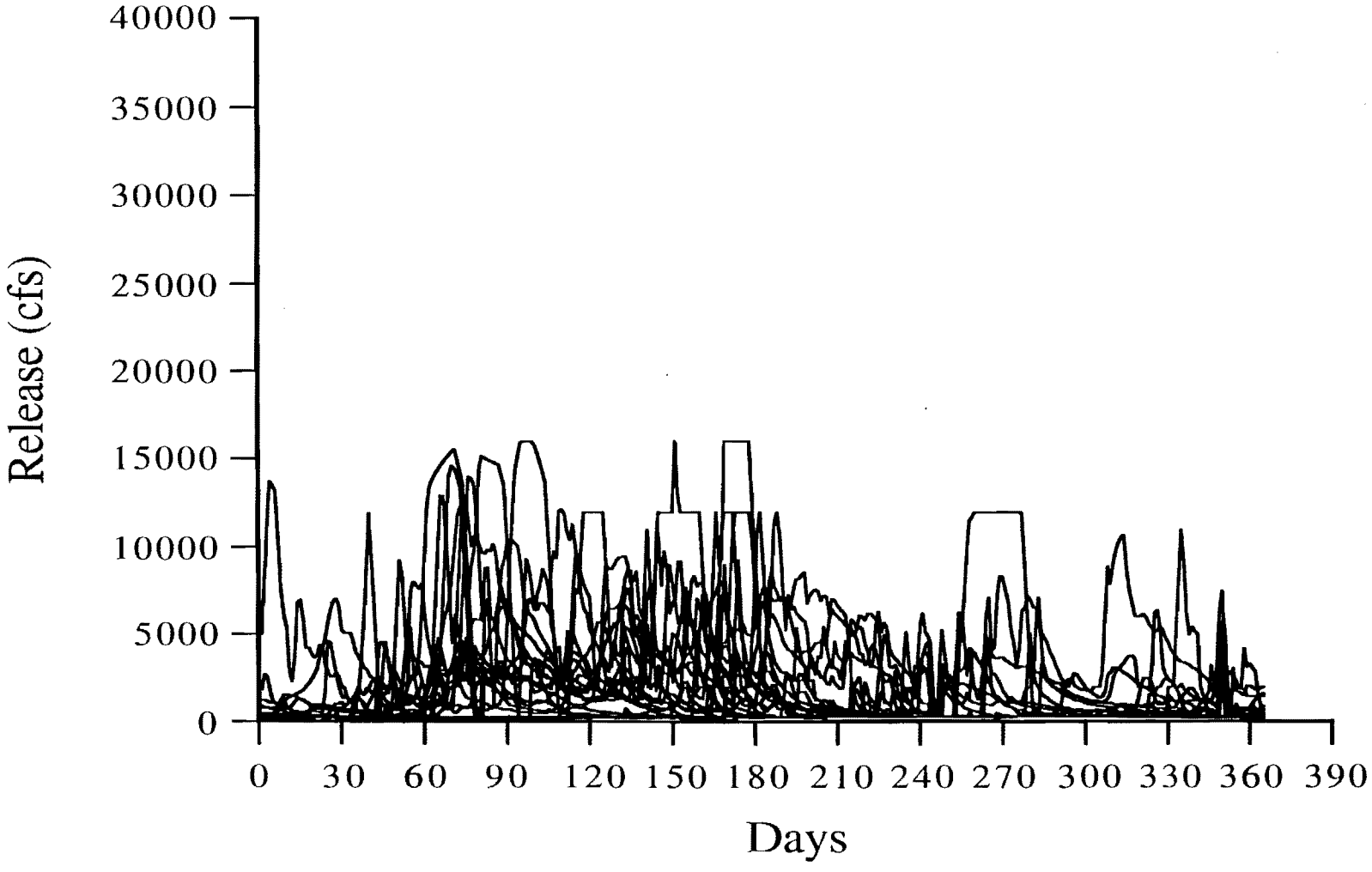

Figure V.27 Current operational practices simulated release sequences, 1925-1944.

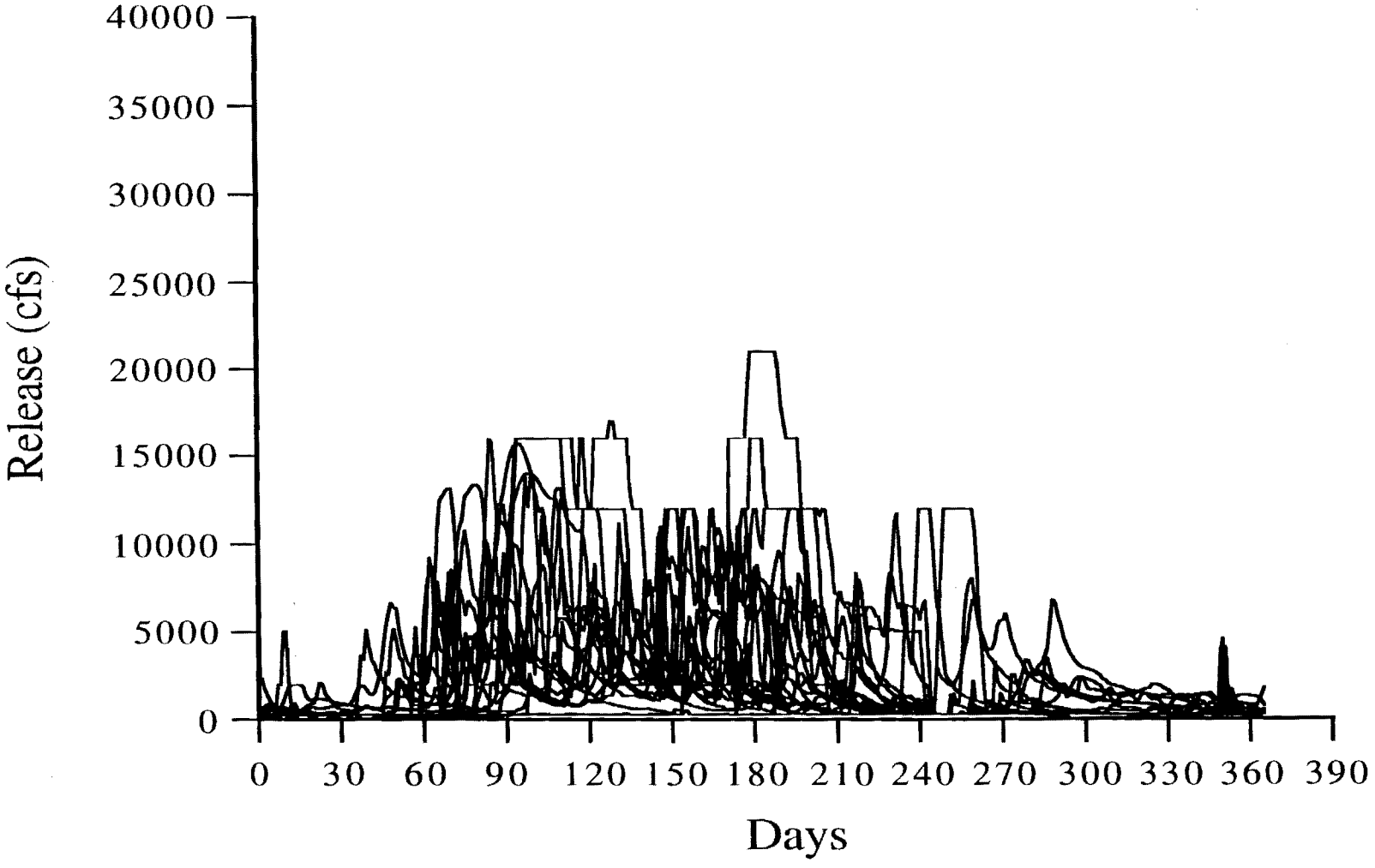

Figure V.28 Current operational practices simulated release sequences, 1945-1964.

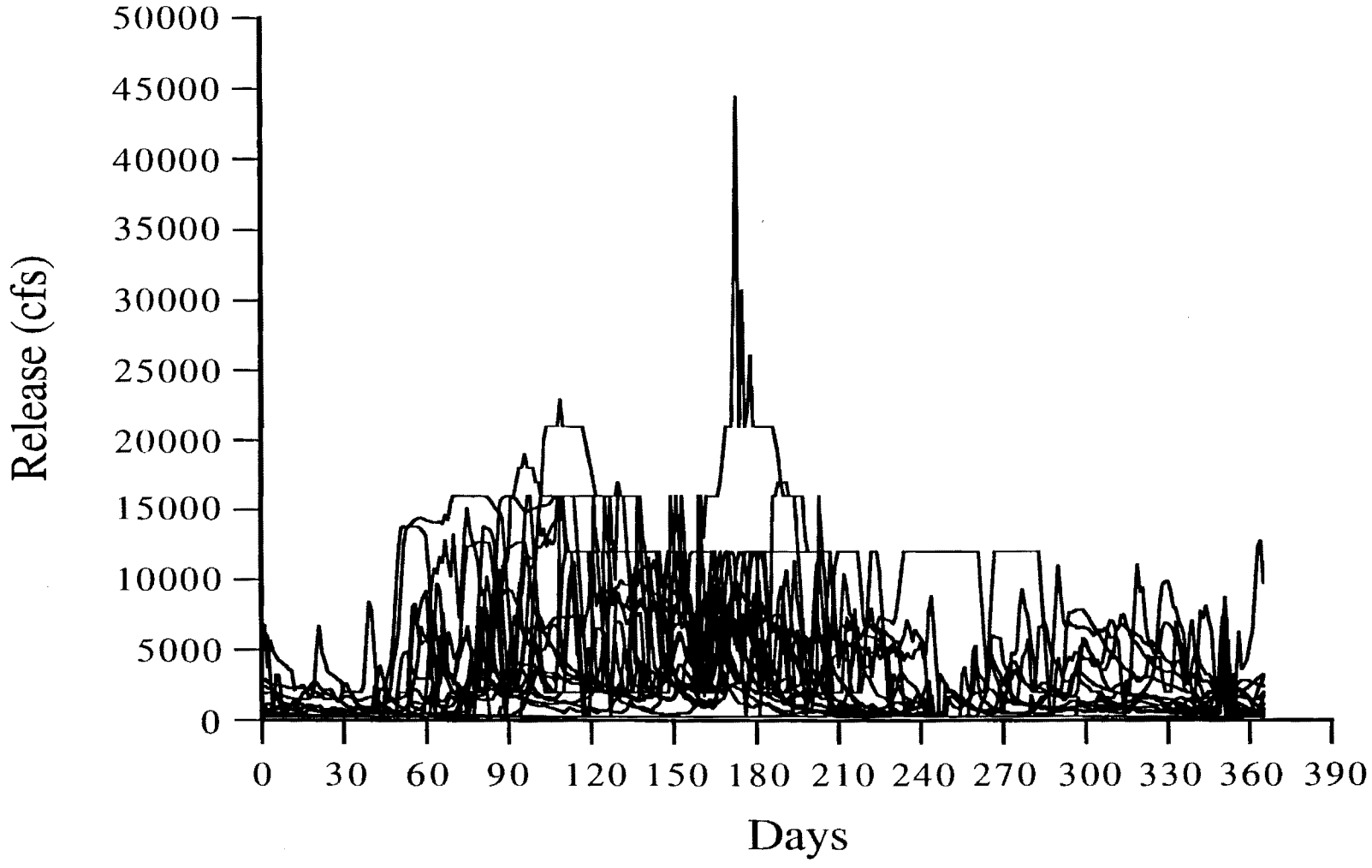

Figure V.29 Current operational practices simulated release sequences, 1965-1984.

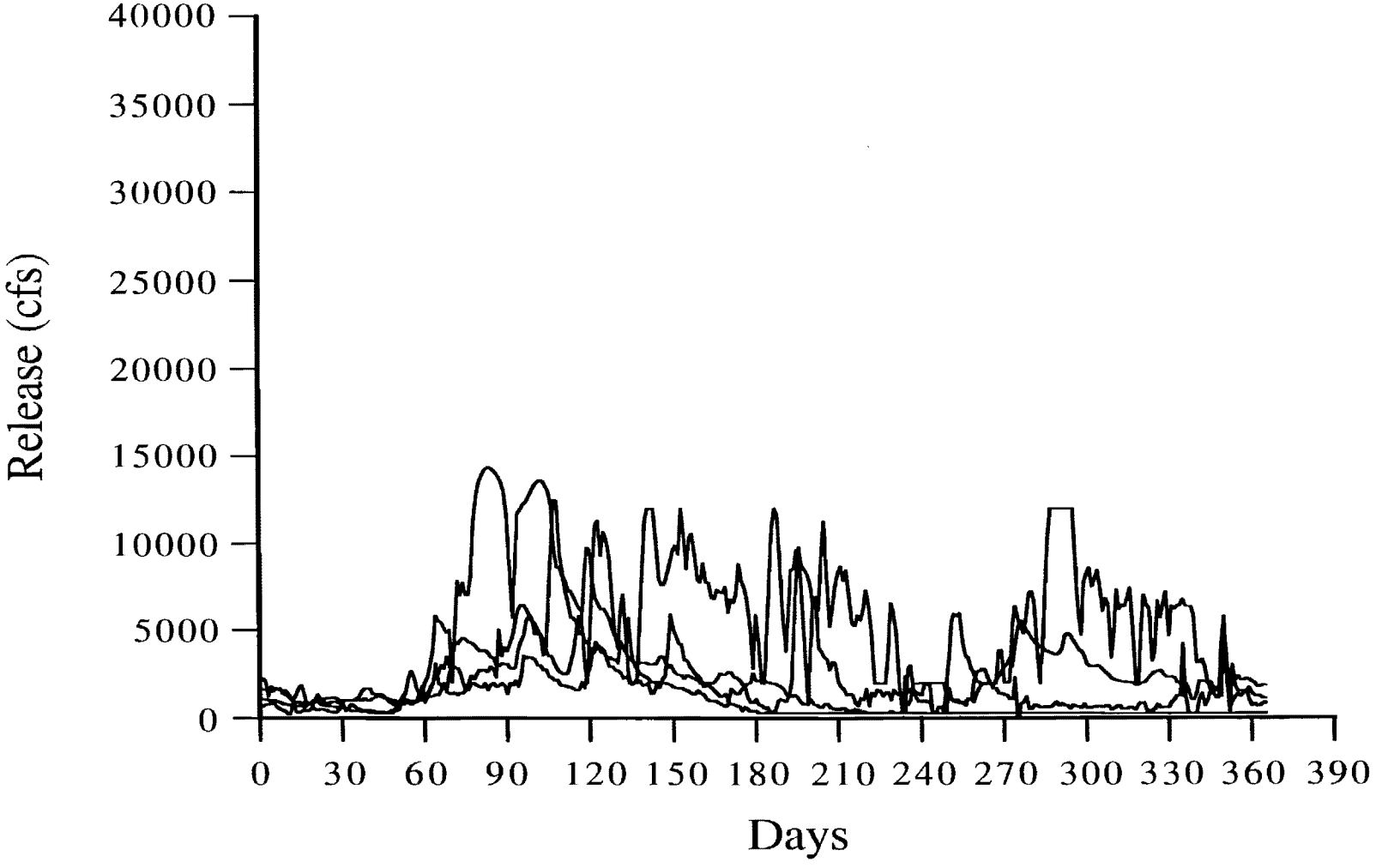

Figure V.30 Current operational practices simulated release sequences, 1985-1988.

VI. SUMMARY, CONCLUSIONS AND RECOMMENDATIONS

The purpose of this work was to determine the sensitivity of the hydrology, the hydrologic forecasts and the operational water management practices to historical climatic forcing in the Upper Des Moines River basin. To the extent that historical climatic periods resemble projected future climatic periods of enhanced greenhouse forcing, the results of this work can be used to assess the sensitivity of forecast/control practices in the basin to potential climate change. The mathematical/numerical tool for the sensitivity study consisted of three main components: the UIFS model, the ESP procedure and an operational reservoir set control procedure. In Chapter III, it was shown that the UIFS model has skill in predicting daily flows in the stream network of the 14,000 km^2 Upper Des Moines River basin.

The sensitivity of the large-basin hydrology was assessed by comparing the atmospheric forcing variables and the model estimated variables for three climatic periods. Key differences in the forcing variables were noted as a) 20 mm/year less mean areal precipitation in the first climatic period, b) a 2°C cooler temperature in the second climatic period compared to the first period and an additional 1°C cooler temperature during the winter of the third period compared to the second, and c) decreasing potential evapotranspiration from the earliest to the latest climatic period. Study of the standardized anomalies of precipitation and temperature over the basin showed no significant co-variation of trends for those two variables. It was found that small differences in the climatic forcing produce large differences in the hydrologic catchment response (i.e., streamflow) which require models of soil water for their understanding and prediction. Differences in the model estimated soil water included a) a greater seasonal range between the maximum and minimum total soil water in the first climatic period and b) a higher value of total soil water in the third climatic period. Differences in temporal scales of soil water content and the interaction between soil water content with precipitation and temperature were also analyzed for each climatic period and were presented in detail in section 4.5. Weak feedback from soil water to surface air temperature was detected on a daily scale. The distribution of soil water anomalies was negatively skewed in almost all cases. While the upper soil water temporal scales were similar during the three climatic periods, those of total water content were significantly different. The latter observation suggests that the main effect of changing climatic forcing on the hydrology of the region is a low frequency one.

The reliability of the ESP forecasts was discussed in Chapter V. The two-standard deviation bounds were adequate to enclose the observed flows for periods of extreme (wettest/driest and coolest/warmest) climatic forcing for most cases. Occasional exceptions were in spring and fall, when extreme flows occur. In general, the worst conditions were

for wettest historical periods when the non-normality of high-flows was apparent. Warmer and drier periods increase ESP reliability. The sensitivity of the hydrologic forecasts and the operational water management practices were also presented in Chapter V. Key findings are that the ESP predictions for a) wet vs. dry and b) cool vs. warm initial conditions show large differences with long persistence in the spring months and small differences for the summer months for all climatic conditions. Exceptions were the wet and dry initial conditions of the first climatic period where there was only a small difference in the spring months. If, in addition to different initial conditions, forcing is categorized as above/below average for precipitation and temperature for each case of corresponding initial condition, ESP predictions show larger differences with longer persistence. The reservoir set controller was seen to adequately handle the climatic variability within each climatic period for all three climatic periods, with minimal excessive and deficit releases. This indicates that the combined forecast-control scheme generally improves reservoir performance and that reservoirs can significantly mitigate the effects of climate changes when controlled effectively.

The main recommendation arising from the results of this study is that management schemes for existing reservoirs be optimized before an assessment of climate impacts is made. Management procedures, as the coupled forecast-control scheme used in this work, would significantly reduce reservoir sensitivities to climatic variability and change. They represent an easily-implementable, inexpensive way to mitigate the adverse effects of a potential change in climatic forcing trends and variability.

REFERENCES

Anderson, E.A., 1973: "National Weather Service River Forecast System-Snow Accumulation and Ablation Model," *NOAA Technical Memorandum NWS HYDRO-17*, Office of Hydrology, National Weather Service, NOAA, Silver Spring, Maryland.

Bae, D.H. and K.P. Georgakakos, 1992: "Hydrologic Modeling for Flow Forecasting and Climate Studies in Large Drainage Basins," *IIHR Report 360*, Iowa Institute of Hydraulic Research and Department of Civil and Environmental Engineering, The University of Iowa, Iowa City, Iowa, 252 pages.

Bae, D.H. and K.P. Georgakakos, 1993: "University of Iowa Forecast System, UIFS, Version 1, A User's Manual," *IIHR Limited Distribution Report No. 205*, Iowa Institute of Hydraulic Research, The University of Iowa, Iowa City, Iowa, 67 pages.

Burnash, R.J.C., Ferral, R.L. and R.A. McGuire, 1973: "A Generalized Streamflow Simulation System-Conceptual Modeling for Digital Computers," National Weather Service-NOAA, and the State of California Department of Water Resources Technical Report, Joint Federal-State River Forecast Center, Sacramento, California, 204 pages.

Crowley, T.J., 1990: "Are There Any Satisfactory Geologic Analogs for a Future Greenhouse Warming?," *Journal of Climate*, Vol. 3 No. 11, pages 1282-1292.

Day, G.N., 1985: " Extended Streamflow Forecasting Using NWSRFS," *Journal of Water Resources Planning and Management*, 111(2), 157-170.

Dooge, J.C.I., 1973: "Linear Theory of Hydrologic Systems," ARS Technical Bulletin No. 1468, Agricultural Research Service, U.S. Department of Agriculture, Washington, D.C., 327 pages.

Farnsworth, R.K., Thompson, E.S. and E.L. Peck, 1982: "Evaporation Atlas for the Contiguous 48 United States," NOAA Technical Report NWS 33, Office of Hydrology, National Weather Service, Silver Spring, Maryland, 26 pages.

Georgakakos, A.P. and H. Yao, 1993: "New Control Concepts for Uncertain Water Resources Systems: 1, Theory," *Water Resources Research*, Vol. 29, No. 6, pages 1505-1516.

Georgakakos, A.P., Georgakakos, K.P. and E.A. Baltas, 1990: "A State Space Model for Hydrologic River Routing," *Water Resources Research*, Vol. 26, No. 5, pages 827-838.

Georgakakos, K.P, 1986: "A Generalized Stochastic Hydrometeorological Model for Flood and Flash-Flood Forecasting, 1, Formulation," *Water Resources Research*, Vol. 22, No. 13, pages 2083-2095.

Georgakakos, K.P., Rajaram, H. and S.G. Li, 1988: "On Improved Operational Hydrologic Forecasting of Streamflows," *IIHR Report No.* 325, Iowa Institute of Hydraulic Research and Department of Civil and Environmental Engineering, The University of Iowa, Iowa City, Iowa, 162 pages.

Giorgi, F and L.O. Mearns, May 1991: "Approaches to the Simulation of Regional Climate Change: A Review," *Reviews of Geophysics*, 29, 2, pages 191-216.

Gleick, P.H., 1987: "Regional Hydrologic Consequences of Increases in Atmospheric CO_2 and Other Trace Gases," *Climate Change*, 10, 137-161.

Gleick, P.H., August 1989: "Climate Change, Hydrology, and Water Resources." *Reviews of Geophysics*, 27, 3, pages 329-344.

Houghton, J.T., Jenkins, G.J. and J.J. Ephraums, 1990: *Climate Change, The IPCC Scientific Assessment*, Cambridge University Press, New York, 365 pages.

Kitanidis, P.K. and R.L. Bras, 1978: "Real Time Forecasting of River Flows," R.M. Parsons Laboratory for Water Resources and Hydrodynamics, Department of Civil Engineering, *MIT, Technical Report No. 235*, 324 pages.

Larson, L.W., 1975: "Precipitation Model," *National Weather Service River Forecast System (NWSRFS) User's Manual*, Hydrologic Research Laboratory, NWS-NOAA, Silver Spring, Maryland.

Larson, L.W. and S. VanDemark, 1979: "Mean Areal Precipitation," *National Weather Service River Forecast System (NWSRFS) User's Manual*, Hydrologic Research Laboratory, NWS-NOAA, Silver Spring, Maryland.

Lettenmaier, D.P. and T.Y. Gan, January 1990:"Hydrologic Sensitivities of the Sacramento-San Joaquin River Basin, California, to Global Warming," *Water Resources Research* Vol. 26, No. 1, pages 69-86.

Lough, J.M., Wigley, T.M.L. and J.P. Palutikof, October, 1983: "Climate and Climate Impact Scenarios for Europe in a Warmer World," *Journal of Climate and Applied Meteorology*, Vol. 22, pages 1673-1684.

Mearns, L.O., Gleick, P.H. and S.H. Schneider, 1990: "Climate Forecasting," *Climate Change and U.S. Water Resources*, ed. P.E. Waggoner, John Wiley and Sons, New York, 41-73.

MINITAB Inc., 1989: "MINITAB Reference Manual, Release 7," Minitab, Inc., State College, Pennsylvania.

Pruitt, W.O., 1966: "Empirical Method of Computing Evapotranspiration Using Primarily Evaporation Pans," *Proceedings on Evapotranspiration and its Role in Water Resources Management*, American Society of Agricultural Engineers, 57-71.

Revelle, R.R. and P.E. Waggoner, 1983: "Effects of a Carbon Dioxide-Induced Climatic Change on Water Supplies in the Western United States," *Changing Climate, Reports of the Carbon Dioxide Assessment Committee*, National Academy Press, Washington, D.C., pages 419-432.

Schneider, S.H., Gleick, P.H. and L.O. Mearns, 1990: "Prospects for Climate Change," *Climate Change and U.S. Water Resources*, ed. P.E. Waggoner, John Wiley and Sons, New York, 41-73.

Smith, J.A., Day, G.N. and M.D. Kane, 1991: "A Nonparametric Framework for Long-Range Streamflow Forecasting," *WMO/TD-No. 428*, World Meteorological Organization, Geneva, Switzerland, 28 pages.

Tennessee Valley Authority, September 1988: "Sensitivity of the Tennessee Valley Authority Reservoir System to Global Climate Change," *Report No. WR28-1-680-101* Tennessee Valley Authority Engineering Laboratory, Norris, Tennessee, 131 pages.

U.S. Army Corps of Engineers, 1968: "Upper Mississippi River Basin, Des Moines River, Iowa and Minnesota, Master Reservoir Regulation Manual," U.S. Army Engineer District, Rock Island, Illinois.

U.S. Army Corps of Engineers, 1983: "Upper Mississippi River Basin, Des Moines River, Iowa and Minnesota, Master Reservoir Regulation Manual, Saylorville Lake" U.S. Army Engineer District, Rock Island, Illinois.

Wei, W.W.S., 1990: *Time Series Analysis, Univariate and Multivariate Methods*, Addison-Wesley Publishing Company, Redwood City, California, 478 pages.

WMO - World Meteorological Organization, 1990: "Scientific Plan for the Global Energy and Water Cycle Experiment, World Climate Research Programme," *WMO/TD-No. 376*, WCRP-40, Geneva, Switzerland, 83 pages.

Yao, H. and A.P. Georgakakos, 1993: "New Control Concepts for Uncertain Water Resources Systems: 2, Reservoir Management," *Water Resources Research*, Vol. 29, No. 6, pages 1517-1526.

APPENDIX

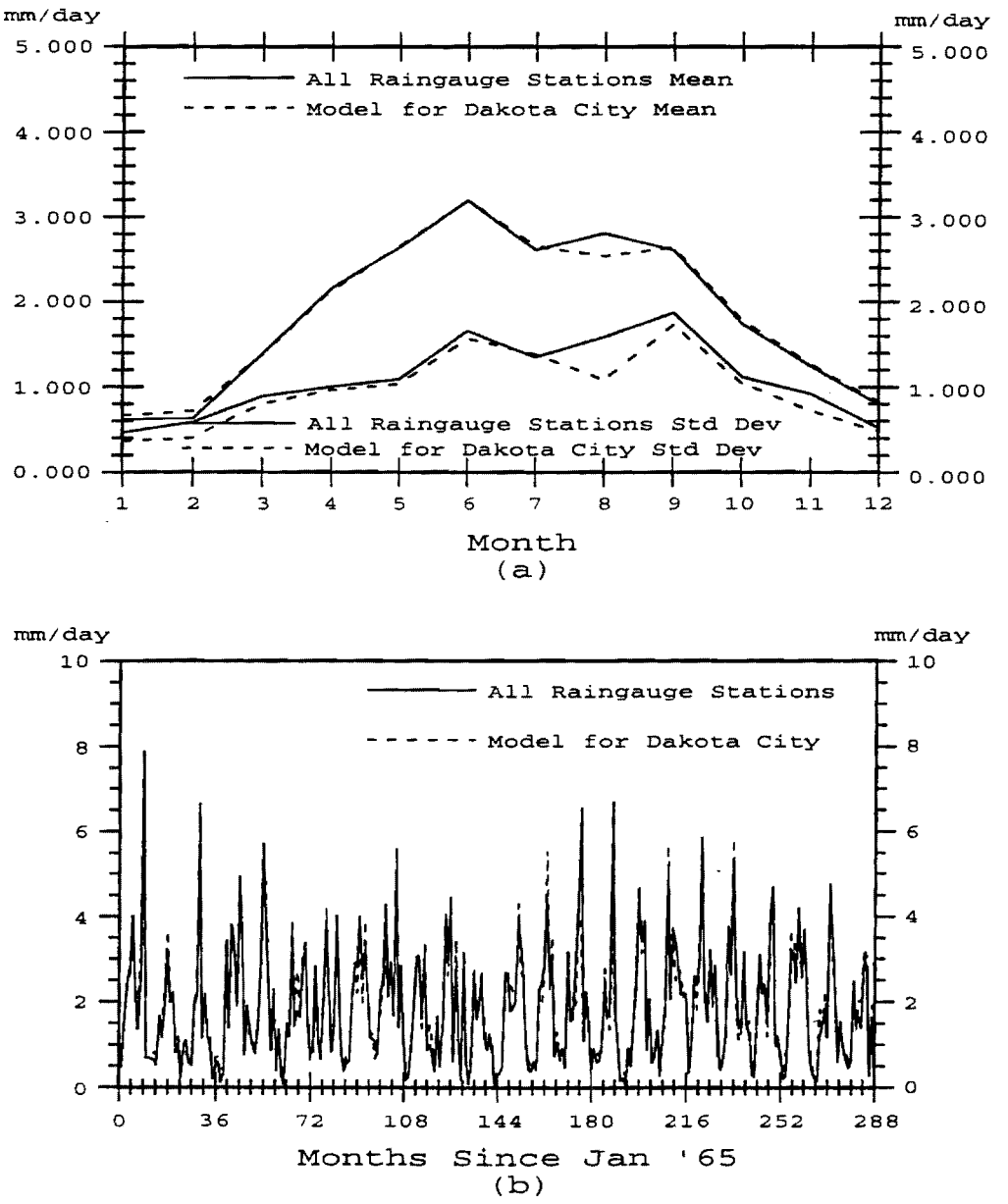

Figure A.1 Monthly precipitation determined by the NWS weighted average method using all described stations (solid) and the regression model (dashed) for Dakota City a) seasonal cycle of means and standard deviations averaged from 1965-1988 and b) monthly means since January 1965.

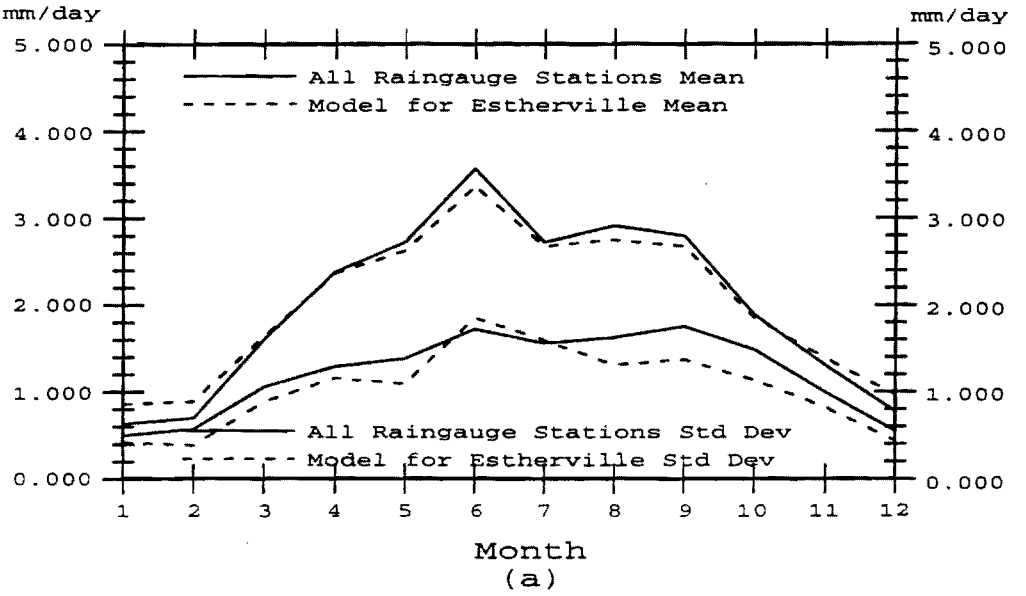

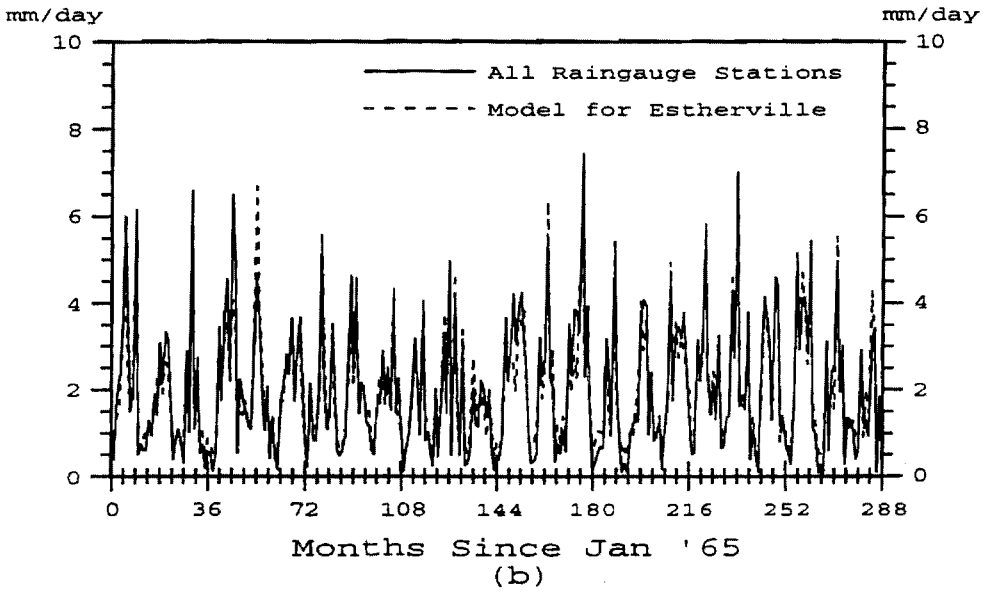

Figure A.2 Monthly precipitation determined by the NWS weighted average method using all described stations (solid) and the regression model (dashed) for Estherville a) seasonal cycle of means and standard deviations averaged from 1965-1988 and b) monthly means since January 1965.

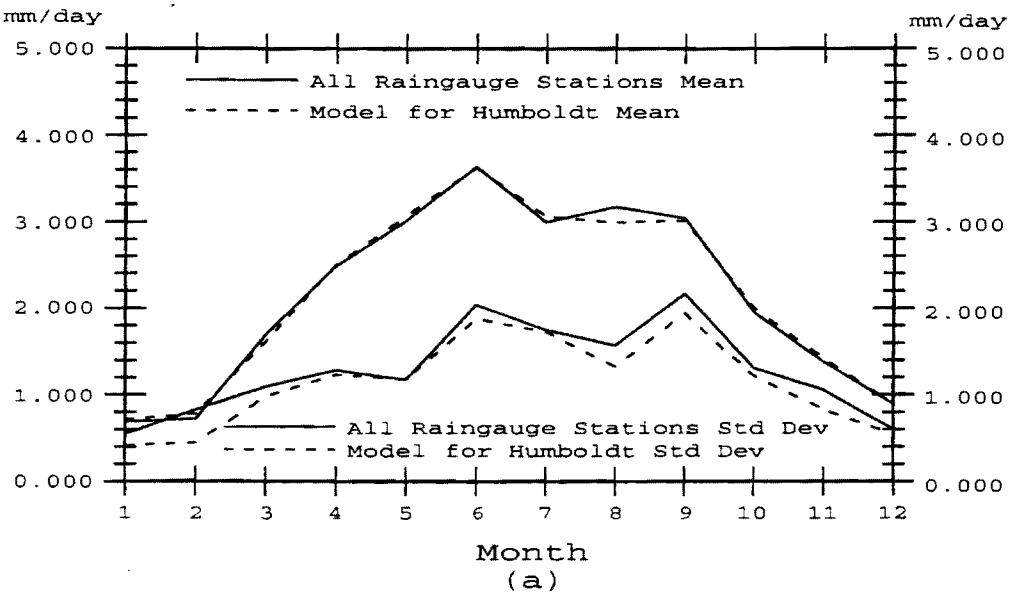

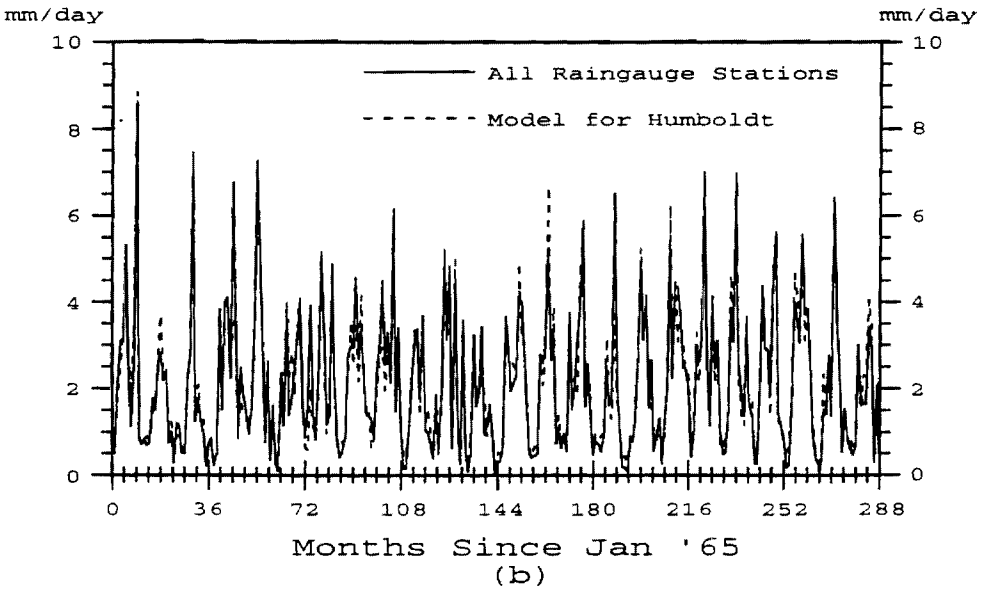

Figure A.3 Monthly precipitation determined by the NWS weighted average method using all described stations (solid) and the regression model (dashed) for Humboldt a) seasonal cycle of means and standard deviations averaged from 1965-1988 and b) monthly means since January 1965.

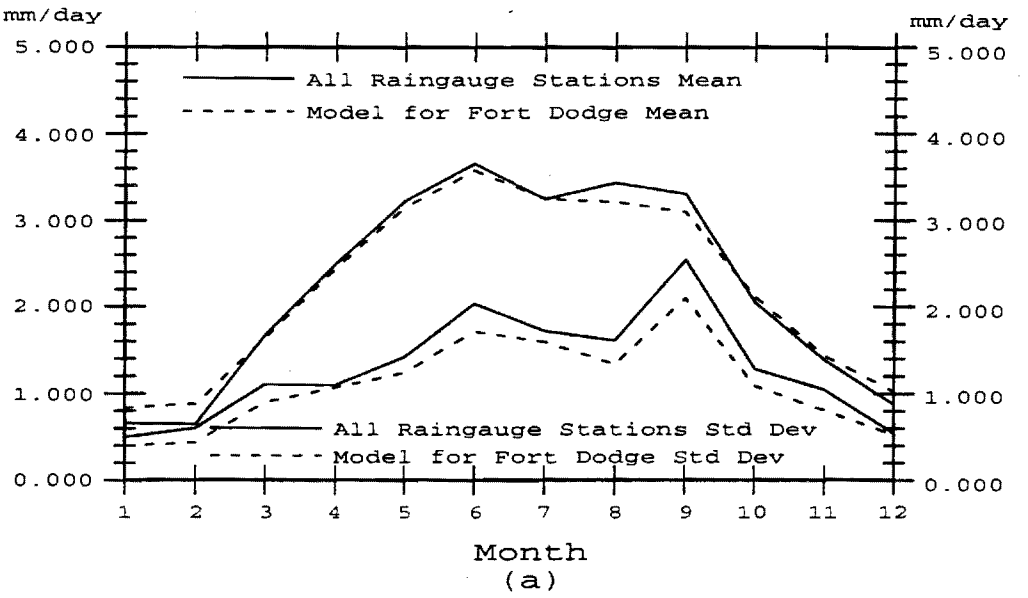

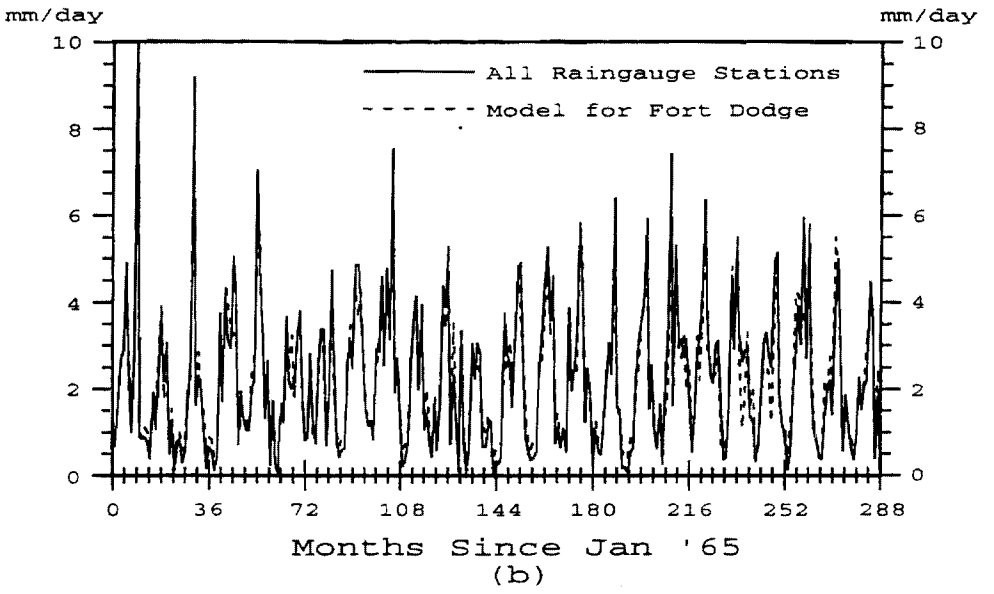

Figure A.4 Monthly precipitation determined by the NWS weighted average method using all described stations (solid) and the regression model (dashed) for Fort Dodge a) seasonal cycle of means and standard deviations averaged from 1965-1988 and b) monthly means since January 1965.

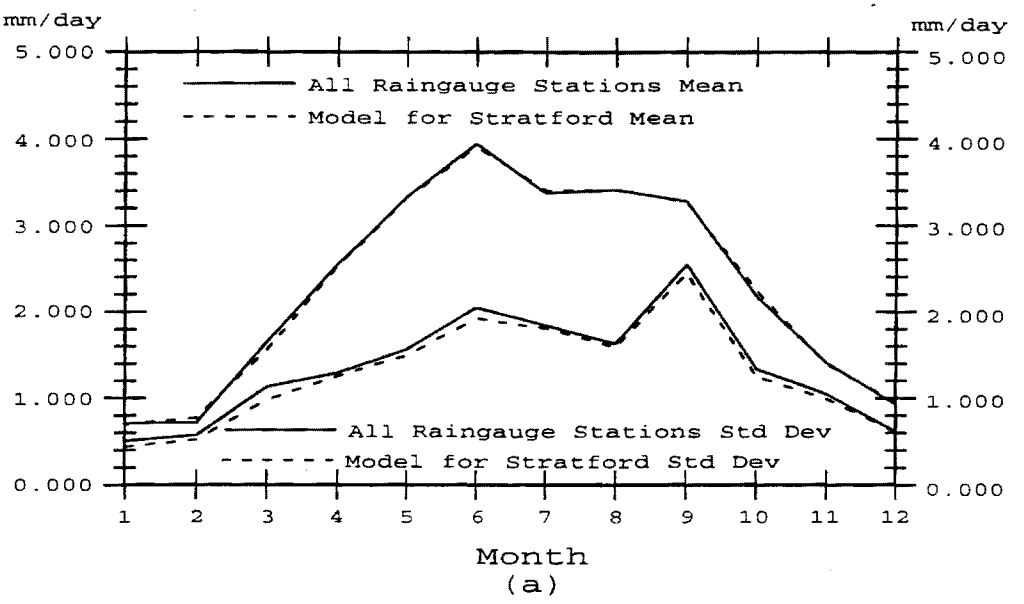

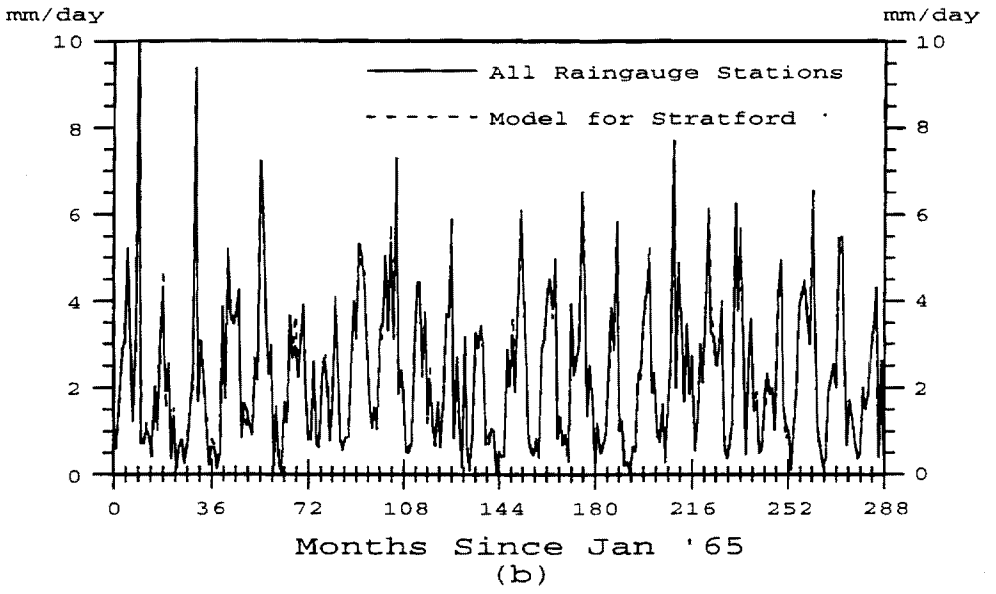

Figure A.5 Monthly precipitation determined by the NWS weighted average method using all described stations (solid) and the regression model (dashed) for Stratford a) seasonal cycle of means and standard deviations averaged from 1965-1988 and b) monthly means since January 1965.

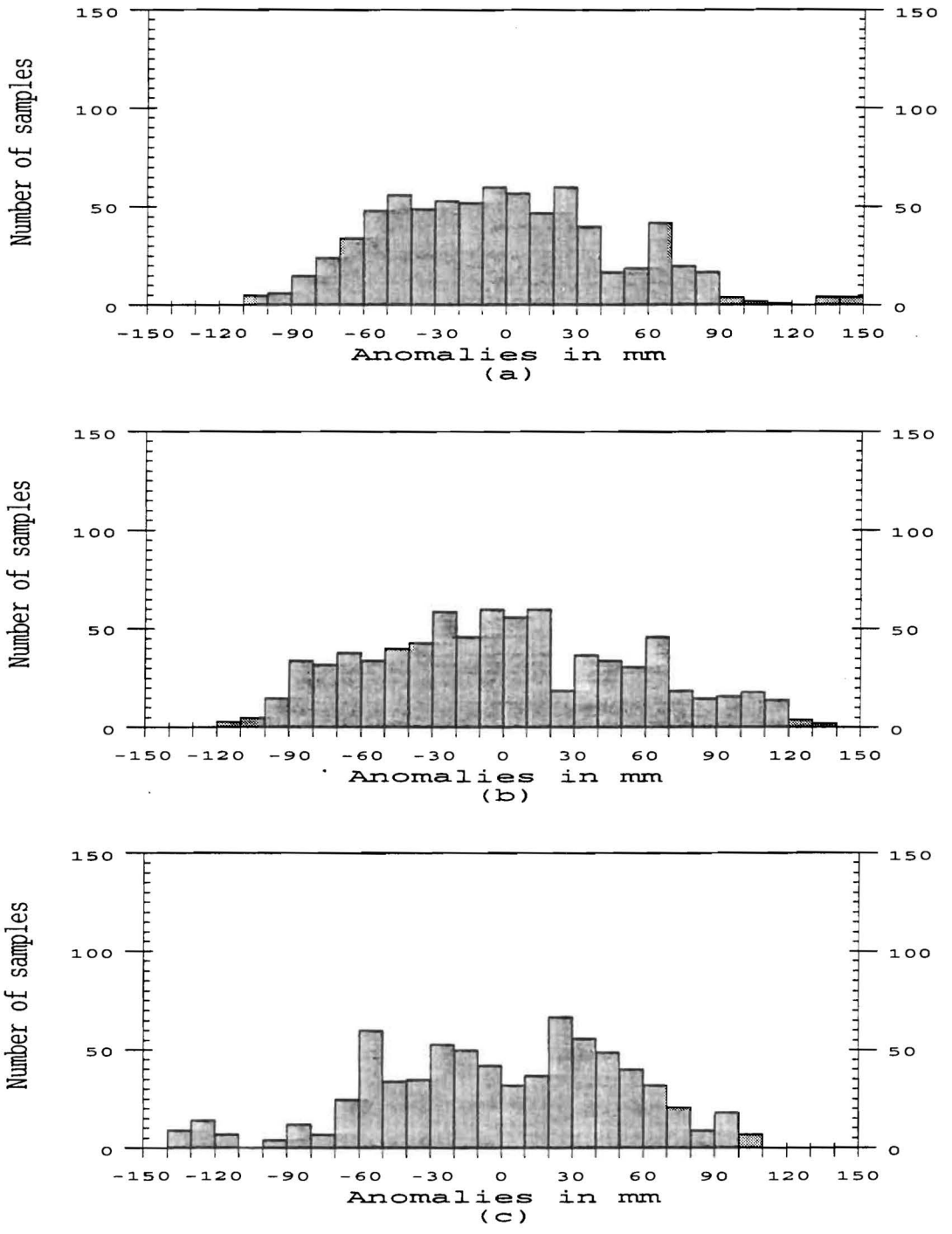

Figure A.6 Total soil water content daily anomaly distribution in September for a) 1925-1949, b) 1949-1974 and c) 1965-1988.

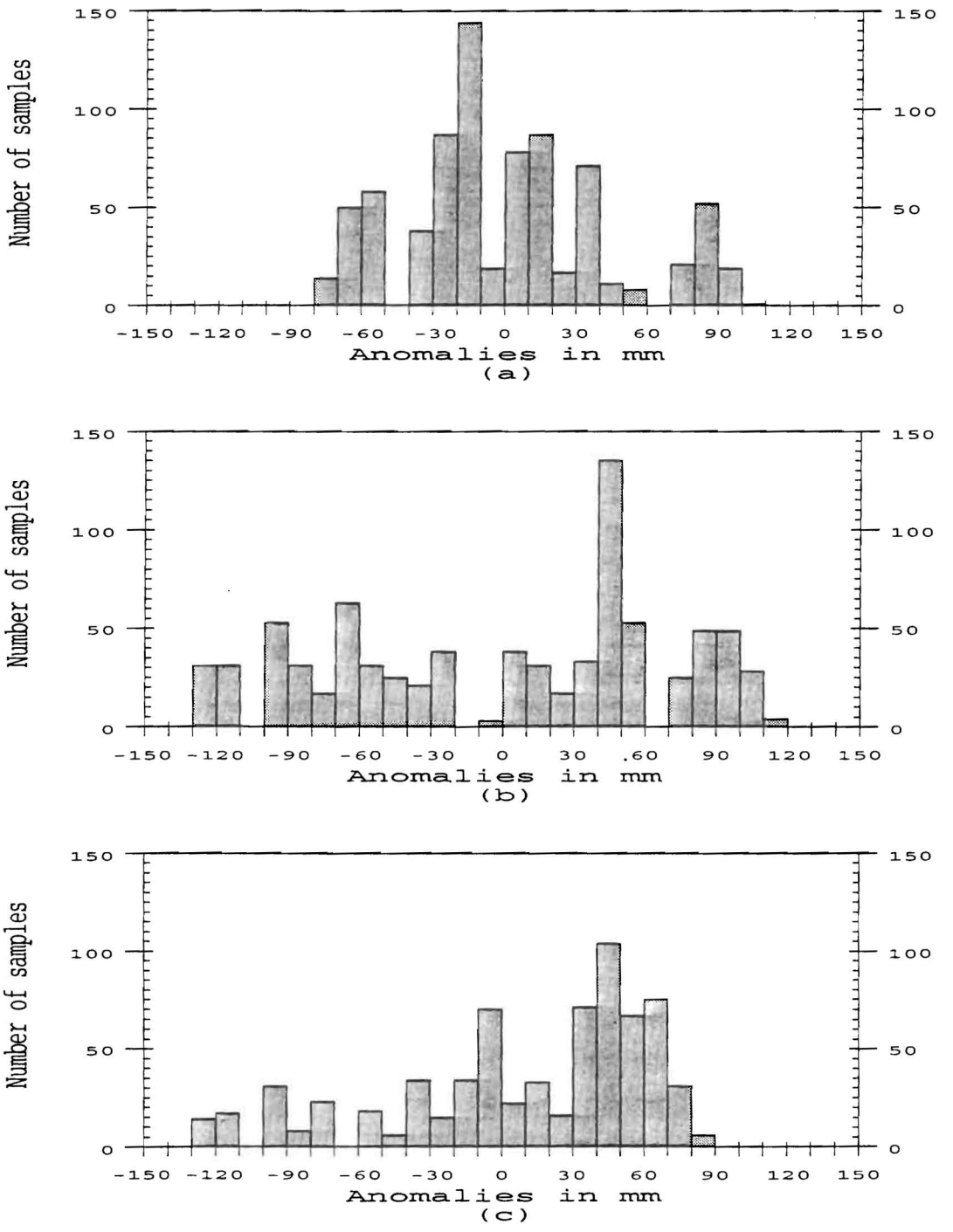

Figure A.7 Total soil water content daily anomaly distribution in December for a) 1925-1949, b) 1949-1974 and c) 1965-1988.

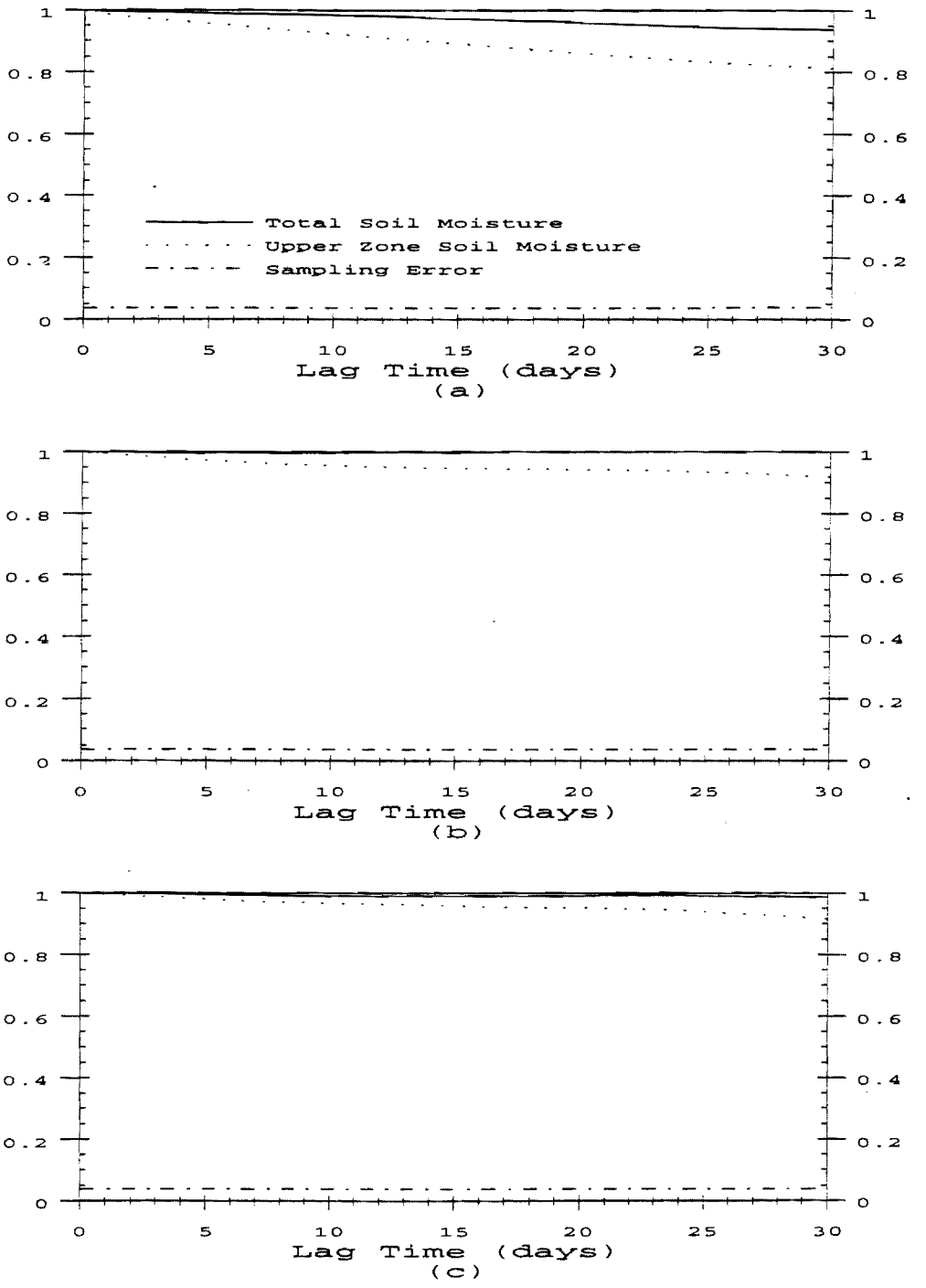

Figure A.8 Auto-correlation of total soil water content (solid line) and upper zone soil water content (dashed line) in December for a) 1925-1949, b) 1949-1974 and c)1965-1988.

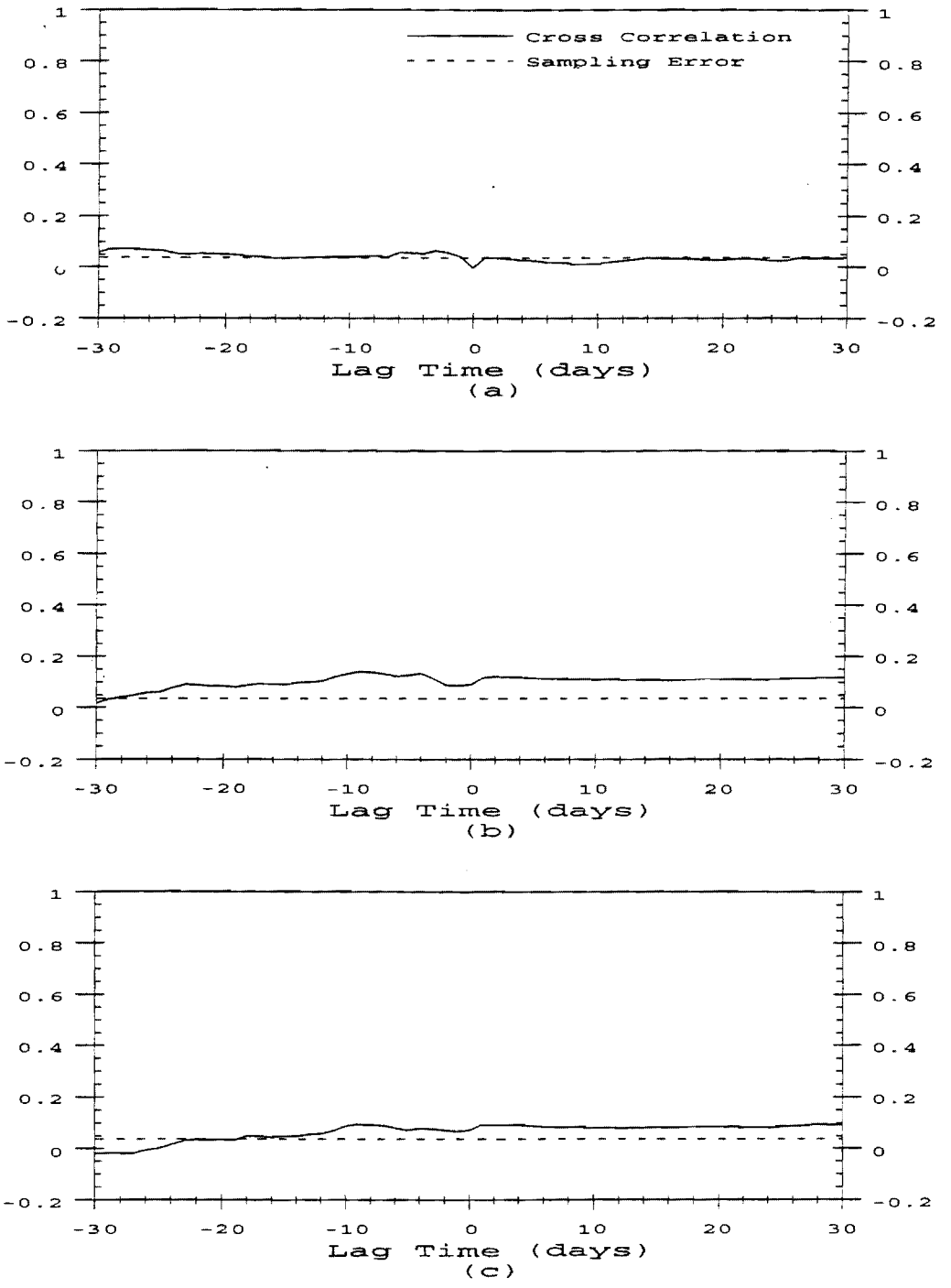

Figure A.9 Cross-correlation of precipitation and upper zone soil water content in December for a) 1925-1949, b) 1949-1974 and c)1965-1988.

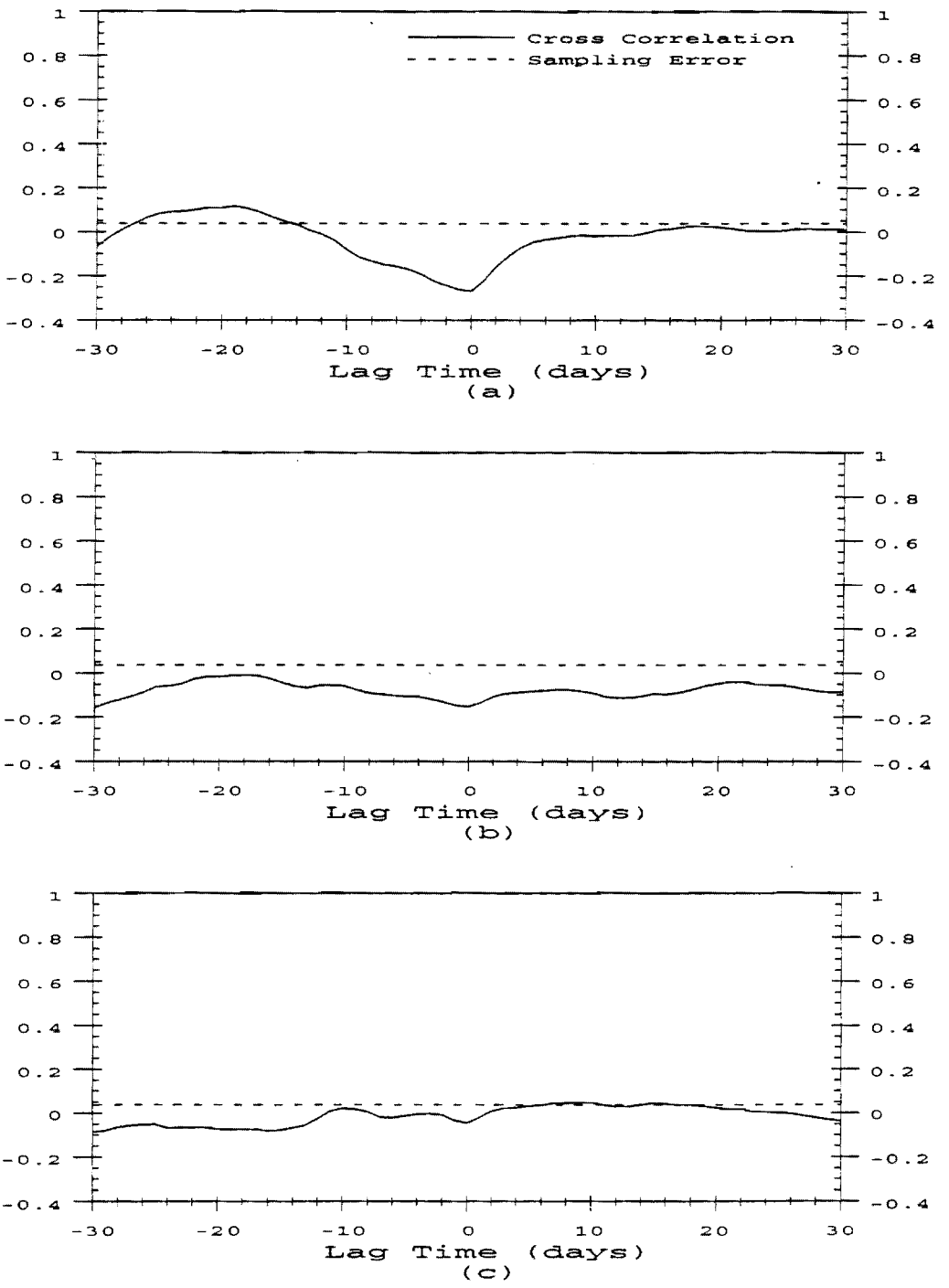

Figure A.10 Cross-correlation of temperature and upper zone soil water content in September for a) 1925-1949, b) 1949-1974 and c)1965-1988.

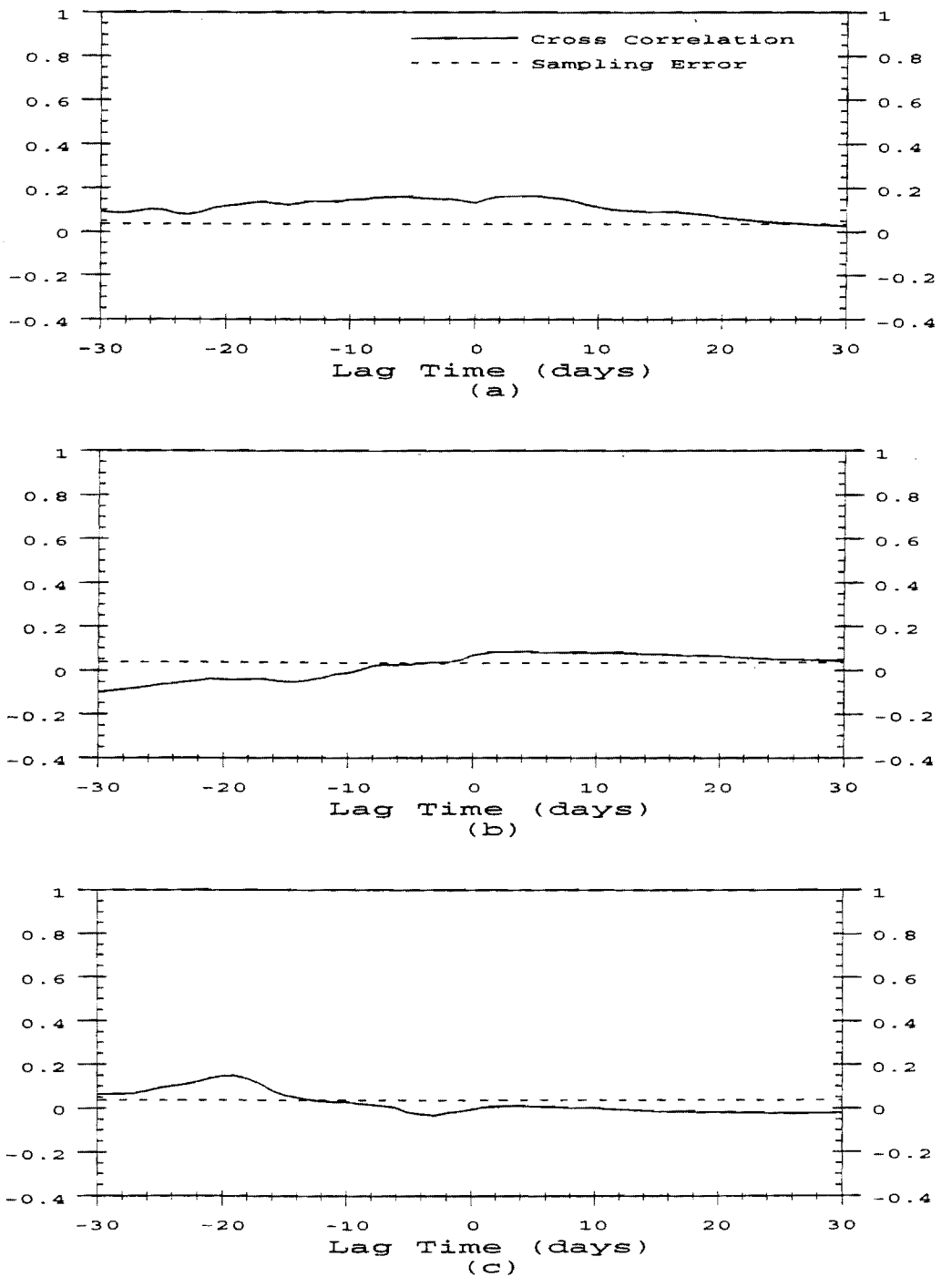

Figure A.11 Cross-correlation of temperature and upper zone soil water content in December for a) 1925-1949, b) 1949-1974 and c)1965-1988.

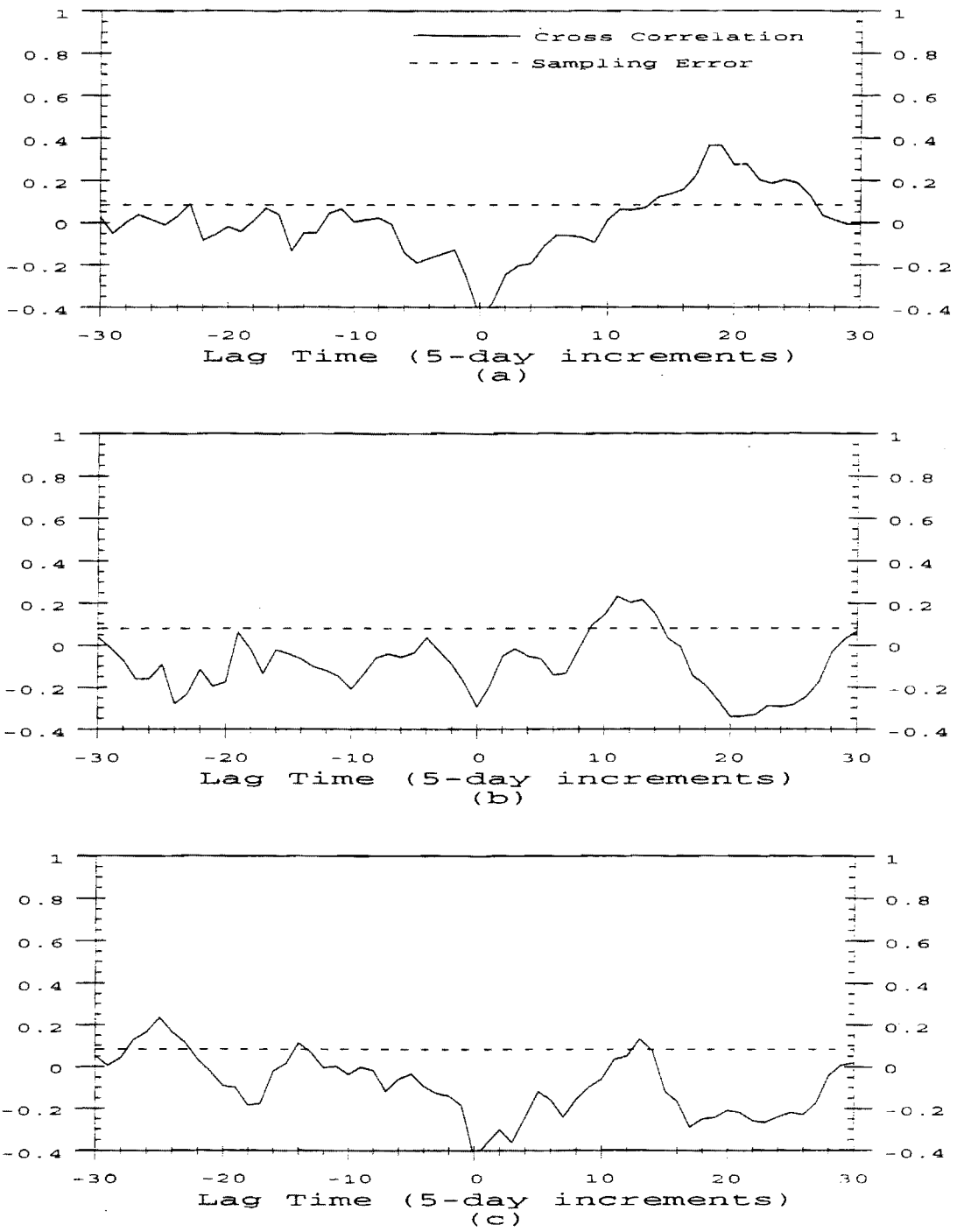

Figure A.12 Cross-correlation of maximum temperature and upper zone soil water content in June for a) 1925-1949, b) 1949-1974 and c)1965-1988. 5-day data.

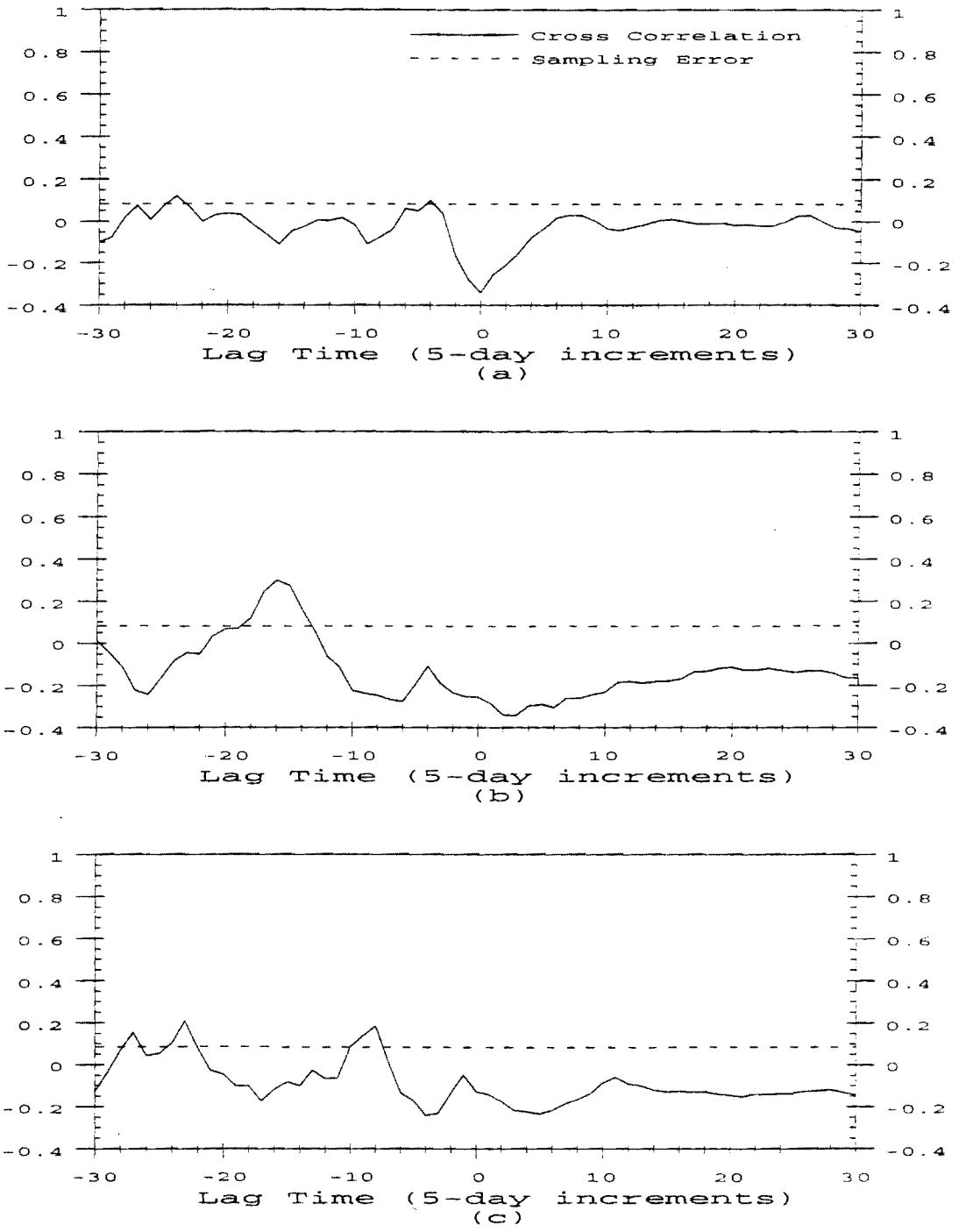

Figure A.13 Cross-correlation of maximum temperature and upper zone soil water content in September for a) 1925-1949, b) 1949-1974 and c)1965-1988. 5-day data.